PHYSICAL CHEMISTRY 2022

16th International Conference
on Fundamental and Applied Aspects of
Physical Chemistry

Proceedings
Volume II

September 26-30, 2022
Belgrade, Serbia

Title: PHYSICAL CHEMISTRY 2022, 16th International Conference on Fundamental and Applied Aspects of Physical Chemistry (Proceedings) **ISBN** 978-86-82475-41-5
Volume II: ISBN 978-53-82475-43-9
Editors: Željko Čupić and Slobodan Anić
Published by: Society of Physical Chemists of Serbia, Studentski Trg 12-16, 11158, Belgrade, Serbia
Publisher: Society of Physical Chemists of Serbia
For Publisher: S. Anić, President of Society of Physical Chemists of Serbia
Printed by: ″Jovan″, <Printing and Publishing Company, Ilije Đuričića 19, Belgrade, 200 Copies
Number of pages: 6+320, Format A4, printing finished in December 2022

Text and Layout: ″Jovan″

200 - *Copy printing*

CONTENT

PHYSICAL CHEMISTRY 2022

16th International Conference on Fundamental and Applied Aspects of Physical Chemistry

Organized by

The Society of Physical Chemists of Serbia

in co-operation with

Institute of Catalysis Bulgarian Academy of Sciences

and

Boreskov Institute of Catalysis Siberian Branch of Russian Academy of Sciences

and

University of Belgrade, Serbia:

Faculty of Physical Chemistry
Institute of Chemistry, Technology and Metallurgy
Vinča Institute of Nuclear Sciences
Faculty of Pharmacy

and

Institute of General and Physical Chemistry, Belgrade, Serbia

International Organizing Committee

Chairman: S. Anić (Serbia)
Vice-chairman: M. Gabrovska (Bulgaria)
A. A. Vedyagin (Russia)
S. N. Blagojević (Serbia)
Members: N. Cvjetićanin (Serbia), S. M. Blagojević (Serbia), M. Daković (Serbia), J. Dimitrić-Marković (Serbia), T. Grozdić (Serbia), Lj. Ignjatović (Serbia), A. Ivanović-Šašić (Serbia), D. Jovanović (Serbia), N. Jović-Jovičić (Serbia), M. Kuzmanović (Serbia), S. Maćešić (Serbia), D. Marković (Serbia), B. Milosavljević (USA), M. Mojović (Serbia), N. Pejić (Serbia), M. Petković (Serbia), A. Popović Bijelić (Serbia), B. Simonović (Serbia), B. Šljukić (Serbia), G. Tasić (Serbia), S. Veličković (Serbia), N. Vukelić (Serbia),

International Scientific Committee

Chairman: Ž. Čupić (Serbia)
Vice-chairman: V. Bukhtiyarov (Russia)
S. Todorova (Bulgaria)
B. Adnađević (Serbia)
Members: S. Anić (Serbia), A. Antić-Jovanović (Serbia), A. Azizoğlu (Turky), R. Cervellati (Italy), A. Clayton (Australia), A. Cristina Silva (Portugal) G. Ćirić-Marjanović (Serbia), V. Dondur (Serbia), R. Faria (Brasil), M. Fronczak (Poland), I. Grinvald (Russia), P. Humpolíček (Czech), M. Jeremić (Serbia), I. Kiss (USA), E. Kiš (Serbia), A.V. Knyazev (Russia), Lj. Kolar-Anić (Serbia), T. Kowalska (Poland), G. Kyzas (Greece), G. Lente (Hungary), Z. Marković (Serbia), S. Mentus (Serbia), K. Novaković (UK), N. Ostrovski (Serbia), V. Parmon (Russia), J. Pérez-Mercader (USA) Z. Petkova Cherkezova-Zheleva (Bulgary), M. Plavšić (Serbia), J. Savović (Serbia), G. Schmitz (Belgium), I. Schreiber (Czech), L. Schreiberova (Czech), D. Stanisavljev (Serbia), N. Stepanov (Russia), Zs. Szakacs (Romania), Z. Šaponjić (Serbia), Á. Tóth (Hungary), M. Trtica (Serbia), H. Varela (Brasil), V. Vasić (Serbia), Nadezda Vasilyeva (Russia), D. Veselinović (Serbia), V. Vukojević (Sweden), A. De Wit (Belgium)

Local Executive Committee

Chairman: S. N. Blagojević
Vice-chairman: A. Ivanović-Šašić
Members: M. Ajduković, I. N. Bubanja, D. Dimić, J. Dostanić, D. Drakulić, S. Jovanović, Z. Jovanović, D. Lončarević, J. Krstić, B. Marković, J. Maksimović, S. Marinović, D. Milenković, T. Mudrinić, M. Pagnacco, N. Potkonjak, B. Stanković, I. Stefanović, A. Todorović, M. Vasić, F. Veljković, M. Pejčić, G. Stevanović, H.Šalipur.K. Milošević, S. Pavlović, V. Kostić, B. Milovanović.

SPONSORS

Ministry of Education, Science and Technological Development of the Republic Serbia

Institute of General and Physical Chemistry, Belgrade

University of Belgrade, Institute of Chemistry, Technology and Metallurgy, National Institute of Republic of Serbia, Belgrade

University of Belgrade, Faculty of Physical Chemistry, Belgrade

H *– Material Science*

EFFECT OF VARIOUS RADIOPACIFIERS ON SELECTED PHYSICAL PROPERTIES AND CYTOTOXICITY OF CALCIUM SILICATE BASED DENTAL CEMENT ENRICHED WITH HYDROXYAPATITE

D. Ćetković[1], A. Dožić[1], A. Despotović[2], K. Janjetović[2], N. Zogović, and Dj. Antonijević[1]

[1] Department of Anatomy, School of Dental Medicine, University of Belgrade, Serbia
[2] Department of Neurophysiology, Institute for Biological Research "Siniša Stanković" – National Institute of the Republic of Serbia, University of Belgrade, Serbia

ABSTRACT

This study aimed to investigate the influence of ZrO_2, Bi_2O_3 and SrF_2 added as radiopacifying agents (30wt.%) into calcium silicate/hydroxyapatite-based dental cement on its physical and biological properties. Among investigated cements, the mixture containing Bi_2O_3 had the highest values of elastic modules and toughness, similarly to control – mineral trioxide aggregate (MTA). SEM analysis of all hydrated cements has shown that bioactive calcite and tobermorite phases were formed. Crystal violet assay showed that pure (undiluted) extracts of experimental cements did not affect cell viability, while MTA exhibited an extremely cytotoxic effect on L929 cells. In 1:4 dilutions all experimental mixtures significantly increased cell proliferation potential after 72h in comparison to untreated cells and MTA, which cytotoxic effect diminished with dilutions. Further studies are needed to determine which radiopacifyer has the most desirable properties for adequate dental cement fabrication.

INTRODUCTION

Bioactive dental cements present a huge advantage in clinical practice since their interaction with host cells may provoke tertiary dentinogenesis [1]. The invention of calcium silicate-based dental materials revolutionized the treatment of pulp capping, apexification/apexogenesis, root canal perforations repair, and root end canal filling surgical procedures [2]. For instance, when used for direct pulp capping, the successful healing rate increased from ~35 % to more than 95 % [3]. Therefore, the research community has been putting significant effort to synthesize various calcium silicate-based dental cements intended for different applications. When formulating dental calcium silicate-based cement, it is imperative to add a radiopacifying component into its composition to allow its visibility on radiographs [2]. The addition of radiopacifiers to dental cements should increase their radio-visibility, but also maintain or even improve their mechanical characteristics. In our previous studies, we have enriched calcium silicate cements with nano-containing hydroxyapatite (CSC-nanoHAP), a known constituent of human bone/tooth [4]. Hydroxyapatite may be a useful compound of dental cement due to its similarity with bone tissue, but on the other side it is known as a brittle material and therefore the physical properties of resulting mixtures may be hampered [5]. Indeed, in some studies, it was shown that hydroxyapatite increases the solubility of calcium silicate/hydroxyapatite mixture [6]. We have evaluated the compressive strength of such a mixture enriched with zirconium oxide (ZrO_2), bismuth dioxide (Bi_2O_3), and strontium fluoride (SrF_2) as radiopacyfing agents [4]. This study went one step further aiming to evaluate elastic modules and the toughness of those formulations. In addition, we investigated the morphology of cement surface and their cytocompatibility.

METHODS

Material synthesis - CSC-nanoHAP was used as a basis for mixing with ZrO_2, Bi_2O_3 and SrF_2. Detailed procedure for CSC and nanoHAP synthesis is given elsewhere [4,5].

Elastic modules and toughness determination – The elastic modules and the toughness of experimental cement specimens (2 cm in length, 4 mm in depth and 4 mm wide) were determined in accordance to International Standard Organization (ISO) 6876 using the universal testing machine (Instron, Norwood, USA, loading rate 50 N/min). For the calculation of elastics modulus, the slope of the tangent to the initial straight line portion of the load deflection curve was drawn and the modulus of elasticity was calculated using the following equation:

$$E = (L^3 \times m)/(4 \times b \times d^3)$$

where E = modulus of elasticity in bending (Nm^{-2}), L = the length of the specimen (m), m = the slope of the initial straight-line portion of the load deflection curve (Nm^{-1} of deflection), b = the width of specimen (m) and d = the depth of the specimen (m).

The toughness was calculated by using area underneath the stress–strain (σ–ε) curve:

U_T = Area underneath the stress–strain (σ–ε) curve = σ × ε.

Scanning electron microscopy (SEM) analysis – Specimens measuring 5 mm in diameter and 1 mm in height were immersed in phosphate buffer saline (PBS) and placed in an incubator at 37°C in a humidified atmosphere with 5 % CO_2 for 14 days. Afterward, the specimens were dried, gold coated, and visualized under scanning electron microscopy (TESCAN, Mira3, XMU USA Inc.).

Cell viability assay – In order to evaluate a dose- and time-dependent response to potentially toxic soluble substances from investigated materials, cell viability was carried out in accordance with the ISO Standard 10993-5/2005 [7]. All materials were manipulated under sterile conditions. Mouse fibroblast L929 cell line (European Collection of Animal Cell Cultures, Salisbury, UK) was cultivated in complete medium, maintained at 37°C in a humidified atmosphere with 5 % CO_2, prepared for experiments using the conventional trypsinization procedure and seeded in 96-well flat-bottom plates (5×10^3 cells/well). Cells were treated 24 h post-seeding with pure extracts of investigated materials (1) and its serial dilutions (1:2 and 1:4 (v:v)), prepared exactly as previously described [4]. Crystal violet (CV) test, based on the inability of dead cells to remain adherent, was assessed after 24, 48 and 72 h treatment. After treatment, the adherent, viable cells were fixed with methanol and stained with 10 % CV solution for 15 min at room temperature. CV dye was dissolved in 33 % acetic acid after rigorous washing with water. The absorbance of dissolved CV dye, corresponding to the number of adherent (viable) cells was measured in an automated microplate reader at 570 nm (Sunrise; Tecan, Dorset, UK). The results were presented as a fold increase in the number of viable cells. The experiments were performed in triplicates.

RESULTS AND DISCUSSION

CSC+HAP+ZrO_2 and CSC+HAP+SrF_2 mixtures showed significantly lower values of elastic modules (260±70 MPa and 190±40 MPa, respectively) than CSC+HAP+Bi_2O_3 (420±80 MPa) and control material – MTA (1290±90 MPa) ($p<0.05$, ANOVA and post+hoc Tukey test). Toughness analysis showed that CSC+HAP+Bi_2O_3 (0.32±0.05 J) was not significantly different than commercially available MTA (0.38±0.05 J) ($p>0.05$), while CSC+HAP+ZrO_2 (0.15±0.06 J) and CSC+HAP+SrF_2 (0.08±0.01 J) had statistically lower toughness values ($p<0.05$, ANOVA and post-hoc Tukey test). Taking into account the obtained physical data it seems that Bi_2O_3 is radiopacyfier of choice to formulate adequate dental material (**Figure 1A**).

SEM analysis of the investigated cements confirmed their bioactivity after soaking in PBS. All the investigated cements exposed the polygonal structures on surfaces, indicating deformation of

tobermoritte phase (calcium silicate hydrate-CSH) (**Figure 1B**). These results showed that hydroxyapatite addition to calcium silicate-based cement does not alter their capability to form biologically active crystals on the surfaces. The purpose of these crystals is to form a thin layer of hydroxyapatite in contact with dental tissue which in turn stimulates odontoblasts for dentinogenesis [1]. However, we believe that the experimental cements may be even more biologically active due to already incorporated hydroxyapatite. This assumption should be confirmed in further biological studies.

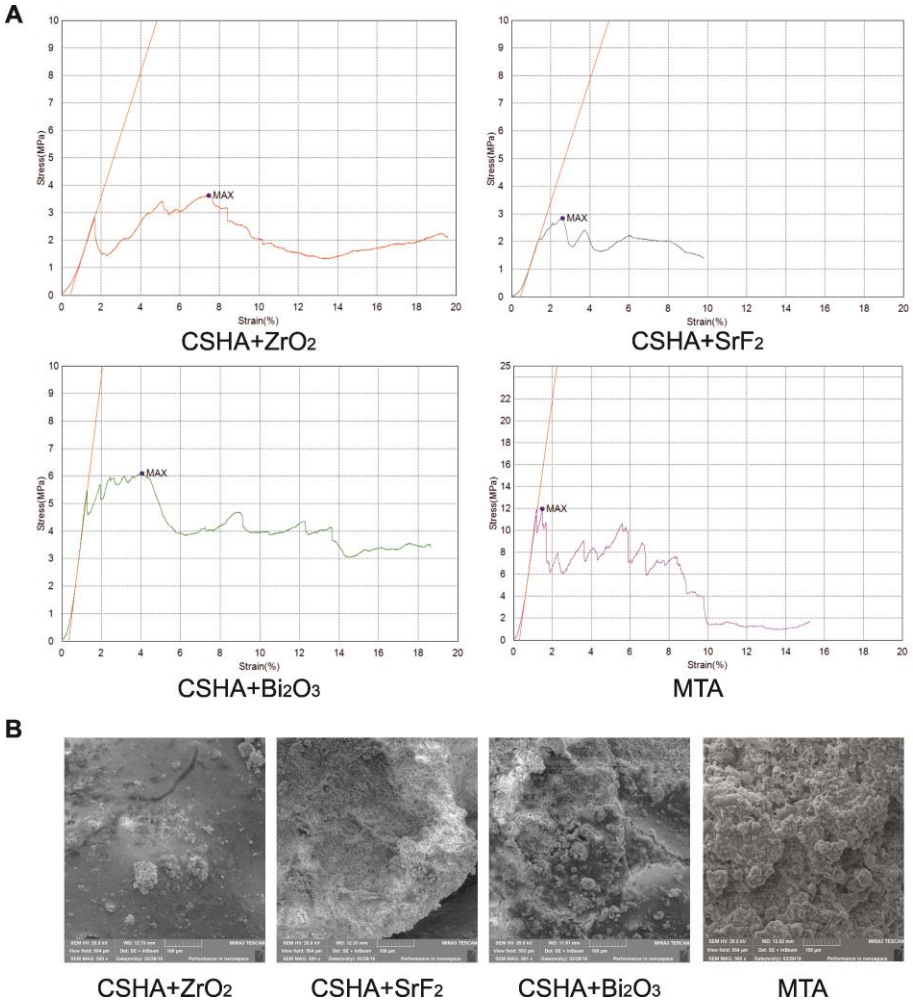

Figure 1. A) Elastic modules and toughness of cements - representative slopes of stress *versus* strain. B) SEM micrographs of the cements surface after soaking in PBS (magnification 500×).

Extracts of experimental cements had no effect on the cell viability after 24 h incubation, while pure extract of MTA exhibited extremely cytotoxic effect on L929 cells, at all time points, which diminished with dilutions. Longer incubation (48 h, 72 h) with ECHA+ZrO_2 and ECHA+Bi_2O_3 extracts (1 and 1:2) decreased cell proliferation rate, but 1:4 dilutions of all experimental cement increased cell proliferation compared to MTA and untreated cells, after 72 h treatment (**Figure 2**).

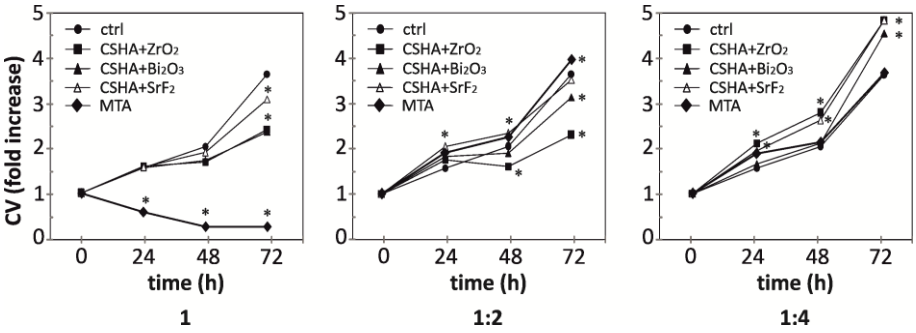

Figure 2. Cell viability (fold increase) evaluated by the crystal violet (CV) assay after 24 h, 48 h, and 72 h exposure of L929 cells to the cements' eluents - pure extract (1) and serial dilutions (1:2 and 1:4 (v:v)). The data are mean of triplicates from a representative of three independent experiments. * $p<0.05$ compared to control, untreated cells (ctrl).

CONCLUSION

Calcium silicate dental cement enriched with hydroxyapatite may be promising material in dentistry. This study has shown that, among investigated radiopacyfing agents, Bi_2O_3 may be considered as a radiopacyfier of choice due to superior physical properties (elastic modulus and toughness) when compared with ZrO_2 and SrF_2. On the other hand, when biocompatibility is taken as selection criteria, SrF_2 may be considered the most promising radiopacifying agent. Further studies should be conducted to examine other physicochemical and biological properties of manufactured cement mixtures to determine which radiopacifyer presents the most desirable properties for adequate dental cement fabrication.

Acknowledgment

This work was supported by the Ministry of Education, Science and Technological Development of the Republic of Serbia (Grant No. 451-03-68/2022-14/200007 and 451-03-68/2022-14/ 200129) and through a bilateral PPP grant provided jointly by the Ministry of Education, Science and Technological Development of the Republic of Serbia and Ministry of Science and Technology of The Peoples Republic of China (Grant No. 451-02-818/2021-09/20).

REFERENCES

[1] D. V. Ilic, D. Antonijevic, V. Biocanin, B. Colovic, V. Danilovic, and V. S. Komlev., Hem. Ind. 73 (2019) 281–294.
[2] M. Torabinejad, T.F. Watson, T.R.P. Ford, J. Endod. 19 (1993) 591–595.
[3] M. Parirokh, M. Torabinejad, J. Endod. 36 (2010) 16–27.
[4] D. Antonijevic, A. Despotovic, V. Biocanin, M. Milosevic, D. Trisic, V. Lazovic, N. Zogovic, J. Milasin, and D.V. Ilic, Ceramics International 47 (2021) 28913–923.
[5] B. Colovic, O. Jankovic, S. Zivkovic, Z. Zizak, I.B. Zizak, and V. Jokanovic, Cer. Int. 45 (2019) 9211–18.
[6] R. Bosso-Martelo, J.M. Guerreiro-Tanomaru, R. Viapiana, F.L. Berbert, M. A. Duarte, M. Tanomaru-Filho, Clin. Oral Invest. 20 (2016) 83–90.
[7] International Organization for Standardization ISO 10993-5. International Organization for Standardization, Geneva, Switzerland, 2009.

SURFACE MORPHOLOGY, COMPRESSIVE STRENGTH AND BIOCOMPATIBILITY OF CALCIUM ALUMINATE DENTAL CEMENT

A. Dožić[1], D. Ćetković[1], A. Despotović[2], K. Janjetović[2], N. Zogović[2] and Dj. Antonijević[1]

[1] *Department of Anatomy, School of Dental Medicine, University of Belgrade, Serbia (djordje.antonijevic@stomf.bg.ac.rs)*

[2] *Department of Neurophysiology, Institute for Biological Research "Siniša Stanković" – National Institute of the Republic of Serbia, University of Belgrade, Serbia*

ABSTRACT

The aim of this study was to investigate the properties of experimental calcium aluminate (CA) dental cement, synthesized from $CaO \times Al_2O_3$ and $CaCO_3$. Calcium silicate (Portland cement, PC) served as a control. The elastic modulus and maximum stress obtained using the universal testing machine showed that CA has greater mechanical resistance than the control PC. Scanning electron microscopy (SEM) analysis of cements specimens before and after soaking in phosphate buffer saline showed that hydrated cements exposed crystal particles of calcite and new aluminum containing phases on their surfaces, suggesting their bioactive potential. Biocompatibility of the CA dental cement was evaluated by observing L929 cells morphology using phase-contrast microscopy. Cells treated with CA extract preserved their structural integrity without any changes in cell morphology, but with a slightly inhibited proliferation rate after 24h treatment, while PC induced changes typical for cell death.

INTRODUCTION

Dental materials engineering has gone through several phases of innovations following new demands that had been placed in front of the research community. In this sense, the concept of manufacturing biologically inert materials has been nowadays replaced with the idea to fabricate bioactive materials. In other words, instead of manufacturing the material that is inert in contact with the surrounding human tissues (i.e. titanium), current trends go in line with formulating the materials capable to provoke a positive response from the host tissue [1]. In the field of dentistry, the revolution occurred when a mineral trioxide aggregate (MTA) was introduced in the nineties at Loma Linda University. MTA is calcium silicate-based dental cement that was intended as a substitute for ~50 years gold standard – calcium hydroxide. Namely, although both materials are capable to release calcium ions and consequently neutralize acidic cariogenic environment, the effect of calcium silicates is measured in the terms of months and years in comparison to ~10 days of calcium hydroxide puferizing capacity [2]. Many calcium silicate-based formulations have been introduced and commercialized such as MTA Angelus (Angelus science and technology, Londrina, Brazil), ProRoot MTA (Dentsply, Tulsa, Oklahoma, USA), MTA Flow (Ultradent, Utah, USA), Bioaggregate (Innovative BioCeramix, Burnaby, Canada), Theracal LCR (Bisco Dental, Illionois, USA), iRoot (IBCeramix, Vancouver, Canada), Endo CPM (Egeo, Buenos Aires, Argentina), Biodentine (Septodent, Saint Maur, France) etc. [1].

Another advantage of calcium silicate cement over calcium hydroxide one is its superior physical properties, i.e. compressive stress of >20 MPa [3,4]. Therefore, recent efforts are directed toward using calcium aluminate-based cements (CA) since they have superior physical properties [5,6]. However, it is not known if the aluminum incorporation can influence cement's biological behavior as well as if the interaction with biological fluids can result in the formation of the apatite-like crystals on its surface. Thus, the aim of this study was to investigate the morphological features on

the surface of hydrated CA cements, cements elastic modulus and maximum stress and their effect on the morphology of L929 cells.

METHODS

Synthesis of experimental calcium aluminate cement - Experimental cement was synthesized from CAC ($CaO \times Al_2O_3$) and calcite ($CaCO_3$) using the protocol described in detail elsewhere [5]. In brief, for the synthesis of CAC, pseudo boehmite sol (AlOOH) was used. Aluminum tri-sec-butoxide was dissolved in a mixture ethanol/water (1:4), wherein a molar ratio of aluminum trisec-butoxide in a mixture ethanol-water was 1:50. This mixture was then heated at 85°C under vigorous stirring. After 2 h of heating, the solution was cooled to room temperature and the sulfuric acid was added dropwise to reach the molar ratio H_2SO_4/aluminum tri-sec-butoxide of 0.04. Calcium chloride tetrahydrate ($CaCl_2x4H_2O$) (Sigma-Aldrich, St. Louis, MO) was used as the precursor for the production of $CaCO_3$. Briefly, the amount of 5 mmol of $CaCl_2x4H_2O$ was dissolved in 50 ml of ethylene glycol (Sigma-Aldrich) and sonicated at 40°C (Elmasonic S_3OH). Afterward, 10 mmol of sodium bicarbonate ($NaHCO_3$) (Sigma-Aldrich), dispersed in 50 ml of ethylene glycol, was added dropwise for 30 min, upon mechanical stirring. Pure calcium silicate – Portland cement (PC, Italcementi, Bergamo, Italy) served as a control material.

Determination of elastic modulus and maximum stress - The elastic modulus and maximum stress were determined in accordance with International Standard Organization (ISO) 6876 by dividing the breaking load (unit: Newton) of every specimen measuring 8 mm in diameter and 1 cm in height on a universal testing machine (Instron 1332, Norwood, USA, loading rate 50 N/min) by the cross-sectional area (Newton per square millimeter). Five specimens per group were tested.

Scanning electron microscopy (SEM) analysis of cements surface morphology - Specimens measuring 5 mm in diameter and 1 mm in height were immersed in phosphate buffer saline (PBS) and placed in an incubator at 37°C for 14 days. Afterward, the specimens were dried, gold coated, and visualized under scanning electron microscopy (JEOL JSM-7500).

Cell culture and treatment - For *in vitro* analysis cements were manipulated under sterile conditions. After mixing, CA and PC cements were placed into pre-sterilized PTFE moulds (5 mm in diameter and 3 mm thick) to set for 24 h in a humidified atmosphere. Specimens were sterilized by ultraviolet irradiation for 2 h and thereafter immersed in 1 ml complete medium Dulbecco's modified Eagle medium (DMEM; Gibco, Thermo Fisher Scientific, Inc., Waltham, MA, USA) supplemented with 5 % fetal bovine serum (FBS), 2 mM L-glutamine and penicillin/streptomycin (all from Capricorn Scientific, Ebsdorfergrund, Germany). After 24 h incubation at 37^{o}C discs were discarded and the supernatants (extracts) were collected for cell treatment.

The mouse fibroblast L929 cell line (European Collection of Animal Cell Cultures, Salisbury, UK) was cultivated in a complete medium and maintained at 37°C, in a humidified atmosphere with 5 % CO_2. Cells were prepared for experiments using the conventional trypsinization procedure with trypsin/EDTA and seeded in 96-well flat-bottom plates (5×10^3 cells/well) for the cell morphology assessment. Cells were treated 24 h post-seeding with pure cements' extracts. Morphological changes were evaluated after 24 h of treatment by phase-contrast light microscope Leica DCF320 (Leica Microsystems DMIL, Wetzlar, Germany). Phase-contrast light microscopy images were taken at 3 random positions within each well at 200× magnification with Leica Microsystems DFC320 camera and Leica Application Suite software (version 2.8.1).

RESULTS AND DISCUSSION

The maximum stress calculated in strain/stress diagram of the experimental CA cement (36±4 MPa) was superior in comparison to that in the PC (12±3 MPa). Elastic modulus of CA cement was 2400±100 MPa, while elastic modulus of PC was 1300±100 MPa. The force to displacement curves

showing maximum loading force are presented in Figure 1. As expected, CA cement showed 3 times greater mechanical resistance than PC and therefore it may be used in clinical applications when the material is subjected to high mechanical stress such as in indirect restorations or when it is used as a direct pulp capping material. In addition, MTA is often used to heal huge bifurcation lesions [2,6]. In this case, the material also suffers great vertical stress which may lead to its fracture and spreading of the infection. It may be assumed that mechanically superior CA cement may be more suitable in this clinical situation.

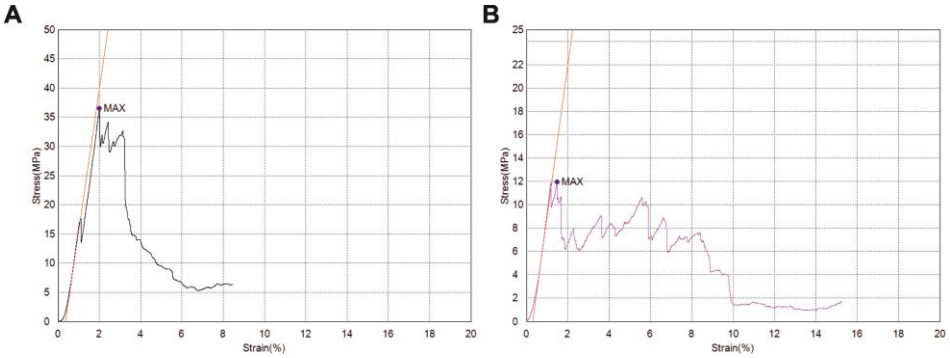

Figure 1. Representative diagram illustrating the amount of force required to fracture A) calcium aluminate and B) Portland cement specimens.

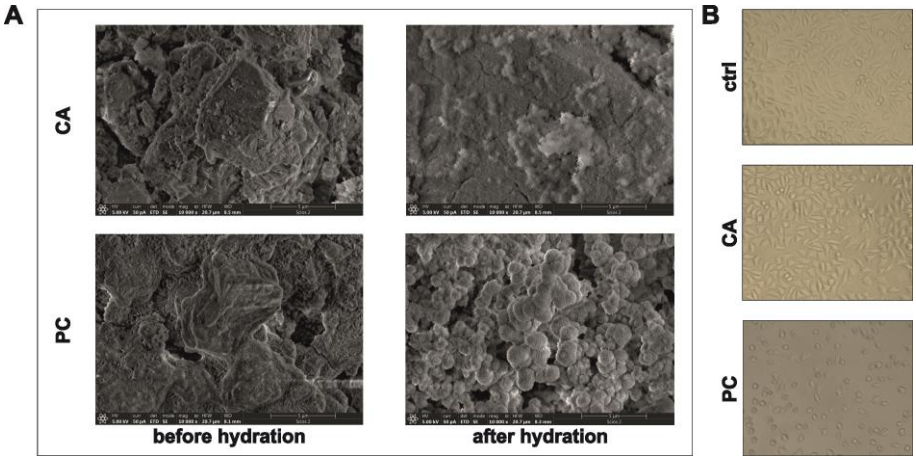

Figure 2. SEM images of cement surfaces and light microscopy images of L929 cells treated with cement extracts. (A) Morphological features of surfaces of calcium aluminate (CA) cement and Portland cement (PC) specimens before and after hydration in PBS. Scanning electron microscopy, magnification 10000×. (B) Effects of CA and PC pure extracts on the morphology of mouse fibrosarcoma cell line L929 in comparison to untreated, control cells (ctrl). Phase-contrast light microscopy (magnification 200×). The data are presented as pictures from one representative of three independent experiments.

The SEM analysis of CA cement showed that, before hydration, the polygonal crystals of calcite measuring 20 μm – 100 μm are observed. In hydrated cement, it can be noticed that morphology has turned mostly into needle-like crystals presumably indicating the formation of new aluminum containing phases (C_3AH_6 and aluminum hydroxide). In PC, the bioactivity of the material is clearly confirmed by changing the shape of the crystals from polygonal (unhydrated) one to globular one after hydration (**Figure 2A**). Similar behavior to PC is reported in the literature for Biodentine [7].

Light microscopy images of L929 cells treated with CA pure extract showed preserved structural integrity and cell morphology after 24h, but with slightly reduced proliferation. Contrary, PC triggered morphological changes typical for cell death – cell shrinkage and rounding and detachment of cells from the bottom well (**Figure 2B**). It may be the consequence of "non-purity" of the PC, because the employed PC was not calcium silicate cement synthesized in the laboratory, but commercially available material of the natural origin that may include in traces elements such as cobalt, mangane and iron [8].

CONCLUSION

Bearing in mind the results presented, CA dental cements have significant potential to become a suitable alternative to calcium silicate cements in dentistry. They showed the surface morphology capable to trigger cell spreading and proliferation. The pure extract of CA cement seems to be non-cytotoxic in L929 cell culture, conversely to PC which induces morphological changes typical for cell death. Superior elastic modulus and maximum stress of CA cements may present a huge advantage in some clinical situations. Further studies are needed to investigate in detail the full potential of CA cements in dentistry.

Acknowledgment

This work was supported by the Ministry of Education, Science and Technological Development of the Republic of Serbia (Grant No. 451-03-68/2022-14/200007 and 451-03-68/2022-14/ 200129) and through a bilateral PPP grant provided jointly by the Ministry of Education, Science and Technological Development of the Republic of Serbia and Ministry of Science and Technology of The Peoples Republic of China (Grant No. 451-02-818/2021-09/20).

REFERENCES

[1] D. V. Ili, D. Antonijevic, V. Biocanin, B. Colovic, V. Danilovic, V. S. Komlev, A. Y. Teterina, and V. Jokanovic, Hem. Ind. 73 (2019) 281–294.
[2] M. Parirokh, M. Torabinejad, J. Endod. 36 (2010) 16–27.
[3] D. Antonijevic, A. Despotovic, V. Biocanin, M. Milosevic, D. Trisic, V. Lazovic, N. Zogovic, J. Milasin, and D.V. Ilic, Ceramics International 47 (2021) 28913–923.
[4] D. Antonijevic, I. Medigovic, M. Zrilic, B. Jokic, Z. Vukovic, and L. Todorovic, Clin. Oral. Invest. 18 (2014) 1597-604.
[5] B. Colovic, O. Jankovic, S. Zivkovic, Z. Zizak, I.B. Zizak, and V. Jokanovic, Cer. Int. 45 (2019) 9211–18.
[6] C. Primus, L.J. Gutmann, R.F. Tay, and B.A. Fuks, J. Am. Cer. Soc. 105 (2022)1841-63.
[7] D. Antonijević, P. Milovanović, C. Riedel, M. Hahn, M. Amling, B. Busse, and M. Djurić, Bio. Micr. 18 (2016) 25.
[8] T. Dammaschke, H.U. Gerth, H. Züchner, E. Schäfer, Dent. Mater. 21 (2005) 731-8.

THE MODIFICATION OF SURFACE CHEMISTRY OF GO AND GO/WPA NANOCOMPOSITES FOR DECOLORIZATION OF METHYLENE BLUE

M. Pejčić[1], Ž. Mravik[1], D. Bajuk-Bogdanović[2], S. Uskoković-Marković[3], B. Nedić Vasiljević[2], S. Jovanović[1] and Z. Jovanović[1]

[1]*Laboratory of Physics, Vinča Institute of Nuclear Sciences – National Institute of the Republic of Serbia, University of Belgrade, P.O. Box 522, 11001, Belgrade, Serbia*
[2]*Faculty of Physical Chemistry, University of Belgrade, P.O. Box 47, 11158, Belgrade, Serbia*
[3]*Faculty of Pharmacy, University of Belgrade, 11000, Belgrade, Serbia*

ABSTRACT

In this study, we investigated the interaction between 12-tungstophosphoric acid (WPA) and graphene oxide (GO) in their nanocomposite based on changes in surface chemistry and adsorption capacity of methylene blue. The methods used in this study enabled better understanding of the type and amount of oxygen surface groups present on GO surface and their behavior once in contact with WPA. Two methods of functional group modification were selected: chemical titration (NaOH, Na_2CO_3, $NaHCO_3$) and thermal treatment (T=450 ^oC, in Ar), while adsorption capacity of methylene-blue was used as an indicator for monitoring the changes of surface chemistry. Titrations showed presence of functional groups of different acidity on pristine GO and that WPA strongly influences this parameter. Color adsorption has shown that functional groups of GO have a positive effect, since their removal reduces the adsorption capacity of the material. In the case of nanocomposite, the presence of WPA is beneficial since adsorption capacity is improved compared to the starting GO. Also, it can be concluded that titration improves the adsorption capacity, while thermal treatment completely blocks the adsorption properties of the composite.

INTRODUCTION

Some carbon materials have a large specific surface area and good conductivity, which are one of requirements for their wider application in energy storage. With isolation of graphene - a stable layer sp^2 hybridized carbon atoms - a new field of research has opened up for carbon nanomaterials with exceptional characteristics. In the case of graphene, all of its atoms are surface atoms which especially emphasizes the importance of its surface chemistry (1). Graphene oxide (GO) is obtained by the oxidation of graphene layers with strong oxidizing agent. GO has a large specific surface area and electrical conductivity that can be optimized, so as such it is used for electrochemical energy storage in supercapacitors, batteries, etc. Surface chemistry plays an important role in the application of GO, which are often the first to interact with the various agents used for functionalization of this material (2). 12-tungstophosphoric acid ($H_3PW_{12}O_{40}$, WPA) belongs to the group of heteropolyacids (HPA) with Keggin structure. These compounds possess exceptional catalytic and redox properties, but also low specific surface area and good solubility in water. Consequently, in many practical applications, their use in composites is resorted to the ones counterparts that have the role of substrate. GO and HPA nanocomposites show significant improvements of their properties as a consequence of interaction between components. The nature of this interaction has been studied in detail in composites in the solid state, however, insufficient is known about the nature of the interaction in suspensions. In our opinion, this is important since this represents the initial step in the preparation and application of nanocomposites. Finally, recent development of composite materials has enriched modern material systems, contributed to sustainable progress in science materials and engineering and improved human life (3).

METHODS

GO and WPA nanocomposites (5 to 50 wt.% of WPA, nominally) were prepared as follows: Initial suspension graphene oxide was ultrasonicated for 1 hour, after which GO suspension was diluted to 1 mg/ml and then a 10 mg/ml solution of WPA was added achieve a weight ratio of 5%, 10%, 15%, 20%, 35% and 50% relative to GO. The part of this suspension was prepared for titration and the other part was left in an oven at 80 °C until completely dry. Two methods of functional group modification were selected: chemical titration (NaOH, Na_2CO_3, $NaHCO_3$) and thermal treatment (T=450 ^oC, in Ar), adsorption of methylene-blue (MB) was used for monitoring the changes of surface chemistry.

RESULTS AND DISCUSSION

As a first step the surface chemistry of GO was investigated which allowed us to monitor changes in GO and GO/WPA composites that occurred during titrations with different titrants and thermal treatment. NaOH, Na_2CO_3 and $NaHCO_3$ were used as titrants where each of them is neutralizing different surface functional groups: NaOH neutralizes all three functional groups –COOR, Ar-OH and –COOH, the Na_2CO_3 neutralizes the –COOR and –COOH groups, while the $NaHCO_3$ neutralizes only the -COOH group (4), (5).

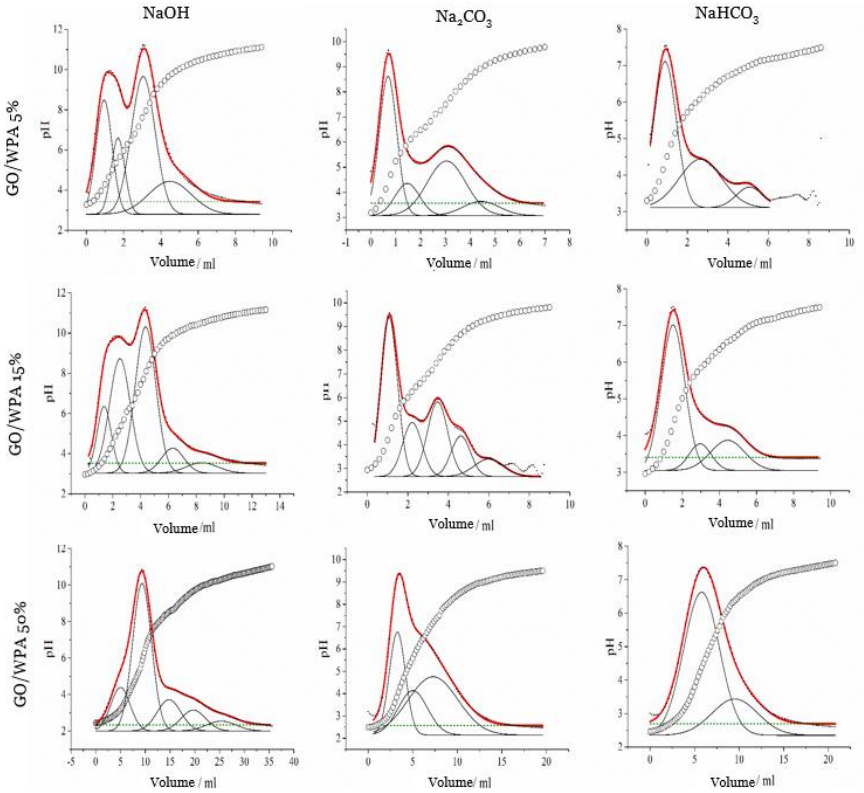

Figure 1. Titration curves (o) and their first derivative (red solid line) of GO/WPA 5%, GO/WPA 15% and GO/WPA 50% with NaOH, Na_2CO_3 and $NaHCO_3$. A deconvolution of the first derivative curve is also shown (black solid line).

When analyzing the titration curves of samples titrated with NaOH, two peaks appear in the first derivative of titration curve, which can be explained by the fact that functional groups of different acidity are present on the GO surface. It can be noticed that as the amount of WPA increases the peaks in derivative curve are becoming wider. This is especially the case for GO/WPA 50%

composite and NaOH titration. In our opinion this is a consequence of WPA influence on the ability of oxygen functional groups to transfer protons. This trend also occurs in samples titrated with Na_2CO_3 solution (Figure 1). Two peaks in derivative curve are visible in the case of NaOH and Na_2CO_3 which is expected results, since in the case of $NaHCO_3$ only carboxyl groups are neutralized.

The photo of GO and GO/WPA suspensions after adsorption of methylene blue is given in Figure 2. It can be seen that the samples that adsorb more methylene blue have a lighter color. Heat-treated samples show more intense blue (lower amounts of adsorbed methylene blue), while samples that are titrated show a lighter color (higher amounts of adsorbed methylene blue).

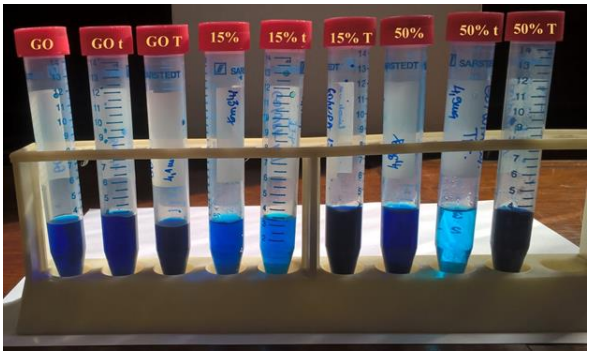

Figure 2. Appearance of samples after adsorption of methylene-blue

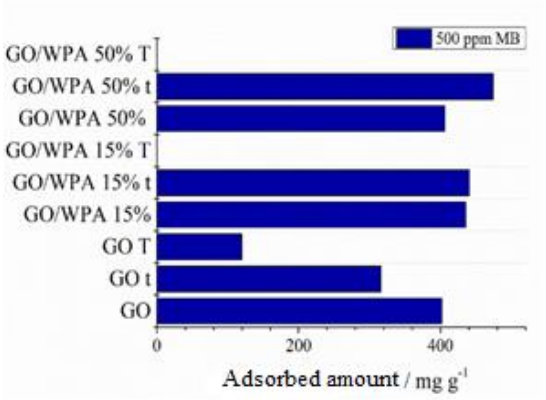

Figure 3. The amount of adsorbed MB. t – titrated (NaOH), T – thermally treated.

Based on the obtained results, a histogram was obtained, which gives a closer insight into the behavior of samples after different treatments (Figure 3). Noteworthy, thermally treated GO/WPA 15% and GO/WPA 50% do not adsorb methylene blue. On the other hand, the presence of WPA in composites plays a role since an increase in adsorption capacity is clearly seen as the amount of WPA in nanocomposite increases. This phenomenon may be associated with changes of surface chemistry of GO, but also structural properties of WPA.

CONCLUSION

The chemical titrations revealed that the presence of WPA affects the ability of surface oxygen groups to transfer protons, which is manifested by widening and merging of the peaks in first derivative of titration curve. This behavior was observed in the case of composites with a higher WPA content (50 wt.%), which had many similarities with the behavior of pure WPA. Hence, it can be concluded that at higher amount of WPA the behavior of nanocomposite is determined by WPA. Adsorption of methylene blue has shown that in the case of pure graphene oxide, oxygen groups have a positive effect, because their loss reduces the adsorption capacity of the material. In the case of composites, the presence of WPA is advantageous because the adsorption capacity is improved compared to the initial GO. Also, it can be concluded that titration improves, while thermal treatment completely blocks the adsorption capacity of nanocomposite. This is an interesting observation and requires more detailed experimental analysis in the future. The results of our study

provide a new insight into the nature of the interaction of GO and WPA and that the selected methods have significant potential to contribute in the future to a better understanding of the interaction of this system in aqueous suspensions.

Acknowledgment
The present study was funded by the Ministry of Science, Education and Technological Development of the Republic of Serbia.

REFERENCES

[1] Verma D, Goh KL. Chapter 11 - Functionalized Graphene-Based Nanocomposites for Energy Applications. In: Jawaid M, Bouhfid R, Kacem Qaiss Ae, editors. Functionalized Graphene Nanocomposites and their Derivatives: Elsevier; 2019. p. 219-43.
[2] Majumder P, Gangopadhyay R. Evolution of graphene oxide (GO)-based nanohybrid materials with diverse compositions: an overview. RSC Advances, 12(9) (2022) 5686-719.
[3] Jovanović Z, Mravik Ž, Bajuk-Bogdanović D, Jovanović S, Marković S, Vujković M, et al. Self-limiting interactions in 2D–0D systems: A case study of graphene oxide and 12-tungstophosphoric acid nanocomposite. Carbon, 156 (2020) 166-78.
[4] Schönherr J, Buchheim JR, Scholz P, Adelhelm P. Boehm titration revisited (part i): Practical aspects for achieving a high precision in quantifying oxygen-containing surface groups on carbon materials. Carbon 204(2) (2018) 21.
[5] Wu H, Lu W, Chen Y, Zhang P, Cheng X. Application of Boehm titration for the quantitative measurement of soot oxygen functional groups. Energy & Fuels, 34(6) (2020) 7363-72.

THE EFFECT OF DIFFERENT SOLVENTS IN THE SYNTHESIS OF WOOD-ALUMINUM SORBENTS. DYE SORPTION INVESTIGATION

N. Velinov, M. Radović Vučić, M. Kostić, M. Petrović, J. Mitrović, D. Bojić and A. Bojić

University of Niš, Faculty of Sciences and Mathematics, Department of Chemistry, Višegradska 33, 18000 Niš, Serbia. (nena.velinov@yahoo.com)

ABSTRACT

Sorbents synthetized by chemically modified wood by aluminum were tested for removal of textile dye Reactive Blue 19 dye. The influence of different solvents polarity and protic/aprotic nature, such as: acetone, ethanol, ether, hexane, and methanol, were analyzed and the best sorbent with the highest removal efficiency of dye was determined. The highest dye removal percentage (100%) and the shortest sorption time (less than 10 min) was achieved for the sorbent synthesized in less polar solvent - hexane. Also, the optimal sorption process conditions for dye removal using the best sorbent, such as: pH, sorbent dose and dye concentration, were examined. The optimal pH was 2.0 with 2.0 g dm^{-3} sorbent dose. Also, wood-aluminum sorbents possess other benefits, such as: mechanical stability, easy synthesis, biocompatibility, which all make it excellent ecologically and economically solution for water treatment of textile dyes.

INTRODUCTION

Dyes are important in many industries, such as: textile, personal care, foodstuff, drugs, and other pharmaco-products. The production and utilization of dyes achieved over 700,000 tones globally [1]. The relies of textile dyes into the water media can impede the growth of large number of water plants due to absorption of sunlight entering the water. Also, dyes can have negative affects the human liver, skin and present a weakly mutagenic effect [2]. So, the removal of dyes from water is very important and the different processes and technologies can be used for that purpose [3].

Among the numerous processes used for dyes removal, the sorption process is presented as highly effective and progressive treatment of wastewaters [1]. Sorbents obtained using eco-friendly natural lignocellulosic polymers, such as wood residue, has become one of the most adjustable and largely used materials due to their high availability, low cost, and the simplicity of synthesis [4]. The wood biowaste material has specific reactive centers – functional groups, such as: aliphatic and phenolic hydroxyl, methoxy, carbonyl groups, which can be used as a good base for chemical modification to produce highly efficient sorbents. The use of wood in the raw state has low removal efficiency of dyes, but chemical modification using inorganic oxides, such as Al_2O_3, can improve the dye sorption capacity of the wood [5]. Therefore, the main aim of this research was the synthesis of a low-cost sorbents from wood by chemical modification using $AlCl_3$ in five different solvents with differently polarity and aprotic/protic characteristics, such as acetone, ethanol, ether, hexane, and methanol. The removal efficiency of the sorbents was evaluated using Reactive blue 19 (RB19). The relationship between the used solvent in the synthesis of sorbent and the sorbent efficiency was discussed in detail and the principal operational sorption conditions, such as: pH, sorbent dose and RB19 concentration, were investigate.

METHODS

The activation agent - $AlCl_3$, organic solvents and RB19 were purchased from Sigma-Aldrich. HNO_3 and NaOH were reagent grade (Merck, Germany). All chemicals were used without further purification. All solutions were prepared with deionized water (18 MΩ). The wood residue was collected from furniture manufacture in Eastern Serbia. Firstly, the wood residue was fractionated by

size and washed with deionized water, then alkali-treated using NaOH for 60 min [5]. After that, 10 g of wood residue each were added into five solutions containing 2.0 g of anhydrous $AlCl_3$ in 100.0 cm^3 of five different solvents: acetone, ethanol, ether, hexane, and methanol and stirred for 30 min. The obtained materials were washed with deionized water, treated by trimethylamine, and dried at 55±1ºC for 5 h. The modification process of wood using $AlCl_3$ enabled the formation of new functional groups or active centers on the wood surface, which can bind the dye molecules and remove it from the solution. The characterization of the sorbent also confirmed the success of the modification using $AlCl_3$. The SEM show very similar porous morphology of the synthesized sorbents such as unmodified wood, but the EDS reveal that in addition to carbon and oxygen which wood contains, the synthesized sorbents also contain the aluminum. The FTIR shows that modification process brings significant change in the spectrum and the intensity of absorption bands of –O–H which appears in the wood spectrum decrease in the sorbent spectrum probably due to Al–OH bonding.

Working model solutions of dye were daily prepared by the appropriate dilution of the stock solutions (1.0 g dm^{-3}). The pH of the solutions was adjusted with 0.1/0.01 mol dm^{-3} $NaOH/HNO_3$ solutions pH-metrically (Orion Star A214, Thermo Fisher Scientific, USA). All experiments were performed at 25.0±0.2°C. The dye concentration was measured at 569 nm using UV-1800 spectrophotometer (Shimadzu, Japan).

The percent of the removed dye (*RE*, %) and amount of the sorbed dye per sorbent mass in the equilibrium (q_e, mg g^{-1}) were calculated using the equations:

$$RE = \frac{c_0 - c_t}{c_0} \cdot 100$$

$$q_e = \frac{(c_0 - c_t) \cdot V}{m}$$

where c_0 is the initial concentrations of the dye, c_t is the concentration of the dye in the solution after time t (mg dm^{-3}), V (dm^3) is the volume of the dye solution and m (g) is the mass of the sorbent. The sorption study was menage to analyze the effects of the pH (2.0–12.0), the sorbent dose (0.5–6.0 g dm^{-3}), and initial RB19 concentration (10.0–1000.0 mg dm^{-3}) on the dye sorption by synthesized sorbent. All experiments were performed in triplicate and ± SD (error bars) are presented in all graphs.

RESULTS AND DISCUSSION

The different solvents (acetone, ethanol, ether, hexane, and methanol) used in the synthesis of sorbents affect the RB19 removal (Figure 1 (1).). The highest dye removal efficiency (100%) was achieved for sorbent synthesized in hexane as a solvent. Sorbents synthesized in ether, acetone, ethanol, and methanol show weaker sorption performance with the removal efficiency 93.71, 71.66, 47.96 and 34.28% respectively. Also, the different nature of solvent affects the rate of sorption and the required time for reaching sorption equilibrium. Sorbent synthesized in hexane, exhibits the fastest sorption performance because it takes less than 10 min for complete dye removal. The complete RB19 removal is achieved after 30, 60, 90 and 120 min with sorbents synthesized in ether, acetone, ethanol, and methanol, respectively. This means that different properties of used solvents play a key role in the sorbent's synthesis. All solvents had different properties, such as: relative polarity and protic/aprotic nature, which have a different impact on anhydrous $AlCl_3$ and its complexation with wood. [6, 7]. The solvent with high values of relative polarity can generate hydrogen bonds and during hydrolysis part of anhydrous $AlCl_3$ may react with used solvent, so a smaller amount of aluminum reacts with the wood. For that reason, the sorbents synthesized in methanol and ethanol with highest relative polarity (0.762 and 0.654, respectively) has the lowest removal efficiency. On the other hand, the sorbent synthesized in hexane, a non-polar solvent with the lowest relative polarity value (0.009), where hydrolysis of the anhydrous $AlCl_3$ does not occur, has maximal dye removal efficiency.

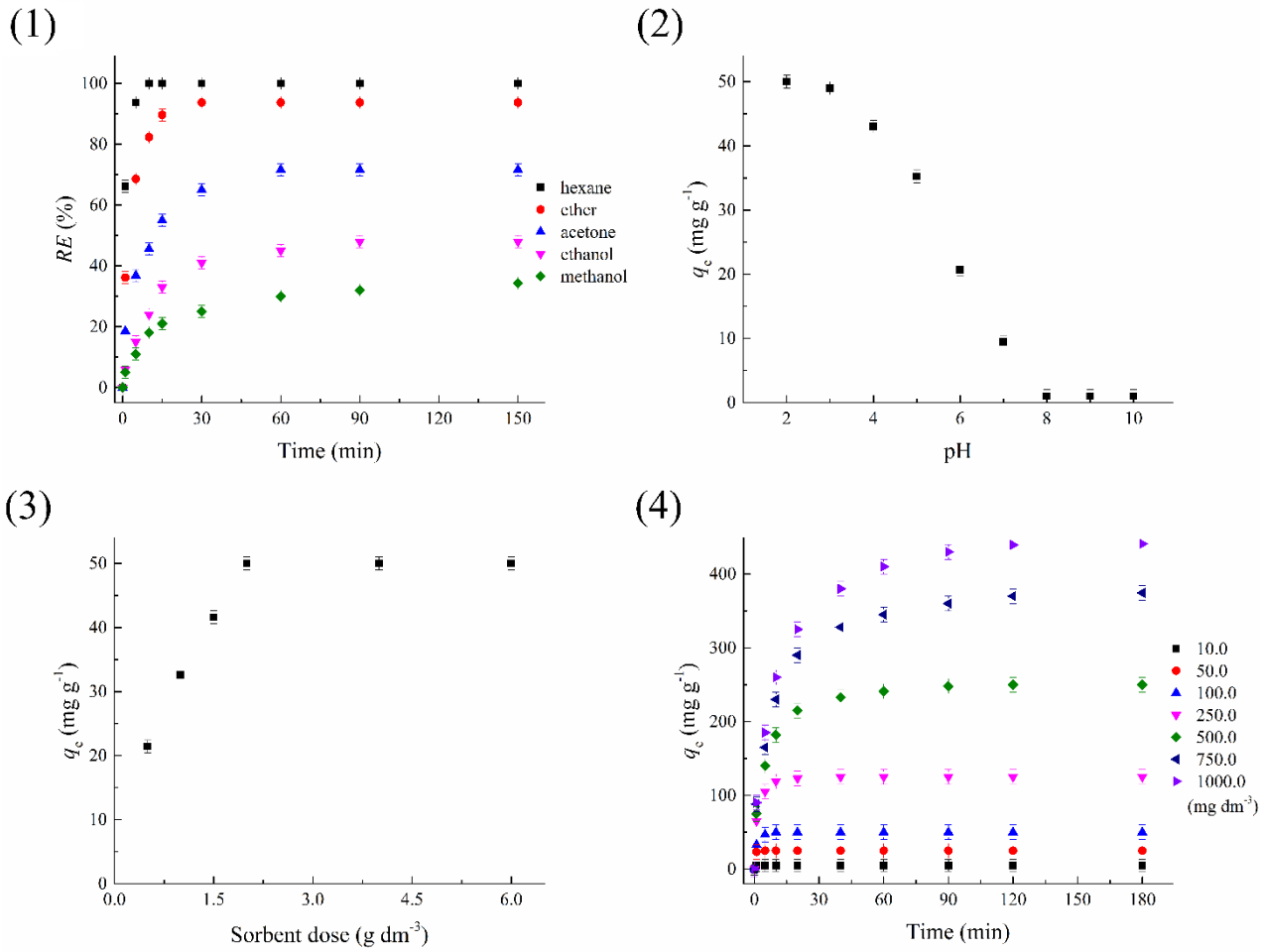

Figure 1. The effects of solvents on the RB19 removal efficiency (1). The effect of pH (2), sorbent dose (3) and dye concentration (4) on amount of the sorbed dye.

The best sorbent was synthesized in hexane, and it was used for further sorption investigations of the optimal sorption parameters, such as: pH, sorbent dose and dye concentration. The pH affects both charge on the sorbent surface and the physico-chemical properties of the dye molecule, so the pH highly affects the amount of sorbed dye by synthesized sorbent. To determine the optimal pH for dye sorption, sorption experiments were caried out in the pH range 2.0–10.0, with other parameters constant (dye concentration 100.0 mg dm^{-3} and dose 2.0 g dm^{-3}). Results show that the amount of sorbed dye decrease from 50.0 to 35.2 mg g^{-1} with the increase of the pH up to 5.0 (Figure 2 (2).). An additional increase of pH up to 10.0 caused a significant decrease of the amount of sorbed dye (1.1 mg g^{-1}). The point of zero charge for wood-aluminum sorbent is 5.41. When the pH is lower, the charge of the sorbent surface is positive and suitable for sorption of the anions. On the other hand, at higher pH, the sorbent surface is negatively charged, and the sorption of cation occurs. Therefore, since the RB19 dye has negatively charged sulfonic group, the higher attraction occurs at the lower pHs. With the increase of the pH, the positive charge on surface of the sorbent decreases, so the amount of the sorbed dye also decreases [8, 9]. The optimal pH for dye sorption is 2.0, which was used in all further experiments.

Also, the dye sorption depends on both sorbent dose and dye concentration. The effect of sorbent dose was examined in the range 0.5–6.0 g dm^{-3}, with other parameters constant (pH 2.0 and dye concentration 100.0 mg dm^{-3}), while the effect of dye concentration was examined in the dye concentration range 10.0–1000.0 mg dm^{-3}, with other parameters constant (pH 2.0 and sorbent dose

2.0 g dm^{-3}). The results show that with the increase of the sorbent dose up to 2.0 g dm^{-3} the amount of sorbed dye quickly increases from 21.4 to 50 mg g^{-1} because the sorbent surface and accessible active sites also increase (Figure 2 (3).). The amount of sorbed dye negligibly changed with higher sorbent doses (4.0 and 6.0 g dm^{-3}), probably because of higher number of active sites onto sorbent surface regarding the dye amount in the solution [8, 9]. Consequently, the optimal sorbent dose for dye sorption was 2.0 g dm^{-3} and it is used in all other experiments. The results show that with the increase of dye concentration, the amount of the sorbed dye also increase (Figure 2 (4).). Lower tested dye concentrations (10.0–200.0 mg dm^{-3}) show very low q_e values but further increase of the dye concentrations up to 1000.0 mg dm^{-3} led to the increase of the amount of the sorbed dye to a 440.8 mg g^{-1}. This is probably a result of the enhancement of the driving force for mass transfer at higher dye concentration and therefore the dye uptakes by the sorbent [8].

CONCLUSION

A new wood-aluminum sorbents were synthesized using five different solvents: acetone, ethanol, ether, hexane, and methanol. Sorption performance of sorbents synthesized in five different solvents strongly depends on their different protic/aprotic nature. The different polarity of the solvents affects the aluminum hydrolysis and its content in the obtained sorbents and thus the sorption efficiency. With an increase in the relative polarity of the solvent, the dye sorption efficiency decreases as well. The highest dye removal percentage (100%) and the shortest time (less than 10 min) was achieved for the sorbent synthesized in hexane as a solvent, because hexane has the lowest relative polarity (0.009), so this sorbent was used further sorption investigations. The optimal pH value where the amount of sorbed dye has the highest value is 2.0. It can be assumed that the main binding mechanism is ion exchange. The amount of sorbent dye is directly related to the sorbent dose and the optimal value was 2.0 g dm^{-3}. With the increase of initial dye concentration, the amount of sorbed dye also increases. The obtained results show that the synthesized sorbent in hexane display very rapid sorption process and high removal efficiency and may become valuable sorbent material in potential applications for environmental protection. Also, the preparation of sorbents using wood biowaste could increase reuse/recycle options of wood.

Acknowledgment

This work was supported by the Ministry of Education, Science and Technological Development of the Republic of Serbia (grant no 451-03-68/2022-14/200124).

REFERENCES

[1] M. Kaya, Wood. Sci. Technol., 52 (2018) 245.
[2] D. M. Leme, G. A. R. de Oliveira, G. Meireles, L. B. Brito, L. de B. Rodrigues, D. J. Palma de Oliveira, Toxicol. Environ. Health. Part. A., 78 (2015) 287.
[3] M. Kadhom, N. Albayati, H. Alalwan, M. Al-Furaiji, Sustain. Chem. Pharm., 16 (2020) 100259.
[4] M. S. Monteiro, R. F. de Faria, J. A. P. Chaves, S. A. Santana, H. A. S. Silva, C. W. B. Bezerra, J. Environ. Manage., 204 (2017) 23.
[5] Y. Djilali, E. H. Elandaloussi, A. Aziz, L.-C. de Menorval, J. Saudi. Chem. Soc., 20 (2016) S241.
[6] C. Reichardt, Solvents and Solvent Effects in Organic Chemistry, Wiley-VCH Verlag, Weinheim, Germany, 2003.
[7] P. C. Sadek, The HPLC Solvent Guide, Wiley-Interscience, New York, 2002.
[8] G. D. Degermenci, N. Degermenci, V. Ayvaoglu, E. Durmaz, D. Cakir, E. Akan, J. Clean. Prod., 225 (2019) 1220.
[9] D. T. Ogunleye, S. O. Akpotu, B. Moodley, Environ. Technol. Inn., 17 (2020) 100616.

CHARACTERIZATION OF IRON-BEARING WOOD MATERIAL FOR APPLICATION IN HETEROGENEOUS FENTON-LIKE PROCESS

M. Radović Vučić, N. Velinov, M. Kostić, J. Mitrović, M. Petrović, S. Najdanović and A. Bojić

University of Niš, Department of Chemistry, Faculty of Science and Mathematics, Višegradska 33, 18 000 Niš, Serbia. (nena.velinov@yahoo.com)

ABSTRACT

The iron-bearing material from wood sawdust was prepared as a catalyst for the degradation of organic pollutants by a heterogeneous Fenton-like process. The materials were thoroughly characterized by several techniques: SEM/EDX and BET surface area and pore size distribution. The use of this modified material will optimize the heterogeneous Fenton-like process economics since they are unexpensive, abundant and require only minimal modifications. The new catalyst can be potentially utilized as a universal catalyst for the degradation of different kinds of organic pollutants in water using solar light as an environmentally friendly and low-cost energy resource.

INTRODUCTION

Various conventional processes are commonly applied for the removal of organic pollutants in contaminated water. However, these methods are usually non-destructive, inefficient, and expensive and in addition, resulted in the production of secondary waste products. Therefore, the development of new technologies for the treatment of wastewater leading to the complete removal of the contaminants now becomes a matter of great concern.

Recently, among the emerging treatment approaches, advanced oxidation processes (AOPs) are considered the most effective and have been proposed as the alternative methods for textile waste-water treatment since they use highly reactive radicals [1]. Due to its simplicity and the lack of toxicity of the reagents. The term “Fenton’s reagent” refers to the mixture of hydrogen peroxide and iron ions. The process can be operated both homogeneously or heterogeneously under various combinations. In the homogeneous phase, a chemical reaction is involved only in the degradation process. It should be pointed out that the homogeneous Fenton process has significant disadvantages. To overcome the disadvantages of Fenton-type processes, considering the possibility of recovering catalysts, the use of heterogeneous solid Fenton catalysts is recommended. In the heterogeneous phase, the physical steps in addition to chemical changes take place on the surface of the catalyst at the active sites where mass transfer limited adsorption of reactant molecules occurs. In other words, physical absorption, and desorption in addition to chemical reactions take place. In the process, iron salts, are adsorbed onto the surface of supported catalysts, and the reduction-oxidation reactions between Fe(II)/Fe(III) take place in the presence of hydrogen peroxide which promotes the formation of reactive components such as (•OH) and (•OOH) radicals [2].

Many studies are focused on the design and synthesis of environmental friendly catalysts. The selection of environment friendly catalyst should also take into account its reusability, ease of product recovery, low temperature and leaching effect of the metal. Many heterogeneous Fenton-like catalysts have recently been reported as alternative methods, such as iron-oxide based catalysts, clay-based catalysts, iron-contained perovskites, two-dimensional carbon-based materials, zeolite-based catalysts, zero-valent iron (ZVI) based catalysts [2, 3].

The aim of this study is to assess the catalytic performance of iron(III) immobilized on wood sawdust as heterogeneous catalyst for the Fenton-like oxidation. The catalyst firstly adsorbs the electro-generated H_2O_2 reducing Fe(III) to Fe(II), and then H_2O_2 can be decomposed to form •OH [2]. Catalyst synthetized by chemically modified wood sawdust by iron was tested for removal of

pharmaceutical Loperamide. Loperamide, which is commercially available as loperamide hydrochloride, is an anti-diarrhoea drug for the fast and effective relief of diarrhoea associated with inflammatory bowel disease [4]. This study is an attempt to further advance the use of wood sawdust, which is a major waste product of wood industries, particularly in furniture manufacturing. Hereby, it is realized to prepare an environmental friendly and low-cost catalyst which can be used in the treatment of wastewaters.

METHODS

The wood sawdust, taken from the local furniture industry, was used as starting lignocellulose raw material for catalyst preparation. The catalyst was prepared by impregnating the metal on activated wood sawdust [5]. A 6.0 g of $Fe(NO_3)_3 \cdot 9H_2O$ (Merck) was dissolved in a beaker containing 20 mL of deionized water. Then, 10 g of wood sawdust was added to this aqueous solution with stirring and maintaining the temperature at 100ºC until the water evaporated. After washing the material with deionized water and drying at 100 degrees, the material used in the experiments was obtained and named wood sawdust-iron catalyst (WS-Fe).

The specific surface area was evaluated by the BET method using N_2 adsorption. A full gas sorption isotherm was run on a Micromeritics Gemini 5 Surface Area Analyser. The pore size distribution was calculated from the desorption branch of the isotherm by the Barrett, Joyner, and Halenda (BJH) method.

SEM–EDX was done by the JEOL5310LV in low vacuum mode with an Oxford Instruments X-Max 50 detector for semi-quantitative EDX analysis. Nominal magnifications of × 5.0 k, 10.0 k and 25.0 k were used when imaging the obtained samples.

The catalyst was dipped into 200 cm^3 H_2O_2 solution (200 mg dm^{-3}), and the pH value was adjusted using 10 % (v/v) H_2SO_4 solution. At the desired time, samples were taken from the reactor for the concentration analysis of total iron ions.

RESULTS AND DISCUSSION

The specific surface area, volume, and average diameter of the pores for unmodified lignocellulosic biomaterial and WS-Fe catalyst were measured using the BET methods and the results are shown in Table 1. The N_2 adsorption/desorption isotherm of WS-Fe is classified as a type IV, with mesoporous nature according to the IUPAC classification [6].

Table 1. Specific surface area and porosity of the raw material and WS-Fe

Parameter	Lignocellulose raw material	WS-Fe
Surface area (m^2/g)	5.71	6.18
Pore volume (cm^3/g)	0.0067	0.0012
Average pore diameter (nm)	5.13	5.9
Colour	Yellow	Brown

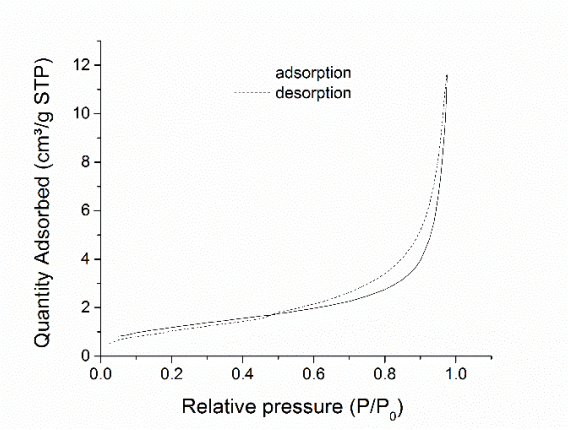

Figure 1. Nitrogen adsorption-desorption isotherms

The images of lignocellulose raw material and obtained wood-based catalyst WS-Fe were shown in Figure 2a and Figure 2b. The SEM images of lignocellulose raw material (Figure 2c) and WS-Fe (Figure 2d) show very similar porous morphology indicating that the modification process and incorporation of WS-Fe in the biomaterial did not bring any significant change to the material surface. The surface of the WS-Fe catalyst is embossed, irregular and porous with characteristic pores of different sizes and shapes, which is similar to the SEM images of basic lignocellulosic material.

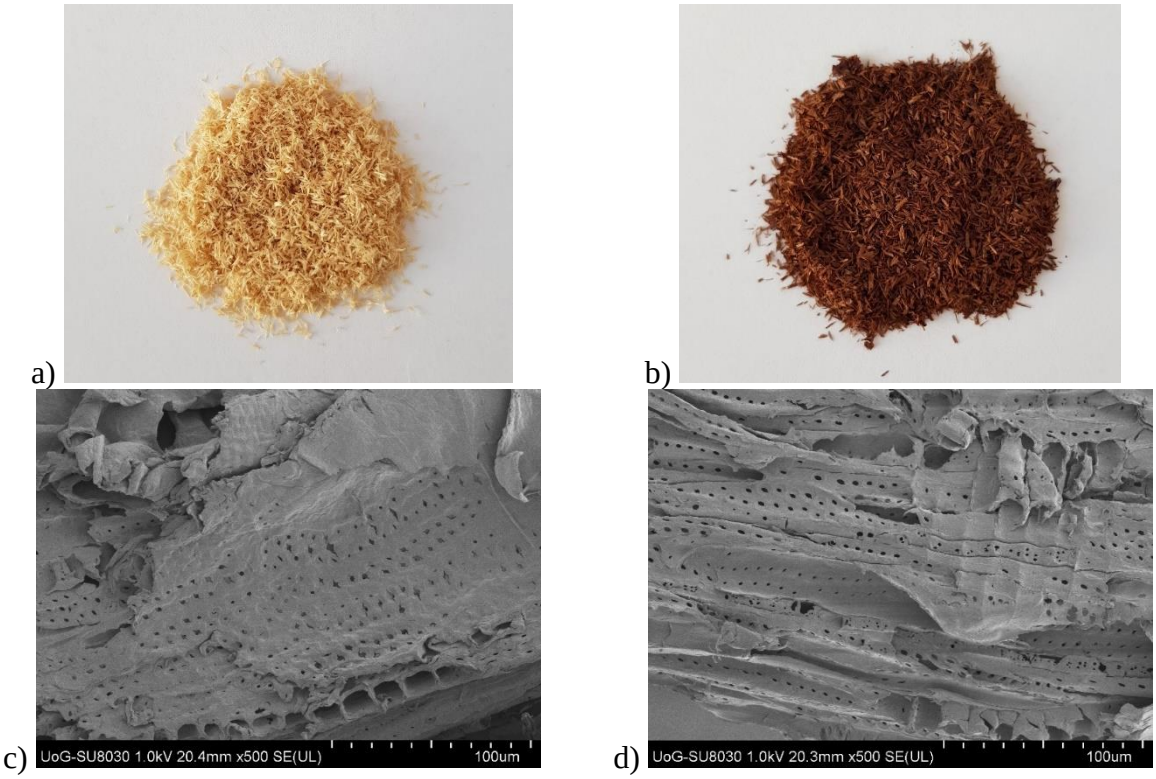

Figure 2. Images of lignocellulose raw material (a) and WS-Fe (b); SEM images of raw material (c) and WS-Fe (d)

EDX analysis shows the presence of carbon and oxygen (Table 1) in unmodified lignocellulosic biomaterial which is characteristic of lignocellulosic materials [7]. In the EDX analysis of WS-Fe, in addition to carbon and oxygen, iron was also detected. Quantification expressed as a percentage by weight showed that unmodified lignocellulosic material consisted of 57.38% carbon and 42.62% oxygen, while WS-Fe consisted of 35.83% carbon, 52.87% oxygen and 11.60% iron.

The leaching amount of iron ions was investigated by dipping 6 g catalyst in 200 mL H_2O_2 solution of 200 mg dm^{-3}. The catalyst dipping of 240 min at pH 3.0 led to the total iron ions concentration of 0.17 mg dm^{-3}. In contrast to the amount of Fe(III) (11.6 mg g^{-1}) on the catalyst, it could be concluded that the catalyst had very low leaching of iron ions.

Table 2. Elemental composition of the raw material and WS-Fe

Element	Lignocellulose raw material	WS-Fe
	Weight (%)	Weight (%)
C	57.38	35.8
O	42.62	52.57
Fe	/	11.60

The suspensions of Loperamide and WS-Fe were magnetically stirred in dark for 30 min to attain adsorption-desorption equilibrium between pharmaceutical and catalyst. The degradation of Loperamide was investigated in a batch test using a beaker containing the working solution (pH 3 adjusted with H_2SO_4) plus 1000 mg dm^{-3} heterogeneous catalyst and H_2O_2 concentration of 10 mM. At required time intervals, 4.0 cm^{-3} of samples were withdrawn, centrifuged (3000 rpm, 5 min) and filtered through a 0.20 μm regenerated cellulose membrane filter (Agilent Technologies, Germany) to separate the catalyst.

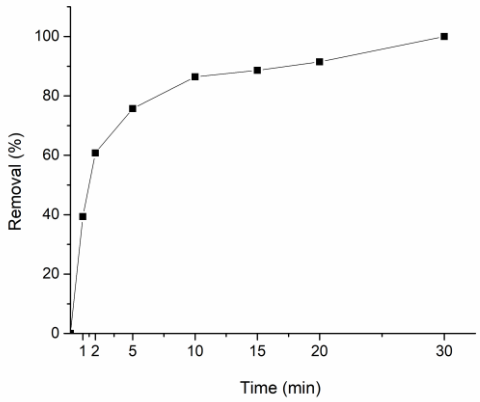

Figure 3. The removal percentages of Loperamide by heterogeneous Fenton-like process.

CONCLUSION

A new catalyst, hybrid material, based on chemical modification of lignocellulosic biomass with Fe was synthesized. As starting biomass, wood sawdust generated from furniture manufacturing was used. In that manner, wood waste could be reduced, and reuse/recycle options of wood sawdust were increased. Chemical modification of the catalyst was confirmed by characterization. SEM micrographs showed that the chemical modification did not change the morphological structure of the biomaterial. The EDX analysis showed the presence of 35.83% carbon, 52.87% oxygen and 11.60% iron. 35.83% carbon, 52.87% oxygen and 11.60% iron. Under optimal conditions, total removal of Loperamide was achieved in less than 30 minutes.

Acknowledgment

This work was supported by the Ministry of Education, Science and Technological Development of the Republic of Serbia (grant no 451-03-68/2022-14/200124).

REFERENCES

[1] S.Samsami, M Mohamadi, M.-H. Sarrafzadeh, E. Rene, M. Firoozbahr, Process Saf. Environ. Prot., 143 (2020) 138.
[2] N. Thomas, D. Dionysious, S. C. Pillai, J. Hazard. Mater., 404 (2021) 124082.
[3] M. Zhang, H. Dong, L. Zhao, D. Wang, D. Meng, Sci. Total Environ., 670 (2019) 110.
[4] F. Faridbod, F. Mizani, M. Ganjali, P. Norouzi, Int. J. Electrochem. Sci., **7**, (2012)7643.
[5] G. Ersoz, Appl. Catal. B, (2014) 353.
[6] K. Sing, Coll. Surf. A: Physicochem. Eng. Asp. 187–188 (2001) 3.
[7] S. Darmawan, N. J. Wistara, G. Pari, A. Maddu, W. Syafii, Bioresouces., 11(2) (2016) 3561.

EFFECT OF pH AND EQUILIBRIUM STUDIE FOR THE DYE SORPTION ONTO LAYERED DOUBLE HYDROXIDE

M. Kostić, N. Velinov, M. Radović Vučić, S. Najdanović, T. Jovanović, D. Bojić and A. Bojić

University of Niš, Faculty of Science and Mathematics, Department of Chemistry, Višegradska 33, 1800 Niš, Serbia. (mk484475@gmail.com)

ABSTRACT

In this study, the removal of Reactive orange 16 (RO16) by layered double hydroxide (MgCoAl-LDH) was investigated. MgCoAl-LDH material was synthesized by the coprecipitation method assisted by ultrasound. MgCoAl-LDH was used for sorption removal of textile dye RO16, chosen as one of the most used reactive dyes. The solution pH was found to strongly influence the uptake of RO16 by MgCoAl-LDH. Moreover, it was found that sorption capacity increased with decrease pH. The sorption capacity of MgCoAl-LDH sorbents was tested using various concentrations of RO16 in the range from 50 to 200 mg dm^{-3} in water. The amount of the sorbed dye at equilibrium (q_e) of MgCoAl-LDH was 240.96 mg g^{-1}.

INTRODUCTION

Anionic clay or layered double hydroxides (LDH) can be represented by general formula $\left[M^{II}_{1-x}M^{III}_{x}(OH)_2\right]^{x+}\left[A^{n-}_{x/n}\right]\times yH_2O$, where M^{II} is a divalent metal cation such as Mg^{2+}, Ca^{2+}, Zn^{2+}, Cu^{2+}, Co^{2+}, Ni^{2+}, etc., and M^{III} is a trivalent metal cation such as Fe^{3+}, Al^{3+}, Ga^{3+}, Cr^{3+}, etc. Electroneutrality of LDH is achieved by the presence of hydrated organic or inorganic anions, such as CO_3^{2-}, NO_3^-, SO_4^{2-}, OH^-, Cl^-, Br^-, etc., in the interlamellar space. In the last few years, many studies dealt with the synthesis of LDHs, but not that much with their application. The coprecipitation [1,2], sol-gel methods [3], hydrothermal synthesis [4] and hydrolysis of urea method [5] were used to obtain LDH materials. LDH materials can be used as drug carriers, flame retardants, for electrocatalytic water splitting and in recent years as sorbents for various organic and inorganic pollutants. Wastewater from the textile, leather, and paper industry contains numerous organic and inorganic pollutants. Different methods have been used in recent years to eliminate the pollutants such as advance oxidation, biological treatments, membrane filtration, nanofiltration, ozonation, as well as sorption. Sorption is one of the most common treatment processes in water treatment because it is very efficient and easy to use [6, 7]. Reactive orange 16 (RO16), as an anionic sulfonated reactive azo and non-biodegradable dye, was chosen as a model pollutant in this study.

In this study, layered double hydroxide (MgCoAl-LDH) was synthesized by the coprecipitation method and applied for sorption of RO16. In brief, the present paper describes the sorption behavior studies by the investigation of the impact of pH and sorption isotherms. The isotherm parameters obtained by nonlinear fitting of the experimental results provided information of the sorption capacity of MgCoAl-LDH.

MATERIALS AND METHODS

RO16 was purchased from Sigma–Aldrich (Germany) (chemical formula: $C_{20}H_{17}N_3Na_2O_{11}S_3$, CI 17757). magnesium nitrate hexahydrate ($Mg(NO_3)_2{\cdot}6H_2O$), cobalt (II) nitrate hexahydrate ($Co(NO_3)_2{\cdot}6H_2O$), aluminum nitrate nonahydrate ($Al(NO_3)_3{\cdot}9H_2O$), sodium hydroxide (NaOH), sodium carbonate (Na_2CO_3) were obtained from Sigma-Aldrich (Germany). All solutions were made by using deionized water (resistivity of 18 MΩ cm^{-1}) and all chemicals were of analytical grade.

MgCoAl-LDH was prepared by the coprecipitation method assisted by ultrasound. Briefly, 150 cm^3 of solution (which contains $Mg(NO_3)_2 \cdot 6H_2O$, $Co(NO_3)_2 \cdot 6H_2O$ and $Al(NO_3)_3 \cdot 9H_2O$ with a molar ratio of Mg:Co:Al=1:2:1) in Erlenmeyer flask with the reflux condenser was placed in the ultrasonic bath (100 W dm^{-3}) and heated to 80 °C. Slow precipitation was performed by adding dropwise a solution containing Na_2CO_3 and NaOH with concentrations of 1.0 and 2.5 mol dm^{-3}, respectively, to pH 10. The suspension was centrifuged, and the precipitate was washed several times with hot deionized water and dried at 80 °C. The obtained carbonate form of LDH was labeled as MgCoAl-LDH. The synthesis procedure was described in detail in a previous study. The MgCoAl-LDH was characterized in previous study [8].

The concentrations of RO16 in the solution were determined by UV–vis technique at λmax = 493 nm using a Shimadzu UV–vis 1650 PC spectrophotometer.

The amount of dye sorbed qt (mg g-1) and the removal efficiency (RE) was determined by using the following equations:

$$q_t = \frac{c_0 - c_t}{m} \times V \quad (1)$$

where c_0 and c_t are the initial and final concentrations of the metal ion and dye in solution (mg dm^{-3}), V is the solution volume (dm^3), and m is the mass of the sorbent (g).

The Langmuir model can be expressed by the nonlinear equation 2 [9]:

$$q_e = \frac{q_m K_L c_e}{1 + K_L c_e} \quad (2)$$

where q_m (mg g^{-1}) is the maximum sorption capacity, K_L (dm^3 mg^{-1}) is Langmuir equilibrium constant.

The affinity between RO16 and the sorbent can be defined by the dimensionless separation factor R_L, presented by equation 3:

$$R_L = \frac{1}{1 + K_L c_0} \quad (3)$$

The Freundlich model can be expressed by the nonlinear equation 4 [10]:

$$q_e = K_F c_e^{\frac{1}{n}} \quad (4)$$

where K_F is Freundlich equilibrium constant ((mg g^{-1}) (dm^3 $mg^{-1})^{1/n}$), n is the exponent associated with the intensity of sorption.

The Sips model can be expressed by the nonlinear equation 5 [11]:

$$q_e = \frac{q_m (b_S c_e)^n}{1 + (b_S c_e)^n} \quad (5)$$

where b_S (dm^3 mg^{-1}) represents affinity constant for sorption, n is exponent.

The sorption study was menage to analyze the effects of the pH from 3.0 to 9.0 and initial RO16 concentration from 50.0 to 200.0 mg dm^{-3} on the sorption with sorbent dose of 0.5 mg dm^{-3}. All experiments were performed in triplicate. The evaluation of all parameters was done using the Origin 2021 (OriginLab Corporation, USA).

RESULTS AND DISCUSSION

Effect of pH on sorption RO16 by MgCoAl-LDH was shown in Figure 1. The sorption capacity of MgCoAl-LDH for RO16 decreased from 199.56 to 60.04 mg g^{-1} when pH increased from 2 to 9 for contact time 180 min.

The sulfonic groups in RO16 molecule were dissociated and negatively charged (–SO_3-) at low pH values. At low pH values the sorbent surface were protonated and positively charged so RO16 molecules might be bound by electrostatic attractions. Conversely, at higher pH more –OH- were

present in solution and compete with the sulfonic groups, which led to a decrease in the number of active sites for RO16 sorption.

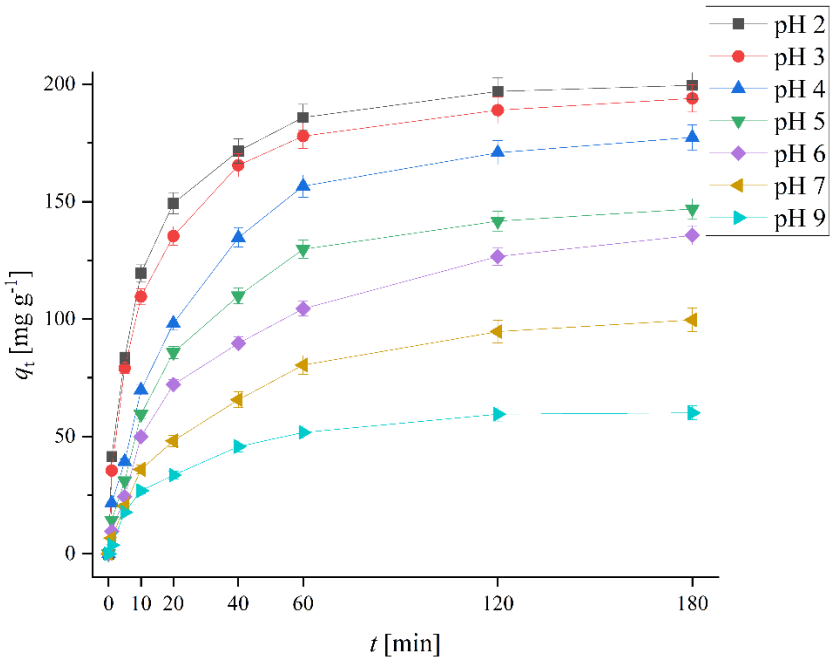

Figure 1. Results of effect of pH on the sorption of RO16 on MgCoAl-LDH (c_0: 100 mg dm^{-3}; sorbent dose: 0.5 g dm^{-3}, steering speed: 280 rpm, temperature: 20 °C).

Equilibrium data for the sorption of RO16 onto MgCoAl-LDH at 20 °C were analyzed using Langmuir, Freundlich and Sips nonlinear isotherm models. From Table 1, the correlation coefficient of the Sips model was slightly larger than that the Langmuir model, which indicates that both models describe the sorption process onto MgCoAl-LDH very well. The Freundlich isotherm did not describe the presented sorption satisfactorily. Also, the maximum sorption capacity calculated on the basis of the Langmuir and Sips isotherm models was close to the experimentally obtained value. This implied that a monolayer sorption was takes place on a structurally homogeneous sorbent surface (all active sites were identical and energetically equivalent and there was no interaction between the adsorbed molecules) [12].

Table 1. The isotherms parameters for sorption RO16 on MgCoAl-LDH at 20 °C

Isotherm parameters								
	$q_{e,exp}$	240.96						
Langmuir	q_m	238.08	K_L	16.99			r^2	0.972
Freundlich	K_F	179.58	n	12.64				0.642
Sips	q_m	235.51	b_s	15.98	n_s	1.36		0.991

R_L values for initial RO16 concentrations from 50.0 to 200.0 mg dm^{-3} ranged from 0.0012 to 0.00029. Such low values indicated the spontaneity of the sorption process (spontaneity increased with the increasing initial concentration of RO16).

The Sips isotherm model exceeds limitations related to the variable energy state of the active centers on the sorbent surface (hybrid of Langmuir and Freundlich isotherms). The good agreement

of experimental results with Sips isotherm model, indicates that in high sorbate concentrations, this predicts monolayer sorption onto surface of sorbent like at the Langmuir isotherm, while at low sorbate concentration, it follows Freundlich isotherm.

CONCLUSION

The sorbent MgCoAl-LDH was synthesized by the coprecipitation method using ultrasound. The experimental results evidenced the strong affinity of RO16 toward the MgCoAl-LDH at low pH. The equilibrium data analysis showed that the Sips and Langmuir models fitted well the experimental data with maximal adsorption capacities of 238.08 and 235.51 mg g^{-1}, respectively, at 20 °C. The experimental sorption capacity for RO16 was 240.96 mg g^{-1} at 20 °C. Based on these findings, MgCoAl-LDH could potentially be an effective sorbent for uptake of dyes from water and further investigations are necessary to estimate the regeneration method and to develop this treatment process at large scale.

Acknowledgment

This work was supported by the Ministry of Education, Science and Technological Development of the Republic of Serbia (Agreement No 451-03-68/2022-14/200124).

REFERENCES

[1] E. H. Mourid, M. Lakraimi, L. Benaziz, E. H. Elkhattabi, A. Legrouri, Appl. Clay Sci. 168 (2019) 87.
[2] M. Kostić, M. Radović, N. Velinov, S. Najdanović, D. Bojić, A. Hurt, A. Bojić, Ecotoxicol. Environ. Saf. 159 (2018) 332.
[3] M. Jitianu, D. C. Gunness, D. E. Aboagye, M. Zaharescu, A. Jitianu, Mater. Res. Bull. 48 (2013) 1864.
[4] L. Feng, Y. Du, J. Huang, L. Cao, L. Feng, Y. Feng, Q. Liu, D. Yang, K. Kajiyoshi, Sustainable Energy Fuels 4 (2020) 2850.
[5] X. Wu, Y. Du, X. An, X. Xie, Catal. Commun. 50 (2014) 44.
[6] G. Crini, Bioresour. Technol. 197 (2006) 1061.
[7] Y. Yasin, A. H. A. Malek, S. M. Sumari, Orient. J. Chem. 26 (4) (2010) 1293.
[8] M. Kostić, Najdanović S., Velinov N., Radović Vučić M., Petrović M., Mitrović J., Bojić A., Environ. Technol. Innov. 26 (2022) 102358.
[9] I. Langmuir, J. Am. Chem. Soc. 40 (1918) 1361.
[10]H. Freundlich, Z. Phys. Chem. 57 (1906) 385.
[11]L. Limousy, I. Ghouma, A. Ouederni, M. Jeguirim, Environ. Sci. Pollut. Res. 24 (2016) 9993.
[12]K. Y. Foo, B. H. Hameed, Chem. Eng. J. 156 (2010) 2.

MODIFICATION OF GRAPHITE ELECTRODE SURFACE BY LASER IRRADIATION-ROLE OF IRRADIATION ATMOSPHERE

D. Aćimović, T. Brdarić, B. Savić, D. Vasić Anićijević, M. Simić, J. Ciganović and M. Momčilović

University of Belgrade, VINČA Institute of Nuclear Sciences - National Institute of the Republic of Serbia, Department of Physical Chemistry, Mike Petrovića Alasa 12-14, 11001 Belgrade, Serbia (tanja.brdaric@vin.bg.ac.rs)

ABSTRACT

In this study, surface modification of the graphite plate electrode induced by laser irradiation treatment is presented. The electrode was irradiated in air and argon atmosphere using the Nd:YAG laser. Surface modifications were analyzed by profilometric measurements. The influence of irradiation atmosphere on electrochemical active surface of graphite electrode was observed using cyclic voltammetry. The results indicate that electrochemical active surface area of graphite electrode was increased using laser irradiation, and highest value was obtained by laser irradiation in air atmosphere. These cognitions can be useful for application of laser-treated electrode in environmental chemistry for detection or removal of organic pollutants.

INTRODUCTION

Graphite, as a crystalline form of carbon, has attracted considerable attention in the field of electrochemical applications. Due to excellent electrochemical characteristics, like high overvoltage for oxygen evolution, high electrical conductivity, large surface area, low-cost synthesis, it is attractive as an anode material for Li-ion batteries, anodic wastewater treatment and electrochemical sensor for various organic pollutants [1-3]. On the other hand, graphite electrodes normally need activation to achieve the desired electrochemical properties, because of the tendency of carbon to adsorb impurities on the surface. Many research studies [4, 5] show that the laser beam interaction with the target electrode surface can be attended to material evaporation or ablation which depends on the irradiation conditions, especially on laser pulse energy. Therefore, the thermal effects of laser irradiation that arise as a consequence of absorption of laser energy by materials lead to desorption of impurities and production of a cleaner, more reactive electrode surface; disruption of the carbon microstructure by thermal stress to the graphite planes and change of the oxide coverage of the electrode. To our knowledge, there are no studies describing the role of irradiation atmosphere on the effectiveness of laser electrode treatment.

Therefore, in this paper we were focused on the examination of the influence of laser irradiation including the surrounding gas atmosphere on the electrochemically active surface of graphite electrode.

METHODS

Laser irradiation was performed on the graphite plate electrode surface 1 cm^2 using Nd:YAG system EKSPLA SL 212/SH/FH. Laser output pulse energy was 15 mJ, pulse duration 150 ps, repetition rate was 10 Hz and laser beam was focused by 15.2 cm focal length quartz lense and target was placed at focus distance. Motion controller was used to scan and modify entire surface of graphite electrode by laser beam. Scanning speed was 0.3 mms^{-1}, and row distance 0.3 mm. The laser irradiation was performed under different gas atmospheres, i.e. air and a flow atmosphere enriched with argon. Morphological characteristics of graphite electrodes surface before and after the laser irradiation treatment were analysed by non-contact optical profilometer ZYGO NewView 7100. Cyclic

voltammetry measurement was employed for determination of electrochemical active surface area of the graphite and laser-treated graphite electrode using three-electrode electrochemical cell. An Ag/AgCl reference electrode and a Pt foil as counter electrode were used, while the graphite plate (1 cm^2) was working electrode. The electrolyte was 5 mM $K_3[Fe(CN)_6]$ in 0.1 M KNO_3 solution (all chemicals is produced from Sigma Aldrich without further purification). The oxidation reaction of ferrocyanide on the working electrode surface was controlled by the diffusion of ferrocyanide ions. Therefore, the peak current is proportional to the electrochemical active surface area of the working electrode and can be expressed by the Randles-Sevcik equation [6]:

$$I_p = (2.69 \cdot 10^5)\, n^{3/2} A D_0^{1/2} v^{1/2} c$$

where *Ip* (A) is the peak current, *n* is the number of electrons transferred in the redox reaction (in this case *n* =1), *A* (cm^2) is the electroactive surface area of electrode, *D* (cm^2s^{-1}) is the diffusion (coefficient for $K_3[Fe(CN)_6]$ is 7.6×10^{-6} $cm^2\ s^{-1}$) [5]), *C* (mol/cm^3) is the concentration of the reaction species in the electrolyte (5×10^{-6} for $[Fe(CN)_6]_4$ here) and *v* (Vs^{-1}) is the scan rate.

RESULTS AND DISCUSSION

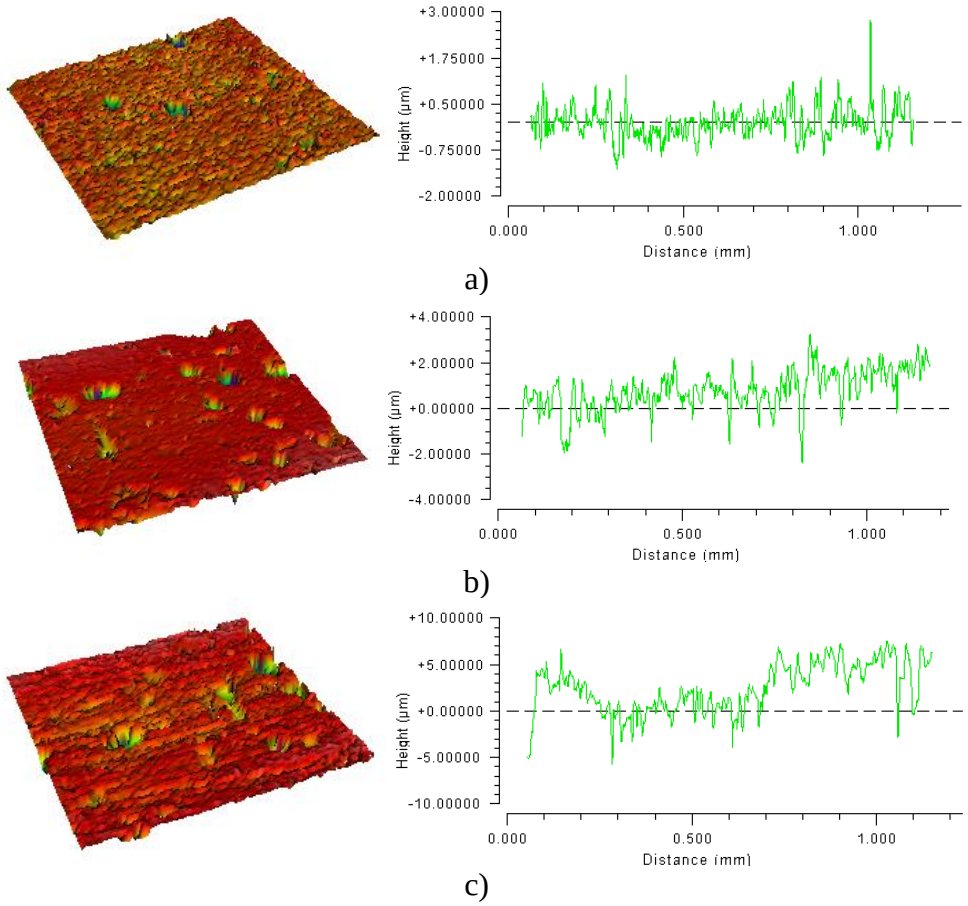

Figure 1. 3D and linear profilometric analysis of the graphite electrode surface before (a) and after irradiation in air (b) and argon (c). Laser pulse output energy was 15 mJ.

Profilometric analysis of non-treated and laser-treated graphite electrode surface was utilized to characterize the altered surface morphology and the laser-induced changes which have occurred in

argon and air atmospheres. The three-dimensional (3D) and linear profiles of the irradiated surface of graphite electrodes showed in Figures 1 a, b and c., indicate that the laser irradiation induced improving of electrode surface roughness. Surface roughness was estimated to increase from 0.33 μm for untreated surface, 0.69 μm for electrodes irradiated in air, and 2.22 μm for targets modified in argon flow atmosphere, and with corresponding rms (root mean square) values of 0.4 (± 0.1) μm, 1.1 (± 0.3) μm, and 2.8 (± 0.3) μm.

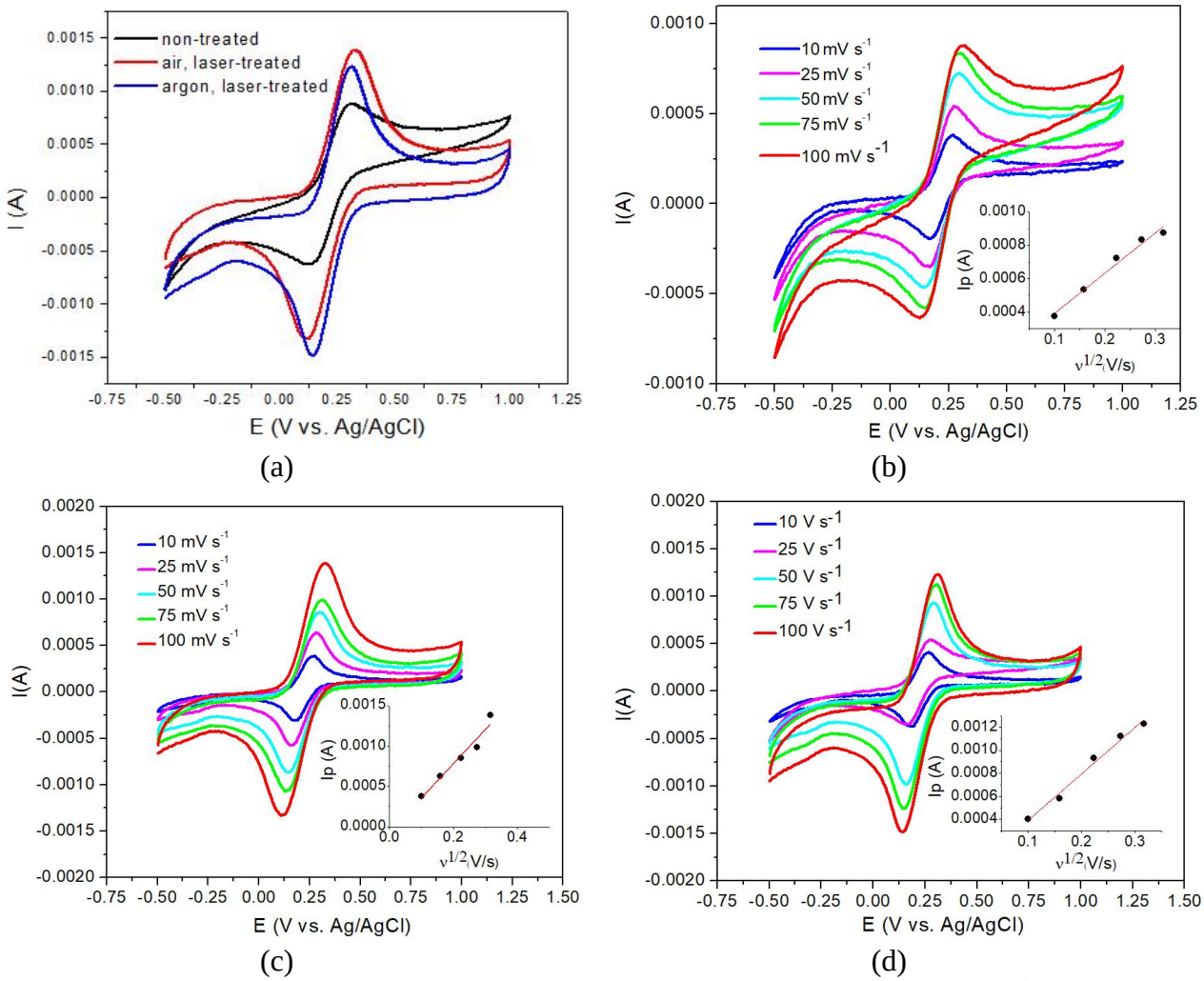

Figure 2. Cyclic voltammograms of 5 mM ferrocyanide in 0.1 M KNO_3 at 100 mVs^{-1} scan rate for laser-treated electrodes (15 mJ energy) in air and argon irradiation atmosphere (a); and cyclic voltammograms at different scan rates for non-treated graphite b); air c); argon d) and Randles–Sevcık fit (insert)

Figure 2. a shows cyclic voltammograms of 5 mM ferrocyanide in 0.1 M KNO_3 at 100 mVs^{-1} scan rate for electrodes treated with laser energies of 15 mJ in air and argon atmosphere. It was found that non-treated and laser-treated graphite electrodes provide an electrochemical response of the tested redox pair. In the case of the laser-treated electrode in argon atmospheres calculated peak-to-peak separation (ΔE) between oxidation and reduction peaks was slightly smaller than in the case of untreated electrode (ΔE from 170 mV to 180 mV). Also, it is important to note that the oxidation and reduction peaks of laser-treated electrodes are better defined with higher currents. This indicates that the laser irradiation procedure increases electrochemical active surface area.

Figure 2 b,c,d depicts the Randles–Sevcık dependence of the oxidation peak current on square root of the scan rate Ip = f ($\nu^{1/2}$). The values of slope of linear curve Ip = f ($\nu^{1/2}$) (see Table 1) proved diffusion-controlled electrode processes. The electrochemical active surface area of graphite electrode was increased using laser irradiation and highest value was obtained by laser irradiation in air atmosferes.

Table 1. The electrochemical surface area

Electrode	Irradiation atmosfere	Slope ($A/(V/s)^{1/2}$)	Electrochemical active surface area (cm^2)
Non-treated graphite	non	0.0024	0.648
Treated graphite	air	0.0043	1.161
Treated graphite	argon	0.0035	0.945

Interestingly, the laser-treated electrode in the air has a lower roughness and a larger electrochemical surface. This can be explained by the loss of laser energy due to surface reactions of carbon with components from the air, e.g. nitride formation, etc. which, on the other hand, affects the growth of the electrochemical surface. However, newly-formed species from the irradiated air can interact with adsorbed impurities and thus act as surface cleaners.

CONCLUSION

Graphite plate electrode was subjected to the laser irradiation under different gas atmospheres, i.e. air and a flow atmosphere enriched with argon, to investigate the influence of the surrounding gas atmosphere on the electrode electrochemical surface characteristics. The results indicated that irradiation atmosphere is one of factors for process of laser modification of surface electrodes. Based on these investigations our future studies will be related to application laser-treated electrode for detection or removal organic pollutant from wastewaters using electrochemical technologies.

Acknowledgment

This work was supported by the Ministry of Education, Science and Technological Development of Republic of Serbia; grant number 451-03-68/2022-14/200017.

REFERENCES

[1] Zhanga H., Yang Y., Ren D., Wang L., He X., Energy Storage Mater., 36 (2021) 147.
[2] Chen Z., Lai W., Xu Y., Xie G., Hou W., Zhanchang P., Kuang C., Li Y., J. Hazard Mater., 405 (2021) 124262.
[3] Annu A., Sharma S., Jain R., Nitin Raja A., J. Electrochem. Soc., 167 (2020) 037501.
[4] McCreery R., Chem. Rev., 108 (2008) 2646.
[5] Alba A., Totoricaguena-Gorrino J., Campos-Arias L., Perinka N., Ruiz-Rubio L., Vilas-Vilela J., Mendez S., Javier del Campo F., Mater. Adv., 2 (2021) 5912.
[6] Shetti N., Nayak D., Malode S., Reddy K., Shukla S., Aminabhavi T., Colloid Surfaces B, 177 (2019) 407.

COMPARATIVE STUDY OF OXYGEN EVOLUTION REACTION KINETICS ON NANOCOMPOSITE METAL OXIDE-CARBON-BASE ANODES

T. Brdarić[1], B. Savić[1], D. Aćimović[1], M. Simić[1], M. Ječmenica Dučić[1], Z. Vranješ[2] and D. Vasić Anićijević[1]

[1]University of Belgrade, VINČA Institute of Nuclear Sciences-National Institute of the Republic of Serbia, Department of Physical Chemistry, Mike Petrovića Alasa 12-14, 11001 Belgrade, Serbia
[2]Public Company "Nuclear Facilities of Serbia", Mike Petrovića Alasa 12-14, 11001 Belgrade, Serbia
(tanja.brdaric@vin.bg.ac.rs)

ABSTRACT
This paper presents a comparative analysis of kinetic parameters of oxygen evolution reaction (OER) on stainless steel (SS), nanocomposites PbO_2-GNR (lead dioxide–graphene nanoribbons) and SnO_2-MWCNT (tin dioxide-multi wall carbon nanotube) anodes in a sodium sulphate electrolyte. Linear sweep voltammetry (LSV) and Tafel plots analysis were used to determine kinetic parameters (Tafel slopes, exchange current density (j_o), and the potential for OER). Experimental results indicate that the highest electrocatalytic activity to OER shows SS, followed by SnO_2-MWCNT and PbO_2-GNR electrode. From these results, it can be predicted that metal oxide-carbon based electrodes can be useful for electrochemical treatment of organic pollutants from textile, communal or industrial wastewaters.

INTRODUCTION
OER has been considered one of the crucial electrochemical processes in technologies for wastewater treatment, especially in the field of electrochemical oxidation (EO) of organic pollutants by indirect mechanisms via hydroxyl radical (•OH). The indirect mechanism of EO is based on the electro-generation of adsorbed •OH on the anode surface as oxygen intermediate from water oxidation. The reaction of organic molecules with electrogenerated electrolytic •OH are engaged in a competition with the side OER resulting in a decrease in the efficiency of the anodic process. Studies [1, 2] have shown that the activity of these electrochemically generated •OH is linked to their interaction with the electrode surface and depends on the nature of anode materials. A low oxidation power anodes with low overpotential for OER are characterized by a strong electrode –•OH interaction resulting in high electrochemical activity for OER (i.e., anodes that are good catalysts for the OER), such as carbon, graphite or platinum, have “active” behavior and leads to partial oxidation of the organic pollutants.

On the contrary, the high oxidation power anode with high overpotential for OER is characterized by a weak electrode –•OH interaction resulting in a low electrochemical activity for the OER (i.e., anodes that are poor catalysts for the OER, have “nonactive” behavior and favors the total mineralization of the organic compounds to CO_2 and H_2O and these electrodes are ideal for wastewater treatment.

Lead dioxide (PbO_2) anodes have been used long for the EO of organics, due to great electrical conductivity, good corrosion resistance and low cost of synthesis.
Tin dioxide (SnO_2) is an n-type semiconducting nanomaterial that has properties such as low cost, chemical stability, poor electric conductivity and non-toxicity.

PbO_2 and SnO_2 electrodes are common examples of nonactive electrodes with high overpotential for OER. The literature review [3] found that their overpotential for OER is 1.8 to 2.0 V vs. SHE and 1.9 to 2.2 V vs. SHE, for PbO_2 and SnO_2, respectively.

Basic electrochemical properties of the these anodes as values of overpotentials for OER can be changed by modifying morphology and reducing grain size to nanometer dimension, doping with metals or mixing with metal- and carbon-based nanomaterials.

Graphene nanoribbons (GNRs) and multi-walled carbon nanotube (MWCNT) are a form of carbon-based materials. Generally, carbon-based anodes show active behavior and have low oxygen evolution overpotential. Consequently, they are good electrocatalysts for oxygen evolution.

For this study, it was of interest to investigate the behavior of electrode which is the combination of both active and nonactive materials. In our previous research [4], we found that nanocomposites PbO_2-GNRs electrodes showed non-active behavior and high efficiency toward EO of phenols compounds, but their values of potential for OER were not determined.

The aim of this work is to determine and compare basic kinetic parameters of OER of SS, nanocomposites PbO_2-GNR and SnO_2-MWCNT anodes in sodium sulphate solutions as supporting electrolytes. This electrolyte is a model for sulphate-rich wastewaters, and the results can be useful for the prediction of electrode behavior towards EO of organic molecules in wastewaters.

METHODS

Nanocomposites PbO_2-GNR anodes were prepared using a procedure that is explained in detail in our previous paper [4]. The nanosized SnO_2 was synthesized by the sol-gel method proposed by Kose et al. [5]. The SnO_2-MWCNT nanocomposite was obtained by mixing synthesized SnO_2 nanoparticles with commercial MWCNT (particle size 7-15nm x 3-6 nm x 0.5-200 μm, Sigma-Aldrich), in deionized water, in a ratio 3:1 (w/w, %) on a magnetic stirrer for 3 hours, until a homogeneous suspension was achieved. The sample was dried at 70 °C. After that, obtained SnO_2-MWCNT nanopowder was dispersed in dimethylformamide (DMF) by sonication for 2 h (5 mg mL^{-1}) and 500μL suspension was applied dropwise to the SS electrodes. The surface area of SS electrode was 2 cm^2 (1x2 cm).

A transmission electron microscope (TEM, Talos F200X, FEI Company) was used to confirm that SnO_2 particles were obtained at the nano-range scale.

Using a Gamry Instrument-Interface 1000 potentiostat/Galvanostat/ZRA 06230, the OER parameters of the electrodes were evaluated by LSV in a conventional three-electrode cell at room temperature. A platinum foil, Ag/AgCl (saturated KCl), and nanocomposites PbO_2-GNR, SnO_2-MWCNT and SS electrode were used as the counter, reference and working electrode, respectively. The measurements were done between 0.0 and 3.0 V (vs. Ag/AgCl) at a scanning rate of 10 mVs^{-1} in 0.1 M Na_2SO_4 with the addition H_2SO_4 to adjust pH to 4.2. Kinetic parameters of OER were determinated by Tafel analysis. OER overpotential was calculated according to the following equation: overpotential (V vs. RHE) = (measurement potential (vs. Ag/AgCl) + 0.059 × pH+ 0.197− 1.229 (vs. RHE)). The Tafel slope was derived from the equation $\eta = b \log j + a$, where η, b, and j are the overpotential, Tafel slope, and current density, respectively.

RESULTS AND DISCUSSION

The TEM micrograph presented in **Figure 1.** shows the synthesized SnO_2 powder.

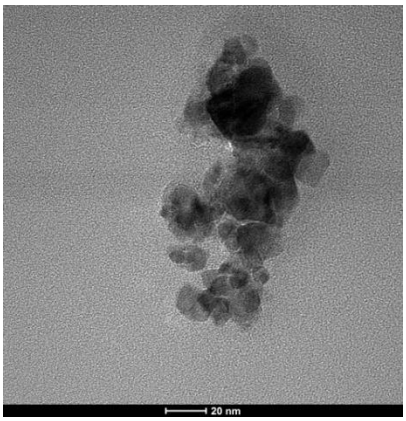

Figure 1. TEM micrograph of SnO_2

As it can be seen in Figure 1. SnO_2 sample consists of particles in form of irregular spherical and polygonal-like structures. The estimated average particle size is about 10 to 15 nm. Similar structures of PbO_2 particles in nanocomposites PbO_2 -GNR were obtained in our previous research [4]. On the other hand, a smaller average particle size of the SnO_2, compared to PbO_2 was observed. This is probably a consequence of the different structural properties of SnO_2 and PbO_2, and different methods of preparation.

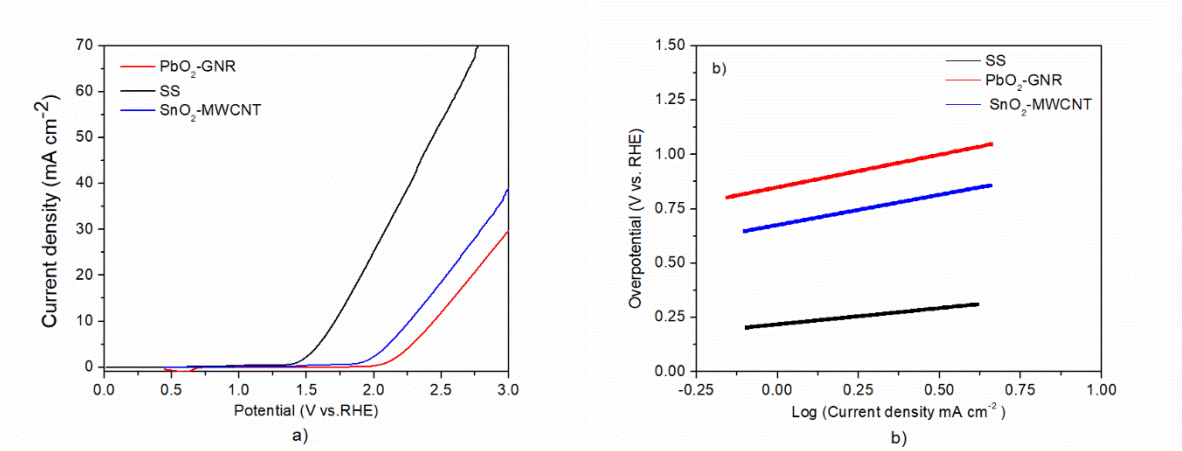

Figure 2. Linear sweep voltammograms (a) linear fitting curves (b) of the SS, SnO_2-MWCNT and PbO_2-GNR electrode in 0.1 mol·L^{-1} Na_2SO_4, scan speed 10 mVs^{-1}

Table 1. Kinetic parametres of OER

Working electrode	a (*V*)	b (V/dec.)	η *(V vs.RHE)*	j_o *(mA cm^{-2})*	*E (V vs, RHE)*
SS	0.2168	0.150	0.173	0.0358	1.403
SnO_2-MWCNT	0.67431	0.270	0.587	0.00318	1.817
PbO_2-GNR	0.84791	0.300	0.817	0.00149	2.047

Figure 2. shows linear sweep voltammograms and Tafel fitting curves of SS, SnO_2-MWCNT and PbO_2-GNR electrode in slightly acid supported electrolyte (0.1 mol·L^{-1} Na_2SO_4, pH 4.2) at applied scan rate 10 mV s^{-1}. The kinetic parameters of OER are given in Table 1. The potential for OER varies significantly on different electrode materials, leading to the significant differences in electrocatalytic activity towards EO of organic molecules. Apparently, the potential for OER of SS, SnO_2-MWCNT and PbO_2-GNR electrodes are in the sequence 1.40, 1.82 and 2.05 V (vs. RHE). This indicates that the OER on the PbO_2-GNR electrode was more difficult to perform, and consequently, has the smallest electrocatalytic activity toward OER. SnO_2-MWCNT showed slightly better activity, but SS electrode has the best electrochemical activity to OER. On the contrary, this means that reaction EO of organic pollutants can be favored on PbO_2-GNR in relation to both investigated electrodes. The exchange current density (j_0) can be used to present the extent to which electrode reactions are blocked. Generally, a larger j_0 value and the smallest Tafel slope (b) imply that OER is more likely to occur. As can be seen in Table 1. the highest j_0 and smallest b, which means the highest electrocatalytic activity to OER, show SS, following SnO_2-MWCNT and PbO_2-GNR electrode.

The obtained results are slightly different than the previously reported results of the other authors which can be explained by the influence of electrode composition, electrolyte composition and concentration, pH, and temperature on OER [6, 7].

CONCLUSION

A comparative analysis of OER kinetic parameters obtained by SS and nanocomposite metal oxide-carbon based anodes in sulphate electrolyte was performed. Particularly, the results indicated that electrode composition is an important factor and significantly affects the parameters of OER. These results provide a starting point for further research in the field application of metal oxide-carbon base anodes for the removal of various organic pollutants by EO in sulfate reach wastewater.

Acknowledgment

This work was supported by the Ministry of Education, Science and Technological Development of the Republic of Serbia; grant number 451-03-68/2022-14/200017.

REFERENCES

[1] A. Kapalka, G. Foti, C. Comninellis in: Electrochemistry for the Environment, Vol.1, C. Comninellis, G . Chen (Eds.), Springer Science+Business Media, LLC, New York, 2010.
[2] M. Panizza in: Electrochemistry for the Environment, Vol.2, C. Comninellis, G . Chen (Eds.), Springer Science+Business Media, LLC, New York, 2010.
[3] Moradi M., Vasseghiana Y., Khataee A., Kobyab M., Arabzade H., Dragoi E., J. Ind. Eng. Chem., 87 (2020) 18.
[4] Savić B., Stanković D., Živković S., Ognjanović M., Tasić G., Mihajlović I., Brdarić T., Appl. Surf. Sci., 529 (2020) 147120.
[5] Kösea H., Aydina A. O., Akbulutb H., Acta Phys. Pol. A, 125 (2014).
[6] Garcıa-Osorio D., Jaimes R., Vazquez-Arenas J., Lara R. H., Alvarez-Ramirez J., J. Electrochem. Soc., 164 (11) (2017) E3321.
[7] Santos D., Lopes A., Pacheco M. J., Gomes A., and Cirıaco L., J. Electrochem. Soc., 161 (2014) H564.

IS IT POSSIBLE TO DESIGN A WATER-RESISTANT MATERIAL FOR CARBON CAPTURE?

D. Vasić Anićijević[1], M. Ječmenica Dučić[1], D. Aćimović[1], B. Savić[1], M. Simić[1], D. Maksin[2] and T. Brdarić[1]

[1]*University of Belgrade, VINČA Institute of Nuclear Sciences - National Institute of the Republic of Serbia, Department of Physical Chemistry, Mike Petrovića Alasa 12-14, 11000, Belgrade, Serbia*
[2]*University of Belgrade, VINČA Institute of Nuclear Sciences - National Institute of the Republic of Serbia, Department of Chemical Dynamics & Permanent Education, Mike Petrovića Alasa 12-14, 11000, Belgrade, Serbia*
(tanja.brdaric@vin.bg.ac.rs)

ABSTRACT
Zeolite based materials are commonly used for carbon capture, as they exhibit satisfactory efficiency in adsorption and desorption of carbon dioxide (CO_2). On the other hand, strong water chemisorption is also a known property of zeolites, so the irreversibly bound water vapor represents a potential problem in CO_2 capturing devices. In this contribution, adsorption of CO_2 and water on a composite zeolite/carbon material was compared, with a potential application in CO_2 capture. Water and CO_2 adsorption properties based on DFT calculated adsorption energies on various crystalline materials were estimated, thus searching for the novel materials that could be more efficient than zeolite in terms of better selectivity for CO_2 and less affinity for water.

INTRODUCTION
Emerging emission and constant increase of CO_2 concentration in the atmosphere, imply a need for urgent implementation of advanced CO_2 capturing technologies. During the last decade, the intensive research was done in field of CO_2 separation from flue gas of major CO_2 emitters: fire coaled power plants, sour natural gas power plants, and syngas plants as well [1]. The facts that any chemical used in a once-through manner to capture CO_2 will rapidly exhaust its global supplies and that any chemical produced from CO_2 as a reactant will rapidly saturate chemical global market [2], underline the necessity for development of novel regenerative capture material.

Zeolite-based materials with high capacity towards CO_2 by adsorption, represent a common choice within CO_2 capture technologies [3]. The energy input for regeneration of the adsorbent is the main criterion for evaluating the cost-effectiveness of CO_2 capture technology [4]. Current strategies include composite materials that are based on commercial zeolites [5] and carbons [6]. The idea is to reduce costs of the regeneration by using the available electric energy from power plants, because the conductivity of carbon component enables efficient adsorbent regeneration by Joule effect [7, 8].

However, a remarkable drawback of zeolite-based composites is their high affinity for water, which is responsible for strong irreversible binding of water vapour from flue gases (10-15 vol. % in power plants) [9]. One possible approach to solve this problem would be finding new, particularly designed adsorbents. Efficient carbon capturing requires highly selective adsorption of CO_2 [10], with little or no adsorption of other combustion gas components (N_2, H_2O).

In this contribution, we pointed a problem that cause non-selectiveness of the state-of-art zeolite-based CO_2 capture materials, since they require drying of the gas mixture prior to the application. In addition, a novel concept to use a DFT screening, in order to design the materials with optimal ratio of CO_2 and H_2O adsorption energies is proposed, that may be further synthetized and examined as remarkably selective adsorbents.

METHODS

Adsorption rates of pure gases (CO_2 and H_2O) were measured in automatic volumetric unit BELsorp-max II (Verder Scientific, Germany).

The composite material was prepared by mixing of 80 wt.% of commercially available zeolite X13 (Chemiewerk Bad Köstriz, Germany) with 20 wt.% of acetylene carbon black (AlfaAesar, Heysham, UK). Carboxymethylcellulose and glycerine were used as binders. Prior to the experiments, composite material was degassed at 150°C under vacuum for a period of 15 h (heating ramp of 2°C/min).

Adsorption rates for both gases were measured at five temperatures, 30°C, 60°C, 90°C, 120°C and 150°C, and at equilibrium pressure of 3.5 kPa. The mass of adsorbent used in the water experiments was smaller in order to reduce the time of measurement (0.2851 g for CO_2 and 0.0804 g for H_2O).

RESULTS AND DISCUSSION

Water chemisorption on zeolite/carbon composite

The adsorption rate of pure CO_2 and H_2O was determined at 30°C, 60°C, 90°C, 120°C and 150°C. The lowest temperature (30°C) was chosen as the highest expectable temperature of flue gases in power plants. The highest temperature (150°C) was chosen as an acceptable limit for material thermo-stability and optimal choice in terms of energy optimization. The other temperatures were examined as expected operational temperatures within CO_2 capture process (during regeneration).

From results (Figure 1. where C, C_{eq} and C_0 represent actual, equilibrium and initial concentration of gas), it is obvious that adsorption rate of water at 30°C is sufficiently higher compared to CO_2: H_2O reaches the equilibrium after approximately 60 s, while equilibrium for CO_2 is not achieved even after 100 s. Very fast decrease of water concentration implies strong binding on adsorption sites in composite. This means that in the case of competitive adsorption such as is separation of flue gases, the water will first occupy available adsorption sites, thus reducing the adsorbent capacity for CO_2.

Similar behaviour is also observed at higher temperatures with the fact that CO_2 adsorption rate increased with increasing temperature of adsorption.

At 150°C adsorption rate of CO_2 and H_2O is approximately equal, which implies that adsorbent regeneration could be difficult in the case of competitive adsorption.

Water adsorption on zeolite involves chemisorption on multiple adsorption sites. For this reason, it is difficult to describe the adsorption rate by any of the simple kinetics models, and the same should be expected for the adsorption isotherms.

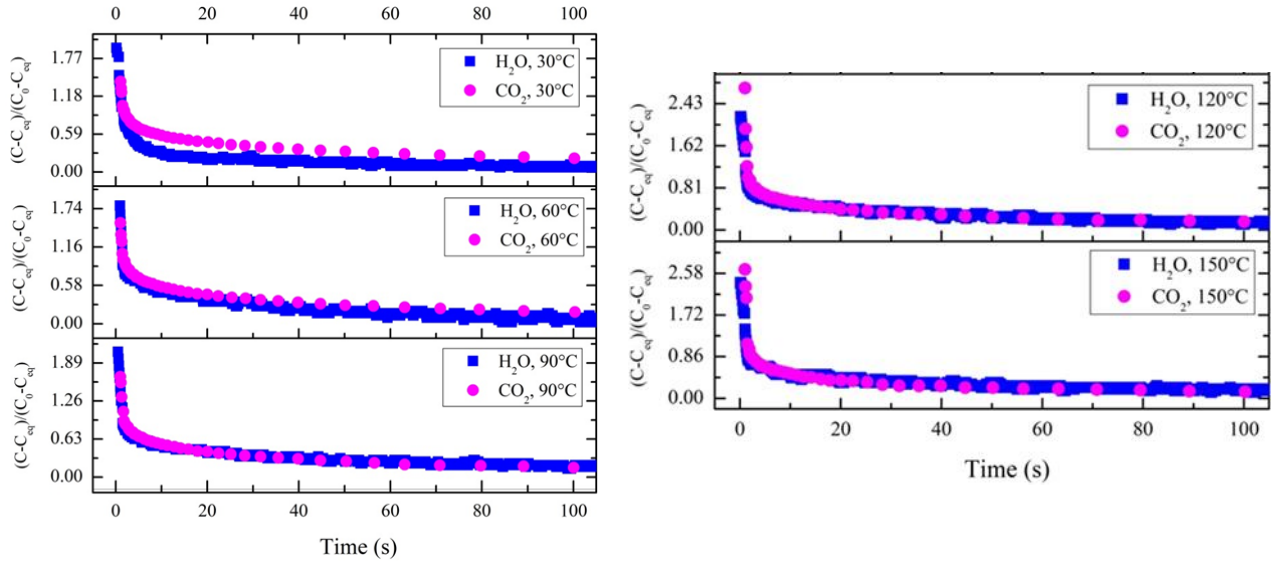

Figure 1. Comparison of adsorption rate of CO_2 and H_2O on zeolite/carbon composite at temperatures 30°C, 60°C, 90°C, 120°C and 150°C.

DFT as a potential screening tool for CO_2 capture materials

Plenty of data on co-adsorption of water and CO_2 on various materials is already available in the literature. Within reported data there are numerous materials with considerably higher affinity for CO_2 than for water (Table 1.) [11-16].

Based on literature data (Table 1.), it is possible to find existing materials with lower affinity for water than for CO_2 adsorption. The DFT calculated adsorption energies of water and CO_2 for materials potentially suitable as adsorbents in CO_2 capture, compared to the corresponding values of zeolite, can serve as a simple and fast criterion. Moreover, there are still plenty of existing materials (for example, MOFs, various dopped carbons etc.), which might be interesting candidates for DFT screening as potential CO_2 capture materials, more selective towards water. Initial design and preparation of the novel materials with controlled H_2O and CO_2 adsorption properties can be guided by DFT calculations. Besides the selectivity, the novel materials should also meet the requirements for CO_2 capture, such as good adsorption capacity or good conductivity.

Table 1. DFT calculated adsorption energies (E_{DFT}) of CO_2 and H_2O on various materials

Material	$E_{DFT,CO2}$, kJ/mol	$E_{DFT,H2O}$, kJ/mol	Reference
As_2O_3	-52	-144	[11]
graphene	-17.9	-20.2	[12]
graphite	-16.5	-14.9	[13]
[a] zeolite (faujasite)	-21 – 36	-58 – 88	[14]
CaO	-243	-146	[15]
Ca_2SiO_4 (olivine)	-82.7	-122.3	[16]
TiO_2(rutile)	-23.6	-10.6	[17]
Al_2O_3	-54.7	-155	[11]

[a] multiple adsorption sites

CONCLUSION

Strong physical and chemical binding of water on zeolites reduces adsorbent capacity for CO_2. The efficiency of regeneration at low temperatures (up to 150°C) is small thus would significantly affect the overall cost-effectiveness of separation process (i.e. CO_2 capture). In further work, the data will be analysed by dynamic model considering the pore diffusion under the batch adsorption operating conditions.

It is possible to define future strategies for the design of novel carbon capture materials, more resistant to water and more selective towards CO_2 compared to currently used zeolites. DFT theory can contribute to the prediction of adsorption properties and guide the sophisticated design of the novel materials.

Acknowldgment

This work was supported by the Ministry of Education, Science and Technological Development of Republic of Serbia (grant number 451-03-68/2022-14/200017).

REFERENCES

[1] Madejski, P., Chmiel, K., Subramanian, N. and Kuś, T., Energies, 15 (2022) 887.
[2] D'Alessandro, D. M., Smit, B. and Long, J. R., Angew. Chem. Int. Ed., 49 (2010) 6058.
[3] Lai, J. Y., Ngu, L. H. and Hashim, S. S., Greenh. Gases: Sci. Technol., 11 (2021) 1076.
[4] A. Cousins, P. Feron, J. Hayward, R. Zhai, K. Jiang, and M. Garcia, Further assessment of emerging CO2 capture technologies and their potential to reduce cost, IEAGHG, Melbourne, 2019.
[5] Khoramzadeh, E., Mofarahi, M. and Lee, C.-H., J. Chem. Eng. Data, 64 (2019) 5648.
[6] Wang, J., Pu, Q., Ning, P. and Lu, S., Greenh. Gases: Sci. Technol., 11 (2021) 377.
[7] Lee, J.-S., Kim, J.-H., Kim, J.-T., Suh, J.-K., Lee, J.-M. and Lee, C.-H., J. Chem. Eng. Data, 47 (2002) 1237.
[8] Regufe, M. J., Ferreira, A. F. P., Loureiro, J. M., Shi, Y., Rodrigues, A. and Ribeiro, A. M., Adsorption, 24 (2018) 249.
[9] Copen, J. H., Sullivan, T. B., Folkedahl, B. C., Weber, G. F. and Carney, B., Proceedings of the International Symposium POWER-GEN, December 6–8th, Las Vegas, Nevada, (2005) 13.
[10] Cheung, O., Bacsik, Z., Fil, N., Krokidas, P., Wardecki, D. and Hedin, N., ACS Omega, 5 (2020) 25371.
[11] Hu, P., Weng, Q., Li, D., Lv, T., Wang, S. and Zhuo, Y., J. Hazard. Mater., 403 (2021) 123866.
[12] Gao, Z. and Ding, Y., J. Mol. Model., 23 (2017) 187.
[13] Rubeš, M., Kysilka, J., Nachtigall, P. and Bludský, O., Phys. Chem. Chem. Phys., 12 (2010) 6438.
[14] Hessou, E. P., Kanhounnon, W. G., Rocca, D., Monnier, H., Vallières, C., Lebègue, S. and Badawi, M., Theor. Chem. Acc., 137 (2018) 161.
[15] Ma, X., Li, Y., Zhang, W., Wang, Z. and Zhao, J., Chem. Eng. J., 370 (2019) 10.
[16] Kerisit, S., Bylaska, E. J. and Felmy, A. R., Chem. Geol., 359 (2013) 81.
[17] Sorescu, D. C., Lee, J., Al-Saidi, W. A. and Jordan, K. D., J. Chem. Phys., 137 (2012) 074704.

SYNTHESIS AND APPLICATION OF WASTE-PET GLYCOLYZATE PLASTISIZER FOR RECYCLED PVC PRODUCTION

M. Vuksanović[1], I.M. Stajčić[1], Z. Veličković[2], J.D. Gržetić[3], F. Veljković[1], S. Veličković[1] and A. Marinković[4]

[1]*University of Belgrade, VINČA Institute of Nuclear Sciences - National institute of the Republic of Serbia, P.O.Box 522, 11001 Belgrade, Republic of Serbia.(ivana_r@vin.bg.ac.rs)*
[2]*University of Belgrade, Military Academy, 11040 Belgrade, Republic of Serbia*
[3]*Military Technical Institute, 11000 Belgrade, Republic of Serbia*
[4]*University of Belgrade, Faculty of Technology and Metallurgy, 11120 Belgrade, Republic of Serbia*

ABSTRACT

Recycling of polymer materials is a promising way of plastic waste reduction and production of compounds that reduce oil-based materials dependence. This paper represents synthesis of waste PET-based plasticizer obtained by esterification of PET depolymerization products (glycolisate) and levulinic (bio-renewable chemical). Depolymerization of the waste PET was performed using diethylene glycol. Morphological and structural analyses confirmed successful depolymerization of waste-PET, as well as esterification of the obtained product with levulinic acid. Good chemical resistance and mechanical properties, *e.g.* elongation at break of 65% and tensile strength of 50 MPa, of recycled PVC modified with synthesized waste-PET based plasticizer proved that depolymerization and modification of waste-PET represent one efficient solution for plastic waste recycling.

INTRODUCTION

The use of polymer-based materials has grown over the last few decades in such manner, that they can be found in every commercial product. As commonly used polymers are not biodegradable, the need for recycling emerged as a solution for plastic waste reduction, in order to protect the environment from pollution [1]. Physical method for recycling involves mechanical treatments, such as cutting, shredding and washing of plastic waste. The resulting product has a shape of granulates, flakes or pellets intended for further processing, which is usually extrusion into desired new product. In order to improve thermal and mechanical stability, the reproduced material can be blended with neat virgin polymer material [2].

Morphological, structural, thermal and mechanical properties of various commercial thermoplastic polymers, such as high-density polyethylene (HDPE), low density polyethylene (LDPE), polyvinyl chloride (PVC), polypropylene (PP) and polyethylene terephthalate (PET) were thoroughly investigated, with the aim of finding the most suitable and efficient recycling method. Polymer blends obtained using recycled PET, PE and PVC represent promising materials from the aspect of morphological and rheological properties [3]. Different blends of the named polymers were created by varying the composition of PET. Each recycled blend contained recycled polymers, with the addition of ethylene propylene diene monomer (EPDM) as a compatibilizer. However, it has been determined that melt flow index (MFI) decreases with the increase of PET concentration in PE/PET/PVC recycled blends. It was also discovered that as the PET content of recycled blends increases, the recycled blends exhibit pseudoplastic behavior [4,5]. Modifications using eco-friendly materials for sustainable applications could enable controllable polymer properties, while at the same time reducing the dependence of oil-based raw materials, which further results in less human impact on the environment [6]. Depolymerization of commercial polymers could result in the production of monomers suitable for industrial-scale polymerization, closing the circle of oil-based materials'

utilization. Furthermore, different products obtained by the controlled decomposition of polymers could be used for the synthesis of eco-friendly plasticizers [7].

This research presents synthesis and characterization of plasticizer obtained by esterification of PET glycolyzates, the product of waste-PET depolymerization, using levulinic acid, the renewable source.

EXPERIMENTAL

MATERIALS

The following materials were used for depolymerization of waste-PET: diethylene glycol - DEG, and Fascat 4100 as a catalyst for the depolymerization reaction. For the esterification of PET-based glycolizates, levulinic acid purchased at Sigma-Aldrich, Germany was used. P-toluenesulfonic acid (from) was used as a catalyst for plasticizer synthesis.

SYNTHESIS OF PET-BASED PLASTICIZER

55 g of DEG and 1.1 g of FASCAT 4100 catalyst were added to a 250 ml three-necked flask equipped with a return condenser and thermometer with vigorous stirring. Then 97 g of PET was gradually added to the flask, raising the temperature to 230/240 ºC with vigorous stirring. The reaction was performed for 9 h. Esterification of waste-PET glycolysate with levulinic acid obtained from natural source was performed in a 250 ml three-necked flask equipped with a Din-Stark nozzle and a thermometer, with azeotropic separation of water from the system by the addition of toluene. 60 g of glycolysate and 65 g of levulinic acid were added. Additionally, 0.64 ml of Fascat 4100 (0.3 wt. %) was added to complete reaction. The reaction was performed at 150 ºC for 3 hours, after what the obtained product, PET/DEG plasticizer was used for PVC recycling.

RECYCLING OF PVC

Waste PVC, provided from RKS Čelarevo ltd, was sieved with a mesh size of 1 mm to 20 mm, and further grinded. The ground PVC waste was dosed into a heating mixer, and the mixing process started at 30 °C. During the mixing, the PET/DEG plasticizer was added to the mixture. When the temperature reached 35 °C, the plasticizer was put to a warm mixer and mixed with waste PVC for up to 5 minutes. When the temperature hits 135 ° C, the batch was emptied into a cool mixer. The hot and doughy mass was changed to a floury form by cooling at 45 °C.

CHARACTERIZATION METHODS

Structural characterization of PET/DEG plasticizer was determined via FTIR spectroscopy using Nicolet™ iS™ 10 FT-IR Spectrometer (Thermo FisherSCIENTIFIC) with Smart iTR™ Attenuated Total Reflectance (ATR) Sam-pling accessories. Spectra were collected in transmittance mode, within a range of 400–4000 cm^{-1}, at a resolution of 4 cm^{-1} and in 20 scan mode.

Elemental analysis (C, H, N) was performed with standard micromethods using ELEMENTAR Vario EL III CHNS/O analyzer. Determination of mechanical properties was done using AG – X ripper plus Universal testing machine, Shimadzu.

RESULTS AND DISCUSSION

FTIR spectrum of the plasticizer obtained by the levulinic acid esterification of PET/DEG-glycolyzate is shown on Figure 1. The strong peak at around 1713 cm^{-1} confirmed the presence of ester carbonyl group.

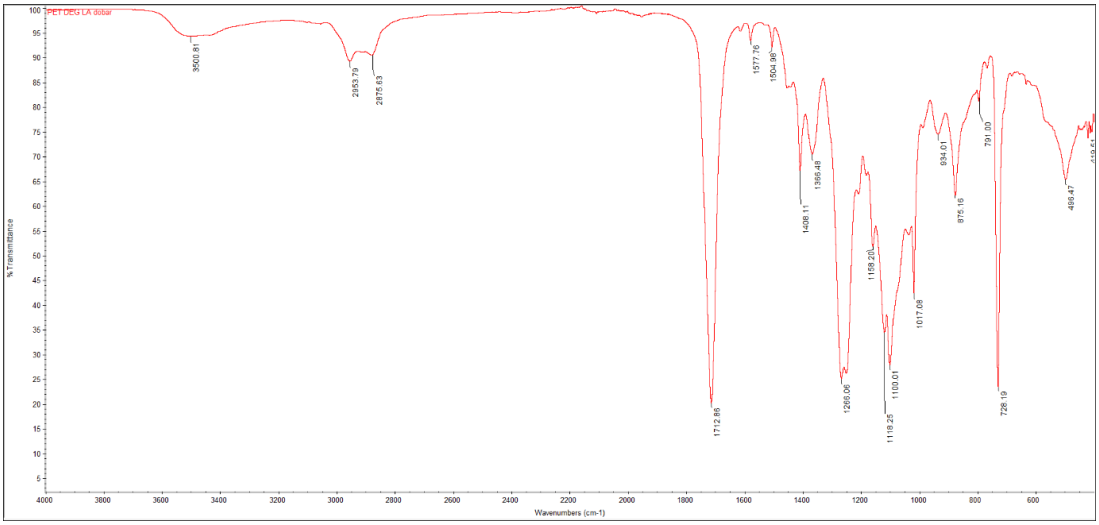

Figure 1. FTIR spectrum of the obtained plasticizer by modification with levulinic acid After two days, the layer on top of the receiving court separated.

Relevant PET/DEG plasticizer structure is presented on Figure 2. Composition of modified PET glycolyzate was in agreement with the expected structure. Determined elemental analysis showed the following composition (experimental): C, 58.33; H, 6.01; O 35.66; (calculated): C, 58.29; H, 6.12; O, 35.59

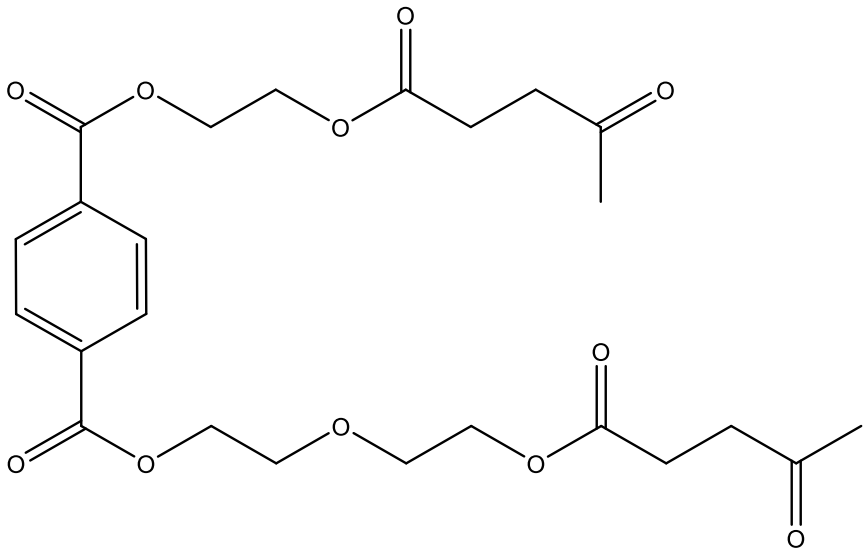

Figure 2. Proposed structure of plasticizer obtained by PET modification with levulinic acid

Table 1 shows comparison of chemical and mechanical properties of the neat recycled PVC and waste PVC recycled using PET/DEG plasticizer. Mechanical properties of modified PVC are significantly improved, making synthesized waste-PET plasticizer a potential candidate for application in thermoplastic commercial polymers.

Table 1. Comparison of chemical resistance and mechanical properties of recycled PVC and recycled PVC/plasticizer from waste PET with the weight ratio 5:1

Chemical resistance		
	Recycled PVC	**Recycled PVC/waste-PET plasticizer**
Acids - concentrated	Good	Good
Acids - diluted	Good	Good
Alcohol	Good	Good
Bases	Good	Good
Aromatic hydrocarbons		
Fats and oils	Good	Good
Halogens	Good	Good
Ketones	Good	Good
Mechanical properties		
Elongation ASTM D638 (%)	92	65
Tensile strength ASTM D638	53 MPa	50 MPa
Bending resistance ASTM D790	59 MPa	49 MPa
Compressive strength ASTM D695	55 MPa	50 MPa
Shor hardness	70	109
Izod toughness (J m^{-1})	24	23

CONCLUSION

Successful esterification of the PET/DEG glycolyzate with levulinic acid from natural sources was confirmed by elemental analysis. Compositional analysis was in accordance with the expected structure. Chemical and mechanical properties showed that the use of waste and bio-based plasticizers has a promising future for modification of recycled PVC and presumably similar thermoplastic polymers.

Acknowledgment

This work was partially supported by the Ministry for Science of the Republic of Serbia (Contract No 451-03-9/2022-14/200017,451-03-9/2022-14/200325 and 451-03-68/2022-14/200135).

REFERENCES

[1] N.M.Özgül, M.Y. Savaşçin, İ.Özkanc,Acta Phys. Pol. A, 132 (2017) 430-443.
[2] M.E.Grigore, Recycling, 2017, https://www.mdpi.com/2313-4321/2/4/2.
[3] G.M.Mamoor, W. Shahid, A. Mushtaq, U. Amjad, U. Mehmood, Chem. Eng. Res. Bull., 16 (2013) 25-32.
[4] Francesco La Mantia, Handbook of Plastics Recycling, iSmithersRapra Publishing, 2002.
[5] S. Levy, J. F. Carley, Plastics Extrusion Technology Handbook, Industrial Press Inc., 1989.
[6] T. O.Azeezin Thermosoftening Plastics, Thermoplastic Recycling: Properties, Modifications, and Applications, G. A. Evingür (Ed.), InTechOpen, 2020.

MODIFYING MESOPOROUS SBA-15 BY A MICROENCAPSULATION METHOD IN THE MATRIX OF SODIUM ALGINATE

M. Kokunešoski[1], M. Pošarc-Marković[1], Dj. Katnić[1], Z. Baščarević[2], S. Ilić[1], A. Grce[1] and A. Šaponjić[1]

[1]University of Belgrade Institute of Nuclear Sciences "Vinča", National Institute of the Republic of Serbia, Mike Petrovića Alasa 12-14, Vinča, 11000 Belgrade, Serbia. (majako@vin.bg.ac.rs)
[2]Institute for Multidisciplinary Research, University of Belgrade, Kneza Višeslava 1, 11030 Beograd, Serbia.

ABSTRACT
The present work represents hydrogel as a composite based on sodium alginate and mesoporous SBA-15. The hydrogel was obtained by modifying mesoporous SBA-15 by a microencapsulation method of the SBA-15 in the sodium alginate matrix. The solution of $CaCl_2$ provided a gelation complex of sodium alginate/SBA-15 in a rigid gel-like structure. The sodium alginate/SBA-15 hydrogels beads of about 3 mm diameter were prepared. Composite material was characterized by using powder X-ray diffraction, scanning electron microscopy and energy dispersive X-ray analysis. This composite material may have potential application in removal of metal ions – pollutants from aqueous solutions.

INTRODUCTION
Mesoporous silica materials such as SBA-15 received considerable attention because of their unique large surface area, well-defined pore size and pore shape [1, 2].

Studies have shown that remarkable surface porosity and functionality strongly affect the properties and efficiency of this material and its applications as drug and gene carrier [3, 4-7], material for enzyme loading [8] as well as material for detection and adsorption of metal ions in living systems [3, 9]. Various procedures have been employed on SBA-15 to improve its adsorption capacity [10]. However, the application of SBA-15 has some limitations due to the difficulty of incorporating functional groups on its surface. These limitations can be overcome by encapsulation of mesoporous silica with alginate.

Development of the hydrogel was driven by the idea to modify the mesoporous SBA-15 by a microencapsulation method with alginate used to protect them from degrading by surrounding them with a semi-permeable biopolymeric matrix. Microencapsulation avoids or retarding their contact with, for example, harmful environmental factors.

Alginate is extracted from various species of algae. Alginate is composed of the linear macromolecule in homopolymeric blocks of each monomer. The macromolecules are composed of (1-4)-linked b-D-man urinate (M) and a- L-guluronate units (G). Properties like low cost, easy use, biodegradability, and biocompatibility make alginate suitable for encapsulation. In the presence of divalent cations, usually, Ca^{2+} alginate is gelling in the form of a rigid gel-like structure, by ion exchange of sodium ions from guluronic acid residues [11-13].

METHODS
Sodium alginate (SA, abcr GmbH), calcium chloride anhydrous powder ($CaCl_2$, 99.99 %, Sigma Aldrich), Pluronic P_{123} non-ionic triblock copolymer (BASF), tetraethoxysilane (TEOS, 98%, Alfa Aesar) hydrochloric acid and (HCl, 35-38%, MACRON) were used.

The SBA-15 was synthesized according to standard procedures [14] using Pluronic P_{123} as a surfactant and TEOS as a source of silica. A 4.0 g of Pluronic P_{123} dissolved in 30 ml of distilled water and 120 g of 2M HCl and stirred at 35 °C for 1.5 h. The 8.5 g of TEOS was added dropwise

into the solution and vigorously stirred at the same temperature for 1.5 h. This was followed by prolonged stirring and subsequent ageing. According to the method proposed by Zhao et al. [14], the mixture was aged in two steps. Firstly, it has aged at 35 °C for 20 h and then at 80 °C for 48 h. The final product is filtered, washed with distilled water until pH was neutral, and dried at room temperature. Calcination has been carried out in flowing air by slowly increasing the temperature from room temperature to 500 °C for 8 h and holding it at 500 °C for 6 h to decompose the remaining triblock copolymer.

Fabrication of sodium alginate/SBA-15 hydrogels in the form of beads (SA/SBA-15) was done. The suspension of 1.5 g of SBA-15 powder and 15 ml distilled water was sonicated for 30 min. One and a half grams of alginic acid sodium salt (SA) was added to 110 mL of water at 35 °C while stirring. The suspension of SBA-15 was added into alginate and then homogenized on a magnetic stirrer (600 rpm) for 2 h at 35 °C.

The obtained new suspension was added in drops into $CaCl_2$ solution through a Pasteur pipette as the next step of synthesizing beads. Gel-type spherical beads were formed during this process. After 3 h of gelation, beads were filtrated and washed with distilled water until pH was neutral. The size of wet beads after filtration was about 3 mm (Figure 1a). After drying at 60 °C, the size of hydrogel beads was about 2 mm. Aqueous $CaCl_2$ solution was prepared by dissolving 0.623 g of $CaCl_2$ in 50 ml distilled water under stirring to neutralize the carboxyl-site covalent bond of alginate with the intention to induce inter-molecular ionic bonds between polymeric chains of alginate [11-13].

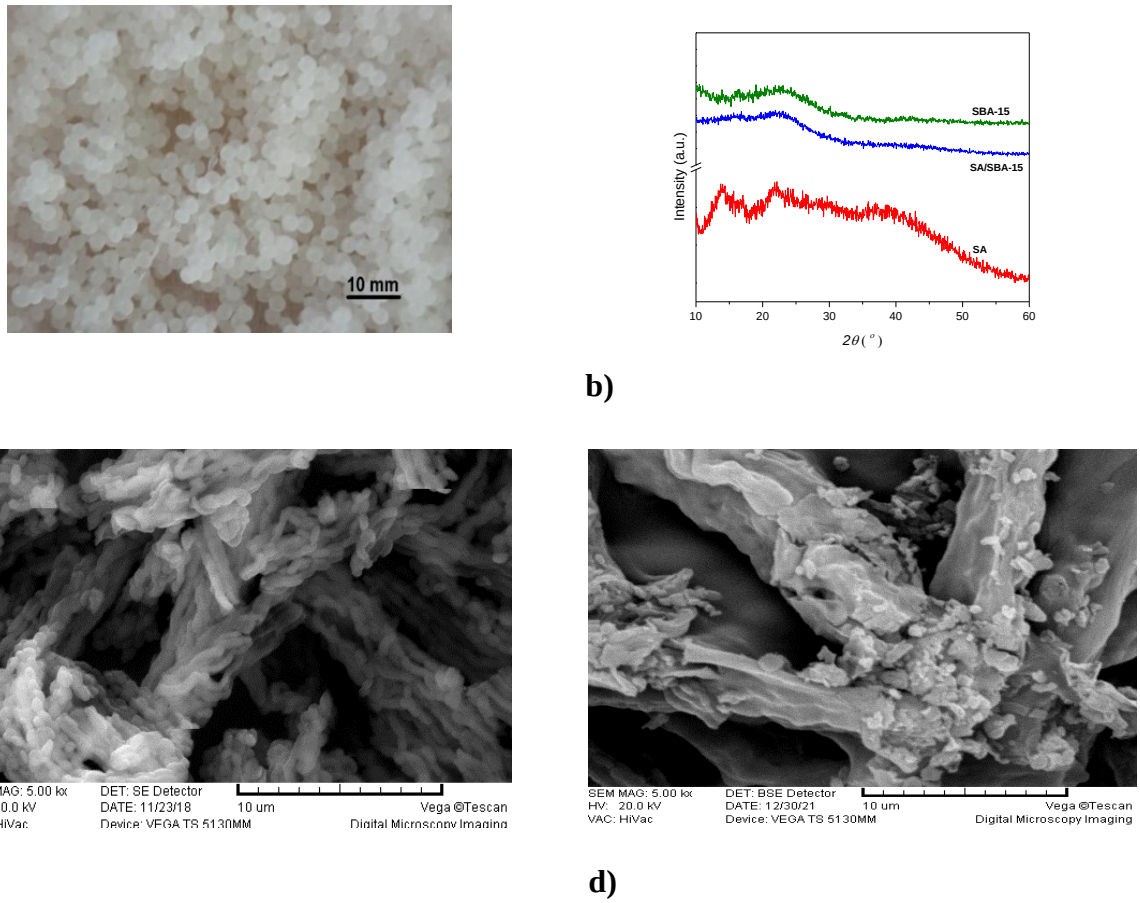

Figure 1. a) Beads of sodium alginate/SBA-15 hydrogel (SA/SBA-15), **b)** XRD patterns of: SBA-15, SA/SBA-15 and SA and SEM images of **c)** SBA-15 and d**)** SA/SBA-15.

X-ray diffraction (XRD) analysis of SBA-15, SA/SBA-15 and SA was performed at room temperature using Ultima IV Rigaku diffractometer, equipped with Cu $K_{\alpha 1,2}$ radiations, with generator voltage 40.0 kV and generator current 40.0 mA. The range of 10°-60° 2Θ was used in a continuous scan mode with a scanning step size of 0.02° at a scan rate of 10 °/min. Microstructure analysis is performed by scanning electron microscope (SEM, VEGA TS 5130 MM, Tescan). Energy-dispersive X-ray analysis (EDS) was carried out with INCA PentaFET-x3, Oxford Instruments.

RESULTS AND DISCUSSION

The XRD patterns of SBA-15, SA/SBA-15 and SA are shown in Figure 1b. Samples SBA-15 and SA/SBA-15 exhibit a single very broad peak at about 2θ = 23°, which is the characteristic of amorphous silica. In contrast, XRD of the SA pattern exhibits very broad peaks at about 2θ = 14° and 22°.

A glimpse at the SEM micrographs of SBA-15 and SA/SBA-15 and (Figure 1c and Figure 1d) discloses the presence of many rod-like agglomerates were approximately 20 μm in length in all studied samples. As the SEM images showed, the average size of grains in all samples was about 1 μm, in which particles have placed themselves along the agglomerated ones like chains. Same chain agglomerate structures (Figure 1c) were reported in an earlier paper [15, 16].

The EDS analysis showed the chemical composition of SBA-15, SA/SBA-15 and SA. The EDS analysis demonstrated that the particles in the SBA-15 sample consist of SiO_2. High levels of carbon (~ 36 at. %) and oxygen (~58 at. %) originate from gases from the air adsorbed by the surface of the SBA-15 [17].

The EDS analysis of SA and SA/SBA-15showed the presence of C, O, Na, K and Cu in SA (Table 1.) and confirmed the presence of C, O, Si, Cl, and Ca in the sample SA/SBA-15. Elements Ca, and Cl originates from $CaCl_2$ solution, used as an agent for sphere formation. However, high levels of carbon (~22 at. %) and oxygen (~59 at. %) originated from SA and air adsorbed by the surface of the samples.

Table 1. Average values of the chemical composition of SA and SA/SBA-15, obtained by EDS analysis (atomic %).

Sample	C	O	S_i	N_a	Cl	K	C_u	C_a	A_g	A_u
SA	56.38	32.56	-	10.21	0.13	0.11	0.11	-	0.08	0.35
SA/SBA-15	21.50	58.71	17.28	-	0.07	-	-	1.65	0.10	0.67

CONCLUSION

Composite hydrogel based on sodium alginate and mesoporous SBA-15 was synthesized by a microencapsulation method of the SBA-15 in the sodium alginate matrix. A gelation complex of sodium alginate/SBA-15 is a form rigid gel-like structure was provided by the solution of $CaCl_2$. The sodium alginate/SBA-15 hydrogels were obtained in the form of beads of about 3 mm in diameter. The X-ray diffraction patterns of SBA-15, SA/SBA-15 and SA exhibit a single very broad peak, which is the characteristic of amorphous silica. A scanning electron microscope discloses that many rod-like agglomerates of all investigated samples were approximately 20 μm in length. As the scanning electron microscope images show, the average size of grains of all investigated samples is about 1 μm. The Energy-dispersive X-ray analysis of the SBA-15 surface content has demonstrated that the particles in this sample are of SiO_2. We intend to investigate the possibility of using the obtained hydrogels of sodium alginat/SBA-15 in the form of pearls to remove metal ions from an aqueous solution.

Acknowledgment
This work was supported by the Ministry of Education, Science and Technological Development of the Republic of Serbia (grant no 451-03-68/2022-14/200017).

REFERENCES

[1] Kresge, C. T., Leonowicz, M. E., Roth, W. J., Vartuli, J. C., Beck, J. S., Nature 359 (1992) 710.
[2] Beck, J. S., Vartuli, J. C., Roth, W. J., Leonowicz, M. E., Kresge, C. T., Schmitt, K. D., Chu, C. T. W., Olson, D. H., Sheppard, E. W., McCullen, S. B., Higgins, J. B. and Schlenker, J. L. J. Am. Chem. Soc., 114 (1992) 1083.
[3] Babić, B., Kokunešoski, M., Miljković, M., Prekajski, M., Matović, B., Gulicovski, J., Bučevac, D., Ceram. Int., 38 (2012) 4875.
[4] Lee, K., Lee, D., Lee, H., Kim, C.K, Wu, Z., Lee, K., Korean J. Chem. Eng., 27 (2010) 133
[5] Valet-Regi, M., Balas, F., Arcos, D., Angew. Chem. Int. Ed., 46 (2007) 7548.
[6] Manzano, M., Aina, V., Arean, C. O., Balas, F., Cauda, V., Colilla, M., Delgado, M.R., Vallet-Regi, M., Chem. Eng. J., 137 (2008) 30.
[7] Lai, C. Y., Trewyn, B. G., Jeftinija, D. M., Jeftinija, K., Xu, S., Jeftinija, S., Lin, V. S. Y., J. Am. Chem. Soc., 125 (2003) 4451.
[8] Nozawa, K., Shoji, A., Sugawara, M., Supramol. Chem., 22 (2010) 389.
[9] Meng, Q., Zhang, X., He, C., He, G., Zhou, P., Duan, C., Adv.Funct. Mater., 20 (2010) 1903.
[10] Boukoussa, B., Mokhtar, A., El Guerdaoui, A., Hachemaoui, M., Ouachtak, H., Abdelkri, S., Ait Addi, A., Babou, S., Boudina, B., Bengueddach, A., Hamacha, R., J. Mol. Liq., 333 (2021) 115976.
[11] Lozano-Vazquez, G., Lobato-Calleros, C., Escalona-Buendia, H., Chavez, G., Alvarez-Ramirez, J., Vernon-Carter, E.J., Food Hydrocolloids, 48 (2015) 301.
[12] Ramdhan, T., Su Hung, C., Prakash, S., Bhandari, B., Food Hydrocolloids, 90 (2019) 232–240.
[13] Kosari, M., Sepehrian, H., Fasihi, J., Arabieh, M., Study, K., J. Appl. Chem. Res. 11 (2017) 135.
[14] Zhao, D., Feng, J., Huo, Q., Melosh, N., Fredrickson, G. H., Chmelka, B. F., Stucky, G. D. Science, 279 (1998) 548.
[15] Kokunešoski, M., Gulicovski, J., Matović, B., Babić, B., J. Optoelectron. Adv. M., 11 (2009) 1656.
[16] Wang, Z., Huang, Y., Wang, M., Wu, G., Geng, T., Zhao, Y., Wu, A., Macroporous calcium alginate aerogel as sorbent for Pb^{2+} removal from water media, J. Environ. Chem. Eng., 4 (3) (2016) 3185.
[17] Kokunešoski, M., Gulicovski, J., Matović, B., Logar, M., Milonjić, S. K., Babić, B., Mater. Chem. Phys. 124 (2010) 1248.

SILICON NITRIDE BASED POWDERS OBTAINED BY CARBOTHERMAL REDUCTION AND NITRIDATION OF DIATOMITE

A. Šaponjić[1], M. Kokunešoski[1], S. Ilić[1], A. Radosavljević Mihajlović[2], T. Barudžija[1] and B. Matović[1]

[1] Institute of Nuclear Sciences "Vinča", National Institute of the Republic of Serbia, University of Belgrade, Serbia (acavuc@vin.bg.ac.rs).
[2] Institute for nuclear technology and other raw materials, Franche D Epere 86, 11000 Belgrade, Serbia.

ABSTRACT

The possibilities of obtaining nanoparticles of non-oxide ceramic powders of silicon nitride (Si_3N_4) by the method of carbothermal reduction and nitriding of diatomaceous earth, a natural bio-amorphous raw material of low crystallinity, were investigated in this paper. Activated carbon was used as a carbon source. In order to obtain better quality Si_3N_4 powder in a faster and more efficient way, commercial α-Si_3N_4 powder was introduced into starting mixtures. The starting mixtures of diatomaceous earth, activated carbon, and differnt amounts of commercial α-Si_3N_4 powder (5, 10, 15, and 20) wt.% were thermally treated for 2 h at 1350 and 1450 ºC. The obtained powders were characterized by the following methods: X-ray diffraction (XRD), infrared spectroscopy with Fourier transform (FTIR) and scanning electron microscopy (SEM).

INTRODUCTION

Due to unique combination of properties, such as high temperature stability, thermal shock resistance, high hardness and toughness and wear and corrosion resistance, silicon nitride (Si_3N_4) powder is important for the production of specific structural materials that pave the way for widespread use in different fields of engineering [1]. One of the most promising methods for production of the non-oxide ceramic powders with important technical uses is carbothermal-reduction reaction (CRR). The process of carbothermal reduction and nitridation (CTRN) is a reaction between a mixture of carbon and SiO_2 precursors in a flow atmosphere of N_2 in the temperature range of 1400-1500°C [2-4]. The final product obtained by this method depends on a number of factors: C / SiO_2 ratio, nitrogen flow rate, reaction temperature, SiO_2 and C particle sizes, as well as their specific surfaces, impurities, etc. This procedure offers the possibility of an economically attractive production route from naturally occurring materials, while obtaining homogeneous fine (nano range) powders [5-11]. Diatomite is a siliceous, sedimentary rock consisting principally of the fossilized skeletal remains of diatom, a unicellular aquatic plant related to the algae. The silica of fossilized diatom skeleton closely resembles opal or hydrous silica in composition (SiO2•nH2O) [9]. In addition, they consist of small amounts of associated organic components, alumina, and even smaller amounts of iron, alkaline earth, and alkali metal oxides. These oxides help to promote the conversion process by formation of liquid phase with a low melting point, thus significantly decreasing the temperature of carbothermic reduction and nitridation reactions. In our previous work it was shown that diatomaceous earth, due to its chemical composition, genesis and submicrometer particle size and porosity, can be successfully used to obtain non - oxide powders (Si_3N_4, SiC, and Si_3N_4,/ SiC) [12]

In this paper, the effect of the amount of silicon nitride seeds on the phase composition of synthesized powders was first preliminarily examined. Diatomaceous earth was used as source of silica, activated carbon as a carbon sources. Commercial powder, α-Si_3N_4 used as a seed, was added in starting mixtures as nucleation centers in order to accelerate reactions that occur during the process of carbothermal reduction and nitridation, as well as to obtained fine silicon nitride powder.

METHODS

The used raw material was a diatomaceous earth of Serbian origin (Kolubara, basin). Diatomaceous earth was chemically treated with a 1 M HCl (p.a. 37%, BDH Prolabo) in order to reduce the content of iron oxide Fe_2O_3. The chemical composition of raw diatomaceous earth includes: SiO_2-73.68, Al_2O_3-12.28, Fe_2O_3-3.29, CaO-0.72, MgO-0.44, Na_2O- 1.01, K_2O-0.12 and loss of ignition (8.26).The chemical compositions of chemically treated diatomaceous earth are determined by classical chemical methods. It was shown that its main composition includes (in wt%): SiO_2-76.58, Al_2O_3-11.34, Fe_2O_3-1.72, CaO-1.22, MgO-0.44, Na_2O- 0.9, K_2O-0.11and loss of ignition (7.13).

Starting mixtures, chemically diatomaceous earth (hereafter d.e.) and the carbon source were homogenized in a FRITSCH-Pulverisette 9 vibratory mill for 2 hours in a tungsten carbide (WC) vessel with an engine speed of 900 min-1. Industrially obtained activated carbon of domestic producer (Miloje Zakić-Kruševac) was used as a source of carbon, with constant C/SiO_2 ratio = 5. The appropriate molar ratio of carbon to d.e., (C/SiO_2) was preliminarily investigated without seeds designated as Starting sample (hereafter S.s.). Commercial powder Si_3N_4 (H. Starck LC 12-SX, as seeds) was subsequently homogenized with starting mixtures, 1 hour in a vibro mill in the presence of distilled water. Prepared samples were designated as I-5, I-10, I-15 and I-20 representing the mixtures of diatomaceous earth, activated carbon and (5, 10, 15, and 20) wt.% α-Si_3N_4 seeds. The samples were heated at two temperatures 1350 and 1450 ºC for 2 h, in the controlled argon flow atmosphere. The argon flow was kept during cooling until 200 ºC.

The reaction products were analyzed by X-ray diffraction analysis, infrared spectroscopy, and scanning electron microscopy. Sample powders, recorded on a diffractometer which is part of the SIEMENS D500 automated system. Diffractograms were recorded with CuKα radiation (λ = 1.54184 Å), at a current in an X-ray tube of 20 mA and a voltage of 35 kV, passed through a Ni-filter. The morphology of the powders was examined with a scanning electron microscope JEOL JSM-3500, an electron beam with a diameter below 1 μm at a voltage of 30 keV. Prior to analysis, the powder samples were steamed with gold.

RESULTS AND DISCUSSION

In X-ray diffraction patterns of S.s. powders obtained by thermal treatment at 1350 ºC and 1450 ºC, (2 h) reflections characteristic for SiC, β-Si_3N_4 (d values: 3.29; 2.65 and 2.49 Å), β′-sialon, and cristobalite were observed. As for samples designated as I-5, I-10, I-15, and I-20 shown in Figure 1 b), weak and diffuse peaks with d values: 4.32; 3.88; 3.37; 2.89; 2.60, 2.55, 2.32, 2.16, and 2.08 Å for sample I-5 originate from α-Si_3N_4. Reflections characteristic for SiO_2 modification, cristobalite (d values: 4.07 and 2.51 Å) are observed. The presence of cristobalite represents unreacted SiO_2 from diatomaceous earth and indicates that under these conditions carbothermal reduction and nitration is not compleete. As can be seen from the presented diffractograms, the intensity of peaks characteristic of α-Si_3N_4 increased with increasing content of α-Si_3N_4, which is expected.

The transformation products at 1450 °C (Figure 1 c, sample I-5) showed very strong α-Si_3N_4 peaks, followed by the reflections of β-Si_3N_4 and of β′-sialon ($Si_3Al_3O_3N_5$) (d values: 3.32; 2.72 and 2.51 Å). Increasing amount of introduced seeds to 20 wt.% did not produced any further increase in reduction and nitridation. This is explained by partial melting of diatomite at this temperature. Thus micro-porous structure was harmed and surface area dramatically reduced with the presence of liquid phase which resulted in decrease in the transport of reaction gases [8]. At 1450 ° C, similar results were obtained for all seeded samples showing the XRD peaks of β-Si_3N_4 and β′-sialon ($Si_3Al_3O_3N_5$) were weaker. Under, normal conditions, α-Si_3N_4 was produced by CTRN process, but liquid phases of oxides such as Na_2O, K_2O, MgO, CaO and Fe_2O_3 contained in the diatomite occurred due to eutectic reaction, led to the formation of β-Si_3N_4 instead of α-Si_3N_4 (8,12,13).

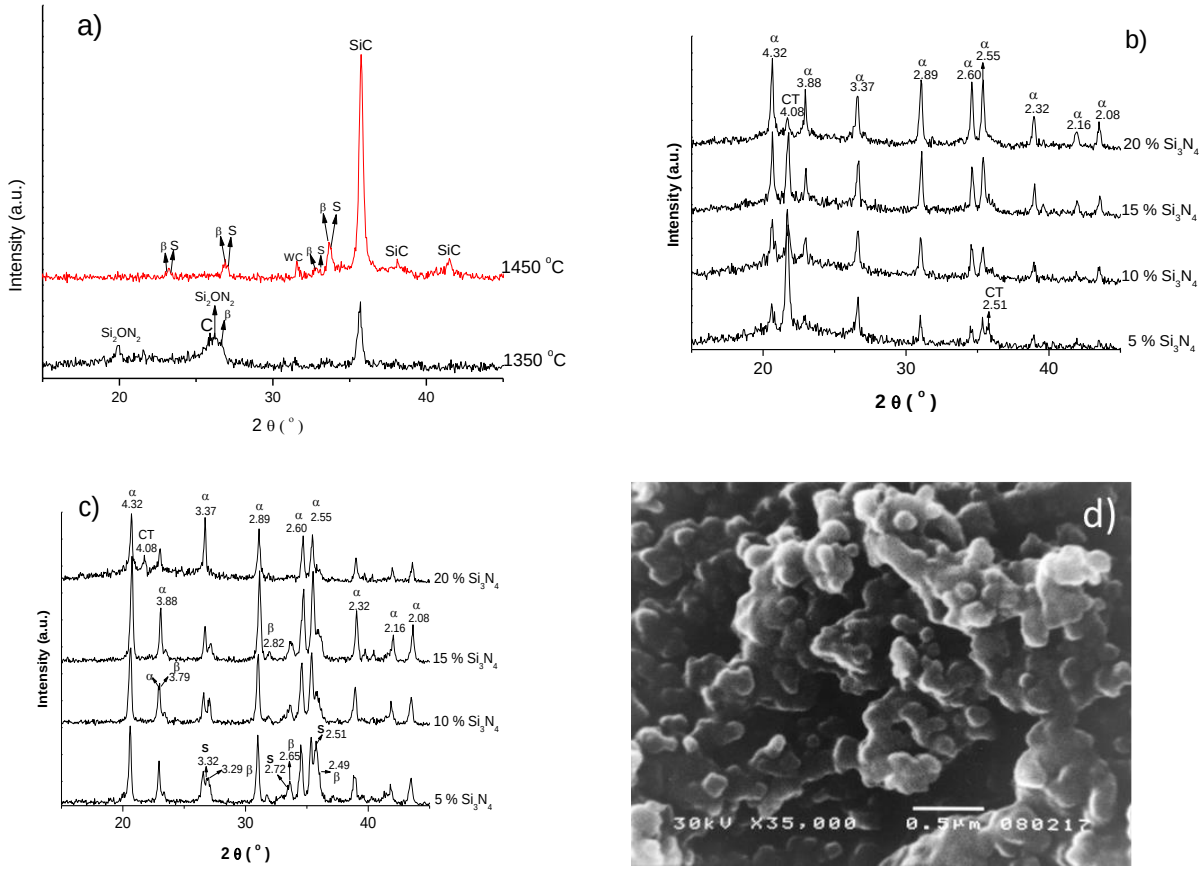

Figure 1. Comparative X-ray diffractograms of powders obtained by thermal treatment of a S.s. (a), samples I-5, I-10, I-15 and I-20 at 1350 ºC (b), at 1450 ºC (c) and SEM, I-20: 1450 °C d). α – α -Si_3N_4; β – β - Si_3N_4; CT – cristobalite; S- $Si_3Al_3O_3N_5$.

The morphological characteristics are given for selected characteristic powder obtained at 1450°C (sample I-20, Figure 1 d). The powder consisted of very fine particles of nanometer dimensions, agglomerated but with a polygonal habitus, which is characteristic for silicon nitride crystals.

CONCLUSION

Non oxide powders based on silicon nitride were prepared by using an inexpensive method carbothermal reduction and nitriding of chemically diatomaceous earth and activated carbon as a source of carbon various source of carbon which were thermally treated for 2 h at 1350 and 1450 ºC.

From the results obtained by X-ray diffraction analysis, it can be concluded that the content of α-Si_3N_4 increased with the addition of commercial powder up to a certain amount of α-Si_3N_4 seeds. The onset of β-Si_3N_4 crystallization at 1450 ºC was observed at content of 5 wt.% of commercial α-Si_3N_4 powder. At lower sintering temperature, the reaction products were a mixture of SiO_2 and α-Si_3N_4. Powders obtained at higher temperature were a mixture of α-Si_3N_4, β-Si_3N_4, and of β′-sialon ($Si_3Al_3O_3N_5$), with recognizable and well-defined crystal geometry of silicon nitride.

Acknowledgment

This research was funded by the Ministry of Education, Science and Technological Development of the Republic of Serbia. Grant no. 451-03-68/2022-14/200017.

REFERENCES

[1] Schwartz, M. M. (1992): Handbook of structural ceramics, McGraw-Hill.
[2] Hofmann, Heinrich, Vogt, U.; Kerber, A.; van Dijen, F 287 (1993) 105–120 MRS Proceedings.
[3] Ličko, T., Figusch, V.& Púchyová, J. Eur. Ceram. Soc. 9 (1992) 219.
[4] Li, J., Tian, J., Dong, L., J. Mat. Sci. Lett. 19 (2000) 1767.
[5] Kljajević, Lj., Šaponjić, A., Ilić, S., Nenadović, S., Kokunešoski, M., Egelja, A., Devečerski, A., Ceram. Int. 42 (2016) 8128.
[6] Ashkin, D. J. Eur. Ceram. Soc. 17 (1997) 1613.
[7] Kurt, A. O., Davies, T. J. J. Mat. Sci. 36 (2001) 5895.
[8] Arik, H. J. Eur.Ceram. Soc. 23 (2003) 2005.
[9] Hadjar, H., Hamdi, B., Jaber, M., Brendlé, J., Kessaïssia, Z., Balard, H. And Donnet, J.B. Microporous Mesoporous Mater. 107 (2008) 219.
[10]Mazzoni, A.D., and Aglietti, E.F., Mater. Chem. and Physics, 37 (1994) 344.
[11]Mizuhara, Y., Noguchi, M., Ishihala, T., Satoh, A., J Am Ceram SOC, 74 (1991) 846.
[12]Šaponjić, A., Matović, B., Babić, B., Zagorac, J., Poharc-Logar, V., Logar, M., Optoel. advan. mater. – rap. comm. Vol., No. 11, November 4 (2010) 1681.
[13]Šaponjić, A., Babić, B., Devečerski, A., Matović, B., Sci. Sint., 41 (2009) 151.

PHYSICO-CHEMICAL CHARACTERIZATION OF BI-LAYERED Au-PNiPAAm/PVA HYDROGEL NANOCOMPOSITES

N. Nikolić, A. Radosavljević, J. Spasojević, U. Stamenović, V. Vodnik, J. Tadić and Z. Kačarević-Popović

Vinča Institute of Nuclear Sciences - National Institute of the Republic of Serbia, University of Belgrade, Mike Petrovića Alasa 12-14, 11351 Vinča, Belgrade, Serbia (nnikolina@vin.bg.ac.rs)

ABSTRACT

In this study, bi-layered hydrogel nanocomposites, based on gold nanoparticles (AuNPs) embedded in poly(*N*-isopropylacrylamide) (PNiPAAm) and poly(vinyl alcohol) (PVA) hydrogel were developed. PNiPAAm with AuNPs represents an active, while PVA represents a passive layer. Crosslinking of polymer matrix with stable 3D structure was obtained by the combination of freeze-thaw and radiolytic methods, while nanoparticles were synthesized using the seed-mediated approach. The UV-Vis absorption spectra and TEM measurements confirm the presence of spherical AuNPs, with a diameter of 30 nm. The influence of AuNPs on the swelling/deswelling behavior and on volume phase transition temperature (VPTT) in distilled water was investigated. The obtained results showed that values of network and diffusion parameters increase with the incorporation of AuNPs and that the swelling transport mechanism is a non-Fickian transport.

INTRODUCTION

Hydrogels are hydrophilic three-dimensional polymeric networks that absorb and retain large amounts of surrounding water while their structure remains stable. Because they are soft materials that contain a significant amount of fluid, they simulate specific properties of bending, shrinking, and changing the shape [1]. Significant progress has been made in the development of multi-layered hydrogels in recent decades. Bi-layered hydrogels could be manufactured as promising biomaterials for soft robotics and medical applications due to their simplicity, versatility, and robustness. Bi-layered hydrogels combine two chemically different hydrogels of stable structures to obtain a material that retains the properties of the basic components but also a material with new, improved properties due to the organization of various functional layers [2]. Among other hydrogels, the thermosensitive poly(*N*-isopropyl acrylamide) (PNiPAAm) is the most studied since undergoes reversible phase transitions at a specific temperature defined as the volume phase transition temperature (VPTT). Poly(vinyl alcohol) (PVA) is a synthetic, water-soluble polymer with a stable 3D structure, porosity, swelling capacity, biodegradability, nontoxicity, and good mechanical properties. These properties, which are widely variable and readily modified, make PVA appropriate for a wide range of applications in different fields such as medicine, pharmaceutics, and robotics [1,3,4]. On the other hand, metal nanoparticles (NPs) exhibit unique optical, chemical, catalytic, and electronic properties, and their presence can improve the existing characteristics of hydrogels and add new ones. The AuNPs/PNiPAAm composite hydrogels possess thermosensitivity as the specific property of PNiPAAm, which can be used to modulate the unique properties of AuNPs. In addition, the photothermal effect of AuNPs supports the composite hydrogels with a light-sensitive character due to their surface plasmon resonance (SPR). Consequently, these smart materials can produce a reversible mechanical deformation under light stimuli. Hydrogel photoactuators represent a relatively new class of composite materials with unique properties and potential applications in various fields, including medicine, microfluidics, and robotics. The synergistic effects of nanoparticles and hydrogel matrices ensure the control of optical, catalytic, and mechanical properties but also specific

advantages such as mimicking human functionality, adaption in aqueous environments, and simple designs [5].

In this research, thermosensitive poly(N-isopropyl acrylamide) (PNIPAm), as the active layer, and non-thermosensitive poly(vinyl alcohol) (PVA) were combined to create a material with an appropriate coefficient of thermal expansion between the layers. Together with gold nanoparticles (AuNPs) embedded in the active layer, these materials have potential applications in soft robotics, artificial muscles, and smart devices.

METHODS

A colloidal dispersion of AuNPs was prepared in a simple process of Au^{3+} ions reduction by sodium citrate, as a reducing and stabilizing agent [6]. In order to achieve a greater concentration of AuNPs, final dispersion was centrifugated (20 min, 12000 rpm). In the obtained precipitate, the amount of the Au determined by inductively coupled plasma-atomic emission spectrometry (ICP-AES) was found to be 0.06 mol dm^{-3}. PVA hydrogel as a passive layer was produced by the freeze-thaw method (3 cycles of freezing and thawing). An aqueous solution containing 2.5 wt% PVA was poured into a mold, frozen at −20°C for 16 h, and then subsequently thawed at 25°C for up to 8 h. Solution of NiPAAm monomer (10 wt%) was prepared in distilled water, and bubbled with argon for 20 min, after which AuNPs ($c = 2.5 \times 10^{-4}$ mol dm^{-3}) were added. The prepared Au/NiPAAm solution was poured over a PVA layer and exposed to gamma irradiation (^{60}Co source, dose rate 0.5 kGy/h up to the total absorbed dose of 25 kGy). Obtained hydrogels were cut into discs, dried to the constant mass, and then extracted in distilled water for 7 days, in order to remove the uncrosslinked polymer. Extracted hydrogels were dried again to the constant weight to determine the weight of the gel fraction. The optical properties of Au-PNiPAAm/PVA hydrogel nanocomposites were investigated by Thermo Fisher Scientific Evolution 600 UV-Vis spectrophotometer. The size and shape of AuNPs were investigated by TEM (Philips EM 400, operated at 120 kV). Dynamic swelling/deswelling processes and volume phase transition temperature were investigated by a gravimetric method in deionized water. All measurements were performed in triplicate.

RESULTS AND DISCUSSION

In order to evaluate the efficiency of the chosen synthesis method, the gel fraction was calculated according to the following equation $W(\%)=(m_{ae}/m_{ab})\cdot 100$, where m_{ae} and m_{be} were the weights of dry samples after and before extraction, respectively [1]. The percentage gelation for PNiPAAm/PVA hydrogel was found to be 91.9%. The obtained bi-layered hydrogel nanocomposites are with clearly visible and defined layers, and stable structures, where the thickness of the passive layer (PVA) is 1 mm, while the thickness of the active layer (Au-PNiPAAm) is 2 mm (Fig. 1a inset).

UV-Vis spectral studies confirmed the presence of AuNPs within the polymer network. The obtained UV-Vis absorption spectra (Fig. 1a) of the Au-PNiPAAm/PVA hydrogel nanocomposites showed the characteristic surface plasmon resonance (SPR) band with the characteristic maximum of absorption at around 520 nm, which confirms that incorporated particles are spherical in shape and with nanometer dimension [1, 4]. A typical TEM micrograph (Fig. 1b) revealed the presence of spherical non-aggregated AuNPs with the size around 30 nm.

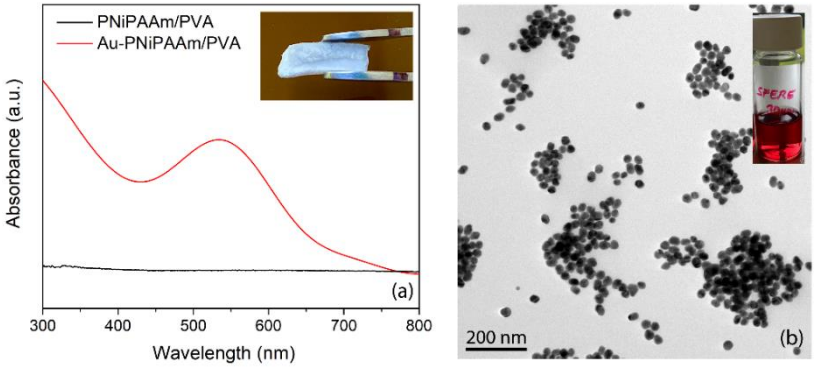

Figure 1. UV-Vis absorption spectra of Au-PNiPAAm/PVA hydrogel nanocomposites (a) (Inset: photograph of bi-layered hydrogel nanocomposite) and TEM micrograph of AuNPs (Inset: photograph of AuNPs -colloid).

Physico-chemical characterization of bi-layered hydrogel nanocomposites was conducted to determine swelling/deswelling properties and volume phase transition temperature (VPTT). All the experiments have been done in triplicate and the mean values are presented in Fig. 2. Equilibrium swelling degree (SD_{eq}) is one of the most important parameters which affect all other parameters and the possibility of application, and it can be described by the following equation: $SD_{eq} = (m_t-m_0)/m_0$, where m_t is a mass of swollen hydrogel at the moment t, and m_0 mass of the xerogel [1]. The results obtained by observing the swelling process show that the incorporation of AuNPs into the polymer network leads to an increase in swelling capacity (Fig. 2a).

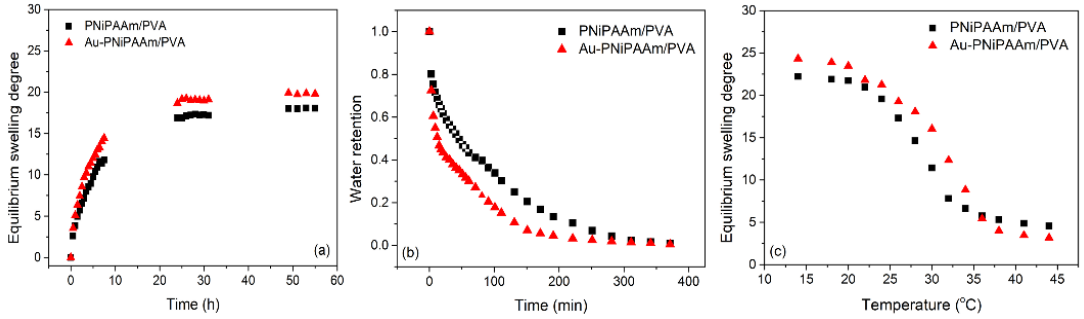

Figure 2. Swelling curves (a), deswelling curves (b), and temperature dependence of SD_{eq} (c) of PNiPAAm/PVA hydrogel and Au-PNiPAAm/PVA hydrogel nanocomposites.

For a complete characterization of the swelling process, it is necessary to determine the liquid transport mechanism of the swelling, by applying a logarithmic form of the equation $SD/SD_{eq}=(kt)^{1/n}$, where k is the kinetic rate constant, while n is a characteristic diffusion exponent describing the mechanism of fluid transport into the polymer matrix. Values of n and k can be calculated from the slope and the intercept, respectively. By monitoring the swelling kinetics, it is possible to determine the diffusion coefficient (D) by using equation $D=((k\pi r^2)/4)^{1/n}$, where r is the radius of xerogels. Calculated values are presented in Table 1. According to the obtained values for n, it could be concluded that the swelling process is affected by both, medium diffusion and relaxation of polymer chains ($n > 0.5$) [1]. As expected, the values of the k are higher for the sample with a higher swelling rate.

Table 1. Physico-chemical parameters: equilibrium swelling degree (SD_{eq}), diffusion exponent (n), kinetic rate constant (k), diffusion coefficient (D), deswelling rate constant (K), and volume phase transition temperature ($VPTT$).

sample	SD_{eq}	n	$kx10^3$, min^{-1}	$Dx10^6$, cm^2min^{-1}	$Kx10^3$, min^{-1}	VPTT, °C
PNiPAAm/PVA	18.0	0.58	20.1	2.65	21.8	29.6
Au-PNiPAAm/PVA	19.8	0.55	27.2	2.78	40.1	32.7

Furthermore, the incorporation of AuNPs leads to a slight expansion of the network and a greater SD_{eq}, resulting in an increase in the diffusion coefficient value, which is consistent with Reinhart and Peppas theory [7]. For the deswelling kinetics studies, the equilibrium swollen hydrogels were transferred into the water at 48°C. The deswelling rate, K, is assumed to follow first-order kinetics and can be determined by a semi-logarithmic plot of first-order rate analysis, as described before [1]. A comparison of deswelling kinetic curves (Fig. 2b) shows that the K was significantly lower in the hydrogel in comparison with the nanocomposites. The thermosensitivity of synthesized systems was investigated through the values of SD_{eq} over the temperature range from 12°C to 48°C, and the swelling profiles were presented in Fig. 2c. Obtained values for VPTT (Table 1) show that incorporation of AuNPs into the polymer matrix moves the phase transition to higher temperatures, due to interaction between polymer chains and nanoparticles, and expansion of the polymer network.

CONCLUSION

In this investigation, hydrogel nanocomposite, consisting of gold nanoparticles embedded in PNiPAAm/PVA bi-layered structure, was successfully synthesized by the combination of freeze-thaw and radiolytic methods. The size and spherical morphology of AuNPs were confirmed by UV-Vis spectroscopy and TEM analysis. The Au-PNiPAAm/PVA hydrogel nanocomposites, compared to PNiPAAm/PVA hydrogel, indicate not only higher swelling capacity and swelling/deswelling rate, but also the VPTT is shifted to the higher values. The diffusion transport mechanism study shows the Fickian transport, indicating that the effects of diffusion and relaxation of polymer chains are comparable.

Acknowledgment

This work was supported by the IAEA (CRP F22070, SRB 23184) and Ministry of Education, Science and Technological Development of the Republic of Serbia (Contract 451-03-68/2022-14/200017).

REFERENCES

[1] J. Spasojević, A. Radosavljević, J. Krstić, D. Jovanović, V. Spasojević, M. Kalagasidis-Krušić, Z. Kačarević-Popović, Eur. Polym. J. 69 (2015) 168-185.
[2] G. Liu, Z. Ding, Q. Yuan, H. Xie, Z. Gu, Front. Chem. 6 (2018) 439.
[3] Z. Chuan-Ling, C. Fu-Hu, W. Jin-Long, Y. Zhi-Long, G. Jin, L. Yang, W. Zhi-Hua, Y. Shu-Hong, ACS Appl. Mater. Interfaces, 9 (2017) 24857−24863.
[4] A.Radosavljevic, D. Bozanic, N. Bibic, M. Mitric, Z. Kacarevic-Popovic, J. Nedeljkovic, J. Appl. Pol. Sci., 125 (2012) 1244–1251.
[5] Q. Shi, H. Xia, P. Li, Y.S. Wang, L. Wang, S.X. Li, G. Wang, C. Lu, L.G. Niu, H.B. Sun, Adv. Optical Mater. 5 (2017) 1700442.
[6] U. Bogdanović, V.V. Vodnik, S.P. Ahrenkiel, M. Stoiljković, G. Ćirić-Marjanović, and J.M. Nedeljković, Synthetic Met., 195 (2014) 122.
[7] C. Reinhart, N. Peppas, J. Membr. Sci. 18 (1984) 227– 239.

EFFECTS OF HIGH-TEMPERATURE HEAT TREATMENT ON STRUCTURAL PROPERTIES OF ALKALI-ACTIVATED MATERIALS

M. Ivanović[1], A. Krstić[2], S. Knežević[1], S. Nenadović[1], Lj. Kljajević[1], M. Mirković[1] and M. Nenadović[3]

[1]*University of Belgrade, „VINČA" Institute of Nuclear Sciences-National Institute of the Republic of Serbia, Department of Materials, Belgrade, Serbia*
[2]*University of Belgrade, „Vinča" Institute of Nuclear Sciences - National Institute of the Republic of Serbia, Department of Physical Chemistry, Belgrade, Serbia. (aleksandar.krstic@vinca.rs)*
[3]*University of Belgrade, „VINČA" Institute of Nuclear Sciences -National Institute of the Republic of Serbia, Department of Atomic Physics, Belgrade, Serbia*

ABSTRACT
In this paper, geopolymer (GP) samples were obtained by alkali activation of metakaolin (MK) as a solid precursor and then thermally treated at 900°C. During the synthesis of geopolymer samples, amorphous phases are formed, which was confirmed by X-ray powder diffraction (XRD). After heat treatment of GP samples, new crystalline phases appeared in all tested samples. Fourier transform infrared spectroscopy (FTIR) confirmed characteristic bands of the Si-O and O-Si-O groups at 1007 cm^{-1} in thermally treated samples. In addition to structural analysis, morphological analysis was performed by SEM analysis. Due to the change of concentrations of NaOH solution as a component of the alkali activator, the change of structure and morphology of thermally treated geopolymer samples was noticed.
Keywords: Alkali-activated material, Metakaolin, Geopolymer, XRD, FTIR, SEM

INTRODUCTION

Alkali-activated material is binder material obtained by reacting an aluminosilicate material with an alkaline activator.Alkaline-activated materials differ and are divided into two subgroups based on the calcium content in the binding phase [1]. The most commonly used materials for geopolymer synthesis are metakaolin and fly ash. In addition, alkali-activated materials have proven to be porous materials with favourable properties, thermal and chemical stability, and widespread use. Previous studies have shown that the amount of vitreous silicon and alumina present in the starting material plays a significant role in the activation reactions and the properties of the reaction product [2-3]. Environment-friendly civil engineering as a challenging issue has become crucial for developing economical and relatively low-cost building materials. Cements are using a lot of energy and emitting gasses into the environment [4-6].

The characteristics of porous materials depend on the size and arrangement of the pores, the porosity (the ratio of total pore volume to material volume), and the material composition. The most important property of geopolymers is their ability to develop high mechanical strength in a short period of time and at moderate temperatures below 100°C [7,8].

The objectives of this research to monitor the microstructure and composition of geopolymers after exposure to temperatures up to 900°C by X-ray diffraction analysis (XRD), Fourier transforms infrared spectroscopy (FTIR), and Scanning Electron Microscopy (SEM).

METHODS

The geopolymer (GP) samples were formed from metakaolin and the alkaline activator solution. Metakaolin (MK) was prepared by calcination of kaolinite (Serbia) at 750 ° C for one h in an air atmosphere. The alkaline activator solutions were prepared from sodium silicate and different

concentrations of aqua solution of NaOH-10, 12, 14, and 16 mol dm^{-3}. The mixtures of MK and alkali activator solutions were cast into covered plastic molds and stored for one day at room temperature. After that, the all samples were put in a sample drying oven for 48 hours at 60±1 °C. Finally, the samples were placed in a desiccator in a controlled condition and aged 28 days. These samples of geopolymers are marked as GPxM, where x is the molarity of a solution of NaOH (GP10M-GP16M). These geopolymers were heated in a furnace in an air atmosphere from 30 to 900°C to investigate changes in their structural properties. The thermally treated geopolymer samples are denoted as $GPxM_{900}$ ($GP10M_{900}$-$GP16M_{900}$).

Changes in the structure of the synthesized material were analysed by various methods: XRD, FTIR, and SEM. XRD analysis is performed by Ultima IV Rigaku diffractometer, equipped with Cu $K\alpha_{1,2}$ radiation. The range of 5–80° 2θ was used for all powders in a continuous scan mode with a scanning step size of 0.02° and at a scan rate of 5°/min. The functional groups of all samples were studied using FTIR spectroscopy at room temperature using a Bomem (Hartmann &Braun) MB-100 spectrometer. The microstructure analysis of the obtained GP materials was performed using a JEOL JSM 6390 LV electron microscope at 25 kV. The samples were previously Au coated to avoid charging problems.

RESULTS AND DISCUSSION

Figure 1a shows XRD results obtained for GP10M-GP16M samples after 28 days of ageing.

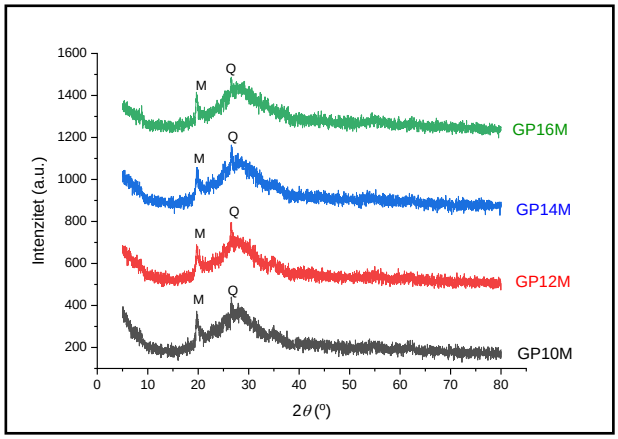

Figure 1. a) XRPD of samples GP10M, GP12M, GP14M, GP16M

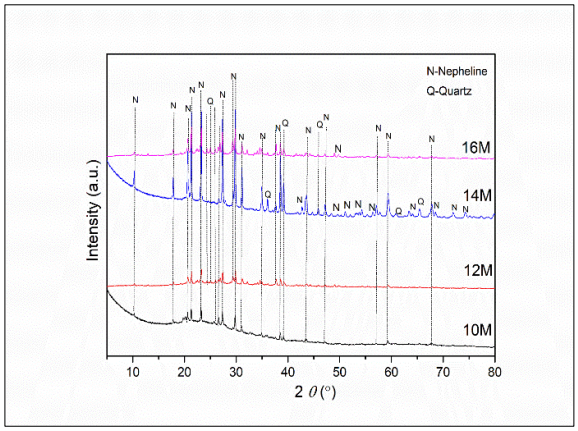

Figure 1. b) XRPD of thermally treated samples $GP10M_{900}$, $GP12M_{900}$, $GP14M_{900}$ and $GP16M_{900}$

XRD of all mentioned samples shows the typical pattern of metakaolin based geopolymer characterized by an amorphous structure (broad diffraction hump from 18 to 34° 2θ with peaks corresponding to muscovite and quartz present as metakaolin impurity. The change in the concentration of NaOH solution as part of the alkaline activator has no significant effect on the samples before thermal treatment. Figure 1b shows XRD results of thermally treated samples $GP10M_{900}$, $GP12M_{900}$, $GP14M_{900}$ and $GP16M_{900}$. It is clear that the increase of the activator concentration leads to a high structural arrangement of the nepheline phase, which is reflected in the sharp and well-defined peaks with high intensities. Based on XRD results, there are almost no amorphous phases in samples 10M-16M. It is evident that by increasing the concentration of the activator by maintaining a constant temperature of 900°C, it is possible to synthesise almost pure monophasic nepheline, which is confirmed in sample $GP16M_{900}$.

Figure 2 shows FTIR analysis of thermally treated samples.

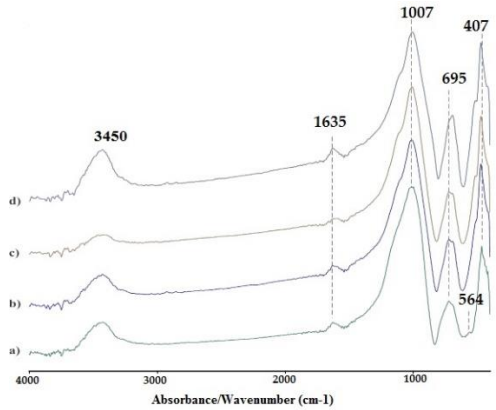

Figure 2. FTIR analysis of thermally treated samples a) GP10M$_{900}$; b)GP10M$_{900}$; c)GP10M$_{900}$; d) GP16M$_{900}$

The FTIR spectra of all samples show broad bands at about 3450 cm^{-1} due to O-H and H-O-H stretching vibrations, and H-O-H bending vibrations are observed in the spectrum at 1635 cm^{-1}. The FTIR band at 1007 cm^{-1} corresponds to Si-O or Si-O-X (X-is Si or OH) elongation [9]. Figure 3 shows SEM micrographs of GP10M and GP16M and corresponding thermally treated samples GP10M$_{900}$ and GP16M$_{900}$

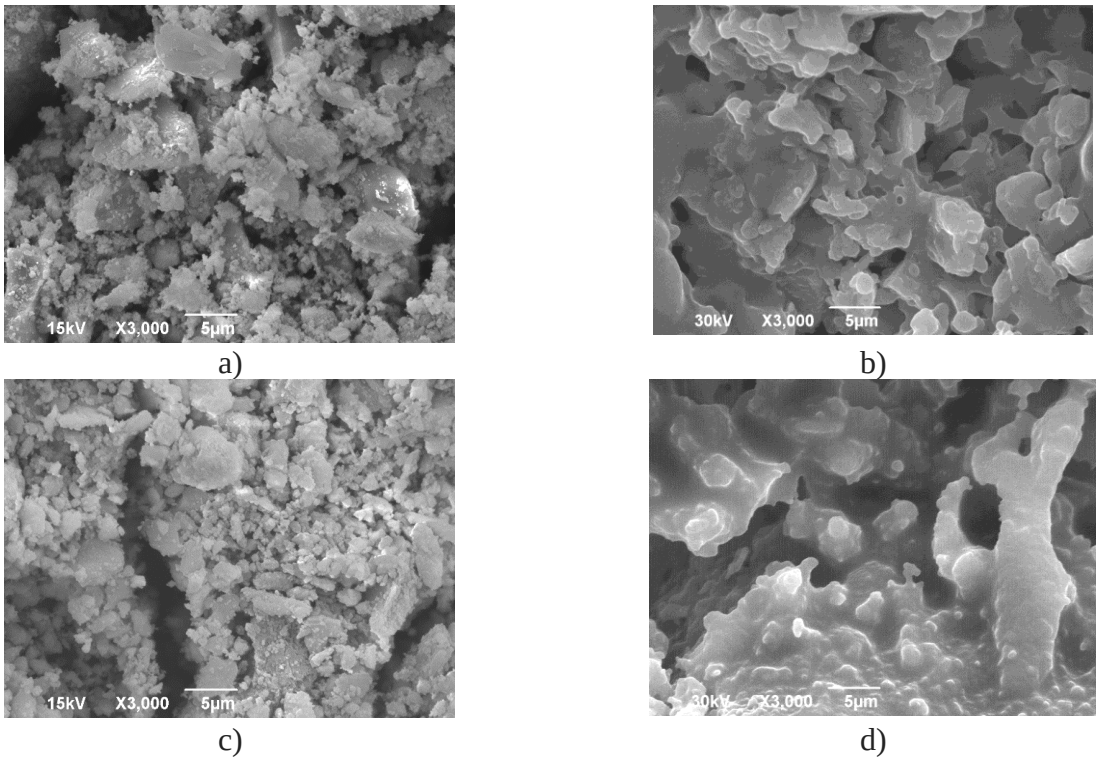

Figure 3. SEM micrographs of a) GP10M and c) GP16M and thermally treated samples b) GP10M$_{900}$ and d) GP16M$_{900}$

After exposure of the geopolymers at 900 °C, new glassy matrix was obtained due to the partial melting of the alumosilicate geopolymer matrix. Geopolymer samples synthesised at 60ºC with different concentrations of NaOH solution as a component of alkali activator are melted and then coagulated, creating a new amorphous matrix withpores of different sizes randomly distributed. The

thermally treated geopolymer samples are transformed from an amorphous geopolymer gel into a new amorphous phase and nepheline and quartz semi-crystalline structure (according to XRD analysis).

CONCLUSION

The present study provided insights into the properties and thermal stability of metakaolin-based geopolymer samples in terms of structural and morphological changes exposed geopolymer samples to high temperatures.The effect of alkaline activator concentration is visible in basic geopolymer and thermally treated geopolymer samples. A new semi-crystalline phase was obtained by the thermal treatment of these samples, and its existence was confirmed by applied methods.

REFERENCES

[1] J. Provis, Geopolymers and other alkali activated materials: why, how, and what?Mater. Struct.47 (2014)11–25
[2] Lj.Kljajević,Z. Melichova, D. Kisić, M.Nenadović, B.Todorović, V. Pavlović, S. Nenadović, Sci. Sint. 51(2018) 163-173.
[3] Lj.Kljajević, Z. Melichova, M. Stojmenović,V. Todorović, N. Čitaković, S. Nenadović, Maced. J. Chem. Chem. Eng**.** 38 (2019) 283-292
[4] M.Ivanović, Lj. Kljajević, M. Nenadović,N. Bundaleski, I.Vukanac, B. Todorović, S.Nenadović, Materiales de Construccion 68(2018)330
[5] Lj Kljajević., Z.Melichova, M.Stojmenović, V.Todorović, N.Čitaković, S. Nenadović, Maced. J. Chem. Chem. Eng.38(2019) 283-292
[6] X.Zhang, C. Bai, Y. Qiao, X. Wang, D. Jia, H. Li, Colombo, P., Applied Science and Manufacturing 150 (2021) 106629
[7] Lj. Kljajević, S. Nenadović, M. Nenadović, N. Bundaleski, B. Todorović, V. Pavlović, Z. Rakočević, Ceramics Internationa l43(9) (2017) 6700-6708
[8] J.Provis, Alkali activated materials: state-of-the-art report, RILEM TC 224-AAM ,Vol. 13. Van Deventer, J. S. (Eds.).Springer Science & Business Media(2013)
[9] K.Komnitsas, D.Zaharaki, Minerals engineering, 20(14) (2007) 1261-1277

CORROSION BEHAVIOR OF Fe-BASED AMORPHOUS AND AMORPHOUS/NANOCRYSTALLINE ALLOYS IN DIFFERENT MEDIA

M. M. Vasić, I. Stojković Simatović and D. M. Minić

Faculty of Physical Chemistry, University of Belgrade, Studentski trg 12-16, Belgrade, Serbia (mvasic@ffh.bg.ac.rs)

ABSTRACT

Four multicomponent iron-based alloys with different chemical composition, $Fe_{40}Ni_{40}B_{12}Si_8$, $Fe_{72}Ni_8Si_{10}B_{10}$, $Fe_{73.5}Cu_1Nb_3Si_{15.5}B_7$, $Fe_{79.8}Ni_{1.5}Si_{5.2}B_{13}C_{0.5}$ (index-at.%), were prepared by melt quenching on a cold rotating disc. The structure and thermal stability of the alloys were examined by XRD and DTA, respectively. Corrosion behavior of the alloys in different media, including 0.5M NaOH, NaCl and HCl, was studied by electrochemical measurements. The chemical composition and microstructure were shown to influence considerably the corrosion behavior of the alloys in various environments.

INTRODUCTION

Numerous positive characteristics of amorphous and nanocrystalline iron-based alloys, including favorable magnetic, electrical, chemical and mechanical properties, make them scientifically interesting for various applications [1, 2]. As a result of their thermodynamic and kinetic metastability, microstructural transformations can occur at high temperatures or pressures, or during prolonged application at moderated temperatures, leading to deterioration or improvement of their functional properties [3]. Therefore, understanding of their thermal stability, mechanism and kinetics of microstructural transformations occurring under different conditions is important for development of materials with targeted properties.

Amorphous and nanocrystalline alloys can be exposed to humid or chloride-containing atmosphere during the practical application, which imposes the need for high corrosion resistance of these materials. Due to their short-range ordered structure, without crystalline defects, amorphous alloys often exhibit better corrosion resistance then the crystalline ones with the same chemical composition [4]. Addition of appropriate amounts of other metal elements (Zr, Cr, Ti, Co, Ni, V, Mo, W, etc.) and metalloids can improve anti-corrosion properties of iron-based amorphous and nanocrystalline alloys [5].

In this work, corrosion behavior of four iron-based alloys of different chemical composition, with amorphous or combined amorphous/nanocrystalline structure, was studied in different environments (0.5 M NaOH, NaCl and HCl) and compared and discussed.

METHODS

For preparation of four multicomponent iron-based alloys of composition $Fe_{40}Ni_{40}B_{12}Si_8$, $Fe_{72}Ni_8Si_{10}B_{10}$, $Fe_{73.5}Cu_1Nb_3Si_{15.5}B_7$ and $Fe_{79.8}Ni_{1.5}Si_{5.2}B_{13}C_{0.5}$ (index-at.%), the technique of rapid quenching of a melt on a cold rotating disc was used. Structural characterization of the obtained alloys was performed by means of X-ray diffractometry (XRD), in Bragg-Brentano geometry, on a Philips PW 1050 device, applying Cu Kα radiation source. Differential thermal analysis (DTA) was performed on a TA SDT 2960 instrument, in an inert atmosphere, at heating rate of 5 $^oCmin^{-1}$.

Electrochemical measurements were carried out in three different media, 0.5 M NaOH, NaCl and HCl, at room temperature, using an Ivium Vertex potentiostat/galvanostat and three-electrode cell. Pt electrode served as counter electrode, while saturated calomel electrode (SCE) was used as reference electrode. Potentiodynamic polarization curves were obtained at a scan rate of 1 mVs^{-1}.

RESULTS AND DISCUSSION

XRD measurements, performed to study initial structure of the as-prepared alloys, revealed combined amorphous/nanocrystalline structure of the $Fe_{72}Ni_8Si_{10}B_{10}$ alloy, while the structure of the other three alloys is completely amorphous, as shown in Figure 1a. The presence of α-Fe nanocrystals in the as-prepared $Fe_{72}Ni_8Si_{10}B_{10}$ alloy is a consequence of the specificity of its chemical composition and limited cooling rate during preparation.

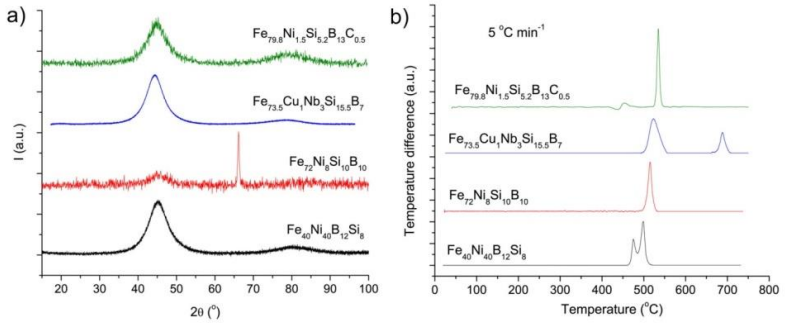

Figure 1. Characterization of the studied multicomponent iron-based alloys: XRD patterns (a) and DTA curves (b).

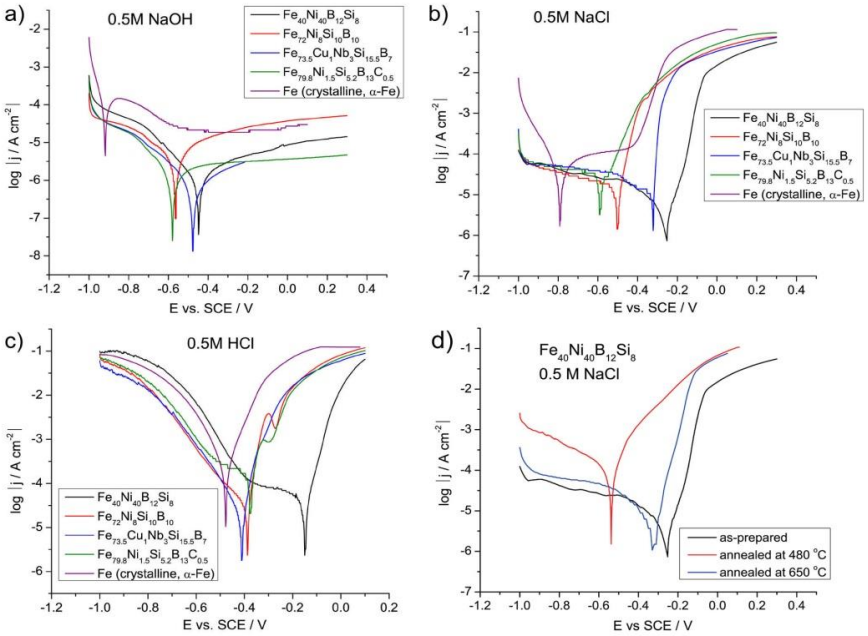

Figure 2. Potentiodynamic polarization curves of multicomponent iron-based alloys in three different media: 0.5M NaOH (a), NaCl (b) and HCl (c); and as-prepared and thermally treated $Fe_{40}Ni_{40}B_{12}Si_8$ alloy in 0.5M NaCl (d).

Thermal stability of the studied alloys is significantly influenced by their chemical composition, as shown in DTA curves presented in Figure 1b. Crystallization onset of the $Fe_{40}Ni_{40}B_{12}Si_8$ alloy at lower temperature than that of the other alloys studied herein is a consequence of large amount of Ni in the composition. The best thermal stability of the $Fe_{79.8}Ni_{1.5}Si_{5.2}B_{13}C_{0.5}$ alloy among the studied alloys results from the optimal chemical composition [6] and completely amorphous structure of the as-prepared alloy sample, without quenched-in nuclei.

Corrosion behavior of multicomponent iron-based alloys was studied by recording potentiodynamic polarization curves in three different media, 0.5M NaOH, NaCl and HCl (Figure 2).

Corrosion patameters (corrosion current density, j_{corr}, and corrosion potential, E_{corr}) determined from the polarization curves are given in Table 1, together with corresponding parameters of pure polycrystalline Fe (α-Fe phase). Much better corrosion resistance of the studied multicomponent iron-based alloys than that of the pure Fe, observed in all media, is a result of their amorphous structure (complete or partial), which lacks grain boundaries and other crystalline defects serving as preferential sites for corrosion, and appropriate chemical composition, including additional metal element and metalloids.

Table 1. Corrosion parameters of multicomponent iron-based alloys in different media, obtained from potentiodynamic polarization curves.

	NaOH		**NaCl**		**HCl**	
	E_{corr} SCE (V)	**j_{corr} (μAcm^{-2})**	**E_{corr} SCE (V)**	**j_{corr} (μAcm^{-2})**	**E_{corr} SCE (V)**	**j_{corr} (μAcm^{-2})**
$Fe_{40}Ni_{40}B_{12}Si_8$ [7]	-0.448	1.6	-0.254	12.4	-0.148	31.6
$Fe_{72}Ni_8Si_{10}B_{10}$ [8]	-0.563	2.0	-0.501	15.4	-0.387	29.9
$Fe_{73.5}Cu_1Nb_3Si_{15.5}B_7$	-0.477	1.2	-0.321	13.7	-0.411	18.6
$Fe_{79.8}Ni_{1.5}Si_{5.2}B_{13}C_{0.5}$	-0.579	1.4	-0.590	30.3	-0.374	97.5
α-Fe (crystalline)	-0.918	68	-0.790	42.2	-0.477	854

Table 2. Corrosion parameters of as-prepared and annealed $Fe_{40}Ni_{40}B_{12}Si_8$ alloy in 0.5M NaCl [7].

As-prepared		**Annealed at 480 ºC, 30 min**		**Annealed at 650 ºC, 30 min**	
E_{corr} SCE (V)	**j_{corr} (μAcm^{-2})**	**E_{corr} SCE (V)**	**j_{corr} (μAcm^{-2})**	**E_{corr} SCE (V)**	**j_{corr} (μAcm^{-2})**
-0.254	12.4	-0.538	64.6	-0.325	17.8

Potentiodynamic polarization curves recorded in 0.5M NaOH reveal the tendency of the studied alloys to passivate in alkaline media, **Figure 2a**. Mechanism of iron corrosion in alkaline media can be represented by the following reactions [9]:

$$Fe + OH^- \rightarrow [Fe(OH)]_{ad} + e^-$$

$$[Fe(OH)]_{ad} \rightarrow [Fe(OH)]^+_{ad} + e^-$$

$$[Fe(OH)]^+_{ad} + OH^- \rightarrow Fe(OH)_2$$

$$Fe(OH)_2 + OH^- \rightarrow HFeO_2^- + H_2O$$

$$HFeO_2^- + OH^- \rightarrow FeO_2^{2-} + H_2O$$

$$Fe(OH)_2 + OH^- \rightarrow FeOOH + H_2O + e^-$$

$$FeOOH + FeOOH \rightarrow Fe_2O_3 \cdot H_2O$$

where $[Fe(OH)]_{ad}$ and $[Fe(OH)]_{ad}^+$ are adsorbed reaction intermediates, while $Fe(OH)_2$, FeOOH, and $Fe_2O_3 \cdot H_2O$ are species related to formation of new phases, which can undergo ageing. In the NaOH environment, the lowest j_{corr} values and thus the lowest corrosion rate is observed for the alloy containing small amounts of Cu and Nb elements ($Fe_{73.5}Cu_1Nb_3Si_{15.5}B_7$), while the alloy with the largest j_{corr} is $Fe_{72}Ni_8Si_{10}B_{10}$ because of the presence of certain amounts of nanocrystalline α-Fe phase in its structure (Figure 2, Table 1).

In chloride environment, metallic dissolution occurs, Figure 2b and c. This process can be represented as [10]:

$$Fe + Cl^- \rightarrow FeCl^-_{ads}$$

$$FeCl^-_{ads} + Fe \rightarrow FeCl^-_{ads}Fe$$

$$FeCl^-_{ads}Fe + OH^- \rightarrow FeOH^+ + Fe + Cl^- + 2e^-$$

$$FeOH^+ + H^+ \rightarrow Fe^{2+} + H_2O$$

where $FeCl^-_{ads}Fe$ is the surface complex formed by adsorbed Cl^- ions at the metal surface. Acidic chloride environment was shown to be more aggressive than NaCl, as expected. Unlike the alkaline environment, the alloy with the largest atomic fraction of Fe ($Fe_{79.8}Ni_{1.5}Si_{5.2}B_{13}C_{0.5}$) exhibits the highest j_{corr} values and the fastest corrosion in NaCl and HCl media, in spite of the fact that its structure is completely amorphous, Figure 2b and c. Larger amount of Ni element in the composition makes the E_{corr} of the $Fe_{40}Ni_{40}B_{12}Si_8$ alloy the most positive among the studied multicomponent iron-based alloys, in all the studied environments.

As an illustration of the influence of thermally induced microstructural changes on corrosion behavior of the alloys, potentiodynamic polarization curves of the $Fe_{40}Ni_{40}B_{12}Si_8$ alloy, recorded in 0.5M NaCl, are given for the as-prepared sample (amorphous), and for the alloy samples annealed at 480 ºC (mostly nanocrystalline) and 650 ºC (completely crystalline) for 30 min, Figure 2d, Table 2 [7]. The sample with completely amorphous structure exhibits the best corrosion resistance, while the one containing large volume fraction of nanocrystals is the most susceptible to corrosion.

CONCLUSION

Corrosion behavior of four multicomponent iron-based alloys of different chemical composition, with amorphous or combined amorphous/nanocrystalline structure, was studied by electrochemical measurements in different media and compared. Significant influence of the chemical composition and microstructure of the alloy on the corrosion parameters (j_{corr}, and E_{corr}) was observed. Due to lack of preferential sites for corrosion in amorphous structure, as well as multicomponent chemical composition, corrosion resistance of all of the studied alloys in the as-prepared form is much better than that of pure polycrystalline iron.

Acknowledgment

This work was supported by the Ministry of Education, Science and Technological Development of the Republic of Serbia (grant No. 451-03-68/2022-14/200146).

REFERENCES

[1] C. Suryanarayana, A. Inoue, Int. Mater. Rev., 58 (2013) 131.
[2] T. Kulik, J. Non-Cryst. Solids, 287 (2001) 145.
[3] H. Gleiter, Prog. Mater. Sci., 33 (1989) 223.
[4] A. Pardo, M.C. Merino, E. Otero, M.D. Lopez. A. M'hich, J. Non-Cryst. Solids 352 (2006) 3179.
[5] S. Wang in: Metallic Glasses – Formation and Properties, B. Mohavedi (Ed.), IntechOpen, London 2016.
[6] M. M. Vasić, D. M. Minić, D. M. Minić in: Metallic glasses, D. Minić, M. Vasić (Eds.), IntechOpen, London, 2020.
[7] M. M. Vasić, T. Žak, N. Pizurova, I. Stojković Simatović, D. M. Minić, Metall. Mater. Trans. A, 52 (2021) 34.
[8] M. M. Vasić, I. Stojković Simatović, Lj. Radović, D. M. Minić, Corros. Sci, 204 (2022) 110403.
[9] R. S. S. Guzman, J. R. Vilche, A. J. Arvia, Electrochim. Acta, 24 (1979) 395.
[10] R. J. Chin, K. Nobe, J. Electrochem. Soc. 119 (1972) 1457.

THE ANALYSIS OF 2,3-DICARBOXIPROPANE-1,1- DIPHOSPHONIC ACID-COATED MAGNETITE NANOPARTICLES UNDER AN EXTERNAL MAGNETIC FIELD

M. Perić[1], M. Radović[1], M. Mirković[1], Z. Milanović[1], D. Stanković[1], A. Vukadinović[1], Đ. Petrović[1], D. Janković[1], S. Vranješ-Đurić[1], I. Krstić[2] and M. Kuraica[2]

[1]*Vinča Institute of Nuclear Sciences, University of Belgrade, P. O. BOX 522, Belgrade, Serbia (markoperic1983@gmail.com)*
[2]*Faculty of Physics, University of Belgrade, Studentski Trg 12, 11001 Belgrade, Serbia*

ABSTRACT
In present study, 2,3-dicarboxypropane-1,1-diphosphonic acid-coated magnetite nanoparticles (Fe_3O_4–DPD MNPs) were evaluated for their theranostic application using different methods. The magnetic hyperthermia efficiency of the Fe_3O_4–DPD MNPs was investigated in saline solution with ionic strengths between 0.05 and 1.0 mol dm^{-3}. For a better understanding of hyperthermia, the behavior of Fe_3O_4–DPD MNPs under a non-alternating magnetic field was studied, and the transparency of the sample was measured.

INTRODUCTION
The biomedical applications of MNPs depend on their colloidal and chemical stability and aggregation levels under physiological conditions. The ionic and protein composition of biological media has a strong influence on the physicochemical and biological behavior of the MNPs. To improve the biocompatibility and colloidal stability of MNPs in biological systems, appropriate surface coatings are necessary. To the best of our knowledge, only a few studies have been reported on the use of bisphosphonates (BPs) as coatings despite their significant affinity towards metal ions and biocompatibility. Bisphosphonates are well-known drugs in osteoporosis treatment and oncology due to their high binding affinity for the surface of metabolically active bone. Moreover, 2,3-dicarboxypropane-1,1-diphosphonic acid (DPD) is a water soluble and biocompatible bisphosphonate, which provides suitable dispersion stability and reduces the cytotoxicity of the naked Fe_3O_4 MNPs [1, 2].

In this study, the interaction of Fe_3O_4–DPD MNPs with an external magnetic field (MF) gradient was analyzed to test the potential of these MNPs for possible applications in the hyperthermia treatment. The heating efficiency of the MNPs under biological conditions remains poorly understood, especially the influence of their dispersion state. Hence, the behavior of Fe_3O_4–DPD MNPs under a non-alternating external MF was monitored by constantly measuring the laser beam transparency through a ferrofluid sample. These measurements were carried out before switching on the MF, when the field was applied, and after switching off the MF. Using the transparency analysis of ferrofluid under a non-alternating external MF and changing the ionic strengths of the sample, the combined effects of the MF and electrolyte were monitored. This provides better comprehension of the behavior of Fe_3O_4–DPD MNPs under an external MF in the absence and presence of an electrolyte and consequently more comprehensive understanding of hyperthermia.

METHODS
The magnetic hyperthermia efficiency of Fe_3O_4–DPD MNPs was tested using a commercial AC applicator (model DM100 by nB nanoscale Biomagnetics). The heat generation of the dispersions of Fe_3O_4–DPD MNPs under an alternating magnetic field (30 mT) and the resonance frequencies between 252 and 577 kHz were measured directly for the samples dispersed in water. The heating

efficiency of the MNPs (2 mg mL^{-1}) is defined as the specific power absorption (SPA) and calculated according to the following formula: $SPA = (C_p \cdot m_w/m_m)(\Delta T/\Delta t)$, where C_p is the specific heat capacity of the medium (C_p–C_{water} = 4.18 J g^{-1} K^{-1}), m_w and m_m are the masses of the medium (water) and magnetic nanoparticles, and $\Delta T/\Delta t$ is the initial slope of the time-dependent temperature curve, respectively. For analysis under a non-alternating external MF, the device developed in our laboratory was used[1]. The Sanyo laser diode DL5147-040 in the single mode regime at the wavelength λ = 655 nm was applied. The transmitted laser light was measured using a photodiode.384

RESULTS AND DISCUSSION

In addition to the applied frequency and field strength, physicochemical characteristics, such as the particle size, shape, and concentration, of the sample strongly affect the behavior of the MNPs under both an alternating and a non-alternating MF. Generally, higher concentrations of MNPs widen the application of different electric and magnetic fields. Upon dilution of the Fe_3O_4–DPD ferrofluid, the SPA values decrease, and at concentrations below 2 mg/dm^3 , the hyperthermia effect cannot be observed (Table 1.).

Table 1. SPA values of Fe_3O_4-DPD MNPs at different concentrations (397 kHz, 30 mT)

Concentration (mg/dm^3)	SPA (W/g)
0.25	0
0.5	0
1	0
2	78
5	89
8	90

The behavior of Fe_3O4–DPD MNPs under a non-alternating MF (30 mT) for different concentrations is depicted in Figure 1. Regardless of the concentration used, at the beginning of the measurement, when the MF was switched-off, the sample showed initial transparency. At the point when the MF was switched on, a rapid decrease in the intensity of the transmitted light was observed. The width and depth of the valley depend on the MF used and on the type of the ferrofluid, as observed previously[3]. After some time, a rapid increase in the intensity of the transmitted light occurred. At a certain point, the saturation effect was noticed. This increase in the intensity is in accordance with the model[4,5] and ascribed to the orientation of the magnetic domains of the nanoparticles caused by the MF. The non-alternating MF forces the magnetic particles along the field lines, similar to the case of magnetic needles. The magnetic domains ordered in this manner are attracted, thus forming magnetic chains. Further, the chains can be organized to form a quasi-lattice of magnetic threads. This aggregation process depends on the field strength and the time interval of the exposure. During this time, the sizes of the scatterers increase due to the formation of doublets, triplets or very small chains. At a certain time interval, a number of scatterers with different sizes satisfy the resonances in the scattering anisotropy and extinction efficiency factors. At minimum transparency, the number of scatterers satisfying the resonance becomes maximum. When the MF is switched off, the sample becomes more transparent, and the intensity of the transmitted light rapidly increases. This is due to the additional attachment of the free magnetic nanoparticles in the solution and their embedment into the magnetic chains. Monitoring of the effect of the non-alternating MF by measuring the transparency of the Fe_3O_4–DPD ferrofluid was not possible at concentrations $\geq$ 5 mg/dm^3 due to the high density of the sample. At the highest tested concentration (2 mg/dm^3), the increase in the ratio between the well depth and the height of transparency is largest. Moreover, the width of the well is

smallest for highest concentration. By dilution of the sample, the increase in the ratio between the well depth and the height of transparency decreases. In addition, the width of the well increases. At lowest concentration, the increase in the transparency is very small, reaching only the initial value (when the MF was switched off). Below 2 mg/dm^3 , the heating capacity of the sample was not observed, and a drastic change in the curve profiles under a non-alternating MF was noticed.

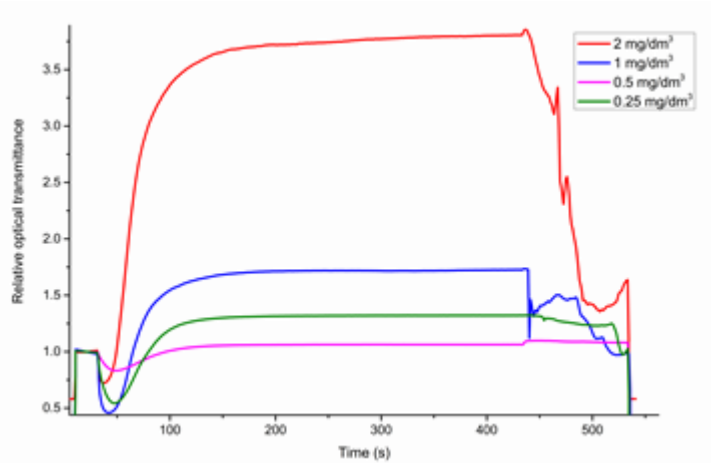

Figure 1. Time dependence of transmitted diode laser light (λ=655nm) for different concentrations of the sample at magnetic field strength of 30mT (lower figure).

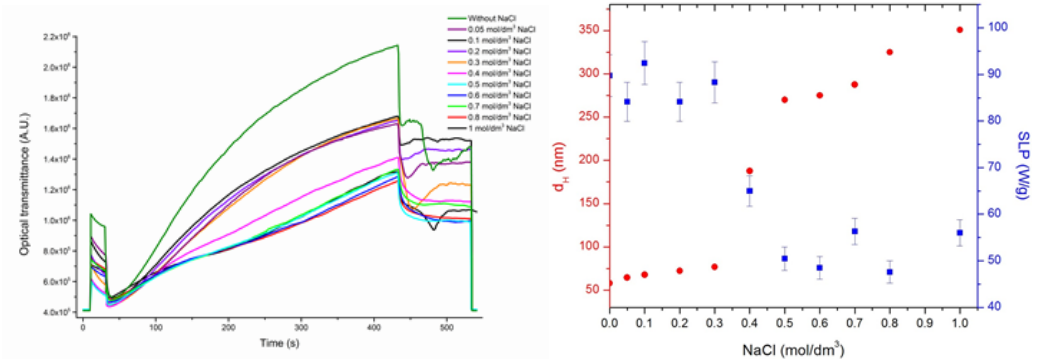

Figure 2. Time dependence of transmitted diode laser light (λ=655nm) for different ionic strengths at magnetic field strength of 30mT, and the dependence of SPA values and hydrodynamic diameter on ionic strength

CONCLUSION

The interaction of the Fe_3O_4–DPD MNPs under an alternating external magnetic field is of special interest due to the possible application of these MNPs in hyperthermia treatment. The results presented imply that the DPD-coated MNPs maintain their heating capacity in the range of 252–577 kHz and thus have potential in biomedical applications. The transparency measurement of the Fe_3O_4–DPD MNPs in the non-alternating MF clarified the mechanism of particle aggregation. These measurements provided us an insight into the orientation of the magnetic domains and aggregate formation in the absence and presence of the electrolyte; this allowed a more comprehensive understanding of hyperthermia.

Acknowledgment
This work was supported by the Ministry of Education, Science and Technological Development of the Republic of Serbia (grant no 451-03-68/2022-14/200017) and through funding the VINCENT Center of Excellence.

REFERENCES

[1] Fatisson, J., Quevedo, I.R., Wilkinson, K.J., Tufenkji, N., Colloids Surfaces B Biointerfaces., 91 (2012) 198.
[2] Safi, M., Courtois, J., Seigneuret, M., Conjeaud, H., Berret, J.-F., Biomaterials., 32 (2011) 9353.
[3] Kuraica, M.M., Iskrenović, P., Perić, M., Krstić, I., Nikolić, A.S., Chem. Pap., 72 (2018) 1535–1542. doi:10.1007/s11696-017-0380-8.
[4] Li, J., Liu, X.-D., Lin, Y.-Q., Huang, Y., Bai, L., Appl. Phys. B., 82 (2006) 81–84. doi:10.1007/s00340-005-2045-5.
[5] Bai, X., Pu, S., Wang, L., Opt. Commun. 284 (2011) 4929.

STRUCTURAL AND OPTICAL PROPERTIES OF CRYSTALLINE TiO_2 NANOPARTICLES − EFFECT OF HEAT TREATMENT

M. M. Milić and N. Jović Orsini

"Vinča" Institute of Nuclear Sciences-National Institute of the Republic of Serbia, University of Belgrade, Mike Petrovića Alasa 12-14, 11351 Vinča, Belgrade, Serbia.
(mikac@vinca.bg.ac.rs)

ABSTRACT

Performance of the TiO_2 nano-objects in various applications is mainly determined by their size and crystalline structure which can strongly vary depending on a route of synthesis. Using a simple sol-gel synthesis we prepared a nanoparticulate TiO_2 sample and subjected it to slow and fast heating protocols to obtain the final product. The calcined samples were experimentally characterized by X-ray diffractometry (XRD), Fourier transform infrared (FTIR) and UV-Vis spectroscopy. It was found that thermally treated samples contained mixture of crystalline TiO_2 phases, and that heating speed strongly affected the phase composition of the prepared samples, as well as their optical properties. The band gap energy values were found to be lower in the fast heated samples.

INTRODUCTION

Having interesting photocatalytic and photovoltaic properties accompanied with low toxicity, good stability and low cost, TiO_2 is a promising candidate for many versatile applications which include solar energy conversion, cosmetic pigments, photocatalyst in waste-water and air treatment etc. [1, 2]. Suitability of TiO_2 particles for each of these applications is mainly determined by their size and phase composition. The TiO_2 crystallize in three structural phases: anatase, brookite and rutile, the anatase being the most thermodynamically stable for crystal sizes below 11 nm, brookite is the most stable for crystal sizes between 11 nm and 35 nm, while the rutile phase shows best stability in the case of crystal sizes above 35 nm [3]. For many applications it is not crucial the TiO_2 to exist as a single phase since it was found that different phases can act synergistically leading to enhanced physical properties. For example the well-known commercial TiO_2 catalyst Degussa P25, which is a mixture of anatase, rutile and amorphous phase, displays better catalytic properties than the single anatase phase TiO_2 [4]. Properties of TiO_2 can be also governed by the presence of the imperfections in its structure developed in the course of the synthesis method as evidenced in the case of the black TiO_2 whose photocatalytic abilities are greatly improved due to existence of oxygen vacancies and structural disorder [5]. Therefore, it is of great importance to investigate different routes of TiO_2 synthesis, as well as various post-synthesis protocols in relation to the phase composition of the resulting product. TiO_2 can be prepared using different methods, the sol gel method being especially convenient since it is conducted at low temperatures, it provides high purity of products and enables good control of product properties by controlling the synthesis parameters [6].

In this work we have prepared TiO_2 sample using a simple sol-gel method starting from titanium(IV) n-butoxide as a Ti ions source. The dried sample was subjected to slow and fast heating protocols at various temperatures. The induced structural changes in the prepared sample were studied using XRD, FTIR and UV−Vis experimental methods. The major contribution of this paper is that it is demonstrated that short annealing time in combination with fast heating rate and proper annealing temperature can be an effective way to prepare TiO_2 samples with lowered the band gap energies (E_g).

METHODS

The material used in synthesis were titanium(IV) n-butoxide ($Ti(BuO)_4$, Acros Organics 98%), absolute ethanol (EtOH, Carlo Erba), NaOH (Labexpert 97%) and distilled water. All chemicals were reagent grade and were used as received. The synthesis protocol of raw TiO_2 nanoparticles was as follows: 0.04g of NaOH was dissolved in 200μL of H_2O and mixed with 30ml of absolute ethanol. Than 1.5ml of $Ti(BuO)_4$ was added dropwise to this solution under vigorous magnetic stirring. The mixture was left to rest at -8°C for two hours and then it was transferred to room temperature. After several days the pale yellow precipitate was collected, and the precipitate was washed with distilled H_2O and EtOH, and then dried at 80°C. Obtained powder was divided in two sets each containing several portions. The TiO_2 aliquots from the first set of was calcined at 500°C, 600°C and 700°C for one hour the heating rate being 8°C/min and these samples were labeled as S500, S600 and S700, respectively. Another set of original raw sample was calcined for 15 minutes at 600°C and 700°C the heating rate being 70°C/min and these samples were labeled F600 and F700.

Structural changes of TiO_2 sample due to thermal treatment were studied at ambient conditions using a Smartlab Rigaku X-ray diffractometer generating CuK_α radiation (λ=1.5406 nm). Diffraction patterns were analyzed using the QualX software [7]. The FTIR spectra were recorded at room temperature in the wavenumber range λ=400-4000cm^{-1} using a Nicolet spectrophotometer operating in ATR mode. Optical properties of the prepared samples were characterized by Genesys 10S (ThermoScientific) UV-Vis spectrophotometer in the wavelength range from 200 to 800 nm with resolution of 2 nm.

RESULTS AND DISCUSSION

Heat triggered evolution of the XRD pattern of the prepared TiO_2 sample is shown in the figure 1. All major diffraction peaks of the S500 samples are indexed to the anatase phase (JCPD 00-073-1764), while the small peak located around 2θ=30.9° indicates onset of brookite phase formation

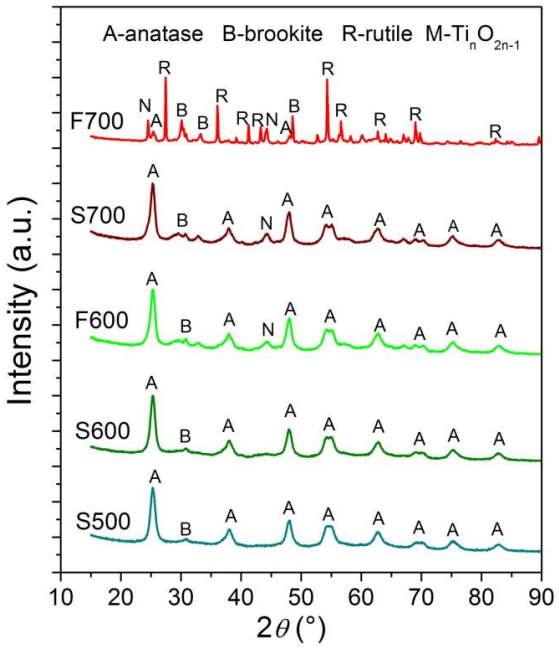

Figure 1. XRD patternes of calcined TiO_2 samples.

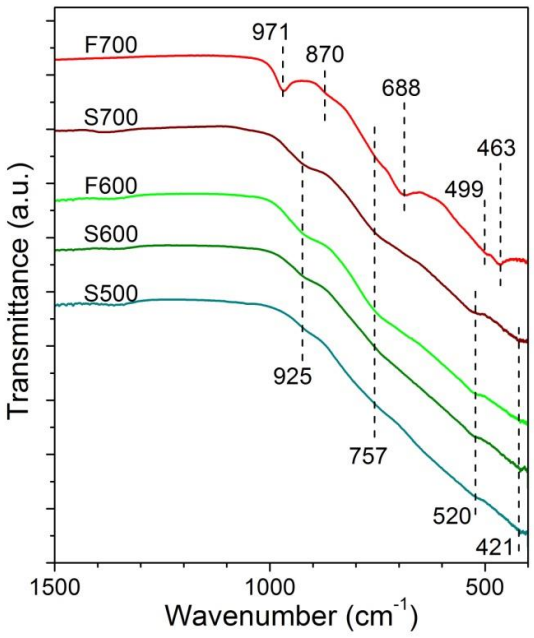

Figure 2. FTIR spectra of prepared TiO_2 samples.

(JCPD 00-720-100). Similar diffraction pattern was observed for S600 sample, while XRD patterns of F600 and S700 sample contain some additional peaks originating from brookite phase indicating its higher content. Low intensity peak at 2θ=45° could not be indexed to any of the above mentioned TiO_2 phases but probably originates from some of nonstoichiometric titanium oxide phases Ti_nO_{2n-1} (Magneli phase) [8]. The sample F700 displays reach diffraction pattern containing reflections that can be indexed to all three TiO_2 phases, the dominant phase being rutile (JCPD 00-901-5662), while the intensity of XRD peaks associated with anatase phase was drastically reduced as compared to those of the samples heated at lower temperatures. The crystallite sizes (c.s.) obtained using Scherrer equation and assuming spherical shape of the prepared titania particles are presented in the Table1. It can be seen that pronounced increase in the crystallite size is observed in the fast heated sample calcined at 700°C.

Table 1. Crystallite sizes (c.s.) and estimated E_g values with corresponding wavelengths λ_g).

	S500	**S600**	**F600**	**S700**	**F700**
Anatase c.s. (nm)	9	9	9	9	15
Brookite c.s. (nm)	ND	ND	ND	12	26
Rutile c.s. (nm)	/	/	/	/	70
E_g(eV)	3.03	3.24	2.92	3.27	3.06
λ_g(nm)	409	383	424	379	405

Structural changes of the prepared sample triggered by thermal treatment were further investigated by infrared spectroscopy. FTIR spectra of calcined TiO_2 samples are shown in the figure 2. Existence of wide transmission band below 1000 cm^{-1} with characteristic peaks that can be attributed to Ti–O stretching and Ti–O–Ti bridging stretching modes, confirms formation of TiO_2 structure [9].

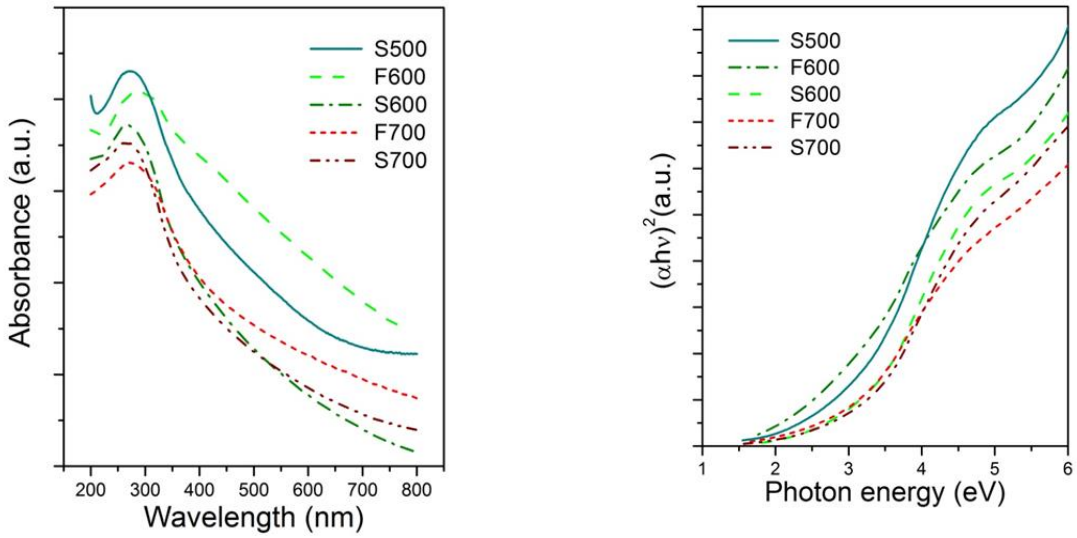

Figure 3. UV-Vis absorption spectra of prepared TiO_2 samples (left) and the corresponding Tauc plots for E_g determination (right).

The figure 3 shows results from the optical absorption measurements carried on the solutions of the calcined samples. As expected, all samples display the best absorbance in the UV region. In the visible spectral region, the best absorbance is shown by F600 sample. Recorded UV-Vis absorbencies spectra were used to construct Tauc plots (figure 3) to determine band gap energies, E_g, corresponding to indirect gap semiconductor transition. Estimated E_g values, together with the corresponding wavelengths, λ_g , are summarized in table 1. The obtained band gap energies values for samples S500, F600 and F700 are lower than the value for pure anatase phase (E_g=3.2 eV). The sample F600, being the mixture of anatase and brookite phases has narrower gap than the pure rutile phase (E_g=3.0 eV) [10].

CONCLUSION

Heat treatment of TiO_2 nanoparticles, prepared starting from $Ti(OBu)_4$ and calcined up to 700°C resulted in the samples containing mixture of TiO_2 crystalline phases. Prevailing phase is anatase, except in the fast heated samples calcined at 700°C, where rutile dominate. It was found that phase composition, as well as the crystallite sizes change significantly upon the heating at 700°C with high heating rate. Optical properties of prepared TiO_2 nanoparticles were also changed during the thermal treatment. Generally, the fast heating resulted in lower band gap energy values as compared to the slowly heated samples, which is most probably due to the fact that fast heating allowed preservation of defects like Ti^{3+} and oxygen vacancies existing in the raw TiO_2 sample, which can induce narrowing of the energy band gap [11]. Formation of these defects in the raw TiO_2 sample can occur in the process of sol gel synthesis due to incomplete hydrolysis of Ti precursor [12].

Acknowledgment

This work was supported by the Ministry of Education, Science and Technological Development of the Republic of Serbia.

REFERENCES

[1] N. Lagopati, K. Evangelou, P. Falaras, E. P. C Tsilibary, P. V. Vasileiou, S, Havaki, A. Angelopoulou, E.A. Pavlatou, and V. G. Gorgoulis, Pharmacol. Ther., 222 (2021) 107795.
[2] S. Peiris, H. B. de Silva, K. N. Ranasinghe, S. V. Bandara and I. R. Perera, J. Chin. Chem. Soc., 68(5) (2021) 738.
[3] H. Zhang and J. F. Banfield, J. Phys. Chem. B, 104(15) (2000) 3481.
[4] S. Banerjee, S.C. Pillai, P. Falaras, K. E. O'shea, J.A., Byrne, and D.D. Dionysiou, J. Phys. Chem., 5(15) (2014) 2543.
[5] T. S. Rajaraman, S.P. Parikh, and V.G. Gandhi, Chem. Eng. J., 389 (2020) 123918.
[6] D.P. Macwan, P.N. Dave, and S. Chaturvedi, J. Mater. Sci., 46(11) (2011) 3669.
[7] A. Altomare, N. Corriero, C. Cuocci, A. Falcicchio, A. Moliterni, and R. Rizzi, J. Appl. Cryst. 48 (2015) 598.
[8] H. Malik, S. Sarkar, S. Mohanty, and K. Carlson, Sci. Rep., 10(1) (2020) 1.
[9] N. Borodajenko, K. Rubenis, A. Pura, N. Mironova-Ulmane, J. Ozolins, and L. Berzina-Cimdina, Key Eng. Mater 604 (2014) 309.
[10] A.J. Haider, Z.N. Jameel, and I.H. Al-Hussaini, Energy Procedia, 157 (2019) 17.
[11] X. Bi, G.H. Du, D.F. Sun, M. Zhang, Y. Yu, Q. Su, S. Ding, and B. Xu, Appl, Surf. Sci. 511 (2020) 145617.
[12] P. Karthik, V. Vinesh, A. M. Shaheer, and B. Neppolian. App. Cat. A: Gen. 585 (2019) 117208.

I *– Photochemistry, Radiation Chemistry, Photonics*

FREESTANDING OR FREE-FLOATING NANOMEMBRANES IN NANOPHOTONICS AND NANOPLASMONICS

Z. Jakšić

University of Belgrade, Institute of Chemistry, Technology and Metallurgy – National Institute of the Republic of Serbia, Njegoševa 12, 11000 Belgrade, Serbia. (jaksa@nanosys.ihtm.bg.ac.rs)

ABSTRACT

This contribution considers the state of the art of nanomembranes/quasi-two-dimensional materials as the emerging building blocks for nanophotonics, nanoplasmonics and optical metamaterials. Nanomembranes may be defined as freestanding or free-floating structures thinner that 100 nm (down to monatomic thickness) and with giant lateral aspect ratios of at least several orders of magnitude. The interest in nanomembranes received an additional boost with the emergence of different families of two-dimensional monatomic and monomolecular structures, including graphene, MXenes, phosphorene, etc. The confinement of the structure along the perpendicular direction results in a multitude of novel physical (electrical, optical, even mechanical), chemical and other properties. These newly discovered properties are frequently unexpected and more often than not even counterintuitive. Yet, nanomembranes are ubiquitous in nature, since lipid bilayer structures represent an unavoidable biological building block – the cell membrane, thus ensuring the existence of the life as we know it. Similar to the biological structures, the usefulness of synthetic nanomembranes becomes vastly greater with their functionalization (inclusion of nanofillers, layering, three-dimensional sculpting, additive and subtractive patterning – even including the formation of artificial ion channels, ion pumps and nuclear pore complexes similar to biological ones). Since we are not limited to the Nature toolbox, we can use unconventional materials and methods to impart various properties not met in biological membranes, for instance plasmonic or metamaterial behavior. Here we give a broad overview of techniques and methodologies used to produce synthetic freestanding or free-floating nanomembranes and to functionalize them in order to achieve the novel properties. Further we focus on the existing applications of nanomembranes in nanophotonics, plasmonics and optical metamaterials and some of their particular uses, e.g. ultrasensitive chemical or biological sensors. We conclude that, even though technologically still in their nascence, nanomembranes open a vast new field for applied research with potentials to introduce some functionalities of living structures into nanooptics and other fields of physics and chemistry, and in certain cases even to exceed them.

J *– Macromolecular Physical Chemistry*

FAST AND FACILE ENHANCED MICROWAVE APPROACH FOR ECO-FRIENDLY POLYMER SYNTHESIS: THE EXAMPLE OF POLYANILINE/CHITOSAN COMPOSITE

M. Gizdavić-Nikolaidis[1], J. M. Pupe [2], A. Jose[1], I. N. Bubanja[3], L. P. Silva[2,4], D. Stanisavljev[3], D. Svirskis[5] and S. Swift[1]

[1]*Department of Molecular Medicine and Pathology, Faculty of Medical and Health Sciences, the University of Auckland, Auckland 1023, New Zealand (m.gizdavic@auckland.ac.nz)*
[2]*Instituto de Ciências Biológicas, Universidade de Brasília, Brasília, DF, 70910-900, Brazil*
[3]*Faculty of Physical Chemistry, University of Belgrade, Studentski trg 12-16, Belgrade, Serbia*
[4]*Embrapa Recursos Genéticos E Biotecnologia, PBI, Pq. Est. Biol. Final W5 Norte, Asa Norte, Brasília, DF, 70770-917, Brazil*
[5]*School of Pharmacy, Faculty of Medical and Health Sciences, the University of Auckland, Auckland 1023, New Zealand*

ABSTRACT

The microwave (MW) irradiation approach is an eco-friendly, rapid and convenient way to produce advanced polymer nanomaterials in high yield at desirable temperatures. In the conventional MW approach, MW irradiation rises the bulk temperature to a maximum set point quickly and then the MW power automatically switches off. The MW enhancement of polymer reactions only occurs during application of MW energy. Conventional MW methods have rarely been used to synthesise conducting polymers (CPs). Recently, our research group introduced an ultrafast and simple enhanced MW approach, for the first time, to produce high yield advanced polyaniline (PANI) based materials at ambient temperature. In contrast with classic chemical synthesis (CS), for which the reaction duration can be several hours or even days, application of microwaves can greatly reduce the reaction duration so that product can be obtained in just 5 min with ca. 76 % yield in the form of nanostructured PANI. The enhanced MW approach keeps a constant reaction temperature over extended time intervals enabling a continuous flow of MW energy into the system. During simultaneously applying irradiating microwaves, the steady amount of energy can be transmitted to the reaction mixture, while preserving a constant temperature by externally cooling the reaction vessel. In this way, enhanced MW approach can be used to fine-tune CP synthesis reaction conditions, directing the morphological and structural properties of PANI based materials.

In this study, we successfully prepared composite products of PANI and chitosan (Chs) of different molecular weights. The oxidizing agent potassium iodate (KIO_3) was used, as it is suitable for scalable bulk production of PANI based composites, achieving a good quality product for a wide range of polymer synthesis parameters. The physical integration of PANI/Ch composites was confirmed using FTIR and SEM analysis. Visible differences in morphology for the resulting MW PANI/Ch or CS PANI/Ch composites were noted depending on the molecular weight of Ch used for synthesis, this finding can be used to tune composite properties toward particular application. All PANI/Ch composites had greater antibacterial efficacy against both Gram-positive and Gram-negative bacteria than pure Ch or PANI. This suggests that the interaction between PANI and Ch in CS or MW prepared composites was able to advance the bactericidal efficacy of both polymers. Understanding the factors which affect the formation of PANI nanofibers in the composite using enhanced MW approach, together with the findings based on CS approach can help tuning PANI formation conditions toward the particular properties of PANI composites for various applications.

SOLID-STATE NMR OF NEGATIVELY CHARGED POLYANIONIC ACID SIDE CHAINS GRAFTED ONTO POLY(3-HEXYLTHIOPHENE): STRUCTURE AND MOLECULAR DYNAMICS

Z. Žujović[1], E. Wai Chi Chan[2] and J. Travaš-Sejdić[2,3]

[1]Centre for NMR, School of Chemical Sciences, the University of Auckland, Private Bag 92019, Auckland 1010, New Zealand. (z.zujovic@auckland.ac.nz)
[2]School of Chemical Sciences, the University of Auckland, Private Bag 92019, Auckland 1010 New Zealand.
[3]MacDiarmid Institute for Advanced Materials and Nanotechnology, Wellington 6140, New Zealand

ABSTRACT

Conducting polymers exhibit the semiconducting and metallic properties of p-conjugated molecular systems while keeping the mechanical and processing characteristics of polymers. The objective of this work is to study and understand the mechanism of conductivity in the copolymers of conducting polymer poly(3-hexylthiophene) grafted with charged poly(acrylic acid) acid (P3HT-g-PAA). The length and the density of the grafts, and the length and mobility of the polymer backbone are critical parameters that affect the flexibility and morphology and, consequently, the electrical properties of a graft copolymer.

Intermolecular interactions and molecular dynamics in *dedoped* conducting graft copolymer P3HT-PAA were investigated by solid-state NMR. Specifically, the relaxation measurements are used to probe spin dynamics by studying low - and high-frequency molecular and chain motion (from tens of kHz to hundreds of MHz). The relaxation measurements of the grafted polymer backbone versus the not grafted polymer backbone allow insights into the degree to which the grafting altered the physical properties of the polymer. The time constants $T_1(^{13}C)$ (carbon spin-lattice relaxation time), $T_2(^{1}H)$ (proton spin-spin relaxation time), $T_{1\rho}{}^{*}(^{13}C)$, and $T_{1\rho}(^{1}H)$ (carbon and proton rotating-frame relaxation) reveal the spin interactions and dynamics at the sub-micron level. Fourier Transform Infrared Spectroscopy (FTIR) and X-Ray Diffraction (XRD) allowed further detailed insight into the structural changes of the doped copolymer caused by *charged* PAA side chains grafted onto P3HT.

THE INFLUENCE OF TiO_2 NANOPARTICLES ON VISCOELASTIC PROPERTIES AND THERMO-OXIDATIVE STABILITY OF POLYURETHANE NETWORK

J. V. Džunuzović [1,2], I. S. Stefanović[2], E. S. Džunuzović[3], S. J. Brzić [4] and C. Marega[5]

[1]University of Belgrade, Institute of Chemistry, Technology and Metallurgy, Center of Excellence in Environmental Chemistry and Engineering, Njegoševa 12, 11000 Belgrade, Serbia.
[2]University of Belgrade, Institute of Chemistry, Technology and Metallurgy, Njegoševa 12, 11000 Belgrade, Serbia. (ivan.stefanovic@ihtm.bg.ac.rs)
[3]University of Belgrade, Faculty of Technology and Metallurgy, Karnegijeva 4, 11100 Belgrade.
[4]Military Technical Institute, Ministry of Defense, Ratka Resanovića 1, 11000 Belgrade.
[5]University of Padova, Department of Chemical Sciences, via Marzolo 1, 35131 Padova, Italy.

ABSTRACT

In this study, unmodified TiO_2 nanoparticles (NPs) and TiO_2 NPs surface modified with lauryl gallate were incorporated into polyurethane (PU) network, based on Boltorn® aliphatic hyperbranched polyester of the second pseudo generation (BH-20) as crosslinking agent and polycaprolactone (PCL) as soft segment (SS). The influence of the applied TiO_2 NPs on viscoelastic properties and thermo-oxidative stability of the prepared PU/TiO_2 nanocomposites (NCs) were investigated by dynamic mechanical analysis (DMA) and thermogravimetric analysis (TGA), respectively. DMA results revealed that addition of unmodified and modified TiO_2 NPs led to the increase of glass transition temperature of SS, decrease of the glass transition temperature of hard segments and crosslinking density of PU network. According to the obtained results, PU/TiO_2 NC loaded with TiO_2 NPs surface modified with lauryl gallate has better thermo-oxidative stability than pure PU and PU/TiO_2 NC prepared with unmodified TiO_2 NPs.

INTRODUCTION

Nano-sized TiO_2 is one of the most versatile materials, often applied as filler for the preparation of polymer based NCs. This metal oxide NPs have become increasingly intriguing because of their excellent chemical and physical stability, nontoxicity, low cost, high specific surface area, high reactivity, unique electro-chemical and photocatalytic properties, and are therefore widely used as UV-resistant material and in the field of chemical fiber production, plastics, printing ink, coatings, self-cleaning ceramics, antibacterial materials, foods packing material, chemical industry, cosmetics, etc. [1]. The main goal for designing PU/TiO_2 NCs is to create stable material with excellent multiple performances, such as improved thermal, mechanical, barrier, dielectric and antimicrobial properties compared to the pure PU matrix. Therefore, the influence of unmodified and modified TiO_2 NPs on the properties of environmentally friendly polyurethane network was investigated in this work.

METHODS

Titanium dioxide NPs (P25, size 25 nm) were obtained from Degussa, while lauryl gallate (LG) and acetonitrile (AN) were purchased from Sigma-Aldrich. TiO_2 NPs were surface modified with lauryl gallate by adding 2 g of TiO_2 in 100 cm^3 solution of LG in AN (concentration 0.01 mol dm^{-3}). After placing the obtained mixture in ultrasonic bath for 10 min and leaving to rest overnight, TiO_2 NPs surface modified with LG (TiO_2-LG) were precipitated in centrifuge, washed twice with AN and dried till constant weight in vacuum oven at 40 °C. For the synthesis of pure PU network, based on PCL, BH-20 and isophorone diisocyanate (IPDI), with soft segment (PCL) content of 30 wt.%,

procedure published elsewhere was applied [2]. The stoichiometric ratio between –NCO and –OH groups was 1.1. The synthesis of NCs was performed in the same manner, by addition of 1.0 wt.% (based on the total weight of PCL, BH-20 and IPDI) of unmodified or modified TiO_2 NPs, dispersed in small amount of THF using ultrasonic bath, during the first step of the reaction.

Density of samples, ρ, was determined at room temperature, using pycnometer and distilled water. The average of three measurements was taken.

Dynamic-mechanical analysis (DMA) of samples was performed using Modular Compact Rheometer MCR-302 (Anton Paar GmbH). Measurements were conducted in a torsion rectangular mode from -80 °C to 180 °C, at strain amplitude of 0.1% and angular frequency of 1 Hz, within the linear viscoelastic region. The crosslinking density of samples, ν, was calculated using the following equation:

$$\nu = \frac{G'}{RT} \tag{1}$$

where G' represents storage modulus, R is the universal gas constant and T is the absolute temperature. The number average molecular weight of polymer chain between crosslinks, M_c, was calculated as follows:

$$M_c = \frac{\rho_{PU}}{\nu} \tag{2}$$

Thermogravimetric analysis (TGA) of samples was done on a TA Instrument SDT 2960 simultaneous TG/DSC system, under an air atmosphere (flow 130 mL/min), from room temperature to 700 °C, with a heating rate of 10 °C/min.

RESULTS AND DISCUSSION

The influence of TiO_2 NPs on viscoelastic properties of PU network was investigated with DMA. Temperature dependences of storage modulus, G', and tan δ of the pure PU and prepared NCs are given in **Figure 1**.

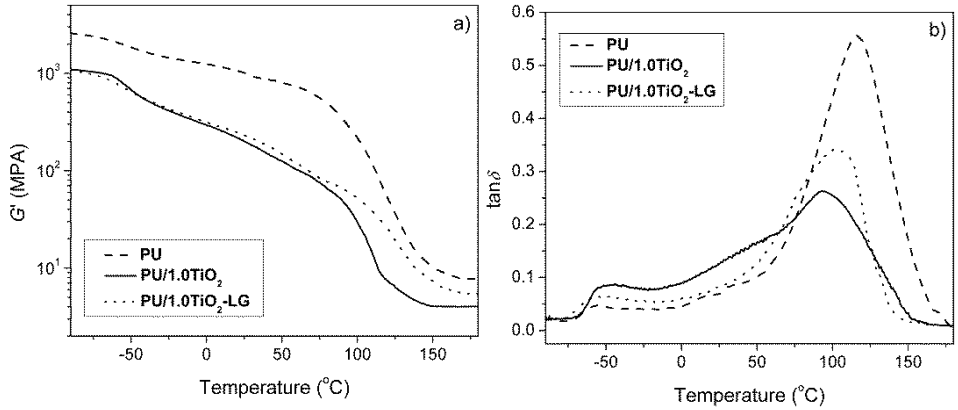

Figure 1. Temperature dependences of a) storage modulus, G' and b) tan δ of the pure PU and prepared NCs.

Obtained results show that all samples have glass transition temperature of the soft, T_{gS}, and hard segments, T_{gH}, due to the presence of microphase separated morphology (Table 1). However, the incorporation of unmodified and surface modified TiO_2 NPs increased T_{gS}, decreased T_{gH}, and, according to the results given in Table 1, also reduced crosslinking density and simultaneously increased M_c value. It can be concluded that the presence of TiO_2 NPs resulted in enhanced segmental mobility of PU. Unmodified TiO_2 NPs have greater effect on viscoelastic properties of PU matrix than TiO_2 NPs surface modified with LG. Also, tan δ peak corresponding to the T_{gH} of

sample PU/1.0TiO_2 is much broader, indicating existence of higher degree of network structure heterogeneity.

Table 1. Values of glass transition temperatures, T_{gS} and T_{gH}, determined as tan δ peak position, storage modulus in the rubbery plateau (at T_{gH} + 60 °C), G'_{RP}, density, ρ, values of the crosslinking density, ν, and number average molecular weight of polymer chain between crosslinks, M_c, of pure PU and NCs

Sample	$(T_{gS})_{\tan\delta}$ (°C)	$(T_{gH})_{\tan\delta}$ (°C)	G'_{RP} (MPa)	ρ (g/cm^3)	$\nu\times10^3$ (mol cm^{-3})	M_c (g mol^{-1})
PU	-55	116	7.7	1.011 ± 0.010	2.06	490
PU/1.0TiO_2	-50	94	4.0	1.024 ± 0.015	1.13	910
PU/1.0TiO_2-LG	-53	103	5.5	1.030 ± 0.018	1.52	680

Thermo-oxidative stability of pure PU and prepared NCs was investigated using TGA under air atmosphere. TG curves of the examined samples are given in Figure 2, while characteristic temperatures of thermo-oxidative degradation T_5, T_{10}, T_{50} and T_{90} (at 5, 10, 50 and 90% weight loss, respectively) and temperatures at which maximum thermal degradation rate occurred are listed in Table 2. The obtained results show that the incorporation of TiO_2-LG NPs in PU network leads to the slight increase of thermo-oxidative stability, indicating that TiO_2 NPs surface modified with LG are involved in inhibition of some thermo-oxidative degradation stages of PU network. According to the literature, during thermo-oxidative degradation oxygen can be adsorbed on the surface of TiO_2-LG, reducing in this manner the amount of oxygen that can reach PU matrix, which further leads to the slower thermo-oxidative degradation than in the case of pure PU [3]. Thermo-oxidative stability of pure PU is somewhat better than for PU/1.0TiO_2, probably due to the reduced crosslinking density after incorporation of unmodified TiO_2 NPs in PU matrix.

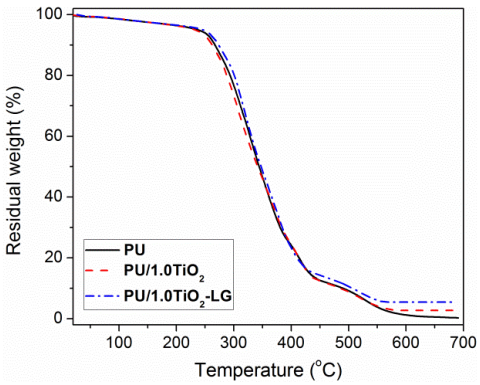

Figure 2. TG curves of the pure PU and NCs, obtained at a heating rate of 10 °C/min, in air.

Table 2. Characteristic temperatures of thermal degradation T_5, T_{10}, T_{50} and T_{90} (at 5, 10, 50 and 90% weight loss, respectively) and temperatures at which maximum thermal degradation rate occurs of the pure PU and NCs, in air atmosphere

Sample	T_5 (°C)	T_{10} (°C)	T_{50} (°C)	T_{90} (°C)	T_{sh1} (°C)	T_{max1} (°C)	T_{max2} (°C)	T_{sh2} (°C)	T_{max3} (°C)
PU	237	267	344	490	275	325	356	413	528
PU/1.0TiO_2	233	262	342	485	268	308	368	412	523
PU/1.0TiO_2-LG	246	274	347	506	279	324	375	412	524

From differential TG (DTG) curves of pure PU and NCs, given in Figure 3, and results listed in Table 2 it can be observed that all samples have three decomposition steps in air. The first DTG peak (T_{max1}) is associated to the degradation of the urethane bonds of the hard segments, which represents the weakest link in PU [2,4]. The second and third DTG peak (T_{max2}) and (T_{max3}) corresponds to the thermo-oxidative degradation of soft segments. It can be observed that incorporation of TiO_2 NPs in PU matrix led to visible splitting of the first and the second DTG peak, which are in DTG curve for pure PU overlapped. The first and the second DTG peak each have one shoulder, the first on its left side (T_{sh1}) corresponding to the thermal degradation of HS, and the second on its right side (T_{sh2}), assigned to the thermal degradation of PCL.

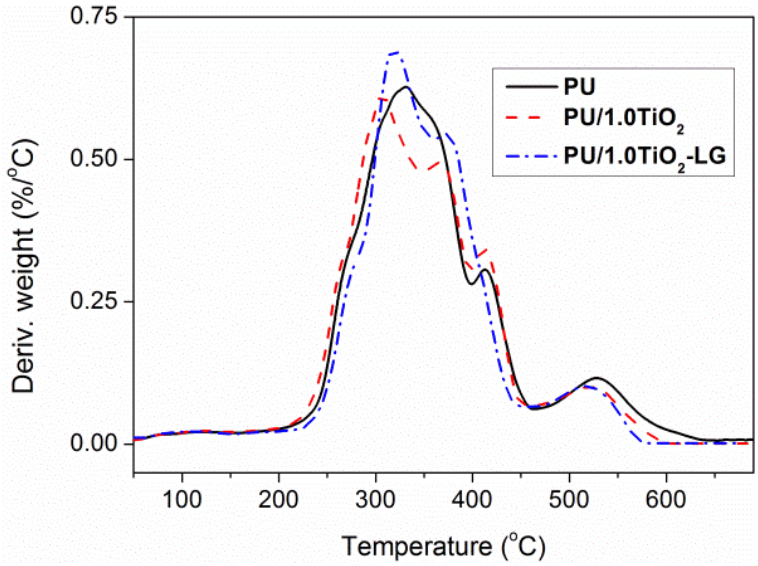

Figure 3. DTG curves of the pure PU and NCs, determined at a heating rate of 10 °C/min, in air.

CONCLUSION

Viscoelastic properties and thermo-oxidative stability of PU matrix are changed after incorporation of unmodified TiO_2 NPs and TiO_2 NPs surface modified with LG. Value of T_{gS} is higher, while T_{gH} and crosslinking density of prepared NCs are lower than for pure PU, while thermo-oxidative stability of PU network was improved by incorporation of TiO_2-LG NPs.

Acknowledgment

This work was supported by the Ministry of Education, Science and Technological Development of the Republic of Serbia (grant no 451-03-68/2022-14/200026 and 451-03-68/2022-14/200135).

REFERENCES

[1] X. Chen, S. S. Mao, Chem. Rev., 107 (2007) 2891.
[2] J. V. Džunuzović, I. S. Stefanović, E. S. Džunuzović, A. Dapčević, S. I. Šešlija, B. D. Balanč, G. C. Lama, Prog. Org. Coat., 137 (2019) 105305.
[3] E. S. Džunuzović, J. V. Džunuzović, A. D. Marinković, M. T. Marinović-Cincović, K. B. Jeremić, J. M. Nedeljković, Eur. Polym. J., 48 (2012) 1385.
[4] D. K. Chattopadhyay, D. C. Webster, Prog. Polym. Sci., 34 (2009) 1068.

STRUCTURE AND MECHANICAL PROPERTIES OF POLYURETHANE/ORGANOCLAY NANOCOMPOSITES

I. S. Stefanović[1], J. V. Džunuzović[1,2], E. S. Džunuzović[3] and C. Marega[4]

[1]University of Belgrade, Institute of Chemistry, Technology and Metallurgy, Njegoševa 12, 11000 Belgrade, Serbia. (ivan.stefanovic@ihtm.bg.ac.rs)
[2]University of Belgrade, Institute of Chemistry, Technology and Metallurgy, Center of Excellence in Environmental Chemistry and Engineering, Njegoševa 12, 11000 Belgrade, Serbia.
[3]University of Belgrade, Faculty of Technology and Metallurgy, Karnegijeva 4 ,11020 Belgrade, Serbia.
[4]University of Padova, Department of Chemical Sciences, via Marzolo 1, 35131, Padova, Italy.

ABSTRACT

Polyurethane/organoclay nanocomposites (PUNs) based on 4,4'-diphenylmethane diisocyanate (MDI) and 1,4-butanediol (BD) as the components of the hard segments (HS) and *α,ω*-dixydroxyethoxy propyl poly(dimethylsiloxane) (EO-PDMS) as the part of the soft segments (SS), were prepared by *in situ* polymerization. Nanocomposites, having different HS content (10 and 20 wt%), were prepared using 1 wt% of organomodified montmorillonite clay (Cloisite 30B®) as nanofiller. Morphology of clay nanoparticles and mechanical properties of PUNs were investigated by XRD analysis and tensile test measurements, respectively. The obtained XRD results revealed that clay nanoparticles were completely delaminated and well dispersed as intercalated or partially exfoliated layers in the polymer matrix. XRD also confirmed that prepared PUNs have amorphous character. Prepared PUNs have good mechanical properties, which allow them to be used for different purposes, such as elastomers, coatings, adhesives, etc.

INTRODUCTION

Segmented thermoplastic polyurethanes (PUs) are linear multiblock copolymers constructed of alternating soft segments (SS) and hard segments (HS). Their physical and chemical properties can be easily controlled and set up with different composition, by the right choice of reactants, synthesis conditions, etc [1]. PUs are widely used due to the good tensile strength, toughness, elasticity and ability to be easily processed.

Despite all good properties, some physical and chemical performances of PUs still can be improved. One of the possible ways to do this is to incorporate different nanoparticle fillers (at very low weight content, lower than 5 wt%), such as layered silicates i.e. clays, into the polymer matrix. In this manner, polyurethane/organoclay nanocomposites (PUNs), that combine properties of organic (polymer) and inorganic (clay) part, are obtained. However, the incorporation of clay nanoparticles into PUs is quite demanding, due to their incompatibility. This obstacle can be overcome by using clays previously modified with organic long-chain cations, such as alkylammonium or alkylphosphonium ions, and by applying sonication during synthesis. In these ways, the polymer/clay interfacial interactions will be improved, leading to the uniform dispersion of clay nanoparticles within the polyurethane matrix [2]. In order to enable better incorporation of polyurethane chains inside clay layers, the distance between them should be increased. In this manner the preferred clay morphologies, such as intercalated or exfoliated, or partially exfoliated or mixed intercalated-exfoliated structure, will be obtained. Surely, the aim is to obtain completely delaminated and well dispersed single clay layers in PUN, in order to achieve improvement of mechanical properties of polymer matrix [3].

EXPERIMENTAL

α,*ω*-Dixydroxyethoxy propyl poly(dimethylsiloxane) (EO-PDMS) was supplied from ABCR, and has M_n = 1000 g/mol and purity 95%. 4,4'-Diphenylmethane diisocyanate (MDI), supplied from Aldrich, was used as received, while 1,4-butanediol (BD) which was also supplied from Aldrich was firstly distilled and then dried over molecular sieves (0.4 nm). *N*,*N*-Dimethylacetamide (DMAc, from Acros) and tetrahydrofuran (THF, from J.T. Baker) were used as solvents and before synthesis were purified by distillation. Dibutyltin dilaurate, supplied from Kefo, was used as catalyst in the form of catalyst solution in THF/DMAc mixture (1/1, v/v). Natural montmorillonite clay was organically modified with methyl-tallow-*bis*-2-hydroxyethyl quaternary ammonium salt. This clay is commercially known as Cloisite 30®.

Two samples of PUNs, based on EO-PDMS and clay Cloisite 30B®, with different HS content (10 and 20 wt%, samples PUN10 and PUN20, respectively), were prepared by *in situ* two-step polyaddition reaction in THF/DMAc mixture (1/1, v/v) and with a molar ratio of –NCO/–OH groups 1.05. In the first step, MDI, EO-PDMS and delaminated clay (1 wt%) were mixed in order to prepare –NCO-prepolymer with addition of catalyst dibutyltin dilaurate, and in the second step BD was added to the reaction mixture at 60 °C for 6 h. The reaction of polymerization took place in an inert atmosphere of argon. After the second step, the reaction mixture was sonicated in an ultrasonic bath (20 min at room conditions), for better dispersion of clay nanoparticles within PUNs. Then, the PUN films were prepared by placing reaction mixtures in the Teflon® dishes, followed by their drying in air and vacuum oven for 24h at 50 °C and 24h at 40 °C, respectively.

XRD analysis were carried out with a Bruker AXS D8 ADVANCE Plus diffractometer in Bragg-Brentano geometry and Cu Kα radiation (λ = 0.154 nm). The data were collected using 0.05°/step and 0.5 s/step. 2θ range was from 5 to 50°.

Mechanical properties (tensile strength, elongation at break and Young's modulus) of PUNs were investigated on an Instron Model 3300 mechanical tester at room temperature. Specimens were cut into rectangular shape, and stress-strain measurements were obtained at strain rate of 2 mm/min. At least three different measurements were performed for each PUN sample.

RESULTS AND DISCUSSION

The XRD analysis was performed to analyze the presence of crystalline structures and to determine the clay layers structure in the prepared PUNs. The obtained XRD patterns of the prepared PUNs and Cloisite 30B® clay are presented in Figure 1.

In the obtained diffraction pattern of the Cloiste 30B® clay there are a few reflections at 2θ = 9.4, 19.9, 35.1 and 43.1° of low intensity. The main and the most intensive reflection at 2θ = 4.8° was omitted, since the restriction of the applied XRD instrument was to start measuring from 2θ = 5.0°. The reflections corresponding to the clay are not observed in the obtained diffraction patterns of the prepared PUNs, which indicates that clay layers are separated into an individual layers, and that intercalated and partially exfoliated morphology of these layers in the PUNs was achieved. Moreover, these reflections can also be hidden due to the low content of clay nanoparticles (1 wt%) or can be overlapped by scattering power noise during the measuring [4, 5].

In the obtained diffractograms of the prepared PUNs, very broad and stretched reflections at 2θ = 12.5 and 21.6° are observed. These reflections are related to the amorphous structure, the first one at 12.5° originates from EO-PDMS blocks from the SS, and the second one at 21.6° originates from the amorphous parts of the HS [4]. Furthermore, the intensity of the first reflection increased, while the second decreased with increasing the content of SS in the PUNs, as expected. XRD diffraction patterns show the absence of distinctive peaks and presences of amorphous halos, which indicate that prepared PUNs have amorphous character.

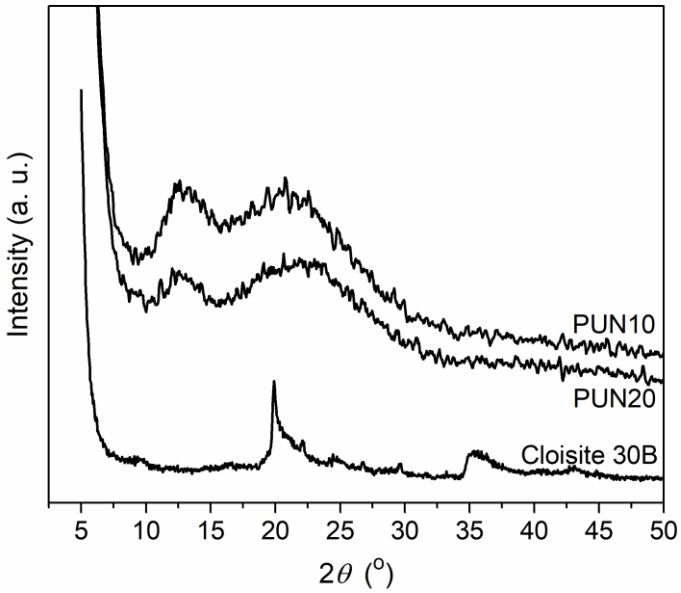

Figure 1. XRD patterns of PUN films.

Table 1. Tensile strength, elongation at break and Young's modulus of the prepared PUNs.

Sample	Tensile strength (MPa)	Elongation at break (%)	Young's modulus (MPa)
PUN10	7.7 ± 0.4	77.2 ± 3.8	39.6 ± 3.1
PUN20	13.6 ± 0.7	42.7 ± 2.9	156.8 ± 8.3

The stress-strain diagrams and obtained values of tensile strength, elongation at break and Young's modulus are presented in Figure 2 and Table 1, respectively.

The tensile strength increased from 7.7 to 13.6 MPa, and Young's modulus increased from 39.6 MPa to 156.8 MPa, while the maximum of elongation dropped from 77.2% to 42.7% with increasing the HS content in the prepared PUNs. According to the obtained results, with increasing the HS content, tensile strength and Young's modulus increase, indicating increase of rigidity of these PUNs. Furthermore, addition of the clay nanoparticles led to improvement of mechanical properties, due to the good dispersion of partially exfoliated and intercalated clay layers (confirmed by XDR analysis) in PU matrix. This probably occurs due to the clay-polymer tethering and hydrogen bonding between clay nanoparticles and polyurethane chains [6]. On the other hand, with increasing the tensile strength and Young's modulus values, the maximum of elongation was expected to decrease, as shown in Table 1.

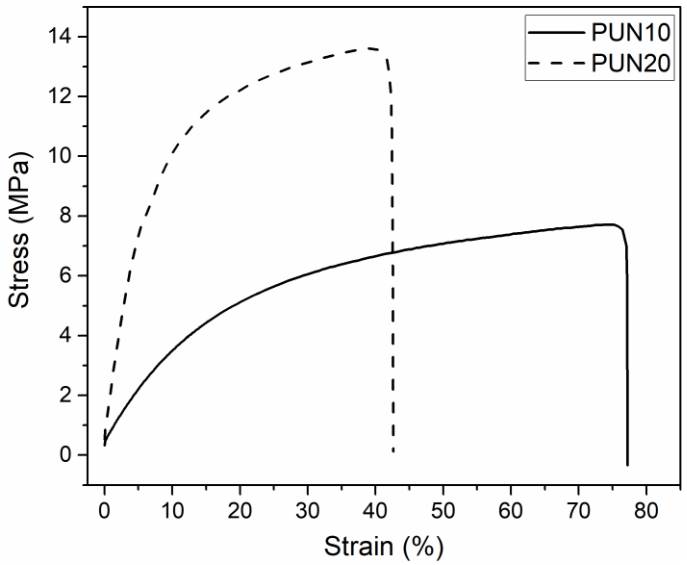

Figure 2. Stress-strain curves of PUN samples.

CONCLUSION

The PUN samples with different HS content (10 and 20 wt%), based on MDI, EO-PDMS, BD and organomodified montmorillonite clay (Cloisite 30B®), were successfully prepared. XRD analysis showed that these PUNs have an amorphous structure and mostly intercalated and partially exfoliated morphology of clay layers in the PUNs. Measurement of mechanical properties showed that these PUNs possess good values of tensile strength, elongation at break and Young's modulus, which are necessary for their use as elastomers, coatings, adhesives, etc.

Acknowledgment

This work was supported by the Ministry of Education, Science and Technological Development of the Republic of Serbia (Grant No. 451-03-68/2022-14/200026 and 451-03-68/2022-14/200135).

REFERENCES

[1] Fenfen, W., Shengli, C., Qiang, W., Rongchun, Z., Pingchuan, S., Polymer 163 (2019) 154.
[2] Ho, M. W., Lam, C. K., Lau, K. tak., Ng, D. H. L., Hui, D., Compos. Struct. 75 (2006) 415.
[3] Paul, D. R., Robeson, L. M., Polymer 49 (2008) 3187.
[4] Stefanović, I., Špírková, M., Ostojić, S., Stefanov, P., Pavlović, V., Pergal, M., Appl. Clay Sci., 149 (2017) 136.
[5] Stefanović, I. S., Marković, B. M., Nastasović, A. B., Vuković, Z. M., Dapčević, A., Pavlović, V.B., Sci. Sinter., 54 (2022), article in press.
[6] Pattanayak, A., Jana, S. C., Polymer, 46 (2005) 3275.

PREPARATION AND SWELLING PROPERTIES OF POLYURETHANE/TiO_2 NANOCOMPOSITES

J. V. Džunuzović[1,2], I. S. Stefanović[2], E. S. Džunuzović[3] and C. Marega[4]

[1]University of Belgrade, Institute of Chemistry, Technology and Metallurgy, Center of Excellence in Environmental Chemistry and Engineering, Njegoševa 12, 11000 Belgrade, Serbia.
[2]University of Belgrade, Institute of Chemistry, Technology and Metallurgy, Njegoševa 12, 11000 Belgrade, Serbia. (ivan.stefanovic@ihtm.bg.ac.rs)
[3]University of Belgrade, Faculty of Technology and Metallurgy, Karnegijeva 4, 11100 Belgrade.
[4]University of Padova, Department of Chemical Sciences, via Marzolo 1, 35131 Padova, Italy.

ABSTRACT

Polyurethane/TiO_2 nanocomposites (NCs) were fabricated from environmentally friendly polyurethane (PU) network, based on polycaprolactone (PCL) and Boltorn® aliphatic hyperbranched polyester of the second pseudo generation (BH-20) as crosslinking agent, and unmodified and surface modified TiO_2 nanoparticles (NPs). The surface modification of TiO_2 NPs was done with lauryl gallate. The chemical structure of the prepared PU/TiO_2 NCs was studied by Fourier transform infrared spectroscopy (FTIR), while their amorphous nature was confirmed by X-ray diffraction (XRD). The influence of type and content of the applied TiO_2 NPs on swelling properties in toluene and tetrahydrofuran (THF) and on water absorption of the prepared PU/TiO_2 NCs were investigated. The obtained results revealed that swelling behavior depends on the used solvent, while percentage of absorbed water decreases with increasing content of TiO_2 NPs and it is generally lower in NCs prepared with modified TiO_2 NPs.

INTRODUCTION

Polymer nanocomposites are materials in which inorganic nano-sized particles, having dimensions less than 100 nm, are dispersed using different procedures in a polymer matrix. In this manner, material with significantly improved physical and mechanical properties, compared to the pure polymer, can be obtained. The improvement of properties is achieved through the establishment of unique synergisms between the properties of polymer and NPs. Properties of polymers, which are often reported in the literature to be improved after incorporation of NPs, include mechanical properties (strength, modulus and dimensional stability), thermal stability and heat distortion temperature, electrical and thermal conductivity, chemical resistance, surface appearance, barrier properties, refractive index and optical clarity, flame resistance and reduced smoke emission, etc [1]. One of the main challenges in developing high performance polymer NC is uniform dispersion of NPs in polymer matrix. This will enable appearance of very large interfacial area per volume between the NPs and applied polymer, and consequently increase the possibility for the improvement of material performances.

In this study, polyurethane/TiO_2 NCs were prepared using environmentally friendly polyurethane network, based on PCL as soft segment and BH-20 as crosslinking agent, and unmodified and surface modified TiO_2 NPs. The surface modification of TiO_2 NPs was done with lauryl gallate. The chemical structure, crystallinity, swelling properties and water absorption of the pure PU and prepared NCs were investigated.

METHODS

Lauryl gallate (LG) and acetonitrile (AN) were obtained from Sigma-Aldrich, while commercial TiO_2 NPs (P25, size 25 nm) were purchased from Degussa. The surface modification of commercial

TiO_2 NPs with lauryl gallate was performed according to the following procedure. In 100 cm^3 solution of LG in AN (concentration 0.01 mol dm^{-3}), 2 g of TiO_2 was added. The mixture was kept in ultrasonic bath for 10 min, and then left overnight. After that, TiO_2 NPs surface modified with LG (TiO_2-LG) were precipitated using centrifuge, washed twice with AN, and dried in vacuum oven at 40 °C until constant weight was achieved. Pure polyurethane network (PU), based on PCL, BH-20 and isophorone diisocyanate (IPDI), with soft segment (PCL) content of 30 wt.%, was prepared by a two-step solution polymerization method, according to the procedure described elsewhere [2]. The stoichiometric ratio between –NCO and –OH groups was 1.1. Nanocomposites PU/TiO_2 and PU/TiO_2-LG were prepared using the same procedure, by addition of adequate amount of unmodified or modified TiO_2 NPs (0.5, 1.0 or 2.0 wt.% based on the total weight of PCL, BH-20 and IPDI) during the first step of the reaction. In order to achieve uniform dispersion of TiO_2 NPs in PU, adequate amount of TiO_2 NPs was first mixed in a small amount of THF for 20 min in ultrasonic bath. The number in the name of prepared NCs stands for NPs content.

FTIR spectra of prepared samples were recorded using ATR Nicolet spectrophotometer Magna System 560, in the scanning range from 400 to 4000 cm^{-1}, at spectral resolution of 4 cm^{-1}, using 64 scans.

X-ray diffraction (XRD) patterns of PCL and prepared samples were obtained with a Bruker AXS D8 ADVANCE Plus diffractometer in Bragg-Brentano geometry, using CuKα radiation (λ = 0.154 nm) ranging from 10° to 35° 2θ, with a step width of 0.05° and a constant counting time of 0.5s per step.

Swelling properties of pure PU and prepared NCs were examined in THF and toluene at room temperature. Square test samples (10.0 mm × 10.0 mm × 1.0 mm ± 0.2 mm) were immersed in selected medium, and their weight, *w*, was periodically measured until constant value (equilibrium swelling). The excess of medium was carefully removed using filter paper, before each weight measurement. The swelling degree, *q*, was calculated according to the following equation:

$$q = \frac{w - w_0}{w_0} \quad (1)$$

where w_0 is the weight of the sample before swelling. The average value obtained from three different specimens was used.

Water absorption of samples (10.0 mm × 10.0 mm × 1.0 mm ± 0.2 mm) was examined after their immersion in distilled water for 48h, at room temperature. The weight percent of the water absorption, *WA*, was calculated as follows:

$$WA = \frac{w_W - w_{W0}}{w_{W0}} \times 100 \quad (2)$$

where w_W is the weight of the sample after 48h and w_{W0} is the weight of dry sample. Results from three different specimens were averaged.

RESULTS AND DISCUSSION

FTIR spectra of PU and NCs prepared with 0.5 wt.% of modified and unmodified TiO_2 NPs are given in Figure 1a. In the FTIR spectra of PU and NCs the band at 2260 cm^{-1} was not observed, indicating completion of the reaction of –NCO groups and formation of urethane bonds. The band which appear around 3330 cm^{-1} is ascribed to the stretching vibrations of hydrogen-bonded urethane N-H groups, while bands at around 2950 and 2870 cm^{-1} correspond to asymmetric and symmetric stretching vibrations of CH_2 groups, respectively. Band characteristic for carbonyl groups appears between 1715 and 1721 cm^{-1} and its position moves to the higher wavenumber for NCs, indicating presence of lower degree of hydrogen bonding after incorporation of modified and unmodified TiO_2 NPs in PU. Furthermore, band ascribed to the deformation vibrations of CH_2

groups appears at 1460 cm^{-1}, while bands characteristic for amide II and amide III vibrations can be observed at around 1540 and 1240 cm^{-1}, respectively. Bands which correspond to asymmetric and symmetric stretching vibrations of C-O-C groups appear at around 1090 and 1030 cm^{-1}, respectively.

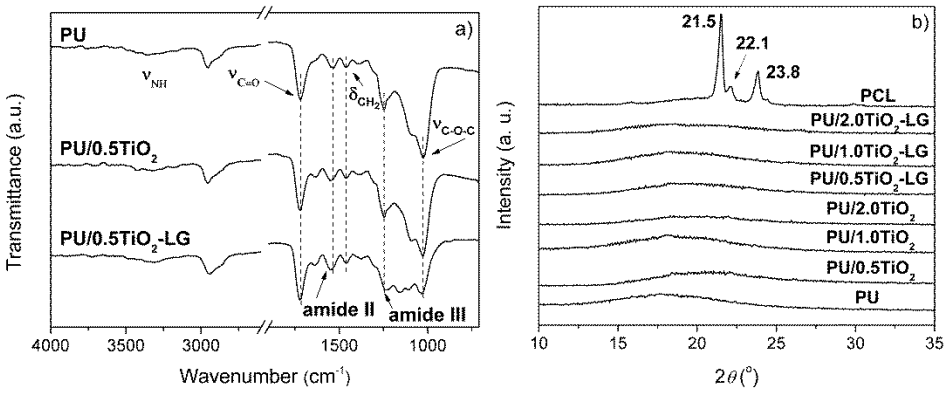

Figure 1. a) FTIR spectra of pure PU and nanocomposites PU/0.5TiO_2 and PU/0.5TiO_2-LG and b) XRD patterns of pure PU and prepared nanocomposites.

XRD patterns of PCL, PU and all prepared NCs are displayed in Figure 1b. The reflections observed in diffractogram of PCL at 2θ = 21.5°, 22.1° and 23.8° correspond to the (110), (111) and (200) planes of PCL orthorhombic crystal lattice (space group $P2_12_12_1$), respectively. These reflections are characteristic for semicrystalline PCL [3]. On the other hand, a broad weak reflection at $2\theta \sim 20.1°$ appeared as a consequence of amorphous contribution in PCL. In XRD pattern of PU and prepared NCs only amorphous halos are present, indicating amorphous character of synthesized samples, due to the presence of crosslinked structure.

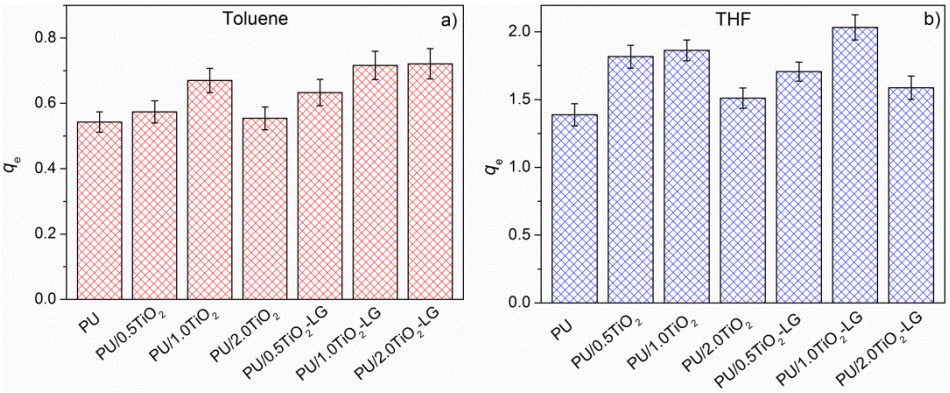

Figure 2. Equilibrium swelling degree (q_e) of pure PU and prepared nanocomposites.

The swelling behavior of PU and prepared NCs was investigated in toluene and THF and obtained results are given in Figure 2. It can be observed that equilibrium swelling degree (q_e) in both solvents depends on type and content of the applied TiO_2 NPs. Since q_e of NCs is in both solvents higher than q_e of pure PU, it can be concluded that the presence of unmodified and surface modified TiO_2 NPs in PU network decreases the crosslinking density of PU. Generally, q_e values are only slightly higher for PU/TiO_2-LG NCs than q_e values of PU/TiO_2 NCs. The increase of the content of TiO_2 and TiO_2-LG NPs up to 1.0 wt.% led to greater swelling of NCs in both solvents, while further increase up to 2 wt.% induced additional slight increase of q_e value only for

PU/2.0TiO_2-LG NC in toluene. The presence of 2 wt.% of the applied NPs probably reduced the diffusion of solvents in prepared NCs and therefore led to the q_e lowering.

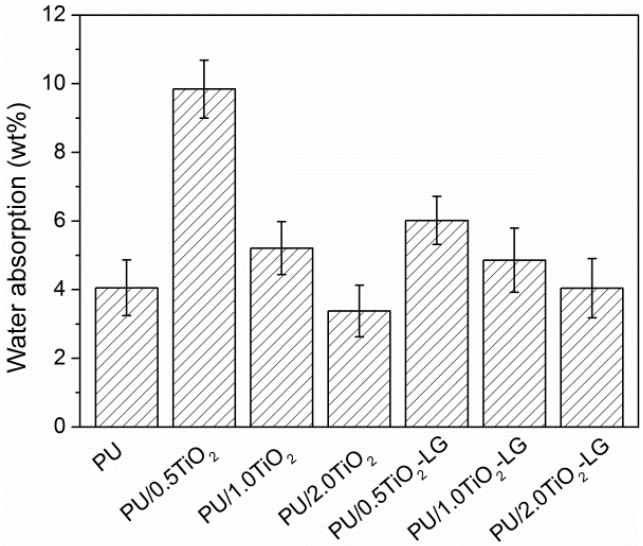

Figure 3.Water absorption of pure PU and prepared nanocomposites.

The water absorption of the pure PU and prepared NCs was examined at room temperature by their immersion in distilled water for 48h, and the obtained results are presented in Figure 3. Polyurethane network itself has hydrophobic character due to the presence of hydrophobic PCL as soft segment [2]. The incorporation of 0.5 wt.% of TiO_2 NPs in PU network reduces its crosslinking density, leading to greater water absorption ability than pure PU. Due to the presence of long hydrophobic aliphatic groups (C12) on the surface of TiO_2 NPs modified with LG, the percentage of absorbed water of PU/0.5TiO_2-LG is lower than for PU/0.5TiO_2. The increase of the content of incorporated unmodified and modified TiO_2 NPs in PU, led to further decrease of water absorption, as a consequence of the hydrophobic character of the applied TiO_2 NPs.

CONCLUSION

Polyurethane/TiO_2 NCs were prepared using different content of unmodified TiO_2 NPs and TiO_2 NPs surface modified with lauryl gallate. The chemical structure of the prepared NCs was examined by FTIR spectra. XRD results revealed amorphous character of pure PU and prepared NCs. Swelling behavior of prepared NCs depends on the used solvent, while percentage of absorbed water decreases with increasing content of TiO_2 NPs and it is generally lower in NCs prepared with modified TiO_2 NPs.

Acknowledgment

This work was supported by the Ministry of Education, Science and Technological Development of the Republic of Serbia (grant no 451-03-68/2022-14/200026 and 451-03-68/2022-14/200135).

REFERENCES

[1] J. W. Krumpfer, T. Schuster, M. Klapper, K. Müllen, Nano Today, 8 (2013) 417.
[2] J. V. Džunuzović, I. S. Stefanović, E. S. Džunuzović, A. Dapčević, S. I. Šešlija, B. D. Balanč, G. C. Lama, Prog. Org. Coat., 137 (2019) 105305.
[3] H. J. Woo, S. R. Majid, A. K. Arof, Solid State Ion., 252 (2013) 102.

VANILLIN-CROSSLINKED CHITOSAN AS BIO-FUNCTIONAL MATERIAL: EFFECT OF MOLECULAR WEIGHT ON SWELLING, POROSITY AND DEGRADATION PROPERTIES

J. Tadić, A. Radosavljević, N. Nikolić, J. Spasojević and Z. Kačarević-Popović

Vinča Institute of Nuclear Sciences - National Institute of the Republic of Serbia, University of Belgrade, Mike Petrovića Alasa 12-14, 11351 Vinča, Belgrade, Serbia
(julijana.tadic@vin.bg.ac.rs)

ABSTRACT
Chitosan is a widely investigated biopolymer with a broad spectrum of biomedical applications, such as wound dressings, tissue engineering and drug delivery systems, due to its excellent biocompatibility and biodegradability. Vanillin is a natural aldehyde, identified as a bio-based crosslinking agent which can simultaneously improve the physical, mechanical and antioxidant properties of chitosan-based materials. Herein, vanillin-crosslinked chitosan scaffolds were synthesized by the freeze-drying method. Different types of scaffolds were prepared by using low and medium molecular weight chitosan. The interactions established between chitosan and vanillin were studied by FT-IR spectroscopy. Furthermore, swelling ratio, porosity and degradation were investigated, and the effect of various molecular weights of chitosan was evaluated. The results indicated that scaffolds with medium molecular weight chitosan have a high potential to be applied as the material for biomedical use.

INTRODUCTION
Chitosan (CS) is an amino polysaccharide derived by deacetylation of chitin, the second most abundant natural polymer after cellulose. Besides its biocompatibility and biodegradability, CS exhibits remarkable properties for biomedical application including wound healing, drug delivery carriers and bone tissue engineering [1]. Most of the CS biological properties arise from the presence of primary amino groups along the CS polymer chain. Namely, these amino groups can be easily protonated, and able to form ionic interactions with various biomolecules. Moreover, CS exhibits antibacterial activity, mucoadhesive, analgesic and hemostatic properties [2]. On the other hand, crosslinking is a well-known method to modify the CS backbone and enhance mechanics properties [3]. Vanillin is a significant bio-based crosslinker, which exhibits antitumor, antiinflammatory, antioxidant and antimutagenic activities, contributing to both, mechanical and biological properties of CS [4]. Molecular weight is an important characteristic of chitosan polymer, which affects properties of chitosan-based materials, such as porosity, biodegradation, crystallinity, and mechanical strength [5]. In other to understand and optimize chitosan materials for biomedical applications, it is significant to examine how molecular weight affects chitosan's physiochemical and biological properties [6]. In this research, the chitosan-vanillin (CS-VAN) scaffolds were synthesized by the freeze-drying method, and the effect of chitosan's molecular weight on swelling, porosity, and degradation properties was investigated.

EXPERIMENTAL
Low molecular weight chitosan (CS-LW; 50-190 kDa) and medium molecular weight chitosan (CS-MW; 190-310 kDa) with 75-85% degree of deacetylation, vanillin (VAN; 99%), acetic acid (glacial), and ethanol (absolute for analysis) were purchased from Sigma Aldrich. Fresh phosphate-buffered saline (pH 7.4) was prepared according to standard procedure, and use as it is.

CS-LW and CS-MW solutions with a concentration of 1% w/v, were prepared by dissolving corresponding CS in aqueous acetic acid solution (2% v/v) under magnetic stirring at 50°C, for 3 h, until their complete dissolution. Vanillin solution was made by dissolving 0.15 g of vanillin in 5 ml of ethanol. Next, the mixtures with a mass ratio of 1:1 (CS:VAN) were prepared by adding the vanillin solution (5 ml) to each, low and medium molecular weight, chitosan solution (15 ml). The mixtures were poured in Petri dishes and frozen. Subsequently, frozen mixtures were freeze-dried for 48h to obtain the 3D porous scaffolds. The scaffolds were immersed in 0.25 M NaOH solution, washed with distilled water, frozen and lyophilized again. Obtained scaffolds were marked as CS-LW-VAN (chitosan-low molecular weight-vanillin) and CS-MW-VAN (chitosan-medium molecular weight-vanillin) and subjected for further investigation.

Fourier transform infrared (FT-IR) spectra of the pure chitosan, vanillin and prepared scaffolds were recorded using a Nicolet™ iS™ 10 FT-IR Spectrometer (Thermo Fisher Scientific) with Smart iTR™ Attenuated Total Reflectance (ATR) sampling accessories. The FT-IR spectra were recorded in the 4000-500 cm^{-1} range with 20 scans per spectrum.

Equilibrium swelling ratio (SD_{eq}) was measured by the conventional gravimetric method [7]. The lyophilized chitosan-vanillin scaffolds (disc; diameter 20 mm, thickness 0.5 mm) were weighed (W_0) and then immersed in deionized water, at temperature 25°C, for 24 h. After incubation of 24 h, swollen scaffolds were weighted (W_s), and the equilibrium swelling ratio was calculated using equation $SD_{eq} = (W_s\text{-}W_0)/W_0$.

The liquid displacement method was used to calculate porosity of the scaffolds [7]. The scaffold was placed in the ethanol bath of known volume (V_1). The volume sum of the ethanol and the scaffold is measured (V_2). The scaffold is removed from this bath and the remaining volume of ethanol in the bath is measured (V_3). The scaffold porosity (P) was calculated as $P = [(V_1\text{-}V_3)/(V_2\text{-}V_3)] \times 100$.

The *in vitro* biodegradation of the scaffolds was tested after 7 days of immersion in PBS at 37°C. Initial weights of the scaffolds were obtained as W_i. After immersion, the scaffolds were washed in distilled water, frozen and lyophilized, and the dry weights were noted as W_d. The percentage of scaffold degradation (D) was calculated using equation $D\ (\%) = [(W_i - W_d)/W_i] \times 100$ [7].

Values of swelling ratio (SD_{eq}), scaffold porosity (P) and scaffold degradation (D) were obtained as mean value of three independent measurements.

RESULTS AND DISCUSSION

The successful preparation of CS-LW-VAN and CS-MW-VAN scaffolds was examined using FT-IR spectroscopy. The FT-IR spectra of neat CS-LW, CS-MW and vanillin were recorded, and compared to the spectra of investigated CS-LW-VAN and CS-MW-VAN scaffolds (Fig. 1a). CS-LW and CS-MW spectra showed characteristic broad bands at 3000-3600 cm^{-1} attributed to the vibrations of –OH and –NH groups. In the case of CS-MW this band was slightly higher in intensity, compared to the CS-LW, which can be ascribed to the longer CS-MW polymer chains with a larger number of –OH and –NH groups. The bands at 1652 cm^{-1} and 1563 cm^{-1} are attributed to amide I and amide II groups, respectively, whereas the peak at 1153 cm^{-1} is assigned to the stretching vibration of the C–O–C bond. In the FT-IR spectrum of vanillin, the broad band at 3170 cm^{-1} is attributed to the stretching vibrations of –OH groups. The peak at 1662 cm^{-1} belongs to the stretching vibrations of the aldehyde group, while the peak at 1262 cm^{-1} is ascribed to the vibrations of the phenolic –OH group. In the CS-LW-VAN and CS-MW-VAN spectra, broad band at 3317 cm^{-1} strongly suggests the formation of hydrogen bonds between hydroxyl and amino groups of CS and hydroxyl groups of vanillin. The peak at 1280 cm^{-1} is attributed to bending vibrations of –OH groups. Also, crosslinking of CS and VAN, in both scaffolds, via azomethine

bond formation, is confirmed by the peak at 1500 cm^{-1}, ascribed to the stretching vibrations of the azomethine C=N group [7,8].

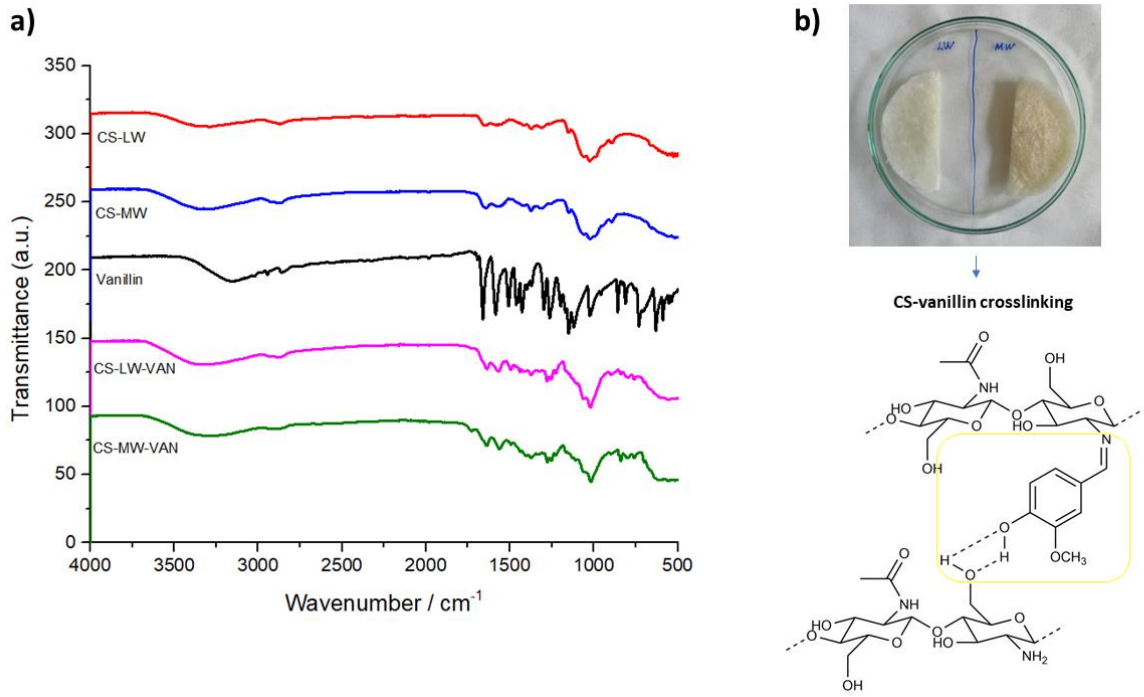

Figure 1. FT-IR spectra of investigated scaffolds (a) and photo of prepared scaffolds with schematic illustration of vanillin-chitosan crosslinking (b).

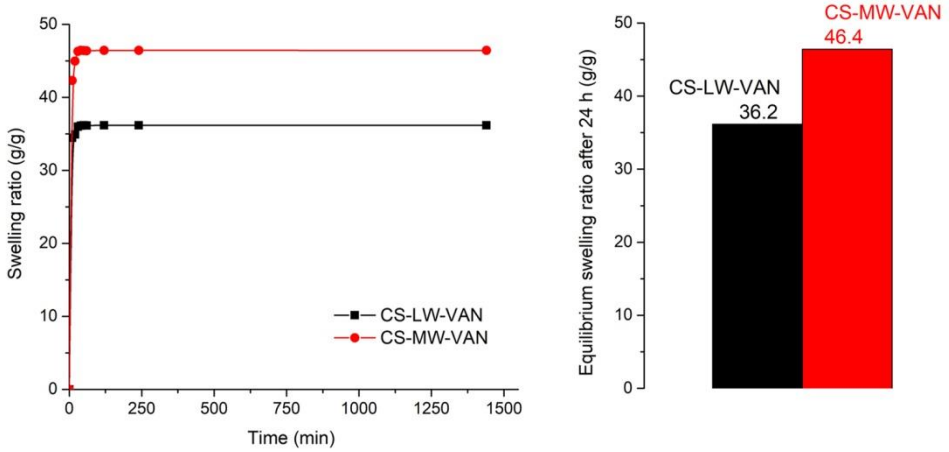

Figure 2. Swelling test for investigated scaffolds.

From the standpoint of biomedical application, good swelling ability, as well as scaffold porosity and degradation are very important factors in scaffold design. Studied CS-LW-VAN and CS-MW-VAN scaffolds swelled rapidly and reached equilibrium swelling ratio within the initial 30 min, which remained steady until the end of the swelling test (Fig. 2). After the 24 h swelling test, the equilibrium swelling ratio was around 22% higher in the case of CS-MW-VAN, which can be

ascribed to the larger and more entangled chitosan chains, leading to a greater expansion of the scaffold's network.

The porous scaffolds for tissue regeneration mimic the extracellular matrix (ECM) for cells, allowing them to adhere, proliferate, and differentiate, whereas the scaffold gradually degrades. Therefore, it is very important to ensure that material for potential application in biomedicine has convenient porosity and biodegradation [7, 9]. The porosity test showed a negligible difference in porous structure between the two investigated scaffolds. The obtained results show that the CS-MW-VAN scaffold has a slightly higher porosity (78%) compared to the CS-LW-VAN scaffold (72%), which is in agreement with the results of the swelling test. Moreover, it is known that biodegradation of chitosan scaffolds decreases with an increase in molecular weight. This study confirmed that CS-LW-VAN degrades faster than CS-MW-VAN scaffold. Namely, after 7 days in PBS, the weight loss of CS-LW-VAN was 10%, while weight loss of CS-MW-VAN was only 5%. These results also indicated stability of the synthesized scaffolds, regarding the uncrosslinked chitosan scaffolds which degradation is very fast [10].

CONCLUSION

In this work, vanillin-crosslinked chitosan scaffolds were synthesized and the effect of various molecular weights of chitosan was evaluated regarding swelling, porosity, and degradation properties. FT-IR spectroscopy indicated the Schiff base and hydrogen bonds formation, confirming the vanillin crosslinking in both CS-LW-VAN and CS-MW-VAN scaffolds. The swelling, porosity and degradation tests pointed out that CS-MW-VAN exhibited better swelling, higher porosity, and high stability during the degradation test in PBS. Hance, medium molecular weight chitosan-vanillin scaffolds have great potential for further development of bio-functional materials.

Acknowledgment

This work was supported by the Ministry of Education, Science and Technological Development of the Republic of Serbia (grant no. 451-03-68/2022-14/200017).

REFERENCES

[1] F. Croisier, C. Jérôme, European Polymer Journal, 49 (2013) 780-792.
[2] W. Wang, C. Xue, X. Mao, International Journal of Biological Macromolecules, 164 (2020) 4532-4546.
[3] M. I. Wahba, Journal of Biomaterials Science, Polymer Edition, 31 (2020) 350-375.
[4] I. Karakurt, K. Ozaltin, E. Vargun, L. Kucerova, P. Suly, E. Harea, A. Minařík, K. Štěpánková, M. Lehocky, P. Humpolícek, A. Vesel, M. Mozetic, Materials Science and Engineering: C, 126 (2021) 112125.
[5] S. Hsu, S. W. Whu, C. L. Tsai, Y. H. Wu, H. W. Chen, K. H. Hsieh, Journal of Polymer Research, 11 (2004) 141-147.
[6] M. M. Mecwan, G. E. Rapalo, S. R. Mishra, W. O. Haggard, J. D. Bumgardner, Journal of Biomedical Materials Research Part A, 97 (2011) 66-73.
[7] J. Hu, Z. Wang, J. M. Miszuk, M. Zhu, T. I. Lansakara, A. V. Tivanski, J. A. Banas, H. Sun, Carbohydrate Polymers, 271 (2021) 118440.
[8] C. Xu, W. Zhan, X. Tang, F. Mo, L. Fu, B. Lin, Polymer Testing, 66 (2018) 155-163.
[9] F. O. M. S. Abreu, C. Bianchini, M. M. C. Forte, T. B. L. Kist, Carbohydrate Polymers, 74 (2008) 283-289.
[10] I. Adekogbe, A. Ghanem, Biomaterials, 26 (2005) 7241-7250.

CO_2 CAPTURE BY AMINE POROUS POLYMERIC SORBENT

B. M. Marković, T. T. Tadić, A. B. Nastasović, N. Radić and Z. M. Vuković

University of Belgrade, Institute of Chemistry, Technology and Metallurgy, Njegoševa 12, 11000 Belgrade, Serbia. (bojana.markovic@ihtm.bg.ac.rs)

ABSTRACT

In this report, magnetic porous polymer functionalized with pentaethylenehexamine (mP-PEHA) was tested as CO_2 sorbent. The sorbent mP-PEHA was characterized by Fourier transform infrared spectroscopy in ATR mode (FTIR-ATR), scanning electron microscopy (SEM) and mercury porosimetry. CO_2 adsorption was determined using a pulse gas chromatographic method. At optimal adsorption conditions (20 °C), the CO_2 sorption capacity reached 10.8 ml CO_2/g (0.48 mmol CO_2/g). Temperature-programmed desorption (TPD) experiments were conducted to calculate the activation energy of CO_2 desorption. Low activation energy (18.34 kJ/mol) and high desorption rate, with a stable uptake in five adsorption/desorption cycles, suggest mP-PEHA as potentially excellent sorbent for CO_2 absorption.

INTRODUCTION

The increasing anthropogenic carbon dioxide (CO_2) emission is considered as the main cause of global warming. Various types of adsorbents can be potentially used for CO_2 captures, such as zeolites, porous organic polymers (POPs), porous carbons, and mesoporous materials [1]. The introduction of various amine groups into porous materials results in sorbents with high CO_2 capture capacity, selectivity, regenerability, and stability [2]. In this study, CO_2 adsorption/desorption performances of chemically stable pentaethylenehexamine (PEHA)-grafted magnetic porous polymer (mP-PEHA) with adjustable surface chemistry and pore structure were tested. The CO_2 uptake, thermodynamics and kinetics and adsorption/desorption cycle stability were determined. The performance of mP-PEHA was investigated over a range of CO_2 partial pressures.

EXPERIMENTAL

Magnetic porous polymer (mP) was prepared following the procedure described elsewhere [3]. Post-functionalization of mP with pentaethylenehexamine (PEHA) was done in a typical procedure, i.e., 7.2 g of mP and 17.7 g of PEHA were added to 300 ml of toluene and heated under stirring at 80 °C for 6 h. The sample mP-PEHA was filtered, washed with ethanol, and dried under vacuum at 40 °C.The amino groups content (C_{AG}) was determined as described in the literature [3]. FTIR-ATR spectra were taken in the range 4000–400 cm^{-1} using a Nicolet 380 spectrometer. The scanning electron microscopy (SEM) micrographs were obtained on JEOL JSM-6460LV. Pore size distributions were collected by a high-pressure mercury intrusion porosimeter Carlo Erba Porosimeter 2000 (Washington, USA, software Milestone 200). The porosity parameters (specific pore volume, V_p, pore diameter which corresponds to half of the pore volume, $D_{V/2}$, and specific surface area, $S_{s,Hg}$) were determined as described in the literature [4].

The CO_2 uptake measurements were performed using a pulse gas chromatographic method. CO_2 desorption was obtained by temperature programmed desorption tests with constant carrier gas stream flow. The experiments were performed on sample mP-PEHA (0.0150 g) in dynamic conditions in a flow system. The content of CO_2 was analyzed online by GC Shimadzu 8a, equipped with a TCD detector using a stainless steel column; 6.5 ft. long and 1/8 in. in diameter, containing 80/100 mesh HayeSep D. For adsorption experiments, the sample was exposed to pulses

of 0.1 ml CO_2 inserted into carrier gas stream (He - 2400 ml/h) at 20 °C. For temperature-programmed desorption tests, the sample was saturated with CO_2 at 20 °C. After that, desorption was performed at heating rates of 10, 20, 30, 40, and 50 °C/min, in the temperature range 20-200 °C with holding of temperature at 200 °C for 2 min. For determination of regeneration stability of mP-PEHA five CO_2 adsorption-desorption cycles were performed, consisting of CO_2 adsorption at 20 °C until saturation, and desorption at 20 to 200 °C (heating rate 30 °C/min), with 2 minutes of retention at 200 °C. After each desorption, for the next cycle, the sample was cooled to an initial adsorption temperature of 20 °C. The reproducibility of the results was verified by performing each test several times.

RESULTS AND DISCUSSION

Characterization of the sorbent

Since the practical application and CO_2 adsorption performances of amino-functionalized porous sorbents strongly depend on their characteristics such as morphology, particle chemistry (amine groups content and location), and pore structure (specific surface area, specific pore volume, pore size, and distribution), a detailed characterization of mP-PEHA was done. In FTIR-ATR spectra (Figure 1a), peaks confirming amino-functionalization are clearly visible, i.e. peaks for δ(NH) and shoulder δ(NH_2), at ~1570 cm^{-1} and ~1650 cm^{-1}, respectively. Also, the magnetic nature of the sorbent is corroborated with the peak for Fe-O vibrations at ~590 cm^{-1}[3].

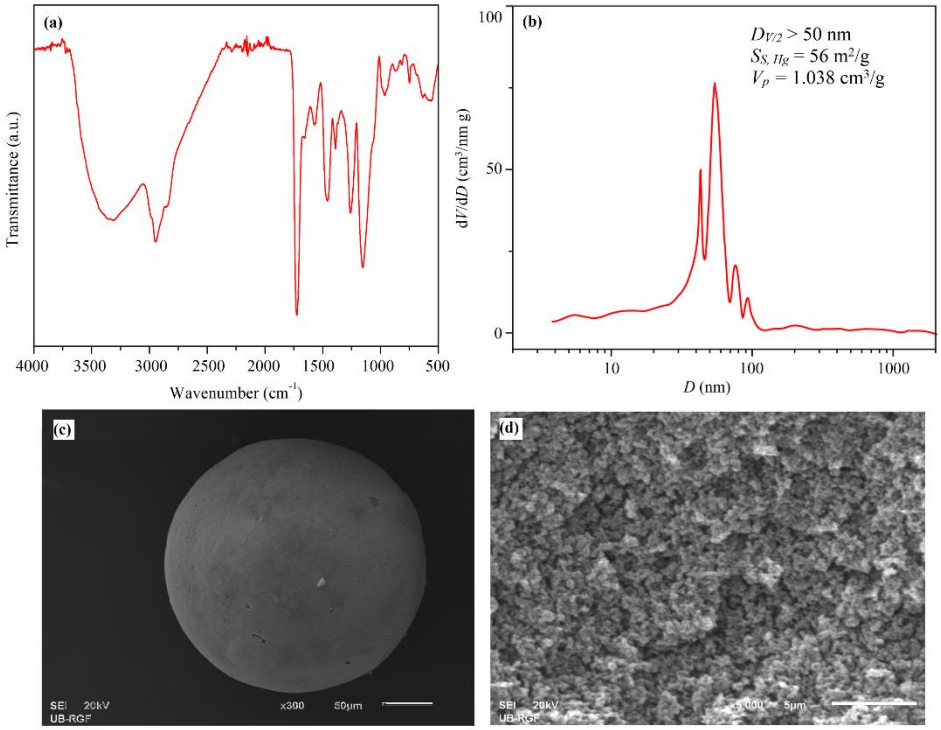

Figure 1. FTIR spectra (a), differential curve of the pore size distribution (b) and SEM microphotographs of particle surface (c) and cross-section (d) for mP-PEHA.

The differential curve of pore volume distribution curves and calculated porosity parameters are given in Figure 1b. As seen, mP-PEHA is macroporous in nature ($D_{V/2}$> 50 nm) with $S_{S,\,Hg}$ = 56 m^2/g and V_p = 1.038 cm^3/g. SEM images of mP-PEHA show a regular globular shape and smooth surface of the particles (Figure 1c), as well as a highly developed three dimensional internal porous

structure composed of a large number of globules and opened pores at the particle cross-section (Figure 1d).

CO_2 Adsorption tests

After successive insertion of a small constant volume of CO_2, polymer mP-PEHA had an adsorption capacity of 10.76 ml CO_2/g (0.48 mmol CO_2/g) which corresponds to the normalized value per unit area of 0.19 ml CO_2/m^2 (8.57 10-3 mmol CO_2/m^2).

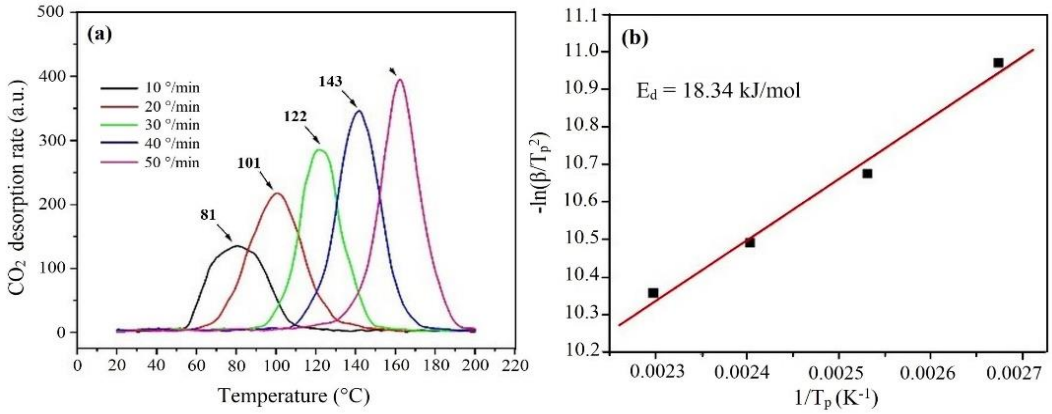

Figure 2.CO_2 desorption vs. temperature (a), relationship between the maximum desorption temperature (T_p) and the heating rate (β) for CO_2 desorption (b) from mP-PEHA [adsorption conditions: He flow rate, 2400 mL/h; adsorption temperature, 20 °C; desorption conditions: carrier gas (He) flow rate, 2400 mL/h; temperature regime: linear increase from 20 to 200 °C, holding at 200 °C for 2 min, heating rates 10, 20, 30, 40, and 50 °C/min; sorbent mass: 0.0150 g].

A series of TPD experiments were conducted at different heating rates (Figure 2a). A plot $\ln(RT_p^2/\beta)$-$1/T_p$ (Figure 2b) was obtained according to the equation (1) [5]:

$$\ln\left(\frac{RT_p^2}{\beta}\right) = \frac{E_d}{R}\left(\frac{1}{T_p}\right) + \ln\left(\frac{E_d}{k_0}\right) \quad (1)$$

where: R is the gas constant, T_p is the peak temperature, β is the heating rate (K/min), E_d is the activation energy for desorption (kJ/mol) and k_0 is the desorption rate coefficient (min^{-1}).

From a linear relationship with a high correlation coefficient (R^2=0.994) (Figure 2b), the activation energy of desorption was calculated to be ~ 18 kJ/mol. Polymer mP-PEHA showed comparable CO_2 adsorption capacity but lower CO_2 desorption energies than their analog amine-modified commercial zeolites [6]. The molecular structures of the amines and their reactions with CO_2 are the main factors affecting polymer properties in CO_2 capture. Thus, the good adsorption-desorption properties of mP-PEHA were attributed to the optimal molecular structure of pentaethylenehexamine which is the main constituent of this polymer. The low activation energies obtained for CO_2 desorption indicate a high CO_2 desorption rate and fast surface regeneration for the energy-saving applications of mP-PEHA in CO_2 capture.

Multiple CO_2 adsorption-desorption cyclic tests were performed to evaluate possible practical applications. As seen (Figure 3), mP-PEHA exhibited high performance in terms of efficient and

cyclic regeneration, since adsorption capacity maintained almost the same after five successive adsorption-desorption cycles.

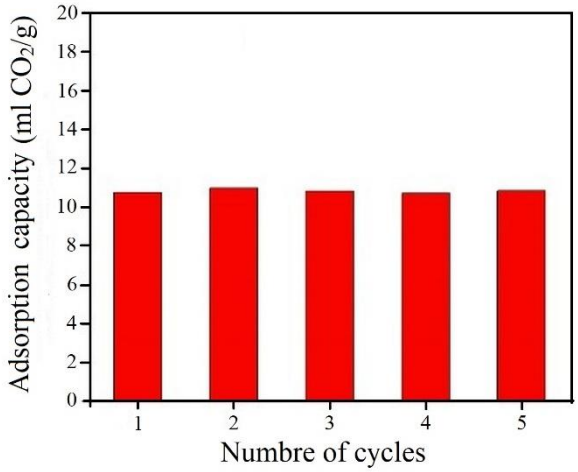

Figure 3. Adsorption-desorption properties of mP-PEHA in repeated cycles of CO_2 adsorption.

CONCLUSION

CO_2 adsorption-desorption properties of mP-PEHA suggests potentially excellent sorbent with a CO_2 adsorption capacity of 10.76 ml CO_2/g (0.48 mmol CO_2/g). It was shown that mP-PEHA could be regenerated successfully in the temperature range from 81 to 162 ^oC, with a stable uptake of ~10.8 ml CO_2/g (0.48 mmol CO_2/g) in five adsorption/desorption cycles. The obtained results showed that CO_2 adsorption on mP-PEHA is comparable to amine-modified commercial materials, Moreover, mP-PEHA showed easier and faster desorption, without reducing the adsorption capacity.

Acknowledgment

This work was supported by the Ministry of Education, Science and Technological Development of the Republic of Serbia (Grant No. 451-03-68/2022-14/200026).

REFERENCES

[1] G. Singh, J. Lee, A. Karakoti, R. Bahadur, J. Yi, D. Zhao, K. AlBahily, and A. Vinu, Chem. Soc. Rev., 49 (2020) 4360.
[2] A. M. Varghese, and G. N. Karanikolos, Int. J. Greenh. Gas Control, 96 (2020) 103005.
[3] B. M. Marković, Z. M. Vuković, V. V. Spasojević, V. B. Kusigerski, V. B. Pavlović, A. E. Onjia, A. B. Nastasović, J. Alloys Compd., 705 (2017) 38.
[4] F. Rodríguez-Reinoso, and A. Sepúlveda-Escribano in: Handbook of Surfaces and Interfacesof Materials, Vol. 5, H. Nalwa (Ed.), Elsevier: Amsterdam, The Netherlands. 2001.
[5] X. Li, H-F. Guo, and H-M. Chen, Adsorp. Sci. Techol., 24 (2006) 907.
[6] H. Cheng, H. Song, S. Toan, K. A. M. Gasem, M. Fan, and F. Cheng, Chem. Eng. J., 406 (2011) 126882.

NON-LINEAR KINETIC ISOTHERMS AND THERMODYNAMIC BEHAVIOR OF As(V) ONTO HYBRID NANOCOMPOSITE

B. M. Marković[1], T. T. Tadić[1], Lj. T. Suručić[2], A. B. Nastasović[1], Z. P. Sandić[3], and A. Onjia[4]

[1]*University of Belgrade - Institute of Chemistry, Technology and Metallurgy, Njegoševa 12, 11000 Belgrade, Serbia.(bojana.markovic@ihtm.bg.ac.rs)*
[2] *Faculty of Medicine, University of Banja Luka, Save Mrkalja 14, 78000 Banja Luka, Republic of Srpska, B&H.*
[3]*University of Banja Luka, Faculty of Natural Science and Mathematics, Mladena Stojanovića 2, Banja Luka, Republic of Srpska, B&H.*
[4]*Faculty of Technology and Metallurgy, University of Belgrade, Karnegijeva 4, 11000 Belgrade, Serbia.*

ABSTRACT
Kinetic, equilibrium and thermodynamic of arsenate sorption onto magnetic polymer sorbent based on glycidyl methacrylate were investigated. The maximum sorption capacity of 0.59 mg/g was obtained. The experimental data were analyzed by seven kinetic models and eight isotherm models. Nonlinear regression method was used to fit the data to the kinetic and isotherm models. Thus, two error functions; coefficient of determination and Chi-square statistic test were applied to evaluate the sorption data. It was shown that arsenate sorption obeys the pseudo-second-order model with evident influence of pore and film diffusion. The Freundlich and all three-parameter isotherm models proved to be the best representatives of arsenate sorption. Thermodynamic studies implied endothermic and spontaneous process in nature.

INTRODUCTION
The presence of arsenic (As) in surface and groundwater is a consequence of natural processes (mineral dissolution, biological activity, erosion) and anthropogenic impact (electronic, petrol, textile, dye and pharmaceutical industry, etc). In the environment, As occurs in oxidation states of ± 3, 5 and 0, predominantly as AsO_3^{3-} and AsO_4^{3-} [1, 2]. It is highly toxic, causing various detrimental effects on human health, such as problems in cognitive development and memory, skin lesions, diabetes and cardiovascular disease to cancer of the skin, lungs, urinary bladder, liver and kidney [3]. Due to the carcinogenic behavior of As, the World Health Organization (WHO) set the maximum contaminant level in drinking water to 10 ppb [4]. Therefore, the removal of As from water is a matter of vital importance. Magnetic polymer materials seem to be very promising adsorbents for the removal of toxic contaminants since they exhibit excellent adsorption properties and have the ability to regenerate and reuse. In this work, we have used a magnetic polymer sorbent based on glycidyl methacrylate (GMA) for removal of arsenate ions. In order to study the kinetics, mechanism and equilibrium of the removal process, the experimental data were analyzed by seven kinetic models and eight isotherm models. Also, the thermodynamic parameters were calculated to determine the feasibility, spontaneity, energy content, and degree of disorderliness of the process.

EXPERIMENTAL
The magnetic polymer sorbent based on GMA was synthesized by in-situ suspension copolymerization in the presence of nanoparticles of magnetite coated with (3-aminopropyl) trimethoxysilane and functionalized with diethylenetriamine according to the procedure described in our previous study [5]. Kinetic, equilibrium and thermodynamic studies of arsenate removal by magnetic polymer sorbent were carried out in non-competitive batch conditions at unadjusted pH

and dosage of sorbent of 10 g/L. The arsenate concentrations in solution were determined by inductively coupled plasma optical emission spectrometry (iCAP6500, Thermofisher Scientific, USA). Kinetic and isotherm parameters were estimated with the non-linear regression method.

RESULTS AND DISCUSSION

For analysis of the kinetic data, pseudo-first order model, pseudo-second-order model, as well as Elovich and fractional power model were used [6]. The resulting kinetic parameters and error function data are presented in Figure 1a and Table 1**.** Arsenate ion sorption kinetics discovers that removal was rapid during the first 25 min but subsequently decreased slightly and plateaued after approximately 60 min. The highest correlation coefficient (R^2 = 0.987) and the lowest Chi-square value (χ^2 = 0.005), indicate the pseudo-second-order model is the best fit for arsenate ion sorption. Also, the sorption capacity at the equilibrium value obtained by the pseudo-second-order model (Q_e^{cal} = 0.60 mg/g) agrees very well with experimental sorption capacity (Q_e^{exp} = 0.59 mg/g) meaning that chemisorption plays an important role in the arsenate sorption onto magnetic polymer sorbent.

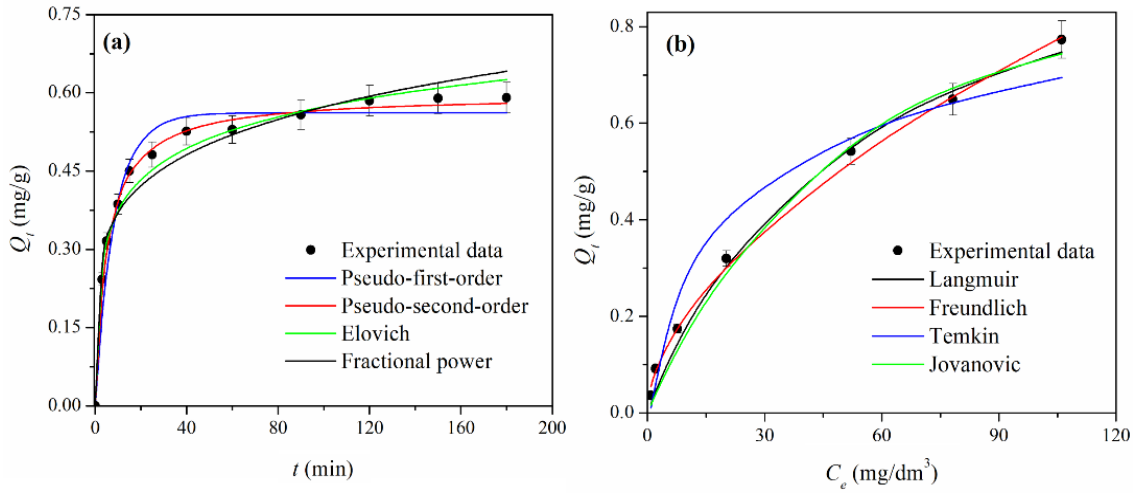

Figure 1. Predicted curve fits for the (a) kinetics and (b) two-parameters equilibrium isotherms of arsenate sorption onto magnetic polymer sorbent.

Table 1. Kinetic parameters and error function data for arsenate sorption onto magnetic polymer sorbent

Pseudo-first-order		Pseudo-second-order		Elovich		Fractional power	
k_1(1/min)	0.13	k_2 (g/mg min)	0.34	α	0.68	k_{FP} (mg/g)	0.24
Q_e^{cal} (mg/g)	0.56	Q_e^{cal} (mg/g)	0.60	β (g/mg min)	11.61	ν(1/min)	0.19
R^2	0.924	R^2	0.987	R^2	0.960	R^2	0.919
χ^2	0.051	χ^2	0.005	χ^2	0.014	χ^2	0.030

Table 2. Sorption mechanism parameters for arsenate sorption onto magnetic polymer sorbent

Intra-particle diffusion model				Bangham diffusion model		Liquid film diffusion model	
Stage	I	II	III				
k_{id}(mg/g min$^{0.5}$)	0.09	0.03	0.01	$k_B \cdot 10^3$ (1/g)	0.21	k_{LFD}(1/min)	0.02
C_{id} (mg/g)	0.09	0.33	0.45	α	0.22	C_{LFD}	-0.84
R^2	0.985	0.999	0.986	R^2	0.913	R^2	0.963

In order to further clarify the rate–determining step and sorption mechanism of the removal process of arsenate ions by magnetic polymer sorbent, the intra-particle diffusion model, Bangham model, and liquid film diffusion model were used and the resulting parameters are shown in Table 2. The high values for the coefficient of determination ($R^2 > 0.900$) for intra-particle diffusion, Bangham, and liquid film diffusion model suggest the influence of pore diffusion as well as film diffusion on the arsenic removal process by magnetic polymer sorbent.

The equilibrium data obtained at different initial arsenate concentrations were fitted using Langmiur, Freundlich, Temkin, Jovanovic, Redlich–Peterson, Sips, Toth and Khan isotherm models [6]. Experimental data and the predicted two-parameters isotherms models by nonlinear analysis for the sorption of arsenate by magnetic polymer sorbent are shown in Figure 1b**.** The parameters for eight isotherms nonlinear fit are presented in Table 3. According to the high R^2 and the low χ^2 values, the Freundlich (two-parameters), Redlich–Peterson, Sips and Khan (three-parameters) isotherms provided a better fit than the other used models. These results suggested that sorption is favorable on the investigated magnetic polymer sorbent as well as that reversible sorption has a significant role in the arsenate sorption process.

Table 3. Isotherm parameters and error function data for arsenate sorption onto magnetic polymer sorbent

Two-parameters isotherm models							
Langmuir		Freundlich		Temkin		Jovanovic	
Q_{max} (mg/g)	1.09	K_F(L^n mg^{1-n}/mg)	0.06	b_T (kJ/mol)	15.29	$Q_{m,J}$ (mg/g)	0.81
K_L (L/mg)	0.02	n	1.81	K_T (L/mg)	0.69	K_J	0.02
R^2	0.991	R^2	0.998	R^2	0.940	R^2	0.987
χ^2	0.070	χ^2	0.007	χ^2	0.158	χ^2	0.114
Three-parameters isotherm models							
Redlich–Peterson		Sips		Toth		Khan	
A (L/g)	0.10	$Q_{m,S}$ (mg/g)	3.13	Q_T(mg/g)	0.42	Q_K(mg/g)	0.09
B (L/mg)	1.05	$K_S \cdot 10^4$ (L^β/mg^β)	1.62	K_T (L/g)	0.04	K	0.63
g	0.53	β	0.64	t	0.45	n	0.49
R^2	0.999	R^2	0.999	R^2	0.998	R^2	0.999
χ^2	0.003	χ^2	0.004	χ^2	0.007	χ^2	0.003

Thermodynamic parameters such as the standard Gibb's free energy change ($\Delta G°$), the standard enthalpy change ($\Delta H°$) and the standard entropy change ($\Delta S°$) were determined from Van't Hoff equation [6]. The calculated values of $\Delta G°$, $\Delta H°$ and $\Delta S°$ for arsenate sorption by magnetic polymer sorbent at different temperatures are given in Table 4.

Table 4. Thermodynamic parameters for arsenate sorption by magnetic polymer sorbent

T, K	$\Delta G°$ (kJ/mol)	$\Delta H°$ (kJ/mol)	$\Delta S°$ (kJ/Kmol)	$T\Delta S°$ (kJ/mol)
298	-1.35	45.87	0.16	47.22
313	-3.25			49.12
328	-6.26			52.13
343	-8.48			54.35

At all investigated temperatures, the $\Delta G°$ values were negative, indicating the feasible and spontaneous nature of arsenate sorption. Sorption of arsenate was more favorable at higher

temperatures due to higher negative $\Delta G°$ values. The positive values of $\Delta H°$ for arsenate removal suggest that the sorption is endothermic in nature, while the positive values of $\Delta S°$ implied an increase in the degree of dispersion of the sorbed arsenate ions.

CONCLUSION

In this work, the sorption behavior of arsenate ions onto magnetic polymer sorbent was investigated. The kinetic data were analyzed using the pseudo-first-order, pseudo-second-order, Elovich, power function, intra-particle diffusion, Bangham and liquid film diffusion models while the equilibrium data were analyzed using Langmuir, Freundlich, Temkin, Jovanovic, Redlich–Peterson, Sips, Toth and Khan isotherm models. The sorption process followed the pseudo-second-order model with the evident influence of the pore and film diffusion. Equilibrium experimental results are the best fitted by the Freundlich, Redlich–Peterson, Sips, Toth as well as Khan isotherm model. Thermodynamic parameters demonstrated that the sorption process was spontaneous and endothermic.

Acknowledgment

This work was supported by the Ministry of Education, Science and Technological Development of the Republic of Serbia (Grants No. 451-03-68/2022-14/200026 and 451-03-68/2022-14/200135).

REFERENCES

[1] H. Garelick, H. Jones, A. Dybowska, E. Valsami-Jones in: Reviews of Environmental Contamination, Vol. 197, D. M. Whitacre (Ed.), Springer, New York, 2009.
[2] B. Liu, K. Kim, V. Kumar, S. Kim, J. Hazard. Mater., 388 (2020) 121815.
[3] T. S. Y. Choong, T. G. Chuah, Y. Robiah, F. L. G. Koay, I. Azni, Desalination, 217 (2007) 139.
[4] G. M. Sawood, S. K. Gupka, Appl. Water Sci., 10 (2020) 131.
[5] B. M. Marković, V. V. Spasojević, A. Dapčević, Z. M. Vuković, V. B. Pavlović, D. V. Randjelović, A. B. Nastasović, Hem. Ind., 73 (2019) 25.
[6] A. Nastasović, B. Marković, Lj. Suručić, A. Onjia, Metals, 12 (2022) 814.

APPLICATION OF MACROPOROUS NANOCOMPOSITE IN MICROEXTRACTION OF AROMATIC AMINE FROM WATER

T. T. Tadić[1], B. M. Marković[1], A. B. Nastasović[1], Lj. T. Suručić[2] and A. E. Onjia[3]

[1] University of Belgrade, Institute of Chemistry, Technology and Metallurgy, Njegoševa 12, 11000 Belgrade, Serbia. (tamara.tadic@ihtm.bg.ac.rs)
[2]Faculty of Medicine, University of Banja Luka, Save Mrkalja 14, 78000 Banja Luka, Republic of Srpska, Bosnia and Herzegovina.
[3]Faculty of Technology and Metallurgy, University of Belgrade, Karnegijeva 4, 11000 Belgrade, Serbia.

ABSTRACT
Magnetic macroporous poly(glycidyl methacrylate-*co*-trimethylolpropane trimethacrylate) nanocomposite was synthesized by suspension copolymerization. The obtained nanocomposite was characterized by Fourier transform infrared spectroscopy (FT-IR), mercury porosimetry and scanning electron microscopy (SEM). Such magnetic nanocomposite was applied as sorbent for a dispersive solid-phase microextraction (DSPME) for aniline preconcentration from water samples. The parameters affecting the microextraction were optimized. The screening of DSPME parameters was determined using Plackett-Burman design (PBD). For the optimization of the most important factors Central Composite Design (CCD) was used. The analysis of the results showed that the pH value and temperature of desorption were the most significant factors.

INTRODUCTION
Aniline is a major raw material in the production of textile dye, herbicides, pesticides, fungicides, plastics and pharmaceuticals [1]. Its considerable consumption in industrial processes has led to the release of aniline in the environment. Aniline is a priory environmental pollutant due to its high toxicity and suspected carcinogenicity and numerous health problems such as vomiting, liver damage and even cyanosis [2]. Because aniline is present in real environmental samples in low concentrations, most analytical techniques rely on some type of preconcentration of samples before analysis. For that reason, DSPME has gained special attention, due to its simplicity, low consumption of sorbent and organic solvent, short extraction time, and high enrichment factor [3]. However, the type of sorbent plays a significant role in the DSPME method. Among different types of sorbents used in DSPME, magnetic polymer nanocomposites have attracted much attention due to their large surface area, chemical, magnetic and physical properties, reusability, and high efficiency and selectivity in the extraction of the target analyte. In this study, magnetic polymer nanocomposite based on glycidyl methacrylate (GMA) was prepared and applied as a potential sorbent for the development of a relatively fast and effective dispersive solid-phase microextraction for aniline preconcentration. The affecting factors on the microextraction recovery were optimized through Design of Experiment (DoE).

EXPERIMENTAL
Magnetic macroporous nanocomposite based on GMA (with 60 wt.% of crosslinker, trimethylolpropane trimethacrylate) was synthesized by radical suspension copolymerization in the presence of 10 wt.% magnetic nanoparticles [4]. FTIR spectra were taken in ATR (attenuated total reflection) mode using a Nicolet 380 spectrometer with a Smart OrbitTM ATR attachment. Pore size distributions were collected by a high-pressure mercury intrusion porosimeter Carlo Erba Porosimeter 2000. SEM micrographs were obtained on JEOL JSM-6460LV instrument. The

DSPME procedure with magnetic nanocomposite sorbent prior to HPLC-MS was used for the detection of aniline according to the procedure described in the literature [5]. A PBD was applied in order to evaluate the significance of eleven variables on the microextraction recovery for the DSPME procedure. Variables were tested at two levels, a high (+1) and a low (-1) level: pH (X_1, 2-10), mass of sorbent (X_2, 10-50 mg), ion strength (X_3, 0-1 wt. %), type of extraction (X_4, vortex-ultrasonic), extraction time (X_5, 1-5 min), extraction temperature (X_6, 10-40 °C), type of eluent (X_7, methanol or acetonitrile), eluent volume (X_8, 200-700 μL), type of desorption (X_9, vortex-ultrasonic), desorption temperature (X_{10}, 10-40 °C) and desorption time (X_{11}, 1-5 min). In the next step, a CCD was used for optimization of the most significant parameters (pH and temperature of desorption) at five levels. For the analysis of the experimental data the statistical software MINITAB was used.

RESULTS AND DISCUSSION

In the FTIR spectrum (Figure 1a), the absorption bands for GMA based nanocomposite at 2995 cm^{-1} and 2950 cm^{-1} (C-H symmetric and asymmetric stretching vibrations), 1730 cm^{-1} (C=O stretching vibrations), 1145 cm^{-1} (stretching vibrations of C-O-C), ~ 1250, ~910 and ~ 840 cm^{-1} (stretching vibrations of C-O) were observed. The absorption band at 640 cm^{-1} (vibrations of Fe–O bonds) indicates the successful incorporation of magnetic nanoparticles in polymer [4]. Values of specific pore volume, V_p, specific surface area, S_{Hg}, and pore diameter which corresponds to half of pore volume, $D_{V/2}$ were 0.77 cm^3/g, 65 m^2/g and 83 nm, respectively. The porosity parameters calculated from the cumulative pore volume distribution curve (Figure 1b) confirmed macroporous structure ($D_{V/2}$> 50 nm).

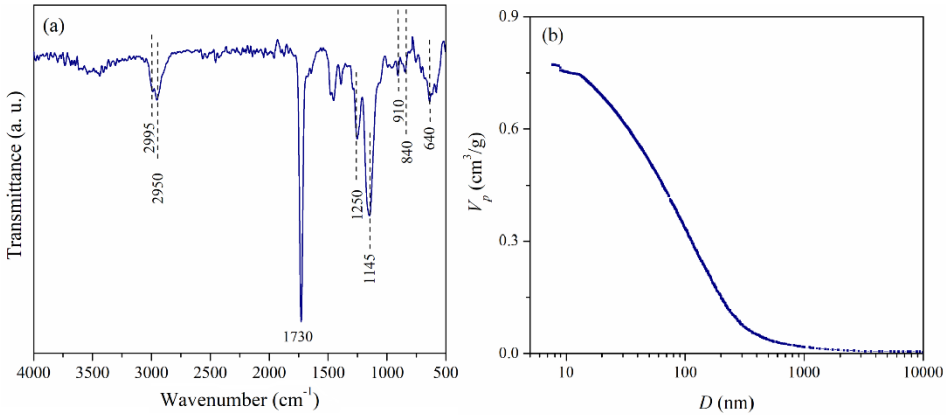

Figure 1.FTIR spectrum (a) and the cumulative pore size distribution curve (b) of magnetic macroporous nanocomposite.

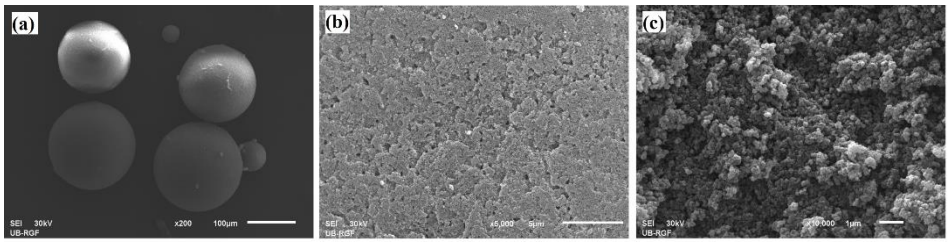

Figure 2. SEM microphotographs of (a) beads (magnification 200×), (b) particle surface (magnification 5000×) and (c) cross-section (magnification 10000×) for obtained nanocomposite.

The appearance and morphology of the surface and cross-section for obtained nanocomposite were investigated by SEM (Figure 2). It can be noticed that nanocomposite has the shape of beads with rough surfaces and porous structures.

The PBD was chosen to screen the eleven independent variables on the microextraction recovery of aniline in 12 runs. The obtained results are presented in Figure 3.

According to the obtained screening results,pH and the temperature of desorption were the most significant variables with a positive effect, while other independent variables had no significant effect on the microextraction recovery. For each factor with no significant effect, the factor level with the optimal response was selected based on the main effects plot (Figure 3). The main effect plot analysis revealed that increaseof the mass of sorbent, extraction time and temperature, and eluent volume as well as decrease of the ion strength and time of desorption led to an increase in microextraction recovery. The optimum for non-significant variables were set as: 50 mg of the sorbent mass, without ion strength, ultrasonic as type of extraction, 5 min for extraction time, 10 °C for extraction temperature, 700 µl of eluent volume, vortex as type of desorption, 1 min for desorption time and acetonitrile as eluent. Two significant factors were selected for the optimization step by CCD.

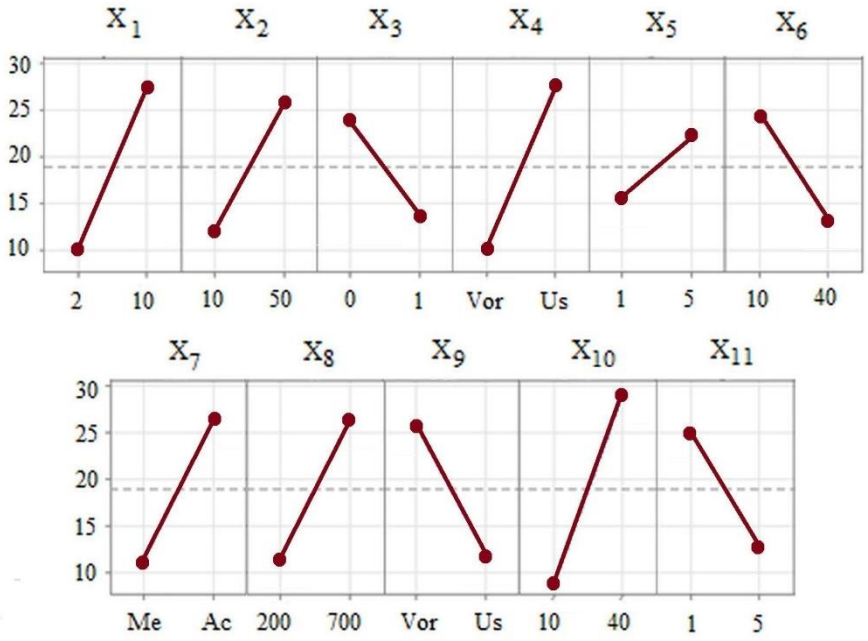

Figure 3. Main effect plot obtained for the PBD of screening experiment.

The CCD design was established to optimize the important factors to obtain the best response. Thirteen experiments were investigated at five levels. The elliptical contours of the contour plot (Figure 4) showed the combined influence of the significant variables on the microextraction recovery. The plot also indicates that the maximum microextraction recovery percent value was found in the middle of the range for each variable. The optimum microextraction recovery for aniline was found at pH 9 and desorption temperature of 20 °C.

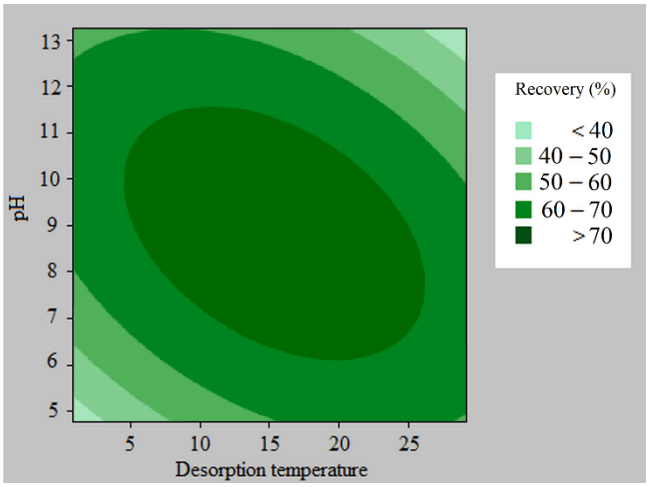

Figure 4. Contour plot desorption temperature – pH obtained for the CCD optimization step.

CONCLUSION

In the present study, a macroporous magnetic nanocomposite was synthesized by suspension copolymerization and used as a sorbent in dispersive solid-phase microextraction of aniline before its determination by HPLC-MS. The synthesized nanocomposite was characterized by FTIR spectroscopy, mercury porosimetry and SEM. FTIR analysis confirmed the presence of magnetite nanoparticles in the polymer matrix, while mercury porosimetry confirmed macroporous structure. The porosity of obtained nanocomposite was proved by SEM. Eleven affecting factors on the extraction recovery were optimized in two steps using the PBD as the screening step and the CCD as the optimization step. Application of DSPME procedure previously optimized with DoE resulted in the successful determination of aniline with good sensitivity, and short extraction and separation time.

Acknowledgment

This work was supported by the Ministry of Education, Science and Technological Development of the Republic of Serbia (Grants No. 451-03-68/2022-14/200026 and 451-03-68/2022-14/200135).

REFERENCES

[1] K. Furukawa, M. Hashimoto, and S. Kaneco, Anal. Sci., 33 (2017) 1189.
[2] M. Zhao, X. Zhang, Y. Li, and W. Chang, Anal. Lett., 33 (2000) 3067.
[3] A. Bazmandegan-Shamili, S. Dadfarnia, A. M. Haji Shabani, M. R. Moghadam, and M. Saeidi, J. Iran. Chem. Soc., 15 (2018) 1181.
[4] B. M. Marković, V. V. Spasojević, A. Dapčević, Z. M. Vuković, V. B. Pavlović, D. V. Randjelović, and A. B. Nastasović, Hem. Ind., 73 (2019) 25.
[5] N. Nazari, M. Masrournia, Z. Es Haghi, and M. R. Boyorgmehr, J. Sep. Sci., 39 (2016) 3046.

POLYMER-SACCHARIDE CONJUGATES

IV. POSSIBILITES FOR INCORPORATION OF OSCILLATORY RESPONSE FOR ANTI-STREES PROTECTION

M.M. Plavšić[1,2]

[1] University of Niš, Faculty of Technology, Bulevar Oslobodjenja 124, Leskovac,
[2]The Academy of Applied Technical Studies, Belgrade (milankaplav@gmail.com)

ABSTRACT

The long standing issue of the unusual impacts of glucose on cell membrane H^+-ATPase activity is revisited, using nowadays computer protein modeling methods, extensive experimental data acquired in the large amount on ATPase enzymes, and theories on enzyme autoinhibition processes. Based on conformational calculations, possible role as a trigger, in oscillatory enzyme activities is proposed for glucose, together with analyses of configurations of its conjugates with this so important polymer molecule.

INTRODUCTION

The P-type of ATPase are membrane enzymes, present in all eukaryote cells but also in fungi, protest and many prokaryotes. It confirms by itself, the importance of this family of enzymes, which subfamily H+-ATPase, characteristic for plants and fungi, is here in focus, but with some properties shared with Na^+ / K+ ATPase and Ca^{2+}-ATPase, considered in parallel [1-6]. In Part-I to -III of our contributions on polymer-saccharide conjugates (the first three parts of it are reported at the same Conference last year) we have considered interactions of ATPase with disaccharides, and oligo-saccharides, in particular with trehalose [7, 8].The P-ATPase are responsible for so vital functions as the transport of some important nutrients into cells, sustaining of cell membrane electrochemical potential and pH values in the cell, for providing energy from ATP reactions and, end for extruding wastes from the cell. When are in vesicle membrane, they provide their main transport functions, as well. Because of that, very early have appeared some (indirect) observations of their functions, but real understanding has begun rather late, due to complexity of structure and function of all those enzymes. The mitigating circumstances are similarities of 3D architecture of all ATPase mentioned, and also the conformational changes that follow from those 3D configurations [1-15].

The characteristics described for all P-typrs mentioned, are valid for the possibility of their oscillatory functions, as well. The first (indirect) evidence of such phenomena is mentioned by D.R. Hoagland, in his (already historic lectures at Stanford and Berkley Universities in 1940[es]. But, much earlier, S. Ringer made similar observations with his galvanic experiments with animal hearts in 1883. But, nowadays are explained some even much earlier methods of heart arrhythmia curing in England of 1770[es] with Na^+ /K^+ ATPase oscillatory control by foxglue plant extracts.

Some experimental investigations of glucose impact on cyclic rhythm of H-ATPase are described by R. Serrano and coworkers in 1980[es] [5]. But at that time focus was on ATPase cycling between E1 and E2 conformational states, essential for providing substrate transport through the membrane, as mentioned above.

But, it doesn't mean that such cycling is permanent, steady process. Obviously, large movements of so huge structure, requires a lot of energy, so it is understandable by itself, that periods of such cycling activity appear only after the increase of some needs, i.e. after some activation threshold, what can be an increase of glucose local concentration, as an impulse. In other words, it is an oscillatory process, with kind of trigger as a starter. Indeed, it was observed, in some experiments with pH leveling needs, that without presence of glucose had been no activity [3-6]. But, its action

upon ATPase, is not here in the glycosylation; this binding is reversible, as some kind of docking. The detailed docking calculations of ATPase require both sophisticated computer programs and detailed data on the protein structure. This is probably, one of the main reasons, why was necessary so long time for understanding some vital characteristics of those so important (but so complex) group of enzymes. In this contribution we use both, nowadays docking computer software and published structural data to investigate the role of glucose in H^+-ATPase activity, more in detail [9,10 ,16,17].

METHODS

For preliminary calculations to identify optimal regions for ligand binding and analyzing AutoGrid interaction energy maps, we considered a number of available data on P-ATPase: PDB, IntEnz, Gene Ontology, PRIAM, BRENDA, ExPASy KEGG, MetaCyc. Pfam, PDBsum. The data clearly identify tree cytosolic domains corresponding to the nucleotide binding -N, phosphorylation -P, and actuator-A. H-ATPase has ten trans-membrane helices. X-ray data mainly describe E1 conformation in quasi-occluded state, with non-hydrolysable ATP analogue bound. It has high structural similarity to Ca^{2+}ATPase that is already well known for some oscillatory activates [5,16].

The Ca^{2+} -ion is most widespread cation in many organisms and is uniquely suited for cell signal transduction. The low basal cytosolic Ca^{+2+} concentrations are kept in equilibrium through a delicate balance between influx and efflux of Ca^{2+} -ions by ATPase. However the equilibrium is often perturbed, causing more Ca^{2+}-ions to enter the cytoplasm then are cleared. This increase of concentration is kind of trigger, and call try to rapidly restore standard concentration by ATPase activation to extrude some ions. The cell inability to regulate and maintain low steady state concentration of some ions (as Ca^{2+}) results in trains of periodic Ca transients. So is generated oscillatory signal by concentrated actions of distinct cellular transporters, what can have large spatial and temporal variations, depending on the type of ion and cell conditions. Despite the many reports on cell oscillatory behavior due to Ca^{2+} concentration impacts, a unifying mechanism, generating the oscillatory response, has not been fully understood. Some additional trigger impacts for the P-ATPase action, are probably involved. Similar P-ATPase behavior can be expected in the case of H_3O^+ excess in the cell, lowering optimal intracellular pH-value. We supposed that glucose here play the role of such triggering actor. It follows that its action should be in C- domain.

To investigate this supposition more in detail, we performed docking calculations of glucose in auto-inhibitory H^+-ATPase, using AutoDock 4.2 program with Discovery Studio 4.0 for protein data adjustment. For Kollman electric interaction calculations and hydrogen polar interactions is used Auto Dock Tools (ADT). So the semi-empirical energy force field with Lamarckian Genetic Algorithm and Geistenger method are applied.

RESULTS AND DISCUSSION

The membrane H^+-ATPase (MHA) structure forms a ring architecture that is about 115 Å high and contains a tightly packed trans membrane region (TMR) and rather flexible cytosolic region **Figure 1a**. Due to the conformational changes directed outward into the cytosolic region, the activated enzyme becomes wider, because six helices become more distinct. In average, the hexamer average diameter increase for 10-15 Å. Both, actuator domain and nucleotide domain stay flexible, what can be concluded from their weaker packing densities. Numerous calculations indicate that only one subunit in the auto-inhibited state, and only two subunits in the activated state have good density for rigid body fitting (what is here of interest) of both A- and N- domains. The C-terminal domain is called C-tail. It is about 40 amino acid residue long, with two α-helixes, creating auto-inhibiting structure. The first α-helix is short, horizontal and partially embedded into membrane region. The second C-tail α-helix is longer and with much more conformational influence. The N- terminal region is more than hundred amino-acid residues long, responsible for binding A-domain, but rather

disordered (and less convenient for precise conformational analyses). There are ten trans-membrane helices in each MHA sub-unit. Three of them line the interior surface of the hexamer ring and four others face the outside surface. Considering all those characteristics and relative rigidity of glucose ring, after some preliminary dockings, in several areas we focused modeling to C-tail area. Some of the results are presented in Figure 1.a,b,c d.

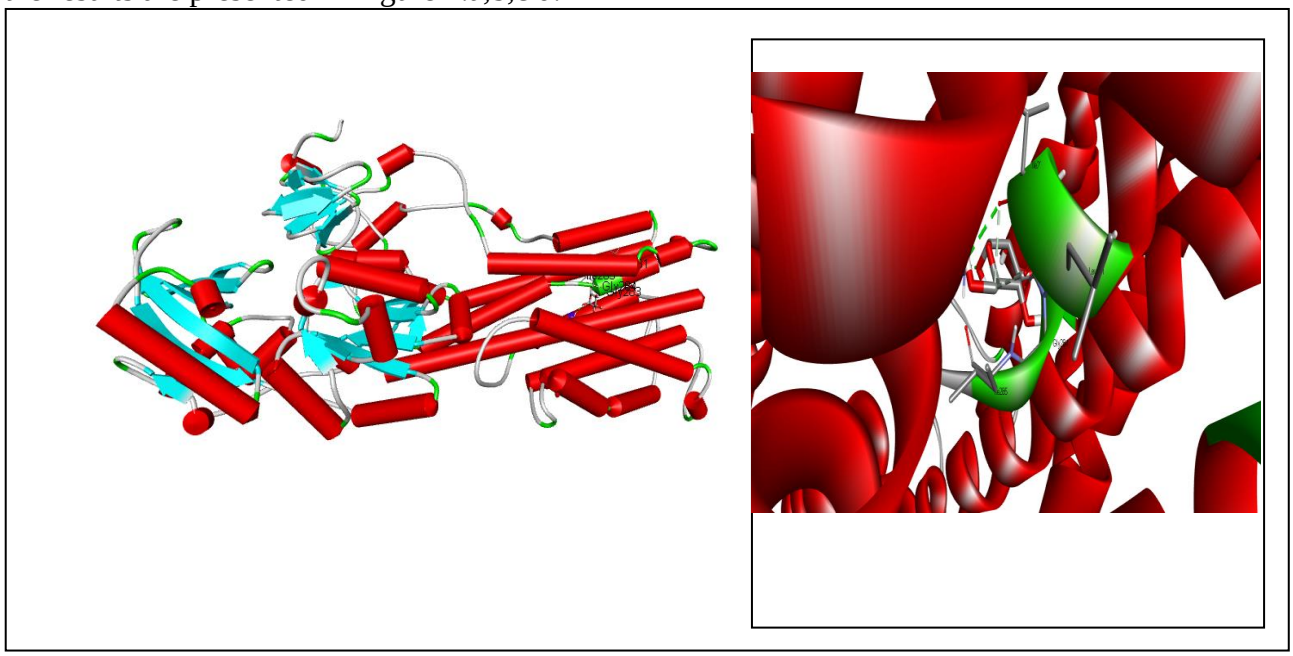

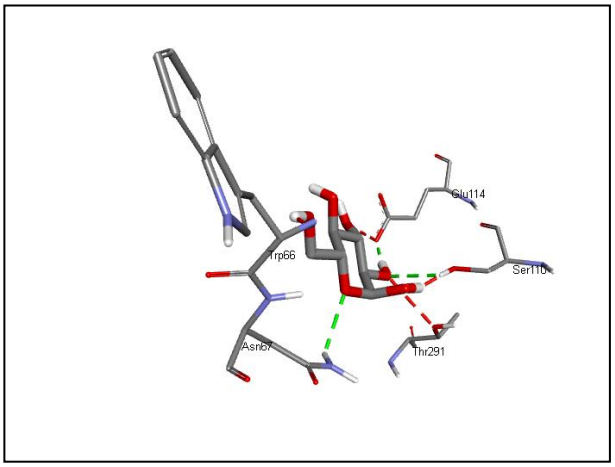

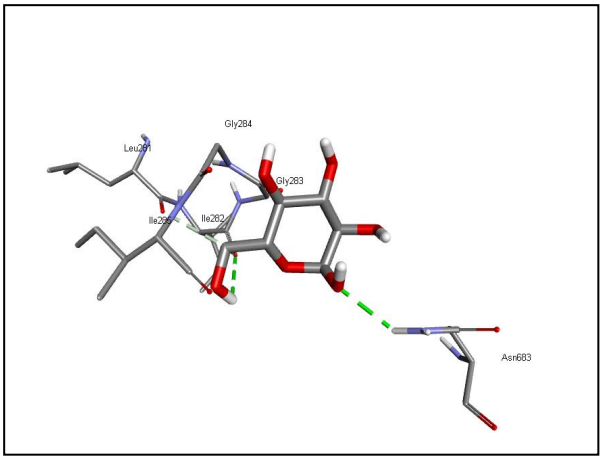

Figure 1. Membrane H+-ATPase conjugate with glucose: 3D structure, and optimal glucose positions and interaction

The position of glucose with lowest energy is between Aspartic acid residue (Asn) at 683 in the chain and several non-polar amino-acid residues in been in a series from 282 to 284 positions in the chain. It follows that glucose in that way makes a bridge between two α-helixes in C-domain. It is interesting that close to Asn 683 lies very important point for MHA autocatalytic activity Arginine 696 (Arg) of base character. Nowadays is believed [10-14] that MHA has two gates in front of its active chamber: the first gate1 (Gt1) and after it, gate2 (Gt2). Both are under dominant impact of Aspartic acid (Asp) residues, been in two opposite α-helix. (Asp 730 and Asp 143). Asp 730 is especially important. It is just in the middle of the membrane bilayer and moreover, the only acidic

residues at the proton transport way [1,11-14]. Such amino -acid residues, and at such location, is conserved in all plant and fungi MHA. In the **active enzyme state**: Asp 730 makes a salt bridge with Arg 695.The surrounding neutral (hydrophobic) groups move away, not to block proton way from Asp730 to Asp 143 (and further through ATPase) . Opposite to it, in **auto-inhibited state**:Asp 730 is blocked (isolated) with hydrophobic groups, and proton transport is blocked (G1 =closed). To open it, Lys 154 must be moved away from the proton path, because of its bulky hydrophobic side group. As can be seen from Figure 1d, glucose in its energetically optimal position, is in interaction with two Isoleucine residues (Ile282 and Ile 2b5) and also Leu261 that is pretty close to it. It follows that glucose at that position, contributes pretty much to be the way open, for hydronium ions, toward Asp730 glucose is in principle neutral molecule, but rigid, with polar (-OH) groups is very convenient to help in that way.

CONCLUSION

The issues of ATPase oscillatory activity in particular, and the issues of their activation and inhibition in general, are very important but, very complex. Here are presented only preliminary results of our conformational calculations of the glucose impact on the autoinhibition domain of cell membrane H^+-ATPase. The protein domains actives usually are rather independent mutually, especially in multifunctional molecules. They retain their function, if they are compactly folded, even been rather isolated. But it is not valid for auto-inhibitory domains, especially not for ATPase. Large conformational changes that they perform for transports through membrane are directly related to position and interaction of structural elements in autoinhibitory domain (AIHD). But, the optimal position for glucose attachment is in less dense domain, but close to AIHD. Its compact, small but rigid molecule, is fixed there on one side with strong interactions with acid side group at protein chain, and in floppy relations with unpolar amino acids on the other side, providing it the significant impact upon hydronium ion transport, when coupled to AIHD and cell conditions are steady. But if the intercellular acidity drops over some threshold, some bases will compete with glucose for that position and so accumulated steric hindrances will stop hydronium ion flow, till the next increase of intercellular pH. It is probably the reason of glucose unique role.

REFERENCES

[1] D. Nelsen, A. Lehninger, M. Cox, Lehninger principles of Biochemistry, Freemann NY (2008)
[2] H. Lodish at al. Molecular cell biology, Fteemann NY (2007)
[3] J. Falhof, at al., Cell (-Molecular Plant) 9 (2016)
[4] J.C. Skou, M. Esmann, J. Bioenergy, Bio-membranes 24 (1992) 249.
[5] R. Serrano, Plasma membrane ATPase, CRC Press, Boca Roton (1985)
[6] D. E. Clapham, Cell 131(2007) 1047
[7] M.M. Plavsic, D.S. Savic, S.R. Savic, 15th Int. Conf.Appl.Fundam. Phys.Chem. Proc.v.2 (2021)
[8] M.M. Plavsic, D.S. Savic, S.R. Savic, M.B. Plavsic Int.Conf. 22YUCOMAT, Proc. (2021) 127
[9] G.M. Morris at al. J. Computational Chem. 30:2785-2791 (2009)
[10] S. Forli at al., Nat. Protoc. 11:905-919 (2016)
[11] S. Benlekbir at al., Nature -Structural & Molecular biology 19 (2012) 1356.
[12] M. Holmgreen at al. Nature, 403 (2 000) 898.
[13] B.P. Pedersen at al. Nature, 460 (2007) 1111.
[14] M. G. Auer at al. , Nature, 392 (1998) 840
[15] S.J. Singer, G.L. Nicolson, Science 175 (1972) 720
[16] R.J..Field, R.M. Noyes, Account Chem. Res. 10: 214-220 (1977).
[17] A. Warshel, J. Florian Proc. Nat. Acad. Sci. USA 95: 5950-5955 (1098).

MECHANISMS OF POLYMER SUPRAMOLECULAR STRUCTURES FORMATION FOR MASS AND HEAT TRANSPORT CONTROL IN CELL SYSTEMS UNDER STRESS

M.M. Plavšić[1,2]

[1]*University of Niš, Faculty of Technology, Bulevar Oslobodjenja 124, Leskovac,*
[2]*The Academy of Applied Technical Studies, Belgrade (milankaplav@gmail.com)*

ABSTRACT
The mechanism of both, formation of the supramolecular structures from two protein molecules in living systems, and of the impact of its formation on well-known phenomena of mass and heat transport, are consider starting from fundamental aspects of polymer conformational principles. Some new approaches to the inhibition processes, for the enzymes involved to those complex structure activities, are proposed.

INTRODUCTION
For the maintenance of life functions in organisms are mass and heat transfers, obviously among the most important mechanisms. Those mechanisms are, also obviously, very complex, but going step by step, a number of issues have been already resolved [1-5]. Any nutrient, taken up by any cell, must at some stage pass the plasma membrane. For ionic and polar particles it is the barrier that can be passed only with the help of membrane proteins. For example, the nutrient in the soil, that is to enter into the plant with roots, needs to be pumped (to enter into space under higher osmotic pressure then outside) and also selected by the organism, as harmless. It is well known nowadays that H^+-ATPase is responsible for the first, but its responsibility for the second, is still under discussion. There are strong indications that proteins (generated for cell membrane and also those generated for immune system) play the main role in such process. Among those proteins important role play ATPase that are present in all eukaryote cells. So researcher's attention has been focused pretty much on structure and functions of those enzymes. Besides the transport of some nutrients into the cell, and some wastes out of the cell, they are responsible for keeping sustained electrochemical potential of cell membranes and providing cell energy balance by ATP reactions. When are in a vesicle membrane, ATPase provide the main transport functions inside the cells [5-10]. The principles of osmotic forces are well understood in physical chemistry, but here have to be extended to cell mechanisms involved. So besides the apoplast transfer (i.e. transfer from the soil into the root), a given nutrient can diffuse through cell system continuum further in plant, by symplast transport (i.e. through cellular continuum). The second mechanism is of even more general importance for both, plants and animals and mostly convenient for studies in plants. The plant products (e.g. fruits), are under control of it, but also the uptake of water and carbon dioxide by leaves in photosynthesis but also in cooling plant by evaporation from leaves through pores on leave surface, involve it. In short: such transfer goes through stomates, pores found in epidermis of leaves, stems and other organs. Air, used for respiration and carbon dioxide, used in photosynthesis pass through a stoma by diffusion and also water vapor diffuse through it, in the process called: transpiration. But, obviously, there is a chance that in parallel to such diffusion processes; also different pathogens can enter through a hole into a plant. For control of all that processes, stoma simply can be opened or closed, According to results from last years, some kind of "switch"- role, (in activating and-inhibiting those processes) can be related to supramolecular structures, formed from ATPase enzymes and of proteins from PIN-class The process involves both: transport

phenomena and some protection mechanisms (even the part of immune protection) from stress, as well.

METHODS

To calculate possible inhibitor docking, responsible for inactivation of ATPase keeping stoma open, we first considered data on H-ATPase pumping activity in relation to its structure: When activated, H+-ATPase pumps proton from the guard cells and increase negative membrane electrical potential. The negative potential opens potassium voltage-gated channels and so an uptake of K^+ occurs. The increase in solute concentration lowers the water potential inside the cell, what results in diffusion of water into the cell. This increases the cell volume and turgor pressure what push guard cells aside each other, and opens the stoma. For precise shifting of guard cells, in tissue exist the cellulose micro-fibrils ring, that prevent them from swelling and transforms turgor forces into stresses that elongate the stoma opening space [4].This example is a good illustration of the importance of systems approach for understanding smart material actions. But, what turns H^+-ATPase actions on and off, at the beginning of those cyclic reactions, as it supposes the models quoted? The concentration changes of PIN4 protein in the guard cells, strongly indicate the importance of its interactions with ATPase, for the mechanism functioning [4]. Based on those data we calculate possible docking of PIN4 to H^+-ATPase, and consider steric hindrances and other interactions, as responsible for ATPase inactivation. We performed first some preliminary optimizations of PIN4 structure, in coiled configuration using Flory method [8] and PDB-data for IDP and obtained rater extended cloudy, flexible configuration. Then is performed Discovery Studio 4.0 adjustment for protein data of both: target and ligand proteins. For Kollman electric interaction calculations and hydrogen polar interactions are used Auto Dock Tools [7-9]. So the semi-empirical energy force field with Lamarckian Genetic Algorithm and Geistenger method are applied and used docking calculations by AutoDock 4.2 program application in active site prediction with auto-ligand mode.

RESULTS AND DISCUSSION

In Figure 1 is presented the supramolecular structure of H-ATPase with PIN4 protein having lowest free energy under proposed condition to be close to the enzyme “gates”:

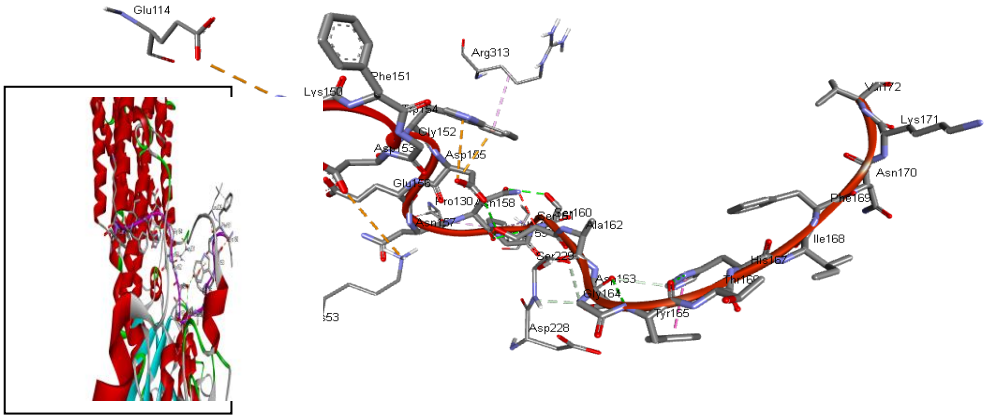

Figure 1. Effects of PIN4 docking on H^+-ATPase a)local interactions b) M-domain position (PFC).

The H^+-ATPase consists of 4 core domains with 2 trans-membrane and 2 cytosolic subdomains, each with 6-8 proteins (called “monomers”) in the core and 6 in domains, shared with membrane region but loosely bound providing huge conformational changes between states E1 and

E2: [3-6]. The enzyme structure has a ring architecture that is about 115 Å high and contains a tightly packed trans membrane region and rather flexible cytosolic region Figure 1a. Due to the conformational changes when directed outward, into the cytosolic region, the activated enzyme becomes wider, because six helices become more distinct. In average, the hexamer average diameter increase for 10-15 Å. Both, actuator domain and nucleotide domain stay flexible, what can be concluded from their weaker packing densities. The calculations indicate that only one subunit in the auto-inhibited state, and only two subunits in the activated state have good density for rigid body fitting of both A- and N- domains. But PIN4 cannot rich that point simply because of its size. So, some other impact must be the reason of its influence.

The important features of H^+-ATPase structure, especially for its autocatalytic activity, are Aspartic acid (Asp) residues Asp 730 and Asp 143. Asp 730 is especially important. It is just in the middle of the membrane bilayer and moreover, the only acidic residues at the proton transport way [3-10]. Such amino acid residue, and at such location, is conserved in all H^+-ATPase of plants and fungi. In the **active enzyme state**: Asp 730 makes a salt bridge with Arg 695 base. In that case the surrounding neutral (hydrophobic) groups move away, not to block proton way from Asp730 to Asp 143 (and further through ATPase). Opposite to it, in **auto-inhibited state**: Asp 730 is blocked (isolated) with hydrophobic groups, and proton transport is blocked (G1 =closed). To open it, Lysine (Lys) 154 must also be moved away from the proton path. So, could be closing of the (substrates) approach to gate G1, the reason of PIN4 impact?

From Figure 1a can be seen that optimal conformation of PIN4 in the supramolecular structure considered, has very extended chain shape. It follows that hydronium ions could easily find the way around it, in such conformation!? But, if we look interaction pares of that part of the complex, we recognize very high concentration of interactions just around the Lys 154 residue: Lys 150, Phe151, Gly152, Asp153,Lys 154, Asp155, Glu156, Asn157, Asn158, Ser160, etc. We shall return to this important feature again, later. Now, let consider possible impacts of conformational dynamics around auto-inhibition center.

The C-terminal domain of H^+-ATPase is called C-tail. It is 38 amino acid residues long, with two α-helix creating, auto-inhibiting structure. The first α-helix is short, horizontal and partially embedded into membrane region. The second C-tail α-helix is longer and with much more conformational influence. The N- terminal region is more than hundred amino acid residues long, responsible for binding A-domain, but rather disordered. There are ten trans-membrane helices in each H^+-ATPase sub-unit. Three of them, line the interior surface of the hexamer ring, and four others face the outside surface. All that elements perform large conformational movement if auto-inhibition is not in action. But is it also the case if some outer forces put them under pressure?!

There is strong experimental evidence on the significant impact of membrane surface pressure on ATPase kinetics, providing similar damping [9, 10]. But the **concentrated forces of the ligand with more than 10 chain amino acid** residues around Lys154 should make the same effect: **PIN4 probably suppress conformational movements of the enzyme, when embedded into the complex,** due to **physical interactions inside supramolecular structure**. In particular, it **prevents Lys 154 to be moved away** as required for opening gate G1. At the same time that could **explain the reversibility of "switch" role in stoma opening and closing**. Due to decrease of concentrated physical attraction (with thermal movement of PIN4 or decreasing turgor in the cell or some other reasons- some reactions close to it, etc.) PIN4 can separate reversibly from the enzyme.

There are some additional facts supporting proposed model: PIN4 is intrinsically disordered protein. In other words it is very flexible and able to envelope the large part of quite huge, but rather extended ATPase molecule as dimensions above quoted, and Figure 1 show. Not many proteins have all those qualities: constitutive compatibility, conformational flexibility, and configuration size. It is the main result of our conformation calculations, although numerous details of this large

structure can be compared to those of similar structures, and to the theories on supramolecul systems, that are still under development, these years.

The mechanism proposed can be easily included in present biological theories on stoma opening and closing, based pretty much on physical chemistry of osmotic processes. As mentioned, the increase of solute concentration results in lower water potential in a cell and diffusion of water into the cell through membrane pores due to osmosis. This increases the turgor pressure. This increase turgor in guard cells causing their elongation around the stoma pore, what opens stoma pore (and gas can diffuse into plant). ("Guard cell" is the name for two cells on both sides of the pore). When conditions are conductive for stoma opening, H^+-ATPase from guard cell membranes, drives hydronium ions from the guard cells. It decrease turgor in guard cell and they lose ability to keep stoma open. It increase in parallel, the charge of guard cell membrane, what starts to opens voltage gated membrane channels, and potassium ions start to enter. When the concentration of that solute is high enough, the cyclic process is repeated. The role of H^+-ATPase is essential for that all. But if the plants sense some concentration of pathogen, they start production of PIN4. It (probably) enters guard cells by symplast transport. Also probably, (because still not enough experimental data exist in the literature), the local flow gradients bring PIN4 close to H^+-ATPase cytoplasmic part, and formation of its supramolecular structure with ATPase starts. It decreases significantly conformational mobility of ATPase and the pumping stops. Lowering of ATPase activity in guard cells decrease the turgor and stoma close, what prevent further pathogen entrance into plant. All of that, rise new ideas and issues: (about possible local heating, change of intracellular dynamics and pH, but also for the impact of turgor change on movements of the plant parts-leaves etc.).

CONCLUSION

The data on supramolecular structures build from ATPase and high polymer molecules, as proteins from PIN class, are still in the early stage of development. But, importance of processes as nutrient transport into cells under different conditions, heat and mass transport and a number of immune mechanisms depending on such complex structures, support further research on it. In this contribution we started from fundamental principles of polymer chain conformations, trying to relate them to the impacts back from the cell. Than to include influences of cell-environment on directions of supramolecular architecture development and grow in nature. So we concluded that usual principles of control from auto-inhibition center are not walled for so large substrates and the indirect impacts still exist, but in combination with other factors, from systems chemistry and systems biology.

REFERENCES

[1] R. Malonis, Chem. Rev. 120 (2019) 3210
[2] C. Molnar Adaptive immune response, Rice Un. Houston (2015)
[3] D.E. Clapham, Cell 131(2007) 1047.
[4] S. Benlekbir at al., Nature -Structural & Molecular biology 19 (2012) 1356
[5] M. Holmgreen at al. Nature, 403 (2 000) 898
[6] B.P. Pedersen at al. Nature, 460 (2007) 1111
[7] A.Warshel, Computer modeling of chemical reactions in enzymes Wiley NY (1997)
[8] S. Forli, at al. Nat. Protoc. 11: 905-919 (2016)
[9] P.J. Flory, Statistical mechanics of chain molecules Wiley NY (1969).
[10] H. Lodish at al. Molecular cell biology, Fteemann NY (2007)
[11] M.M. Plavsic, D.S. Savic, S.R. Savic, 15th Int. Conf.Appl.Fund. Phys.Chem. Proc.v.2 (2021)
[12] M.M. Plavsic, D.S. Savic, S.R. Savic, M.B. Plavsic Int.Conf. 22YUCOMAT, Proc. (2021) 127

K *– Environmental Protection,*
Forensic Sciences,
Geophysical Chemistry,
Radiochemistry,
Nuclear Chemistry

CHITOSAN-MODIFIED POLYMERIC MATERIAL FOR WASTEWATER TREATMENT

D. A. Gkika[1], N. Malesic-Eleftheriadou[2], E. Evgenidou[2], M. Lazaridou[2], D. N. Bikiaris[2], D.A. Lambropoulou[2], A. C. Mitropoulos[1] and G. Z. Kyzas[1]

[1]Department of Chemistry, International Hellenic University, Kavala, Greece
[2]Department of Chemistry, Aristotle university of Thessaloniki, Thessaloniki, Greece
kyzas@chem.ihu.gr

ABSTRACT

One of the most important decontamination techniques is considered to be adsorption. It is fast, simple, low-cost with many opportunities to modify the initial materials after appropriate synthesis routes etc. Numerous adsorbent materials are prepared the last years having as ultimate scope to remove some pollutants especially from contaminated waters (effluents originated from industries). But the composition of each type of effluents is varying. Dyes, heavy metals, pharmaceutical compounds are some major components of industrial wastewaters. In the last years, polymers attracted many researchers employing with adsorption technique, because of their excellent properties. Researchers proceeded with that and achieved even more effective polymeric adsorbents making some modification to initial polymeric chains in order to enhance the adsorption capacity and improve the rigidity, preparing many polymeric composites. The present lecture summarizes the application of a synthesized cross-linked and grafted zwitterionic chitosan derivative to the removal of a mixture of five anti-inflammatory compounds from aqueous matrix. An effective bio-based adsorptive material was synthesized using 2-(methacryloyloxy)ethyl]dimethyl-(3-sulfopropyl)ammonium hydroxide as monomer. According to the functional groups of derivative and adsorption efficiency of chitosan (the polymeric substrate used), results indicated a high adsorption ability of tested material for disposal of the certain remedies from aqueous systems. Parameters like the pH of the solution, the initial concentration of the compounds, the temperature and the contact time between the novel, bio-based adsorptive material and the target compounds proved to affect the process. The optimum pH appears to be pH=4 and adsorption was ascribed to various electrostatic interactions that may take place between the adsorptive material and the drug affected by the functional groups, and the substituents of molecules. For adsorption isotherms, it was found that the Langmuir equation provided a better fitting than the Freundlich equation. Increase of temperature favours the adsorption capacity of the new material while 180 min were found to be the time required for the process to be completed. Also, the cost process might be negatively affected by a series of factors, thus additional research identifying the critical attributes and analyzing their financial potential is crucial. This study describes the total cost of ownership (TCO) model settings, equations and input data as well as the result and discussions. This constitutes the first time that the total cost of ownership has been applied for adsorption and photocatalysis at lab scale. A TCO synthesis model was employed to provide quantitative estimates on the actual need and economic potential of recipes. The importance of looking beyond the synthesis process and making use of a safe by design approach during the design process has been highlighted.A thorough financial assessment is required for the calculation of indirect costs, considering they impose a significant economic burden. The research considered costs related to capital and operation. For the adsorption cycle, those steps (and their costs) are the actual adsorption, regeneration, desorption, acid wash and material recovery. Both cases revealed that labor and accident costs account for 80% of the synthesis TCO. For this material energy and maintenance cost was insignificant. This study stressed the importance of a practical implication. It forms the basis of a TCO model that will be employed across a number of adsorbents.

Acknowledgment

The financial support received for this study from the Greek Ministry of Development and Investments (General Secretariat for Research and Technology) through the research project "Intergovernmental International Scientific and Technological Innovation-Cooperation. Joint declaration of Science and Technology Cooperation between China and Greece" with the topic "Development of monitoring and removal strategies of emerging micro-pollutants in wastewaters" (Grant no: T7DKI-00220) and it is gratefully acknowledged.

LEMNA MINOR AS AN INDICATOR OF POTENTIALLY TOXIC ELEMENTS ON THE BEGEJ RIVER SURFACE

D. Đukić[1], A. Krstić[2], I. Bracanović[3], A. Kalijadis[3], K. Jakovljević[1] and M. Mirković[3]

[1]*University of Belgrade-Faculty of Biology, Institute of Botany and Botanical Garden, Takovska 43, 11000 Belgrade, Serbia*
[2]*University of Belgrade-„Vinča" Institute of Nuclear Sciences - National Institute of the Republic of Serbia - Department of Physical Chemistry„ 11000 Belgrade, Serbia (aleksandar.krstic@vinca.rs)*
[3]*University of Belgrade, „Vinča" Institute of Nuclear Sciences - National Institute of the Republic of Serbia-Department of Materials, 11000 Belgrade, Serbia*

ABSTRACT

The use of the floating aquatic plant *Lemna minor* as a bioindicator of freshwater pollution with potentially toxic elements (PTE) has many advantages, including accessibility, high biomass, rapid growth and reproductive rate. In this study, *L. minor* was sampled from the Begej River in the urban area of Zrenjanin and used to determine the PTE pollution of the river near the former successful textile factory, in the navigable part of the river. The concentrations of different PTEs in Begej water and *L. minor* samples were determined. The results showed that *L. minor* can accumulate the analyzed PTEs in extremely high concentrations, in the following order: Fe> Cr> Ni> Mn> Ti> Zn> Mo> Cu> Co> As> Pb> Cd> V> Ag. Moreover, they indicate that the plant can be considered a hyperaccumulator of Ni and Cr. Despite the low concentration of the analyzed PTEs in the Begej water, the results of *L. minor* indicate presumably periodic pollution of the surface of the river by anthropogenic activities.

INTRODUCTION

Due to natural processes and anthropogenic activities, potentially toxic elements (PTE) can be released into the environment. PTE's natural sources are mainly certain types of geological deposits (such as ultramafites) and volcanic eruptions, while anthropogenic sources are much more diverse [1]. Common anthropogenic sources of PTEs in freshwater include the overuse of fertilizers, pesticides, and industrial effluents, such as textile effluents from dyeing and finishing processes [2, 3]. Most of these elements accumulate in the soil and sediments of water bodies [4]. Some of these elements are essential for plant growth and development, while others are toxic even in low concentrations. However, even though they are necessary, these elements can become toxic when present in elevated concentrations in plant tissues [5]. Plants have developed several defense mechanisms that control the uptake, accumulation, and translocation of PTE. One of the mechanisms is to prevent the uptake of PTEs into root cells by immobilizing them in the apoplast by binding to released organic acids or anions on cell walls. However, when they enter the plant, most of the potentially toxic elements are stored in the root cells, limiting their translocation to the aboveground organs and thus protecting leaf tissues (especially the metabolically active photosynthetic cells) from damage. The final defense mechanism that non-tolerant plants develop when exposed to long-term high concentrations of potentially toxic elements is the increased activity of cellular antioxidant systems that counteract oxidative stress [6].

The duckweed *Lemna minor* L. (Figure 1) is often chosen as a model organism for this type of study because of its accessibility and availability. As a free-floating, freshwater plant, it can also serve as an indicator of water pollution in several specific locations [7]. In this case, the plant material collected from the Begej River is located about 10 meters from the former successful textile factory. Pollution of the Begej is due to industrial and urban wastewater, as well as runoff from surrounding

agricultural lands during periods of heavy rainfall [4, 8]. In Serbia, therefore, the water of the Begej is used only for irrigation and to supply fish ponds, while upstream in Romania, where it rises, it is used, among other things, to supply the population of Timisoara with drinking and service water [8].

Considering the characteristics of *L. minor*, the aim of this study was to monitor the pollution of the Begej River with different PTEs using this floating plant.

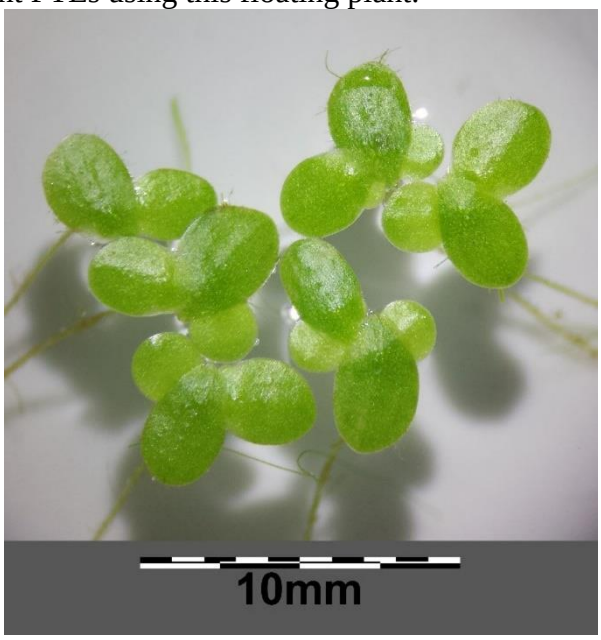

Figure 1. *Lemna minor* [9]

METHODS

The plant sample was collected in September 2020, during the flowering period, in the urban area of Zrenjanin (45°38′26.98″ N, 20°40′16.39″ E, alt. 77.5 m a.s.l.). The water from the river was collected together with the plant material and stored in round bottom flasks.

The collected plant sample was filtered from Begej water and washed with distilled and deionized water. Afterward, the plant material was dried in a dryer at 60°C for 12h. The total of 11.8 mg of the dry weight of the plant was measured and ground until a fine powder was obtained. The remaining water filtrate from the river was stored and analyzed together with plant material. After processing, the plant material was digested with hot (70-80°C) concentrated nitric acid (HNO_3) and 30% hydrogen peroxide (H_2O_2) for about 2 hours. After digestion, 5 ml of the solution remaining after evaporation was filtered, and the filtrate was diluted with deionized water.

Both the plant and water samples were analyzed in triplicates using ICP-OES (Thermo Fisher Scientific, model iCAP ™ 7400 Duo) to determine the concentrations of arsenic, cadmium, iron, chromium, cobalt, copper, lead, manganese, molybdenum, nickel, silver, zinc, titanium, and vanadium.

RESULTS AND DISCUSSION

The results presented in Table 1 show the concentrations of the different PTEs in the sample from the Begej River and in the plant material sample. The results show that the concentrations of PTEs in the plant material are much higher than expected compared to the PTE content in the water. Moreover, the experiment shows that the concentrations of the analyzed PTEs in the water of the Begej River are within the limits of World Health Organization for drinking water [10]. The determined concentrations of PTEs in *L. minor* are in the following order: Fe > Cr > Ni > Mn> Ti > Zn > Mo > Cu > Co > As > Pb > Cd > V > Ag.

Table 1. Average concentration of the different PTEs in *L. minor* and water from the Begej River

Potentially toxic element	Sample	
	Begej water (mg/L)	*Lemna minor* (mg/kg)
As	<0.010	58.223
Cd	<0.002	7.4420
Fe	0.129	55969
Cr	0.022	9832.1
Co	<0.005	75.075
Cu	<0.002	182.87
Pb	<0.010	56.062
Mn	0.086	1348.1
Mo	0.008	400.02
Ni	0.007	5526.0
Ag	<0.001	0.1700
Zn	0.007	403.37
Ti	<0.001	747.46
V	<0.002	1.5680

Previous studies have shown that *L. minor* tolerates high concentrations of various PTEs, e.g., it can survive in water containing up to 100 mg/L Zn, Fe, and Pb [11], and it can play an important role in their removal from the contaminated waters [12]. Due to the specific sampling site and the frequent exposure of *L. minor* to the different PTEs, the results obtained in this experiment show that this plant has the ability to accumulate these ions and even hyperaccumulate them in the case of Ni and Cr [12]. Moreover, this could indicate that the absorption rate of the different PTEs by *L. minor* is very high due to the unstable, periodically high exposure. This assumption is supported by the fact that the concentration of PTEs in the Begej water sample was low at the time of sampling. The study from Skadar Lake showed that *L. minor* contains more than five times lower concentrations of Cd, Cu and Pb, although the concentration of these PTEs in the water samples is similar [13]. Finally, the obtained results are consistent with previous research and show that *L. minor* can be used as a bioindicator for monitoring PTE pollution of fresh waters, especially their surfaces, caused by anthropogenic activities.

CONCLUSION

The results of this study show that *L. minor* is a good indicator of surface contamination of freshwater, specifically their surface, occasionally exposed to industrial effluents containing high concentrations of PTEs. This is because, although the water sample from the Begej has low concentrations of PTEs, the concentrations obtained by analysing the plant show the opposite. This fact indicates a significant potential of the studied species for the remediation of waters exposed from time to time to high concentrations of PTE. Rapid growth and reproductive rate, high biomass, accessibility, accumulation of a wide spectrum of PTEs and their high adsorption represent an additional advantage that places this species in the group of species suitable for the remediation of aquatic ecosystems.

Acknowledgment

This research was funded by the Ministry of Education, Science and Technological Development of the Republic of Serbia, record number 451-03-68/2021-14/200017, and grant No. 1702202.

REFERENCES

[1] G. Tomović, S. Đurović, U. Buzurović, M. Niketić, Đ. Milanović, N. Mihailović, K. Jakovljević, Accumulation of Potentially Toxic Elements in Viola L. (Sect. Melanium Ging.) from the Ultramafic and Non-ultramafic Soils of the Balkan Peninsula, Water, air, and soil pollution 232 (2021).

[2] M.M. Onakpa, A.A. Njan, O.C. Kalu, A Review of Heavy Metal Contamination of Food Crops in Nigeria, Annals of global health 84 (2018) 488-494.

[3] V. Bhardwaj, P. Kumar, G.K. Singhal, Toxicity of Heavy Metals Pollutants in Textile Mills Effluents, International Journal of Scientific & Engineering Research 5 (2014) 664-666.

[4] M. Dubovina, D. Krčmar, N. Grba, M.A. Watson, D. Rađenović, D. Tomašević-Pilipović, B. Dalmacija, Distribution and ecological risk assessment of organic and inorganic pollutants in the sediments of the transnational Begej canal (Serbia-Romania), Environmental Pollution 236 (2018) 773-784

[5] R. Nieder, D.K. Benbi, F.X. Reichl, Role of Potentially Toxic Elements in Soils, Soil Components and Human Health (2018) 375–450.

[6] A. Kushwaha, R. Rani, S. Kumar, A. Gautam, Heavy metal detoxification and tolerance mechanisms in plants: Implications for phytoremediation, Environmental Reviews 24 (2016) 39-51.

[7] M.A. Khan, G.A. Wani, H. Majid, F.U. Farooq, Z.A. Reshi, A.M. Husaini, M.A. Shah, Differential Bioaccumulation of Select Heavy Metals from Wastewater by Lemna minor, Bulletin of Environmental Contamination and Toxicology 105 (2020) 777-783.

[8] B. Dalmacija, M. Prica, I. Ivancev-Tumbas, A. van der Kooij, S. Roncevic, D. Krcmar, I. Bikit, I. Teodorovic, Pollution of the Begej Canal sediment-metals, radioactivity and toxicity assessment, Environment International 32 (2006) 606-615.

[9] Wikipedia: https://commons.wikimedia.org/wiki/File:Lemna_minor_sl1.jpg.

[10]World Health Organization, Guidelines for drinking-water quality, 4th ed, World Health Organization (2011).

[11] S.M. Hafez, A.M. Hassan, R.M. El-Shahat, M.A. Kassem, Accumulation of Iron, Zinc and Lead by Azolla pinnata and Lemna minor and activity in contaminated water, Egyptian Journal of Chemistry 64 (2021) 5017-5030.

[12] M. Gałczyńska, N. Mańkowska, J. Milke, M. Buśko, Possibilities and limitations of using Lemna minor, Hydrocharis morsus-ranae and Ceratophyllum demersum in removing metals with contaminated water, Journal of Water and Land Development 40 (2019) 161-173.

[13] V. Kastratović, Ž. Jaćimović, D. Đurović, M. Bigović, S. Krivokapić, Lemna minor L.: As bioindicator of heavy metal pollution in Skadar lake: Montenegro, Kragujevac J. Sci**.** 37 (2015) 123-134.

RADIOACTIVITY IN SOIL FROM REGION DONJI MILANOVAC, NP ĐERDAP IN 2018-2020

A. Čučulović[1], J. Stanojković[1], R. Čučulović[2], S. Nestorović[3] and N. Radaković[3]

[1]University of Belgrade, INEP- Institute for the Application of Nuclear Energy, Banatska 31b, 11080 Zemun-Belgrade, Serbia. (anas@inep.co.rs)
[2]University of MB, Faculty of Business and Low, Teodora Drajzera 21, 11000 Belgrade, Serbia.
[3]Public Company Đerdap Nationalni Park, Kralja Petra I 14a, 19220 Donji Milanovac, Serbia.

ABSTRACT
From June 2018 to 2020, 87 soil samples were collected from 10 locations in the National Park Đerdap, region of Donji Milanovac. The radionuclide content (Bq kg^{-1}) in collected soil was: for ^{40}K 80.6-1005; ^{238}U 7.4-60.2 and ^{232}Th 5.3-13.1. The apsorbed dose rate in air (nGy h^{-1}) on the territory of NP Đerdap is in the range of 18.5 to 98.8, with an average value of 53.6. Values of the external gamma dose were in the range of expected values and close to the average values in the world. The mean value of the annual effective dose in the region Donji Milanovac is 0.066 mSv and is lower than the mean value in the world.

INTRODUCTION
NP Đerdap is located in the North-Eastern part of Serbia and covers part of the area of the Đerdap gorge (Iron Gate) in the middle course of the Danube. It includes parts of the Severni Kučaj, Miroč and Štrbac massive 2-10 km wide, and also a part of the Danube that belongs to the Republic of Serbia. The very complex relief in NP Đerdap, specific climate, a large number of relic species and phytocenosis, and also a great variety in the lithological composition of rocks, genetic affiliation, and geological age have caused the formation of a variety of soil types with different properties and production potential [1]. The land is a dynamic system in which different physic-chemical and biological processes occur. It is composed of two components: mineral and organic. Rocks that are part of the Earth's crust contain a certain concentration of natural radionuclides (uranium, radium, thorium, and potassium) that are also present in the soil formed when they decompose and their contribution to natural radioactivity in the environment is the highest [2]. Primordial radionuclides such as ^{238}U, ^{232}Th and ^{40}K have a long physical half-life and significantly differ in physical and geochemical properties from other radionuclides. Radionuclides such ^{238}U, ^{232}Th and ^{40}K are present more homogeneously in the environment than manmade ones with worldwide average activity concentrations in soil 400 Bq kg^{-1}, 30 Bq kg^{-1}, and 35 Bq kg^{-1}, respectively [3]. Knowledge of their distribution and concentration plays a significant role in radiation protection.

EXPERIMENTAL
Soil samples (87) were collected in the NP Đerdap, the Donji Milanovac region, from 10 management units (MU) (Boljetinka (*1*), Crni vrh (*2*), Pecka bara (*3*), Kosovica (*4*), Manastirički gaj (*5*), Prapežešće (*6*), Brzujka (*7*), Zlatica (*8*), Boljetinska reka (*9*), Porečke šume (*10*)), up to the depth of 10 cm, in June from 2018 to 2020. Localities were carefully chosen based on the results obtained for bioindicator radioactivity in previous years [4]. After arrival at the laboratory, the samples were cleaned by removing visible impurities, dried, mechanically chopped, homogenized, and packed into Marinelli's vessels with a volume of 0.5 L, hermetically sealed with paraffin, and left to sit for 40

days to establish radioactive stability of post-radon series members ^{238}U, prior to gamma spectrometric analysis. The ^{238}U content was determined based on gamma lines: ^{234}Th (63 and 93 keV) and ^{234}Pa (1001 keV). The ^{232}Th content was determined based on gamma lines ^{228}Ac (338, 911 and 969 keV). The ^{40}K content was determined based on the gamma line at 1460 keV. The sample mass was up to 600g. Detector calibration was performed using three different radioactive reference materials in the Marinelli geometry: 1) Silicone resin (Czech Metrological Institute Praha (CMI Praha), Cert. No. 1035-SE-40517-17, Type MBSS 2 (^{241}Am, ^{109}Cd, ^{139}Ce, ^{57}Co, ^{60}Co, ^{137}Cs, ^{113}Sn, ^{85}Sr, ^{88}Y, ^{51}Cr), 490.0g, density: 0.98 ± 0.01 gcm^3, vol. 500.0 ± 5.0 cm^{3}ref. date 1.9.2017); 2) silicone resin CMI Praha, Cert. No. 1035-SE-40661/14, Type MBSS 2 (^{241}Am, ^{109}Cd, ^{139}Ce, ^{57}Co, ^{60}Co, ^{137}Cs, ^{113}Sn, ^{85}Sr, ^{88}Y, ^{51}Cr), 490.0g, density: 0.98 ± 0.01 g/cm^3, vol. 500.0 ± 5.0 cm^3, ref. date 1.10.2014). All samples were measured for 60000 s. A semiconducting germanium high purity detector of the n-type, ORTEC – AMETEK, USA, with 8192 channels, resolution of 1.65 keV, and relative efficiency of 34% at 1.33 MeV for ^{60}Co was used for detection. Spectra were analyzed using the Gamma Vision 32 software package [5]. The total standard error of the method was estimated to be around 20%. The absorbed dose rate in air (nGy h^{-1}) and the annual effective dose calculations were performed according to the recommendations of UNSCEAR [6].

RESULTS AND DISCUSSION

Table 1 shows the mean value obtained from measuring the content of radionuclides (^{40}K, ^{232}Th and ^{238}U) in soil, collected from 2018 to 2020 on the territory of the D. Milanovac region. Also, values of the apsorbed dose rate in air D (nGy h^{-1}) and annual effective dose D_E (mSv) are given in Table 1. The mean value (Bq kg^{-1}) of the radionuclide content in soil collected on the region D. Milanovac (in 2018, 2019, 2020) was ^{40}K 498 (536, 497, 470), ^{238}U 32.1 (33.4, 35.5, 27.9) and ^{232}Th 29.6 (34.4, 32.4, 23.2). The content (Bq kg^{-1}) in soil collected in region Donji Milanovac in 2018 (2019, 2020) was: ^{40}K 106-887 (80.6-918, 245-1005), ^{238}U 16.9-60.2 (8.8-53.9, 7.4-46.1) and ^{232}Th 13.1-60.6 (8.2-55.7, 5.3-45.3). These values are in the range determined in our previous research and in the worldwide research [6].

The values of Pearson's coefficient for U-Th are 0.891, which indicates a very strong correlation and common origin; while for K-U 0.489 and K-Th 0.571 indicate a correlation.

The apsorbed dose rate in air (nGy h^{-1}) radiation originating from activity of radionuclides in soil can be calculated using the following equation:

$$D(nGyh^{-1}) = 0.462xC_{Ra} + 0.604xC_{Th} + 0.0417xC_K \quad (1)$$

where C_{Ra}, C_{Th}, C_K are the radionuclide content in soil, while according to recommendations of UNSCEAR, corresponding conversion coefficients are: 0.462 nGy h^{-1}/(Bq kg^{-1}), 0.604 nGy h^{-1}/(Bq kg^{-1}), 0.0417 nGy h^{-1}/(Bq kg^{-1}), respectively [3]. The apsorbed dose rate in air (nGy h^{-1}) in 2015 on the territory of NP Đerdap is in the range from 9.8 to 70.5, while in 2016 it was from 4.6 to 66.3 [7]. The mean value of the apsorbed dose rate in air (nGy h^{-1}) in the period from 2018 to 2020 is 58.8, 56.8, and 46.7. The mean value of the apsorbed dose rate in air (nGy h^{-1}) is in the range of 23.1 to 98.8. These values are in the range of values obtained in the previous research globally [6].

The annual effective dose was determined as

$$D_E\ (mSv) = Dx0.7x0.2x365x24 \quad (2)$$

The annual effective dose (mSv) in 2015 was from 0.014 to 0.087, while in 2016 it was from 0.006 to 0.081 and they are the same order of magnitude as values determined on other locations in Serbia [7]. The mean value of the annual effective dose in the region Donji Milanovac is in the range from

0.023 to 0.121 mSv. The average value of the annual effective dose (mSv) in soil collected in the period from 2018 to 2020 is 0.072, 0.070, and 0.057. These values are within the measurement range of the mean value globally determined (0.070 mSv).

Table 1. Mean value radionuclide content (Bq kg^{-1}) in soil collected from 2018 to 2020 in the Donji Milanovac region and values of the apsorbed dose rate in air D (nGy h^{-1}) and annual effective dose D_E (mSv)

MU* (samples)	Year	^{40}K	^{238}U	^{232}Th	D	D_E
		(Bq kg^{-1})			(nGy h^{-1})	(mSv)
1 (3)		229	23.7	18.3	31.6	0.039
2 (9)		503	38.4	38.6	62.2	0.076
3 (4)		793	39.6	47.1	80.1	0.098
4 (2)		502	33.4	35.8	58.1	0.071
5 (2)	2018.	211	18.7	14.8	26.4	0.032
6 (2)		710	34.1	33.4	65.7	0.081
7 (2)		823	27.4	33.6	67.5	0.083
1 (6)		425	27.4	24.0	45.00	0.055
2 (14)	2019.	478	41.9	50.8	62.5	0.077
3 (3)		788	46.6	45.2	81.9	0.101
8 (3)		503	27.2	24.0	48.2	0.059
9 (5)		457	25.8	23.7	45.4	0.056
1 (4)		344	22.5	21.5	37.8	0.046
2 (9)	2020.	510	39.3	36.7	61.8	0.076
3 (3)		706	42.2	41.8	74.4	0.097
8 (7)		454	20.2	11.6	35.4	0.043
9 (4)		353	16.5	9.90	28.5	0.035
10 (5)		474	22.9	16.0	40.2	0.049

*MU management unit

Based on the Guidelines [3,6] the annual effective dose for the population is increased if it is higher than 1 mSv for a year. The calculated average values show that the effective dose for the population in the Donji Milanovac region is low.

CONCLUSION

Radionuclides ^{40}K, ^{238}U, and ^{232}Th were detected and measured in all investigated samples. The average values of radionuclide content in soil collected from 2018 to 2020 are in the range of average values of radionuclide content in the soil worldwide.

The apsorbed dose rate in air originating from radionuclide activity in soil was calculated. Total and annual effective doses were calculated and they are in the range of average values throughout the world.

Acknowledgment

The research presented in this work was performed with the financial backing of the Ministry for Education, Science and Technological Development of the Republic of Serbia, as part of financing scientific research at the Institute for the Application of Nuclear Energy – INEP, contract number 451-03-68/2022-14/200019.

REFERENCES

[1] M. Medarević, Šume Đerdapa, JP Nacionalni park Đerdap - Donji Milanovac i IP Ecolibri, Beograd, 2001.
[2] A. Dangić in: Jonizujuća zračenje iz prirode, Jugoslovensko društvo za zaštitu od zračenja, Institut za nuklearne nauke Vinča. Jugoslovensko društvo za zaštitu od zračenja, Beograd, Srbija, 1995, 41.
[3] Republika Srbija, Agencija za zaštitu od jonizujućih zračenja i nuklearnu sigurnost Srbije, Izveštaj o sistematskom ispitivanju sadržaja radionuklida u zemljištu u 2014. godini, Beograd, 2015.
[4] A. Čučulović, R. Čučulović, M. Sabovljević, M. Radenković, D. Veselinović, Arh. Hig. Rada Toksikol., 67 (2016) 31-37.
[5] ORTEC, Gamma Vision 32, Gamma-Ray Spectrum Analysis and MCA Emulation, ORTEC, Oak Ridge, Version 5.3, 2001.
[6] UNSCEAR Sources and Effects of Ionizing Radiation. Annex B: Exposure from natural radiation sources. United Nations, New York, 2000.
[7] A. Čučulović, R. Čučulović, S. Nestorović, N. Radaković, D. Veselinović, Radioactivity in soil from NP Đerdap in 2015 and 2016, Eco TER18, 26th International Conference Ecological Truth & Environmental Research, 12-18 June 2018, Hotel Jezero, Bor, Lake, Serbia, 140-145.

MANGANESE REMOVAL FROM ACIDIC MINE EFFLUENTS BY THERMALLY TREATED bovine BONES

I. Smičiklas, M. Jović, A. Čupić and S. Dragović

University of Belgrade, „VINČA" Institute of Nuclear Sciences - National Institute of the Republic of Serbia, Mike Petrovića Alasa 12-14, 11000 Belgrade (ivanat@vin.bg.ac.rs)

ABSTRACT

Along with the European Union's aspiration to double the rate of circular material use in the next decade, the search for acid mine drainage (AMD) remediation agents among waste materials and by-products is increasingly intense. Manganese removal from acidic effluents is particularly challenging due to the high pH values necessary for its precipitation. This study explores the effectiveness of alternative calcium phosphate materials obtained by treating crushed animal bones at different temperatures. The calcination of bones at 1000°C is beneficial for Mn separation from acidic effluents, bringing equilibrium pH to a neutral value, but sulfate ions commonly present in AMD significantly suppress Mn removal by such sorbent. The materials produced at 400°C-800°C proved to be more favorable Mn sorbents in acidic solutions with high sulfate content. All tested bone-derived materials, including the commercial bone char, proved to be more effective than synthetic hydroxyapatite.

INTRODUCTION

Mining activities worldwide cause significant environmental issues, one of which is the formation of acid mine drainage (AMD) with a wide range of toxic heavy metals concentrations and high sulfate content. Depending on the AMD composition, generated quantities, technical and economic factors, treatment methods based on metals` precipitation, adsorption, ion exchange, and membrane separation are in use. Still, treatment of more than 90 % of the AMD globally is currently being carried out using hydrated lime, and while most heavy metals can be removed straightforwardly by AMD neutralization, Mn separation stands out as the most challenging due to the very high pH values necessary for its complete precipitation [1].

Except for using alkane reagents, adding phosphate-rich materials to heavy metal contaminated effluents is a promising approach for converting contaminants from soluble to insoluble and less hazardous forms. The unique physicochemical properties of hydroxyapatite $Ca_{10}(PO_4)_6(OH)_2$ make it particularly advantageous for the separation of different pollutants, including a variety of heavy metals [2]. Promising Mn removal efficiencies were obtained using apatite-based materials of synthetic [3], mineral [4], and biogenic origin [5]. Given that the phosphorus scarcity has become one of the greatest concerns of the global society, and increasing rates of P reuse are urged, animal bones with typically 60 % (w/w) of bioapatite represent a rich secondary source of P that justifies further research in the field of environmental protection.

This study aimed to evaluate the influence of bone treatment temperature on the Mn separation ability from highly acidic media and the influence of sulfate ions on this process. The performance of sorbents obtained by treatment of bovine bones at 400°C-1000°C was compared with the efficiency of synthetic hydroxyapatite and a commercial bone char.

METHODS

According to the procedure described previously [6], the sorbents were prepared by heating crushed bovine bones for 4 h in an ambient air atmosphere at 400°C, 600°C, 800°C, and 1000°C (samples

B400-B1000). The samples were milled and sieved, and the fraction with the particle size 45–200 μm was used in further experiments. In addition, a commercial bone char (BRIMAC®, denoted BC) was tested for comparison, as well as the pure hydroxyapatite (HAP) synthesized by the neutralization method [7].

Model AMD solutions (100 mg/L Mn and 100 mg/L Mn combined with 2000 mg/L sulfate anions) were prepared by dissolving appropriate amounts of $MnCl_2$ and Na_2SO_4 in distilled water. The initial pH was adjusted to 2.5 with 1 M HCl. Batch sorption experiments were conducted by mixing the reagents and solutions at the solid/solution ratio of 5 g/L for 24 to reach the equilibrium. After filtering through qualitative filter paper, the equilibrium solution pH values were measured. The residual concentrations of Mn and concentrations of Ca ions released from the sorbents were measured by Inductively Coupled Plasma Optical Emission Spectrometry (Perkin Elmer Avio 200). Blank experiments (distilled water with initial pH set at 2.5) were conducted under the same conditions. The experiments were conducted in duplicate.

RESULTS AND DISCUSSION

The Mn separation efficacy from model AMD solutions (initial pH 2.5) by investigated materials is presented in Figure 1. With less than 20 % Mn removed from 100 mg/L solution, synthetic HAP was less effective than bone-derived products. The efficacy of bovine bones treated at 400°C and 600°C was similar (73.2 % and 66.0 %) and comparable with the performance of the commercial BC (68.3 %), while samples annealed at 800°C and 1000°C displayed superior properties (87.9 and 96.9 %, respectively). Except for HAP, Mn removal showed a reduction in the presence of a sulfate anion. Samples BC, B400, and B600 exhibited a slight decrease (3.2 - 7.0 %), using B800 Mn removal decreased by 11.4 %, while the most significant negative impact of sulfate was determined by applying B1000 (72.6 % reduction).

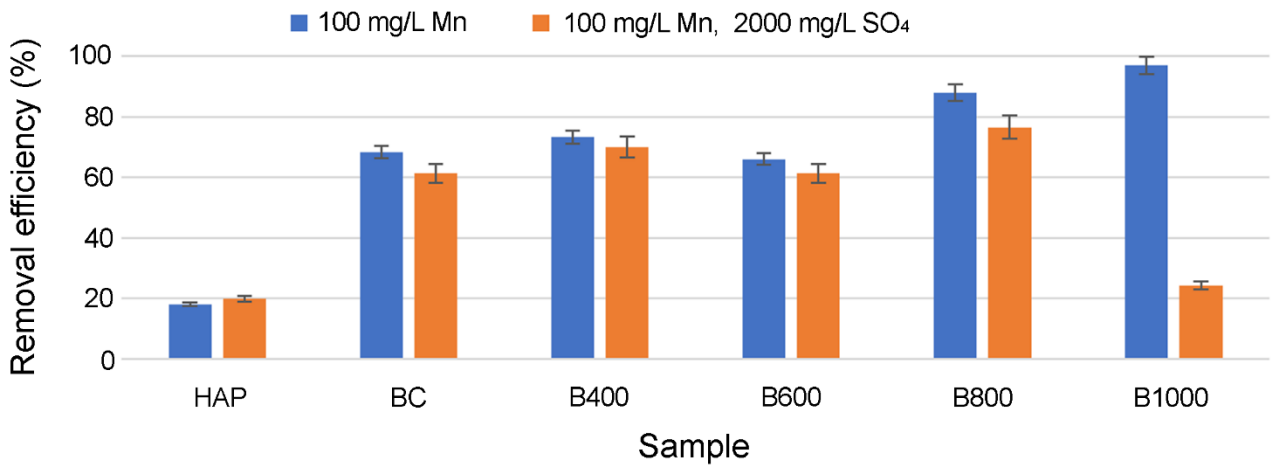

Figure 1. Mn removal efficiency from model AMD solutions by synthetic and bone-derived apatite samples.

The results presented in Figures 2 and 3 indicate the partial dissolution of investigated sorbents after reaction with acidic model AMD and blank solutions (initial pH 2.5), resulting in equilibrium pH increase and release of Ca ions from apatite structures. The Mn ion removal efficiency is a function of the equilibrium pH values, which explains the lowest efficiency of HAP and the highest for B1000 (equilibrium pH 4.9 and 7.0, respectively). Compared with blank experiments, removing Mn ions by apatite sorbents was accompanied by a significant increase in the released amounts of Ca ions (Figure 3), pointing out that ion exchange is one of the main operating mechanisms.

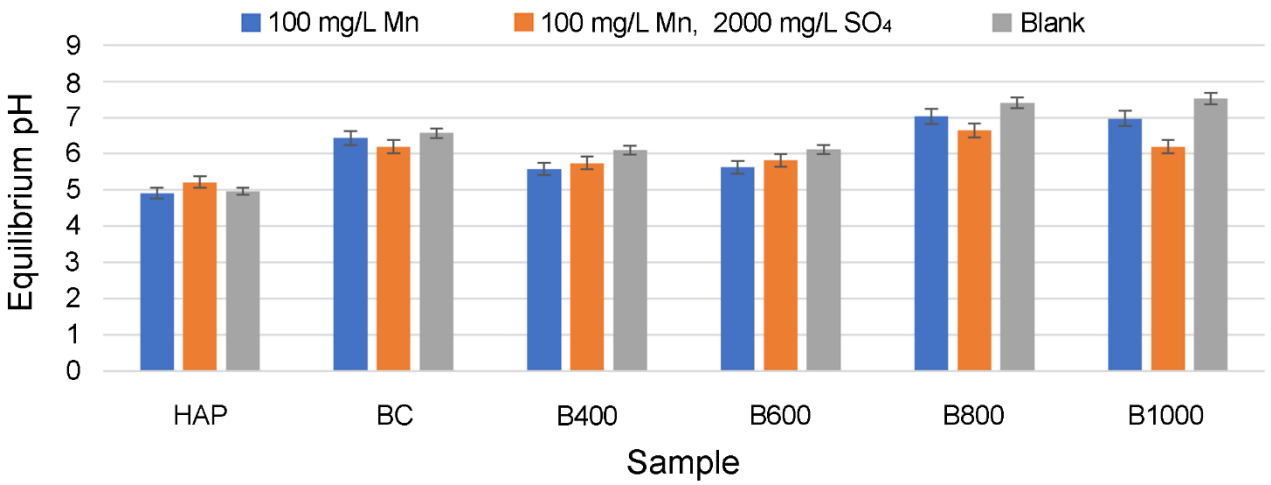

Figure 2. Equilibrium pH values in model AMD and blank solutions after treatment with apatite-based samples.

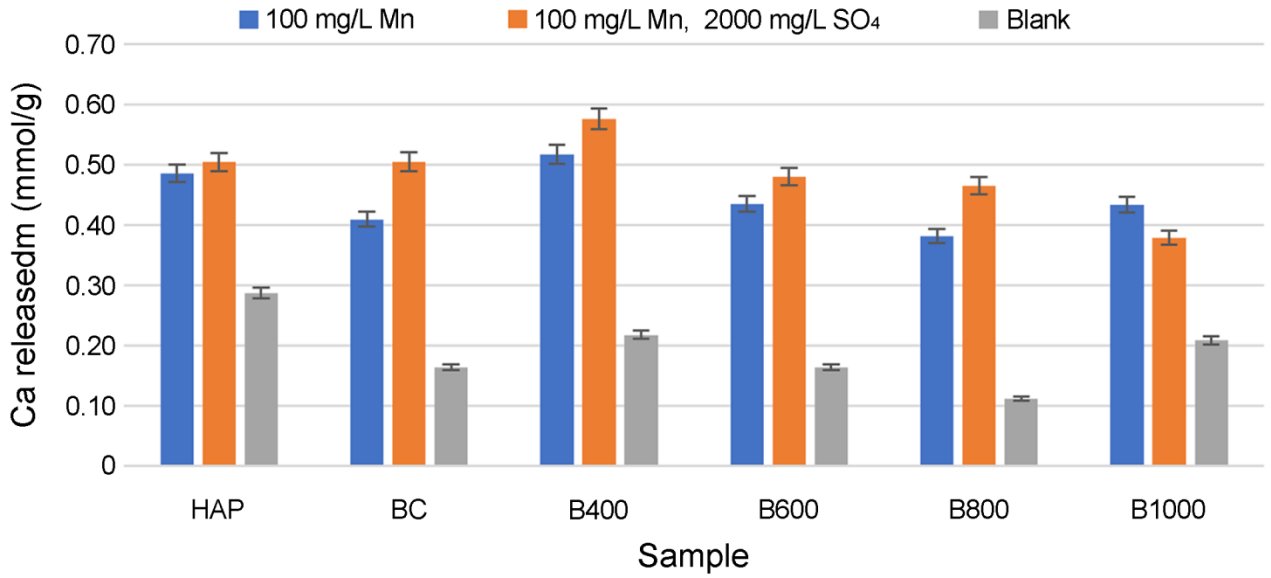

Figure 3. The amounts of Ca ions released from the apatite-based samples in model AMD and blank solutions.

Due to different origin and preparation routes, investigated sorbents displayed significantly different physicochemical properties [6-8]. The amounts of Mn ions sorbed from model solutions (mmol/g) were in correlation with the specific surface area (Sp,BET) [6-8] of the samples HAP, BC, B400, and B600, i.e., the higher the Sp,BET the higher the amount of Mn sorbed (Figure 4). Quite the contrary, a radical decrease in Sp,BET caused by hydroxyapatite particles sintering at higher temperatures (800°C and 1000°C) and an increase in pH values of these sorbents due to the formation of CaO and MgO [6] was associated with high Mn removal rates. Increased solubility of B800 and particularly B1000 can cause precipitation of $CaSO_4$ in contact with sulfate-containing AMD, which may be the explanation for the reduced Mn removal efficiency.

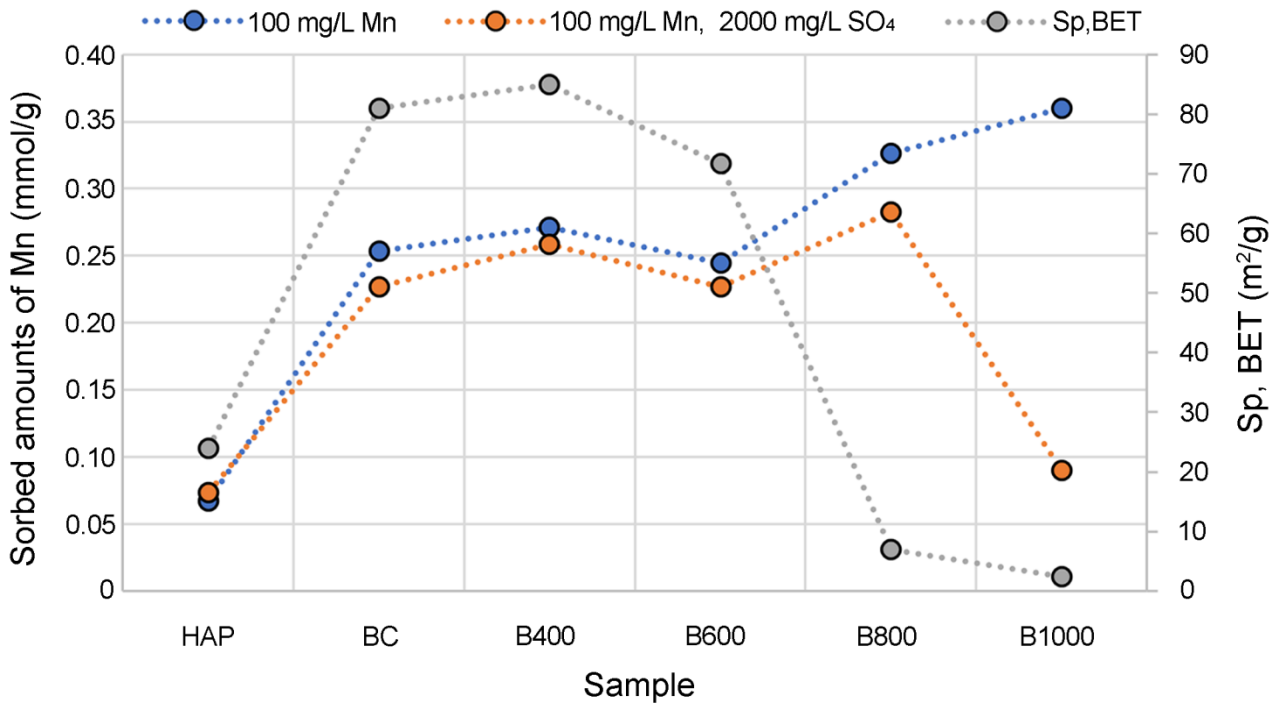

Figure 4. Relationships between the specific surface area of the apatite-based samples [6-8] and the amounts of Mn sorbed from model AMD solutions.

CONCLUSION

This study indicates a good prospect for thermal conversion of animal bones, a food industry waste, into calcium phosphate materials capable of Mn separation from acidic effluents. Sorbents obtained by thermal treatment of bovine bones demonstrated both AMD neutralization and Mn removal effects, superior to synthetic HAP. The results represent a basis for further study of the Mn sorption mechanism and the stability of the obtained residues to optimize the bone processing conditions.

Acknowledgment

This work was supported by the Ministry of Education, Science and Technological Development of the Republic of Serbia (grant no 451-03-68/2022-14/200017).

REFERENCES

[1] C. M. Neculita, E. Rosa, Chemosphere, 214 (2019) 491–510.
[2] A. N. Amenaghawon, C. L. Anyalewechi, H. Darmokoesoemo, H. S. Kusuma, J. Environ. Manage., 302 (2022) 113989.
[3] R. Carrillo-González, M. C. A. González-Chávez, G. O. Cazares, J. L. Luna, Environ. Monit. Assess., 194 (2022) 280.
[4] V. Vandeginste, C. Cowan, R. L. Gomes, T. Hassan, J. Titman, J. Hazard. Mater., 389 (2020) 122150.
[5] D. C. Sicupira, T. T. Silva, V. A. Leão, M. B. Mansur, Brazilian J. Chem. Eng. 31 (2014) 195–204.
[6] S. Dimović, I. Smičiklas, I. Plećaš, D. Antonović, M. Mitrić, J. Hazard. Mater., 164 (2009) 279–287.
[7] I. Smičiklas, S. K. Milonjić, P. Pfendt, S. Raičević, Sep. Purif. Technol., 18 (2000) 185–194.
[8] S. Dimović, I. Smičiklas, M. Šljivić-Ivanović, I. Plećaš, L. Slavković-Beškoski, J. Environ. Sci. Health A, 46 (2011) 1558–1569.

RECOVERY OF COPPER FROM ORE DUMP USING BIOLEACHING APPROACH

J. Avdalović[1], N. Lugonja[1], T. Šoštarić[2], M. Lukić[3], J. Milić[1],
J. Milojković[2] and V.Conić[4]

[1]University of Belgrade, Institute of Chemistry, Technology and Metallurgy, Njegoševa 12, 11000 Belgrade, Serbia. (jelena.avdalovic@ihtm.bg.ac.rs)
[2]Institute for Technology of Nuclear and Other Mineral Raw Materials, Bulevar Franše d'Eperea 86, Belgrade, Serbia.
[3]University of Belgrade, Faculty of Chemistry, Studentski trg 12-16, 11000 Belgrade, Serbia.
[4]Mining and Metallurgy Institute Bor, Zeleni bulevar 35, 19210 Bor, Serbia.

ABSTRACT
Bioleaching is an environmentally-friendly approach for the extraction of useful metals from low-grade ores and secondary mineral materials.
The object of this paper was to examine the possibility of microbiological solubilisation of copper from ore dump by *Acidithiobacillus* sp. B2.

Leaching experiments were performed by the shake flask testing technique at 28 ^{o}C, during two-week period. The percentage of the copper leached at the end of this experiment was 31%.

INTRODUCTION
Bioleaching is a process in mining and biohydrometallurgy (natural processes of interactions between microbes and minerals) that extracts valuable metals from a low-grade ore with the help of microorganisms such as bacteria or archaea.

Microbial methods for recovering metals are important for following reasons:
1) Waste materials is being used as a raw material giving the metal as that final product, that would be irretrievably lost; 2) Microbial leaching methods are several times cheaper compared to the conventional one that are inapplicable for the low grade ores; 3) Minimum threats to the environment [1].

In order to extract copper from the ore dump, microbial leaching has been conducted in laboratory using the culture of *Acidithiobacillus* sp. B2. Parameters, like chemical characteristics of tailings, solid-liquid ratio, numberof bacteria, leaching time, pH decreasing, percentage of pyrite sulphur consumption as well as the percentage of the leached copper, were determined.

METHODS
Chemical analysis of the ore dumps
Silicate analysis of the ore dumps was conducted using the conventional method, by alkaline fusion with $NaKCO_3$ and dissolution in HCl [2]. From the filtrate Fe, Al, Ti, Ca and Mg, were determined whilethe residue was further treated with HF in order to obtain volatile SiF_4, from which the SiO_2 content was determined. The remaining precipitate was treated again as silicate material.

For the determination of alkaline metals and copper, the sample was decomposed with a mixture of $HClO_4$ and HF, while for the determination of phosphorus, the sample was decomposed witha mixture of aqua regia and $HClO_4$.

The alkaline metals and copper were determined by atomic emission flame spectrophotometry; Fe, Al, Ti, Ca, Mg by atomic absorption flame spectrophotometry. Sulphide sulphur from the ore dumps was determined gravimetrically after oxidation with $KClO_3$ and HNO_3 followed by

precipitation as $BaSO_4$. Correction on sulphate sulphur from the ore dumps was determined in the "soda-extract" (boiling solution of Na_2CO_3), as $BaSO_4$ [2].

Analysis of 16S rRNA gene sequences

Isolation of microorganisms Iron-oxidizing *Acidithiobacillus* sp. B2 was performed from water samples taken from Lake Robule, in the copper mine in Bor, Serbia. Analysis of 16S rRNA gene sequences The genomic DNA of iron-oxidizing *Acidithiobacillus* sp. B2 was extracted using DNeasy Blood & Tissue Kit (Qiagen, USA). The 16S rRNA genes were amplified by PCR using 27F(50-AGAGTTTGATCMTGGCTCAG-30;and 1492R (50-TACGGYTACCTTGTTACGACTT-30. Amplified fragments were purified with the QIAquick PCR Purification Kit (Qiagen, USA) and sequenced using the commercial MACROGEN (Netherland) service. The isolated strain was identified using the EzTaxon-e server on the basis of 16S rRNA sequence data. The iron-oxidizing *Acidithiobacillus* sp. B2 strain isolated exhibited the following characteristics: motility, cell size 1.5 0.5 lm, growth using sulphur, thiosulfate, ferrous iron, and pyrite as electron donors. The identification was performed by sequence analysis of the 16S rRNA gene, and the gene sequence of analyzed strain was deposited in NCBI GenBank under accession number KC691309. Molecular characterization indicated that the isolated strain belongs to the genus *Acidithiobacillus* with 99.28 % pairwise similarity with *Acidithiobacillus ferrivorans* NO-37(T) (AF376020), 98.54% with *Acidithiobacillus ferridurans* ATCC 33020(T) (AJ278719) and 98.21% similarity with *Acidithiobacillus ferrooxidans* ATCC 23270(T) (CP001219) [3].

Leaching experiments design

The leaching experiments were carried out with bacterium *Acidithiobacillus* sp. B2. Experimental conditions were: leaching period of 14 d, leaching solution (g/dm^3): $FeSO_4x7H_2O$ (5), $(NH_4)_2SO_4$ (3), K_2HPO_4 (0.5), $MgSO_4$ (0.5), KCl (0.1), $Ca(NO_3)_2$ (0.01), (1K) at a pH of 2.5 in 500 mL Erlenmeyer flasks at a pulp454 density of 10% (m/V) (10 g leaching substrate in 100 ml solution). The control suspension had the same chemical content and pH value as the suspension with *Acidithiobacillus* sp. B2, but the *Acidithiobacillus* sp. B2 culture had been inactivated by sterilization. Experiment was performed on a horizontal shaker New Brunswick Scientific. The incubation temperature was 28 °C and the rotation speed 180 rpm. Number of microorganisms, concentration of copper and pH were analysed every seventh day during the period of 14 day.

The bacteria oxidized pyrite to sulfuric acid and $FeSO_4$, which was then microbiologically oxidized to iron(III) sulphate ($Fe_2(SO_4)_3$). Iron(III) sulphate is very important in the bioleaching process, because this compound is a strong oxidizing agent, so pyrite oxidation continued.

Bioleaching occurs according to the following chemical reactions:

$2FeS_2 + 7O_2 + 2H_2O \rightarrow 2H_2SO_4 + 2FeSO_4$

$2FeSO_4 + H_2SO_4 + 0.5O_2 \rightarrow Fe_2(SO_4)_3 + H_2O$

$FeS_2 + Fe_2(SO_4)_3 \rightarrow 3FeSO_4 + 2S\downarrow$

$2S + 3O_2 + 2H_2O \rightarrow 2H_2SO_4$

Key role of *Acidithiobacillus* sp. B2 is to regenerate sulphur acid and Fe^{3+}, which is strong oxidizing agent. All these things lead to lower pH and leaching of copper from solid phase.

RESULTS AND DISCUSSION

Samples were taken from eight different locations on Bor ore dumps. Chemical analyses of ore dumps are presented in Table 1.

Table 1. Chemical analyses of ore dump

Component	SiO_2	Al_2O_3	CaO	MgO	Na_2O	K_2O	S	P_2O_5
%	59.29	14.56	2.65	1.03	0.98	1.30	2.80	0.070
Component	Fe_{total}	Fe^{2+}	Cu	Cu_{ox}	$S_{sulphide}$	$S_{sulphate}$	MnO	LOI
%	8.38	4.20	0.22	0.02	1.3	1.5	0.01	8.07

The X-ray powder diffraction analyses show that ore dump contents quartz, feldspars, amphibole, pyrite,talc.

The initial number of microgranisms was $3x10^7$ per ml. This number increased during experiment, and after seven days itwas $4x10^8$/ml, and on the end of the experiment it was $2x10^8$/ml.

During the leaching process, pyrite sulphur (sulphide sulphur) content in suspension with *Acidithiobacillus sp.* B2 decreased from 1.3% to 0.7%, while in the control suspension its content decreased from 1.3% to 1.2%. Obtained results confirm the role of microorganism in pyrite oxidation, as well as in process of copper leaching from ore dump.

Change of pH and percentage of copper leached in suspension with bacteria, aswell as in control suspension, were determined on start and on the 7th and 14th day of experiment. The results obtained are presented on Figure 1. and Figure 2.

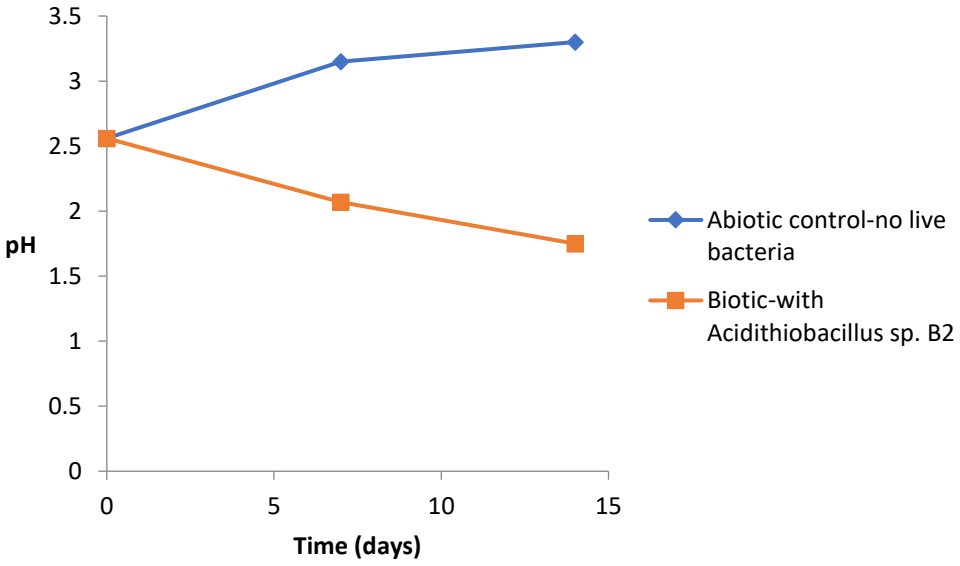

Figure 1. pH profiles during bioleaching of ore dumps in suspension with *Acidithiobacillus* sp. B2 and control suspension

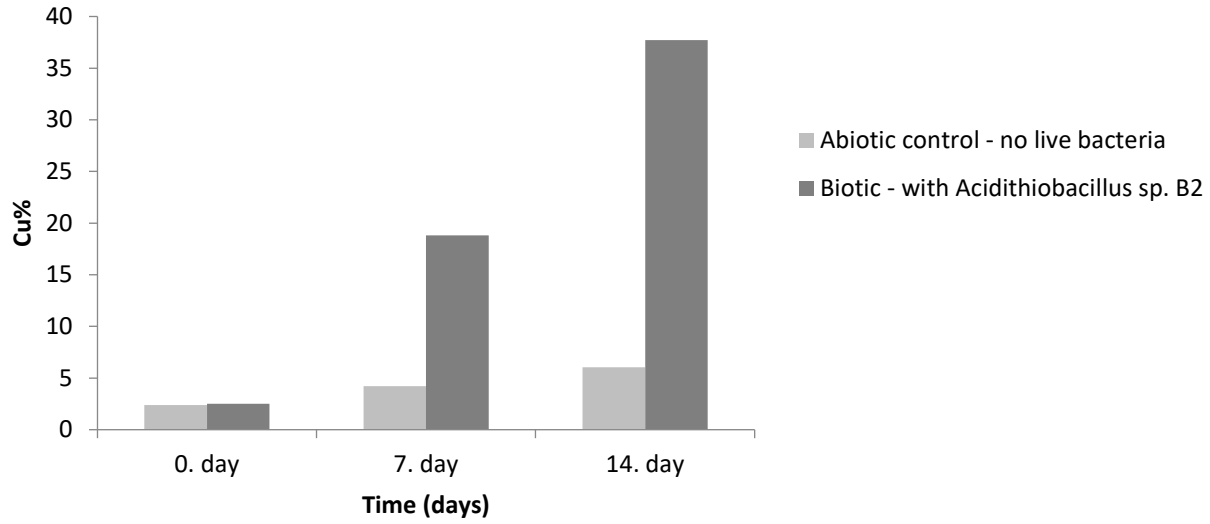

Figure 2. Amount of Cu leached during the process on shaker

Obtained results indicate that there is relationship between copper leaching and decrease of pH value, which is directly correlated with concentration of bacterially produced sulfuric acid in leaching medium.

The percentage of leached copper, resulting from the activity of *Acidithiobacillus* sp. B2, *(i.e.* the effective metal leaching), was calculated by subtraction of percentage metal leaching in the control suspension from that in the *Acidithiobacillus* sp. B2 suspension, and it equals 31%.

CONCLUSION

These results showed that microbiological treatment of ore dump had been efficient, and the future task is tooptimize this process in order to get larger amount of copper leached. It could be probably achieved by increasing the number of microorganisms in suspension, or increasing the time of leaching.

Microbial methods of leaching ore dump plays very important role for obtaining the additional amounts of metals and in the concept of environmental protection, because it allows use of relatively simple technology to control and redirect uncontrolled loss of metals into the soil and watestreams.

Acknowledgment

This work was supported by the Ministry of Education, Science and Technological Development of the Republic of Serbia (grant no 451-03-68/2022-14/200026 and grant no 451-03-68/2022-14/200023).

REFERENCES

[1] M. M. Vrvić, Fundamental and applied aspects of interaction of thionic bacteria with sulphide substrates, PhD thesis (in Serbian), University of Belgrade, Faculty of Chemistry, Belgrade, 1991.

[2] J. S. Jekić, V. P. Beškoski, G. Gojgić-Cvijović, M. Grbavčić, M. M. Vrvić, J. Serb. Chem. Soc., 72 (2007) 615.

[3] J. Avdalović, V. Beškoski, G. Gojgić-Cvijović, M.L. Mattinen, M. Stojanović, S. Zildžović, M. M. Vrvić, Miner. Eng., 72 (2015) 17.

REMOVAL EFFICIENCY OF Pb(II), Zn(II) AND Cu(II) IN MONO- AND MULTIMETAL SYSTEMS BY ALKALI TREATED APRICOT SHELLS BIOSORBENT

T. Šoštarić[1], J. Milojković[1], J. Avdalović[2], N. Lugonja[2], V. Adamović[1], A. Antanasković[1] and Z. Lopičić[1]

[1]Institute for Technology of Nuclear and Other Mineral Raw Materials, Belgrade, Franchet d'Esperey St. 86, Belgrade, Serbia
[2]University of Belgrade, Institute of Chemistry, Technology and Metallurgy, Njegoševa 12, 11000 Belgrade, Serbia. (jelena.avdalovic@ihtm.bg.ac.rs)

ABSTRACT
The mutual interaction of metal ions (lead, zinc and copper) on removal efficiency in binary and ternary systems, by biosorbent based on alkali treated apricot shells (*Prunus armeniaca* L.) was examined. The evaluation was done in batch system at two metals concentrations: 0.2 and 0.5mmol/ dm^3. Tested biosorbent exhibited preferential uptake of lead in a multimetal systems. It is evident that mutual inhibition exists in all multimetal systems, but systems containing lead ex-hibited extreme inhibition toward copper and zinc ions. Process of sorption depends not only on specific chemistry of each metal, their affinity toward binding sites and the type of metal binding onto biosorbent, but also on sorbent chemical and morphological characteristics. In multimetal systems, tested sorbent showed preferential sorption orders: Pb (II)>Cu (II)>Zn (II).

INTRODUCTION
Research focusing on biosorption offers a stepping stone for developing a whole new environmental technology aiming to the removal or the recovery of various pollutants from water systems. It's not surprising that many papers have been published about this topic in the past decades [1,2]. Although, biosorption is a technology that has been seen with great potential for wastewater treatment, it has to be commercialized [3]. The number of published papers for single metal removal by biosorption is many times higher compared to multi-metal removal [4]. Considering that wastewater contains a mixture of metal ions, it is necessary to study and understand multicomponent sorption under competitive conditions by using low-cost biosorbents [5]. It is well known that when several different metal ions are in solution a few possible interactions can be expected: synergism (resulting in an increase in sorption efficiency), antagonism (resulting in a decrease in sorption of individual ions from the mixture) or no interactions [6]. This work focuses on the removal efficiency of Pb(II), Zn(II) and Cu(II) in mono- and multimetal systems by alkali treated apricot shells.

METHODS
The apricot stones were obtained from Juice Factory "Vino Župa" Aleksandrovac. Seeds were manually separated from shells and for further experiments only apricot shells were used. Dried shells were grounded (KHD Humbolt Wedag AG) at fraction less than 1.0 mm. Furthermore, modification was performed by mixing of 50 g of dried/grinded/sieved biomass sample with 1.0 dm^3 of 1.0 mol/dm^3 NaOH on a magnetic stirrer (at 250 rpm) for 3h. Afterwards, the suspension was filtered and residue was repeatedly washed with distilled water until stable pH value was observed. Subsequently, it was dried at 50°C until reaching a constant mass. It was labeled as SHM.

The mutual interaction of the examined metals on the removal efficiency by SHM was investigated in solutions of binary and ternary mixtures of metals. The following binary solutions of metal ions were tested: Pb(II) and Cu(II); Pb(II) and Zn(II); Zn(II) and Cu(II), at each metal concentration of 0.2

and 0.5 mmol/dm^3. At the same concentrations, the ternary solution of metal ions: Pb(II), Cu(II) and Zn(II) were tested, too. The experiments were performed at sorbent concentration of 2.0 g/dm^3, the initial pH value 5.0 (adjusted by 0.1 mol/dm^3 HNO_3 or KOH solution). The suspensions were stirred on orbital shaker at 250 rpm for 120 minutes. After this time the suspensions were filtered and the filtrates were analyzed by using atomic adsorption spectrophotometer (Perkin Elmer AAnalyst 300). Stock solutions were prepared by dissolving precise amount of $Cu(NO_3)_2 \times 3H_2O$; $ZnSO_4 \times 7H_2O$ and $Pb(NO_3)_2$ (p.a. grade) in distilled water. Metal solutions of specific concentrations were prepared by dilution of the stock solution. Using pH meter (SensIon MM340), pH value was adjusted to the required values with 0.1 M HNO_3 and 0.1 M NaOH solutions.
The biosorption efficiency of SHM was calculated using the following equation:

$$R\ (\%) = \frac{(C_i - C_{eq})x100}{C_i}$$

where: C_i and C_{eq} (mg/dm^3) are the initial and final equilibrium metal ion concentration, respectively.

RESULTS AND DISCUSSION

Previous study confirmed that alkaline treatment of apricot shells had successfully improved adsorption capacity by 154, 61 and 90% for Cu(II), Zn(II) and Pb(II), respectively [7]. In order to determine the efficiency of SHM in complex systems simulating the real effluents, biosorption experiments in binary and ternary systems, with Cu(II), Zn(II) and Pb(II) were investigated and the results of testing are presented in Figure 1. As can be seen, sorption efficiency of lead ions in a mixture with copper ions decreases by 18 % at both concentrations, while with zinc ions decreases by 7% and 15% at initial concentration 0.2 and 0.5 mmol/dm^3, in comparison to the sorption efficiency from solution which contains only lead ions. However, the sorption efficiency of lead ions in the ternary system decreases more by 28 and 23%, at same initial concentrations. Sorption efficiency of SHM toward copper ions in a mixture with lead ions decreases even more by 30% and 40% and with zinc ions by 19% and 2% at same initial concentrations, in comparison to the sorption efficiency from solutions where copper ions were individually present. The sorption efficiency of copper ions in the ternary system decreases by 28% and 53%, at same initial concentrations. However, SHM sorption efficiency of zinc ions in the mixture with lead ions decreases drastically by 63% and 46% and with copper ions by 60% and 47% at initial concentration 0.2 and 0.5 mmol/dm^3 in comparison to the sorption efficiency from the solution where zinc ions were individually present. The sorption efficiency of zinc ions in the ternary system decreases by 83% and 49% at same initial concentrations. It is evident that the efficiency of heavy metals removal from solutions containing individual ions is significantly higher in relation to the efficiency of metals removal from multimetal solutions. Evidently, there is antagonism between ions as a consequence of competition for available active sites on the SHM surface. Suppression of sorption by other metal ions is most pronounced with lead ions and least pronounced with zinc ions present in solution. The complexity of the process is reflected in interaction between sorbent and metals, which is related to sorbent chemical and morphological characteristics and to the chemical and physical properties of metals. According to authors previous research alkaline treatment causes an increase in porosity (by 20%), total pore volume (by 24%), specific surface area (by 33%) and average pore diameter (by 20%) in comparison to untreated apricot shells [7,8]. Metal ion characteristic parameters: ionic radius, electronegativity, hydrated radius, covalent index, hydration enthalpy, charge-to-radius ratio are listed in Table 1/Figure 1. Metals with higher electronegativity adsorb more readily because metal ions with larger ionic radius have lower charge density and lower electrostatic attraction that limits the interaction of the metal ions with the adsorption sites [9]. Also, the higher the electronegativity, the stronger the bond that is established between metal ions and oxygen atoms from functional groups on the surface of the SHM and experimental results showed that SHM affinity followed the order Pb(II)>Cu(II)>Zn(II) which is

consistent with the electronegativity values. Hillel [10] explained that the smaller the ionic radius and the higher the valence, the closer and stronger the ion is adsorbed. However, on the other hand, the higher the hydration of the ion, the further it is from the surface of the adsorbent and the weaker the adsorption. Since the attraction of water molecules around ions depends on the charge density of ions, smaller ions will attract more water molecules leading to an inverse relationship between the ionic radius and the hydrated ionic radius. The ionic radius grows in the following order: Cu(II)>Zn(II)>Pb(II), while the radius hydrated ions decrease in the following order: Zn(II)>Cu(II)>Pb(II) (Table 1). With an increase of the ionic size, the absolute value of enthalpy of hydration decreases. According to the values of enthalpy of hydration Pb(II) ions will have greater accessibility to the SHM surface. The results of these experiments showed that in multimetal systems, tested sorbent exhibited preferential sorption order: Pb(II)>Cu(II)>Zn(II). Similar results were obtained by Milojković [11] examining the removal of Pb(II), Cu(II), Cd(II), Ni(II), and Zn(II) ions from aqueous solution by application of the *Miriophylum spicatum* compost. According to that study the biosorbent showed the highest affinity for Pb(II) and Cu(II), while the biosorption capacity decreased in the order Pb(II)>Cu(II)>Cd(II)>Zn(II)>Ni(II), at pH 5.0.

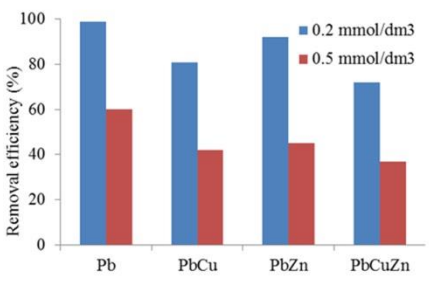

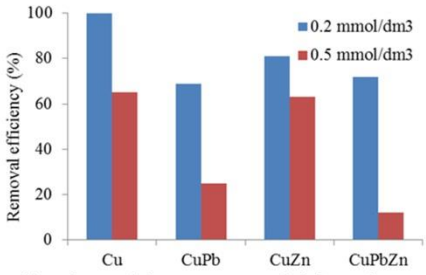

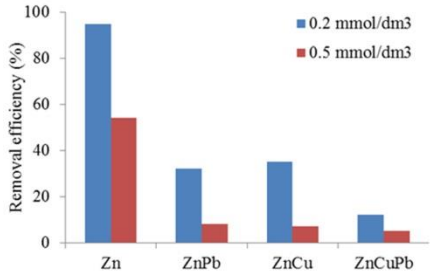

Table 1 Metal ion characteristic parameters and their trends

Metal	Ionic radius (pm) [12]	Hydrated radius (pm) [13]	Electronegativity (Pauling) [12]	Covalent index, $Ci = X_m^2 (r + 0.85)$ (pm)	Hydration enthalpy (kJ/mol) [12]
Pb(II)	120	401	2.33	1,113	−1,480
Cu(II)	73	419	1.9	578	−2,100
Zn(II)	74	430	1.65	433	−2,044
Ionic radius (pm)			Pb(II) > Zn(II) > Cu(II)		
Electronegativity (Pauling)			Pb(II) > Cu(II) >Zn(II)		
Hydrated radius (pm)			Zn(II) > Cu(II)> Pb(II)		
Covalent index (pm)			Pb(II) > Cu(II) > Zn(II)		
Hydration enthalpy (kJ/mol)			Pb(II) > Zn(II) > Cu(II)		
Charge-to-radius ratio (electrostatics effect on ionic bonding)			Cu(II) > Zn(II) > Pb(II)		

Figure 1. SHM removal efficiency of lead, copper and zinc ions in binary and ternary systems

CONCLUSION

In this study, the application of the biosorbent based on alkali treated apricot shells was tested for removal of Pb(II), Cu(II) and Zn(II) ions from multimetal solution. SHM showed the highest affinity for Pb(II) and the lowest affinity for Zn(II). Antagonism between metal ions as a consequence of competition for available active sites on the SHM surface has been evident. The resulting biosorption efficiency decreased in the order Pb(II)>Cu(II)>Zn(II), at pH 5.0.

Acknowledgment
This work was supported by the Ministry of Education, Science and Technological Development of the Republic of Serbia (grant no 451-03-68/2022-14/200023 and grant no 451-03-68/2022-14/200026).

REFERENCES

[1] M. Abdulaziz, S. Musayev, Pol J Environ Stud, 26 (2017) 1433–1441.
[2] H. I. Syeda, I. Sultan, K. S. Razavi, P.-S. Yap, J Water Process Eng, 46 (2022) 102446.
[3] M. Fomina, G. M. Gadd, Bioresource Technol, 160 (2014) 3–14.
[4] M. Long, H. Jiang, X. Li, Sci Rep 11 (2021) 11527.
[5] H. E. Reynel-Avila, D. I. Mendoza-Castillo, V. Hernández-Montoya et al., Chapter 5: Multicomponent removal of heavy metals from aqueous solution using low-cost sorbents In: Water Production and Wastewater Treatment Editor: B. Antizar-Ladislao et al., 2010 Nova Science Publishers
[6] D. L. D. Mitić, Uklanjanje teških metala iz vode bosorbentom na bazi *Lagenaria vulgaris*, Univerzitet u Nišu, Prirodno-matematički fakultet. Doktorska disertacija, Niš, 2012.
[7] T. D. Šoštarić, M. S. Petrović, F. T. Pastor, D. R. Lončarević, J. T. Petrović, J. V. Milojković, M. D. Stojanović, J Mol Liq, 259 (2018) 340-349.
[8] T. Šoštarić, M. Petrović, J. Stojanović, M. Marković, J. Avdalović, A. Hosseini-Bandegharaei, Z. Lopičić, Biomass Convers Biorefin (2020) https://doi.org/10.1007/s13399-020-00766-2
[9] M. Minceva, , L. Markovska, V. Meshko, Maced J Chem Chem En, 26 (2) (2007) 125–134. [10] D. Hillel, Environmental Soil Physics. Academic Press, San Diego, CA, 1998.
[11]J. V. Milojković,, M. D. Stojanović, M. L. Mihajlović, Z. R. Lopičić, M. S. Petrović, T. D. Šoštarić, M. Đ. Ristić, Water Air Soil Poll 225 (2014) 1927.
[12]G. Wulfsberg, Principles of descriptive chemistry. Monterey CA:Brooks/Cole Publishing, 1987.
[13]E. R. Nightingale, J Phys Chem, 63 (1959) 1381–1387.

SPENT COFFEE GROUNDS AS AN ADSORBENT FOR MALATHION AND MALAOXON

V. Milanković, T. Tasić, S. Mitrović, S.Brković, I. Perović, and T. Lazarević-Pašti

University of Belgrade, VINČA Institute of Nuclear Sciences - National Institute of the Republic of Serbia, Mike PetrovicaAlasa 12-14, 11000 Belgrade, Serbia. (ivanaperovic@vin.bg.ac.rs)

ABSTRACT

Extensive use of organophosphate pesticide malathion led to its abundant presence in the environment. An additional concern is its transformation to the more toxic form, malaoxon, due to environmental conditions. Malathion and malaoxon omnipresence in water and soil raise the need to explore efficient procedures for their elimination. We used bio-waste material as an adsorbent for two pesticides. The kinetics and efficiency of the malathion and malaoxon adsorption on the low-cost bio-waste material obtained from non-treated spent coffee grounds were investigated. The results showed that the experimental data are a good fit with the pseudo-second-order model. The calculated rate constants were 0.108 g mg^{-1} min^{-1} and 4.343 g mg^{-1} min^{-1} for 1 mg mL^{-1} and 10 mg mL^{-1} of adsorbent, respectively. It was shown that 1 g of investigated material is capable of adsorbing up to 40.76 mg of malathion. A satisfactory agreement of experimental results with the Freundlich isotherm model suggests the multilayer adsorption on the heterogeneous surface. Adsorption efficiency of investigated adsorbent for malaoxon was higher than for malathion.

INTRODUCTION

Organophosphorous pesticides (OPs) are esters or thioesters of phosphoric acid widely used in agriculture for the control of pests. OPs are primarily neurotoxicants, as they inhibit the enzyme acetylcholinesterase (AChE). Therefore, they prevent brake-down of the neurotransmitter acetylcholine (ACh) and increase the duration of action and level of ACh in nerve endings [1].

Malathion is an OP insecticide with a broad range of use. The toxicity of malathion is moderate, but by ingestion or adsorption into the human body, it goes through the process of oxidation. In the oxidation process of malathion, a sulfur atom from the thio-group is replaced by an oxygen atom, forming a more toxic oxo-form of malathion – malaoxon [2].

Removal of OPs from water is a major concern, and it has been greatly studied for decades. The least invasive and safest way of removing OPs from water without forming more toxic products is adsorption. The search for the material with a good balance of adsorption properties and chemicals/energy used in its production is still on. Non-treated waste materials have the advantage of low-cost production, making them interesting for research [3].

Coffee is one of the most used products in the world. Nearly 10 billion kg of coffee is produced yearly. After use, coffee grounds are tossed away, presenting the problem of environmental pollution [4].

The aim of this work was to investigate the kinetics and efficiency of the malathion and malaoxon adsorption on bio-waste material obtained from non-treated spent coffee grounds.

METHODS

Spent coffee grounds were dried for 5 days at ambient temperature. The obtained bio-waste material was dispersed in double-distilled water (stock solutions were 2 mg cm^{-3} and 20 mg cm^{-3}), and the desired amount of malathion and malaoxon stock solutions were added to provide the targeted concentration of adsorbent and OP. Then, the vessel containing the adsorbent + OP mixture was placed on a laboratory shaker and left for the desired amount of time. After the incubation, the mixture

was centrifuged for 10 min at 14 500 rpm, and the supernatant was filtered through a nylon filter membrane. The concentrations of malathion and malaoxon were determined using Ultra-performance liquid chromatography (UPLC). For UPLC measurement, Waters ACQUITY UPLC system with a photodiode array (PDA) detector, controlled by the Empower software, was used. The analyses were done using ACQUITY UPLC™ BEH C18 column (1.7 μm, 100 mm × 2.1 mm, Waters GmbH, GER) under isocratic conditions with a mobile phase A consisting of 10% acetonitrile in water (v/v), and a mobile phase B, which was pure acetonitrile. The eluent flow rate was 0.2 cm^3 min^{-1} in all cases, and the injection volume of 5 μL was used. The same mobile phase was used for both OP, composed of 40 % A and 60 % B. Under these experimental conditions, the retention time of malathion was 3.2 min and 1.6 min for malaoxon. Both OPs were detected at 200 nm. Control experiments were performed identically but without adsorbent.

RESULTS AND DISCUSSION

In order to investigate the kinetic parameters of the adsorption process, 1 mg cm^{-3} and 10 mg cm^{-3} of investigated adsorbent was incubated with malathion in the concentration 5×10^{-5} mol dm^{-3} for various intervals (1-60 min) at 25 °C. The concentration of adsorbed malathion was calculated as a difference between its initial concentration (C_0) and the equilibrium concentration (C_e) of malathion measured with UPLC after removing the adsorbent. The obtained data are presented in Figure 1 and Table 1. The presented results showed that the experimental data fit better with the pseudo-second-order model. The calculated rate constants were 0.108 g mg^{-1} min^{-1} and 4.343 g mg^{-1} min^{-1} for 1 mg cm^{-3} and 10 mg cm^{-3} of bio-waste adsorbent, respectively.

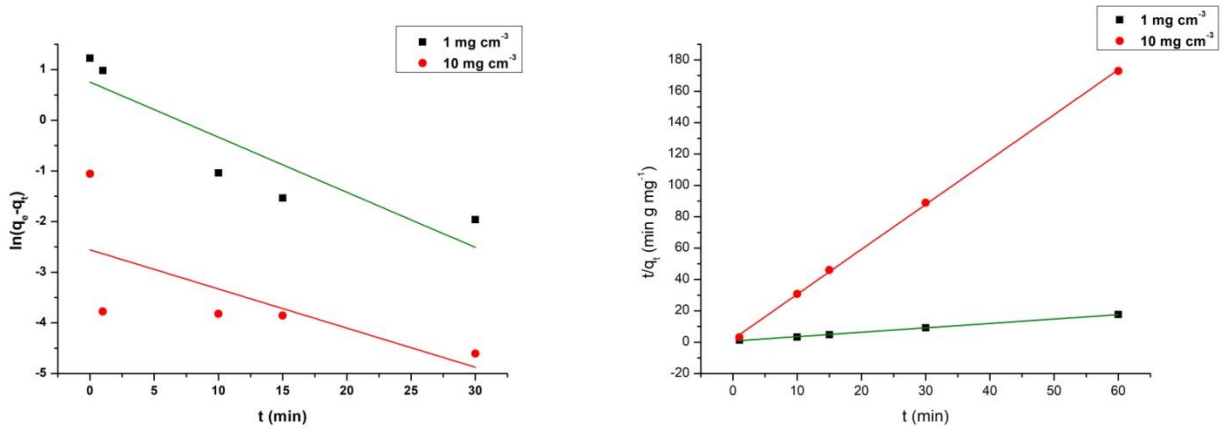

Figure 1. Corresponding plots of pseudo-first-order (left) and pseudo-second-order model (right) for 5×10^{-5} mol dm^{-3} malathion and 1 mg cm^{-3} and 10 mg cm^{-3} of bio-waste adsorbent.

Table 1. Kinetic parameters of the pseudo-first-order and pseudo-second-order models for 5×10^{-5} mol dm^{-3} malathion and 1 and 10 mg cm^{-3} of bio-waste adsorbent.

	1 mg cm^{-3}		10 mg cm^{-3}	
Parameter	pseudo-first-order	pseudo-second-order	pseudo-first-order	pseudo-second-order
k*	0.108	0.108	0.077	4.343
R^2	0.759	0.999	0.305	0.998

*(min^{-1}) for pseudo-first-order model and (g mg^{-1} min^{-1}) for pseudo-second-order model

In order to further study the process of adsorption, 1 mg cm^{-3} and 10 mg cm^{-3} of investigated adsorbent was incubated with malathion in the concentration range from 5×10^{-6} mol dm^{-3} to 1×10^{-4} mol dm^{-3} for 24 h at 25 °C. The concentration of adsorbed malathion was calculated as a difference between its initial concentration (C_0) and the equilibrium concentration (C_e) of malathion measured with UPLC after removing the adsorbent. Adsorption capacity (Y_{max}) represents the equilibrium concentration of malathion *per* 1 g of adsorbent. Experimental results were evaluated with the Langmuir and Freundlich isotherm models to determine the specific parameters of adsorption. The results are presented in Figure 2 and Table 2.

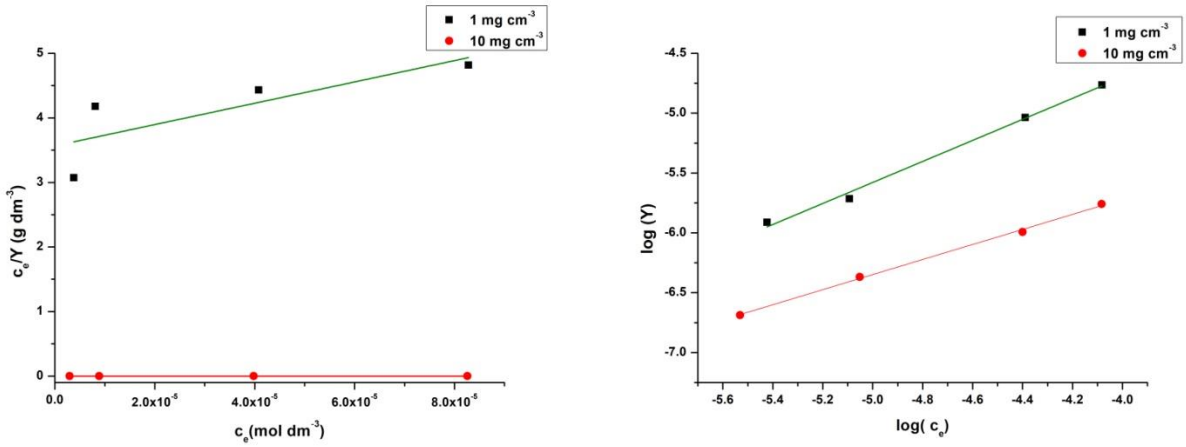

Figure 2. Experimental data for 1 and 10 mg mL^{-1} adsorbent and malathion fitted with Langmuir (left) and Freundlich (right) adsorption isotherms.

From the data presented in Figure 2 and Table 2, it was obvious that 10 mg cm^{-3} of investigated adsorbent can adsorb a higher concentration of malathion compared to the lower studied concentration of material (1 mg cm^{-3}). Furthermore, the experimental data showed a satisfactory agreement with the Freundlich isotherm model. Agreement with this model suggests the multilayer adsorption on the heterogeneous surface. Moreover, the results indicated that 1 g of investigated bio-waste material could adsorb up to 40.76 mg of malathion. Compared to literature data, this value is very good [5], especially considering there is no aggressive and environmentally harmful pre-treatment of the bio-waste material.

Table 2. Fitting parameters of Langmuir and Freundlich isotherm models

Parametar	1 mg cm^{-3}		10 mg cm^{-3}	
	Langmuir	Freundlich	Langmuir	Freundlich
Y_{max} (mg g^{-1})	6.06×10^{-5}	-	40.76	-
K_{ads} (g dm^{-3})	5.89×10^{4}	-	1.56×10^{-9}	-
n	-	1.14	-	1.59
k	-	6.46×10^{-2}	-	6.31×10^{-4}
R^2	0.4770	0.9923	0.9640	0.9974

The results are even more promising when it comes to the malaoxon adsorption on investigated bio-waste material. Namely, the experiments showed that 1 mg cm^{-3} of adsorbent could adsorb 1.03×10^{-5} mol dm^{-3} of malathion after 60 minutes of incubation with 5×10^{-5} mol dm^{-3} malathion. Under the same experimental conditions, 2.13×10^{-5} mol dm^{-3} of malaoxon is adsorbed. It shows that the adsorption efficiency for malaoxon is more than two times higher compared to malathion.

CONCLUSION

Bio-waste material obtained from the spent coffee ground was used for malathion and malaoxon removal from water. The results showed that the experimental data fit better with the pseudo-second-order model. The calculated rate constants were 0.108 g mg^{-1} min^{-1} and 4.343 g mg^{-1} min^{-1} for 1 mg cm^{-3} and 10 mg cm^{-3} of bio-waste adsorbent, respectively. It was shown that 1 g of investigated material is capable of adsorbing up to 40.76 mg of malathion. A satisfactory agreement of experimental results with the Freundlich isotherm model suggests the multilayer adsorption on the heterogeneous surface. Adsorption efficiency of investigated adsorbent for malaoxon was higher than for malathion. Remediation of malathion and malaoxon using the investigated adsorbent was successful.

Acknowledgment

This work was partially supported by the Ministry for Science of the Republic of Serbia (Grant no. 451–03–9/2022–14/200017).

REFERENCES

[1] Milankovic V., Lazarević-Pašti T., The Role of the Cholinergic System in Lung Diseases, Springer, Singapore, 2021.

[2] Mirković M., Pašti T., Došen A., Čebela M., Rosić A., Matović B., et al. RSC Adv., 6 (2016) 12219.

[3] Singh R., Singh P., Tiwari J., Singh P., Gode F., Sharma Y., Jour. Wat. Res. Protect., 2 (2010) 322.

[4]https://www.ico.org/#:~:text=World%20consumption%20for%20coffee%20year,in%20coffee%20year%202020%2F21.

[5] Jocić A., Breitenbach S., Pašti I., Unterweger C., Fürst C., Lazarević-Pašti T., Environ. Sci. Poll. Res., 29 (2022) 35138.

COMPARATIVE ANALYSIS OF Pb^{2+} SEPARATION USING NATURAL AND SYNTHETIC SILICATE MATERIALS

T. Stanišić[1], M. Đolić[2], M. Ristić[2] and A. Perić Grujić[2]

[1]Innovation Center of the Faculty of Technology and Metallurgy, Karnegijeva 4, 11000 Belgrade, Serbia. (tstanisic@tmf.bg.ac.rs)
[2]University of Belgrade, Faculty of Technology and Metallurgy, Karnegijeva 4,11000 Belgrade, Serbia.

ABSTRACT
In this study, the adsorption capacity and removal efficiency of lead using various metal-oxide materials from aqueous solution have been analyzed. Two SiO_2-based materials, natural (loam) and synthesized (metal-oxide heterostructures – MOH) were investigated. The characterization of these samples was performed using X-ray powder diffraction (XRD) and Fourier-transform infrared spectroscopy (FTIR). Adsorption tests were performed in a batch system by varying the mass of tested materials. The highest adsorption capacity for Pb^{2+} was achieved using 5 mg of MOH (166.6 μg g^{-1}), while the removal efficiency using the optimal mass (10 mg) of MOH and loam was 99.3 and 94.2 %, respectively. Based on the obtained results, it was concluded that the synthetic material has higher adsorption capacity and removal efficiency than the natural material for the selected ion.

INTRODUCTION
Water contamination with heavy metals such as lead (Pb), cadmium (Cd), mercury (Hg), copper (Cu) and metalloids as arsenic (As) can occur with the use of chemicals, industrial or other waste. These pollutants have long been known of their hazardous nature even in very low concentrations (ppb) and their presence deteriorate the water quality and renders it inapt for its intended uses [1]. Currently, there are several efficient methods reviewed for the removal of heavy metals such as chemical precipitation, ion exchange, coagulation, flocculation, floatation, reverse osmosis, electrodialysis, ultrafiltration, nanofiltration, etc. Adsorption as a very simple, economical, effective and versatile process has become one of the most applied methods for removal of toxic pollutants from aqueous solution [2]. Besides, there are many different materials used as adsorbents where the main distinction is according to their origin - natural and synthetic. Metal(hydr)oxides have a great potential as promising adsorbents for the separation of lead ions due to their exceptional properties, such as a high removal capacity, selectivity towards heavy metals, their high surface area to mass ratio, high surface reactivity, and unique catalytic activity [3]. The most common oxide-based materials for the adsorption process are iron (III) oxides (Fe_2O_3), zinc oxides (ZnO), titanium oxides (TiO_2), aluminum oxides (Al_2O_3), magnesium oxides (MgO), cerium oxides (CeO_2), as well as their mixtures [4]. The adsorption reaction of silicate minerals comprises the following metal–surface complex reactions: inner-sphere metal complexes (metal sorption at the surface forming bonds with oxygen atoms in the tetrahedra framework; 2) and outer-sphere metal complexes (adsorption at the surface on silanol groups, Si–OH, which are formed by the cleavage of Si–O–Si bonds) [5]. This paper presents the adsorption of Pb^{2+} onto natural and synthesized samples, which consist of several metal oxides (mainly SiO_2, Fe_2O_3, Al_2O_3, TiO_2).

METHODS
The standard solution of initial concentration of 100 μg L^{-1} was prepared for lead ion. The singular batch experiments were conducted according to the following procedure: the different mass of the adsorbents (5, 7.5, 10 and 20 mg) were placed in flask of 10 mL containing concentration of 100 μg L^{-1}

standard solutions. The other parameters such as pH value (5), concentration (100 µg L^{-1}), contact time (24 h), and temperature (25 ºC) were kept constant. After the adsorption process the samples were filtered through a 0.45-mm pore diameter membrane filter and analytes were acidified with nitric acid (1:1, v/v). The concentration of lead was determined using inductively coupled plasma mass spectrometry (ICP-MS) on an Agilent 7500ce. Limits of quantification were quite low for the ICP-MS (0.1–1.5 µg L^{-1}), enabling analyses of very low levels of metals in drinking water.

The adsorption capacity, *q*, and removal efficiency, *R*, of the adsorbent was calculated according to the following equation:

$$q = \frac{C_i - C_f}{m} x\, V \quad (1)$$

$$\%R = \frac{C_i - C_f}{Ci} x\, 100 \quad (2)$$

where *Ci* and *Ce* are initial and final metal concentrations of examined ion in the solution (µg L^{-1}), respectively, *m* is the dosage of the adsorbent (mg), and *V* is the volume of solution (mL).

In addition, X-ray diffraction (XRD) and Fourier transform infrared spectroscopy (FTIR) were used to characterize the materials, chemical structures and compositions.

RESULTS AND DISCUSSION

The structural analyses of the loam and MOH are presented in Figure 1a. The loam sample is a heterogeneous material that predominates in the content of quartz (60.9 wt. %) and kaolinite (22.6 wt. %), while diopside (84 wt. %) predominates in the MOH sample. For the loam sample, quartz (SiO_2) is the dominant phase whose diffraction peaks appear in 2θº = 20.8, 27.2, 50.7 and 60.1 [6]. The absorption peaks of kaolinite in loam appear at 2θ° = 12.4, 21.5, 25.0 and 34.9. On the other hand, in MOH sample the main constituent is diopside/diopside aluminum phase with characteristic peaks at 2θº =29.9, 30.4, 35.8, 39.3, 42.5, 52.3 and 65.6 [7].

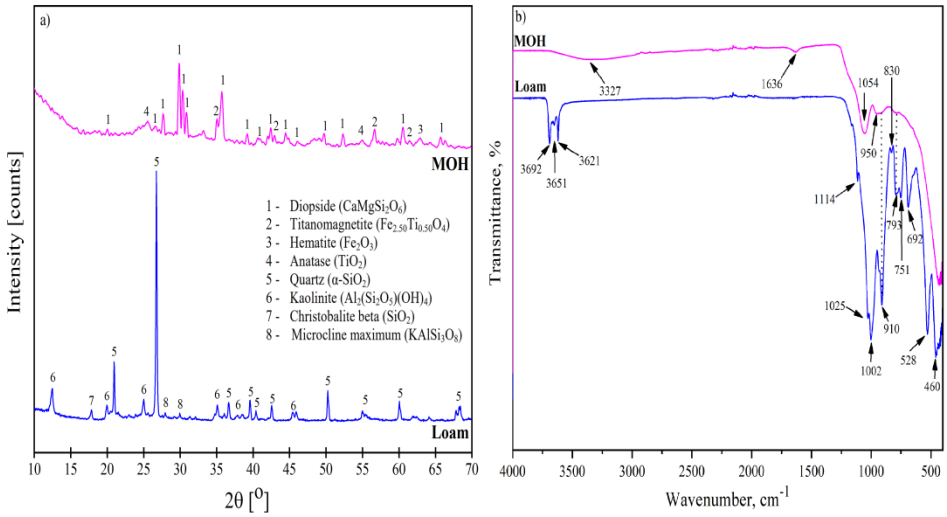

Figure 1. The characterization of MOH and loam samples by a) XRD (on the left) and b) FTIR spectra (on the right)

The FTIR spectra obtained for tested samples are showed in Figure 1b. On the IR absorption of loam material the most dominant aluminosilicate hydroxyl structural units (e.g., Si–O, Si–O–Al, Al–OH, O–H), were discovered. The Figure 1b is shown the FTIR spectra characteristic of the hydroxyl

group at: 3692, 3651, 3621 and 3327 cm^{-1} [8]. The peak of very low intensity at 1634 cm^{-1} (MOH sample) was evidence of the bending vibrational mode of absorbed H_2O. The intense bands located at 1114, 1054, 1025 and 1002 cm^{-1} are assignable to the Si–O–Si symmetric stretching vibrations [9] The Si-O-Ti vibration are observed only in the sample MHO at 950 cm^{-1} [10]. The absorbance at 950–600 cm^{-1} represents intensive spectra confirming the OH bending vibrations of Al–OH.

The investigations of the influence of the adsorbent mass were performed under the same experimental conditions (Figure 2). The effect of mass of adsorbent was studied with several different masses of loam and MOH in the range of 5-20 mg, while other parameters such as pH, concentration, contact time, and stirring rate were kept constant. The results showed that the removal efficiency of lead increased with the increasing the mass of adsorbents, while for the adsorption capacity it decreased (Figure 2).

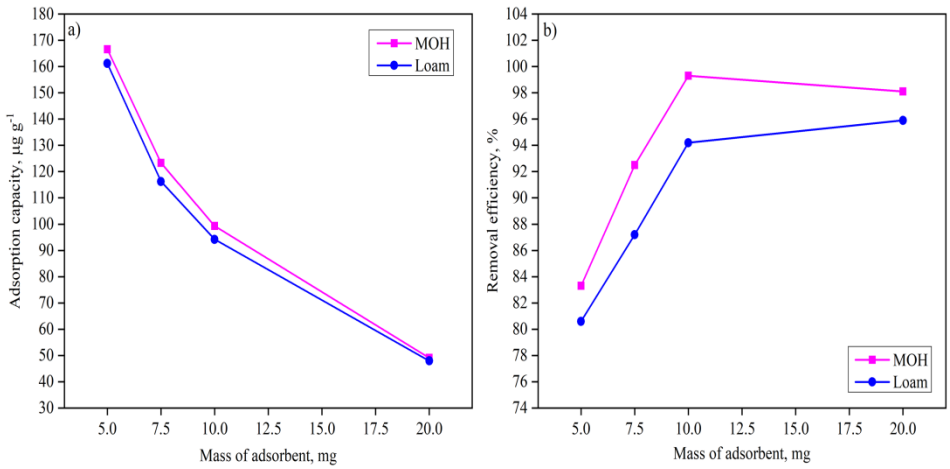

Figure 2. The effect of adsorbent mass on a) adsorption capacity and b) percentage of removal of lead onto loam and MOH

In Figure 2a, significant reduction adsorption capacity for both adsorbents can be observed. From the results, it is apparent that the quantity of adsorbent and the adsorbed amount per unit weight are inversely proportional to each other. The maximum adsorption capacity of 166 and 161.2 µg g^{-1} was achieved using 5 mg of MOH and loam, respectively.

It was found that removal efficiency of lead increased with increasing the amount of both tested adsorbents from 5 to 10 mg (Figure 2b), which can be attributed to the availability of larger surface area and the quantity of the adsorption sites. Further increase in adsorbent mass from 10 to 20 mg showed negligible change, the adsorbent mass of 10 mg was selected as the optimal mass in further adsorption procedures. The removal efficiency of lead ions on MOH and loam was 99.3 % and 94.2 %, under the optimal conditions (m_{ads}=10 mg).

CONCLUSION

The separation of lead using natural and synthetic silicate materials has been investigated. Two materials were analysed, natural (loam) and synthesized (MOH), which mainly consist of different oxides such as silicon dioxide, aluminium oxide and iron (III) oxides. On one hand, the efficiency of lead removal increased with increasing the mass of tested adsorbents. The maximum removal efficiency of lead ions under optimal conditions (C_i= 100 µg L^{-1}, m_{ads} = 10 mg and pH 5) was 99.3 % and 94.2 % for MOH and loam, respectively. On the other hand, the adsorption capacity of the material decreased with increasing the mass of both adsorbents. The highest adsorption capacity was

achieved using 5 mg of MOH sample (166.6 μg g^{-1}), and for loam it was slightly lower (161.2 μg g^{-1}). Based on the results obtained, the synthesized material, MOH, was more efficient for lead ions separation from aqueous solutions. Finally, the analysed silicate materials, both natural and synthesized, can be used as effective adsorbents to remove lead ions from water systems, bearing on mind that the application of environmentally and economically acceptable materials for water purification presents a great challenge nowadays.

Acknowledgment
This work was supported by the Ministry of Education, Science and Technological Development of the Republic of Serbia (grant nos. 451-03-9/2022-14/200135 and 451-03-9/2022-14/200287).

REFERENCES

[1] Abdellaoui, Y., Olguín, M. T., Abatal, M., Ali, B., Díaz Méndez, S. E., and Santiago, A. A, Superlattice Microst, 127(2019) 165–175.
[2] Lakherwal, D., International Journal of Environmental Research and Development, 4 (2014).
[3] Wagle, D., and. Shipley, H. J., Environ. Eng. Sci., 33 (2016) 299–305.
[4] Yang, J., Hou, B., Wang, J., Tian, B., Bi, J., Wang, N., and Li, X., Nanomaterials-Basel, 9 (2019) 1-39.
[5] Đolić, M.B., Rajaković, V.N., Marković, J.P., Janković-Mandić, L.J., Mitrić, M.M., Onjia, A.E., and Rajaković, Lj., Appl. Surf. Sci. 324 (2015) 221–231.
[6] Dewi, R., Agusnar, H., Alfian, Z., and Tamrin, J. Phys. Conf. Ser., 1116 (2018) 0–6.
[7] Li, Q., Liu, F., Zhang, X., Yang, H., Xue, X., and Niu, X., J. Alloys Compd., 657 (2016) 152–156.
[8] Margenot, A.J., Calderón, F.J., Goyne, K.W., Dmukome, F.N., and Parikh, S.J., Encycl. Spectrosc. Spectrom., (2016) 448–454.
[9] Choudhary, R., Vecstaudza, J., Krishnamurithy, G., Raghavendran, H.R.B., Murali, M.R., Kamarul, T., Sasikumar, S., and Locs, J., Mater. Sci. Eng., 68 (2016) 89–100.
[10] Novack, A.M., dos Reis, G.S., Hackbarth, F. V., Marinho, B.A., Đolić, M.B., Valle, J.A.B., Sampaio, C.H., Lima, E.C., Dotto, G.L., Ulson de Souza, A.A., Vilar, V.J.P., and Guelli Ulson de Souza, S.M.A., Environ. Sci. Pollut. Res., 28 (2020) 23568–23581.

FLY ASH MODIFIED WASTE COTTON AND COTTON-POLYESTER YARNS FOR REMOVAL OF HEAVY METALS FROM WATER

M. Maletić[1], A. Lazović[2], N. Karić[1], M. Vukčević[2], K. Trivunac[2], M. Ristić[2] and A. Perić-Grujić[2]

[1]Innovation Centre of the Faculty of Technology and Metallurgy, Karnegijeva 4, 11000 Belgrade, Serbia. (mvukasinovic@tmf.bg.ac.rs)
[2]University of Belgrade, Faculty of Technology and Metallurgy, Karnegijeva 4, 11000 Belgrade, Serbia.

ABSTRACT
Using two types of industrial waste materials (yarns and fly ash), adsorbents for removing heavy metal ions from water were obtained. To improve the adsorption efficiency of cotton and cotton-polyester yarns, modification using fly ash and sodium alginate as a binder, was applied. Characterization of materials was performed by Scanning electron microscopy and Fourier transform infrared spectroscopy, while the concentration of lead and cadmium ions was determined using atomic absorption spectroscopy. The modification of the material has contributed to an increase in the adsorption efficiency of lead and cadmium by up to twice in comparis onto the unmodified materials. It was found that the kinetics of the metal adsorption process can be better described by a second-order pseudo model. The results showed that by combining two types of industrial waste, cotton and cotton/polyester yarns and fly ash, highly efficient adsorbents for removing lead and cadmium from aqueous solutions are obtained.

INTRODUCTION
Heavy metals reach the environment through the industrial activities of metallurgy, nuclear industry, batteries, leather, pesticides, fertilizers, oil and textile industries. Unlike organic pollutants, heavy metal ions in the aquatic environment have a great tendency to bioaccumulate, because they do not decompose naturally, which can cause various health problems in humans. Toxicity can be manifested even at very low concentrations, when organ damage, growth retardation, headaches, mental disorders, skin diseases, and nervous system dysfunction can occur [1]. Therefore, the removal of heavy metals from wastewater is of great importance to reduce their harmful effects. Among conventional techniques used to remove heavy metals from water, adsorption is most effective because other techniques have inherent limitations such as high sludge production, low efficiency, sensitive working conditions, and costly disposal. The adsorption method provides flexibility in design, ease of application, economy, high-quality treated effluent, reversibility of the process, and reuse of the adsorbent [2]. From the aspect of environmental protection, the conditions for wastewater discharge are becoming more stringent, while the application of environmentally and economically acceptable adsorbents for wastewater treatment is a great challenge today. Therefore, in this study, the possibility of using easily available waste materials as efficient adsorbents for removing heavy metal ions from aqueous solutions was investigated. Fly ash, obtained from thermal power plants as a by-product, was used to modify and improve the adsorption efficiency of cotton and cotton-polyester yarns, which were obtained as waste from the textile industry. Lead and cadmium have been used, as models to determine the effectiveness of unmodified and modified materials in removing heavy metal ions.

METHODS

Waste cotton (C) and cotton-polyester yarns (CP) (50% cotton-50% polyester) were obtained from the production processes of the textile factory SIMPO Dekor (Vranje, Serbia). The materials were modified in a two-cycle process. 0.1 g of material was weighed and immersed in 4 ml of a mixture of 0.5% aqueous sodium alginate solution and 0.1 g of fly ash for 10 minutes. Thereafter, the materials were dried at 60 °C for 1 h. After the second modification cycle, the materials were dried at 60 °C overnight, and the modified materials were labelled as C-alg-FA and CP-alg-FA, for modified cotton and cotton-polyester, respectively. The morphological characteristics of the surface of unmodified and modified materials were examined by scanning electron microscopy (SEM), while examination of the content of functional groups on the surface of the material was performed by Fourier transform infrared spectroscopy (FTIR). The adsorption efficiency of Pb and Cd from aqueous solutions using unmodified and modified yarns was tested in a batch system and at room temperature. The yarn samples, weighing 0.02 g, were immersed in 20 ml of an aqueous solution of metal ions with a concentration of 10 mg dm^{-3} and stirred constantly at 150 rpm for 3 h. Metal ion concentrations after adsorption were determined by atomic absorption spectroscopy. The adsorption efficiency (%A) of the tested materials in the removal of metal ions was calculated using the following equation (1):

$$\%\,A = \frac{(C_0 - C_e)}{C_0} \times 100 \quad (1)$$

where C_e is the equilibrium and C_0 is the initial concentration of metal ions in solution (mg dm^{-3}). The two kinetic models, the pseudo-first order model (equation (2)) and the pseudo-second order model (equation (3)) were used to calculate the adsorption rate [3].

$$q_t = q_e \cdot \left(1 - e^{-k_1 \cdot t}\right) \quad (2)$$

$$q_t = q_e - \left(\frac{1}{q_e} - k_2 \cdot t\right)^{-1} \quad (3)$$

where q_t is the amount of metal ions adsorbed at the time t (mg g^{-1}), q_e is the adsorption quantity at equilibrium (mg g^{-1}), k_1 is the pseudo-first-order kinetic rate constant (min^{-1}), and k_2 is the pseudo-second-order kinetic rate constant (mg g^{-1} min^{-1}).

RESULTS AND DISCUSSION

The SEM micrographs of the unmodified cotton and cotton-polyester yarns and modified with fly ash are shown in Figure 1.

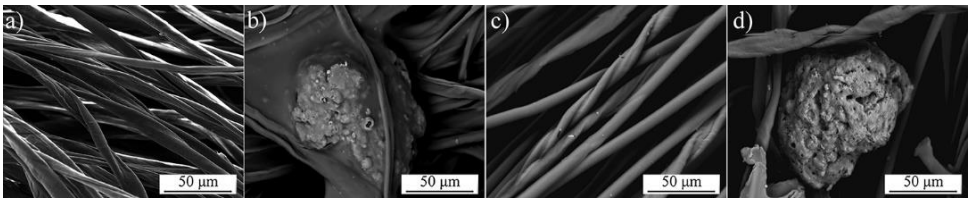

Figure 1. SEM micrographs of a) cotton yarns, b) C-alg-FA, c) cotton-polyester yarns, and d) CP-alg-FA.

It can be seen that the untreated cotton yarns (Figure 1a) are intertwined, with the cotton fibers spirally twisted with a relatively smooth surface. Figure 1c shows the morphology of unmodified cotton-polyester yarns, where in addition to the cotton component, the presence of polyester fibers with a uniform tubular structure and smooth surface is observed. Fly ash is incorporated between cotton and polyester component (Figures 1b and 1d), and bound to them with sodium alginate, which acts as a binding agent.

FTIR spectra of modified materials are shown in Figure 2a. The presence of a wide absorption band at 3300 cm^{-1} in the structure of all materials originates from the vibration of the O-H bond in the hydroxyl group, while the peak at 2900 cm^{-1} is the characteristic peak of the stretching vibration of the C-H bond in the methyl or methylene group of cellulose molecules. The peak at 1612 cm^{-1} in the spectra of samples C and C-alg-FA may be related to the presence of water in the cotton fibers. The adsorption peaks at 1427 and 1406 cm^{-1} are associated with the CH_2 symmetric bending of the cellulose while the peaks at 1312 and 1335 cm^{-1} originate from the bending vibrations of the C-H and C-O groups of the aromatic rings in cellulose structure. The intense band at 1021 cm^{-1} in spectra of all materials is related to the C=O and C-O stretching vibrations of the polysaccharide in cellulose, while the peak at 895 cm^{-1} indicates the presence of β-glycosidic linkages between monosaccharides [4]. The FTIR spectra of CP and CP-alg-FA, compared to the spectra of cotton yarns, have additional absorption peaks at 1711 cm^{-1} and 1234 cm^{-1}, which indicates the presence of ester groups in polyester chains [5].

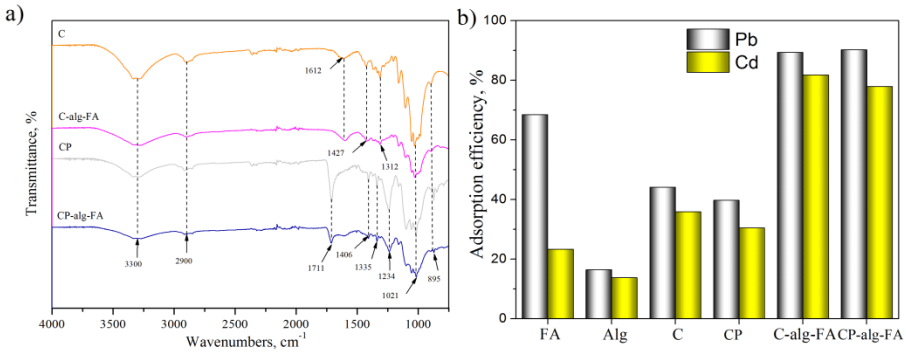

Figure 2. FTIR spectra (a) and adsorption efficiency (b) of unmodified and modified materials.

Figure 2b shows the efficiency of the modified samples (C-alg-FA and CP-alg-FA) in removing Pb and Cd from aqueous solutions, compared with the adsorption efficiency of unmodified samples (C and CP), alginate particles (Alg), and fly ash (FA). It can be noted that the modification of the material increased the efficiency of Pb and Cd removal almost twice. The removal efficiency of both metals on the modified materials ranged from 80 to 90%, with a slightly higher removal efficiency of Pb. High efficiency in the removal of metal ions may be due to the presence of a large number of hydroxyl and carboxyl groups on the surface of the modified materials.

Graphs of pseudo-first and pseudo-second-order models are given in Figure 3, while the kinetic constants and correlation coefficients for Pb and Cd adsorption are shown in Table 1. The pseudo-first order and pseudo-second order equations were used to evaluate the adsorption kinetic data and investigate the adsorption mechanism.

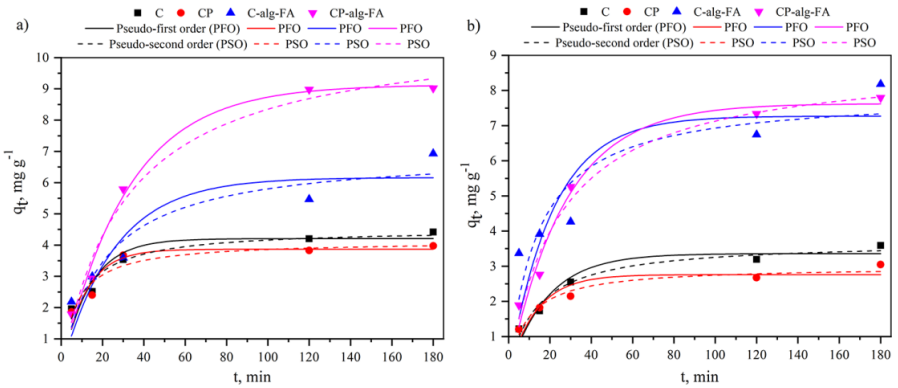

Figure 3. Nonlinear kinetic adsorption models of metals Pb (a) and Cd (b) on tested samples.

Based on the results of kinetic models, it can be seen that the process of metal adsorption on all tested materials was relatively fast and that equilibrium was reached at about 30 min for Cd and 60 min for Pb. The highest adsorption capacity was achieved using C-alg-FA material for Pb removal. Also, by comparing the correlation coefficient (R^2), it can be concluded that the pseudo-second order model has a greater ability to describe the kinetic behaviour of the adsorption process, which means that the dominant mechanism of adsorption is chemisorption.

Table 1. Kinetic constants and correlation coefficients for Pb and Cd adsorption on samples C, C-alg-FA, CP, and CP-alg-FA.

Metal	Material	Pseudo-first order			Pseudo-second order		
		q_e, mg g^{-1}	k_1, min^{-1}	R^2	q_e, mg g^{-1}	k_2, g mg^{-1} min^{-1}	R^2
Pb	C	4.20	0.0743	0.818	4.52	0.0252	0.933
	C-alg-FA	6.16	0.0390	0.838	6.99	0.0069	0.888
	CP	3.86	0.0879	0.758	4.13	0.0339	0.852
	CP-alg-FA	9.13	0.0314	0.984	10.9	0.0029	0.975
Cd	C	3.35	0.0534	0.899	3.70	0.0189	0.955
	C-alg-FA	7.27	0.0468	0.526	7.91	0.0089	0.704
	CP	2.76	0.0743	0.800	2.99	0.0363	0.938
	CP-alg-FA	7.62	0.0367	0.967	8.87	0.0045	0.968

CONCLUSION

In this study, adsorbents based on waste industrial materials, yarns and fly ash, for the removal of lead and cadmium ions from aqueous solutions were successfully obtained. The adsorption properties of cotton and cotton-polyester yarns were improved by mixing with fly ash and sodium alginate as a binder. Structural and morphological characterization of the materials confirmed that the modification was successful. Adsorption results showed that all tested materials show slightly better efficiency of lead adsorption compared to cadmium. Also, the results show that the modification of waste yarns with fly ash has contributed to the increase in the efficiency of lead and cadmium ions removal almost twice.

Acknowledgment

This research was supported by the Science Fund of the Republic of Serbia, GRANT No 7743343, Serbian Industrial Waste towards Sustainable Environment: Resource of Strategic Elements and Removal Agent for Pollutants - SIW4SE.

REFERENCES

[1] Beni, A.A., and Esmaeili, A., Environ. Technol. Innov., 17 (2020) 0100503.
[2] Agarwal, R. M., and Singh, M., J. Water Reuse Desal., 230 (2019) 278.
[3] Lekniute-Kyzike, E., Bendoraitiene, J., Danilovas, P. P., and Zemaitaitis, A., Desalin. Water Treat., 57 (2016) 23728–23738.
[4] Portella, E. H., Romanzini, D., Angrizani, C. C., Amico, S. C., and Zattera, A. J., Mater. Res., (2016) 1-7.
[5] Jiang, S., Xia, Z., Farooq, A., Zhang, M., Li, M., and Liu, L., Cellulose, 28 (2021) 3235-3248.

MODIFICATION OF CELLULOSE-BASED WASTE MATERIALS FOR REMOVAL OF METHYLENE BLUE FROM WASTEWATER

M. Vukčević[1], M. Maletić[2], N. Karić[2], B. Pejić[1], K. Trivunac[1] and A. Perić Grujić[1]

[1]University of Belgrade, Faculty of Technology and Metallurgy, Karnegijeva 4, 11000 Belgrade, Serbia. (marijab@tmf.bg.ac.rs)
[2]Innovation Center of Faculty of Technology and Metallurgy, Karnegijeva 4, 11000 Belgrade, Serbia.

ABSTRACT

Different natural fibers and yarns (hemp, flax, and cotton), obtained as a waste from textile industry, were used for the removal of methylene blue from aqueous solution. In attempt to increase the adsorption efficiency, examined fibers and yarn were modified by sodium hydroxide solution. Characterization of examined samples was performed by scanning electron microscopy and Fourier transform infrared spectroscopy. It was shown that applied modification caused the differences in the distribution of hemicelluloses in the structure of examined fibers and fibers in yarn, inducing the changes in morphology and surface chemistry. These changes slightly improved the adsorption properties of hemp fibers, while in the case of cotton yarn modification had a negative effect on methylene blue adsorption. Nevertheless, adsorption efficiency of these waste fibers and yarns highly increase with the pH of the solution, enabling their utilization for methylene blue removal from wastewaters.

INTRODUCTION

Intensive growth of world population along with the frequent changes in clothing fashion trends and furniture industry lead to the excessive consumption of textiles to meet human needs. Also, there is a growing demand for clothes made from comfortable, biodegradable, biocompatible and ecological fibers. Therefore, after quite a long period of intensive application of synthetic fibers, natural fibers take precedence over the synthetic ones, especially in regard to comfort and ecological properties. As the result of increased production in textile industry, the amount of solid textile waste (in the form of short and entangled fibers, natural or synthetic yarns, pieces of clothing etc.) considerably increases. The reckless disposal of textile wastes can cause serious soil, water and air pollution, and it is of great significance to find a new way to reuse these wastes, rather than their commutation.

In the recent years, attention has been devoted to the utilization of different waste materials, as cheap and efficient sorbents for removal of organic and inorganic pollutants from wastewater [1, 2]. The application of these biosorbents for purification of waste and drinking water is a very cost-effective method that can be used as an alternative for adsorption on commercially available activated carbons. Due to the specific structure, heterogeneous chemical composition, and surface functional groups, natural fibers as biosorbent offer an effective way to decrease the concentration of pollutants in wastewaters [3, 4].

In this paper, we report on utilization of different natural fibers and yarns (hemp, flax, and cotton), readily available in large quantities as a waste from textile industry, as an adsorbents for removal of methylene blue from wastewater. To increase the adsorption efficiency, natural fibers and yarns were modified, using cheap and simple treatment of mercerization. Mercerization implies soaking the cellulose fibers in a dilute solution of sodium hydroxide (NaOH), resulting in the dissolution of hemicellulose and rearrangement of microfibrils in a more compact manner.

METHODS

The fibers used as a starting material in this investigation were short flax fibers (L) obtained from Banja Luka (Republic of Srpska, Bosnia and Herzegovina) [5], and short hemp fibers (K) obtained from ITES Odzaci (Serbia) [6], while waste cotton yarn (P) was obtained from textile factory SIMPO Dekor Vranje (Serbia) [4].

Waste fibers and yarn (approximately 1 g), were immersed in 50 ml of 18% NaOH solution. Chemical modification was performed with constant stirring (150 rpm), at room temperature for 60 minutes. After chemical treatment, fibers and yarn were neutralized with 1% acetic acid solution, washed with distilled water and dried at 60 ^{o}C overnight. The modified flax and hemp fibers, and cotton yarn are labeled as L_{mod}, K_{mod} and P_{mod}, respectively.

The morphological characteristics of examined samples were assessed by scanning electron microscopy (Mira3, Tescan and SEM JEOL JSM-6610LV). FTIR spectra of the samples, within a range of 400-4000 cm^{-1}, were recorded using a Nicolet™ iS™ 10 FT-IR Spectrometer (Thermo Fisher Scientific).

Adsorption efficiency of unmodified and alkali modified fibers and yarn to remove methylene blue (MB) were tested in batch system with constant shaking at room temperature. The influence of initial pH value on adsorption efficiency was examined by adjusting the initial pH (2, 4, 6, 8 and 10), and adsorption onto 0.02 g of examined samples was performed from 20 cm^3 of methylene blue solution (20 mg/dm^3). Adsorption kinetics was examined by soaking 0.1 g of unmodified and modified samples in 100 cm^3 of MB solution (20 mg/dm^3), and concentration of MB was measured in defined period of time (5, 15, 30, 60, 120 and 180 minutes) by UV/Vis spectrophotometer.

RESULTS AND DISCUSSION

The structure and surface morphology of unmodified and alkali modified samples are shown in Figure 1. The changes in morphological characteristics of samples L and K, induced by applied chemical treatment, are visible in Figures 1d, and 1e. Removal of hemicelluloses from the structure of L and K, induced by mercerization, led to the formation of new open spaces between distinctly liberated elementary fibers in the structure of L_{mod} and K_{mod}. On the other hand, modification of P sample caused only a relative peeling of yarns' surface (Figure 1f).

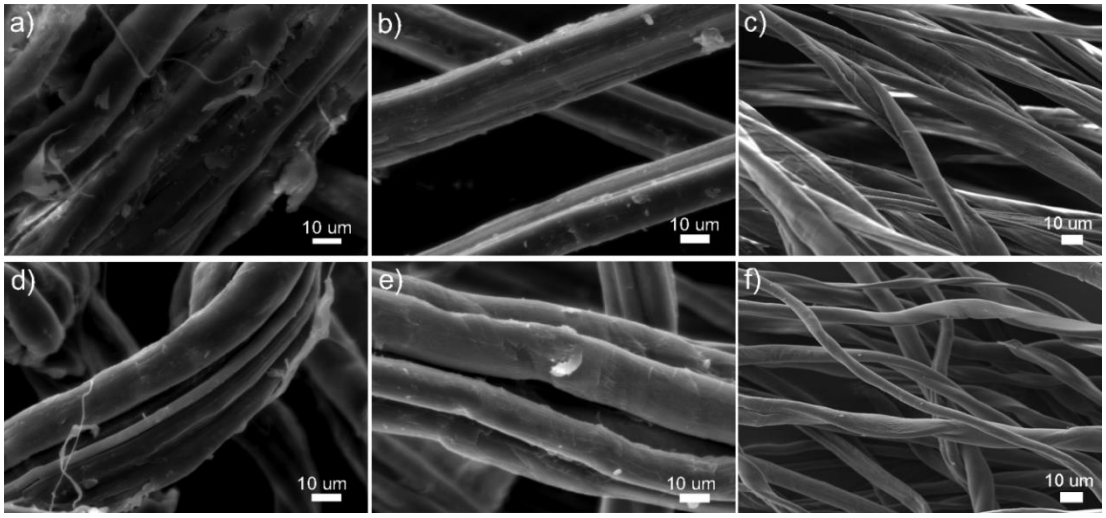

Figure 1. SEM photographs of a) L, b) K, c) P, d) L_{mod}, e) K_{mod}, and f) P_{mod}

FTIR spectra for all samples (Figure 2) show a broad band around 3300 cm^{-1}, originating from stretching of O-H bond in hydroxyl groups. Spectra of modified samples also show two shoulders at 3478 cm^{-1} and 3436 cm^{-1}, attributed to hydroxyl groups in cellulose II, and to the specific hydrogen

bonds between O(3)H and O(5), respectively [5]. Peaks at 2850 cm^{-1} and 2920 cm^{-1} originate from the symmetrical and asymmetrical vibrations of C-H bond in methyl and methylene groups of cellulose, and hemicelluloses [7] in the structure of examined fibers and yarns. The changes in FTIR spectra in this wavenumber region, observed for modified samples, originate from hemicelluloses removal by applied mercerization. Also, as a consequence of modification, the peak near 1730 cm^{-1}, attributed to C=O stretching of carbonyl or ester groups of hemicelluloses [7, 8], decreases in intensity for samples L_{mod} and K_{mod}, and disappears for sample P_{mod}. The similar behavior is observed for the bands in the region 1000-1370 cm^{-1}, which are related to the C-O and C-C stretching in polysaccharides, cellulose, and hemicelluloses. The peak around 890 cm^{-1} indicates the presence of glucopyranose ring in the structure of all examined samples. Results of FTIR analysis also showed that applied modification cause the changes in the distribution of hemicelluloses in the structure of examined fibers and yarn.

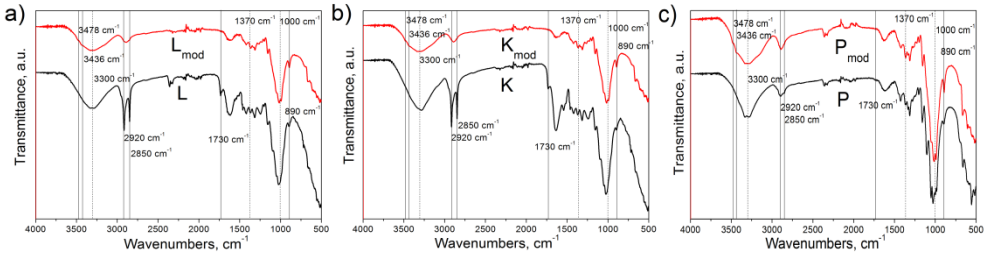

Figure 2. FTIR spectra of unmodified and modified a) flax fibers, b) hemp fibers, and c) cotton yarn.

The influence that applied modification has on adsorption properties of flax and hemp fibers, and cotton yarn, was examined through the adsorption of methylene blue. The solution pH value can be a critical factor that affects adsorption of MB on examined samples through the ionization of surface oxygen containing groups, which represents the binding sites for adsorption. The effect of pH was investigated by varying the initial values of pH solution from 2 to 10, and obtained results are shown in Figure 3. The initial pH of solution has considerable influence on the amount of MB adsorbed. Removal efficiency of methylene blue in the case of P and P_{mod} increases from 5 % on pH 2, to the 50 % on pH 10, while in the case of unmodified and modified L and K samples, removal efficiency increases with the pH even more, up to 75 %. Being the biopolymers, examined fibers and yarns, consist mainly from cellulose and hemicellulose chains, which, at higher pH may get negatively charged, and enhance the adsorption of positively charged dye through electrostatic forces of attraction.

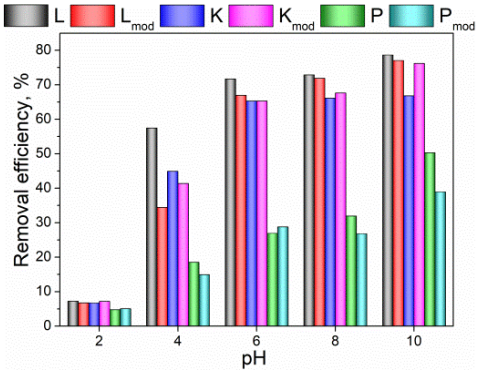

Figure 3. Influence of initial pH on removal efficiency of MB

The increase in adsorption capacities with an increase of contact time is noticeable for all tested samples (Figure 4). Unmodified and modified fibers samples (L, L_{mod}, K and K_{mod}) showed higher

adsorption capacities, and higher rates of adsorption (Figure 4a and 4b) than yarns samples (P and P_{mod}) (Figure 4c), most likely due to the different form of samples, i.e. larger contact surface and easier adsorption on the samples in the form of fibers, than in form of yarns. Applied modification has different influence on adsorption capacities: no effect in the case of flax fibers, slight increase for hemp fibers, and negative effect for cotton yarns. Experimental data were examined by the pseudo-first and pseudo-second order kinetic models (Figure 4). Adsorption of methylene blue onto examined fibers and yarns better fits with pseudo-second order kinetic model, suggesting that adsorption process is characterized by chemisorption.

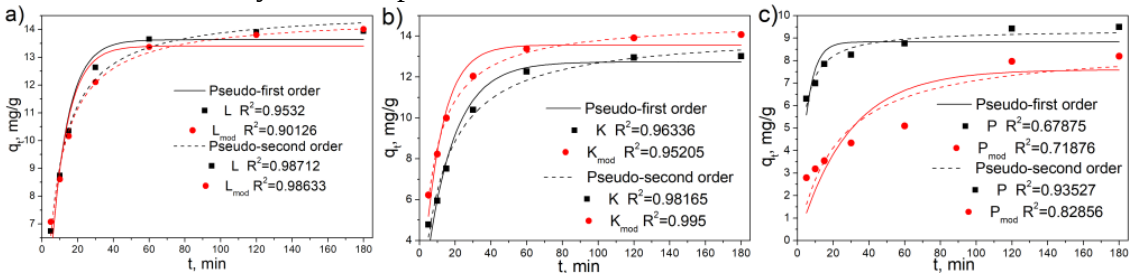

Figure 4. Effect of time on MB adsorption onto unmodified and modified a) flax fibers, b) hemp fibers, and c) cotton yarn.

CONCLUSION

Different natural fibers and yarns (hemp, flax, and cotton), readily available in large quantities as a waste from textile industry, were chemically modified and used as an adsorbents for removal of methylene blue from wastewater. Applied chemical modification caused the differences in the distribution of hemicelluloses in the structure of examined fibers and fibers in yarn, inducing the changes in morphology and surface chemistry. These changes slightly improved the adsorption properties of hemp fibers, while in the case of cotton yarn modification had a negative effect on methylene blue adsorption. Nevertheless, adsorption efficiency of these waste fibers and yarns highly increase with the pH of the solution, enabling their utilization for methylene blue removal from wastewaters. Results obtained in this work showed that waste natural fibers and yarns may be used as sustainable and renewable low cost biosorbent.

Acknowledgment

This research was supported by the Science Fund of the Republic of Serbia, GRANT No 7743343, Serbian Industrial Waste towards Sustainable Environment: Resource of Strategic Elements and Removal Agent for Pollutants - SIW4SE.

REFERENCES

[3] B. Dhir, Environ. Sci. Pollut. Res., 21 (2014) 1614.
[4] M. Fawzy, M. Nasr, H. Nagy, S. Helmi, Environ. Sci. Pollut. Res., 25 (2018) 5875.
[5] W. Yuan, J. Cheng, H. Huang, S. Xiong, J. Gao,J. Zhang, S. Feng, Ecotoxicol. Environ. Saf., 175 (2019) 138.
[6] S. Mihajlović, M. Vukčević, B. Pejić, A. Perić-Grujić, M. Ristić, K. Trivunac, J. Nat. Fibers, (2021) https://doi.org/10.1080/15440478.2021.1993414.
[7] B. D. Lazić, B. M. Pejić, A. D. Kramar, M. M. Vukčević, K. R. Mihajlovski, J. D. Rusmirović, M. M. Kostić, Cellulose 25 (2018) 697.
[8] M. M. Vukčević, A. M. Kalijadis, T. M. Vasiljević, B. M. Babić, Z. V. Laušević, M. D. Laušević, Microporous Mesoporous Mater., 214 (2015) 156.
[9] H. Zhang, R. Ming, G. Yang, Y. Li, Q. Li, H. Shao, Polym. Eng. Sci., 55 (2015) 2553.
[10]M. A. Sawpan, K. L. Pickering, A. Fernyhough, Composites, Part A., 42 (2011) 888.

THE EFFECT OF STARCH MODIFICATION ON THE DYE ADSORPTION EFFICIENCY

N. Karić[1], M. Vukčević[2], M. Maletić[1], M. Ristić[2] and K. Trivunac[2]

[1]*Innovation Centre of the Faculty of Technology and Metallurgy, Karnegijeva 4, 11000 Belgrade, Serbia. (nkaric@tmf.bg.ac.rs)*
[2]*University of Belgrade, Faculty of Technology and Metallurgy, Karnegijeva 4, 11000 Belgrade, Serbia.*

ABSTRACT
Researches in the field of nanotechnology indicate the possibility of the development and application of bionanocomposites based on clay minerals and biopolymers as promising materials for the removal of pollutants from contaminated water. Therefore, this study is based on an examination of the effect of intercalation of starch or cationic starch with kaolin clay or diatomaceous earth on the adsorption properties of the obtained materials for the removal of anionic and cationic dyes from aqueous solutions. Structural characterization of the obtained materials was performed by Fourier transform infrared spectroscopy while the morphology of the samples was determined by Scanning electron microscopy. The removal efficiency of methyl orange and crystal violet dyes was tested in a batch system, while the dye concentration after the adsorption process was determined by UV-Vis spectrophotometry. It was found that modification of cationic starch with clay and diatomaceous earth improved the efficiency for removing crystal violet dye from an aqueous solution.

INTRODUCTION

The discharge of wastewater with a high content of dyes used in various industries, such as textile, tanning, paper, food, pharmaceutical and cosmetic industries, can lead to contamination of surface and groundwater [1], [2]. Adverse effects can be reflected on flora and fauna, because the dyes in their structure may contain complex, carcinogenic, mutagenic, and toxic compounds, with chromophore groups of high molar mass, high water solubility, and low biodegradability. In addition to the negative impact on the environment, dyes can enter the human food chain, causing damage to human health. Dyes can causes many health problems such as allergies, dermatitis, skin irritation, cancer, and dysfunction of the reproductive system, as well as the central nervous system [3], [4].

Adsorption is considered one of the most applicable methods for dye removal from wastewater due to its high efficiency, simplicity, economy, and reusability [5]. An alternative to conventional adsorbents to remove dyes present in wastewater is the use of adsorbents based on the natural polymeric material, starch, due to the abundance of sources in nature, renewability, low cost, biodegradability, and non-toxicity. Among natural materials, clays also stand out as materials with good adsorption properties due to high surface area and cation exchange capacity, swelling, microporosity, layered structure, nano-size, as well as their lower cost compared to conventional adsorbents [6], [7].

The biocompatibility of clay and the biodegradability of starch make their combination a successful approach for the development of nanocomposites that can be used as effective adsorbents for dyes removal from aqueous solutions [7].

The aim of this study was to investigate the effect of starch modification with clay materials on dye adsorption efficiency. The prepared materials are based on starch/cationic starch and clay/diatomaceous earth. Structural characterization of the materials was performed by Fourier transform infrared spectroscopy (FTIR) technique while morphological properties were determined by Scanning electron microscopy (SEM). The possibility of their application for the removal of

anionic dye, methyl orange (MO) and cationic dye, crystal violet (CV) from an aqueous solution was investigated.

METHODS

Native wheat starch, cationic starch modified with glycidyltrimethyl ammonium chloride (with cationic degree 0.2), clay (kaolin), and diatomaceous earth were used for the preparation of adsorbent. The anionic dye – methyl orange and the cationic dye – crystal violet were used for the adsorption study. FTIR (Nicolet iS10, Fisher Scientific) and SEM (SEM JEOL JSM-6610LV) were used to characterize the tested adsorbents. A UV-Vis spectrophotometer for the visible range was used to determine the concentration of the tested dyes at 464 and 582 nm for MO and CV, respectively.

The preparation of the materials was performed in a two-stage procedure, according to the literature [8], [9] with some changes. 5 g of native starch (St) or cationic starch (CSt-G) was dispersed in 30 mL of deionized water and heated to 70 °C with constant stirring at 400 rpm for 1 h. Thereafter, 0.5 g of clay - kaolin or diatomaceous earth was dispersed in 30 mL of deionized water and added to a gelatinized native starch or cationic starch solution. The mixture was heated at 60 °C with stirring at 400 rpm for 3 h. The obtained materials were dried in an oven at 100 °C for 3 h and then ground into a powder.

Adsorption tests were performed in the batch system at room temperature. The adsorption efficiency of MO and CV was determined for constant adsorbent mass (0.05 g), solution volume (25 cm^3), and initial concentration (10 mg/dm^3) after 180 min of constant stirring of the dye solution. The amount of adsorbed dye was determined by measuring the concentration in the solution before and after the adsorption process, after time t. The adsorption efficiency (% E) of dyes from aqueous solutions, R, is calculated according to the equation (1) [10]:

$$\% E = \left(\frac{C_0 - C_t}{C_0}\right) \cdot 100 \quad (1)$$

where C_0 and C_t are the concentration of the dye at the initial time and after time *t* (mg dm^{-3}), V is the volume of solution (cm^3), and m is the amount of the adsorbent (g).

RESULTS AND DISCUSSION

The results of the FTIR analysis are shown in Figure 1.

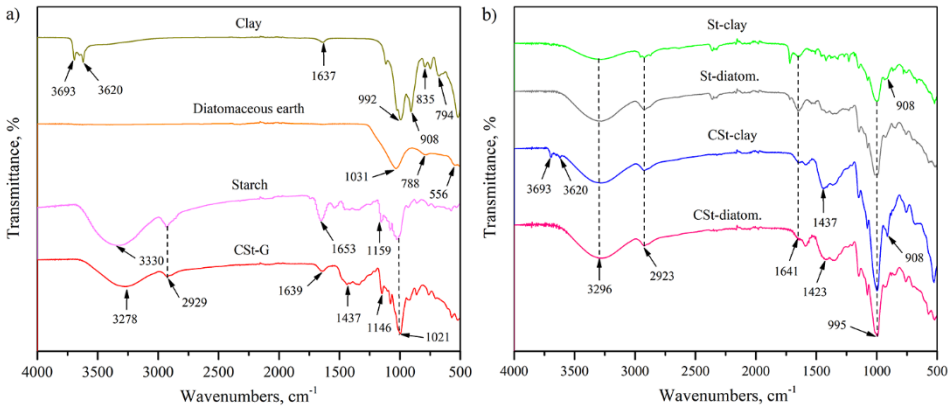

Figure 1. FTIR spectra of a) raw clay - kaolin, diatomaceous earth, native starch, and cationic starch and b) St-clay, St-diatomaceous earth, CSt-clay, and CSt-diatomaceous earth.

The spectra with characteristic peaks for the materials structures before the modification are shownin Figure 1a. For kaolin clay, bands at 3620 and 3693 cm^{-1} correspond to the vibration of OH stretching which is bonded with Al on the surface. A peak corresponding to the O-H bending of water molecules appeared at 1637 cm^{-1}. For Si-O stretching, a broad intense peak was detected at 992 cm^{-1}

while the band at 908 cm^{-1} represents Al-O stretching of the kaolin structure. The bands at 835 and 794 cm^{-1} represented Fe-OH and Si-O stretching vibration [11]. On the FTIR spectrum of diatomaceous earth, a wide absorption band appears at 1031 cm^{-1}, which corresponds to Si-O-Si vibrations. The peak at about 788 cm^{-1} also corresponds to the structure of the silicate. The absorption peak of lower intensity at about 556 cm^{-1} corresponds to Si-O deformation and Al-O stretching [12]. For native starch and cationic starch, bands at 3330 and 3278 cm^{-1} corresponds to O-H stretching, 2929 cm^{-1} for C-H stretching, 1653 and 1639 cm^{-1} for H-O-H bending, while the signals at about 1000-1200 cm^{-1} were due to C-O stretching vibration. An additional peak at CSt-G spectrum at 1437cm^{-1} originates from C-N stretching the quaternary ammonium cationic group (R_4N^+) [1]. All major peaks in the FTIR spectra of the synthesized samples (Figure 1b) coincide with the FTIR spectra of the starting materials (Figure 1a) with a slight shift of the peaks.

SEM micrographs of the prepared materials are shown in Figure 2. The main difference between the modification with native starch and cationic starch is in the appearance of the surface of the material. The surface of the materials in Figures 2a and 2b is smoother due to the smooth surface of the native starch, compared to the materials with cationic starch (Figures 2c and 2d), which has a rough surface with protrusions and holes. Also, in Figures2a and 2c layered structures originating from clay can be seen, while in Figures2b and 2d parts of the rod shape structure originating from diatomaceous earth are visible. The loss of clear boundaries between the materials, i.e. the connection of the starch structure with the structure of clay and diatomaceous earth, indicates a successful modification.

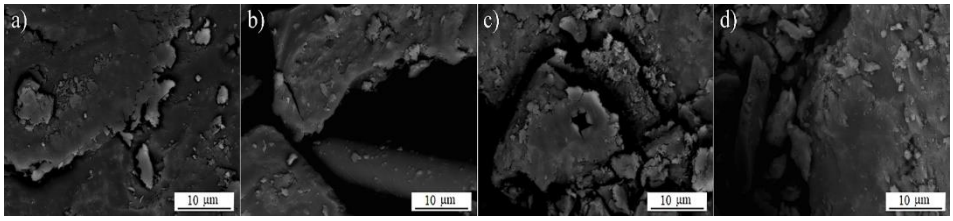

Figure 2. SEM micrographs of a) St-clay, b) St-diatomaceous earth, c) CSt-clay, and d) CSt-diatomaceous earth.

The results of the adsorption study are shown in Figure 3.

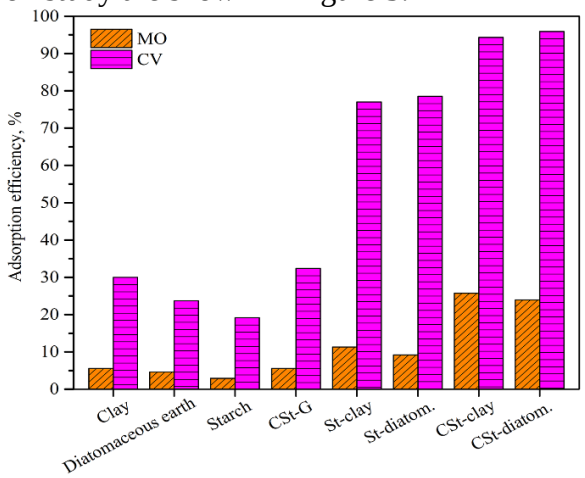

Figure 3. Adsorption efficiency of MO and CV dyes on the different materials.

Modification of starch and cationic starch contributed to the increase of adsorption efficiency in relation to the starting materials for both dyes. The results show that the prepared materials are more efficient in removing the CV dye from an aqueous solution compared to the MO dye. The differences

in the efficiency of CV and MO dye removal can be due to different dye structures, as well as differences in molar mass. Adsorption efficiency of over 90% was achieved for CV dye on cationic starch modified with clay and diatomaceous earth.

CONCLUSION

In this paper, the influence of starch modification with kaolin clay and diatomaceous earth on the adsorption properties of final materials was investigated. Adsorption was tested for the removal of methyl orange and crystal violet dyes from aqueous solutions. The results of the FTIR analysis indicated the presence of characteristic groups for the structure of starch, cationic groups for the structure of cationic starch, as well as silicate groups in the structure of kaolin clay and diatomaceous earth. SEM analysis also confirmed that the material modification was successful. Cationic starch modified with clay and diatomaceous earth proved to be a very effective material for removing crystal violet dye from an aqueous solution.

Acknowledgment

This work was supported by the Ministry of Education, Science and Technological Development of the Republic of Serbia (Contract No. 451-03-9/2022-14/200135 and 451-03-9/2022-14/200287).

REFERENCES

[1] Lawchoochaisakul, S., Monvisade, P., and Siriphannon, P., Carbohydr. Polym., 253 (2020) 117230.
[2] Aly, A. A., and Hebeish, A. A., Int. J. Sci. Res., 4 (2015) 4-12.
[3] Lellis, B., Fávaro-Polonio, C. Z., Pamphile, J. A., and Polonio, J. C., Bio. Res. Innov., 50 (2019) 1-16.
[4] Berradi, M., Hsissou, R., Khudhair, M., Assouag, M., Cherkaoui, O., El Bachiri, A., and El. Harfi, A., Heliyon, 5 (2019) e02711.
[5] Pirbazari, A. E., Hashemian, S. F., and Yousefi, A., J. Chem. Eng. Process Technol. 6 (2015) 1000231.
[6] Awad, A. M., Shaikh, S. M. R., Jalab, R., Gulied, M. H., Nasser, M. S., Benamor, A., and Adham, S., Sep. Purif. Technol., 228 (2019) 115719.
[7] Orta, M. M., Martin, J., Santos, J. L., Aparicio, I., Medina-Carrasco, S., and Alonso, E., Appl. Clay Sci., 198 (2020) 105838.
[8] Jain, S. K., Duttu, A., Kumar, J., and Shakil, N. A., Arab. J. Chem., 13 (2020) 7990-8002.
[9] Koriche, Y., Darder, M., Aranda, P., Semsari, S., and Ruiz-Hitzky, E., Dalton Trans., 43 (2014) 10512.
[10]Ilgin, P., Ozay, H., and Ozay, O., Cellulose, (2020) 1-16.
[11]Kourim, A., Malouki, M. A., Ziouche, A., Boulahbal, M., and Mokhtari, M., Defect and Diffus. Forum, 406 (2021) 457-472.
[12]Hanna, A. A., Sherief, M. A., and Aboelenin, R. M. M., Res. J. Pharm., Biol. Chem., 5 (2014) 198-205.

INFLUENCE OF pH OF AQUEOUS SOLUTIONS ON XANTHATES REMOVAL BY USING WASTE SLAG

A. Vasić*, N. Nišić, K. Nikolić, I. Kandić, M. Stojmenović, J. Gulicovski and M. Kragović

"VINČA", Institute of Nuclear Sciences- National Institute of the Republic of Serbia, University of Belgrade, Serbia, Mike Petrovića Alasa 12-14, 11351 Belgrade,
(andrijana.nedeljkovic@vin.bg.ac.rs)

ABSTRACT
Xanthates are the most widely used reagents in flotation processing of the sulfide ores, and, therefore largely present in tailings. Since xanthates pose certain toxicity and numerous negative effects from the ecological point of view it is very important to find a proper solution for their removal from the wastewater. In this study, xanthate absorption by using raw as well as modified waste slag as promising adsorbents was investigated with a focus on the impact of the pH value of the polluted water on the efficiency of the overall process. The raw waste slag showed poor performance removing only ~ 13 % of the xanthates, while the modified waste slag was significantly better adsorbent and removed ~ 99 % of xanthates. The results showed that the best adsorption capacity for ethyl xanthate modified slag was obtained at pH 9-10 (12 mmol/g). The obtained result for modified slag adsorption capacity is a good starting point for future research in the field of removal of xanthates from aqueous solutions.

Keywords: *slag, xanthate, pH, wastewater, tailings*

INTRODUCTION
Collectors, including xanthates, are considered to be of great importance among different reagents used in the flotation of sulfide minerals, and their application is inevitable for achieving required efficiency of these processes. Despite the tendency to exclude xanthates from these technological operations and find proper alternatives that are ecologically more acceptable, they are still widely present in industrial plants. Moreover, their consumption is growing which may lead to a number of issues. Global consumption of xanthate in the mining industry has always been significant, amounting to 52,000 tons in the 80s and since then it's on the increase. What is more, it is estimated to be around 372,000 tons by the year of 2025 [1]. On average, current consumption of xanthate amount to about 10 g per 0.1 wt% of metal empirically. Although xanthates are used to extract useful elements from the ore and therefore end up in the final product (i.e. concentrate), due to the technological limitations a significant amount remains as well in the waste material and is disposed of in tailings.

According to the chemical composition, as anionic collectors, xanthates consist of a hydrocarbon nonpolar radial part and a polar group that is considered highly toxic to the environment and human well-being [2]. Therefore, residual xanthates and other by-products from their decomposition in wastewater, even at very low concentrations (< 1 mg/dm^3) can be hazardous, causing serious negative consequences to the environment, affecting human health and hindering the survival of flora and fauna in the surrounding of the mining area. It is especially important to point out their ability to bioaccumulate in living organisms and enhance the augmentation of heavy metals, which can lead to numerous diseases and adverse effects on human health [3]. The effects caused can be either neurological or reproductive [4]. Among other things, that is the reason why flotation tailings are regarded as environmentally extremely harmful by-products. Therefore, having considered all of the above mentioned, it is mandatory to develop an adequate technique for the treatment and removal of xanthate from the wastewater from mining facilities. The literature survey evidenced that there are

many studies related to the treatment or removal of xanthates in mining wastewaters following different methodologies [5-10]. Some of the studies suggested different mechanisms of degradation such as one biological [5] or photocatalytic activity [6, 7]. However, adsorption appears to be the simplest, most efficient, but still, cost-effective solution especially if used in combination with environmentally friendly adsorbents, such as materials that are obtained from waste which itself is environmentally problematic [11]. So far, researchers reported various materials as effective adsorbents for xanthate-contaminated wastewater. For example, Panayotova et al., [8] investigated the removal of potassium ethyl xanthate from wastewater using silver nanoparticles and zeolite composites. In the work of Rezaei et al., [8] modified bentonite was examined as an absorbent for the residual xanthate in flotation tailings. The same to Rezaei et al., [9], modified bentonite was investigated for the same purpose in the paper of Amrollahier al., [10]. However, modification of bentonite was performed using magnetic nanoparticles.

Nevertheless, there haven't been any literature reports on application of waste products, such as waste slag as an absorbent material for the purpose of xanthate removal from mining wastewater so far. Since there is a tendency among scientific circles towards zero-waste principles, finding a potential application of harmful by-products like slag, that are in great volumes generated and disposed in the environment, might be very significant. In order to establish optimal parameters for the adsorption of xanthates using waste slag different factors must be taken into account and one of them is pH value of the contaminated water.

In this study we examined the impact of the initial pH of polluted wastewater on the xanthate adsorption process, which might contribute to establishment of conditions under which waste slag can remove the most of the present xanthates.

METHODS

Waste slag used in this investigation was sampled from an industrial landfill from Valjevo environs. Slag sample was dried throughout the night on temperature 105 °C, then homogenized and grinded. Waste slag was rinsed several times until pH reached 7 before modification. All other chemicals used in this research are analytically clean. The pH of solution was determined with pH meter Cole Parmer. Initial and final concentrations of xanthate were determined on UV-VIS spectrometer UV-1900 Shimadzu $\lambda = 301$ nm.

The waste slag was modified by magnetic nanoparticles previously described by Amrollahi et al., [10] ($Cu(NO_3)_2 \times 3H_2O$ and $Fe(NO_3)_3 \times 9H_2O$) were dissolved in distilled water with magnetic stirring for 20 minutes. The washed slag was added to the suspension and stirred for another 30 minutes on a magnetic stirrer. The pH was adjusted to 10 with 5M NaOH and then the suspension was heated at 100 °C for 2 hours. The resulting particles were washed several times with distilled water and dried at 105 °C.

Initially, the preliminary test for xanthates removal were performed using raw washed and modified slag while following experimental conditions were applied: initial pH 10; initial xanthates concentration 20 mg/dm^3, volume 50 cm^3, mass of the adsorbent 0.01 g, reaction time 24 h. The prepared suspensions were stirred continuously for 24 h with rate of 250 rpm at ambient temperature. Additionally, the suspensions were centrifuged for 10 min at 10000 rpm. Afterwards, the final xanthates concentrations were determined. Measurements of initial final xanthates concentrations were performed using UV-VIS spectrometry.

The influence of the pH on the xanthates removal by using modified waste slag was tested as follows: five Erlenmeyer's of 100 cm^3 were used; in each one 10 mg of modified slag was put and overflown with 50 cm^3 of 0.125 mM of xanthates. Desired pHs were accomplished using a 0.1M solution of KOH. Suspension was shaken for 24 h, after which all the solutions were centrifuged. The concentrations of xanthates in filtrates were determined.

Prior to this study, stability of xanthates in the range of pH 2-10 was investigated. It was shown that xanthates are stable at pH above 8, which was the reason why pH value in the present experiments considering the influence of pH on xanthate removal was chosen to be in the range of 8-12.

RESULTS AND DISCUSSION

The results of the determination of the removal percentage of the raw (IS), and modified (SM) waste slag are shown in (Figure 1.).

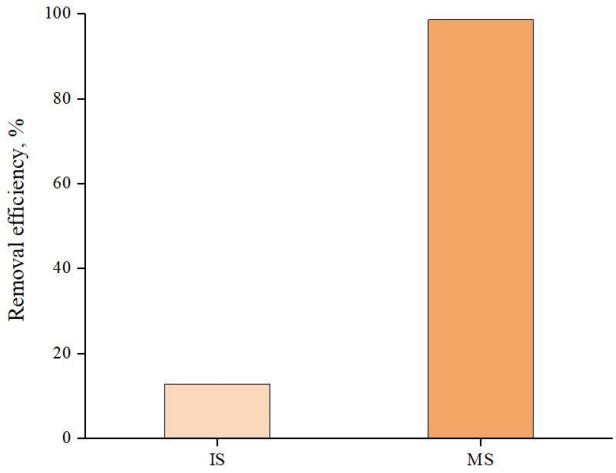

Figure 1. Results of xanthates removal by IS and MS

As presented in Figure 1, efficiency of xanthate removal is rather different comparing raw and modified slag as adsorbents. After slag modification, the removal of xanthate from the solution was improved, rising from 12.73 % to 98.60 %, which indicated that new active binding centres of xanthate on the slag surface appeared as the consequence of the slag treatment.

The pH of the solution plays a significant role in the adsorption efficiency of xanthate. In adsorption experiments, the initial pH varied in the range of 8-12. The results show that the removal of xanthates increases until pH of the solution reaches 10, after which it starts to decrease. For example, at pH 10 percentage of xanthates adsorption was measured to be 98.6 %, after which it dropped to 82.7 % at pH 12. The experiment determined that the maximum adsorption capacity of xanthate is in the pH range of 9-10 on modified slag.

Comparison of adsorption capacity of modified waste slag with literature values of other adsorbents for xanthates removal is in Table 1. Literature review did not show data connected to slag as possible adsorbent. It can be seen that adsorption capacity of modified slag is significantly higher than other adsorbents for xanthates removal.

Table 1. Compresion of adsorption capacities of various adsorbents

Adsorbents	pH	q_{max} (mmol/g)	Reference
AgNPs-clinoptilolite	8-10	0.0235	[8]
Al-Be	12.2	1.31	[9]
Be-Cu-Fe_2O_4	9.2	1.15	[10]
Mn-Ce-Al_2O_3	7.22	1.064	[12]
CuFe3O4-slag	9-10	12	This paper

CONCLUSION

From the present results, it can be concluded that optimal xanthate adsorption capacity of modified slag can be accomplished at pH 9-10 amounting to 12 mmol/g. According to the literature overview, it is obvious that use of waste slag as adsorbent for xanthate provide noticeably better result, higher for a whole order of magnitude compared to results of other materials for the same purpose. This study gives good basis for future research aimed at enhancement of the performance of modified waste slag as adsorbent for xanthates.

Acknowledgment

These investigations were supported by the Ministry of Education, Science and Technological Development of the Republic of Serbia (Contract numbers 451-03-495 68/2022- 14/200017) through the realization of research themes 1702203 and 1702205.

REFERENCES

[1] Harris, G. H., Kirk-Othmer Encyclopedia of Chemical Technology,2000.
[2] Boening, D. W., Min. Eng., Colorado, USA, 1998.
[3] Xu, Y., Lay, J. P., and Korte, F., Bull. Environ. Contam. Toxicol, United State, 41(1988) 5.
[4] Bach, L., Nørregaard, R. D., Hansen, V., Gustavson, K., Scientific Report, 2016.
[5] Lin, H., Qin, K., Dong, Y., and Li, B., J. Environ. Manage., 316 (2022)115304.
[6] Jiang, M., Zhang, M., Wang, L., Fei, Y., Wang, S., Núñez-Delgado, A., and Han, N.Chem.Eng.J., 431(2022)134104.
[7] Zhang, M., Han, N., Fei, Y., Liu, J., Xing, L., Núñez-Delgado, A., and Liu, S., J. Environ. Manage., 297(2021) 113311.
[8] Panayotova M., Mintcheva N., Gicheva G., Djerahov L., Panayotov, V., AndIvanov B., *J.* Int. Sci. Publ.: Ecol. Saf., 13(2019) 58-67.
[9] Rezaei R., Massinaei M., andMoghaddam A. Z., Miner. Eng., 119(2018) 1-10.
[10] Amrollahi A., Massinaei M., and Moghaddam A. Z., Miner. Eng., 134(2019) 142-155.
[11] Ćalić N., Teorijski osnovi pripreme mineralnih sirovina, Rudarsko-geološki fakultet Univerziteta u Beogradu, Beograd, 1990.
[12] Yaping, Z., Chonghu, W., Zhengzhong, L., andJinmei, L., IEEE (2011, February) 1998-2001.

WOOD-WASTE-DERIVED ACTIVATED POROUS CARBON MATERIAL FOR PESTICIDE REMOVAL FROM WATER

T. Tasić, V. Milanković, M. Kokunešoski, A. Šaponjić, A. Valenta Šobot, A. Grce and T. Lazarević-Pašti

University of Belgrade, VINČA Institute of Nuclear Sciences - National Institute of the Republic of Serbia, Mike PetrovicaAlasa 12-14, 11000 Belgrade, Serbia. (majako@vin.bg.ac.rs)

ABSTRACT

Organophosphate pesticides are primarily used in agriculture despite their high neurotoxicity to humans and the environment. Malathion is used in agriculture as a means of controlling the development of pests, but also in the protection of public health, to control mosquitoes and lice. However, this organophosphate compound is hazardous to human health. We used wood-waste-derived activated porous carbon material as an adsorbent for malathion removal from water. The kinetics of the malathion adsorption process on investigated carbon material at different temperatures was studied. The results showed that the experimental data are a good fit with the pseudo-second-order model. The calculated rate constants were 0.009 and 0.007 g mg^{-1} min^{-1} at 20 and 40 °C, respectively. The equilibrium was reached after 60 minutes at both investigated temperatures. It was shown that 1 g of the studied material could adsorb up to 186.22 mg of malathion at 20 °C.

INTRODUCTION

Organophosphate pesticides (OP) are an effective group of pesticides that are widely used. They are used in agriculture and many green areas as insecticides, in households as a remedy against lice, and in veterinary medicine [1]. However, excessive use of pesticides increases the risk of their harmful effects on the human body. Organophosphate toxicity is reflected in the inhibition of the enzyme acetylcholinesterase (AChE), which plays a key role in the transmission of nerve impulses. Organophosphates are irreversibly bound to AChE, leading to symptoms such as tachycardia, hypertension, anxiety, bronchial prostheses, and many others [2].

Malathion is a broad-spectrum organophosphate pesticide used to control pests on agricultural land, green areas, gardens, and veterinary and public health. [1] Residues of malathion can be found in soil, drinking water, rainwater, rivers, fruits and vegetables. [3] Pure malathion is a colorless, odorless liquid, while industrial malathion is characterized by certain impurities that make the solution yellowish and smell like garlic [4].

Exposure to malathion is associated with an increased risk of prostate cancer, thyroid cancer, leukemia and other endocrine, hematological and reproductive problems [3]. Therefore, it is important to remove malathion from the environment effectively. Methods for removing this toxic pesticide are numerous, and one of the most effective is its adsorption on carbon materials. This method is economical, simple, not harmful to the environment and does not cause chemical transformations of pesticides, potentially leading to the creation of even more dangerous products. In addition, due to the large specific surface area of carbon materials, diverse surface chemical composition, and various pore structures, carbon materials have great potential for organophosphate adsorption [1].

The aim of this work was to investigate the kinetics of the malathion adsorption process on wood-waste-derived activated porous carbon material at different temperatures.

METHODS

Beech wood waste was dried for 24 h at 95 °C. Then, the dried material was carbonized in a chamber furnace under a nitrogen atmosphere with a heating rate of 1.0 °C min^{-1} and held isothermal for 30 min at 900 °C. Afterward, the carbonized fibers were activated in a rotary kiln at 870 °C for 165 min in a CO_2-flow of 80 Lh^{-1}. The obtained carbon material was dispersed in double-distilled water (1 mg cm^{-3}), and the desired amount of malathion (Figure 1) stock solution was added to provide the targeted concentration of adsorbent (0.5 mg cm^{-3}) and OP (5×10^{-4} mol dm^{-3}). Then, the vessel containing the adsorbent + OP mixture was placed on a laboratory shaker and left for the desired amount of time. After the incubation, the mixture was centrifuged for 5 min at 10000 rpm, and the supernatant was filtered through a nylon filter membrane. The concentration of malathion was determined using Ultra Performance Liquid Chromatography (UPLC). For UPLC measurement, Waters ACQUITY UPLC system with a photodiode array (PDA) detector, controlled by the Empower software, was used. The analyses were done using ACQUITY UPLC™ BEH C_{18} column (1.7 µm, 100 mm × 2.1 mm, Waters GmbH, GER) under isocratic conditions with a mobile phase A consisting of 10% acetonitrile in water (v/v), and a mobile phase B, which was pure acetonitrile. The eluent flow rate was 0.25 cm^3 min^{-1}, and the injection volume of 5 mm^3 was used. The mobile phase was composed of 40 % A and 60 % B. Under these experimental conditions, the retention time of malathion was 2.6 min. OP was detected at 205 nm. Control experiments were performed identically but without adsorbent. The representative chromatogram of malathion is presented in Figure 2.

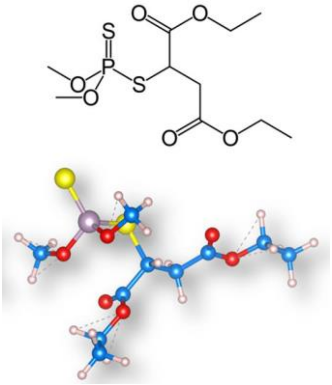

Figure 1. 2D structure and 3D model of malathion

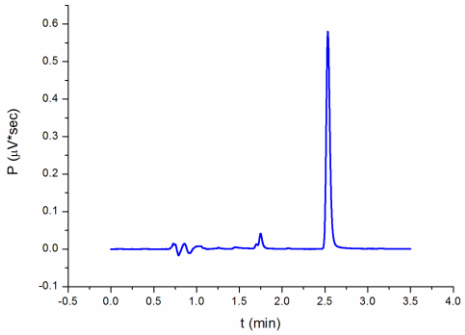

Figure 2. Chromatogram of 5×10^{-4} mol dm^{-3} malathion under the experimental conditions described above

RESULTS AND DISCUSSION

In order to study the kinetic parameters of the adsorption process, 0.5 mg cm^{-3} of investigated adsorbent was incubated with 5×10^{-4} mol dm^{-3} malathion for various intervals (1-120 min) at two different temperatures (20 and 40 °C). The concentration of adsorbed malathion (C_{ads}) was calculated as a difference between its initial concentration (C_0) and the equilibrium concentration (C_e) of malathion measured with UPLC after removing the adsorbent. The obtained data are presented in Figure 3.

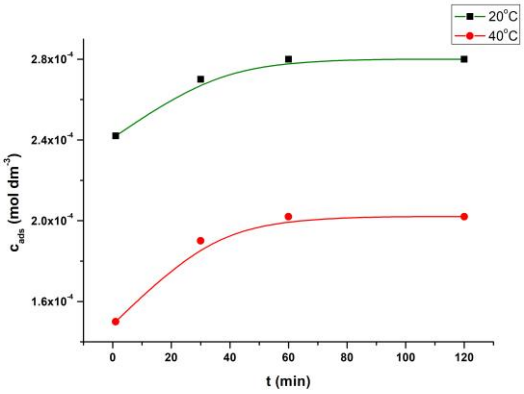

Figure 3. The concentration of adsorbed malathion (C_{ads}) as a function of time obtained at two different temperatures (20 and 40 °C).

From the data presented in Figure 3, it was obvious that the equilibrium was reached after 60 minutes at both temperatures. The results also showed that the adsorption is more efficient at a lower temperature. It implies that the physisorption took place and that the increase in the temperature negatively influenced the formation of non-covalent bonds between malathion and carbon material. The effect of pH was also tested and shown not to influence the adsorption efficiency. Experimental data were then fitted with pseudo-first and pseudo-second-order models. The obtained results are presented in Figure 4 and Table 1. The presented results showed that the experimental data fit better with the pseudo-second-order model. The calculated rate constants (k) were 0.009 and 0.007 g mg^{-1} min^{-1} (this unit is common when adsorption capacity, q_e, is given in mg g^{-1}) at 20 and 40 °C, respectively. Moreover, the results indicated that 1 g of investigated bio-waste material could adsorb up to 186.22 mg of malathion. Compared to literature data, this value is satisfying [5].

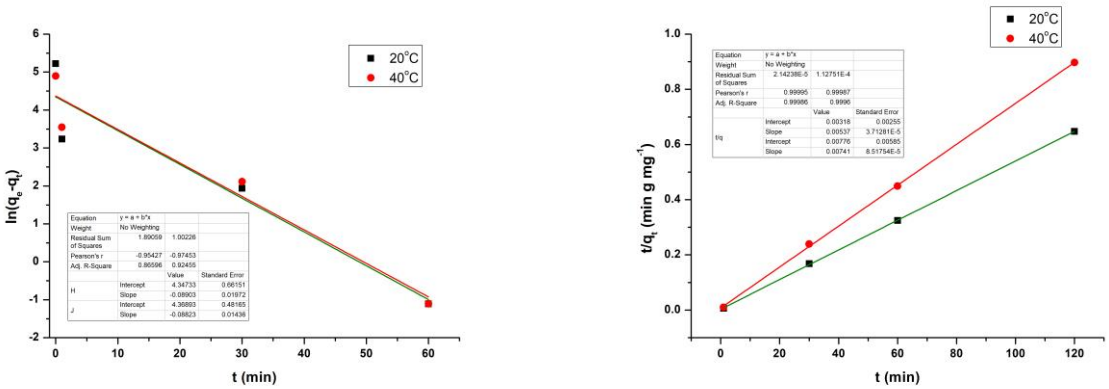

Figure 4. Corresponding plots of pseudo-first-order (left) and pseudo-second-order model (right) for 5×10^{-4} mol dm^{-3} malathion and 0.5 mg cm^{-3} of adsorbent at two different temperatures (20 and 40 °C). q_e - equilibrium adsorption capacity, expressed as the mass of adsorbed malathion *per* unit mass of adsorbent, given in (mg g^{-1}). q_t - adsorption capacity for a defined time, t.

Table 1. Kinetic parameters of the pseudo-first-order and pseudo-second-order models for 5×10^{-4} mol dm^{-3} malathion and 0.5 mg cm^{-3} of adsorbent at two different temperatures (20 and 40 °C). k – adsorption rate constants; q_e- equilibrium adsorption capacity.

	Pseudo first order		Pseudo second order	
T (^oC)	20	40	20	40
k*	0,089	0,089	0,009	0,007
q_e (mg g^{-1})	77,484	79,177	186,220	134,953
R^2	0,866	0,925	0,999	0,999

*(min^{-1}) for pseudo-first-order model and (g mg^{-1} min^{-1}) for pseudo-second-order model

The interparticle diffusion kinetics model was applied to elucidate the diffusion mechanism. The two divided linear plots suggest the diffusion process occurs via two steps on both investigated temperatures (data not shown). The first segment of the plot denotes boundary layer diffusion, in contrast to the second segment representing interparticle diffusion of malathion throughout the open cavities of the adsorbent. Values for k_i (adsorption rate constant for interparticle diffusion model) were 29.00 and 11.16 mg g^{-1} $min^{-1/2}$ at 20 and 40 °C, respectively.

CONCLUSION

Wood-waste-derived activated porous carbon material was used as an adsorbent for malathion removal from water. The rate constants were 0.009 and 0.007 g mg^{-1} min^{-1} at 20 and 40 °C, respectively, calculated from the pseudo-second-order model. The adsorption efficiency was higher at 20 °C, indicating physisorption. It was shown that 1 g of the studied material could adsorb up to 186.22 mg of malathion. The interparticle diffusion kinetics model indicated that the diffusion process occurs via two steps. pH was shown not to influence the adsorption efficiency. Remediation of malathion using the investigated adsorbent was successful.

Acknowledgment

This work was partially supported by the Ministry for Science of the Republic of Serbia (Grant no. 451–03–9/2022–14/200017).

REFERENCES

[1] Lazarević-Pašti, T. (Ed.) Organophosphates: Detection, Exposure and Occurrence. Volume 1: Impact on Health and the Natural Environment. Nova Science Publishers, New York, USA, 2022.

[2] Adeyinka A, Muco E, Pierre L. Organophosphates. 2021 Jul 29. In: StatPearls [Internet]. Treasure Island (FL): StatPearls Publishing; 2022 Jan–. PMID: 29763035.

[3] Pluth, T. B., Zanini, L. A. G. and Battisti, I. D. E., Pesticide exposure and cancer: an integrative literature review. Saúde em Debate [online]. 2019, 43 (122) [Accessed 30 May 2022] , pp. 906-924.

[4] https://pubchem.ncbi.nlm.nih.gov/compound/Malathion

[5] Jocić, A., Breitenbach, S., Pašti, I.A. *et al.* Environ Sci Pollut Res 29 (2022) 35138–35149.

THE POTENTIAL HEALTH RISK OF HEAVY METALS IN HERBAL TEA COMMERCIALLY AVAILABLE IN ŠABAC, SERBIA

K. Popović[1], M. Antonijević Nikolić[1], B. Dražić[2] and S. Tanasković[2]

[1]*Academy of Applied Studies Šabac, Department for Medical, Business and Technological Studies, Šabac, Serbia*
[2]*Faculty of Pharmacy, University of Belgrade, Vojvode Stepe 450, 11000 Belgrade, Serbia.*

ABSTRACT
The chemical components in tea have received great interest because they are related to health. In this study the content of five heavy metals including Cu, Fe, Mn, Zn and Ni were determined by atomic absorption spectrometry on samples of herbal teas: *Quercus cortex, Gentianae radix, Althaeae radix, Uvae ursi folium* and *Glycyrrhizae radix* collected from Šabac's market, Serbia. Based on the obtained content of the metals in the analyzed herbal teas, estimated daily intake (*EDI*) was determined. Both target hazard quotient (*THQ*) and hazard index (*HI*) were employed to assess the potential health risk of studied metals in teas. The herbal tea samples analysed contain essential heavy metals (Cu, Fe, Mn, Zn) and probably essential in trace (Ni) and could contribute to the daily dietary requirements. The *THQ* from $7.76 \cdot 10^{-4}$ to $5.75 \cdot 10^{-1}$ and *HI* from 0.1059 to 0.6151 values for tea samples were lower than 1, suggesting that consumption of tea would not cause significant health risks for consumers.

INTRODUCTION
Herbal teas have complex chemical compositions, and chemical substances they contain can exhibit biological activity in humans. Consequently, herbal teas represent sources of various organic and inorganic components that can influence the human health. Tea is a rich source of minerals and trace elements that are essential to human health and drinking of teas can be an important source of some essential minerals . Essential minerals, including the trace elements, are inorganic elements that have a physiological function within the body. These must be provided in the diet and vary from grams per day for the major minerals through milligrams to micrograms per day for the trace elements . A deficiency, as well as elevated concentration of essential elements, can have a negative impact on human health. Special attention is devoted to determining the content of heavy metals in teas which are easily absorbed by plants and aquatic species and subsequently enter the food chains and then the human body.Teas contain both essential (Fe, Cu, Mn, Zn) and toxic elements (As, Cd, Hg, Pb). The biological effects of heavy metals depend on their concentration [1] and thus should be carefully controlled.The content of metals in food is defined in terms of maximum allowed concentrations, which represent the amount of toxic substance in the adult weighing 70 kg, consumed over all their lives, will not cause unwanted toxic effects. The content of heavy metals in herbal teas depend on climatic, geographic, other environmental factors and specific methods of the production of certain sorts of tea. The distribution of the heavy metals among plant organs is selective and dependent on the part of the plant, surface characteristics of the plant organ, and the element that is examined.

METHODS
All samples used in this research are herbal teas collected from local health food stores in Šabac, Serbia. The samples were herbal teas *Quercus cortex, Gentianae radix, Althaeae radix, Uvae ursi folium* and *Glycyrrhizae radix* sold in bulk.

Preparation of tea samples for analysis of heavy metals was performed by dry digestion, burning and dissolving the ash in a suitable acid. In dry digestion, about 3 g of the sample (exact mass

measured to 4 decimal places) was calcined gradually by raising the temperature by 50°C/h, from room to 450° C, at which the sample was kept for 8 h. The resulting ash was dissolved in 5 ml hydrochloric acid (c= 6 M) and the solution was evaporated in water bath to dryness. The residual precipitate was dissolved in ~10.0 ml nitric acid (c=0.1 mol/dm^3), filtered, washed with deionized water. The final volume was 50 ml [2]. The blank sample was prepared in the same way with no tea. Atomic absorption measurements were made using a Perkin-Elmer spectrophotometer AAS-5100/PC with background correction and hollow cathode lamps. Air–acetylene flame was used for determination of all the elements.

The contents of heavy metals in herbal teas were used to evaluate the estimated daily intake of heavy metals (*EDI*), target hazard quotients (*THQ*) and hazard index (*HI*) for adults.

The estimated daily intake (*EDI*) (mg/kg body weight/day) of heavy metals is a fundamental parameter for metal transfer from plant to human. It can be calculated using the following equation (1) [3]:

$$EDI = \frac{C \cdot F_{IR} \cdot TR}{W_{AB} \cdot 1000} \qquad (1)$$

where C is the heavy metal content (mg/kg) in herbal tea, F_{IR} is the herbal tea ingestion rate (g/person/day), TR is the transference rate of the heavy metal from herbal tea to herbal tea infusion, and W_{AB} is the average body weight.

The targeted hazard quotient (*THQ*) was used to estimate the potential noncarcinogenic effects of individual heavy metals present in the herbal teas. The equation (2) was employed to calculate the *THQ*:

$$THQ = \frac{EDI}{RfD} \qquad (2)$$

where the *THQ* is the target hazard quotient and is dimensionless, the *EDI* is the estimated daily intake of heavy metals (mg/kg body weight/day), and the *RfD* is the oral reference dose for the heavy metals (mg/kg body weight/day) [3] which does not induce a lifetime harmful effect. The *RfD* values of the tested heavy metals are shown in Table 1.

Table 1. The literature oral reference doses (*RfD*) [4, 5].

Heavy metal	**Cu**	**Fe**	**Ni**	**Mn**	**Zn**
The oral reference dose (*RfD*) (mg/kg body weight/day)	0.04	0.7	0.02	0.014	0.3

HI can be estimated by the sum of the target hazard quotients of all studied pollutants [3].

RESULTS AND DISCUSSION

In this paper quality of five herbal tea samples were analyzed. Herbal tea samples were collected from the local health food markets on the territory of Šabac, Serbia. Analyzed samples were in bulk, without adequate evidence of their quality. The metal contents (Fe, Cu, Zn, Mn, Ni) of herbal tea samples were analyzed by using Atomic absorption spectroscopy (AAS) are in Table **2**. Herbal teas showed the concentration of the heavy metals Cu, Fe, Mn, Zn and Ni in the range: 22.2-5.9 mg/kg, 489.0-144.5 mg/kg, 150.0-19.0 mg/kg, 39.0-6.5 mg/kg and 10.0-2.7 mg/kg, respectively.

According to the equation (1), the estimated daily intakes (*EDI*) values of heavy metals (Cu, Fe, Ni, Mn and Zn) of tested herbal teas from Serbia were calculated and were showed in Table **2**. In the Table **2**, also were given the values of the recommended daily intakes expressed by body weight

(mg/kg body weight/day) i.e. the recommended daily intakes recalculated for adults weighing 70 kg. The *EDI* values of the studied heavy metals in tested herbal teas were the following: Zn >Fe > Mn > Cu > Ni, because the mean average of *EDI* were $3.99\cdot10^{-3}$, $2.71\cdot10^{-3}$, $1.72\cdot10^{-3}$, $2.99\cdot10^{-4}$, $2.16\cdot10^{-4}$ (mg/kg bw/day), respectively (Table **2**). This means that the contribution of Fe was the largest among the daily intakes of analyzed heavy metals which has been obtained in other studies [3].

The *EDI* for Cu, Fe, Ni, Mn and Zn in all tested herbal teas are lower than the recommended daily intakes expressed by body weight (Table **2**). This indicates that the daily intake of these heavy metals surveyed as a five cups of the herbal tea infusion are much lower than human body needed. According, consuming herbal tea can supplement essential in traces elements (Cu, Fe, Mn and Zn) and probably essential in traces elements (Ni) [6] needed by human body, but their contents are much lower than human body needs.

The *EDI* values in this research were all below the oral reference dose (*RfD*) (mg/kg body weight/day) values for all investigated heavy metals in the samples, indicating that the drinking of the analyzed herbal teas did not appear to pose a health risk to consumers.

Table 2. Total contents of heavy metals (mg/kg dry weight) in herbal teas, estimated daily intakes (*EDI*) (mg/kg bw/day) of heavy metals for adults due to the consumption of analyzed herbal teas of Serbia as well as the mean average of *EDI* (mg/kg body weight/day) and the recommended daily intakes expressed by body weight (mg/kg body weight/day).

No	**Herbal tea**	**EDI (mg/kg body weight/day) for adults (Content of heavy metals (mg/kg))**				
		Cu	**Fe**	**Ni**	**Mn**	**Zn**
1	*Quercus cortex*	$4.46\cdot10^{-4}$ (8.2±0.4)	$4.15\cdot10^{-3}$ (238.0±0.7)	$4.49\cdot10^{-4}$ (6.5 ± 0.5)	$8.05\cdot10^{-3}$ (150.0 ± 1.5)	$2.33\cdot10^{-4}$ (6.5 ± 0.4)
2	*Gentianae radix*	$5.28\cdot10^{-4}$ (9.7 ± 0.6)	$4.69\cdot10^{-3}$ (269.0 ± 1.5)	$6.91\cdot10^{-4}$ (10.0 ± 1.1)	$5.95\cdot10^{-3}$ (111.0 ± 1.1)	$1.40\cdot10^{-3}$ (39.0 ± 0.9)
3	*Althaeae radix*	$1.21\cdot10^{-3}$ (22.2 ± 0.9)	$2.52\cdot10^{-3}$ (144.5 ± 0.8)	$3.80\cdot10^{-4}$ (5.5 ± 0.4)	$1.05\cdot10^{-3}$ (19.5 ± 0.9)	$7.17\cdot10^{-4}$ (20.0 ± 1.1)
4	*Uvae ursi folium*	$3.21\cdot10^{-4}$ (5.9 ± 0.4)	$8.53\cdot10^{-3}$ (489.0 ± 1.7)	$4.49\cdot10^{-4}$ (6.5 ± 0.7)	$1.10\cdot10^{-3}$ (20.5 ± 1.2)	$1.24\cdot10^{-3}$ (34.5 ± 1.8)
5	*Glycyrrhizae radix*	$4.84\cdot10^{-4}$ (8.9 ± 0.6)	$7.17\cdot10^{-3}$ (411.0 ± 1.2)	$1.87\cdot10^{-4}$ (2.7 ± 0.2)	$1.02\cdot10^{-3}$ (19.0 ± 5.8)	$4.12\cdot10^{-4}$ (11.5 ± 0.6)
The mean average of *EDI* (mg/kg body weight/day)		$2.99\cdot10^{-4}$	$2.71\cdot10^{-3}$	$2.16\cdot10^{-4}$	$1.72\cdot10^{-3}$	$3.99\cdot10^{-3}$
Recommended daily intakes expressed by body weight (mg/kg body weight/day) which calculated for men (women) weighing 70 kg (*RDI*)		$1.29\cdot10^{-2}$	$1.14\cdot10^{-1}$ ($2.57\cdot10^{-1}$)	$7.14\cdot10^{-3}$	$3.29\cdot10^{-2}$ ($2.57\cdot10^{-2}$)	$1.57\cdot10^{-1}$ ($1.14\cdot10^{-1}$)

The target hazard quotient (*THQ*) of samples varied from $8.03\cdot10^{-3}$–$1.12\cdot10^{-2}$ for Cu, $6.70\cdot10^{-3}$–$1.22\cdot10^{-2}$ for Fe, $7.28\cdot10^{-2}$–$5.75\cdot10^{-1}$ for Mn, $7.76\cdot10^{-4}$–$4.66\cdot10^{-3}$ for Zn and $9.33\cdot10^{-3}$–$3.46\cdot10^{-2}$ for Ni, Table **3**. The *THQ* for tested heavy metals from the all samples were less than one, which is regarded as secure for human use.

Table 3. Target hazard quotient (*THQ*) and hazard index (*HI*) values of heavy metals for adults due to the consumption of analyzed herbal teas of Serbia.

No	Herbal tea	*THQ* for adults					*HI* for adults
		Cu	Fe	Ni	Mn	Zn	
1	*Quercus cortex*	$1.12\cdot10^{-2}$	$5.93\cdot10^{-3}$	$2.25\cdot10^{-2}$	$5.75\cdot10^{-1}$	$7.76\cdot10^{-4}$	0.6151
2	*Gentianae radix*	$1.32\cdot10^{-2}$	$6.70\cdot10^{-3}$	$3.46\cdot10^{-2}$	$4.25\cdot10^{-1}$	$4.66\cdot10^{-3}$	0.4844
3	*Althaeae radix*	$3.02\cdot10^{-2}$	$3.60\cdot10^{-3}$	$1.90\cdot10^{-2}$	$7.47\cdot10^{-2}$	$2.39\cdot10^{-3}$	0.1299
4	*Uvae ursi folium*	$8.03\cdot10^{-3}$	$1.22\cdot10^{-2}$	$2.25\cdot10^{-2}$	$7.85\cdot10^{-2}$	$4.12\cdot10^{-3}$	0.1254
5	*Glycyrrhizae radix*	$1.21\cdot10^{-2}$	$1.02\cdot10^{-2}$	$9.33\cdot10^{-3}$	$7.28\cdot10^{-2}$	$1.37\cdot10^{-3}$	0.1059

The *HI* values of all investigated heavy metals via the consumption of herbal tea infusions are given in Table **3.** It was discovered that *HI* values for all the tested heavy metals, in the samples herbal teas, were below 1. This enabled us to conclude that there is actually no carcinogenic risk from the drinking of infusions of these herbal teas, in amounts and with the frequency assumed in this paper.

CONCLUSION

This study determined levels of five heavy (toxic and essential) metals in five samples herbal tea. The samples were collected from local markets in Šabac, Serbia. The heavy metal content was determined by AAS. Essential metal concentration of Mn, Fe, Zn, Cu and Ni in the herbal tea decreased in the order of Fe > Mn > Zn > Cu. > Ni. The variations of heavy metal concentrations were observed in this paper probably could be due to the tea types and different plant organs (roots, branches and leaves) present in the herbal tea. The influence of physico-chemical characteristics of growing regions, methods of production of certain types of tea, dishes used for tea processing can not be excluded, too.The herbal tea samples analysed contain trace elements (Fe, Cu, Zn, Mn and Ni) and could contribute to the daily dietary requirements. The noncancer health risk assessment indicated that herbal teas health risk to consumers.

Acknowledgment

This work was supported by the Ministry of Education, Science and Technological Development of the Republic of Serbia (grant no 452-03-9/2020-14/200014-0902105).

REFERENCES

[1] D. A. Schuschke, J. T. Saari, F. N. Miller, D. G. Lominadze, J. Trace Elem. Exp. Med., 9 (1996) 63-72.
[2] Official Methods of Analysis of AOAC International, 17th Ed. Official Method 999.11. Gaithersburg, MD, USA: AOAC International, (2000).
[3] J. Zhang, R. Yang, R. Chen, et al., Int J Environ Res Public Health.,15(1) (2018) 133-155.
[4] M. Harmanescu, L. M. Alda, D. M. Bordean, et al., I. Chem Cent J., 5 (2011) 64-74.
[5] United States Environmental Protection Agency, Handbook for Non- Cancer Health Effects Evaluation. US Environmental Protection Agency, Washington (DC) (2000).
[6] V. Daničić, Vitaminologija, sve o vitaminima i mineralima [in Serbian], Tarifa, Beograd (2012).

MALATHION REMEDIATION IN WATER BY BIOWASTE-BASED CARBON MATERIAL

K. Kokanov[1], T. Tasić[2], V. Milanković[2], N. Potkonjak[2] and T. Lazarević-Pašti[2]

[1]University of Belgrade, Faculty of Physical Chemistry,
Studentski Trg 12, 11000 Belgrade, Serbia.
[2]University of Belgrade, VINČA Institute of Nuclear Sciences,
National Institute of the Republic of Serbia,
Mike Petrovica Alasa 12-14, 11000 Belgrade, Serbia.
(npotkonjak@vin.bg.ac.rs)

ABSTRACT

Widespread use of organophosphate pesticide malathion raises the need to develop efficient procedures for its elimination from the environment. We used biowaste-derived carbon material as an adsorbent for malathion. It was shown that 1 g of investigated material is capable of adsorbing 18.34 mg of malathion at 25°C. A satisfactory agreement of experimental results with the Freundlich isotherm model suggests the multilayer adsorption on the heterogeneous surface.

INTRODUCTION

Pesticides are extensively used, improving food production by enhancing the yield quality and quantity, ensuring food security for the ever-growing population around the world. Pesticides are extensively used in modern agriculture to improve agricultural production and control various pests and disease vectors in public health. However, despite their many benefits, excessive or improper application of pesticides in agricultural activity leads to the pollution of soils and aqueous environments, which may produce a range of hazardous effects to non-target species such as humans and animals [1].

Organophosphorus pesticides (OPs) are widely used to improve agricultural manufacture. However, an extensive application of OPs leads to high-level OP residues in food and the environment, which is highly undesirable due to its harmful nature. The toxic effects of OPs are related to the irreversible inhibition of the enzyme acetylcholinesterase (AChE) [1].

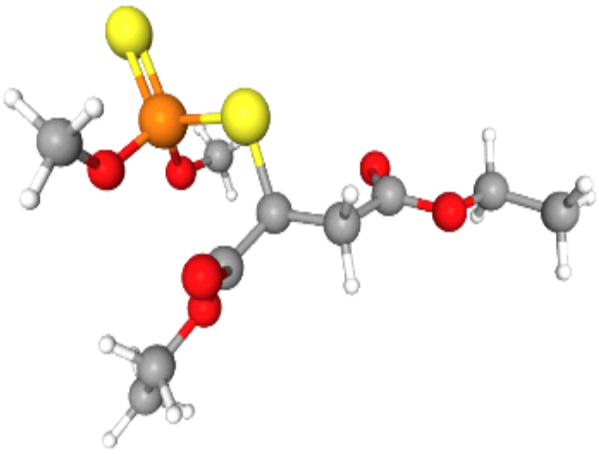

Figure 1. 3D structure of malathion.

Malathion (Figure 1.) is a broad-spectrum organophosphate pesticide used to control pests on agricultural land, green areas, gardens, and veterinary and public health. Residues of malathion can be found in soil, drinking water, rainwater, rivers, fruits and vegetables. Malathion is moderately toxic. However, absorption or ingestion of malathion into the human body results in its transformation to malaoxon, which is significantly more toxic.

Efficient removal of OPs is necessary to control the levels of these compounds in food and the environment. Different adsorbents have been applied to remove malathion from wastewaters, such as activated carbon, rice husk and activated rice husk, bagasse fly-ash from sugar industry waste, clays and organ clays [2]. Carbon materials proved to be very efficient adsorbents for the removal of OPs [1, 3]. Various types of waste are gaining increasing importance as precursors for the production of cheaper activated carbon materials with specific structures and properties. Recently, special attention has been given to biowaste since it is easily accessible, low cost, and environmentally friendly.

In this contribution, we synthesized biowaste-based carbon material and used it as an adsorbent for the removal of malathion from water. In addition, we evaluated experimental results with the Langmuir and Freundlich isotherm models to determine the specific parameters of adsorption.

METHODS

In this study, spent rodent cage bedding was used as a biowaste-based carbon material. Firstly, it was dried at 90 °C for 24 h. Then, it was carbonized in a chamber furnace under a nitrogen atmosphere with a heating rate of 5.0 °C min^{-1} and held isothermal for 60 min at 650 °C. The obtained carbon material was dispersed in double-distilled water. In order to investigate the process of adsorption, 1 mg mL^{-1} of adsorbent was incubated with malathion in the following concentration range from 5×10^{-6} to 5×10^{-4} mol dm^{-3}. Incubation was done at 25 °C for 24 h. Then, the vessel containing the adsorbent + malathion mixture was placed on a laboratory shaker. Incubation was done at 25 °C for 24 h, to ensure that equilibrium was reached. After equilibration, the mixture was centrifuged for 10 min at 14,500 rpm, and the supernatant was filtered through a nylon filter membrane.

The concentration of adsorbed malathion was calculated as a difference between its initial concentration (C_0) and the equilibrium concentration (C_e) of malathion measured with UPLC after removing the adsorbent. Adsorption capacity (Y_{max}) represents the equilibrium concentration of malathion *per* 1 g of adsorbent. Experimental results were evaluated with the Langmuir and Freundlich isotherm models to determine the specific parameters of adsorption. The concentration of malathion was determined using UPLC analysis [2]. Control experiments were performed identically but without adsorbent.

RESULTS AND DISCUSSION

Results obtained are presented in the Table 1. and Figure 2. From the presented data it can be concluded that a satisfactory agreement was achieved with the Freundlich isotherm model. This suggests the multilayer adsorption on the heterogeneous surface. Furthermore, it appears that 1 g of biowaste-derived carbon material is capable do adsorb 18.34 mg of malathion. Compared to literature data, this value is rather modest. Still, one must keep in mind the low cost and green waste management principles connected to this biowaste-based material production [4].

Table 1. Fitting parameters of Langmuir and Freundlich isotherm models

Parameter	Langmuir isotherm	Freundlich isotherm
Y_{max} (mg g^{-1})	18.340	/
K_{ads} (g dm^{-3})	6.030×10^{3}	/
$1/n$	/	0.485
log k	/	2.658
R^2	0.6255	0.9384

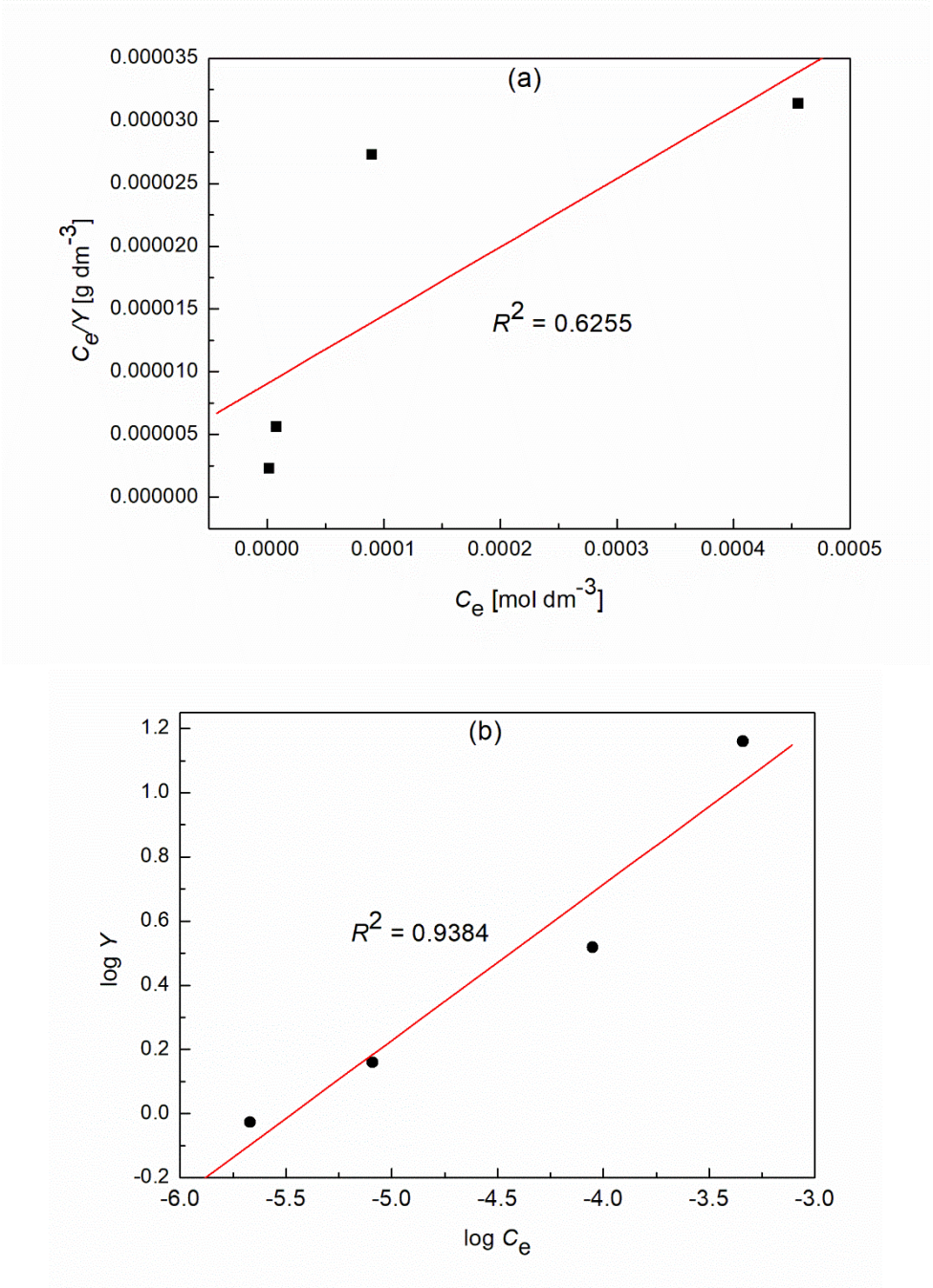

Figure 2. Experimental data for 1 mg mL^{-1} adsorbent and malathion fitted with Langmuir (a) and Freundlich (b) adsorption isotherms.

CONCLUSION

Biowaste-based carbon material was used for malathion removal from water. It was shown that 1 g of investigated material is capable of adsorbing 18.34 mg of malathion. A satisfactory agreement of experimental results with the Freundlich isotherm model suggests the multilayer adsorption on the heterogeneous surface. Remediation of malathion using the selected adsorbent was successful.

Acknowledgment

This work was partially supported by the Ministry for Science of the Republic of Serbia (Grant no. 451–03–9/2022–14/200017).

REFERENCES

[1] T. Lazarević-Pašti, I. Pašti, B. Jokić, B. Babić, and V. Vasić, RSC Advances, 6 (2016) 62128.
[2] M. Mirković, T. Lazarević-Pašti, A. Došen, M. Čebela, A. Rosić, B. Matović, B. Babić, RSC Adv., 6 (2016) 12219.
[3] T. Lazarević-Pašti, V. Anićijević, M. Baljozović, D. Vasic Anićijević, S. Gutić, V. Vasić, and N. Skorodumova, I. Pašti, Env. Sci. Nano, 5 (2018) 1482.
[4] A. Jocić, S. Breitenbach, I. A. Pašti, et al., Environ. Sci. Pollut. Res., 29 (2022) 35138.

REMOVAL OF PHARMACEUTICAL RESIDUES FROM AQUEOUS SOLUTION BY DOPED CRYOGELS MATERIALS

A. Krstić[1], I. Bracanović[1], P. Batinić[2], D. Vasić-Anićijević[1], Dj. Katnić[1] and A. Kalijadis[1]

[1]*University of Belgrade, Vinca Institute of Nuclear Sciences - National Institute of the Republic of Serbia, Mike Petrovića Alasa 12-14, Belgrade, Serbia*
[2]*Institute of Medicinal Plants Research "Dr Josif Pancic", Tadeuša Koščuška 1,11000 Belgade, Serbia*
E-mail: aleksandar.krstic@vinca.rs

ABSTRACT
The aim of this work was a synthesis of nitrogen and sulfur co-doped carbon cryogel (CCNSs) (with nominal concentrations of 2 and 6 wt.%), as well as pristine carbon cryogel (CC). Samples were tested for removal of pharmaceutical residues carbamazepine (CBZ) and naproxen (NPR) which are recognized as water contaminants. Composition and surface characterization were performed by elemental and BET analysis. Kinetics and equilibrium adsorption studies were investigated using a batch experimental approach. Effect of pH of pharmaceutical solution on adsorption efficiency was also investigated. Determination of pharmaceuticals was performed by the UPLC technique coupled with a PDA detector. Obtained results showed that by functionaliziation of carbon materials through the doping/co-doping, it is possible to improve their adsorption characteristics which was the goal of this work.

INTRODUCTION
Carbon cryogel are relatively novel carbon material prepared by sol-gel polycondensation of resorcinol and formaldehyde in the presence of base as a catalyst [1]. Carbonization in the inert gas stream was used for obtaining the final carbon material. These materials have well-developed porosity, low density and high surface area and makes them as a suitable sorbent [2]. The cryogels doped with heteroatoms (N, S) showed more benefits than pristine cryogel, such as adsorption and storage properties, electrocatalyst, and conductivity. The incorporation of N and S into the cryogel structure improves their structural and surface characteristics, such as porosity, formation of new functional groups on the surface, and electronic properties, which significantly impact the adsorption characteristics of these materials. Research reported that the dual doping with N and S may decrease adsorption energy between adsorbate-functional groups on the carbon surface to a lower distance, which leads to better and stronger adsorption [3]. Also, N and S contain a lone electron pair and act as a Lewis base and can donate and form a stronger bond with an aromatic ring of adsorbate [4].

METHODS
Carbon cryogel samples were synthesized by policondenzation reaction of resorcinol and with formaldehyde in water solution with Na_2CO_3 as a basic catalyst followed by freeze-drying and carbonization in the inert atmosphere at 900^0C. For nitrogen and sulfur doping, thiourea was added to the precursor solution as a nitrogen and sulfur source to obtain the nominal nitrogen concentrations 2 and 6 wt.%. Before drying, the obtained samples are rinsed with t-butanol. After that, samples were pre-frozen at -30^0C and then freeze-dried for 24h under vacuum (0,4mbar). [5]. These synthesized co-doped samples as marked as $CCNS_1$ and $CCNS_2$. For the adsorption experiments, the active

substances from the commercial drugs (Karbapin® 375 mg (CBZ), Naproxen® 500 mg (NPR), were used. The CC and CCNSs samples were characterized by elemental and BET analysis. Kinetics and equilibrium adsorption studies were investigated using a batch experimental approach. All experiments were performed by mix two pharmaceutical solution with initial concentration of 5 ppm at room temperature^{0}C). UPLC system coupled with PDA detector (Waters, Milford, Massachusetts, USA) was used to quantify pharmaceutical residue before and after adsorption.

RESULTS AND DISCUSSION

The addition of melamine and thiourea into the CC precursor resulted in nitrogen and sulfur incorporated in final materials up to 1.01 wt.% and 0.42 wt.%, respectively. Results of elemental and BET analysis are given in Table 1 [6]. The specific surface area values are in the range of 592-1070 m^2/g. Dual doping with nitrogen and sulfur leads to a significant increase in specific surface area values compared to the pristine CC sample, especially for the $CCNS_2$ (1070 m2/g) sample, but mesoporosity for all samples is preserved [5].

Table 1. Elemental analysis and porous properties of CC and CCNSs samples [6]

Sample	C (wt.%)	H (wt.%)	N (wt.%)	O (wt.%)*	S (wt.%)	S_{BET} m^2/g	S_{meso} m^2/g
CC	88,47	1,49	0,00	10,04	0,00	592	318
$CCNS_1$	84,77	1,88	0,95	11,88	0,52	780	440
$CCNS_2$	82,31	2,24	1,01	14,02	0,42	1070	580

*Calculated by the difference

Effect of pH was investigated in the pH range 2-12 for all pharmaceuticals. The experiments were performed in a mix pharmaceutical solution concentration of 5 ppm. Equilibration time was 3h. The results showed that the adsorption efficiency of CC for CBZ is at about 75%, at pH 8, while NPR adsorption is the highest at pH 4 (>90%). Based on these results optimal pH value for further experiments on CC samples was adjusted at pH 4 for NPR and at pH 8 for CBZ. The co-doped samples show the highest adsorption at the pH 4 for both pharmaceuticals and this pH value is optimal for further experiments. The pH_{pzc} experiments showed that the adsorbent surface at the pH<7 is positively charged while the pH>7 is negatively charged. Based on this, NPR in the pH range 3-6 is present as an anion (pH>pKa) and interacts with a positively charged adsorbent surface that adsorption is favorable. On the other hand, the pH 2-4 CBZ is present as a cation (pH<pKa) and interacts with the negatively charged adsorbent surface and the adsorption is favorable. Obtained results suggested that the possible adsorption mechanism may be ion-dipole and Van der Waals interaction.

Adsorption kinetics experiments were performed in the 0-24h time interval. Obtained results showed significantly better adsorption characteristics for CCNSs samples than pristine CC (Figure 1). In first hour of adsorption all samples adsorbed more than one half concentration of the pharmaceuticals (for the CBZ adsorption, 47% on the CC sample, 50 % on the $CCNS_2$ and 66% on the $CCNS_3$ sample, respectively; for the NPR adsorption, 53% on the CC sample, 56% on the $CCNS_2$ and 71% on the $CCNS_3$ sample, respectively). Obviously, in the first hour of adsorption, co-doped samples adsorbed a higher quantity of adsorbate. These is might be a consequence of a higher specific surface area and higher numbers of active sites co-doped sample surfaces. After a steady state (24h adsorption), co-doped samples adsorbed more than 96% of both pharmaceuticals compared to pristine CC, which adsorbed 86% of analyts (Figure 2). The experimental kinetics data was fitted with pseudo

first order and pseudo second order and obtained results showed better correspond with pseudo second order (R^2>0,99). These differences in the adsorption process between co-doped samples indicate that the more developed specific surface area is not crucial for higher adsorption performance. Obtained results can be explained by the effect of nitrogen and sulfur incorporation into the turbostratic carbon structure, leading to charge redistribution on the carbon surface and an increase of electron density. This phenomenon leads to stronger electrostatic and dipole-dipole interactions between the ionizable pharmaceutical and charged adsorbent surfaces.

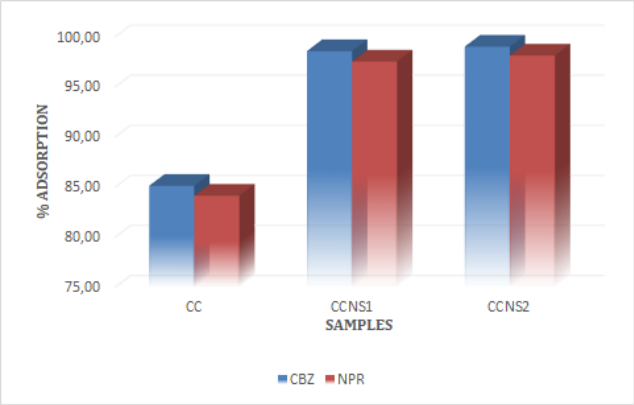

Figure 1. Adsorption of CBZ and NPR after 24h of equilibration on samples CC_0, $CCNS_1$ and $CCNS_2$

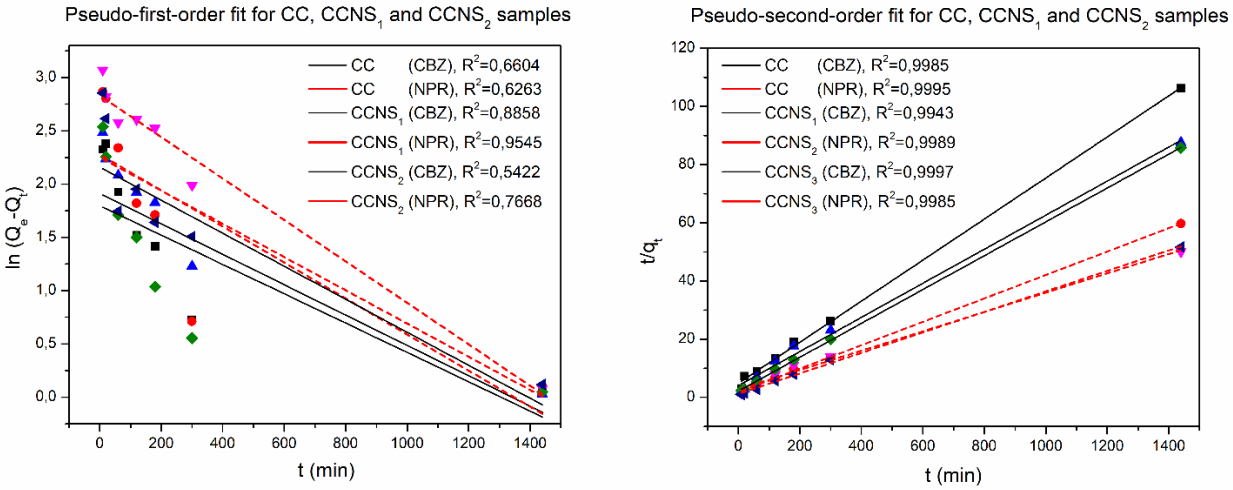

Figure 2. Pseudo-first and pseudo-second-order fit for CBZ and NPR onto CC and CCNSs samples

CONCLUSION

In this work using of nitrogen and sulfur co-doped carbon cryogels for the removal of pharmaceutical residues such as carbamazepine and naproxen from the water was investigated. The elemental analysis confirmed the successful incorporation of nitrogen and sulfur. BET analysis confirmed the significant increase of the specific surface area of co-doped samples than pristine carbon cryogel (up to 1070 m^2/g). The increase is greatest for the sample with the highest nominal concentration of nitrogen and sulfur. The batch adsorption experiments such an effect of pH and adsorption kinetics, were performed. The results of these experiments showed better adsorption performance of N, S co-

doped samples than pristine CC. Further investigation will provide a better insight into the adsorption mechanism. Based on these results, the carbon cryogel and nitrogen and sulfur co-doped carbon cryogel could be a potentially good sorbent for removal carbamazepine and naproxen from water.

Acknowledgment
All authors thank to the Ministry of Education, Science and Technological Development of the Republic of Serbia for the financial support of the research through institutional funding (contract number 451-03-68/2022-14/200017).

REFERENCES

[1] R. W. Pekala, "Organic aerogels from the polycondensation of resorcinol with formaldehyde" *Journal of Materials Science* 24 (1989) 9
[2] P. Veselá and V. Slovák, "N-doped carbon xerogels prepared by ammonia assisted pyrolysis: Surface characterisation, thermal properties and adsorption ability for heavy metal ions" *Journal of Analytical and Applied Pyrolysis* 109 (2014) 266-271
[3] B. Liu, X. Ren, L. Chen, X. Ma, Q. Chen, Q Sun, L. Zhang, P. Si, L. Ci, "High efficient adsorption and storage of iodine on S, N co-doped graphene aerogel" *Journal of Hazardous Materials* 373 (2019) 705-715
[4] Y. Ren, F. Chen, K. Pan, Y. Zhao, L. Ma, S. Wei, "Studies on kinetics, isotherms, thermodynamics and adsorption mechanism of methylene blue by N and S co-doped porous carbon spheres" *Nanomaterials* 11 (2021) 7
[5] A. Kalijadis, N. Gavrilov, B. Jokić, M. Gilić, A. Krstić, I. Pašti, B. Babić, Composition, Structure and Potential Energy Application of Nitrogen Doped Carbon Cryogels, *Mater. Chem. Phys*. 239 (2020) 122120
[6] A.Krstić,A Lolić, M. Mirković, J.Kovač, T. Minović-Arsić, B. Babić, A.Kalijadis, "Synthesis of nitrogen doped and nitrogen and sulfur co-doped carbon cryogels and their application for pharmaceuticals removal from water" – ***Manuscript under review***

CHARACTERIZATION OF GROUNDWATER QUALITY IN THE ALLUVIAL AREA OF DANUBE RIVER NEAR KOSTOLAC BASIN, SERBIA USING CHEMOMETRIC TECHNIQUES

G. Devic[1], M. Pergal[1] and M. Pergal[2]

[1]University of Belgrade, Institute of Chemistry, Technology and Metallurgy National Institute of the Republic of Serbia, Njegoševa 12, 11000 Belgrade, Serbia
[2]Faculty of Chemistry, University of Belgrade, Studentski trg 12-16, Belgrade 11000, Serbia

ABSTRACT

Chemometric techniques were used to analyze the quality of groundwater data sets. Thirteen water quality parameters: T °C, pH, EC, the cations Na^+, K^+, Ca^{2+} and Mg^{2+},the anions Cl^-, SO_4^{2-} NO_3^-, PO_4^{3-}, Total N, Toatal P and eight trace elements Pb, As, Ni, Cu, Cd, Hg, Zn and Cr were measured at 12 different key sampling sites for the winter period of 2017. Cluster Analysis (CA) grouped the sample sites into two clusters based on the similarities of the characteristics of the groundwater quality. Factor analysis (FA) was applied on the log-transformed data sets and allowed the identification of a reduced number of factors with hydrochemical meaning. The results showed severe pollution with EC, Total N, NO_3^-, SO_4^{2-}, Cd, and Pb whereby anthropogenic origin of these contaminants was indicated. The pollution comes from scattered point sources (industrial effluent) and diffuse source agricultural activity. These samples may not be suitable for human consumption; the water quality belongs to class III/IV (contaminated). The concentrations of the other parameters did not exceed the guidelines (WHO and MWQ) for safe water. The results of the chemical analyses showed that the groundwater in the alluvial area of Danube River near Kostolac Basin, Serbia is generally of chemical quality suitable for domestic or agricultural use at most of the tested locations; water quality of class II.

Keywords: alluvial area of Danube River near Kostolac basin, groundwater, heavy metals, water quality parameters, multivariate statistical methods

INTRODUCTION

Water is critical for sustainable development and is indispensable for human health and well being. The global goal of ensuring that human beings have access to acceptable quality water and sufficient quantity faces a number of challenges in the years to come. To provide safe drinking water especially to rural populations, groundwater has been sought as the source in many developing and under developed countries. Groundwater quality in a region is largely determined by both natural processes (dissolution and precipitation of minerals, groundwater velocity, quality of recharge waters and interaction with other types of water aquifers) and anthropogenic activities [1]. The concentrations of nitrate and sulfate increase notably as a result of the large amount of chemical fertilizers used in agriculture Various anthropogenic activities under the shadow of urbanization and the industrial development results in effluent disposal, which introduced into the groundwater system high concentrations of trace metal [2]. Many of these metals are considered essential for human health, but human consumption of poor quality water can lead to different kinds of health, while the use of poor quality water for irrigation reduces crop productivity [3]. According to the WHO organization, about 80% of all the diseases in human beings are caused by water. Groundwater is the principal natural water resources for both drinking and agricultural purposes. In areas where population density is high and human use of the land is intensive, groundwater is especially vulnerable.Virtually any activity whereby chemicals or wastes may be released to the environment, either intentionally or accidentally,

has the potential to pollute groundwater. When ground water becomes contaminated, it is difficult and expensive to clean up. The Danube is an international waterway river, second largest in Europe, with a total length of 2800 km. It belongs to the Black Sea Basin. A large number of industrial and electricity production plants are located on the banks of this river, In Serbia, the only thermal power plant located on the banks of Danube is power plant Kostolac.The purpose of this study was to evaluate the importance of water quality parameters: T °C, pH, EC, cations Na^+, K^+, Ca^{2+} and Mg^{2+}, anions Cl^-, SO_4^{2-} NO_3^- PO_4^{3-}, Total N, Total P, and eight trace elements Pb, As, Ni, Cu, Cd, Hg, Zn and Cr, throughout the application of multivariate techniques and to distinguish the influence of the impact of natural processes and anthropogenic input on the composition of groundwater in alluvial area of Danube River near Kostolac basin. These results provide information to be used for developing better pollution control strategies for the groundwater of Danube River near Kostolac Basin, Serbia.

METHODS

In the current study, 12 well samples were collected and 21 parameters (T, pH, EC, Na^+, K^+, Ca^{2+} and Mg^{2+}, Cl^-, NO_3^-, SO_4^{2-}, PO_4^{3-}, Total N, Total P, Ni, Cd, Cu, Cr, Hg, Pb, As, and Zn) were analyzed using standard procedures [4]. The electrical conductivity (EC), pH and temperature (T) were measured on-site. The concentrations of heavy metals were determined by atomic emission spectrometer (Varian SpectrAA 20-plus). All concentrations of the chemical parameters are expressed in mg/L or μg/L, except for pH (units) and EC (μS/cm). Application of standard methods, careful standardization, procedural blank measurements, and duplicate samples reflect the methodologic quality and results obtained in the research.

Results and Discussion

There was a relatively uniform temperature regime in most groundwater samples (5.7 to 6.9 °C). The pH values of the groundwater samples varied from 6.9 to 7.4 which indicates the water is neutral in nature.

Comparing with the World Health Organization (WHO) and the Water Act and Regulations on the Monitoring of Water Quality introduced by the Government of the Republic of Serbia (MWQ), the variables pH, PO_4^{3-}, all cations, metals such as Ni, As, Cr, Cu, Hg and Zn were less than the maximum or equal to the permissible levels. The concentrations of EC, NO_3^-, total N, Cl^-(only one site exceeded permissible levels), SO_4^{2-}, and metals (Pb and Cd), however, exceeded the standards set by the MWQ and the WHO.

Electrical Conductivity (EC) is considered as one of the important parameters to classify the drinking water quality. Higher EC values indicate increased concentration of dissolved solids and high ionic strength of the groundwater [5]. The EC always showed significantly positive correlations with the cations, and anions. The EC of the studied water samples ranges from 417 to 2030 μs/cm with a mean of 920.10 μs/cm. Though mean value lies within the permissible limits, but 30% samples exceed the limits recommended by MWQ. The order of the relative abundance of the major cations in groundwater was Ca>Mg> Na> K (mg/L) while that of the anions was SO_4^{2-}>Cl^->, > NO_3^-> PO_4^{3-}.

The Danube River is polluted by industrial waters from Kostolac basin in analyzed area and therefore higher values of SO_4^{2-}, (478 mg/L) and NO_3^- (90.63mg/L) are in our samples, but generally values are lower than of waters in worldwide polluted regions around urban and industrial areas [6]. The water quality is of class III. However, these high concentrations of anions may also indicate that the water contains harmful bacteria or other pollutants. Agricultural runoff, inputs of animal and human wastes water, and local point pollution sources are the most significant causes of nutrient enrichment in the analyzed alluvial area. These anions may in higher concentrations render

the water unfit for living organisms, humans. EC, SO_4^{2-}, and Zn showed the highest variance in the distribution of their concentrations-large spatial variations (Fig.1), howeever concentrations of Zn (65- 1980mg/L) in all the groundwater samples were below or equal to the permissible levels. The heavy metals Cd and Pb are known to have a number of negative impacts on human health, such as DNA damage, cancer and damage of the central nervous system. As the Cd (3mg/L) and Pb (77mg/L) levels exceeded the WHO and MWQ a guidelines in 30% samples these heavy metals should actually considered as having a impact on the disease burden of people living in analyzed areas.The water quality belongs to class III/IV (contaminated). The highest pollution by mentioned trace metals comes from scattered point sources (industrial effluent).

The results of the chemical analyses showed that the groundwater in analyzed area at the other tested locations is generally of a chemical quality suitable for domestic or agricultural use, and the water quality is of class II. PCA with Varimax normalized rotation was perfomed in this research. There were two main components indetified. PC 1 explains 59.5% of total variance and these parameters result from mineralization processes and suggests a primarily geogenic origin while PC2 explains 32.8% of the total variance and responsible for the values of the risk ecological index. HCA grouped the sample sites into two clusters based on the similarities of the characteristics of the groundwater quality and in accordance with PCA analyses.

CONCLUSION

Chemometric methods were successively applied to evaluate the spatial variations in groundwater quality and pollution source identifications in the alluvial area of Danube River near Kostolac Basin, in Serbia indicating that the different methods are effective and harmonious with each other. The results suggested that most of the variations are explained by the set of soluble salts (natural) and anthropogenic pollutants. The pollution comes from scattered point sources (industrial effluent) and diffuse sources-agricultural activity. The measured contents of metals in the groundwaters of Serbia indicate the presence of pollution. With 30% of the studied wells being contaminated by EC, Total N, NO_3^- , SO_4^{2-} , Cd and Pb this is an alarming result, and they are the key factors impairing the water quality of the groundwater. The region with the highest trace metal pollution Pb (77 μg/L) and Cd (3 μg/L) is located which is exposed to large uncontrolled metal inputs from anthropogenic sources. The samples containing large amounts of Cd, Pb, , EC, NO_3^- and SO_4^{2-} fall thus into class III/IV. According to the Serbian Water Act regulations, class III/IV water is of unacceptable quality and requires sanitation. The concentrations of other parameters and metals did not exceed the guidelines for safe water. The results of the chemical analyses showed that the ground water is generally of chemical quality suitable for domestic or agricultural use, at most locations tested; water quality of class II.

Acknowledgment

The authors would like to thank the Ministry of Education, Science and Technological Development (Grant No: 146008).

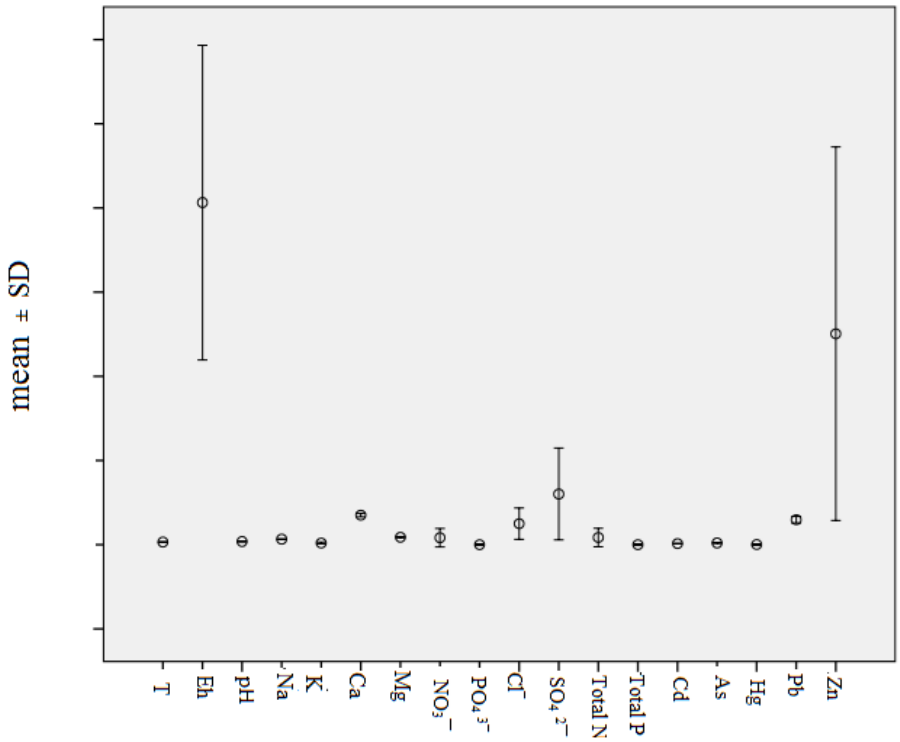

Figure 1. Box and whisker plot showing the variation of chemical constituents in the studied groundwater samples from alluvial area of Danube River near Kostolac Basin

REFERENCES

[1] Andrade E, Palacio HAQ, Souza IH, Leao RA, Guerreiro MJ., Environ Res, 106 (2008) 170–7.
[2] Papaioannou A, Dovrili E, Rigas N, Plageras P, Rigas I, Kokkora M, et al.,Water Resour Manag, 24 (2010) 3257–78.
[3] Azizullah A, Khattak MNK, Richter P, Hader D-P., Environ Int, 37 (2011) 479–97.
[4] Md Bodrud-Dozaa, S.M. Didar-Ul Islam, Md. Tareq Hasan, Ferdous Alam, Md. Morshedul Haque, M.A. Rakib, Md. Ashadudzaman Asad, Md. Abdur Rahman, 2019, *Groundwater for Sustainable Development*, https://doi.org/10.1016/j.gsd.2019.100219
[5] A. Groundwater, Quality and Its Regulating Geochemical Processes in Assiut Province, Egypt, 2022, Exposure and Health, https://doi.org/10.1007/s12403-021-00445-1
[6] B. Choi, S.Yun,Bernhard Mayer,Gi-Tak Chae,Kyoung-Ho Kim,Kangjoo Kim,Yong-Kwon Koh, Hydrological Processes, 24 (2010) 317-330.

HEAVY METAL CONTENTS AND ASSESSMENT OF SOIL CONTAMINATION IN KOSTOLAC BASIN, SERBIA

G. Devic[1], M. Pergal[1] and M. Pergal[2]

[1]University of Belgrade, Institute of Chemistry, Technology and Metallurgy National Institute of the Republic of Serbia, Njegoševa 12, 11000 Belgrade, Serbia
[2]Faculty of Chemistry, University of Belgrade, Studentski trg 12-16, Belgrade 11000, Serbia

ABSTRACT
The aim of this paper is to determine the impact of Power Plants and Mines Kostolac, (TE-KO) on the quality of soil in the surrounding environment. The investigation included the surface soil layer that was sampled and tested during 2017. A total of 20 samples of Kostolac soil were analyzed for the content of 8 heavy metals: Cu, Pb, Cd, Zn, Hg, As, Cr and Ni. The analyses were carried out by atomic absorption spectrophotometer technique according to the EPA method and the following conclusions were made: Kostolac coal ash affects the quality of the surrounding soil in terms of Ni and Cu as evidenced by the strong correlation of the Ni-Cu pair (r = 0.88). The anthropogenic origins of Pb, and Cd elements were addressed due to energy plants activities. Except that, in the area surrounding the analyzed area there is a network of local roads with active traffic, maybe as well response to high valeas of Pb and Cd. The negative correlation between Hg and other heavy metals could be the occurrence of a different causal factor, or a different source of the soil contamination, unburned coal residues and mineral fertilizers. Microelements (Cr, Zn and As) were mostly of a geological origin. The results suggested that most of the variations could be explained by a set of natural inputs and anthropogenic pollution. Among the investigated elements, Ni, Cd, and Hg showed a higher potential ecological risk, than the other metals. Determined indices for the researched heavy metals indicate that some sampling sites do have a moderate ecological risk to the environment in these areas**.**

Keywords: Power Plants and Mines Kostolac, soil; heavy metal; traffic network, intensive farming activities

INTRODUCTION
Soil pollution by heavy metals is a global problem that has recently received a great deal of attention [1]. Globally, more than 10 million soil sites are polluted, and more than 50% of these soil sites are contaminated with heavy metals. Soils may become contaminated by the accumulation of heavy metals and metalloids through emissions from the rapidly expanding industrial areas, mine tailings, disposal of high metal wastes, leaded gasoline and paints, land application of fertilizers, animal manures, sewage sludge, pesticides, wastewater irrigation, coal combustion residues, spillage of petrochemicals, and atmospheric deposition [1]. Heavy metals constitute an ill-defined group of inorganic chemical hazards, and those most commonly found at contaminated sites are lead (Pb), chromium (Cr), arsenic (As), zinc (Zn), cadmium (Cd), copper (Cu), mercury (Hg), and nickel (Ni). Soils are the major sink for heavy metals released into the environment by aforementioned anthropogenic activities and unlike organic contaminants which are oxidized to carbon (IV) oxide by microbial action, most metals do not undergo microbial or chemical degradation [2], and their total concentration in soils persists for a long time after their introduction [2]. Heavy metal contamination of soil may pose risks and hazards to humans and the ecosystem through: direct ingestion or contact with contaminated soil, the food chain (soil-plant-human or soil-plant-animal-human), drinking of contaminated ground water, reduction in food quality (safety and marketability) via phytotoxicity,

reduction in land usability for agricultural production causing food insecurity, and land tenure problems [3].

This paper focused on the objectives determination of soil pollution state from surrounding of Power Plants and Mines Kostolac, (TE-KO) by the important heavy metals pollutants, to evaluate the degree of contamination, and improving their monitoring in the analyzed area.

METHOD

Power Plants and Mines Kostolac, (TE-KO) is located in the northeast of Serbia, about 90 km east of Belgrade. This basin extends over an area of 100 km^2. The Coal-Fired Power Station Kostolac consists of two production plants, which participate in the annual electricity production of the Republic of Serbia with about 14%. One of the main problem associated with electricity generation from coal-combustion is the energy-waste issue. Fly and bottom ash, and unburned coal residues are considered as energy waste and they are very easily dispersed during deposition due to their fine granular size. On the studied area, 20 measuring points were sampled in 2017. On each sampling site, at least three grab samples of active fine-grained surface soils were collected from different places in an area of 5 m2. From this material, a composite sample was taken which weighed up to 1.5kg. This procedure decreased the possible bias caused by local variability. After sampling, the soils were dried in air at room temperature and then sieved through 63μm sieves. Total content of heavy metals (copper (Cu), lead (Pb), cadmium (Cd), zinc (Zn), mercury (Hg), arsenic (As), chromium (Cr) and nickel (Ni) in the soil was extracted by digestion with *aqua regia* in duplicate (0.5 g of soil sample + 10 mL ($HCl:HNO_3$ = 3:1), and concentrations of heavy metals were determined on atomic emission spectrometer (Varian SpectrAA 20-plus).

RESULTS AND DISCUSSION

Basic information-The solubility of trace metals is often a function of pH, and it is affected by the type and content of organic matter (OM). The studied surface samples were typically neutral to sub-alkaline in nature due to the presence of basic salts, i.e. Ca, Mg and K salts, with pH values in the range of 7.36–8.23, and OM contents was from 1.61% to 6.13%, with a mean value 3.81%±2.82% , which means that the sediments were weakly to moderately fortified with OM. In such slightly alkaline sediments, heavy elements are likely to be in a less mobile form. Clay contents of the analysed samples varied from 5.33% to 8.03%, with an average value of 6.67% Table 1 show the results of chemical analysis of heavy metal content in soil samples near the Kostolac basins for copper (Cu), lead (Pb), cadmium (Cd), zinc (Zn), mercury (Hg), arsenic (As), chromium (Cr) and nickel (Ni). The results are compared with the permissible and remediation limit values in compliance with relevant legislation [4]. Higher concentrations of Ni (76.20 ± 9.84 mg/kg), Cu (38.08 ± 8.35), Hg (35.1 ± 8.93 mg/kg), Cd (1.49 ± 0.39 mg/kg) and Pb (86.65 ±8.80 mg/kg) in soil samples have been observed, so after comparing them with guidelines, it can be said that there is a potential risk for human health. In the world, the average concentration of Ni in the soil is determined at 40 mg/kg of soil, while in almost all analyzed samples the concentrations of Ni significantly above of 40 mg/kg. Although the origin of Ni in the soil is very variable and it is difficult to focus on just one source of emission, the impact of ash is undeniable. In the area surrounding the Kostolac coal basin, nickel was previously shown to have an increased concentration.The element that exceeds the limit value, but not above the remediation value in most samples collected from the Kostolac soil is copper. The correlation coefficient ($r=0.88$; $p = 0.01$) for the pair Cu-Ni indicates their common origin and the fact that Kostolac ash is their main source. Interestingly, the high concentration of these heavy metals in the soil is a very common occurrence in the vicinity of coal-fired power plants and many studies concluded that lignite combustion and its unburned residuals are responsiblen for this situation. The concentrations of Cd (80% of all samples) and Pb (16% of all samples) were exceeded only the

Serbian limit values, and the anthropogenic origins of these elements were addressed due to energy plants activities. Except that, in the area surrounding the analyzed area there is a network of local roads with active traffic, maybe as well response to high valeas of Pb and Cd. In contrast, to mentioned metals, the negative correlation between Hg and other heavy metals could be the occurrence of a different causal factor, or a different source of the soil contamination. Unburned coal residues and mineral fertilizers usually represent the main source of mercury in the soil, pesticides can also be a significant source. Howeever, it is very important to emphasize that mercury has the tendency to transform and volatilize in the presence of microorganisms in the soil. Based on the pollution indices, except Ni and Cd, Hg made the most dominant contribution, with a higher contamination risk being determined in this studied area The heavy metals that do not exceed the permissible values in any of the analyzed samples are chromium, zinc and arsenic and were mostly of a geological origin.

Table 1. Descriptive Statistics of investigated heavy metals in soil samples in the surroundings of Kostolac basin

Chemical Element (mg/kg)	Minimum	Maximum	Mean ±St. Deviation	Permissible values	Remediation values
Cr	1.38	8.03	3.38±1.80	100	380
Pb	27.83	86.65	39.36±8.80	85	530
Cd	0.17	1.49	0.92±0.390	0.8	12
Cu	8.22	38.08	21.66±8.35	36	190
Ni	40.67	76.20	59.23±9.84	35	210
Zn	33.71	103.83	62.28±18.04	140	720
As	0.05	1.1	0.33±0.36	29	55
Hg	0.05	35.1	3.02±8.93	0.3	10

CONCLUSION

In this paper, we reached the conclusion that the soil from the Kostolac landfill affects the quality of surrounding soil in terms of contamination by nickel (Ni), copper (Cu), cadmium (Cd), lead (Pb) and mercury (Hg) whose concentrations in the analyzed samples are above the permissible limit values. The Ni and Cu contents correlated closely among each other carrying the similar information, Kostolac ash is their main source. As for heavy metals such as lead and cadmium whose concentrations exceeded the limit values in Kostolac soil samples, the investigations suggest that apart from ash, other sources may be responsible for this contamination, such as motor vehicle traffic on the roads in subject area. The maximum concentration of Hg in soil samples of the study area is 35 mg/kg with an average value of 3.02 mg/kg. The negative correlation between Hg and other heavy metals could be the occurrence of a different source of the soil contamination, like mineral fertilizers or pesticides. Arsenic, zinc and chromium mainly derived from the process of soil formation, natural source. Based on the pollution indices, except Ni and Cd, Hg made the most dominant contribution, with a higher contamination risk being determined in this studied area. Therefore, increasing attention shall be needed for monitoring the heavy metal pollution in soils in the areas, Kostolac basin.

Acknowledgment

The authors would like to thank the Ministry of Education, Science and Technological Development (Grant No: 146008).

REFERENCES

[1] Jiang, Y.; Chao, S.; Liu, J.; Yang, Y.; Chen, Y.; Zhang, A.; Cao, H. Source apportionment and health risk assessment of heavy metals in soil for a township in Jiangsu Province, China. Chemosphere, 168 (2017) 1658–1668

[2] Peng, X.; Shi, G.S.; Liu, G.; Xu, J.; Tian, Y.; Zhang, Y.; Feng, Y.; Russell, A.G. Source apportionment and heavy metal health risk (HMHR) quantification from sources in a southern city in China, using an ME2-HMHR model. Environ. Pollut. 221 (2017) 335–342

[3] Raymond A. Wuana, Felix E. Okieimen, "Heavy Metals in Contaminated Soils: A Review of Sources, Chemistry, Risks and Best Available Strategies for Remediation", *International Scholarly Research Notices*, vol. 2011, Article ID 402647, 20 pages, 2011. https://doi.org/10.5402/2011/402647

[4] Official gazette of RS 88/2010. Program of systematic monitoring of soil quality indicators for assessing the risk of soil degradation and methodology for development of remediation programs.

CONTENT OF ^{90}Sr IN MONASTERY SPRING WATERS

N. Sarap[1], M. Ničić[2] and M. Janković[1]

[1]University of Belgrade, Vinča Institute of Nuclear Sciences, National Institute of the Republic of Serbia, Radiation and Environmental Protection Department, Mike Petrovića Alasa 12-14, 11001 Belgrade, Serbia. (natasas@vinca.rs)
[2]HBIS GROUP SERBIA IRON & STEEL D.O.O. BEOGRAD, Carigradska 55, Radinac, 11300 Smederevo, Serbia.

ABSTRACT
The research was focused on the examination of level of ^{90}Sr, as one of the most toxic radionuclides of artificial origin, in spring waters from the yards of selected monasteries from the territory of the Republic of Serbia, as well as the Montenegro, considering that their radiological quality assessment has not been confirmed so far. After collection and appropriate chemical-analytical treatment of samples, the ^{90}Sr activity concentration was determined by beta spectrometry method. Knowing the level of ^{90}Sr activity in drinking water is extremely important because it allows comparison with the recommended value, above which it is assessed whether the presence of the radionuclide in drinking water poses a risk to human health, which requires protection measures or remedial measures to improve water quality in accordance with the requirements for the protection of human health from the point of view of protection against ionizing radiation.

INTRODUCTION
The worldwide presence of ^{90}Sr, to measurable amount, has been caused intentionally or accidentally since the 1940s, as a consequence of various human nuclear activities. Chernobyl NPP's accident has become an important source of ^{90}Sr after 1986 [1]. Radionuclide ^{90}Sr is one of the main fission products of uranium in the nuclear reactor and can be obtained from the reprocessing of spent nuclear fuels. The ^{90}Sr has maximum β radiation energy of 0.546 MeV and a half-life of 28.8 years [2]. The radiotoxic effect of ^{90}Sr is additionally increased by progeny ^{90}Y that can be generated from the beta decay of ^{90}Sr. The ^{90}Y is a pure β particle emitting radionuclide that emits a strong beta radiation with maximum energy at 2.28 MeV while it has a short half-life of 64 h. The product of ^{90}Y decay is ^{90}Zr, which is a stable isotope [3].

Due to fact that ^{90}Sr emits the low energy and range of β particles, this radionuclide poses a threat to health only if it is introduced into the body by inhalation or ingestion or if it is brought into direct contact with the skin. Food and drinking water are the largest sources of exposure. Grain, leafy vegetables, and dairy products contribute the greatest percentage of dietary ^{90}Sr to humans [2]. In order to maximally protect against the toxic effects of the mentioned radionuclide, methods for its determination in water samples, soil, air, food products, etc. have been developed [4]. Limited data are available for ^{90}Sr due to its complicated and time-consuming sample preparation [5]. Since ^{90}Sr is a pure beta emitter and therefore one has to prepare pure beta sources, meaning extraction and clean-up of the sample, before it can be analyzed by beta spectrometry method.

The waters in the monastery yards are regularly subjected to chemical and bacteriological analysis. The aim of conducted research was to confirm the radiological safety of spring waters from the yards of the selected monasteries. For this purpose, determination of ^{90}Sr in monastery spring water samples was performed by application of developed radiochemical analytical procedure based on the approach is to isolate the daughter nuclide of ^{90}Y, which is in equilibrium with ^{90}Sr. After separates ^{90}Y from ^{90}Sr by precipitation, this radionuclide is measured with beta spectrometry. The beta decay of ^{90}Y (half-life of 64 h) is measured through several consecutive counts by means of a beta gas proportional

counting system. This method is highly sensitive and suitable for activities in the mBq range, but sometimes time is limiting factor.

METHODS

The sampling was conducted during the May of 2019. The drinking water samples collected from the yards of the following monasteries at the territory of the Republic of Serbia, as well as the Montenegro (Figure 1.): Monastery Rajinovac (Begaljica, Belgrade), Monastery Rakovica (Rakovica, Belgrade), Monastery Sveti Stefan (Lipovac, Aleksinac), Monastery Žiča (Kraljevo), Monastery Mileševa (Prijepolje) and Monastery Sveta Trojica (Pljevlja).

Figure 1. The map of sampling sites

The initial volume of water samples was approximately 10 L. The each water sample was evaporated to dry residue under infrared lamp, then mineralized at 450 °C. The mineralized residue was dissolved in hydrochloric acid, and then further steps of radiochemical analytical procedure for determination of ^{90}Sr was performed. After applied procedure the samples were stored for 18 days to reach the radioactive equilibrium between ^{90}Sr and ^{90}Y. After 18 days ^{90}Y departed on collector $Al(OH)_3$, which was then fired till oxide. Measurement was performed on low level gas flow proportional counter THERMO EBERLINE FHT 770 T (ESM Eberline Instruments GmbH, Erlangen, Germany). The used counter is suitable for measuring low β activities, which makes it ideal for ^{90}Sr analysis. The counting time was 5400 s. The efficiency of counter for a beta count was approximately 35 %.

The activity concentration of ^{90}Sr (A_{Sr}) in water samples given in Bq/L was calculated by equation:

$$A_{Sr} = \frac{(R - R_0) \cdot e^{\frac{\ln 2}{T_{1/2}} \cdot t}}{\varepsilon \cdot \eta_{Al} \cdot \eta \cdot V}$$

where R is count rate of the measured sample (1/s), R_o denotes background count rate (1/s), t is time elapsed from ^{90}Y separation (h), $T_{1/2}$ is half-life of ^{90}Y (h), ε is efficiency of the detector, η_{Al} is yield factor of aluminium for the measured sample, η is yield factor of the used method and V is the volume of water sample (L).

The minimum detectable activity (*MDA*) was evaluated using formula:

$$MDA = \frac{LD \cdot e^{\frac{\ln 2}{T_{1/2}} \cdot t}}{V}$$

where LD is detection limit of beta radiation (1/s) which is automated calculated by used software.

The annual effective dose rate to an individual, D (Sv) caused by absorption of artificial radionuclide ^{90}Sr in water can be calculated using formula [6]:

$$D = A_{Sr} \cdot \eta \cdot V$$

where η is the age dependent dose conversion factor (Sv/Bq) and V is the annual consumption water of 730 L based on assumption daily consumption water of 200 mL.

RESULTS AND DISCUSSION

The activity concentrations of ^{90}Sr in investigated monastery spring water samples are presented in Table 1. The obtained values showed that the activity concentrations of ^{90}Sr in the investigated waters were below detection limit. The derived activity concentration of ^{90}Sr in drinking water is 4.9 Bq/L [7]. Given that the obtained activity concentrations of ^{90}Sr in analyzed monastery drinking water samples are less than above mentioned value, the all investigated samples met the criteria defined by Regulation on limits of radionuclide content in drinking water, foodstuffs, feeding stuffs, drugs, items of general use, building materials and other goods to be placed on the market [7].

Table 1. The activity concentrations of ^{90}Sr in investigated monastery spring water samples

The name of the monastery	Measured activity concentration of ^{90}Sr (Bq/L)
Rajinovac	< 0.0060
Rakovica	< 0.0072
Sveti Stefan	< 0.0046
Žiča	< 0.0052
Mileševa	< 0.0058
Sveta Trojica	< 0.0053

The measurement results found in this study can be used to determine effective dose rates stemming from ingestion of artificial radionuclide ^{90}Sr due water consumption. The annual effective dose equivalent due to consumption of investigated waters is calculated based on the corresponding age dependent dose conversion factor for ^{90}Sr [6]. Considering the measured activity concentrations of ^{90}Sr in all water samples were below MDA, the obtained values of annual effective dose are lower than 0.1 mSv recommended reference level [7].

CONCLUSION

The subject of this study was to determine level of ^{90}Sr activity in spring drinking waters from the yards of the selected monasteries at the territory of the Republic of Serbia, as well as the Montenegro. Determination of artificial radioactivity level in drinking water has importance because it allows the assessment of population exposure to radiation due consumption of the water. To our knowledge, we are the first to report of this investigation type. Therefore, our results represent valuable data guiding us into further research on tracking ^{90}Sr content and behavior in this type of water. In the future, the investigation will be expanded and the research should cover a larger number of monasteries.

Acknowledgment

This work was supported by the Ministry of Education, Science and Technological Development of the Republic of Serbia (grant no 451−03−68/2022−14/200017).

REFERENCES

[1] Cwanek, A., Lokas, E., Dinh, C. N., Zagórski, P., Singh, S. M., Szufa, K., Tomankiewicz, E., J. Radioanal. Nucl. Ch., 327 (2021) 485.
[2] Agency for Toxic Substances and Disease Registry (ATSDR), Toxicological profile for strontium, U.S. Department of health and human services, Public Health Service, Toxicology Information Branch, Atlanta, 2004.
[3] Pichestapong, P., Sriwiang, W., Injarean, U., Energy Procedia, 89 (2016) 366.
[4] Vajda, N., Kim, C. K., Appl. Radiat. Isotopes, 68 (2010) 2306.
[5] Zehringer, M., Abraham, J., Kammerer, F., Syla, V., Wagmann, M., J. Chem. Chem. Eng., 11 (2017) 116.
[6] Janković, M. M., Sarap, N. B., Todorović, D. J., Joksić, J. D., Nucl. Technol. Radiat. Prot., 28 (2013) 284.
[7] Official Gazette of the Republic of Serbia, No. 36/2018, 2018.

L *– Phase Boundaries, Colloids, Liquid Crystals, Surface-Active Substances*

FORMATION AND STRUCTURE OF TRANSIENT PHASE STATE NEAR SOLID SURFACE IN ORGANIC SYSTEMS

I.I. Grinvald and R.V. Kapustin

Nizhny Novgorod State Technical University n.a. R.E. Alekseev
Minin str. 24, 603950 Nizhniy Novgorod, Russia (grinwald@mts-nn.ru)

ABSTRACT

This work discusses the appearance mechanism and structure of a transient phase state in the gas-liquid layers of organic systems forming near a solid surface at evaporation-condensation process in terms of IR and DFT study. Due to its ambiguous phase spectral characteristics, this state resembles a supercritical fluid that forms at high temperature and pressure and represents both gas and liquid. Under ambient conditions, these layers represent an intermediate stage of the gas-liquid phase transition. Similar transformations caused by supramolecular and variable spatial arrangement of organic liquids play a crucial role in the heterogeneous catalysis.

The substituted methane, ethane, silane, and aromatic organic systems have been selected because they are involved in many preparative and technological processes, where the transient phase state phenomenon might provide the reaction mechanism. Besides, this selection allows to evaluate the role of different intermolecular bonding types in the near-surface transformation.

The experimental approach to the gas-liquid layers preparation and its investigation by IR spectral methods includes four possible pathways: 1) evaporation into a small and enclosed space of an optical cell at ambient temperature combined with a compression-expansion procedure; 2) evaporation by heating between optical windows in a wide temperature range from 320 to 400 K; 3) compressing a liquid with an optical material (KBr) into a solid matrix; 4) low-temperature films freezing-defrosting procedure in a wide temperature range from 20 to 200 K.

IR study of the methane systems (CCl_4, $CHCl_3$, CH_2Cl_2, CH_3I, CH_3NO_2, CH_3CN, CH_3OH) has revealed the formation of the transient phase state with dual gas-liquid properties provided by different cluster shapes of the molecular system. Transformations of a similar state in the silane systems ($SiCl_4$, $SiHCl_3$, SiH_2Cl_2) lead to a significant change in their properties, particularly, in the considerably growing resistance to an air oxidation.

IR data for the substituted ethane systems (1,2-$C_2H_4Cl_2$, 1,1,2-$C_2H_3Cl_3$, 1,1,2,2-$C_2H_2Cl_4$) show that the evaporation-generated layers have both liquid and gas phase properties like in methane systems. Presumably, this transient state is integrated into the spatial arrangement of the liquid bulk due to the intermolecular hydrogen bond.

IR data for aromatic systems (C_6H_6, C_4H_4O, C_4H_4S) also indicate the near-surface transformations that can be assigned to the transient phase formation. The behavior of this state reminds the disintegrating of the aromatic rings' stack arrangement in the gas-liquid systems.

DFT modeling of the transient state formation and transformations shows that it possibly appears due to the mobile molecular clusters' appearance not only in the liquid, but in the gas phase as well. These clusters have different structure accompanied by halogen–carbon or halogen–silane interactions, classic hydrogen bond formation, or intermolecular π-bonding as in aromatic systems.

All of the above leads to the conclusion that at the condensation-evaporation process of the organic liquids, the transient phase state with the dual gas-liquid properties forms near a solid surface. The most significant property associated with the formation of these layers is the activation of the initial components, bypassing the stage of a complex formation with a catalyst. This state to some extent can be considered as a fluid-like system forming at ambient conditions.

M – Complex Compounds

NEW MACROCYCLIC Cu(II) COMPLEXES WITH LEUCINE/ISOLEUCINE CO-LIGANDS

M. Antonijević Nikolić[1], B. Dražić[2] and S. Tanasković[2]

[1]*Academy of Applied Studies Šabac, Department for Medical, Business and Technological Studies, Šabac, Serbia (nikanto@ptt.rs)*
[2] *Faculty of Pharmacy, University of Belgrade, Belgrade, Serbia.*

ABSTRACT
Two new bridged dinuclear Cu(II) compounds of tpmc (*N,N',N'',N'''*-tetrakis(2-pyridylmethyl)-1,4,8,11-tetraazacyclotetradecane) and co-ligands L-leucine or L-isoleucine have been synthesized and characterized. The complexes were prepared in the reaction [Cutpmc]$(ClO_4)_4 \cdot 6H_2O$ and aminocarboxylates. The complexes were characterized by elemental analysis (C, H, and N), molar electrical conductivity and spectral methods (UV/vis and FTIR). The analytical data of the complexes show the formation of binuclear complexes with the proposed formula $[Cu_2(L)tpmc](ClO_4)_4$, L=L-leucine (**1**) and L=L-isoleucine (**2**). The spectroscopic data suggested that the tpmc is coordinated to Cu(II) through eight N donors and amino carboxylate ligands via their carboxylate ion moieties.

INTRODUCTION
Macrocyclic ligands are polydentate ligands having their donor atoms either incorporated in or attached to a cyclic backbone. Macrocyclic ligand N,N',N",N"'-tetrakis(2-pyridylmethyl)-1,4,8,11-tetraazacyclotetradecane (tpmc) is polydentate ligand with four 2-pyridylmethyl groups and with eight N donors. The flexible macrocyclic ring usually coordinates two metal ions in exo-coordination mode. In order to achieve a stable structure, additional ligands bridge the central atoms in complexes. Macrocyclic compounds have attracted interest because of their unlimited applications in various fields of research [1].

A great number of mixed-ligand Cu(II) complexes containing pendant macrocycle tpmc and one or two additional ligands of various type have hitherto been described [2-4]. On the other hand, the fact is that amino acids or their derivate are attractive ligands due to their biological activity (acids are the building blocks of proteins and take part in all major processes in organisms), often used as ligands in the synthesis of coordination compounds. Amino acid, like other aminocarboxylato ligands, are bonded in one of many modes: as *N*-monodentate; *N,O*-bonded as chelate in mononuclear complexes or in binuclear as a bridging ligand between two metallic centers, *N,O,O*'-mode. Also, one or both oxygens are included in the coordination and $–NH_2$ group resting uncoordinated. They are bonded: unsymmetrically, symmetrically or in a combined chelate-bridged manner [5].

In addition, copper shows significant biochemical action. It is found as a trace metal and as an ingredient in various exogenously applied compounds in humans. It has a role in biological processes related to human physiology and pathology. Copper (II) complexes are potential antimicrobial, antiviral, anti-inflammatory and antitumor agents, enzyme inhibitors or chemical nucleases. The biochemical effect of the Cu complexes are significant nonsteroidal anti-inflammatory drugs (NSAIDs). Numerous Cu (II) NSAID complexes show enhanced anti-inflammatory and anti-ulcerogenic activity, as well as reduced gastrointestinal toxicity compared to non-complex drugs [6]. The difference in response of tumor cell and normal cell towards copper possibly laid the foundation of copper complexes evolution as anticancer agents. However, a large number of copper complexes with various sets of ligands have been prepared for this cause and displayed noteworthy *in vitro* cytotoxicity.

The aim of this paper is the preparation and characterization of Cu(II)tpmc complexes with L-leucine/L-isoleucine as co-ligands (Figure 1).

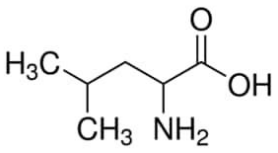

L-leucine
2-amino-4-methylpentanoic acid

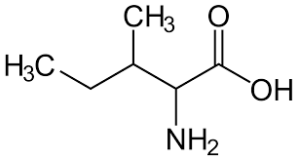

L-isoleucine
2-amino-3-methylpentanoic acid

Figure 1. Aminocarboxylate co-ligands

METHODS

Preparation

To a stirred CH_3CN solution (10 mL) containing $[Cu_2tpmc](ClO_4)_4\cdot$(0.1506 g) was added a 5 mL solution (mixture CH_3CN and H_2O) of leucine (leu) or isoleucine (ileu) (0.0302 g), pH = 6. After stirring and reflux during 1,5 h on the 80ºC blue reaction solution was cooled to room temperature. The resulting solution was filtered and left in the fridge. After a few days blue products are separated by suction. Obtained complexes were washed with H_2O.

$[Cu_2(leu)tpmc](ClO_4)_4$ (1), Yield 81 %. Anal. Found C 39.51; H 4.39; N 10.81. Calcd.for $C_{40}H_{57}O_{18}N_9Cu_2Cl_4$ (FW = 1220.91) C 39.35; H 4.70; N 10.33. Solubility (t=20±2 °C) wellsoluble in CH_3CN, DMSO and DMF, insoluble in EtOH, CH_3OH, $(CH_3)_2CO$ and H_2O.

$[Cu_2(ileu)tpmc](ClO_4)_4$ (2), Yield 78 %. Anal. Found C 38.92; H 4.34; N 10.68. Calcd.for $C_{40}H_{57}O_{18}N_9Cu_2Cl_4$ (FW = 1220.91) C 39.35; H 4.70; N 10.33. Solubility (t=20±2 °C) well soluble in DMSO, $(CH_3)_2CO$ and DMF, insoluble in EtOH, CH_3OH, CH_3CN and H_2O.

Measurements

Elemental analyses were performed by standard methods in the Centre for Instrumental Analyses, ICTM in Belgrade. Electronic absorption spectra of complexes in CH_3CN ($c=1\cdot10^{-3}$ M) were recorded on GBC UV-Vis spectrophotometer Cintra 20. FTIR spectra were recorded on NICOLET 6700 FTIR (ATR technique) in the range 400-4000 cm^{-1}. Molar conductivities were measured on conductometer HANNA instruments HI 8820N (at 20 ± 2ºC) in CH_3CN ($c=1\cdot10^{-3}$ M).

RESULTS AND DISCUSSION

In the reaction of the $[Cu_2tpmc](ClO_4)_4\cdot6H_2O$ with the aminocarboxylate ligands L-leucine or L-isoleucine, two new binuclear complexes were obtained. The composition of the complex was proposed based on the results of elemental analysis. The electrical molar conductivity (Λ_M =527 Scm^2mol^{-1} (1) and Λ_M =481 Scm^2mol^{-1} (2)) corresponds to the electrolyte type 1:4.

Spectral studies

The electronic spectra of both complexes reveal a single broad d–d bands in the visible region at 681.5 nm (ε=570 and 534 (**1**) $dm^3mol^{-1}cm^{-1}$ (**2**)). As expected, the transition energies are in the typical region for five-coordinate copper(II) complexes [7].

The absorption bands in the electronic spectra of similar Cu(II) complexes are also in the range 645–648 nm [8] for glicine or alanine co-ligands. According to this result, it can be assumed that new complexes have the same chromophore (CuN_4O) and five-coordinate Cu(II) as in the similar compounds. In UV part of spectra several sharp unresolved bands in the range from 210 to 290 nm (ε = 5000-5711 $dm^3\ mol^{-1}\ cm^{-1}$) were assigned to intraligand transitions bands. Intraligand transitions were found in the spectra of ligands in the range 220–280 nm.

In FTIR spectra of both complexes the following characteristic bands were found: 1611 cm^{-1} from skeletal vibrations of the pyridine from coordinated tpmc ligand (sharp) which was found at 1588 in the spectrum of free tpmc, ~1100 cm^{-1} from $\nu(ClO_4^-)$ (intensive) shows no splitting, indicating the absence of coordinated ClO_4^- in the complexes and at 630 cm^{-1} from $\delta(ClO_4^-)$ (medium), 2965 cm^{-1} from $\nu(NH_3^+)$ which was found at 2959 and 2967 cm^{-1} in the spectra of L-leucine or L-isoleucine.

As co-ligand in dinuclear complexes aminocarboxylate ligand could be coordinated on several modes represented on **Figure 2**.

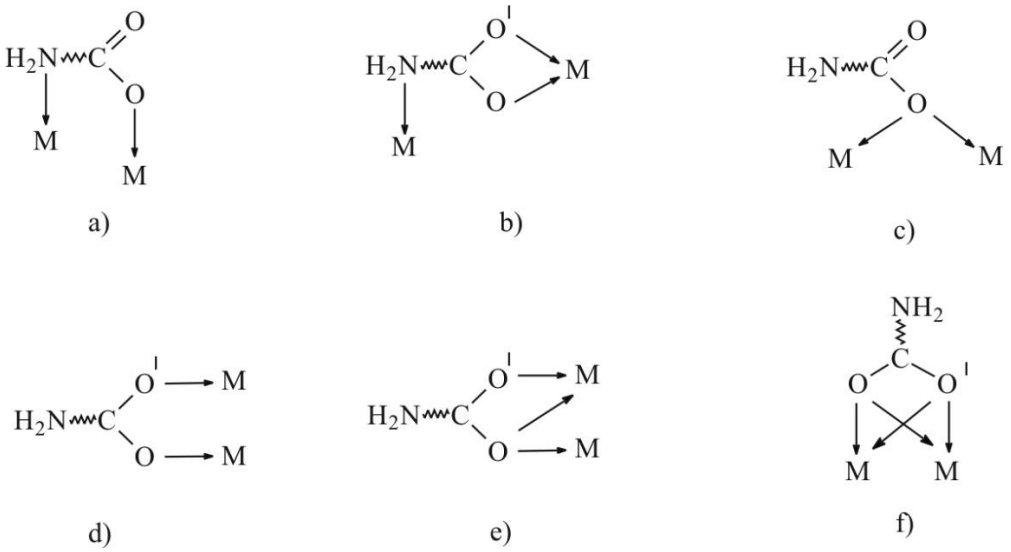

Figure 2. Some of the possible coordination modes of aminocarboxylate ligands.

The FTIR spectra exhibit significant features in the $\nu(NH_3^+)$ and $\nu(COO^-)$ regions. Free amino acids exist as zwitterions ($^+$NH3CH(R)COO^-). The FTIR spectra show evidence in support of the involvement of carboxylate group in coordination.

In comparison with free amino acids (zwitterions), the $\nu_{asym}(OCO^-)$ and $\nu_{sym}(OCO^-)$ shows shifts, which confirm the coordination of the carboxylate group, which is the case when OCO- participates in coordination. Two characteristic strong bands observed at 1574 and 1374 cm^{-1} are attributed to the asymmetric $\nu_{asym}(COO^-)$ and symmetric $\nu_{sym}(COO^-)$ carboxylate stretches respectively, indicating the coordination of the carboxylate oxygen to metal ions in the complexes. The characteristic bands $\nu_{asym}(COO^-)$ and $\nu_{sym}(COO^-)$ at 1584 and 1367 cm^{-1} for L-leucine and bands at 1584 and 1354 cm^{-1} for L-isoleucine were observed.

The mode of coordination of the carboxylate can be deduced from the magnitude of separation between the $\nu_{asym}(COO^-)$ and $\nu_{sym}(COO^-)$, that is, $\Delta\nu(COO^-)$. For the synthesized metal complexes, values for $\Delta\nu(COO^-)$ are 200 cm^{-1}, while for L-leucine or L-isoleucine is 217 cm^{-1} ond 230 cm^{-1} respectively. This could indicate the presence of carboxylate bridging mode of metal-oxygen-carbon-oxygen-metal (M-O-C-O-M) type between two metal centers in complexes (**Figure 2d**) [8,9]. This type of coordination mode of ligands L-glicine or L-alanine was confirmed by X-ray structure analyses of the Cu(II)-tpmc complexes [8].

On the basis spectral and other methods it is proposed that both Cu(II) ions are *exo* penta-coordinated using, besides oxygen atom, two cyclam's and two pyridyl nitrogens. Macrocycle ligand tpmc is *exo* coordinated to Cu(II), probably in the boat conformation [8].

CONCLUSION

New binuclear Cu (II) complexes with octaazamacrocyclic ligand tpmc and L-leucine/L-isoleucine were obtained and characterized by elemental analysis (C, H, and N), molar electrical conductivity and spectral methods (UV/vis and FTIR). Based on that data it is proposed that carboxylic group of aminocarboxylate bridges two Cu(II) ions.

Acknowledgment

This work was supported by the Ministry of Education, Science and Technological Development of the Republic of Serbia (Grant No. 451-03-68/2020-14/200161).

REFERENCES

[1] W. Sibert, A. H.Cory, J. G.Cory, Chem. Commun., 2 (2002) 154-155.
[2] P. M. Reddy, R. Rohini, E. Ravi Krishna, A. Hu, V. Ravinder, Int. J. Mol. Sci., 13 (2012) 4982-4992.
[3] R. S. Prabhat, R. Singh, S. Pawar, A. Chauhan, J. Am. Sci., 6(9) (2010) 559-564.
[4] C. S. Dilip, V. Sivakumar, J. J. Prince, Indian J. Chem. Tech., 19 (2012) 351-356.
[5] M. Antonijević-Nikolić, J. Antić-Stanković, S. B. Tanasković, M. J. Korabik, G. Gojgić-Cvijović, G. Vučković, J. Mol. Struct., 1054–1055 (2013) 297–306.
[6] I. Iakovidis,I. Delimaris, S. M. Piperakis, Molecular Biology International, 2011 (2011) Article ID 594529
[7] P. Comba, T. W. Hambley, M. A. Hitchman, H. Stratemeier, Inorg. Chem., 34 (1995) 3903–3911.
[8] M Antonijević Nikolić, B. Dražić, B. Cristóvão, A. Bartyzel, B. Miroslaw, S. Tanasković, J. Mol. Struct, 1252 (2022) 131969.
[9] N. Raman, J. Joseph, A. Sakthivel, R. Jeyamurugan, Journal of the Chilean Chemistry Society. 54(4) (2009) 354 – 357.

COMPARISON OF NH···O INTERACTION OF COORDINATED AMMONIA AND ETYLENEDIAMINE

J. M. Živković[1], S. S. Zrilić[1] and S. D. Zarić[2]

[1] *Innovative Centre of Department of Chemistry, Studentski trg 12-16, 11000 Belgrade, Serbia. (andric_jelena@chem.bg.ac.rs)*
[2] *University of Belgrade, Faculty of Chemistry, Studentski trg 12-16, 11000 Belgrade, Serbia.*

ABSTRACT
The NH···O interactions for coordinated ammonia and ethylenediamine were compared. The results have shown that in crystal structures coordinated ammonia have more pronounced tendency to build bifurcated interactions than coordinated ethylenediamine. The calculations revealed that coordinated ethylenediamine has stronger interaction due to higher electrostatic potential on interacting atom and less side repulsive interaction.

INTRODUCTION
Hydrogen bonding has been widely studied between water molecules. The interaction energy between two water molecules estimated at CCSD(T)/CBS level is -4.84 kcal/mol [1]. When one water molecule coordinates to a metal ion, the hydrogen bond interaction with non-coordinated water molecule is stronger, due to higher positive electrostatic potentials at hydrogen atom of coordinated water molecule. The interaction energy of hydrogen bond of water molecule in doubly charged zinc tetrahedral complexes is -24.0 kcal/mol [2]. The increased strength of interaction upon coordination can be observed as shortening of d_{HO} distances in the analysis of crystal structures from the Cambridge Structural Database (CSD). The peaks of d_{HO} distance in the crystal structures for non-coordinated water molecules are between 1.8-2.0 Å and 1.6-1.8 Å when one water molecule is coordinated.
Hydrogen bond interactions of coordinated water in octahedral complexes with different nucleic acid bases are also strong and span from -6.7 kcal/mol to -49.9 kcal/mol [3]. These interaction energies are several times stronger than for non-coordinated water-nucleic acid bases (-4.6 to -8.7 kcal/mol) [3].
The hydrogen bonds of ammine group were studied in different systems [4,5]. The NH···O hydrogen bond interactions are found in DNA and protein chains, where they play important role in stabilizing DNA and proteins. Recently, the results about hydrogen bond interactions of ammine groups have been published [4,5]. Here we made comparison between NH···O interactions for coordinated ammonia and ethylenediamine.

METHODS
The Cambridge Structural Database (CSD) search was used to find contacts for coordinated ammonia/water and coordinated ethylenediamine/water molecules. The criteria for contacts were the d_{HO} distance less than 4.0 Å, and the angle α (N-H···O) larger than 110° (Figure 1) [4,5].
The energy of NH···O hydrogen bond interactions was calculated at the M06L-GD3/def2-TZVPP level, since it produces results that are in good agreement with the CCSD(T)/CBS method which is considered as the gold standard in quantum chemistry [4,5].
The electrostatic potentials for cobalt(II) complexes were computed at M06L-GD3/def2-TZVPP level, on surfaces defined as the 0.001 au (electronbohr^{-3}) contours of the electronic densities. The positive potentials on hydrogen atoms involved in the interaction for rigid monomers (Vs) were calculated at the same level of theory [4,5].

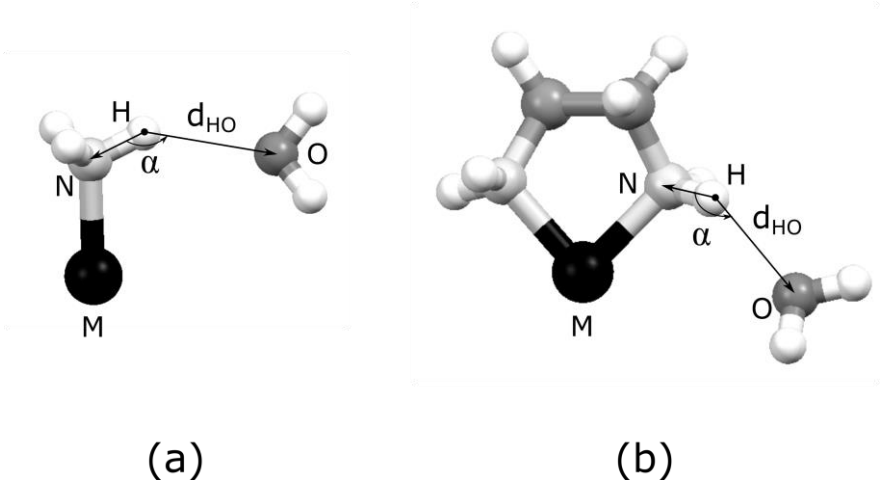

Figure 1. The geometrical parameters used for search and analysis of CSD data were d_{HO} distance and α angle for hydrogen bond for coordinated ammonia/water (a), and coordinated ethylenediamine/water (b).

RESULTS AND DISCUSSION

The results from CSD search for coordinated ammonia have shown that the peak of d_{HO} distance for coordinated ammonia is in the 2.0 Å to 2.2 Å range, while the peak of d_{HO} distance for ethylenediamine is shorter, lying within the 1.8 Å to 2.0 Å range (Figure 2). The results for distributions of α angle for coordinated ammonia and ethylenediamine do not show particular tendency for certain angle. The maximum of the distribution of angle α for coordinated ammonia is at 160° - 170°, while for coordinated ethylenediamine is at 150° - 160° (Figure 2). These data indicate the existence of monofurcated and bifurcated interactions for both coordinated ammonia and ethylenediamine, while tendency for bifurcated interactions is more pronounced for coordinated ammonia. The interaction energies and d_{HO} distances of the most stable geometries were calculated for rigid model systems, where the geometries of monomers were optimized, however systems with hydrogen bonds were not optimized. In addition, the interaction energies of fully optimized systems with hydrogen bonds were also calculated.

In the rigid systems, the calculated interaction energies for free ammonia and free ethylenediamine are both -2.3 kcal/mol and the calculated d_{HO} distances are the same, 2.2 Å. The coordination of ammonia and ethylenediamine molecules leads to stronger interactions (Table 1). The interaction for $[Co(NH_3)_3Cl_3]/OH_2$ is repulsive due to side repulsive interactions with chlorine atoms. The interaction energies for singly and doubly charged ammonia complexes are -5.0 kcal/mol and -10.7 kcal/mol. The interaction energies for neutral, singly and doubly charged ethylenediamine complexes are stronger than for ammonia. They are -6.7 kcal/mol, -11.8 kcal/mol and -19.9 kcal/mol.

The interactions for coordinated ethylenediamine are stronger than for coordinated ammonia due to higher values of electrostatic potentials (Table 1) and less side repulsive interactions in model systems [5]. Additionally, the calculated d_{HO} distances for coordinated ethylenediamine are shorter than for coordinated ammonia molecule. This is in accordance with the data observed in the crystal structures (Figure 2).

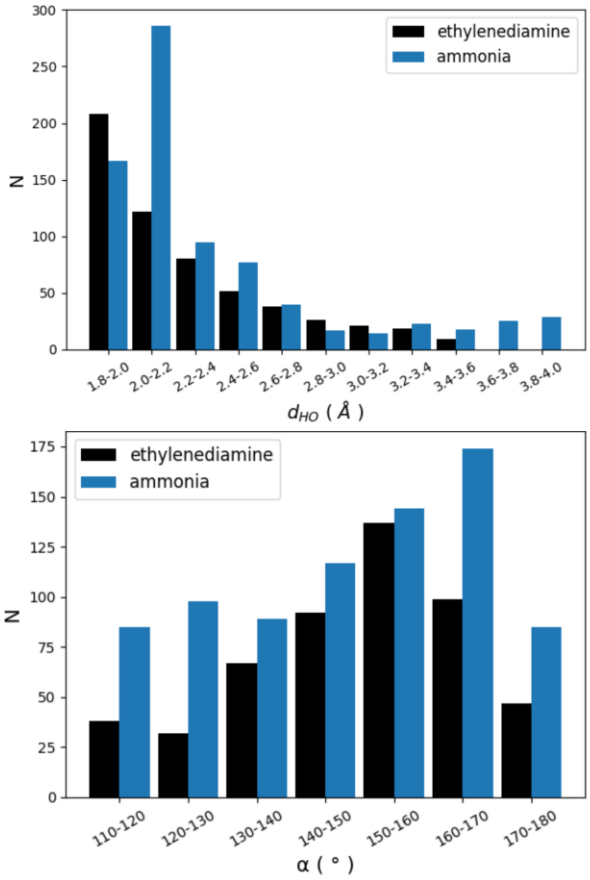

Figure 2. The distribution of d_{HO} distance (left) and angle α (˚) (right) for coordinated ammonia/water and ethylenediamine/water interactions found in the CSD.

Table 1. The d_{HO} distance (Å), the positive electrostatic potential on hydrogen atom involved in monofurcated interaction (Vs), and interaction energy (ΔE (kcal/mol)) for rigid systems.

	d_{HO}	**Vs**	**ΔE**
NH_3/OH_2 [a]	2.2	27	-2.3
$NH_2CH_2CH_2NH_2/OH_2$ [a]	2.2	20	-2.3
$[Co(NH_3)_3Cl_3]/ OH_2$ [b]	/	14	/
$[Co(NH_3)_4Cl_2]^+/ OH_2$ [b]	2.2	98	-5.0
$[Co(NH_3)_5Cl]^{2+}/ OH_2$ [b]	2.0	179	-10.7
$[Co(H_2O)enCl_3]/OH_2$ [b]	2.0	49	-6.7
$[Co(H_2O)_2enCl_2]^+/OH_2$ [b]	1.9	135	-11.8
$[Co(H_2O)_3enCl]^{2+}/OH_2$ [b]	1.9	214	-19.9

[a] calculated at CCSD(T)/CBS level [4,5]
[b] calculated at M06L-GD3/def2-TZVPP level [4,5]

Table 2. The d_{HO} distance (Å), the positive electrostatic potential on interacting site (Vs), and interaction energy (ΔE (kcal/mol)) for optimized systems.

	$\mathbf{d_{HO}}$	**Vs**	**ΔE**
NH_3/OH_2 [a]	/	/	/
$NH_2CH_2CH_2NH_2/OH_2$ [a]	2.21	-8	-7.2
$[Co(NH_3)_3Cl_3]/ OH_2$ [b]	2.02	26	-16.3
$[Co(NH_3)_4Cl_2]^+/ OH_2$ [b]	2.05	110	-15.0
$[Co(NH_3)_5Cl]^{2+}/ OH_2$ [b]	1.91	174	-23.9
$[Co(H_2O)enCl_3]/OH_2$ [b]	2.02	29	-18.8
$[Co(H_2O)_2enCl_2]^+/OH_2$ [b]	2.16	43	-22.3
$[Co(H_2O)_3enCl]^{2+}/OH_2$ [b]	2.06	194	-28.1

[a] calculated at CCSD(T)/CBS level [4,5]
[b] calculated at M06L-GD3/def2-TZVPP level [4,5]

The optimized model system NH_3/OH_2 did not have N-H···O hydrogen bond. In the optimized model systems, coordinated ammonia and ethylenediamine form bifurcated interactions with water molecule, hence interaction energies are stronger **(Table 2) than for rigid systems (Table 1).** As for rigid systems, interaction energies for optimized systems are stronger for coordinated ethylenediamine/water than for coordinated ammonia/water systems. For almost all optimized ammonia/water and ethylenediamine/water systems, the d_{HO} distances are longer than in rigid systems. This is the consequence of bifurcated interactions in optimized systems.

CONCLUSION

The results of the crystal structure study of NH···O hydrogen bond for coordinated ammonia show peak in the 2.0 Å to 2.2 Å range, while, for coordinated ethylenediamine the peak lies in 1.8 Å to 2.0 Å range. This is in accordance with calculated data; coordinated ethylenediamine forms stronger hydrogen bonds with shorter distances. The distribution of α angle in crystal structures is slightly different for coordinated ammonia and ethylenediamine, indicating more pronounced tendency of coordinated ammonia to form bifurcated interactions. The computational study has shown that interactions for coordinated ethylenediamine are stronger due to higher electrostatic potentials and less side repulsive interactions in model systems.

Acknowledgment

This work was supported by the Serbian Ministry of Education, Science and Technological Development (Contract numbers: 451-03-68/2022-14/200168 and 451-03-68/2022-14/200288).

REFERENCES

[1] J. M. Andrić, G. V. Janjić, D. B: Ninković, S. D. Zarić, Phys. Chem. Chem. Phys., 14 (2012) 10896-10898.
[2] J. M. Andrić, M. Z. Misini-Ignjatović, J. S. Murray, P. Politzer, S. D. Zarić, D. B. Ninković, ChemPhysChem, 17 (2016) 2035-2042.
[3] J. M. Andrić, I. M. Stanković, S. D. Zarić, Acta Crystallogr. A, B75 (2019) 301-309.
[4] J. M. Živković, D. Ž. Veljković, S. D. Zarić, Cryst. Growth Des. 22 (2022) 148–158.
[5] J. M. Živković, M. Milovanović, S. D. Zarić, Cryst. Growth Des, submitted.

NOVEL Ru(II) COMPLEX WITH 1-NAPHTHYLHYDRAZINE - SYNTHESIS, STRUCTURAL CHARACTERIZATION, AND INTERACTIONS WITH TRANSPORT PROTEIN

M. Đošić[1], T. Eichhorn[2], D. Dimić[1], J. Dimitrić Marković[1], E. Avdović[3], N. Pantelić[4], D. Simijonović[3] and G. N. Kaluđerović[2]

[1]University of Belgrade, Faculty of Physical Chemistry, Studentski trg 12-16, 11000 Belgrade, Serbia. (ddimic@ffh.bg.ac.rs)
[2]Department of Engineering and Natural Sciences, University of Applied Sciences Merseburg, Eberhard-Leibnitz-Straße 2, DE-06217 Merseburg, Germany
[3]Department of Science, Institute for Information Technologies, University of Kragujevac, Jovana Cvijića bb,34000 Kragujevac, Serbia
[4]Department of Chemistry and Biochemistry, Faculty of Agriculture, University of Belgrade, Nemanjina 6,11080 Belgrade, Serbia

ABSTRACT

Ruthenium complexes have attained attention in the scientific literature as promising anticancer agents due to their lower toxicity to healthy cells, increased selectivity, lower resistivity, and antimetastatic properties. A novel Ru(II) complex, [Ru(η^6-cym)Cl_2(1-$NNHNH_2$)], was obtained from p-cymene Ru(II) dimer with 1-naphthylhydrazine (1-$NNHNH_2$) under mild conditions. The structure of the compound was confirmed by the ^{1}H NMR, IR, and Raman spectroscopies. The spectrofluorometric measurements were employed to study the binding affinity toward transport proteins. It was shown that this process occurs spontaneously, with the change in Gibbs free energy of reaction being -30 kJ mol^{-1}. It is assumed that π-π interactions are the dominant ones between the surrounding amino acids and p-cymene/naphthalene moieties of the title compound.

INTRODUCTION

Cancer is one of the leading causes of death worldwide. The available treatment of patients is limited to surgery, radiotherapy, and the use of cytotoxic agents, although most of them are associated with resistance and known side effects. In the past years, Ru(II) complexes have been widely investigated for their promising antitumor and antibacterial properties. Due to the toxic side effects of more conventional compounds used in chemotherapy, like cisplatin, these complexes continue to be a vast and open field of interest and investigation due to their low toxicity against normal cells [1]. Although many of the non-platinum metal complexes are described in the literature, only a few of them match the clinical efficiency of cisplatin [2,3]. Nevertheless, ruthenium complexes are promising agents because of the antimetastatic properties and lower resistivity of advanced tumors. For this reason, it is of utmost importance to study interactions of these complexes with transport proteins, for example, bovine serum albumin (BSA) and human serum albumin (HSA). These experiments usually include spectrofluorimetric measurements through the BSA or HSA intrinsic fluorescence quenching by the complex at different temperatures. The thermodynamic parameters are then calculated and correlated with the interactions taking place in the observed system.

In this paper, the synthesis and structural characterization of a new Ru(II) arene complex bearing 1-naphtylhydrazine ligand, [Ru(η6-cym)Cl2(1-NNHNH2)], is reported. The binding affinity towards bovine serum albumin was investigated by spectrofluorometry and the thermodynamic parameters governing this process were calculated.

METHODS

Synthesis

In the first step, 0.2 mmol of Ru(II) dimer was suspended in 5 mL of absolute methanol and stirred for 15 min under a stream of nitrogen. After that, 0.6 mmol of LiOH monohydrate was added to the solution and stirred for an additional 15 min until Ru(II) dimmer was completely dissolved.
Afterward, 0.6 mmol of 1-naphthylhydrazine hydrochloride was added to the clear red solution at room temperature. The reaction mixture was allowed to stir for 20 min under a stream of nitrogen until the reactants were completely dissolved. The precipitated product was filtered off under a vacuum and washed with diethyl ether. ^{1}H NMR (400 MHz, Chloroform-d) δ (ppm): 7.94 – 7.87 (m, 1H, **C5''-H**), 7.85 (s, 2H, **C8''-H**, **C6''-H**), 7.86 – 7.79 (m, 1H, **C3''-H**), 7.51 (ddd, J = 9.4, 7.1, 4.9 Hz, 1H, **C4''-H**), 7.37 (t, J = 7.9 Hz, 1H, **C7''-H**), 7.05 (d, J = 7.4 Hz, 1H, **C2''-H**), 6.94 (s, 1H, NH), 5.59 – 5.50 (m, 2H, **C2-H**, **C6-H**), 5.38 (d, J = 5.7 Hz, 2H, **C3-H**, **C5-H**), 3.48 (s, 1H, NH), 3.04 (p, J = 6.9 Hz, 1H, **H-1'**), 2.30 (s, 3H, **CH3-4'**), 1.34 (d, J = 7.0 Hz, 6H, C2'-H3-2', **CH3-3'**)

Chemical characterization

Characterization of the novel complex was performed using IR (Thermo Nicolet – model Avatar 370, KBr pellet, 1 mg of substance to 150 mg of KBr, 4000-400 cm^{-1}, spectral resolution 2 cm^{-1}), Raman (Thermo Scientific – model DXR Raman Microscope, solid sample, 3500-400 cm^{-1}, objective lens 50×, laser output 10 mW, acquisition time 10 s with 10 scans, fluorescence correction) and ^{1}H-NMR spectroscopy (Inova 500, $CDCl_3$ as solvent, TMS as standard, 500 MHz).

Spectrofluorometric measurements

The Stern-Folmer diagrams for the BSA binding study were obtained using the Cary Eclipse MY2048CG03 instrument. Excitation and emission slits were both set to 5 nm. The excitation wavelength was 280 nm and the emission spectrum was recorded between 300 to 500 nm. The scan rate was 600 nm/min and the PMT voltage was set to medium.

For the spectrofluorometric study of bonding with BSA, a 100 ml of BSA solution (5×10^{-6} M) was prepared in PBS buffer (pH~7.4), as well as a 10^{-4} M solution of the synthesized ruthenium(II) complex in DMSO. The method used was the Stern-Folmer fluorescence quenching method.

The BSA solution was then titrated with the solution of the ruthenium complex at different temperatures (33, 35, 37, 39˚C). After each added volume of the complex, the emission fluorescence spectra were recorded. Recording of the spectra was done 3 minutes after each addition of the complex to the BSA solution for each temperature, as it was previously shown that this time interval is sufficient for the system to reach an equilibrium state and constant temperature.

RESULTS AND DISCUSSION

Ru(II) dimer reacted with 1-naphthylhydrazine in the presence of LiOH yielding [Ru(η^6-cym)Cl_2(1-$NNHNH_2$)] (Scheme 1.).

In the 1H-NMR spectrum of [Ru(η^6-cym)Cl_2(1-$NNHNH_2$)], hydrogen atoms from the methyl groups resonate at 1.34 ppm and 2.30 ppm. Septet at 3.04 ppm was ascribed to hydrogen atom from the CH-isopropyl moiety. Hydrogen atoms belonging to the p-cymene moiety and 1-naphthylhydrazine resonate from 7.00-7.95 ppm.

The vibrational spectra of the obtained complex are presented in (Figure 1). The doublet at around 3280 and 3200 cm^{-1} belongs to the NH stretching vibration of the ligand. Bands above 3000 cm^{-1} belong to the CH stretching vibrations of the aromatic ring in the p-cymene and 1-naphthylhydrazine ligands, while the signals below 3000 cm^{-1} are from the CH stretching vibrations of methyl groups in the p-cymene moiety.

From the intercept values on the Stern-Folmer diagrams, as well as the double log Stern-Folmer equation, the binding constants at operating temperatures were determined (Table 1). These values were further used to construct the graphs $\ln K_b = f(T^{-1})$, from which the Gibbs free energy, as well as enthalpy and entropy changes for the reaction, were determined (Figure 2).

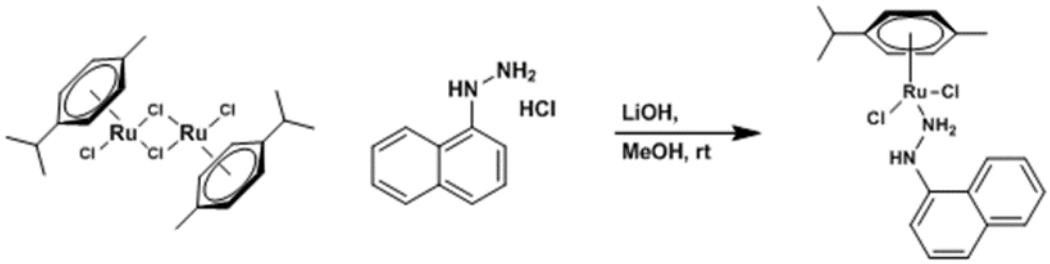

Scheme 1. Synthesis of $[Ru(\eta^6\text{-cym})Cl_2(1\text{-}NNHNH_2)]$

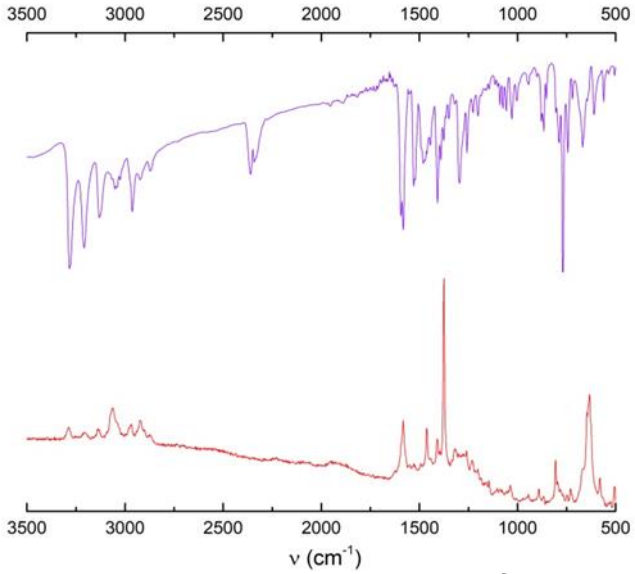

Figure 1. IR (violet) and Raman (red) spectra of $[Ru(\eta^6\text{-cym})Cl_2(1\text{-}NNHNH_2)]$

Table 1. Values of binding constants, number of bonding sites and the Gibbs free energy

T (K)	$\log K_b$	$K_b(\times 10^5)$	$\ln K_b$	n	ΔG^0_b (kJmol^{-1})
306.15	5.630	4.266	12.964	1.13	-32.996
308.15	5.163	1.455	11.888	1.05	-30.457
310.15	4.760	0.575	10.960	0.95	-28.262
312.15	4.488	0.308	10.334	0.91	-26.819

As can be seen from the results, the values for the binding constant are quite large at lower temperatures (~105) but decrease rapidly as the temperature increases. The obtained values for the change in Gibbs free energy are negative, which proves the spontaneity of the process. When the values for the change in enthalpy and entropy of this process were calculated, the following values were obtained: ΔH0b = -350.47 kJ mol-1 and ΔS0b = -1,04 kJ mol-1K-1. Based on these values, it can be concluded that the binding process is enthalpically driven which contributes the most to the change in Gibbs free energy. From the structural point of view, it can be assumed that the most numerous interactions with surrounding amino acids include π-π (with benzene and naphthalene

moieties), and probably some σ-π interactions. The electronegative atoms in the structure are well protected by the surrounding groups, as well as the Ru(II) ion, therefore interactions with these parts are not probable. Additional investigation including molecular docking/molecular dynamics calculations is required to verify these assumptions.

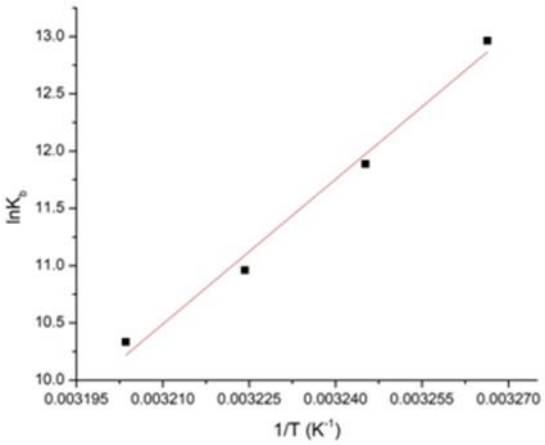

Figure 2. The Van't Hoff graph for different temperatures (R^2=0.98225)

CONCLUSION

A novel Ru(II) complex, [Ru(η^6-cym)Cl_2(1-$NNHNH_2$)], was obtained from the appropriate Ru(II) dimer with 1-naphthylhydrazine. The structure of the complex was confirmed by ^{1}H-NMR, IR, and Raman spectroscopies. The spectrofluorometric measurements proved the spontaneity in binding between obtained complex and bovine serum albumin, with the change of Gibbs free energy of reaction being around 30 kJ mol^{-1}. The binding is driven by the exothermicity of the reaction due to the formation of π-π bonds. Additional theoretical calculations are needed to verify the binding mode of the title complex and transport proteins.

Acknowledgment

The authors gratefully acknowledge financial support from the Science Fund of the Republic of Serbia (Serbian Science and Diaspora Collaboration Program: Knowledge Exchange Vouchers: Project TumorSelCoum 6388843) and the Ministry of Education, Science, and Technological Development of the Republic of Serbia (grant no 451-03-68/2022-14/200146).

REFERENCES

[1] Scolaro, C., Bergamo, A., Brescacin, L., Delfino, R., Cocchietto, M., Laurenczy, G., Geldbach, T., Sava, G., and Dyson, P. J., J. Med. Chem., 48 (2005) 4161.
[2] Kostova, I., Curr. Med. Chem., 13 (2006) 1085.
[3] Huang, S., Peng, S., Su, W., Tang, Z., Cui, J., Huang, C., and Xiao, Q., RSC Advances, 6 (2016) 47043.

BINUCLEAR RUTHENIUM(II) COMPLEX WITH 1-NAPHTHYLHYDRAZINE – STRUCTURAL OPTIMIZATION, HIRSHFELD SURFACE ANALYSIS, AND BOVINE SERUM ALBUMIN BINDING STUDIES

S. Mišić[1,2], T. Eichhorn[2], F. Kolbe[1,2], D. Dimić[1], J. Dimitrić Marković[1], T. Rüffer[3], D. Milenković[4], J. Đorović Jovanović[4], N. Pantelić[5] and G. N. Kaluđerović[2]

[1]*University of Belgrade, Faculty of Physical Chemistry, Studentski trg 12-16, 11000 Belgrade, Serbia (ddimic@ffh.bg.ac.rs)*
[2]*Department of Engineering and Natural Sciences, University of Applied Sciences Merseburg, Eberhard-Leibnitz-Straße 2, DE-06217 Merseburg, Germany*
[3]*Institute of Chemistry, Chemnitz University of Technology, Straße der Nationen 62, D-09111 Chemnitz, Germany*
[4]*Department of Science, Institute for Information Technologies, University of Kragujevac, Jovana Cvijića bb,34000 Kragujevac, Serbia*
[5]*Department of Chemistry and Biochemistry, Faculty of Agriculture, University of Belgrade, Nemanjina 6,11080 Belgrade, Serbia*

ABSTRACT

Piano-stool ruthenium(II) complexes with aromatic ligands are promising candidates as antitumor compounds. The novel binuclear ruthenium(II) complex with a 1-napthtylhydrazine (1-$NNHNH_2$) ligand, $[\{Ru(\eta^6\text{-cym})Cl\}_2(\mu\text{-1-}NNHNH_2)(\mu\text{-Cl})]PF_6$ is described in this contribution from the structural point. The crystallographic structure was obtained by X-ray crystallography and described. The Hirshfeld surface analysis was performed to obtain quantitative parameters for the stabilization interactions between various contact atoms. The importance of intermolecular hydrogen bonds was shown. The optimization of structure at the B3LPYP level of theory with a 6-31+G(d,p) basis set for ligand and LanL2DZ for ruthenium(II) was done based on the experimental structure. The most prominent bonds were compared and the applicability of chosen level of theory was shown. The interactions of title compound with bovine serum albumin, a model of transport protein, were investigated by spectrofluorometry. The binding process is spontaneous, with the change in Gibbs free energy being around -30 kJ mol^{-1} for the investigated temperature range.

INTRODUCTION

Cisplatin is one of the most used antitumor drugs, obtained in 1845 and licensed for medical use since 1978, although some major disadvantages are known. Some of these include nephrotoxicity, neurotoxicity, and ototoxicity. One of the ways to suppress these side effects was to change the ligands which led to the synthesis of carboplatin and oxaliplatin, but these were still very toxic due to the presence of platinum. Several other metals are suitable for the antitumor drugs and these include titanium(IV), gallium(III), gold(III), and tin(IV) [1].

Ruthenium complexes have received considerable attention in the field of medicinal chemistry, due to the increased stability in aqueous and alcoholic solutions, as well as lower sensitivity to oxygen and sulfur. In physiological conditions, the ruthenium ion is stable in two oxidation states, Ru(II) and Ru(III), with the former being more reactive [2]. Both oxidation states accommodate a six-coordinate octahedral configuration, but it is also possible to obtain complexes with different geometries and it is expected that they can participate in various biological redox reactions. Organoruthenium(II/III) compounds are also suitable for medicinal use as lower general toxicity was observed. Besides significant improvement in the selectivity towards tumor cells, antimetastatic activity was shown. It

is also known that some of the antitumor drugs can form complexes with ruthenium to overcome the resistance of the tumor cell lines. The stabilization of the +2 oxidation state of ruthenium can be accomplished through the π-bonded arene ligands, which partially influence the solubility and possible resistance of tumor cells towards these compounds [3].

This contribution describes the synthesis, crystal structure, optimization of the structure, and Hirshfeld surface analysis of novel binuclear ruthenium(II) complex with a 1-naphthylhydrazine ligand. The structure optimization is performed to verify the applicability of the chosen level of theory for future calculations and activity prediction. The binding affinity towards bovine serum albumin (BSA) was determined by spectrofluorimetry to discuss the possibility the interactions with the transport proteins.

METHODS

The crystallographic structure of the complex was determined based on the X-ray diffraction analysis of a single crystal on a Rigaku Oxford Gemini S diffractometer at 110 K using Mo-Kα radiation. Absorption was corrected by multiscanning with the SCALE3 ABSPACK algorithm as implemented in the CrysAlisPro software. The direct method was used for solving the structure by SHELXS-2013 and refined in the same program by full-matrix least-square routines against F^2. Non-hydrogen atoms were refined with anisotropic parameters, while hydrogen atoms bonded to the carbon atoms were placed in the calculated positions, according to the riding model. The crystallographic structure was visualized in ORTEP III [4]

The structure of the title complex was optimized in the Gaussian program package [5] starting from the crystallographic structure. The employed functional was B3LYP with a 6-31+G(d,p) basis set for H, C, and N atoms and LanL2DZ for Ru. The absence of imaginary frequencies proved that the minimum in energy was reached during the optimization. The Natural Bond Orbital analysis was performed on the optimized structure. The analysis of crystal structure allows detailed investigation of the intermolecular interactions that govern the stability of the obtained structure. The Crystal-Explorer 17 was utilized for this analysis which is based on the graphical representations of two distances, de, and di. The first one represents the distance between the two nearest nuclei and the section is the distance between the nuclei to the external surface. The normalized distance is then represented by various colors depending on the relative size that is compared to the van der Waals separations. These colors include red, white, and blue if the distance is shorter, equal, or larger than the van der Waals separations. Interactions between specific atoms are shown in the fingerprint plots and allow calculations of the relative percentages for the two atoms' interactions.

The binding affinity of complex towards bovine serum albumin (BSA) was investigated by spectrofluorometry on the Cary Eclipse MY2048CG03 instrument. The excitation wavelength characteristic for the tryptophan residues was set to 280 nm, and the emission spectrum was recorded between 300 and 500 nm. The concentration of BSA was held constant at 5×10^{-6} M, while the concentration of complex was between 1.5 and 9.9×10^{-6} M. The successive addition of complex resulted in the decrease in intrinsic fluorescence of protein. The analysis followed a double log Stern-Folmer quenching. The scan rate was set to 600 nm min^{-1}, with both slits being 5 nm. The measurements were repeated at three temperatures (30, 33, and 37ºC) to mimic body temperature.

RESULTS AND DISCUSSION

Single crystals of binuclear ruthenium(II) complex with 1-naphthylhydrazine (1-$NNHNH_2$), [{Ru(η^6-cym)Cl}$_2$(μ-1-$NNHNH_2$)(μ-Cl)]PF_6, were obtained by X-ray diffraction. The crystal structure of the title compound is shown in (Figure 1). As it can be seen, the compound crystallized as discreet cations and anions. The structure is characterized by the presence of two Ru(II) ions bridged by a chlorine atom and a hydrazine group of 1-naphthylhydrazine. Two additional chlorine atoms are directly

bonded to one of the Ru(II) atoms. In the crystal structure, two methanol molecules additionally stabilize the structure by intermolecular hydrogen bonds. One hydrogen bond is formed between the N-H group of hydrazine and the OH group of methanol, while the second is present between two methanol molecules. The bond lengths Ru–Cl are between 2.406 and 2.429 Å, which is in the expected range for similar compounds. The bond distance between Ru and N atoms is 2.137 and 2.192 Å.

The stability interactions in the crystal structure were analyzed by the Hirsfeld surface analysis. Due to the presence of electronegative oxygen atoms in methanol, fluorine atoms in PF_6^-, and chloride ligands several hydrogen bonds were observed. These bonds are represented by one of the following N–H···F, C–H···Cl, O–H···Cl, and C–H···F. The highest contribution was calculated for the H···H contacts (59%), which is expected due to the multitude of hydrogen atoms in naphthylhydrazyl and p-cymene moieties. Mentioned hydrogen bonds significantly contribute to the stability, with the most prominent being H···F (22.5%) and H···Cl (7.6%). A much lower contribution was calculated for H···O contacts (1.1%). The contacts including carbon atoms amount to only several percentages, namely C···H (8.1%), C···C (1.1%), and C···F (0.2%).

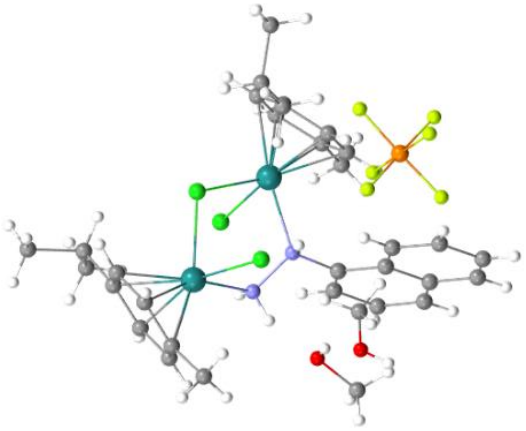

Figure 1. Crystal structure of cation in the $[\{Ru(\eta^6\text{-cym})Cl\}_2(\mu\text{-1-NNHNH}_2)(\mu\text{-Cl})]PF_6$ (Pd–dark green, Cl–green, N–blue, O–red, C–grey, P–orange, F–yellow, H–white)

The structural optimization was performed to verify the applicability of the chosen level of theory. The optimized bond lengths are compared to the most prominent bonds in the crystallographic structure. The optimized Ru-Cl bond lengths are between 2.478 and 2.503 Å, while Ru-N are 2.185 and 2.259 Å. The experimental Cl-Ru-Cl are 85.64 and 86.20°, while the theoretical are 87.88 and 87.76°. The average angle between Ru and hydrazine group is 116° in the crystallographic structure and 114° in the theoretical one. These values reproduce well the experimental ones, bearing in mind that the structure was optimized in a vacuum with the methanol and PF_6 removed. The elongation of Ru-Cl bond lengths is due to the relaxation of the structure that is separated from the other structural units. These values proved the applicability of the chosen level of theory.

The fluorescent spectra of BSA before and after various additions of a complex are presented in (Figure 2). As it can be seen, there is a decrease in fluorescence intensity in a concentration-dependent manner. When the fluorescence intensity was plotted against the concentration, the binding constants were determined from the double log Stern-Folmer equation at three different temperatures. These values were dependent on temperature, as shown in (Figure 2). From these values, the thermodynamic parameters governing the binding process were determined. The change in the enthalpy of reaction is 189 kJ mol^{-1}, the reaction being endothermic. On the other side, the change in entropy of reaction is 719 J $mol^{-1}K^{-1}$. The reaction is entropically driven. The change in Gibbs's free energy of reaction is between -28.97 and -34.01 kJ mol^{-1} in the examined temperature range. It can be assumed that during

the binding process, weak interactions stabilize the structure, probably by disintegrating the structure of the complex. Further theoretical studies are needed to elucidate the possible binding mechanism.

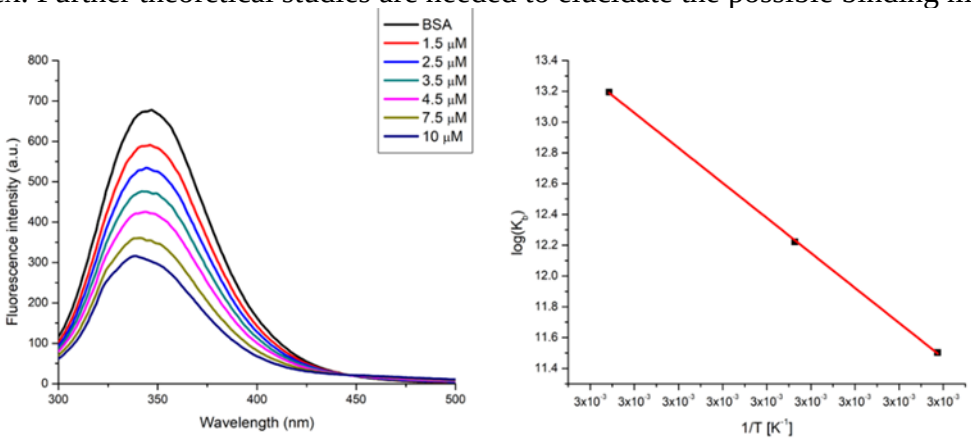

Figure 2. The decrease in intrinsic fluorescence of BSA after the addition of complex (left) and van't Hoff plot for a binding process (right)

CONCLUSION

A novel binuclear ruthenium(II) complex with 1-naphthylhydrazine was obtained. This compound is crystalized as a discreet cation and anion. In the structure, two Ru atoms were bridged by chlorine atom and hydrazyl moiety, while two methanol molecules and PF_6^-anion were present. The hydrogen bonds were important for the overall stability of the crystal structure, as shown by the Hirshfeld analysis. These contacts, namely H···F and H···Cl contributed 22.5 and 7.6% to the total number of interactions. The structure optimized at the B3LYP level of theory showed great resemblance to the experimental one, especially when Ru-Cl and Ru-N bonds are concerned. The addition of complex led to the decrease in the fluorescence intensity of BSA in a concentration-dependent manner. The spontaneity of the process was reflected in the change of Gibbs free energy of around -30 kJ mol^{-1} for the temperature interval between 30 and 37ºC.

Acknowledgment

The authors gratefully acknowledge financial support from the Science Fund of the Republic of Serbia (Serbian Science and Diaspora Collaboration Program: Knowledge Exchange Vouchers: Project TumorSelCoum 6388843) and the Ministry of Education, Science, and Technological Development of the Republic of Serbia (grant no 451-03-68/2022-14/200146).

REFERENCES

[1] Arlt, S., Petković, V., Ludwig, G., Eichhorn, T., Lang, H., Rüffer, T., Mijatović, S., Maksimović-Ivanić, D., and Kaluđerović, G. N., Molecules, 26 (2021) 1860.
[2] Kostova, I., Curr. Med. Chem., 13 (2006) 1085.
[3] Huang, S., Peng, S., Su, W., Tang, Z., Cui, J., Huang, C., and Xiao, Q., RSC Advances, 6 (2016) 47043.
[4] Farrugia, L. J., J. Appl. Cryst., 45 (2012) 849.
[5] M.J. Frisch, G. W. Trucks, H. B. Schlegel, et al. Gaussian 09, Revision C. 01, Gaussian Inc. Wallingford, CT. USA, 2010.

N – Food Physical Chemistry

CONTEMPORARY METHODS OF TESTING HUMAN MILK QUALITY

N. Lugonja[1], J. Avdalović[1], M. Ilić[1], Z. Lopičić[2], T. Šoštarić[2], D. M. Stanković[3,4] and S. Spasić[1]

[1]University of Belgrade, Institute of Chemistry, Technology and Metallurgy, Njegoševa 12, Belgrade, Serbia. (jelena.avdalovic@ihtm.bg.ac.rs)
[2]Institute for Technology of Nuclear and other Mineral raw materials, Bulevar Franše d'Eperea 86 Belgrade, Serbia.
[3]University of Belgrade, Faculty of Chemistry, Studentski trg 12-16, Belgrade, Serbia.
[4] University of Belgrade, Vinča Institute, Belgrade, Serbia.

ABSTRACT

Infant nutrition is essential for their growth and development. This research aims to determine the total antioxidant capacity of the infant food for preterm infants and indicate adequate methods for testing the quality and biological value of milk and infant food. The total antioxidant capacity (TAC) was determined in human milk and an infant formula for premature infants. The determination of the total antioxidant capacity was made using cyclic and differential pulse voltammetry, potentiometry and electron paramagnetic resonance spectroscopy. The results of three comparative electrochemical methods indicate that human milk has a higher antioxidant potential compared to infant formula, which contributes to better physiological development of the child. Fenton-based electron paramagnetic resonance spectroscopy method provides additional insight into TAC analysis, whereby a carbon-centered radical and an ascorbyl radical are formed in infant food. All methods can be used to determine TAC, since the results obtained individually with each method follow the same trend.

INTRODUCTION

Adequate nutrition is essential for the growth and development of infants and young children. Human milk is the most complete source of nutrients, especially adapted to baby's needs. When breast milk is not available, infant formulas are an adequate source of macro and micronutrients for infant development. The nutrition of premature babies poses a specific challenge, because it requires a high-energy intake, adequate nutrients and antioxidants. In a complex system such as milk, several redox systems are active at the same time, and their effect on antioxidant potential depends on several factors, such as system reversibility, oxidant-reductant ratio and concentration of active system components[1].

In addition to the commonly used enzymatic and spectrophotometric methods, modern electrochemical techniques—differential pulse voltammetry (DPV), cyclic voltammetry (CV), and potentiometry (POT)—are used to determine the total antioxidant capacity (TAC) of biological samples [2]. These methods could find their application in the daily control of milk quality before thermal treatments. The addition of fortifier to human milk is very important for the nutrition of premature infants, so it is necessary to determine the antioxidant capacity for infants in neonatal units. Electron paramagnetic resonance spectroscopy (EPR) is a "fingerprint method" for determining the activity of biologically active compounds [3].

There is no simple method to determine the freshness of milk. The freshness and quality of milk reflect its redox state. The aim of this paper is to compare electrochemical methods that determine the redox potential of infant food, as carriers of protective activity and milk quality.

METHODS

Human milk samples (MM) were collected from mothers of preterm infants, delivered before 37 weeks of gestation, at the Institute of Neonatology, Belgrade, Serbia (E82501/4). Special infant formula (IF) for preterm and low birth weight infants was produced in Serbia in accordance with recommendations (Codex Alimentarius Commission FAO / WHO). IF was prepared by dissolving 16g of powder in 90 ml of water, for the final volume of 100ml of meal.

Potentiometric determination of the total antioxidant capacity of milk samples is based on the Noyhouzer method [4], which determines the redox state and redox capacity of milk. Total antioxidant activity of milk was determined potentiometrically using iodine / iodide redox reaction in a two-electrode cell. Fisher's Pt electrode was a working electrode, and saturated calomel electrode was the reference. Redox potential was measured in solution after adding constant volumes of redox mediator 0.1 M J^-/ J2. Portions (10 μL) were added to 50 ml of the titrant solution every 90 s. Cyclic and differential pulse voltammograms were recorded on a CHI760B instrument (CHInstruments, Austin, USA), in a three-electrode cell: a glass electrode (GC) was used as the working electrode (Model CHI 104) and an additional large Pt electrode (platinum wire) (Model CHI 221) and Ag / AgCl electrode (Model CHI 111) as auxiliary and reference electrodes. Electrochemical cells have a volume of 5 ml. The measurements were performed in an anaerobic atmosphere, with the introduction of nitrogen into the cell. Voltammogram CV was recorded in the range -400 to +1000 mV, with a recording scan rate of 100 mVs^{-1}, DP voltammogram from -100 to +700 mV with a scan rate of 100 mVs^{-1}. Before each recording, the working GC electrode was polished with aluminum powder (1 and 0.5 μm, Buehler, IL, USA), and then washed with distilled water [2]. The EPR spectrum was recorded on a Varian E104-A EPR spectrometer (Varian, Palo Alto, CA.USA) X-band (9.572 GHz). Spin-trap stimulation of 5-tert-butoxycarbonyl-5-methyl-1-pyrroline-N-oxide (BMPO) was used [3]. All data were expressed as means ± Standard Deviation (SD). Comparison between groups was done using NCSS-2001 (NCSS, Kaysville, UT) statistical software. Kruskal–Wallis ANOVA test was used for multiple comparisons.

RESULTS AND DISCUSSION

The total antioxidant capacity was examined in HM and IF for the nutrition of premature infants. Table 1 shows the results obtained by different methods used to determine TAC.

Table 1. Comparison of methods for determination of TAC of milk and IF

Method	MM	IF
POT (mV)	250±2	205±2
CV (μC)	0.398±0.263	0.204±0.011
DPV (μC)	0.737±0.298	0.532±0.016
EPR*	81±10	107±15

* The signal intensity of the BMPO adduct with carbon-centered radical

Mechanisms for determining the TAC by CV and DPV differ from potentiometry. CV and DPV reactive species are electrons from the electrode, while in potentiometry, reactive species are electron donors, while iodine solution as an oxidant is an acceptor, which is an indicator of the measured antioxidant potential. The values of antioxidant potential in CV and DPV were in good agreement (MM 100%, and IF 80% activity), while the results obtained by potentiometry show slightly higher values (IF 82% of total activity compared to MM). This can be explained by the longer measurement time, since in potentiometric analyzes the time between adding two aliquots of iodine is 90 s, which is enough time to use up all iodine—it oxidizes with antioxidants from milk—and to get a more realistic insight into antioxidant content. By comparing the three electrochemical

methods (CV, DPV and POT, Figure 1) to determine the total antioxidant potential of breast milk and infant formula, it is shown that human milk gives a significantly stronger TAC, i.e., it has a higher redox potential compared to infant formula.

Based on the above results, it can be concluded that all three methods can be used to determine TAC, since the results obtained individually with each method follow the same trend. The Kruskal-Wallis multiple Z-value comparison test (Table 2), which shows that the Z value for the confidence interval does not exceed the critical value (z-value 1.9600), confirmed the experimental results and showed that potentiometry, CV and DPV can be equally used to determine TAC of different milk samples.

Table 2. Kruskal-Wallis Multiple-Comparison Z-Value Test

Variable	POT	CV	DPV
POT	0.0000	0.0271	0.4611
CV	0.0271	0.0000	0.4339
DPV	0.4611	0.4339	0.0000

Regular Test: Medians significantly different if z-value > 1.9600
Bonferroni Test: Medians significantly different if z-value > 2.3940

The disadvantage of the potentiometric method is that the time required for analysis is longer—about half an hour per sample analysis—while the time required to obtain the TAC by cyclic and differential pulse voltammetry is much shorter, since the analyses only take a few seconds.

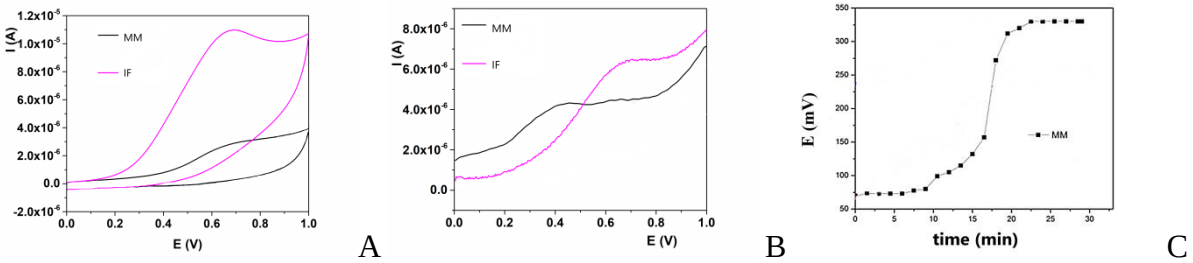

Figure 1. Application of different electrochemical methods for detection of human milk quality: A) CV; B) DPV; C) Potentiometry

Mother's milk and infant formula catch the hydroxyl radical to form carbon-centered and ascorbyl radical. The formation of these species is lower, with the equal production of ·OH radicals in IF compared to MM (Table 1). Both MM and IF scavenge the ·OH radical, whereby a carbon-centered radical and an ascorbyl radical are formed in MM, and a carbon-centered radical is formed in IF. The TAC of breast milk is obviously 3 times higher than IF, especially if we consider that the carbon-centered radical targets different biological molecules (Figure 2).

The applied electrochemical methods are very fast, cheap and reliable in determining the total antioxidant capacity of human milk because they are based on direct measurement of the electron-donating components of milk and enable quantitative determination of TAC of MM and IF. Electrochemical methods are very important for milk freshness control, especially in neonatal units. Spectroscopic examination using electron paramagnetic resonance with spin trapping, tests the ability of human milk and infant formula to reduce the production of free radicals in the Fenton system. Fenton-based EPR method completes the insights into TAC analysis of MM and IF. This is particularly important for the immature defense system of infants, which makes them more sensitive

to various environmental stressors and disorders within the system associated with the production of reactive oxygen species.

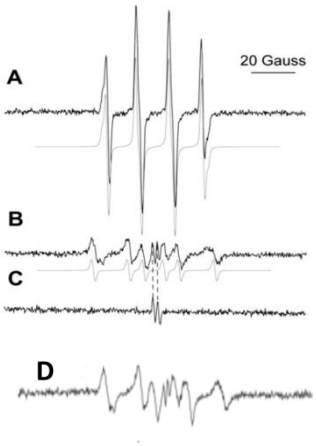

Figure 2. Application of EPR for detection of human milk (B and C) and IF (D) quality (A: Fenton system)

CONCLUSION

Our results represent valuable data guiding us into further research on electrochemical methods for rapid, routine and daily determination/monitoring of TAC in human milk and infant formulas. Electrochemical techniques can exceed the limits of spectrophotometric analysis, such as lower sensitivity and slower response, and can be successfully applied as a replacement for long-running spectrophotometric methods and in clinical trials.

Acknowledgment

This work was supported by the Ministry of Education, Science and Technological Development of the Republic of Serbia (Grant No. 451-03-9/2022-14/200026 and 451-03-68/2022-14/200023).

REFERENCES

[1] N. Lugonja and S. Spasić in: New Research on Breastfeeding and Breast Milk, Kai Santos Melo Eds., Nova Science Publishers, Inc, New York 2020.
[2] N. Lugonja, D. Stanković, B. Miličić, S. Spasić, V. Marinković, M. Vrvić, Food Chem., 240 (2018) 567–572.
[3] N. Lugonja, S. Spasić, O. Laugier, A. Nikolić-Kokić, I. Spasojević, Z. Oreščanin-Dušić, M. Vrvić,Nutrition, 29(2) (2013) 431–435.
[4] T. Noyhouzer, R. Kohen, D. Mandler, Anal. Meth., 1 (2009) 93–99.

ENHANCEMENT OF NUTRITIONAL, PHYSICAL AND STRUCTURAL CHARACTERISTICS OF APPLE POMACE FLOUR BY AGGLOMERATION WITH PREBIOTICS USING FLUID-BED GRANULATION

S. Zlatanović[1], D. Micić[1], M. Đuriš[2], S. Ostojić[1], F. Pastor[3], M. Jovanović[1] and S. Gorjanović[1]

[1]*Institute of General and Physical Chemistry, Studentski trg 12-16, P.O. Box 45, 11158 Belgrade 118, Serbia (snezana.zlatanovic@gmail.com)*
[2]*Institute of Chemistry, Technology and Metallurgy—National Institute of The Republic of Serbia, University of Belgrade, Njegoševa 12, 11000 Belgrade, Serbia*
[3]*University of Belgrade, Faculty of Chemistry, Studentski trg 12-16, 11000 Belgrade, Serbia*

ABSTRACT

Apple pomace flour (APF) obtained by dehydration of minimally processed apple pomace and subsequent grinding represents a rich source of dietary fibers (DF) and polyphenolics. The nutritional, physical and structural property of APF was further enhanced by fluid-bed granulation with inulin and pectin (10% w/w). Maltodextrin (5% w/v) was used as a binder. Chosen prebiotics additionally improve ratio of carbohydrates to DF and consequently the anti-obesity effect of APF while its transformation into dust-free granules can enable easier manipulation, consumption or compression into tablets. Significantly improved flowability of granulated mixtures was confirmed. Particle size increased up to 3 times compared to starting material. Carr index decreased from 27.5 to 16.8 and 28.6 to 21.9 while the Hausner ratio from 1.38 to 1.20 and 1.40 to 1.28 for APF mixture with inulin and pectin, respectively. An increase in glass transition temperature along with a water activity decrease implied better storability.

INTRODUCTION

Apple pomace, a valuable by-product rich in dietary fibers and polyphenolics, is still underutilized in Serbia and the region. Apple pomace flour (APF) produced at an industrial scale level by a recently patented technological procedure expressed significant antioxidant, anti-obesity and anti-diabetic effects [1, 2]. APF versatile applicability as a food ingredient was demonstrated [3]. However, its applicability could be further expanded while physical properties improved. Pectin and inulin as prebiotics with a wide range of functional properties are frequently used to enrich food products or supplements [4].

Fluidized bed granulation, a technique of particle enlargement by agglomeration, is often a method of choice to increase the density of the mixture, so that it occupies less volume per unit weight for better storage and shipment, and to facilitate metering or volumetric dispensing. The primary methods by which the agglomerated granules are formed include solid bridges, sintering, chemical reactions, crystallization and deposition of colloidal particles. Besides, binding can also be accomplished through adhesive and cohesive forces by utilizing high viscous binders. The series of mechanisms by which granules are formed from the powder particles encompass wetting and nucleation, coalescence or growth, consolidation, and attrition or breakage [5].

Water activity (aw) can be used to predict the stability and safety of food. The determination of the minimum value of aw that allows the growth of certain microorganisms and the mechanical and thermal equilibrium of the material with the surroundings are the most important parameters that characterize the stability of the material. The equilibrium moisture content has a fundamental role in the food industry and technology from the aspect of design and optimization of drying processes

and equipment, design of packing materials for dried products, prediction of quality and stability, as well as for calculation of changes in the moisture content of dried material during its storage.

Most food products with reduced moisture content are partly or totally amorphous. Depending on the storage temperature and their composition (mainly water content), they may be glassy and expected to be rigid (eventually crispy) and stable, or contain a rubbery or liquid phase and then be soft and prone to physical and chemical changes.

The aim of this work was to explore the possibility to enhance the nutritional, physical and structural characteristics of APF by its fluid-bed co-granulation with the prebiotics pectin/inulin, using maltodextrin as a binder. Improvement of flowability, thermal stability and storability of the granulated product was shown. Based on a decrease in carbohydrates to dietary fibre (DF) ratio nutritional improvement was confirmed and further enhancement of the prominent anti-diabetic and anti-obesity effect of APF by agglomeration with inulin or pectin was indicated.

METHODS

Apple pomace flour was produced at an industrial scale level by a recently patented technological procedure [1]. Inulin ((Digestive Inulina. Inulin Frutafit IQ, Fornatura- food supplements), pectin (Grindsted® Pectin LA 415, Dupont Nutrition & Health) and maltodextrin (Maxumalium Maltodextrin, Inexall Company) were used.

The process of wet granulation in a fluidized bed (pilot-scale device, Innovation Project IP 16-10 2018) was performed to obtain granulated APF with the addition of pectin and inulin. Upon sterilization of the mixture of APF with particle size ≤ 200 μm (300g) and inulin/pectin (30g) in the preheated column (78 ℃) of a fluidized bed dryer (10 min), temperature was reduced to 60 ℃. The mixture was granulated via top spraying of 150 ml of aqueous maltodextrin solution (5% w/v). The pressure through a two-fluid nozzle was 1.6 bar. The mean fluid flow rate and airflow rates were 3.5 ml/min and 38 m^3/h, respectively. The granulated mixture was dried by fluidization at 50℃ for 15 min. To prevent the disintegration of the formed granules due to collision and attrition, the airflow rate in the drying phase was reduced to 20-25 m^3/h.

Physical and technological properties of APF mixture before and after granulation, including bulk and tap density, flowability, Carr Index (C_I), Hausner ratio (H), particle size distribution, and water activity (aw meter Novasina LabSwift Bench-model Water Activity Meter (Neutec Group Inc., Farmingdale, NY, USA) at 25 ± 2 °C, were determined and compared [2,4].

A differential scanning calorimeter (DSC, Q1000, TA Instruments, New Castle, DE, USA) was used to perform DSC experiments. Samples (5-7 mg) were placed in aluminium pans with pin holes lids, cooled from 20 to -90 °C, equilibrated for 5 min and scanned initially from -90 to 150 °C, with a controlled heating rate of 5 °C /min under the N2 purge flow of 50 mL/min. Each thermogram was analyzed by TA Advantage Universal analysis 2000 software, version 4.5A. Glass transition is characterized by onset temperature (T_{gon}), midpoint temperature (T_g) and end temperature (T_{gend}) of the change in heat capacity (ΔCp).

The total content of dietary fibers and carbohydrates in APF was previously determined and the ratio of carbohydrates to dietary fibre in obtained granulated materials was calculated [1].

RESULTS AND DISCUSSION

The raw apple pomace flour showed a mean particle size of 200μm, bulk and tapped density of 435 g/dm^3 and 635 g/dm^3. However, with particle enlargement the product became free flowing, resulting in a good homogeneity and a nearly normal distribution of the agglomerated product. The addition of inulin and pectin to APF without a granulation process did not improve the physical properties according to the Carr index and Hausner ratio (Table 1.). Maltodextrine, known to

increase the glass transition temperature (T_g) of the food products promoting the subsequent preservation of physical and chemical properties, was chosen as a binder [6].

Improvement of physical properties upon granulation was explained by the agglomeration of particles, not only due to the binding agent maltodextrin but also due to the presence of inulin and pectin [8]. After granulation, the physical characteristics of the obtained material were significantly improved compared to the initial one (Table 1., Figure 1.).

Table 1. Physical characteristics of APF with inulin and pectin before and after granulation

	Starting material				**Granulated material**			
	ρ_{bulk} g/ml	**ρ_{tapped} g/ml**	**C_I**	**H**	**ρ_{bulk} g/ml**	**ρ_{tapped} g/ml**	**C_I**	**H**
APF+Inulin	0.4793	0.6614	27.53	1.38	0.2908	0.3498	16.85	1.20
APF+Pectin	0.4832	0.6766	28.58	1.40	0.2982	0.3819	21.91	1.28

Significant improvement of granulated material flowability was confirmed. Particle size increased 2.75 and 2.5 times compared to starting material, Carr Index decreased from 27.5 to 16.8 and 28.6 to 21.9 while Hausner ratio from 1.38 to 1.20 and 1.40 to 1.28 for APF mixture with inulin and pectin, respectively.

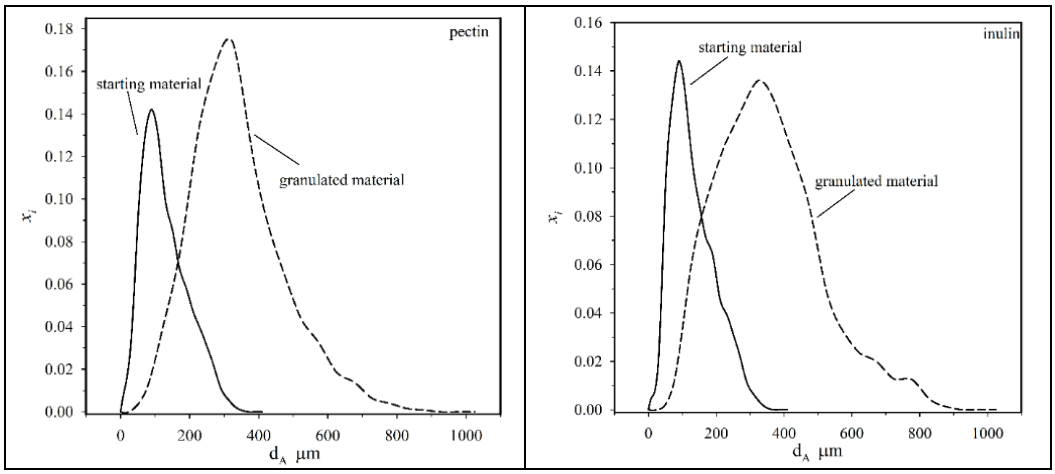

Figure 1. Fractional particle distribution of APF with pectin and inulin before and after granulation

According to the obtained DSC curves, analyzed samples showed similar thermal behavior at the temperature range 0 and 140 °C. It was observed that for a given material, T_g decreased as aw increased (Figure 2.). This is a characteristic behavior observed in sugar-rich systems such as inulin, attributed to the plasticizer effect of water promoted by the formation of hydrogen bonds on the hydrophilic groups [7]. Low aw achieved by technological procedures applied, as well as glass transition well above the storage temperature, ensures prolonged shelf life of granulated material.

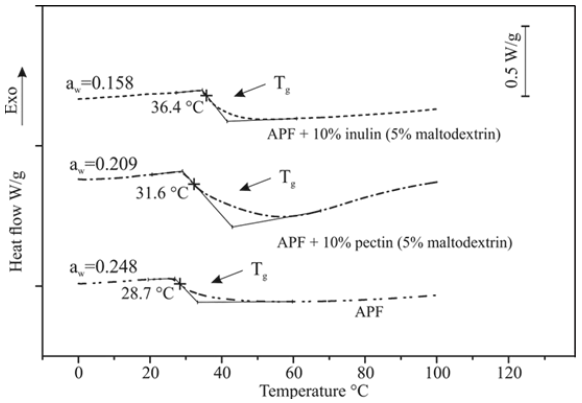

Figure 2. Thermograms of APF and granulated mixture (APF+inulin) and (APF+pectin) obtained at a heating rate of 5 °C/min in nitrogen flow of 50 ml/min, with water activity indicated

Finally, fiber- and sugar-based metrics was applied to compare and differentiate the nutritional quality of APF, before and after granulation. In addition to their prebiotic effect inulin and pectin added in a significant amount (10% w/w) improved the already favourable ratio of carbohydrates to DF [9]. The ratio decrease leads to the conclusion that the prominent anti-obesity and anti-diabetic effects of APF could be further enhanced by agglomeration with inulin or pectin.

CONCLUSION

To our knowledge, this is the first report on the improvement of the nutritional, physical and structural characteristics of APF using its co-granulation with pectin/inulin by a fluidized bed. Significant improvement of followed properties was achieved. APF granulated with prebiotics represent an upgraded material with a more favourable ratio of carbohydrates to DF, superior flowability and thermal stability. The applicability of the granulated APF in both the food and pharmaceutical industries needs to be further investigated.

Acknowledgment

This work was supported by the Ministry of Education, Science and Technological Development of the Republic of Serbia (grant no 451-03-68/2022-14/200051).

REFERENCES

[1] Zlatanović, S., Gorjanović, S., Ostojić S., Micić D., Pastor F., Kalušević A., Laličić-Petronijević J., Patent Registration number 63010 issued by The Intellectual Property Office of Republic of Serbia 3/2022
[2] Gorjanović, S., Micić, D., Pastor, F., Tosti, T., Kalušević, A., Ristić, S., Zlatanović, S., Antioxidants, 9 (2020) 413.
[3] Zlatanović, S., Kalušević, A., Micić, D., Laličić-Petronijević, J., Tomić, N., Ostojić, S., Gorjanović, S., Foods, 8 (2019) 561.
[4] J.M.Li, S.P. Nie, Food Hydrocolloids, 53 (2016) 46-61.
[5] S. M. Iveson, J. D. Litster, K. H. Bryan, J. Ennis, Powder Technol., 117 (2001) 3-39.
[6] Đuriš, M., Arsenijević, Z., Jaćimovski, D., Radoičić, T.K., Powder Technol., 302 (2016) 177–186.
[7] Z. Saavedra-Leos, C. Leyva-Porras, S. B. Araujo-Díaz, A.Toxqui-Terán, & A. J. Borrás-Enríquez, , Molecules (Basel, Switzerland), 20 (2015) 21067–21081.
[8] R. Agrawal and N. Yadav, Inter. J. of Pharm. Front. Res. 1 (2011) 65-83.
[9] M. Blumfield, A. McConnell, T. Cassettari, P. Petocz, M. Warner Campos, et al P.ONE 16 (2021) e0253582.

PHENOLIC COMPOSITION AND CYTOTOXIC ACTIVITY OF RED WINE

N. Đorđević[1], N. Todorović Vukotić[1], L. Korićanac[1], J. Žakula[1], S. Pejić[1], S. B. Pajović[1] and V. Tešević[2]

[1]*University of Belgrade, Institute of nuclear sciences Vinča, National Institute of the Republic of Serbia, Mike Petrovića Alasa 12-14, 11351 Vinča-Belgrade, Serbia. (neda@vin.bg.ac.rs)*
[2]*University of Belgrade, Faculty of Chemistry, Studentski trg 12-16, Belgrade, Serbia.*

ABSTRACT
Positive effects of moderate wine consumption in individuals with cardiovascular disease, hypertension, diabetes, and cancers have been shown in numerous epidemiological and clinical studies. This research examined the phenolic content of commercial and two clonal Merlot wines as well as their biological potential. The obtained results indicated that all analyzed samples were a good source of phenolic compounds. Cytotoxicity assay on melanoma (A375) and cervical (HeLa) cancer cell lines have shown that all analyzed wines inhibited the growth of human cancer cells *in vitro* with differing susceptibility among tested cell lines. Clonal wines in the volume ratio of 10 and 20% showed to be more efficient anti-proliferative agents than commercial wine regarding the A375 cells. This could be connected with higher total phenolic content in clonal wines. The effect of all analyzed samples on the A375 cells was greater compared to HeLa cell line.

INTRODUCTION
Red wine is a rich source of phenolic compounds significant for reducing the risk of developing chronic human diseases like cardiovascular, inflammatory diseases, cancer and diabetes [1]. Besides beneficial activity of phenolic compounds related to scavenging of reactive oxygen species (ROS), nitrogen radicals and chlorine species, these compounds also show anticancer activity through inducing cell cycle arrest, apoptosis, autophagy, deoxyribonucleic acid (DNA) damage and p53 signaling, leading to the death of cancer cells [2]. Besides, phenolic compounds can increase the ability of cancer cells to differentiate and transform into normal cells. In previous years, it has been found that naturally occurring phenolic compounds have positive effects on stopping cell migration by epithelial/mesenchymal transition interference, cell invasion, and extravasation [3]. Thus, phenolic compounds support the localization of cancer cells and make them more sensitive to drug treatment.

Although melanoma has the lowest prevalence rate (5-10%), it is responsible for the 80% of mortality cases from skin cancer [4]. Its lethality arises from its rapid progression, easy metastasis and drug-resistance as well. Shortcomings of the current treatments for the management of metastatic and/or non-metastatic melanoma like high cost, high toxicity and increasing inefficiency due to resistance, especially in metastatic form, lead to necessity to investigate new effective therapeutic strategies. Cervical cancer is the fourth most frequent cancer type among women worldwide. Surgical interventions, radiotherapy and chemotherapy are used for treatment of cervical cancer, but because of the adverse effects they have, in the last years the emphasis has been on alternative medicine, especially on phytochemicals that could help in cancer therapy [5].

METHODS
For the purpose of this research wine samples were obtained from developing sector of "Plantaže 13. juli" A.D. winery (Podgorica, Montenegro). They included commercial wines (Comm) along with two novel red wine clones of Merlot variety (VCR1 and VCR101), vintages 2010 and 2011.

Samples were produced using standard vinifications. Prior to analysis they were stored at 10 °C in the dark and analyzed immediately after opening.

Total phenolic content was analyzed using colorimetric Folin–Ciocalteu (FC) procedure adapted to the analysis of wine [6]. Absorbance was measured at 740 nm. Total flavonoid content was determined by spectrophotometric method using aluminium(III)-chloride as reagent [7]. The absorbance of the formed complexes was monitored at 410-440 nm. Total anthocyanin content was measured using pH differential method [8]. The absorbance was measured at 520 and 700 nm by UV-VIS spectrophotometer (GBC Cintra 40) which was used for all the aforementioned measurements. All the analyses were performed in triplicate and the data were expressed as mean ± STDEV. Value for total phenolic, total flavonoid and total monomeric anthocyanin content was expressed as gallic acid equivalent (mg GAE/L), rutin equivalent (mg RTE/L) and cyanidin-3-glucoside equivalent (mg CGE/L), respectively. Results were analyzed using One-way ANOVA followed by a post-hoc Tukey's test. $p < 0.05$ was defined as statistically significant.

Cytotoxic activity of analyzed wines (vintage 2011) on A375 and HeLa cell lines was determined using SRB assay. The test was performed according to method of Skehan et al. [9] after 72h of treatment with different wine volume percentage (5, 10 and 20%). Absorbance was measured at 550 and 690 nm using Wallac, VICTOR^2 1420 Multilabel counter (PerkinElmer, Turku, Finland). Cytotoxic effect of wines was exspressed as percentage of control untreated cells (set as 100%). All data were expressed as means ± STDEV. Results were analyzed using Factorial ANOVA followed by a post-hoc Tukey's test. $p < 0.05$ was defined as statistically significant.

RESULTS AND DISCUSSION

The obtained results showed that VCR101 sample was the richest in total phenolic and flavonoid content within 2010 vintage. It has significantly higher content of total phenolic content compared to Comm wine ($p < 0.001$) and VCR1 wine ($p < 0.01$) (Table 1**.**). The VCR1 and VCR101 samples from 2011 vintage have the similar total phenolic content, which was significantly lower in Comm wine compared with VCR101 sample from the same vintage ($p < 0.05$). The clonal wines analyzed in this study had significantly higher total phenolic content than other clonal wines from the same variety analyzed in other studies [10, 11]. All the samples from 2011 vintage had the similar content of total flavonoid, while total anthocyanin content was the highest in VCR101 sample (Table 1.). Comparing contents of total phenolic, flavonoid and anthocyanin in wines from 2011 and 2010 vintages it is obvious that the weather conditions with higher number of sunny hours and less rainy days influenced the better quality of wines from 2011 vintage.

Table 1. Total phenolic, flavonoid and anthocyanin content in analyzed wine samples.

Sample		Total phenolic content (mg/L)	Total flavonoid content (mg/L)	Total anthocyanin content (mg/L)
2010	Comm	2184 ± 94 ^{a,A}	298 ± 7 ^{a,A}	173 ± 2 ^{a,C}
	VCR1	2370 ± 82 ^{a,A}	299 ± 8 ^{a,A}	90 ± 2 ^{a,A}
	VCR101	2775 ± 49 ^{a,B}	365 ± 5 ^{a,B}	152 ± 3 ^{a,B}
2011	Comm	2989 ± 142 ^{b,A}	376 ± 11 ^{b,A}	215 ± 4 ^{b,A}
	VCR1	3256 ± 91 ^{b,AB}	393 ± 6 ^{b,A}	204 ± 4 ^{b,A}
	VCR101	3338 ± 115 ^{b,B}	397 ± 9 ^{b,A}	230 ± 7 ^{b,B}

* Comm – commercial Merlot wine; VCR1/VCR101 – wine obtained from VCR1/VCR101 vine clone. Value for total phenolic, total flavonoid and total monomeric anthocyanin content is

expressed as gallic acid equivalent (mg GAE/L), rutin equivalent (mg RTE/L) and cyanidin-3-glucoside equivalent (mg CGE/L), respectively. All values are represented as mean ± SD (triplicate). Different letters within each column show statistically significant differences (Tukey HSD test, $p < 0.05$). The lowercase letters represent statistically significant differences within the same variety through different vintages, while the uppercase letters show statistically significant differences between different varieties in the same vintage.

The test of cytotoxic activity showed significant cytotoxic activity of all analyzed wines. Cell viability ranged between 18 and 45%, compared to control cells. At 10 and 20 volume percentage of analyzed wines, the VCR1 and VCR101 samples showed higher cytotoxic activity on A375 cells than commercial wine (Figure 1.). This could be related to higher total phenolic content in clonal wines. Cytotoxic activity of wine samples on HeLa cell line was similar at levels of 5 and 10%, while VCR101 sample had the highest cytotoxic activity at 20% of wine. Furthermore, it is clear that all wines showed higher cytotoxic effect on A375 cell line.

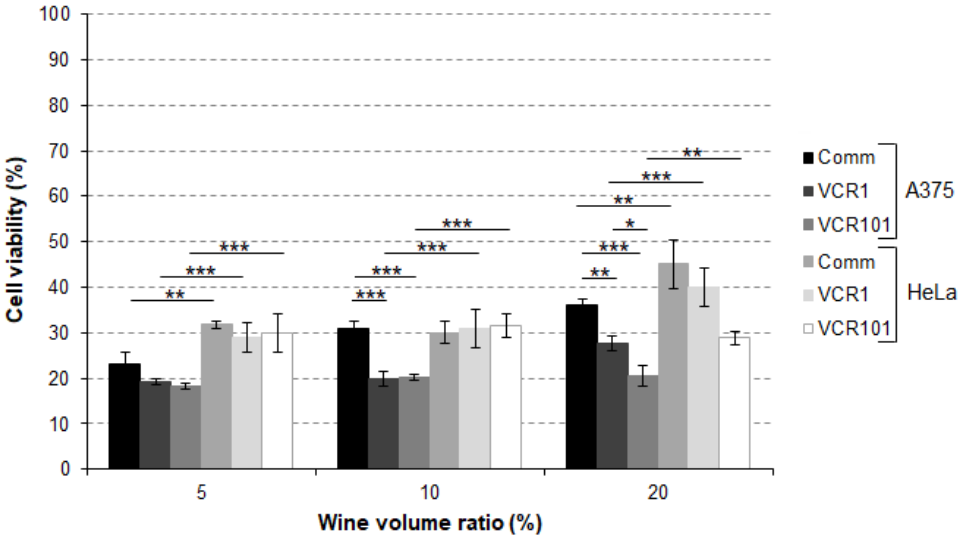

Figure 1. A375 and HeLa cell viability after treatment with different wine volume ratio of commercial wine (Comm) and wine obtained from two vine clones VCR1 and VCR101. All measurements were done in triplicate and the obtained results are expressed as mean value ± SD. Different letters show significant differences between obtained values ($p < 0.05$), according to Tukey's HSD test. Asterisks indicate statistically significant difference between treated groups *p<0.05; **p <0.01; ***p <0.001.

CONCLUSION

This study showed that all analyzed wines are notable source of bioactive phenolic compounds. They all expressed cytotoxic effect on both A375 and HeLa cell lines, although the effect on the A375 cell line was greater. The activity of clonal wines stands out and highlights them as natural products with specific biological activity.

Acknowledgment
This work was supported by the Ministry of Education, Science and Technological Development of the Republic of Serbia (grant no 451-03-68/2022-14/200017).

REFERENCES

[1] S. Arranz, G. Chiva-Blanch, P. Valderas-Martínez, A. Medina-Remón, R. M. Lamuela-Raventós, R. Estruch, Nutrients, 4 (2012) 759-781.
[2] J. Duan, H. Guo, Y. Fang, G. Zhou, Food Nutr Res, 65 (2021) 6507.
[3] Y. Ci, J. Qiao, M. Han, Molecules, 21(12) (2016) 1634.
[4] K. V. Laikova, V. V. Oberemok, A. M. Krasnodubets, N. V. Gal'chinsky, R. Z. Useinov, I. A. Novikov, Z. Z. Temirova, M. V. Gorlov, N. A. Shved, V. V. Kumeiko, T. P. Makalish, E. Y. Bessalova, I. I. Fomochkina, A. S. Esin, M. E. Volkov, A. V. Kubyshkin, Molecules, 24(8) (2019) 1516.
[5] G. Dretcanu, C. I. Iuhas, Z. Diaconeasa, Int J Mol Sci, 22 (2021) 8812.
[6] V. L. Singleton, R. Orthofer, R. M. Lamuela-Raventos, Methods Enzymol, 299 (1998) 152-178.
[7] C. C. Chang, M. H. Yang, H. M. Wen, J. C. Chern, J Food Drug Anal,10 (2002) 178-182.
[8] M. M. Giusti, R. E. Wrolstad in: Current Protocols in Food Analytical Chemistry, ed. by R.E. Wrolstad, Wiley, London, 2001, F1.2.1-1.2.13.
[9] P. Skehan, R. Storeng, D. Scudiero, A. Monks, J. McMahon, D. Vistica, J. T. Warren, H. Bokesch, S. Kenney, M. R. Boyd, J Natl Cancer Inst, 82 (1990) 1107-1112.
[10] D. Vujovic, B. Pejin, J. Popovic Djordjevic, M. Velickovic, V. Tesevic, Nat Prod Res, 30 (2016) 987-990.
[11] T. M. Majkić, Lj. D. Torović, M. M. Lesjak, D. D. Četojević-Simin, I. N. Beara, Food Res Int, 121 (2019) 151-160.

TOMATO AND CARROT POMACE FLOUR PRODUCED AT INDUSTRIAL SCALE LEVEL BY DEHYDRATION AS A NUTRIENT SOURCE IN FOOD FORTIFICATION

S. Gorjanović[1], F. Pastor[2], D. Micić[1] and S. Zlatanovic[1]

[1]*Institute of General and Physical Chemistry, Studentski trg 12-16, P.O. Box 45, 11158 Belgrade 118, Serbia (snezana.zlatanovic@gmail.com)*
[2]*University of Belgrade, Faculty of Chemistry, Studentski trg 12-16, 11000 Belgrade, Serbia*

ABSTRACT
At the industrial scale level, minimally processed tomato and carrot pomace was subjected to dehydration below 55 °C, stabilization, and grinding to desired particle size without heating. Tomato and carrot pomace flour (TPF and CPF) with low content (≤ 7%) and water activity (aw) (0.4), as well as the temperature of glass transition (T_g) significantly above the standard temperature of storage (39 ºC), was further analyzed as a source of nutrients lacking in the modern diet. Proximate composition was determined. Very high content of dietary fibre (DF) was confirmed, while carbohydrate content was significantly lower than in apple pomace flour (APF). The ratio of carbohydrates to DF proved that TPF (0.3) and CPF (1.0) addition can lower the glycaemic index and/or glycaemic load of various food formulations. High content of polyphenols, as well as prominent antioxidant activity, determined upon *in vitro* digestion additionally confirm the high potential of TPF and CPF in food fortification. In addition, TPF can be claimed as high in protein.

INTRODUCTION
Besides fruit pomace, the juice industry generates a significant amount of minimally processed vegetable pomace containing a high amount of health related biomolecules and low content of sugar. Prior to further application or introduction into food formulation perishable pomace need to be preserved. At the industrial scale level, low-cost preservation without compromising the structure and activity of phytochemicals is still a challenge. Pomace preserved in a sustainable manner could profitably be utilized for the supplementation of various food formulations, including gluten-free and vegan products.

Tomato (*Lycopersicon esculentum L*) is the world's second largest vegetable crop while carrot (*Daucus carota* L) is one of the most popular root vegetables and an important source of dietary carotenoids. Tomato pomace (TP) resulting from the processing of tomato in the industry represents 5%–30% of the raw fruit [1]. The carrot juice yield is 60% to 70% while carrot pomace (CP) contains up to 80% of total carotene [2]. TP is composed of a mixture of peels that contain DF and a much higher amount of lycopene than the pulp, seeds representing a large portion that contains up to 20% crude oil and up to 22% protein and residual pulp is rich in various phenolic compounds such as hydroxycinnamic acid and quercetin derivatives, flavanones and naringenin-chalcone. CP represents a good source of chlorogenic, and caffeic acid, catechin and epicatechin, and contains a high amount of carotene and DF [2].

Here, a recently patented technological procedure used for industrial scale production of thermally stable apple pomace flour (APF) with long shelf life and significant effect on glucose metabolism and body weight management was applied to produce tomato and carrot pomace flour (TPF and CPF) [3], [4], [5]. The first aim of this study was to adjust the technological parameters of the procedure that includes dehydration below 55 °C, stabilization, and subsequent grinding without heating to achieve low water activity (aw) and obtain stable TPF and CPF with high temperature of glass transition while the second one was to analyze nutritional properties. Proximate composition

of TPF, CPF, and APF were analyzed in parallel as well as polyphenols and antioxidant activity of flour digested in simulated gastrointestinal fluids were determined. Potential of TPF and CPF to fortify common cereals and pseudocereals flour was discussed based on a comparison of the content of DF and polyphenolics and carbohydrate/DF ratio.

METHODS

Production at industrial scale level - Immediately upon juice production in Zdravo. Selenča, RS raw tomato and carrot pomace (150 kg) with approx 80 % of moisture were transported to dehydration device, and subjected to a dehydration at 55 °C according to slightly modified technological procedure until desired (aw) value [3]. Water activity (aw) was determined at 25 ±2 °C (Novasina LabSwift Bench-model Water Activity Meter, Neutec Group Inc., Farmingdale, NY, USA). Dehydrated pomace was ground without heating to desired particle size (mean particle size of 200μm).

Proximate composition - Moisture content was determined at 105 ± 5 °C in a thermostatically controlled dry oven until a constant weight was reached. The chemical composition of flour was analyzed in terms of fats and proteins, DF, and total carbohydrates. Protein, total dietary fibre and fat content were determined by AOAC methods. Standard enzymatic-gravimetric AOAC method 985.29 was used to determine the content of DF [6].

***In vitro* digestion** - Flour samples were digested in simulated gastrointestinal fluids according to the adapted Infogest protocol. The blank solution was prepared with all reagents but without the sample.

The total content of phenolics and antioxidants activity - Total phenolic content, FRAP, and DPPH were determined using a slightly modified procedures described previously [5].

Thermal stability - A differential scanning calorimeter (DSC, Q1000, TA Instruments, New Castle, DE, USA) was used to perform DSC experiments. Samples (5-7 mg) were placed into aluminium pans with pin holes lids, cooled from 20 to -90 °C, then equilibrated for 5 min and scanned initially from -90 to 150 °C, with a controlled heating rate of 5 °C /min under the N_2 purge flow of 50 mL/min. Each thermogram was analyzed by TA Advantage Universal analysis 2000 software, version 4.5A. Glass transition is characterized by onset temperature (T_{gon}), midpoint temperature (T_g), and end temperature (T_{gend}) of the change in heat capacity (ΔCp).

RESULTS AND DISCUSSION

Dehydration, stabilization, and grinding parameters were optimized to achieve low water content and activity. Upon 4 and 6 hours of dehydration followed by approx. 2 hours of stabilization moisture and aw values lower than 7% and 0.4 were reached. The temperature of glass transition (T_g) well above standard storage temperature (39 ºC) proved thermal stability. Along with low (aw), high (T_g) indicated long shelf life at standard storage conditions.

The proximate composition of obtained flour was determined (Table 1). Much higher content of DF than required to claim high DF content (6/100g) (Figure 1a) was ascribed to TPF and CPF. Similar to APF they possess several folds higher content of DF than common cereal and pseudocereal flour but lower content of sugar. They can be claimed as a good or excellent source of fiber (10 % or 20 % of the daily value that increases to 2.8 or 5.6 grams per serving) [6]. Chinoa flour made by milling the whole seed contained 7.1 g/100 g followed by sorghum and teff flours with approx. 4.5 g/ 100 g, oat with 4.1 g/100 g, and maize with 2.6 g/100 g. Dehulled and milled buckwheat contain mainly starchy endosperm and low DF content (2.2 g/100 g) as well as dehulled white rice flour with almost negligible DF content of 0.4 g/100 g [7]. For comparative reasons content of DF in vegetable flour was shown in parallel with APF and some commonly used flours (Figure 1). In addition, with more than 20% of its energy value provided by proteins TPF can be

claimed as high in proteins. Wheat flour commonly used for bread making has a protein content of approximately 11%, teff and buckwheat flour approx. 12%, quinoa flour 13.5%, sorghum and maize flour 4.7% and 5.5%, rice and oat 7.3% and 6.9% [7].

Table 1. Proximate composition of TPF, CPF and APF

%	TPF	CPF	APF
Proteins	23.1±1.7	8.8±0.6	3.6±0.2
Fat	7.3±0.6	1.8±0.2	2.7±0.2
Dietary fibre	50.2±1.2	42.9±2.3	37.0±4.0
Carbohydrates	15.2±1.6	44.5±4.6	56.0±6.0

The carbohydrate to DF metrics, based on the finding that higher DF carbohydrate food has a lower glycaemic index and/or glycaemic load and slows down the absorption of sugar and insulin spikes, compared to food with the same carbohydrate content with low DF, was applied here to stress vegetables pomace flour potential to enrich standard or gluten free ones food formulations (Figure 1a) [8]. Obtained pomace flour fits the ≤ 10:1 carbohydrate to fiber ratio rule used to identify healthy food associated with low cardiometabolic risk factors. Several folds lower ratio for TPF, APF, and CPF confirm their potential to fortify common flours efficiently (Figure 1b).

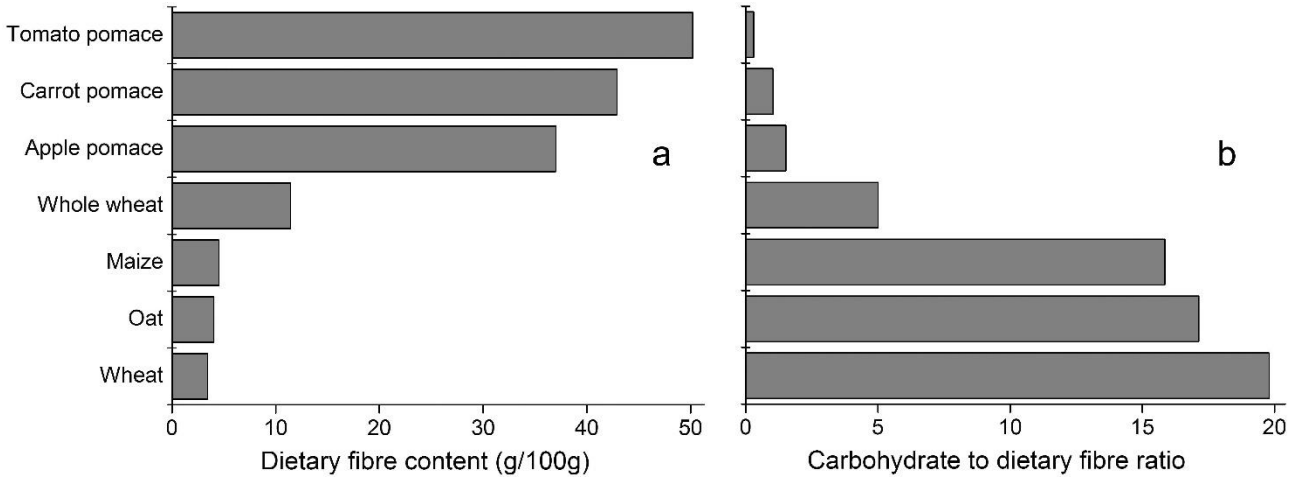

Figure 1. Content of DF (**a**) and ratio of carbohydrates to DF (**b**) in TPF, CPF and APF in comparison to commonly used flour (as reported in Hager at al [7])

Upon *in vitro* digestion in simulated gastro-intestinal fluids total content of phenolics (TPC), radical scavenging activity (DPPH), and ferric reducing antioxidant power (FRAP) were determined. In Table 2 obtained values for digested samples of TPF, CPF and APF were given in parallel. The content of TPC in common cereal and pseudocereal flour extracts was much lower [6]. Among the different common flours, the highest value was observed in buckwheat (4.6 mg/g) and teff (1.8 mg/g) and decreased in the following order: buckwheat > teff > sorghum > maize > wholewheat > quinoa > rice > oat [7].

Table 2. Total content of phenolics (TPC), radical scavenging activity (DPPH) and ferric reducing antioxidant power (FRAP) determined in TPF, CPF, and APF digested according to Infogest protocol.

	TPC (mg GAE/g)	**FRAP (μmol TE/g)**	**DPPH (μmol TE/g)**
TPF	9.2±1.3	25.7±1.4	15.8±1.9
CPF	5.0±1.2	19.7±1.5	16.4±1.3
APF	5.7±0.8	22.7±1.8	22.3±2.0

Some cereal grains contain phytic acid with a high chelating activity that decreases the bioavailability of calcium, magnesium, iron, and zinc, and adversely affects the absorption of nutrients such as amino acids, proteins, and starch. Teff and quinoa flour contained 1.52 g/100 g, and 1.34 g/100 g, followed by wholewheat, buckwheat, and sorghum (0.77 g/100 g, 0.64 g/100 g and 0.49 g/100 g). White wheat flour, rice, oat, and maize flour showed low phytate concentrations while TPF, CPF, and APF do not contain anti-nutritional factors such as phytic acid or gluten [7].

CONCLUSION

The possibility to efficiently preserve tomato and carrot pomace at an industrial scale level by dehydration was demonstrated. The technological parameters of dehydration and grinding were successfully adjusted to obtain stable TPF and CPF with low aw, and T_g well above the temperature of storage. Both TPF and CPF can be claimed as high in DF while TPF as high in proteins. According to the content of DF and polyphenolics with prominent antioxidant activity as well as low carbohydrate/fiber ratio, TPF and CPF addition in various food formulations can contribute to lowering glycaemic index and/or glycaemic load providing cardiometabolic risks prevention.

Acknowledgment

This work was supported by the Ministry of Education, Science and Technological Development of the Republic of Serbia (contracts no 451-03-68/2022-14/200051 and 451-03-68/2022-14/200168).

REFERENCES

[1] S. Yagci, R. Calıskan, Z.S. Gunes, E. Capanoglu, M. Tomas, Food Chem. 368 (2022) 130847.
[2] K.D. Sharma, S. Karki, N.S. Thakur, S. Attri, J. Food Sci. Technol. 49 (2012) 22–32.
[3] S. Zlatanović, S. Gorjanović, S. Ostojić, D. Micić, F. Pastor, A. Kalušević, J. Laličić-Petronijević, Process for Production of Gluten Free Flour from Apple Pomace and the Flour Obtained by Said Process, Patent Registration number 63010, 2022.
[4] S. Zlatanović, S. Ostojić, D. Micić, S. Rankov, M. Dodevska, P. Vukosavljević, S. Gorjanović, Thermochim. Acta 673 (2019) 17–25.
[5] S. Gorjanović, D. Micić, F. Pastor, T. Tosti, A. Kalušević, S. Ristić, S. Zlatanović, Antioxidants 9 (2020) 413.
[6] Method AOAC Official Method 985.29 Total Dietary Fiber in Foods Enzymatic-Gravimetric, (1985).
[7] A.S. Hager, A. Wolter, F. Jacob, E. Zannini, E.K. Arendt, J. Cereal Sci. 56 (2012) 239–247.
[8] J. Liu, C.D. Rehm, P. Shi, N.M. McKeown, D. Mozaffarian, R. Micha, PLoS One 15 (2020) e0231572.

TG-DTG ANALYSIS OF FRUIT-BASED WASTE PYROLYSIS: A CASE STUDY OF GOJI BERRY MESOCARP

F. Veljković[1], S. Veličković[1], N. Manić[2], I. Stajčić[1] and B. Janković[1]

[1]*VINČA Institute of Nuclear Sciences - National Institute of the Republic of Serbia, University of Belgrade, Serbia*
[2]*Laboratory for Thermal Analysis, Faculty of Mechanical Engineering, University of Belgrade, Serbia*

ABSTRACT
This work considers possible uses of fruit-based waste for the production of valuable chemicals and biofuel precursors through recycling by thermochemical conversion. Slow pyrolysis of Goji berry mesocarp (GBM) as sugar-rich feedstock was investigated using simultaneous thermal analysis (STA) measurements in non-isothermal conditions. Results reveal that pyrolysis of GBM represents a promising route to obtain important key platform chemical - 5-hydroxymethylfurfural (5-HMF). It was found that autocatalytic dehydration of fructose (in a presence of Lewis acids) is responsible for production of 5-HMF at a low heating rate (5.0 K/min) with a maximum 5-HMF theoretical yield of 63.20 %. Higher heating rates (10.0 and 15.0 K/min) trigger fructose autogenesis behavior which opens the transferability channel to glucose engagement for 5-HMF theoretical high yield production.

INTRODUCTION
Waste as by-products in fruit or vegetable industry processing is a significant biomass source for the production of key platform chemicals through both, throughout chemical routes and biological processes. For example, anaerobic digestion as a biochemical treatment favors the high moisture content biomass, such as food waste (FW), by reducing transportation and pre-treatment costs, especially when treated *in situ* [1]. Biochemical processes are operationally constrained by the formation of inhibitors, online monitoring of temperature, pH, mixing, and organic load concentration. Therefore, these parameters affect the bio-gas, the production and process stability, especially at commercial scales [2]. On the other hand, thermochemical processes are much shorter and almost completely utilize biomass components. Therefore, lignocellulosic biomass can be converted into liquid biofuels through thermochemical processes, such as pyrolysis. Forasmuch capital and operating costs, GHG (greenhouse gas) emissions, the consumption of process chemicals and carbon efficiency and thermochemical conversions, with an indication of the pyrolysis process, are more effective [3]. Fruit mesocarp (the inner flesh) is used in the fruit pulp processing within the fruit juice production technology, and it is the most basic food product obtained from fresh fruit treatment as well as belonging to a broad category of industrial food waste (IFW). Given the large abundance of nutritional and bioactive compounds in these berries, the chosen residue - Goji berry mesocarp (GBM) was investigated in this work ought to show significant potential as biomass feedstock for the production of value-added chemicals and precursors to biofuels through the pyrolysis monitored by simultaneous thermal analysis (STA) measurements under non-isothermal conditions.

METHODS
Sample preparation
Fresh Goji berries were provided by A&S UNION D.O.O. Goji farm located in the Subotica City (North-Backi county), in the Republic of Serbia. All harvested fruits (harvest was done in July

2019) were randomly collected in the orchard from different plants and analysed as air-dried. The collected berries (about 1.0 kg of fresh berries packed in a plastic sealed bag) were frozen in the refrigerator at -8.0 °C before use. For experimental analyses, defrosting of a single bulked sample was performed naturally in the current sealed bag at room temperature. The passive drying of the sample was performed by lying of Goji berries out onto dry trays, and leaving them in a warm, airy place, away from the direct light until thoroughly dried.After drying, the separation of Goji berry mesocarp from other parts (seeds and exocarp) of dried fruit was performed mechanically, with increased care to avoid mesocarp damage. One part of dried berries was set aside for mesocarp preparation in thermal analysis (TA) measurements. For the mechanical separation of fruit parts, the singled scalpel-knife was used for the mesocarp secluding without the exocarp.

TA measurements

The effect of pyrolysis process under an inert atmosphere was investigated by simultaneous thermogravimetry (TG) and derivative thermogravimetry (DTG) using NETZSCH STA 445 F5 Jupiter (Erich NETZSCH GmbH & Co. Holding KG, Germany) thermal analyzer equipment. The purging gas was argon (Ar) (Class 5.0) with a flow rate of φ = 40 mL/min. The following heating rate values were used β = 5.0, 10.0 and 15.0 K/min. The heating rates were chosen to estimate the best conditions for performing a slow pyrolysis process. To reduce the influence of the sample quantity on the analyses, about (5.10± 0.01) mg of the sample was used in a platinum pan for each measurement analysis. The mesocarp samples were submitted to a linear temperature gradient (programmed heating in a linear mode) ranging from room temperature (RT) up to 710 °C. TA device has user-friendly menus combined with automated routines within Proteus® software for processing thermo-analytical experimental data.

RESULTS AND DISCUSSION

The mass loss (TG) and derivative mass loss (DTG) curves (as absolute mass loss rate curves) of the GBM feedstock sample in Aratmosphere at different heating rates (5.0, 10.0 and 15.0 K/min) are presented in Fig. 1 a) and b**)**.

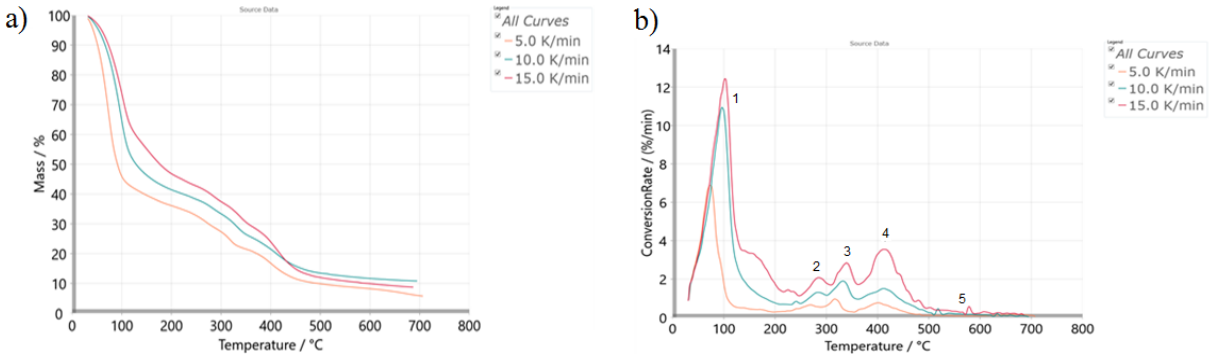

Figure 1. a) TG) curves and b) absolute DTG (conversion rate) curves of GBM pyrolysis at 5.0, 10.0 and 15.0 K/min (ordinal numbers "1 – 5" represent identified reaction stages).

It can be observed from TG features at all heating rates (Fig. 1 a)) that GBM feedstock retains a significant amount of water after air drying, where moisture removal intensifies to approximately 125 °C (step 1). The mass loss of the sample in this stage gradually decreases with an increasing of heating rate. This drop of the sample mass is a consequence of the water loss during the temperature rise (parallel with raising the heating rate value). So, the first phase of the process can be attributed to thermal dehydration of GBM, but it is possible to expect and decarboxylation process in labile

compounds.Within reaction step 1, the water evaporation is more intensive, but applying highest heating rate, the broader “shoulder” appears on DTG curves at about 150 ^{o}C (Fig. 1 b)).

The main pyrolysis temperature intervals related to reaction steps 2, 3 and 4 which are clearly differentiated can be attributed to decomposition of fibers, such as hemicelluloses (200 ^{o}C– 300 ^{o}C) and cellulose (300^{o}C– 360 ^{o}C) (peaks ‘2’ and ‘3’ – the hollocellulose pyrolysis), and decomposition of carbohydrates (sugars) with most prominent DTG peak (Fig. 1 b)) for 360 ^{o}C – 475 ^{o}C [4]. Since it has been reported that lignin decomposition take place over a wide temperature interval [5], the main lignin pyrolysis zone probably occurs above 500 ^{o}C (considering step 5). It should be emphasized that biomass feedstock with high volatile matter (VM) content may generates a lot of large molecular compounds, so that a more activation energy was needed to overcome the energy barrier and drive pyrolysis process further. Thus, at high *T*, some of lipid molecules may evaporate and remote decomposition of them, demanding more activation energy inputs. Therefore, these lipids can repair pyrolysis activation energy at the end of entire process. The production of key intermediate platform chemical such as 5-hydroxymethylfurfural (5-HMF) emerges fromD-fructose dehydration proceeds *via* higher activation energy, where reaction takes place in a higher temperature region (Fig. 1) [6]. Using NETZSCH Kinetics NEO advanced tool package (product version: 2.6.0.1, build date: 2/16/2022; for more information the reader is referred to https://kinetics.netzsch.com, kinetics.neo@netzsch.com), the complex reaction curve at each heating rate was resolved into the sum of individual peaks attached to every identified reaction step within the established scheme *code p*:;, with the possibility of extracting the desired reaction step of interest. Using Gaussian and Fraser-Suzuki (asymmetric Gaussian) functions together with a set of defined concentrations and application of Akaike information criterion (AIC), theoretical estimation of %-yield of 5-hydroxymethylfurfural (5-HMF) forfructose dehydration route (in a presence of Lewis acids as catalysts) was determined at each heating rate used. Fig. 2 a) – c) shows 3-D color map surface as spatial dependence of temperature (^{o}C) – time (min) – 5-HMF yield (%) at various heating rates. Change in %-yield of produced 5-HMF at observed heating rate is given through color spectrum in a legend of presented figure.

a) b) c)

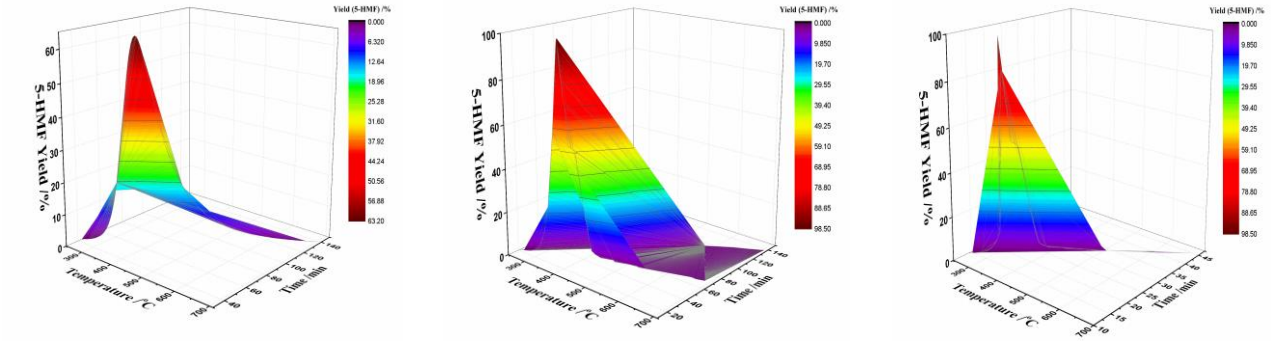

Figure 2. 3-D color map surface of temperature (^{o}C) – time (min) – 5-HMF (theoretically) yield (%) for: a) 5.0 K/min, b) 10.0 K/min, and c) 15.0 K/min.

It can be observed that applied heating rate has a strong influence on the spatial geometric shape of surface, increasing asymmetry as heating rate increases. Also, the yield of 5-HMF strongly depends on the applied heating rate, whereby at lowest heating rate, the 5-HMF-yield of 63.20 % is achieved (Fig. 2 a)). Above 5 K/min, the yield of 5-HMF shows a large increase up to 98.50 %, but yield then becomes independent at higher heating rates (Fig. 2 b) and 2 c)). The emergence of interesting phenomenon should be emphasized here. With an increase of heating rate magnitude,

maximum temperature (T_{max}) as well as maximum time (t_{max}) at which a given yield of 5-HMF is achieved decrease, moving towards lower values in apparently low-temperature region (Table 1).

Table 1. 5-HMF yield, maximum temperature (T_{max}) and maximum time (t_{max}) at 5.0, 10.0 and 15.0 K/min

β /K/min	5-HMF-yield /%	T_{max}/°C[a]	t_{max} /min
5.0	63.2	356.7	65.3
10.0	98.5	350	32
15.0	98.5	310.3	18.7

[a]Temperature differences ΔT: 5.0 → 10.0 K/min = 6.7°C; 10.0 → 15.0 K/min = 39.7°C.

This means that fructose acts as an inhibitor for forward reaction route *via* rehydration to obtain levulinic acid (LA) and the formic acid (FA). Considering this fact, the rehydration reaction can be neglected. Then, fructose opens a "new" catalytic pathway, shifting reaction backwards, unto the glucose isomerization path, forcing glucose to dehydrate and producing a very high yield of 5-HMF (Figs. 2 b) and **2** c)). This is a direct consequence of fructose autogenic behavior with constraining coupling. Therefore, high heating rates causes increased production of fructose, which thus opens a new reaction pathway which due to falling entropy extends unfavorable route regenerating glucose molecules, where other chemical entities (as already present Lewis acids) isolate glucose, for the one-pot conversion [7] to 5-HMF in a short time and obviously with a lower activation energy. Therefore, heating rate magnitude affects on "organized work" of fructose, and thus maintaining its active capacity for transferability to glucose. Calculated high yield of 5-HMF is achieved *via* transferable pathway to glucose at higher values of heating rates (≥ 10.0 K/min) which significantly shortens the conversion.

CONCLUSION

This work aimed to verify abilities of Goji berry mesocarp (GBM) to provide the production of value-added chemicals and precursors to biofuels through slow pyrolysis process, performed by simultaneous TG-DTG measurements. It was reported that autocatalytic dehydration of fructose is responsible for achieving a lower yield 5-HMF at lower heating rate (5.0 K/min). The higher heating rates (10.0 and 15.0 K/min) triggered the fructose autogenesis behavior, which opens transferability channel to the glucose engagement for 5-HMF high yield production.

Acknowledgment

This work was supported by the Ministry of Education, Science and Technological Development of the Republic of Serbia (grant no 451-03-68/2022-14/200017).

REFERENCES

[1] V. Strezov, Properties of Biomass Fuels. In: Biomass Processing Technologies, V. Strezov& T.J. Evans (Eds.), CRC Press, Taylor & Francis Group, Boca Raton, FL, USA, 2014, pp. 1-32.
[2] Opatokun, S.A., Strezov, V., and Kan, T., Energy, 92 (2015) 349-354.
[3] Anex, R.P., Aden, A., Kazi, F.K., Fortman, J., Swanson, R.M., Wright, M.M., Satrio, J.A., Brown, R.C., Daugaard, D.E., Platon, A., Kothandaraman, G., Hsu, D.D., and Dutta, A., Fuel, 89 (2010) S29-S35.
[4] Jo, J-H., Kim, S-S., Shim, J-W., Lee, Y-E., and Yoo, Y-S., Energies, 10(8) (2017) 1191.
[5] Brebu, M., and Vasile, C., Cellulose Chemistry and Technology, 44(9) (2010) 353-363.
[6] Kunov-Kruse, A.J., Riisager, A., Saravanamurugan, S., Berg, R.W., Kristensen, S.B., and Fehrmann, R., Green Chemistry, 15 (2013) 2843-2848.
[7] Liang, F., Chen, D., Liu, H., Liu, W., Xian, M., and Feng, D., ACS Omega, 4(5) (2019) 9316-9323.

ANTIRADICAL ACTIVITY OF NEW STRAWBERRY CULTIVAR EXTRACTS INCORPORATED INTO LIPOSOMES – AN EPR STUDY

Đ. Nakarada [1], D. Milosavljević [2], J. Milivojević [3], J. Dragišić Maksimović [2] and M. Mojović[1]

[1]University of Belgrade, Faculty of Physical Chemistry, Studentski trg 12-16, 11000 Belgrade, Serbia. (djura@ffh.bg.ac.rs)
[2]University of Belgrade, Institute for Multidisciplinary Research, Kneza Viseslava 1, 11030 Belgrade, Serbia,
[3]University of Belgrade, Faculty of Agriculture, Nemanjina 6, 11080 Belgrade, Serbia

ABSTRACT
Strawberries are rich in various health-promoting compounds. A particularly high yield of these molecules could be extracted using methanol which is unfortunately harmful to living beings. To surpass the problem of solvent toxicity, in this paper, we have incorporated methanol extracts of two novel strawberry cultivars into liposomes. Our results show that both extracts possess significant antiradical activity towards hydroxyl and DPPH radicals, unaltered by lipids from liposome membranes. These results indicate that otherwise toxic extracts could easily be turned into a promising pharmaceutical product.

INTRODUCTION
Strawberries are among the most consumed berry fruits in the world. They are rich in antioxidant compounds such as vitamins, melatonin, polyphenols, and bioactive sugars. The most abundant phenolic compounds found in strawberries are anthocyanins, flavan-3-ols, ellagitannins, glycosides of quercetin, and kaempferol. These compounds contribute to the sensorial and organoleptic attributes of strawberries, and most importantly, to their health-promoting properties. With large-scale production, several new cultivars of strawberries are introduced each year. 'Tea' and 'Aprika' are two new strawberry cultivars that are in the testing phase with still unexplored antioxidant potential. Extraction is the crucial step in studying biologically active compounds of plants, and it plays an important role in the results and conclusions. Various techniques as well as various solvents and their mixtures have been used to obtain strawberry extracts with high concentration and high variety of biologically active compounds, thus having high antioxidative activity. Previous studies indicate that extracts prepared using 80% methanol (MeOH) possess a plethora of compounds responsible for the high antioxidative activity. However, due to its harmful health effects, MeOH extracts are not suitable for pharmaceutical applications. On the other hand, many of the antioxidant molecules which are present in MeOH extracts have low solubility in water, making their antioxidative activity towards biologically relevant radicals difficult to study. Electron paramagnetic resonant (EPR) spectroscopy is the only experimental technique capable of direct radical detection. EPR technique has high selectivity and detection limit and obtained results do not depend on the optical characteristics of substances. During redox analysis, biologically relevant free radicals, like $^{\bullet}OH$, $^{\bullet}O_2^-$, and $NO^{\bullet}$, have to be generated using water as a solvent. Using other organic solvents give rise to carbon-based radicals as artifacts during their interaction with reactive oxygen species, seriously bringing into question the usability of the obtained results.

To overcome an issue of pharmaceutical applicability of MeOH strawberry extracts, as well as the problem of studying their antiradical activity, the extracts of two novel strawberry cultivars have been incorporated into the membrane of 1,2-dipalmitoyl-sn-glycero-3-phosphocholine (DPPC) liposomes. The antiradical activity of these liposomes towards hydroxyl ($^{\bullet}OH$) and 2,2-diphenyl-1-picrylhydrazyl (DPPH) radicals was studied to determine the radical scavenging potential of

strawberry extracts and to evaluate whether lipids from the liposome membranes affect the obtained results.

METHODS

Extracts of two strawberry cultivars ('Tea' and 'Aprika') have been prepared by homogenization of 1 g of frozen fruit with 3 ml of 80% methanol. The mixture was transferred into the microcentrifuge tube and centrifuged for 10 min at 10 000 rpm. The obtained extracts were further filtered through the 0.22 µm HPLC filter. Extracts were stored at -80 °C until analysis. Multilamellar liposomes were prepared from strawberry extracts and DPPC by the modified thin-film method [1]. This was done by dissolving 2.5 mg of DPPC in the mixture of chloroform and methanol (4:1 v/v) in a rotary flask, followed by the addition of 250 µl of the strawberry extract. The solvent was slowly evaporated at room temperature using a rotary vacuum evaporator. The remaining thin film was hydrated with 2 ml of 18 MΩ water in increments of 250 µl, each followed by 3 min of vigorous vortexing and 3 min of sonication using an ultrasound ice bath. The suspension was further sonicated for 20 min. In order to obtain the uniform size of liposomes, the suspension was extruded through a 100 nm membrane. Finally, liposomes were concentrated to the volume of 250 µl using a vacuum concentrator. Control liposomes were prepared following the same procedure, without the addition of strawberry extracts. To determine the size and stability of liposomes, 750 µl of the suspension was placed into the disposable cuvette and size/zeta-potential was measured using Malvern Zetasizer Nano ZS90 dynamic light scattering (DLS) analyzer.

EPR spin-trapping technique was employed in order to trap short-lived free radical species generated directly in the liposome suspension and to quantify the amount of their interaction with liposomes. To study the interaction of hydroxyl radicals with strawberry-derived antioxidant compounds from the liposomes, the intensity of the hydroxyl spin-adduct EPR signal was measured. 26 µl of the liposome suspension was mixed together with 2 µl of 5 mM H_2O_2 and 1 µl of 100 mM 5-(diethoxyphosphoryl)-5-methyl-1-pyrroline-N-oxide (DEPMPO). After the addition of 1 µl of 5 mM $FeSO_4$, the mixture was transferred into a 1 mm diameter Teflon tube, and EPR spectra were recorded using Bruker ELEXSYS-II E540 EPR spectrometer [2].

The interaction of DPPH free radicals with strawberry-derived antioxidant compounds from the liposomes was studied by measuring the intensity of the DPPH EPR signal. 26 µl of the liposome suspension was mixed with 3 µl of deionized water and 1µl of 3.2 mM DPPH, prior to transferring the mixture into a 1 mm diameter Teflon tube and recording the EPR spectra.

All EPR spectra were recorded using the following parameters: center field 3500 G, microwave power 10 mW, microwave frequency 9.85 GHz, modulation frequency 100 kHz, and modulation amplitude 1 G. Control experiments have been made following the same procedures, using water instead of liposome solution.

RESULTS AND DISCUSSION

The results of the DLS measurements showed that the size of liposomes containing strawberry extracts ranged between 65 and 69 nm, while their mean zeta potential was -6 mV. This indicates the overall uniform size distribution and relative stability of the liposomes. The decrease of the intensities of DEPMPO/OH adduct and DPPH EPR signals were measured 2 min after mixing experimental solution in the suspension of liposomes containing strawberry extracts (Figure 1). The reduction of the EPR signal was calculated using the formula:

$$\Delta h = \frac{h_i - h_2}{h_i} \times 100\ (\%)$$

where h_i and h_2 refer to the intensities of the control free radical signal and the signal after 2 min (liposomes containing strawberry extracts). The calculated percentage of the DEPMPO/OH adduct

EPR signal reduction was 92.65% for liposomes containing extract of 'Tea', and 78.00% for those containing extract of 'Aprika' strawberry cultivar. Regarding DPPH$^{\bullet}$ free radical, the calculated EPR signal reduction amounts to 30.10% for 'Tea' and 16.26% for 'Aprika' cultivar. These results indicate that liposomes containing strawberry extracts have a rather strong antioxidant capacity and that they react more selectively with $^{\bullet}$OH than with DPPH radicals. Liposomes containing extracts of 'Tea' strawberry cultivar showed stronger antiradical activity compared to 'Aprika' cultivar. These findings are very interesting having in mind that DPPH radicals are routinely used in antioxidant scavenging assays despite that they have no biological relevance, while $^{\bullet}$OH radicals are of great importance considering their role in many physiological processes. To confirm that obtained results arise only from strawberry-derived antioxidant compounds from the liposomes, and not from DPPC, control experiments were performed using 100% DPPC liposomes (prepared using the same procedure previously described). These experiments showed no EPR signal reduction (data not shown). Altogether, the results presented in this paper strongly indicate that strawberry-derived antioxidant compounds incorporated into the membrane of the DPPC liposomes have rather significant antioxidant potential, which is not affected by the DPPC.

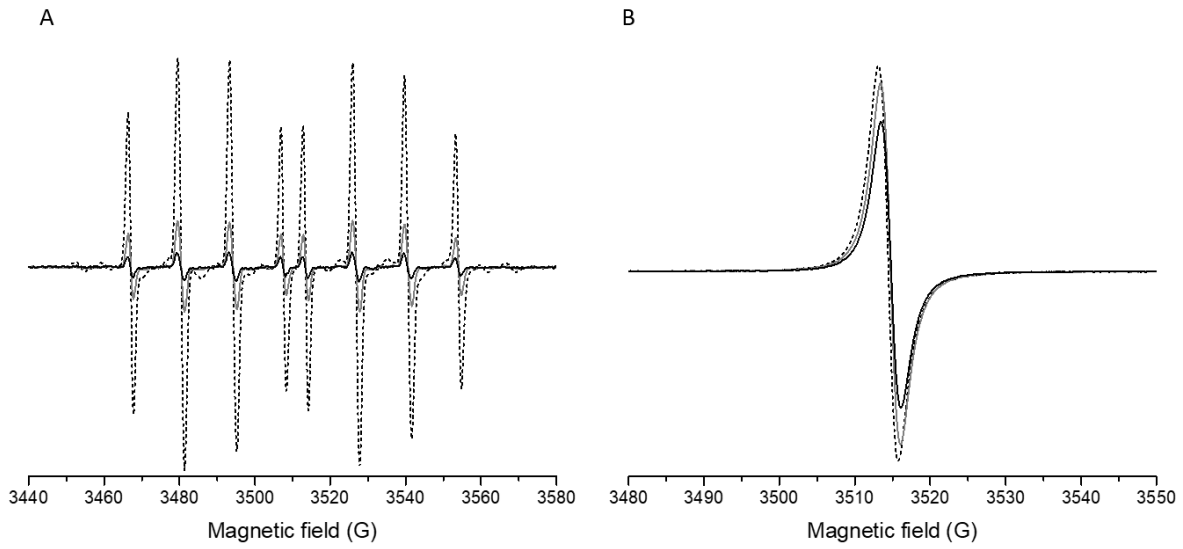

Figure 1. EPR spectra of DEPMPO/OH adduct (A) and DPPH radical (B) recorded in the control sample (dotted) and 2 min after mixing the experimental solution in the suspension of liposomes containing 'Aprika' (grey) and 'Tea' (black) strawberry extracts.

These findings further confirm the validity of the recent approach for measuring the antioxidative activity of water-insoluble molecules towards biologically relevant radicals, developed by our group [3]. To additionally validate selectivity in terms of the antiradical activity of strawberry extracts, experiments on other free radical species (such as NO$^{\bullet}$, $^{\bullet}O_2^-$ and Asc$^{\bullet}$) will be performed. Experiments obtaining strawberry extracts using different solvents should be performed to determine the type of extract bearing the strongest antiradical activity and being the most appropriate for liposomal encapsulation.

CONCLUSION

Liposomes are important nanostructures suitable for studying the antioxidant activity of various hydrophobic and hydrophilic molecules. In this paper, the method of incorporating biologically active compounds into liposomes was applied for MeOH extracts of two novel cultivars of strawberries, assessing their antioxidative activity towards $^{\bullet}$OH and DPPH radicals. Liposomes

obtained using 'Tea' strawberry extract in MeOH have reduced DEPMPO/OH adduct EPR signal by 92.65% while the reduction rate was 78.00% for those obtained using MeOH extract of 'Aprika' strawberry cultivar. The calculated DPPH EPR signal reduction amounts to 30.10% for 'Tea' and 16.26% for 'Aprika' cultivar. These results indicate strong and selective antiradical activity of liposomes containing strawberry-derived antioxidant compounds, unaffected by lipids from the liposomes. Taken altogether, the findings of this study demonstrate the significant potential of the encapsulation of strawberry-derived antioxidant compounds obtained from MeOH extracts into liposomes and their promising use for various pharmaceutical purposes.

Acknowledgment
This work was supported by the Ministry of Education, Science and Technological Development of the Republic of Serbia (Contracts No 451-03-68/2022-14/200146, 451-03-68/2022-14/200053; 451-03-68/2022-14/200116).

REFERENCES

[1] V. Weissig, Liposomes: Methods and Protocols, Vol. 1: Pharmaceutical Nanocarriers, Humana Press, Mumbai, 2010.
[2] M. Mojović, M. Vuletić, G. Bačić, Detection of Oxygen-Centered Radicals Using EPR Spin-Trap DEPMPO: The Effect of Oxygen, Ann. N. Y. Acad. Sci., 1048 (2006) 471 – 475.
[3] Đ. Nakarada, B. Pejin, G. Tommonaro, M. Mojović, Liposomal integration method for assessing antioxidative activity of water insoluble compounds towards biologically relevant free radicals: example of avarol, J. Liposome Res., 30 (3) (2019) 218–226.

MICROWAVE ASSISTED ISOLATION OF PECTIN FROM RED ORANGE PEELS USING GREEN SOLVENTS

A. Gavran, A. Jevremović, D. Bajuk-Bogdanović, M. Milojević-Rakić, M. Mojović and A. Pavićević

Faculty of Physical Chemistry, University of Belgrade, Studentski trg 12-16, 11000 Belgrade, Republic of Serbia (aleks.pavicevic@ffh.bg.ac.rs)

ABSTRACT

Food waste is becoming a burning issue intertwined with various other environmental problems that require urgent attention. Citrus waste comprises a large portion of the total food waste generated upon production of juices, jams and essential oils. Its disposal into the soil presents an environmental threat, due to high oxygen and nitrogen consumption, and CO_2 emission upon degradation by a soil microbiome. Bearing in mind that citrus waste is composed of very valuable compounds, their extraction may help in the reduction of generated biowaste. However, extraction procedures need to be optimized in order to reduce their impact on the environment. In the present study, we suggest a microwave-assisted method for pectin isolation from red orange peels by using citrate solution as a "green" alternative extraction agent. The results indicate that this procedure gives high yields of low-esterified, negatively charged pectin, that may be a suitable candidate for a variety of applications.

INTRODUCTION

Citrus crops are among the most popular fruits, grown in around 140 countries in the subtropical and tropical regions. They belong to the family of *Rutaceae*, which encompasses around 1300 species [1]. According to the "Citrus Fruit Fresh and Processed Statistical Bulletin 2020" published by the Food and Agriculture Organization (FAO), the world production of citrus crops in 2019 was approximately 143 million tons, among which it is estimated that roughly 30% is utilized for processing, mainly for juice, essential oils, and citric acid production [2]. Citrus processing generates cca. 60 million tons of biowaste annually worldwide in the form of peels, seeds and membrane residues [1]. Even though this waste is biodegradable, if untreated, it still represents a serious environmental threat, due to the high oxygen consumption, CO_2 emissions, and depletion of soil nitrogen upon bacterial decomposition at the waste disposal site. Thus, there is a significant effort in the scientific community to develop eco-friendly methods for the extraction of very valuable compounds from citrus waste, such as cellulose and pectin fibers, essential oils (limonene), polyphenols, flavonoids and vitamins [1,3]. In this study, we have addressed the extraction of pectin from red orange peels, due to the high demands for pectin in food industry as a gelling agent [1], and on the other hand, for its applicability as a biosorbent for heavy metals [4]. Pectin is a heteropolysaccharide comprised of mainly galacturonic acid (GalA), whose carboxylic group can be methyl-esterified. The degree of methyl-esterification (DE) determines physicochemical properties of pectin, and accordingly it can be classified as high- (DE > 50%) and low-methyl-esterified (DE < 50 %) pectin [5]. Common industrial procedures for pectin isolation include treatment of raw peel material with hot mineral acids for several hours, which lead to the corrosion of the machinery, and also pose a hazard to the environment. Citric acid and citrate buffers have been suggested as "green" substitutes for mineral acids, given that citric acid is regarded as safe, and approved as direct human food ingredient by the Food and Drug Administration (FDA) [5]. Hence, in this study we attempt to improve the suggested extraction methods in terms of energy efficiency, yield and

environmental impact by utilizing microwave (MW) radiation and citric acid to extract pectin from red orange peels.

METHODS

Red oranges were bought at the local store and manually peeled. Peels were air-dried for a couple of days and ground until a very fine powder was obtained, which was in the next step passed through a sieve. Samples for MW assisted extraction were prepared by mixing 4 g of dry peel powder with 100 ml of 0.1 M citrate solution (pH 8.0). Afterwards, the flask with the mixture was placed inside a MW-oven and heated up at 160 W for 10, 20 and 30 min, respectively. Due to the high extent of water evaporation, after MW digestion samples were filled up to 100 ml by adding deionized water, and left to cool down to room temperature. Subsequently, samples were centrifuged at 7000×g for 20-40 minutes. Pellet was discarded, while supernatant was transferred to glass beakers, mixed with 1.5-fold volume of 96% ethanol for pectin precipitation and left in fridge at 4 ^{o}C overnight. The precipitated pectin was further washed twice with 60 % ethanol, and dried in an oven at 60 ^{o}C until a constant mass was obtained. Pectin yield was calculated as ratio of dried pectin mass and mass of starting dried peel powder.

In order to characterize obtained pectin, Fourier-transform infrared spectroscopy (FT-IR) was performed using a Nicolet iS20 FT-IR spectrophotometer equipped with a diamond crystal for the attenuated total reflection (ATR) analysis, by collecting 32 scans at 2 cm^{-1} resolution.

RESULTS AND DISCUSSION

In order to establish optimal conditions for obtaining the product of a satisfying quality, while on the other hand employing an energy efficient procedure, the duration of MW heating was varied at the lowest available MW power. Yields calculated for the different experimental setups are summed in Table 1.

Table 1. Pectin yields obtained by extraction from dried red orange peels at different MW irradiation times.

Time (min)	Yield (%)
10	13.8 ± 0.2
20	28.8 ± 0.2
30	33.4 ± 0.2

It can be clearly observed that prolonged MW heating has a significant impact on the final product quantity, which is in line with literature findings [6]. These yields are comparable to the ones obtained in a similar study where pectin extraction from sour orange peels was performed at varying citrate solution pH values, MW powers and irradiation times [6]. In that study, maximum yield achieved was 26.4% at pH 1.5, and 700 W MW irradiation for 3 min [6]. Even though comparison between the results obtained in these two studies may imply that in the present study the selected parameters are less energy efficient, such a conclusion needs to be drawn carefully, since variations in experimental setups, namely, different orange varieties (and thus peel pectin content), pH values (8.0 vs. 1.5), starting amounts of dried orange peel powders (4 g vs. unknown), and total citrate solution volumes (100 ml vs. unknown) may alter the final outcome of the extraction procedure. Also, it should be highlighted that extraction performed in acidic and alkaline solutions yield pectins of different physicochemical properties [5].

Furthermore, the extraction product was investigated by ATR FT-IR spectroscopy in order to confirm presence of pectin. ATR FT-IR spectra are given in Figure 1. All the typical peaks found in literature for pectin could also be observed in Figure 1 [5–7]. The pronounced peak between 3300

and 3500 cm^{-1} corresponds to the stretching vibrations of -OH groups [6]. The smaller peak observed in the region of 2850-3000 cm^{-1} is assigned to different C-H vibrational modes [6]. The characteristic peak reported for pectin at around 1750 cm^{-1} originates from the C=O stretching of methyl-esterified-carboxylic groups [5,6]. This peak is very weak in all three spectra depicted in Figure 1, which is coherent with the results obtained by other authors, showing that the extraction performed in slightly alkaline solutions yields low-methyl-esterified pectin [5,7]. Two peaks at approx. 1630 cm^{-1} and 1440 cm^{-1} are assigned to an asymmetric and symmetric stretching of unesterified carboxylic group, respectively [5,6]. However, in the spectra shown in Figure 1. these peaks are shifted to 1595 and 1405 cm^{-1}, indicating the presence of carboxylic groups in a dissociated form, i.e. Na^+ salt [5,7].

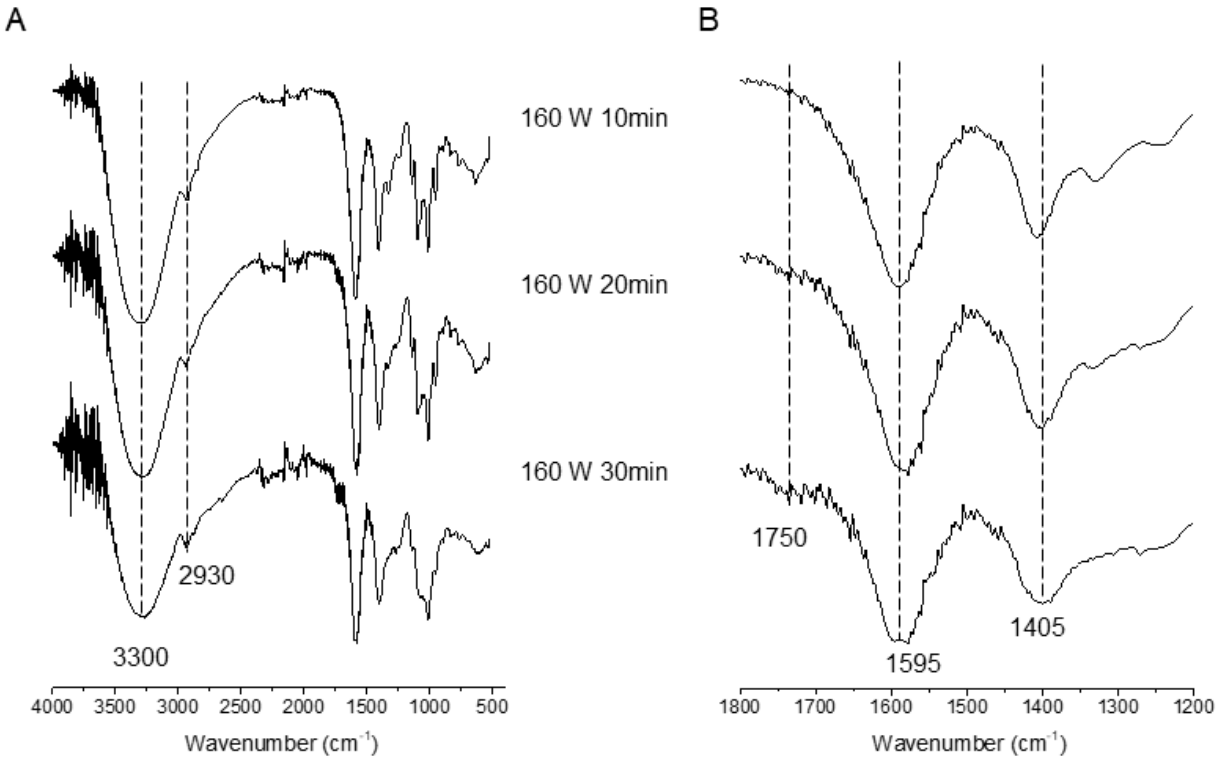

Figure 1. ATR FT-IR spectra of three preparations of pectin, obtained by MW (160 W) irradiation for 10, 20 and 30 minutes in the range of: A) 4000-400 cm^{-1} and B) 1800-1200 cm^{-1}.

CONCLUSION

In this study it was demonstrated that pectin was successfully isolated from red orange peels at very high yield by using a slightly alkaline citrate solution. Moreover, it was shown that the yield was significantly increased by extending the duration of MW irradiation. Identification of peaks in FT-IR spectra showed that the obtained pectin is low-methyl-esterified and negatively charged. The presented results are just the pilot study, and further characterization is needed in terms of mono- and disaccharide content, degree of methyl-esterification etc. However, from the data provided it can be already suggested that the described method for pectin extraction may have multiple environmental benefits – citrus biowaste generated by food industry can be reduced and upcycled to pectin, that is produced by employing a "green" solvent, and the final product can potentially be used as a biosorbent for heavy metals, and other cations, thereby reducing pollution.

Acknowledgment
This work was supported by the Ministry of Education, Science and Technological Development of the Republic of Serbia (grant no. 451-03-68/2022-14/200146).

REFERENCES

[1] N. Mahato, Foods, 8 (2019) 523.
[2] Citrus Fruit Fresh and Processed Statistical Bulletin 2020, Food and Agriculture Organization of the United Nations, (n.d.). https://www.fao.org/policy-support/tools-and-publications/resources-details/en/c/1439010/
[3] M. Anticona, Foods. 9 (2020) 811.
[4] R. Wang, Trends Food Sc. Technol., 91 (2019) 319.
[5] C. He, ACS Sustainable Chem. Eng. 9 (2021) 833.
[6] S.S. Hosseini, Carbohydr. Polym., 140 (2016) 59–65.
[7] O. Kurita, Carbohydr. Polym., 74 (2008) 725.

O *– Pharmaceutical Physical Chemistry*

DIFFERENT EFFECT OF ZALEPLON ON GABAERGIC SIGNALING IN THE PREFRONTAL CORTEX AND HIPPOCAMPUS OF MALE WISTAR RATS

J. Martinovic[1], S. Ivkovic[1], M. Zaric Kontic[1], I. Gusevac Stojanovic[1], N. Mitrovic[1], I. Grkovic[1] and J. Samardzic[2]

[1]*Department of Molecular Biology and Endocrinology, VINČA Institute of Nuclear Sciences-National Institute of the Republic of Serbia, University of Belgrade, Belgrade, Serbia. (jelenazlatkovic@vinca.rs)*
[2]*Institute of Pharmacology Clinical Pharmacology and Toxicology, Faculty of Medicine, University of Belgrade, Belgrade, Serbia.*

ABSTRACT
Insomnia is a highly prevalent sleep disorder affecting 33-50% of adult population. Z drugs arose as suitable insomnia treatment due to binding selectivity and pharmacokinetic, with reduced potential for abuse and lower affinity for tolerance and withdrawal syndrome. Zaleplon binds selectively to the α1 subunit of the γ-aminobutyric acid receptor ($GABA_AR$) and, as positive allosteric agonist, increases the efficacy of $GABA_AR$ channel opening. Although been on the global market for a long time, molecular studies related to Zaleplon and other Z drugs are scarce. We examined GABA level across the rats' prefrontal cortex (PFC) and hippocampus (HIP) and expression of synaptic $GABA_AR$ α1 subunit in these brain regions following 5-days Zaleplon treatment. Increased GABA and $GABA_Aα1$ levels were observed in the HIP while in the PFC GABA were unchanged and $GABA_Aα1$ level decreased. This region-specific effect and potential cross-talk between GABA and other signaling will be further examined.

INTRODUCTION
According to *Diagnostic and Statistical Manual of Mental Disorders, 5th ed.* (DSM-5) insomnia is disorder characterized by poor sleep quality or quantity that causes distress or impairment in important areas of functioning, sometimes to such an extreme that patients' work or social life suffers. According to statistics, about one-third of adults experienced symptoms of insomnia, while six to ten per cent of individuals meet the criteria for insomnia disorder. Although behavioral-cognitive therapy is recommended as the first-line treatment of insomnia, it is not readily accessible and medication is still the treatment of choice. Drugs approved for treating insomnia target receptors involved in the regulation of the sleep and wake cycle such as γ-aminobutyric acid (GABA), melatonin, histamine, and orexin/hypocretin receptors [1].

GABA is the main inhibitory neurotransmitter in the CNS that affects brain function via two distinct classes of receptors. $GABA_A$ receptor ($GABA_AR$) is a ligand-gated chloride channel that mediates fast inhibitory signals through rapid postsynaptic membrane hyperpolarization, whereas the metabotropic $GABA_B$ receptors produce slow and prolonged inhibitory signals via G proteins and second messengers [2]. In mammals, $GABA_ARs$ are assembled in a heteropentameric structure as a combination of 19 subunits (α1–6, β1–3, γ1–3, δ, ε, θ, π, and ρ1–3), which affect their biophysical properties and affinity for GABA, pharmacology and location on the cell [3]. The majority of mammalian brain $GABA_AR$ receptors consist of αβγ2 subunits that are located on the synapse and represent the site of action of several different classes of drugs. Positive allosteric $GABA_AR$ agonists bind at specific sites on the receptor, distinct from the GABA-binding site, change the shape of the receptor oligomer and increase the efficacy of GABA for opening the channel. This results in

sedative, anxiolytic, muscle-relaxant, and hypnotic effects [4], widely exploited in medicine (e.g., for the general anesthesia, as treatment for anxiety disorders, or sleep disorders). Benzodiazepines (BDZ) are traditionally used clinically to treat anxiety and insomnia, however, the development of tolerance and dependence after long-term treatment, as well as the abuse potential, limit their use. Although sharing similar mechanism of action, Z drugs (Zaleplon, Zopiclone, eszopiclone, and zolpidem) emerged as 'safe' BZD substitutes due to their binding selectivity and pharmacokinetic, with reduced potential for abuse and lower affinity for tolerance and withdrawal syndrome. However, current data suggest that the misuse, abuse, dependence, and withdrawal issues also may be associated with the use of all Z drugs, although zaleplon may present comparatively lower levels of risk [5].

Zaleplon is a selective full agonist of the $GABA_AR$ that acts preferentially at α1 subunit [6], indicated for the short-term treatment of insomnia (review in detail in [7]). Although it has been on the market since 1980s, there are no molecular studies related to Zaleplon, as most studies refer to clinical observation [8] [9] [10] or pharmacological and behavioral studies [11] [12]. Hence, for the first time, we strived to examine the molecular mechanism of Zaleplon action, with emphasis on GABAergic signaling in different brain regions. We have already reported that, in rats, repeated Zaleplon administration at a lower dose affects the level of vesicular GABA transporter (VGAT), protein responsible for GABA packaging into synaptic vesicles [13]. Further analysis involved investigation of GABA level across the prefrontal cortex (PFC) and hippocampus (HIP) as well as expression of α_1 subunit of $GABA_AR$ in the synaptosomes of these brain regions.

METHODS

All experimental procedures were conducted in accordance with the rules of the Ethical Committee for the Use of Laboratory Animals of the VINCA Institute of Nuclear Sciences (authorization reference number: 323-07-06688/2020-05), and the European Communities Council Directive (2010/63/EU). Adult male Wistar rats were kept under standard housing conditions: regular 12h light/12h dark cycle with constant temperature (21 ± 2°C) and humidity. Commercial rat pellet and tap water were available *ad libitum*. For the purpose of the experiment rats were randomly divided to two groups: one group received Zaleplon (0,625 mg/kg, *i.p.*) for 5 days (Zal, n=9) while control group (Con, n=9) received the same volume of vehicle. At the end of the treatment rats were sacrificed using small animal guillotine (Harvard Apparatus, USA), brains were carefully isolated from the scull and processed according to further analyses.

For the immunoblot analysis, following brain removal, PFC and HIP were dissected and placed in ice-cold isolation medium (0.32 M sucrose, 5 mM Tris-HCl pH 7.4) for immediate preparation of synaptosomes. After homogenization and centrifugation at 3000 rpm for 10 min at 4°C supernatant was again centrifugated 20 minutes at 9800 rpm at 4°C. Obtained crude synaptosomal pellet was layered onto a Ficoll gradient and synaptosomes were collected after centrifugation at 65,000 g at 4°C for 55 min. The protein content was determined according to the modified Lowry method [14] using bovine serum albumin as a standard.

Equal amount of total protein from each sample (25 μg) diluted with Laemmli sample buffer (250 mM Tris-HCl pH 6.8, 10% SDS, 30% glycerol, 5% β-mercaptoethanol, 0.02% bromophenol blue) was separated on 10% SDS– PAGE gel and transferred to PVDF membranes (Imobilion-P membrane, Millipore, USA). Membranes were blocked in TBS containing 10% BSA and 0.1% Tween 20 (TBST) for 1h, incubated overnight at 4 °C with primary ANTI-$GABA_A$ Receptor (α1 subunit) (Sigma Aldrich, G4416), following by appropriate horseradish peroxidase conjugated secondary antibody. After washing in TBST, the membranes were incubated with the enhanced chemiluminescence system (Immobilon Western Chemiluminescent HRP Substrate, Millipore, USA) and immunoreactive bands were detected on X-ray films in the dark chamber. β- actin (Thermo Fisher Scientific, USA; PA1-21167) was quantified and used as a loading control. The signal intensity was

evaluated using Image J software package and results were expressed relative to the control value (Con group).

For the immunohistochemical analysis additional 3 brains per group were carefully isolated from the skull and fixed in 4% paraformaldehyde (dissolved in 0.1 M PBS) for 24h at 4 °C. After fixation, brains were transferred into graded sucrose (10% - 30% in 0.2 M phosphate buffer) for cryoprotection at 4 °C. The dorsal HIP (-3.12 to -3.84 mm AP to Bregma) and PFC (5.16 to 3.00 mm AP to Bregma, Paxinos et al 2005) were cryosectioned in 25 µm thick coronal section, air-dried for 2h at room temperature (RT) and stored at -20 °C until further use.

Prior to analysis slides were tempered at RT for 30 min and washed in phosphate-buffered saline (PBS). After washing, slides were permeabilized using Triton X-100 (0.5%) in PBS (PBT) for 30 min at RT and then incubated with 10 % normal donkey serum (Abcam, UK) for 1h at RT to block nonspecific binding. This was followed by the incubation with polyclonal rabbit anti-GABA antibody (Sigma 2062, 1:500) overnight at 4 °C in a humid chamber to prevent drying. Next day, slides were washed in PBS and probed with goat anti-rabbit AlexaFluor (488, 1:400) conjugated secondary antibody (Molecular probes) for 2h at RT. After washing in PBS, the sections were stained with DAPI (4',6-Diamidino-2-fenilindol), covered with Mowiol-mounting media (Sigma) and evaluated using fluorescent microscopy. Sections were visualized and images captured on an Axio Observer Microscope Z1 using an AxioVision 4.6 software system (Carl Zeiss, Germany). The findings reported as microscopic images were representative of staining performed in three brain sections per group.

RESULTS AND DISCUSSION

GABA is expressed in the inhibitory neurons in the cortex and HIP. The effect of GABAergic inhibition depends on the GABA levels but on the presence of GABAR as well.

GABA fluorescence was quite evident within the cell bodies of GABAergic neurons and was also visible in the main dendritic arbors and axonal terminals. We found that the levels of GABA expression in the HIP of Zaleplon-treated rats were elevated compared to the controls (Figure 1 B, D). In the same time GABA immunohistochemistry revealed that the levels of GABA expression in the PFC remained unaltered in the Zaleplon-treated rats (Figure 1 A, C).

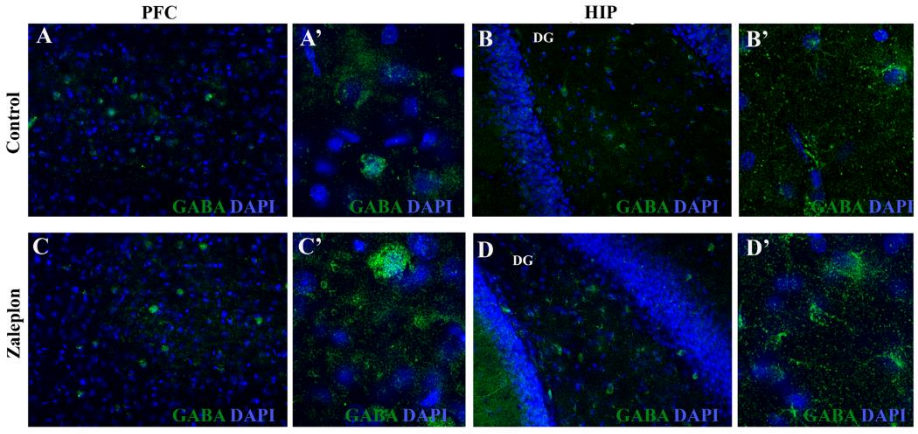

Figure 1. The expression of GABA in the rat prefrontal cortex (PFC A, C) and hippocampus (HIP B, D) in control animals (A, B) and following Zaleplon treatment (C, D). GABA – green, DAPI – blue, DG – dentate gyrus. Magnification 20x, A', B', C', D' – magnified areas from A, B, C, D; respectively.

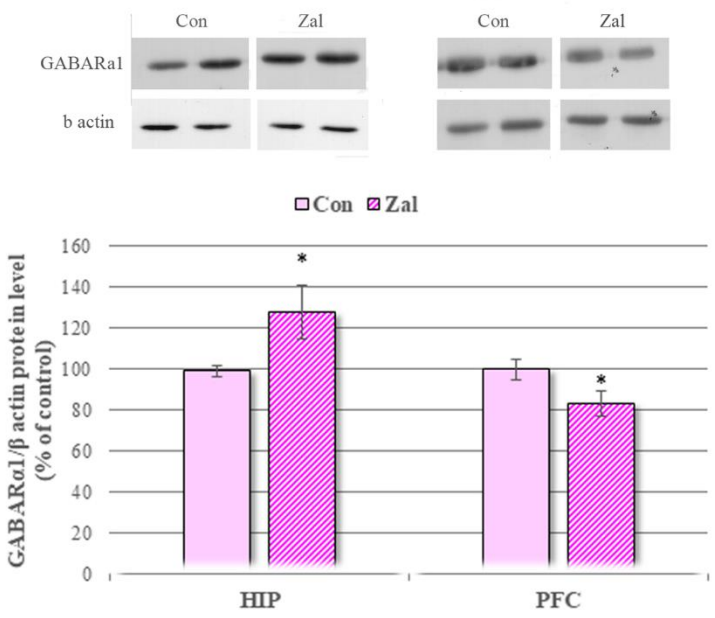

Figure 2. $GABA_AR\alpha1$ level in the synapses of the hippocampus (HIP) and prefrontal cortex (PFC) of male Wistar rats. Data are presented as the mean ± SEM, and the values of the control group were set as 100 %. Symbol * indicates significant difference compared to Con group ($p<0.05$). Representative blots are presented above the graph.

One-way ANOVA revealed significant effect of Zaleplon treatment on $GABA_AR$ α1 subunit protein expression in both PFC and HIP ($F_{1,11}=5,111$, $p<0.05$; $F_{1,11}=5,066$, $p<0.05$, respectively).

However, treatment had opposite effect in these brain regions as *post hoc* Tuckey test detected significant increase of $GABA_AR$ α1 level in HIP ($p<0.05$), while in the PFC significant decrease was observed ($p<0.05$) compared to Con (Figure 2).

Neural circuits and networks are based on the neurotransmitter-mediated interconnection of cells via synapses. In GABAergic synapses vesicular transporter VGAT enables packaging of newly synthesized GABA into synaptic vesicles that will be docked into the plasma membrane of the cell. Following membrane depolarization, released GABA diffuses through the synaptic cleft toward postsynaptic receptors. In the case of $GABA_AR$, the presence of GABA provokes postsynaptic membrane hyperpolarization that results in inhibition of effector (postsynaptic) cells and reduction of neuronal excitability [3]. Although Zaleplon, as positive allosteric agonist of $GABA_AR$, potentiate this pharmacological effect, up to date no studies were conduct toward elucidation of its' effects on GABAergic system at the molecular level. For the first time, we revealed overall changes of the GABAergic signalization in healthy animals subjected to repeated Zaleplon treatment. Based on the pharmacodynamic properties we can seemingly conclude that Zaleplon-induced increase in GABA signaling is expected. Interestingly, different change pattern was observed in the HIP and PFC, as all parameters indicate augmented GABAergic activity in the HIP while in the PFC components of GABAergic signaling remained unchanged and/or decreased. It has been known that the balance between the insertion, lateral diffusion, internalization and recycling of $GABA_AR$ in the neuronal plasma membrane determines the strength of GABAergic synapses [15] [16]. Due to continuous cycle of receptors between the plasma membrane and intracellular compartments as well as between the synaptic and extrasynaptic locations, decrease and/or increase of α1 subunit does not necessary implies degradation or *de novo* synthesis and assemblance od $GABA_AR$. Hence, it should be determined whether herein reported results depict plasticity of GABAergic synapses following Zaleplon treatment, or indicate the alteration at the mRNA level.

Bidirectional effects of Zaleplon may be explained by different role of investigated brain regions. Namely, PFC is involved in planning complex cognitive behavior, personality expression, decision making and social behavior moderation *i.e.*, coordination of thoughts and actions in accordance with internal goals [17]. Hence, lack of changes in the PFC may be the related to one of the Zaleplon characteristics as, due to binding selectivity and pharmacokinetic profile, it has been reported minimized possibility of side-effects (such as next day sedation, dependence, and withdrawal) when Zaleplon is taken as recommended.

One should bear in mind that GABAergic synapse cannot be singled out and observed alone, this main inhibitory system is tightly connected with main excitatory glutamate system. Numerous studies point to a down-modulation of GABAergic synapses [18] [19] [20] or increased synaptic expression of $GABA_AR$ [21] [22] following glutamate N-methyl-D-aspartate receptor (NMDAR) activation. It is considered that strong activation of NMDAR down-regulates the surface expression and the synaptic clustering of $GABA_AR$, while moderate stimulation of NMDAR induces the opposite response [15]. Results of our ongoing research reveal associated increase of components of glutamatergic signalization in the HIP, indicating preserved balance between these two systems. Given the importance of equilibrium of these two systems for neuronal excitability, synaptic plasticity, and cognitive functions, it is not surprising that novel pharmaceuticals rely on GABA/glutamate balance.

CONCLUSION

The study indicated region-specific and opposite effects of Zaleplon on GABAergic signaling in HIP and PFC. Increased protein expression of $GABA_AR$ α1 subunit and GABA level together with our previously obtained data of VGAT augmentation clearly point to enhanced GABAergic signaling in HIP. However, it seems that GABAergic signaling in PFC stayed relatively stable where the only observed change was the decrease of $GABA_AR$ α1 subunit protein expression. It is possible that these bidirectional Zaleplon effects in HIP and PFC, the regions highly important for cognition, emotional balance and behavior, may explain Zaleplon reduced potential for abuse and lower affinity for tolerance and withdrawal syndrome. Perhaps the enhanced inhibitory activity in HIP could be "overcame" by increased excitatory activity in PFC providing therefore the functional counterbalance and better overall clinical outcome in patients using Zaleplon and Z-drugs compared to BDZ and other similar drugs.

Acknowledgment

This work was funded by the Ministry of Education, Science and Technological Development of the Republic of Serbia, Grant 451-03-68/2022-14/200017.

REFERENCES

[1] American Psychiatric Association (2013) *Diagnostic and Statistical Manual of Mental Disorders* (5th ed.). Arlington, VA: American Psychiatric Publishing.

[2] D.N. Neubauer, S.R. Pandi-Perumal, D.W. Spence, K. Buttoo, J.M. Monti, Journal of central nervous system disease 10 (2018) 1179573518770672.

[3] M. Terunuma, Proceedings of the Japan Academy. Series B, Physical and biological sciences 94 (2018) 390.

[4] A. Ghit, D. Assal, A.S. Al-Shami, D.E.E. Hussein, Journal, genetic engineering & biotechnology 19 (2021) 123.

[5] M.T. Liu, The American journal of managed care 26 (2020) S85.

[6] F. Schifano, S. Chiappini, J.M. Corkery, A. Guirguis, The international journal of neuropsychopharmacology 22 (2019) 270.

[7] E. Sanna, F. Busonero, G. Talani, M. Carta, F. Massa, M. Peis, E. Maciocco, G. Biggio, European journal of pharmacology 451 (2002) 103.
[8] M. Dooley, G.L. Plosker, Drugs 60 (2000) 413.
[9] V. Scharner, L. Hasieber, A. Sonnichsen, E. Mann, BMC geriatrics 22 (2022) 87.
[10] D.R. Drover, Clinical pharmacokinetics 43 (2004) 227.
[11] E.K. Stranks, S.F. Crowe, Journal of clinical and experimental neuropsychology 36 (2014) 691.
[12] H. Noguchi, K. Kitazumi, M. Mori, T. Shiba, Naunyn-Schmiedeberg's archives of pharmacology 366 (2002) 183.
[13] W.E. Heydorn, Expert opinion on investigational drugs 9 (2000) 841.
[14] European College of Neuropsychopharmacology., European neuropsychopharmacology : the journal of the European College of Neuropsychopharmacology. Elsevier, Amsterdam, 1990, p. volumes.
[15] M.A. Markwell, S.M. Haas, L.L. Bieber, N.E. Tolbert, Analytical biochemistry 87 (1978) 206.
[16] M. Mele, G. Leal, C.B. Duarte, Journal of neurochemistry 139 (2016) 997.
[17] M. Mele, R.O. Costa, C.B. Duarte, Frontiers in cellular neuroscience 13 (2019) 77.
[18] S. Funahashi, Frontiers in neuroscience 11 (2017) 431.
[19] H. Bannai, S. Levi, C. Schweizer, T. Inoue, T. Launey, V. Racine, J.B. Sibarita, K. Mikoshiba, A. Triller, Neuron 62 (2009) 670.
[20] J. Muir, I.L. Arancibia-Carcamo, A.F. MacAskill, K.R. Smith, L.D. Griffin, J.T. Kittler, Proceedings of the National Academy of Sciences of the United States of America 107 (2010) 16679.
[21] F. Niwa, H. Bannai, M. Arizono, K. Fukatsu, A. Triller, K. Mikoshiba, PloS one 7 (2012) e36148.
[22] E.M. Petrini, T. Ravasenga, T.J. Hausrat, G. Iurilli, U. Olcese, V. Racine, J.B. Sibarita, T.C. Jacob, S.J. Moss, F. Benfenati, P. Medini, M. Kneussel, A. Barberis, Nature communications 5 (2014) 3921.
[23] K.C. Marsden, J.B. Beattie, J. Friedenthal, R.C. Carroll, The Journal of neuroscience : the official journal of the Society for Neuroscience 27 (2007) 14326.

TOXICITY EVALUATION OF PROMISING CONTRAST-ENHANCING STAINING AGENTS FOR MICRO-COMPUTED TOMOGRAPHY

M. B. Čolović

Department of Physical Chemistry, "Vinča" Institute of Nuclear Sciences-National Institute of the Republic of Serbia, University of Belgrade, Serbia. (colovicm@vin.bg.ac.rs)

ABSTRACT

Cytotoxicity and prooxidative properties evaluation of three Wells-Dawson polyoxotungstates that were published as potential contrast-enhancing staining agent (CESA) candidates for micro-computed tomography (microCT): parent Wells-Dawson POM α_2-$K_6P_2W_{18}O_{62}\cdot 14H_2O$ (**parent WD)**, monolacunary Wells-Dawson POM α_2-$K_{10}P_2W_{17}O_{61}\cdot 20H_2O$ (**lacunary WD**), and 1:2 hafnium(IV)-substituted Wells-Dawson POM $K_{16}[Hf(\alpha_2\text{-}P_2W_{17}O_{61})_2]\cdot 19H_2O$ (**Hf-WD 1:2**), was carried out *in vitro*. Oxidative stress indicators, reduced glutathione (GSH) and malondialdehyde (MDA) levels were determined in human blood plasma after 4 and 24 h treatment with the selected polyoxotungstates, within the concentration range 1-100 μM at 37 °C, and polyoxotungstate-induced cytotoxicity was assessed by monitoring cell viability in peripheral blood mononuclear cells (PBMCs). The results demonstrated that each of the studied promising CESAs resulted in a decrease of human PBMC viability in concentration- and time-dependent manner, and **Hf-WD 1:2** exhibited the strongest cytotoxic properties inducing up to 50% decrease of the cell viability related to corresponding control. However, only **Hf-WD 1:2** might be considered a potential prooxidant that resulted in a significant decrease of human plasma GSH level, whereas none of the investigated polyoxotungstates did not cause membrane lipid damage. Conclusively, **parent WD**, **lacunary WD**, and **Hf-WD 1:2** could not be considered safe primarily from a cytotoxic point of view, thus more extensive *in vitro* and *in vivo* studies are needed for the toxicological profile assessment of the studied promising CESA candidates for the soft tissue visualization using microCT.

INTRODUCTION

Compounds based on 2,4,6-triiodinated benzene have been used as standard contrast agents in computed tomography (CT). However, these iodine derivatives were confirmed to induce side effects after their injection such as acute kidney injury. In addition, iodinated agents are specially dangerous for thyroid disease and renal impaired patients [1, 2]. Therefore, scientific studies have been directed to finding low-toxic contrast-enhancing staining agents (CESAs) for microCT with satisfactory imagining properties [3, 4]. Recent studies [5, 6] revealed tungsten-based polyoxometalate (POM) clusters as novel promising CESAs for 3D imagining soft biological tissues. Firstly, Keggin structure polyoxotungtsate, phospho-tungstic acid has been reported as an effective agent for 3D visualization using CE-CT, but this POM damages tissue integrity due to its strong acidic properties [7]. In a recent study [8] the following Wells-Dawson POM species: parent Wells-Dawson POM α_2-$K_6P_2W_{18}O_{62}\cdot 14H_2O$ (**parent WD)**, monolacunary Wells-Dawson POM α_2-$K_{10}P_2W_{17}O_{61}\cdot 20H_2O$ (**lacunary WD**), and 1:2 hafnium(IV)-substituted Wells-Dawson POM $K_{16}[Hf(\alpha_2\text{-}P_2W_{17}O_{61})_2]\cdot 19H_2O$ (**Hf-WD 1:2**) (Figure 1) were confirmed as promising CESAs to visualize murine long bones and kidneys using microCT. Moreover, these POMs are interesting because of their cost-effectiveness and do not require much time to be synthesized.

Many novel agents with confirmed biomedical effects were not approved for clinical application due to their harmful effects for healthy tissues. Taking into account the fact that toxicity is the main limitation for drug development, in this study *in vitro* cytotoxicity towards normal non-target cells

and prooxidative properties of the above promising Wells-Dawson POM CESA candidates for microCT were evaluated using human blood as a model system.

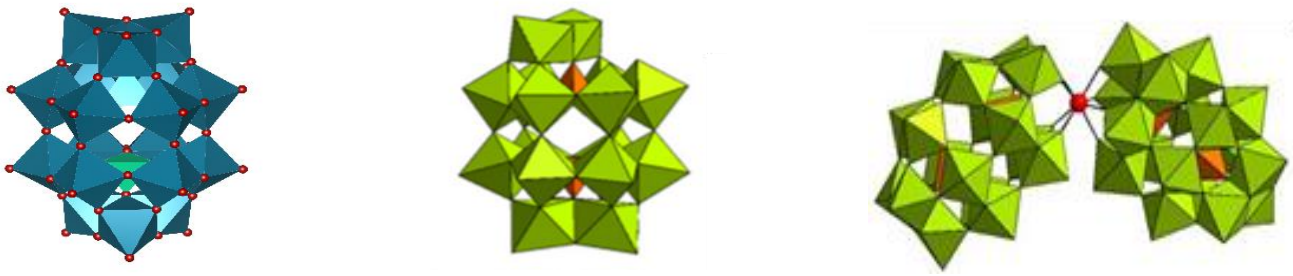

Parent WD *Lacunary WD* *Hf-WD 1:2*

Figure 1. Structures of the investigated Wells-Dawson polyoxotungstates: **parent WD, lacunary WD**, and **Hf-WD 1:2**.

EXPERIMENTAL

Parent WD, **lacunary WD**, and **Hf-WD 1:2** were synthesized according to procedures available in literature [9]. Stock aqueous solutions of **parent WD**, **Hf-WD 1:2** (10 mM), and **lacunary WD** (0.5 mM) were prepared by vortex mixing at the room temperature, and working solutions were prepared by diluting (water) the stock solutions up to desired concentrations.

Blood samples were taken from a healthy male and a female young donor, who gave informed consent to participate in this study, which was approved by the Institutional Ethics Committee and observed the ethical principles of the Declaration of Helsinki. The individuals were not exposed to ionizing radiation or genotoxic chemicals for a year before the blood sampling, which might have interfered with the results of the testing. The blood was drawn by antecubital venipuncture into vacutainers (Becton Dickinson, Franklin Lakes, USA) containing lithium heparin as anticoagulant. For the treatment, 100 μL of the stock/working solutions of **parent WD**, **lacunary WD**, and **Hf-WD 1:2** were added to 900 μL of human whole blood samples to achieve desired final concentrations, which then were incubated at 37 °C for 4 and 24 h.

The cytotoxicity of the WD polyoxotungstates was assessed by following the cell viability of peripheral blood mononuclear cells (PBMCs) in the absence (control) and presence of different POM concentrations. For this aim, differential staining with acridine orange (AO) and ethidium bromide (EB) and fluorescence microscopy were applied [10]. The difference in the cell viability between control and exposed samples was done by the Student *t* test. Data were considered statistically significant at $p < 0.05$.

Oxidative stress parameters were determined in blood plasma that was separated from the control and POM treated whole blood samples. Then, 5% trichloroacetic acid solution was added to the plasma samples (1:1 volume ratio) to precipitate –SH-containing proteins and avoid their interferention with the chromogenic reagent for the detecting –SH groups. After centrifugation (12500 rpm, 15 min) the supernatant was used for the subsequent determination of oxidative stress parameters. The extent of lipid peroxidation was mesaured as the concentration of thiobarbituric acid (TBA) reactive product malondialdehyde (MDA) by spectrophotometrical method at 532 nm [11]. Reduced glutathione (GSH) concentration was determined by a spectrophotometrical method at 412

nm based on the addition of 5,5'-dithio-bis-(2-nitrobenzoic acid) (DTNB) as a chromogenic reagent to form a measurable yellow-colored product (2-nitro-5-thiobenzoic acid) [11]. All measurements were done in triplicates.

RESULTS AND DISCUSSION

The results of cytotoxicity evaluation demonstrated that all studied concentrations of **parent WD** (1-100 μM) and **lacunary WD** (1-50 μM) did not significantly affect the PBMC viability after 4 h treatment. However, **Hf-WD 1:2** (10 and 100 μM) induced a statistically significant decrease of the cell viability (15 and 25%, respectively), whereas the least investigated **Hf-WD 1:2** concentration (1 μM) did not result in a cytotoxic activity. Then, the 24 hour-exposure exhibited a more potent POM induced effect, even up to 50% decrease of the PBMC viability for 100 μM **Hf-WD 1:2**. All studied POMs induced a concentration-dependent cytotoxicity toward normal human PBMCs. **Hf-WD 1:2** was detected with the strongest cytotoxic action, which reduced the cell viability from 25 to 45% related to the corresponding control. On the other hand, the weakest cytotoxic influence was observed for **parent WD** that did not affect PBMC viability at the concentration of 1 μM **parent WD**.

The results obtained for GSH, as a main non-enzymatic antioxidant against free radicals and a marker of induced oxidative stress, showed various effects of the studied promising CESAs. **Parent WD** did not influence human plasma GSH concentration within the investigated concentration range of 1-100 μM. Its monolacunary derivative, **lacunary WD** (1-50 μM) resulted in up to 20% decrease of GSH level. Finally, **Hf-WD**, containing two monolacunary Hf-substituted units, exhibited a concentration-dependent effect. The highest concentration (100 μM) decreased plasma GSH about 40% compared to the corresponding control. Therefore, **Hf-WD 1:2** could be considered a prooxidant capable of inducing excess free radical generation and thus oxidative stress resulting in different toxic occurences. On the contrary, the exposure to **parent WD** did not affect plasma GSH concentration, accordingly prooxidative properties could not be associated with this POM-based potential CESA.

MDA level, as a marker of lipid peroxidation and membrane damage, was measured in the human plasma in the absence (control) and presence of **parent WD** and **Hf-WD 1:2** (1-100 μM), and the highest investigated **lacunary WD** concentration was 50 μM because of the limitation in its water solubility. In the case of **parent WD**, the *in vitro* influence on lipid peroxidation after 24 h exposure implied a non-significant effect compared to the untreated control for all studied concentrations. Then, **lacunary WD** and **Hf-WD 1:2** treatments resulted in a decrease in plasma MDA level comparing with the control. The observed effects suggest that **parent WD** does not have a strong prooxidative potential or antioxidant defense systems overcame free radical-induced the membrane lipid harm. Then, **lacunary WD** and **Hf-WD 1:2** could not be regarded as strong prooxidants being able to cause the final membrane damage.

CONCLUSION

The obtained results demonstrated that all studied polyoxotungstate-based CESA candidates affected human PBMC viability in concentration- and time-dependent manner. The most potent cytotoxic activity was found for **Hf-WD 1:2**, whereas **parent WD** exhibited the weakest effect on the cell viability *in vitro*. The evaluation of oxidative stress parameters suggested a non-significant influence of **parent WD** on both human plasma GSH and MDA levels. Prooxidative properties might be ascribed to **Hf-WD 1:2** resulting in a significant reducing human plasma GSH concentration *in vitro*. Nevertheless, additional studies considering other relevant oxidative stress indicators are needed to confirm this assumption. Finally, **parent WD**, **lacunary WD**, and **Hf-WD 1:2** could not be regarded as toxicologically safe, thus more extensive *in vitro* and *in vivo* studies are necessary for the toxicological assessment of the studied potential CESA candidates for the soft tissue visualization using microCT.

Acknowledgment
This research was funded by the Ministry of Education, Science and Technological Development of the Republic of Serbia (contract no. 451-03-9/2022-14/200017), Science Fund of the Republic of Serbia (POMCACT project no. 6526393), the Institute for Medical Research and Occupational Health and Faculty of Pharmacy and Biochemistry, University of Zagreb, Croatia. The authors also gratefully acknowledge the bilateral project Serbia-Croatia (no. 337-00-205/2019-09/19) and Erasmus+ KA103 European Mobility Program (author M.Č.).

REFERENCES

[1] Seeliger, E., Sendeski, M., Rihal, C. S., and Persson, P. B., Eur. Heart J., 33 (2012) 2007.
[2] Zhang, P., Ma, X., Guo, R., Ye, Z., Fu, H., Fu, N., Guo, Z., Zhang, J., and Zhang, J., Molecules, 23 (2021) 7063.
[3] Cormode, D. P., Naha, P.C., and Fayad, Z.A., Contrast Media Mol. Imaging, 9 (2014) 37.
[4] Lusic, H., and Grinstaff, M. W., Chem. Rev., 113 (2013) 1641.
[5] De Clercq, K., Persoons, E., Napso, T., Luyten, C., Parac-Vogt, T.N., Sferruzzi-Perri, A,N, Kerckhofs, G,, and Vriens, J., Proc. Natl. Acad. Sci. USA, 116 (2019) 13927.
[6] Kerckhofs, G., Stegen, S., van Gastel N., Sap, A., Falgayrac, G., Penel, G., Durand, M., Luyten, F. P., Geris, L., Vandamme, K., Parac-Vogt, T., and Carmeliet, G., Biomaterials, 159 (2018) 1.
[7] Buytaert, J., Goyens, J., De Greef, D., Aerts, P., and Dirckx, J., Microsc. Soc. Can., 20 (2014) 1208.
[8] de Bournonville, S., Vangrunderbeeck, S., Ly, H. G. T., Geeroms, C., De Borggraeve, W. M., Parac-Vogt, T.N., and Kerckhofs, G., Acta Biomater., 105 (2020) 253.
[9] A.P. Ginsberg, Inorganic Syntheses, Wiley, 1990.
[10] Isakovic, A. M., Čolović, M. B., Ma, T., Ma, X., Jeremić, M., Gerić, M., Gajski, G., Misirlic-Dencic, S., Kortz, U., and Krstić, Z., J. Biol. Inorg. Chem., 26 (2021) 957.
[11] Gajski, G., Gerić, M., Domijan, A.-M., Golubović, I., and Žegura, B., Toxicon, 187 (2020) 93.

PROLONGED ALPRAZOLAM TREATMENT DIFFERENTALLY MODULATES THE PROTEIN EXPRESSION OF EXCITATORY AMINO ACID TRANSPORTERS 1 AND 2 BOTH IN VIVO AND IN VITRO

M. Zarić Kontić[1], M. Dragić[2], J. Martinović[1], K. Mihajlović[2], N. Mitrović[1], I. Guševac Stojanović[1] and I. Grković[1]

[1] *Department of Molecular Biology and Endocrinology, VINČA Institute of Nuclear Sciences - National Institute of the Republic of Serbia, University of Belgrade, Belgrade, Serbia (marinazaric@vin.bg.ac.rs)*

[2] *Laboratory for Neurobiology, Department for General Physiology and Biophysics, Faculty of Biology, University of Belgrade, Belgrade, Serbia*

ABSTRACT

Benzodiazepine alprazolam is used for treatment of anxiety, panic and sleep disorders. Prolonged alprazolam action on GABAergic signaling indirectly induces adaptive changes in other neurotransmission circuits in the brain including glutamatergic neurotransmission contributing to commonly observed side effects. Excitatory amino acid transporters 1 and 2 (EAAT1/2) are two major glutamate transporters in the brain responsible for glutamate uptake and regulation of its synaptic level. Therefore the aim was to investigate potential effects of prolonged ALP treatment on protein expression of EAAT1/2 in hippocampus of adult male Wistar rats as well as *in vitro* in isolated astrocytes. Results indicated increased protein expression of EAAT1 *in vivo* as well as *in vitro* while EAAT 2 was decreased in both conditions. These findings provide strong evidence for modulation of glutamatergic neurotransmission that may contribute to side effects of prolonged alprazolam (benzodiazepine) treatment.

INTRODUCTION

Alprazolam (ALP) is one of the most prescribed benzodiazepines (BDZs) worldwide approved for treatment of anxiety, panic and sleep disorders. It produces sedative, anxiolytic, muscle relaxant and anticonvulsant effects providing thus the relief of the symptoms. Due to complexity of mentioned disorders (and recreational abuse), ALP and other BZDs are often applied long-term which is not recommended but is usually necessary. Nevertheless, prolonged ALP treatment is almost always detrimental for the patient causing tolerance, dependence and withdrawal syndrome [1].

ALP, and all other BDZs, are positive allosteric modulators of γ-aminobutyric acid (GABA) type A receptors ($GABA_aR$). They increase the affinity of GABA for $GABA_aR$ and thereby the frequency of chloride channel opening, potentiating $GABA_aR$-mediated inhibitory responses in the central nervous system (CNS) [2]. Prolonged action of ALP on $GABA_aR$ and GABAergic signaling indirectly induces adaptive changes in the function of other receptors and neurotransmission circuits in the brain therefore leading to development of numerous side effects including tolerance [3]. So far, experimental data had suggested that BDZs tolerance may be associated with modulated/enhanced glutamatergic transmission and that it may contribute to dependence and withdrawal following abrupt discontinuation of the treatment [4]. Glutamate as the major excitatory neurotransmitter in the vertebrate CNS elicits a large array of functions, thus it's crucial to maintain its level in the synaptic cleft in physiological range [5]. The only efficient and reliable way to regulate the level of synaptic glutamate is by removal from the extracellular space through its uptake by neurons and glial cells via high affinity excitatory amino acid transporters (EAATs). EAAT type 1 (EAAT1) and EAAT type 2 (EAAT2) represent major glutamate transporters in the brain responsible for glutamate uptake mainly by astrocytes [5]. Therefore, our aim was to investigate potential effects of prolonged ALP treatment

on protein expression of EAAT1/2 in hippocampus (HIP) of adult male Wistar rats as well as *in vitro* effects on astrocytes.

METHODS

All experimental procedures were approved by the Ethics Committee for the Use of Laboratory Animals of Vinca Institute of Nuclear Sciences (license number: 323-07-06136/2020-05) according to the guidelines of the EU registered Serbian Laboratory Animal Science Association.

For *in vivo* part of the research, adult male Wistar rats were divided into three experimental groups (eight animals *per* group): a) intact animals without treatment (INT), b) animals injected i.p. with 2% Tween 80 dissolved in normal saline, used as ALP vehicle, for 14 days (VEH); c) rats treated i.p. with 2 mg/kg ALP for 14 days (ALP). At the end of the treatment, rats were euthanized, brains were removed and crude synaptosomal fraction (P2) of HIP was isolated as described previously [6]. *In vivo* results indicated alteration of EAAT1/2 following prolonged ALP treatment so the next part of the research was directed toward evaluation of EAAT1/2 protein expression in isolated astrocytes *in vitro*. For that purpose, primary astrocyte culture was prepared from cortex of 2 days old male Wistar rats, as previously described [7]. The astrocyte cultures (4 *per* group) were maintained to reach 90 % confluence and then treated with vehicle (VEH, 0.02 % Tween 80 dissolved in sterile dH2O) or increasing concentrations of ALP (0.01, 0.1, 1 and 10 μM ALP, dissolved in sterile dH2O containing 0.02 % Tween 80 and added to the cells in DMEM+ growth medium) for 48 h. After determining protein concentration using the modified method of Lowry [8] (*in vivo* samples) / commercial BCA Protein Assay Kit (Rockford, USA) (*in vitro* samples), Western blot analysis was performed to determine protein expression of EAAT1 and EAAT2. Equal amount of total protein from each sample diluted in Laemmli sample buffer (250 mM Tris–HCl pH 6.8, 10% SDS, 30% glycerol, 5% β-mercaptoethanol, 0.02% bromophenol blue) was separated on 10% SDS-PAGE gel and transferred to PVDF membranes (Imobilion-P membrane, Millipore, USA). Membranes were blocked in TBS containing 5% non-fat milk (Sigma-Aldrich, USA) and 0.1% Tween 20 (Sigma-Aldrich, USA) for 1 h and incubated overnight at 4 °C with primary antibodies (Table 1). The next day membranes were incubated with appropriate horseradish peroxidase conjugated secondary antibody (Table 1). After washing in TBST, the membranes were incubated with the enhanced chemiluminescence system (Immobilon Western Chemiluminescent HRP Substrate, Millipore, USA) and immunoreactive bands were detected on X-ray films in the dark chamber, scanned and saved in .tiff format. β-Actin was used as a loading control. The signal intensity was evaluated using Image J software.

All data were expressed as means ± S.E.M. Results were analyzed using One-way ANOVA followed by a post-hoc Tukey's test. $p < 0.05$ was defined as statistically significant.

Table 1. List of primary and secondary antibodies used for Western blot analysis

Antigen	Manufacturer and Catalog No	Species and Dilution
EAAT1	Cell Signaling Techonology, USA; # 5684T	rabbit monoclonal
EAAT2	Abcam, UK; ab69098	rabbit monoclonal
β-actin	Thermo Fisher Scientific, USA; PA1-21167	rabbit polyclonal; 1:5000
mouse IgG	R&D systems, bio-techne, USA; HAF007	goat polyclonal; 10 000
rabbit IgG	Invitrogen, USA ; # 31460	goat polyclonal; 1:10 000

RESULTS AND DISCUSSION

Significant effect of ALP was observed on protein expression of EAAT1 ($F = 14.36$, $p = 0.0002$; $F = 6.910$, $p = 0.0011$) and EAAT2 ($F = 8.040$, $p = 0.003$; $F = 6.718$, $p = 0.0011$) both *in vivo* and *in vitro*, respectively. Protein expression of EAAT1 *in vivo* was increased in ALP group (***$p < 0.001$, ^^^p

< 0.001) compared to INT and VEH, respectively, as well as *in vitro* in 0.01 uM ALP (**p < 0.01), 0.1 uM ALP (*p < 0.05), 10 uM ALP group (*p < 0.05) compared to INT. On the contrary, post hoc test revealed that EAAT2 protein expression was decreased *in vivo* in ALP group compared to INT (**p < 0.01) which was also observed *in vitro* in 0.1 uM ALP (*p < 0.05, ^p < 0.05), 1 uM ALP (*p < 0.05, ^p < 0.05) and 10 uM ALP group (*p < 0.05) compared to INT and VEH, respectively (Figure 3).

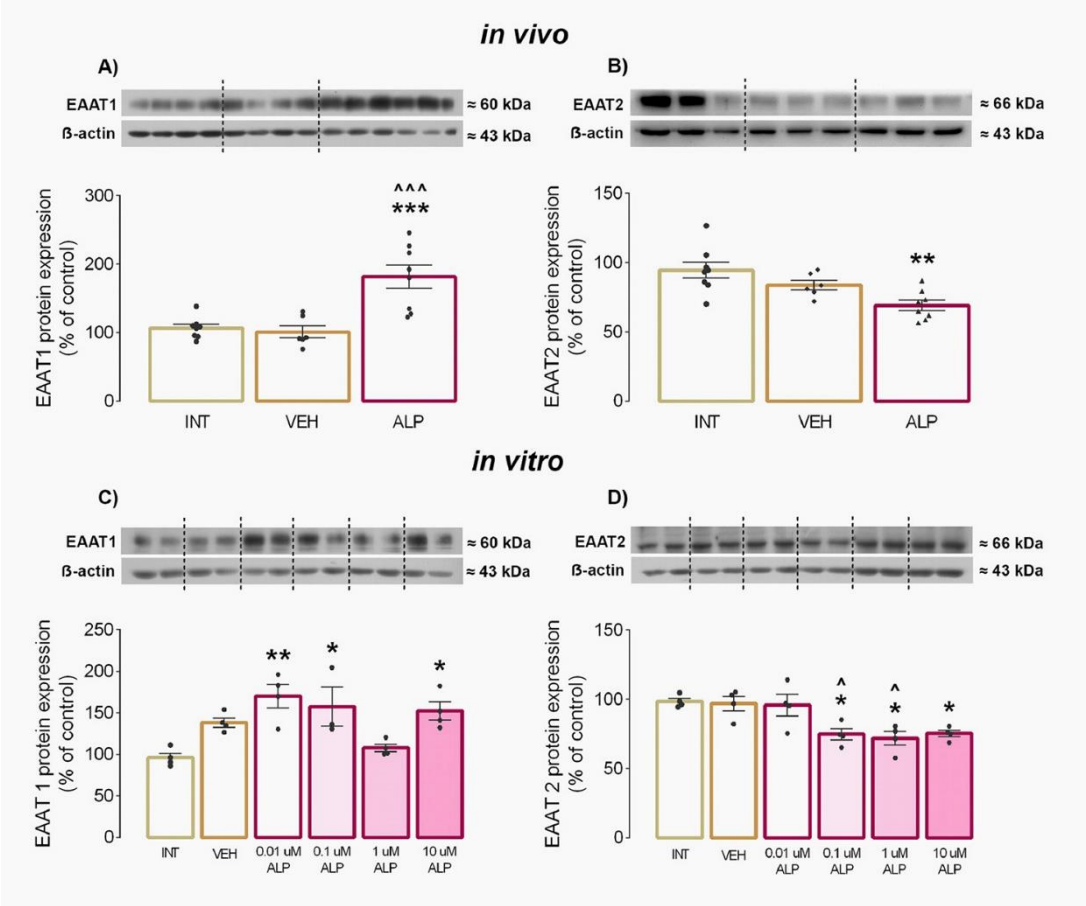

Figure 1. Protein expression of EAAT 1 *in vivo* (A) and *in vitro* (C) and EAAT2 *in vivo* (B) and *in vitro* (D). Data are presented as the mean ± SEM, and the values of INT group were set as 100 %. Symbol * indicates statistically significant difference between INT and ALP groups while symbol ^ represents the difference between VEH and ALP group. Intermittent lines on representative blots mark the end of sample loading of certain group and the beginning of other group (sample order the same as on the graph below the representative blot).

Obtained results suggest differential modulation of EAAT 1 and EAAT2 in HIP which was also detected in primary astrocyte cell culture following ALP treatment. These two transporters represent critical components of glutamatergic transmission as they control the level of extracellular glutamate and indirectly the glutamatergic firing rate. They prevent uncontrolled and persistent activation of glutamate receptors, enable the recycling of the transmitter and thus confer protection from hyperexcitability and excitotoxicity. EAAT2 is responsible for more than 90% of glutamate uptake, being the major glutamate transporter in the brain [5] which could result in decreased glutamate uptake and it enhanced level in the synaptic cleft. On the other hand, observed EAAT1 increase may

represent a compensatory mechanism counteracting the potential rise of synaptic glutamate. Therefore, observed alteration of EAAT1 and EAAT2 protein expression may influence all components of glutamatergic signaling and contribute the occurrence of side effects characteristic for long-term ALP use. Indeed, our research indicated the alteration of other components of glutamatergic signaling including increase of protein expression of N-Methyl-D-aspartate receptor (NMDAR) subunits and decrease of vesicular glutamate transporter type 1 (vGlut1) following prolonged ALP treatment (data not shown) which may altogether represent a compensatory mechanism due to prolonged suppression of glutamatergic neurons by enhanced inhibitory impulses deriving from GABAergic neurons.

CONCLUSIONS

The results indicate different modulation of EAAT1 and EAAT2 protein expression following protracted ALP treatment which could influence the glutamate level in the synaptic cleft and provide a fine tuning of glutamatergic excitatory neurotransmission. Our findings provide strong evidence for modulation of glutamatergic neurotransmission that may contribute to side effects of prolonged ALP (BDZ) treatment such as tolerance or withdrawal symptoms.

Acknowledgment

This work was funded by the Ministry of Education, Science and Technological Development of the Republic of Serbia, Contract 451-03-1/2022-14/13-0902202.

REFERENCES

[1] N. Ait-Daoud, A.S. Hamby, S. Sharma, D. Blevins, Journal of addiction medicine 12 (2018) 4.
[2] B.J. Van Sickle, A.S. Cox, K. Schak, L.J. Greenfield, Jr., E.I. Tietz, Neuropharmacology 43 (2002) 595.
[3] M.C. Gravielle, Pharmacological research 109 (2016) 92.
[4] E. Izzo, J. Auta, F. Impagnatiello, C. Pesold, A. Guidotti, E. Costa, Proceedings of the National Academy of Sciences of the United States of America 98 (2001) 3483.
[5] A.G. Rodriguez-Campuzano, A. Ortega, Neuropharmacology 192 (2021) 108602.
[6] N. Mitrovic, I. Gusevac, D. Drakulic, M. Stanojlovic, J. Zlatkovic, J. Sevigny, A. Horvat, N. Nedeljkovic, I. Grkovic, General and comparative endocrinology 235 (2016) 100.
[7] K.D. McCarthy, J. de Vellis, The Journal of cell biology 85 (1980) 890.
[8] M.A. Markwell, S.M. Haas, L.L. Bieber, N.E. Tolbert, Analytical biochemistry 87 (1978) 206.

THE PROTOLYTIC EQUILIBRIA OF RALOXIFENE

M. Popović Nikolić[1], M. Čakar[2] and G. Popović[2]

[1]*University of Belgrade, Faculty of Pharmacy, Department of Pharmaceutical Chemistry, Vojvode Stepe 450, 11221 Belgrade, Serbia. (majap@pharmacy.bg.ac.rs)*
[2]*University of Belgrade, Faculty of Pharmacy, Department of General and Inorganic Chemistry, Vojvode Stepe 450, 11221 Belgrade, Serbia.*

ABSTRACT
The apparent ionization constants (pK_a*) of raloxifene have been determined potentiometrically in methanol–water mixtures (45% - 55% wt/wt) and the pK_a values (pK_{a1}=7.21±0.02, pK_{a2}=7.86±0.02, pK_{a3}=9.97±0.04) which define the ionization in aqueous media were obtained by extrapolation of the pK_a* values to 0% of methanol. Obtained pK_a values were assigned to corresponding ionization centers. On the basis of the ionization constants determined in this study distribution of raloxifene equilibrium forms have been calculated.

INTRODUCTION
Raloxifene is the nonsteroidal benzothyophene referred as the first selective estrogen receptor modulator (SERM) approved for the prevention and therapy of osteoporosis fractures in postmenopausal women which does not increase the risk of breast and endometrial cancer [1]. The selective action is the result of partial similarity with the chemical structure of estradiol.

From perspective of a chemical structure raloxifene is an ampholyte (Figure 1) with two acidic centers (phenolic hydroxyl group and hydroxyl group attached to benzo-[b]thien), and one basic center (piperidine nitrogen).

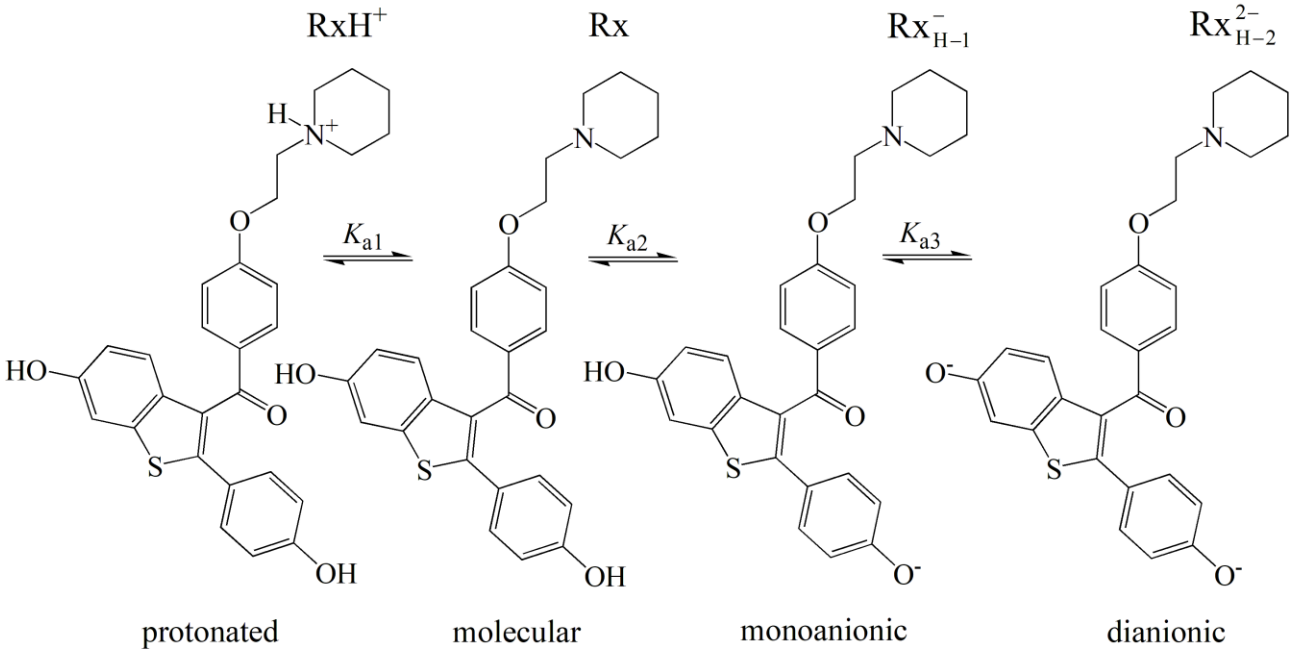

Figure 1. The ionization profile of raloxifene (Rx).

Crystal structure of the ligand-binding domain (LBD) of estrogene receptor (ER) in complexes with raloxifene reported in literature [2] shows that raloxifene is bound to the LBD of ER by a direct hydrogen bonds involving its ionization centers, both acidic groups and piperidine ring nitrogen.

In pharmaceutical formulations raloxifene occurs in the form of hydrochloride salt and expresses poor aqueous solubility. It is predicted that raloxifene ionization directly affects its solubility because the possibility of intramolecular folding of raloxifene to satisfy the positive and negative charges of the zwitterion contributes to low water solubility. Thus the investigation of raloxifene protolytic equilibria can help in consideration of bioavailability enhancement by developing of pharmaceutical dosage forms for oral administration.

There is lack of the raloxifene pK_a values in the literature and for neither the available data neither experimental approach employed nor the experimental conditions are described [3].

METHODS

Automatic titrator 798 MPT Titrino (Metrohm, Switzerland) with a combined electrode LL unitrode Pt 1000 (Metrohm, Switzerland) was used for potentiometric determinations. The electrode was regularly calibrated with standard buffer solutions (pH 4.01, 7.00, and 9.21). Raloxifene hydrochloride, [6-hydroxy-2-(4-hydroxyphenyl)benzo-[b]thien-3-yl][4-[2-(1-piperidinyl)ethoxy]-phenyl]ethanone hydrochloride, was kindly donated from Hemofarm AD. Standard HCl and CO_2-free NaOH solutions were standardized by potentiometry.

Potentiometric titrations were carried out at 25°C with a continuous magnetic stirring. Constant ionic strength was adjusted to 0.1 M with KNO_3. The apparent ionization constants (pK_a*) were obtained in the different methanol-water mixtures (45%, 50%, 55% wt/wt). In order to prevent dissociation of the acidic groups and to achieve total protonation of piperidine nitrogen, 0.5 mL of HCl solution (0.1041 M) was added to 40 mL solutions of raloxifene hydrochloride (5×10^{-4} M) in the methanol-water mixtures, and titrated with the 0.02 mL aliquots of standard NaOH solution (0.0996 M).

The measured pH values are expressed as pcH values (pcH = -log [H^+]), according to the relation pcH = pH - A. The correction factor A was determined experimentally for every single methanol-water mixture by titration of the standard HCl solution at the ionic strength of 0.1 M (KNO_3) with the standard NaOH solution. On the basis of the data obtained by potentiometric titrations, the pK_a* values were calculated using a computer program Hyperquad, which enables determination of equilibrium constants in complex systems containing the overlapped acid-base equilibria.

RESULTS AND DISCUSSION

Raloxifene can be chemically considered as an ampholyte containing three ionizable groups, one basic group (piperidine nitrogen) and two acidic groups (phenolic hydroxyl group and hydroxyl group attached to benzo-[b]thien). Very slight raloxifene solubility disabled the potentiometric pK_a determination in pure aqueous media, without the use of cosolvents. The apparent pK_a* values of raloxifene (Table 1) were determined in different methanol-water mixtures 45 % to 55 % (wt/wt). Methanol was used as a cosolvent because its effect on the ionization constants is close to that of pure water [4].

Table 1. The pK_a* values of raloxifene determined by potentiometry in different methanol-water mixtures at I = 0.1 M (KNO_3) and t = 25 °C.

%MeOH	pK_{a1}	pK_{a2}	pK_{a3}
45	8.90±0.04	9.03±0.04	10.41±0.05
50	8.60±0.04	9.31±0.05	11.18±0.06
55	8.65±0.04	9.30±0.05	11.15±0.05

The pK_a values (pK_{a1}=7.21±0.02, pK_{a2}=7.86±0.02, pK_{a3}=9.97±0.04) which define the raloxifene ionization in aqueous media were obtained by extrapolation of the apparent pK_a* values to 0% of methanol (Figure 2). In the mixed solvent solutions methanol contributes to the better raloxifene solubility but expressed relatively high effect on the pK_a values.

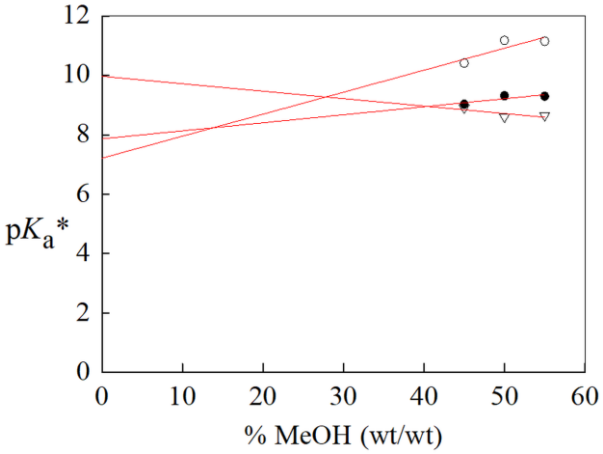

Figure 2. Plots of the pK_a* values versus % MeOH (wt/wt).

The pK_a values experimentally determined in this study were assigned to corresponding ionization centers taking into account their chemical properties and electrical effects. The pK_{a1}=7.21 corresponds to the ionization of piperidine ring nitrogen, influenced by the inductive electron-withdrawing effects of the electronegative oxygen atom, makes it less basic in a relation to the pK_a expected for piperidine (11.2) [5]. In addition to this, difference form piperidine ionization could be a consequence of the specific orientation of the raloxifene molecule, or of some intramolecular interactions occurring in the solution. The electrons of the hydroxyl group oxygen attached to benzo-[b]thien moiety are more delocalized comparing to electrons of the phenolic hydroxyl group. This indicates that the pK_{a2}=7.86 can be assigned to phenolic hydroxyl group and the pK_{a3}=9.97 to hydroxyl group attached to benzo-[b]thien moiety.

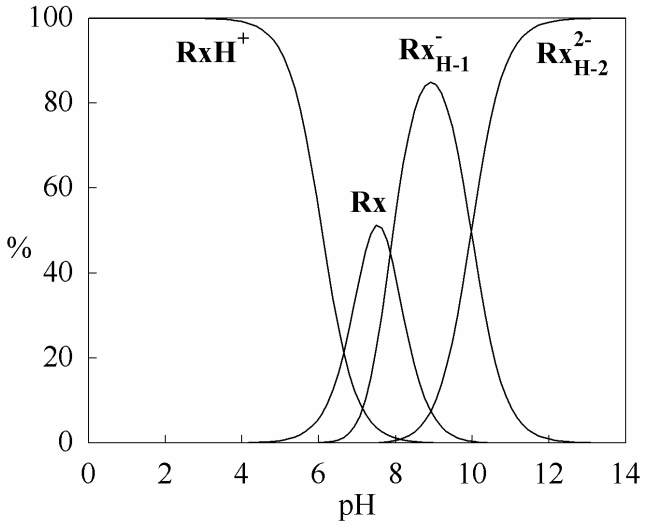

Figure 3. Distribution of the raloxifene equilibrium forms as a function of pH.

The pK_a values of raloxifene determined throughout the present study were somewhat lower than those reported in the literature (pK_{a1}=8.95, pK_{a2}=9.83, pK_{a3}=10.91)[3], probably because of differences in experimental approach.

The ionization of raloxifene includes four equilibrium forms present in solution, described in detail in Figure 1, protonated form, molecular form (free base), monoanionic form and dianionic form. On the basis of equations which describe the ionization of compound with three ionizable centers and the pK_a values determined in this study the distribution of equilibrium forms as a function of pH is calculated and presented in Figure 3.

CONCLUSION

The protolytic equilibria of raloxifene in aquous media have been defined providing a real insight in the overlapped protolytic equilibria and all the potential equilibrium species present in the solution. This results can help to improve design of pharmaceutical dosage forms possessing optimum dissolution, oral bioavailability and pharmacokinetic profile.

Acknowledgment

This research was funded by the Ministry of Education, Science and Technological Development, Republic of Serbia through Grant Agreement with University of Belgrade-Faculty of Pharmacy No: 451-03-68/2022-14/200161.

REFERENCES

[1] Delmas, P. D., Bjarnason, N. H., Mitlak, B. H., Ravoux, A. C., Shah, A. S., Huster, W. J., Draper, M., Christiansen, C., N. Eng. J. Med., 337 (1997) 1641.
[2] Brzozowski, A.M., Pike, A.C.W., Dauter, Z., Hubbard, R.E., Bonn, T., Engstrom, O., Ohman, L., Greene, G.L., Gustafsson, J.A., Carlquist, M., Nature, 389 (1997) 753.
[3] Teeter, J.S., Meyerhoff, R.D., Environ. Toxicol. Chem., 21 (2002) 729.
[4] Avdeef, A., Absorption and Drug Development: Solubility, Permeability, and Charge State, Hoboken, NJ: John Wiley & Sons, 2012.
[5] Eicher, T., Hauptmann, S., Speicher, A., The chemistry of heterocycles: structures, reactions, synthesis, and applications. John Wiley & Sons, 2013.

THE DETERMINTAION OF THE IONIZATION PROFILE OF CEFTAZIDIME

M. Popović Nikolić[1], J. Mudrić[2] and G. Popović[3]

[1]*University of Belgrade, Faculty of Pharmacy, Department of Pharmaceutical Chemistry, Vojvode Stepe 450, 11221 Belgrade, Serbia. (majap@pharmacy.bg.ac.rs)*
[2]*University of Belgrade, Faculty of Pharmacy, Department of Pharmaceutical Technology and Cosmetology, Vojvode Stepe 450, 11221 Belgrade, Serbia.*
[3]*University of Belgrade, Faculty of Pharmacy, Department of General and Inorganic Chemistry, Vojvode Stepe 450, 11221 Belgrade, Serbia.*

ABSTRACT

The ionization constants (pK_a) of ceftazidime, third generation cephalosporin, were determined by potentiometry. Ceftazidime is an ampholyte with four ionizable centers, three acidic centers (two carboxyl groups and amide group) and one basic center (aminothiazole). Potentiometric determinations were performed at 25 °C and constant ionic strength of 0.1 M (NaCl). Experimental data were analyzed by computer software Hyperquad and four pK_a values were derived: pK_{a1} 2.55; pK_{a2} 3.94; pK_{a3} 4.54 and pK_{a4} 7.55. According to the obtained pK_a values distribution diagram as a function of pH was constructed and distribution of the ceftazidime equilibrium forms was calculated at a pH values of biopharmaceutical significance (pH 1.2, 4.5, 6.8 and 7.4). In addition, based on the chemical structure of ceftazidime the order of ionization were suggested.

INTRODUCTION

Ceftazidime is a semisynthetic, broad-spectrum, third-generation cephalosporin antibiotic that is bactericidal through inhibition of enzymes responsible for cell-wall synthesis, primarily penicillin-binding protein 3 (PBP3) [1]. Chemically, ceftazidime is a complex ampholyte with three acidic (two carboxyl groups and amide) and one basic (aminothiazole) ionizable centers (Figure 1). It is commercially available in the form of a powder for solution containing sodium carbonate as excipient.

A complex system of protolytic equilibria is established in the reconstituted solution involving the

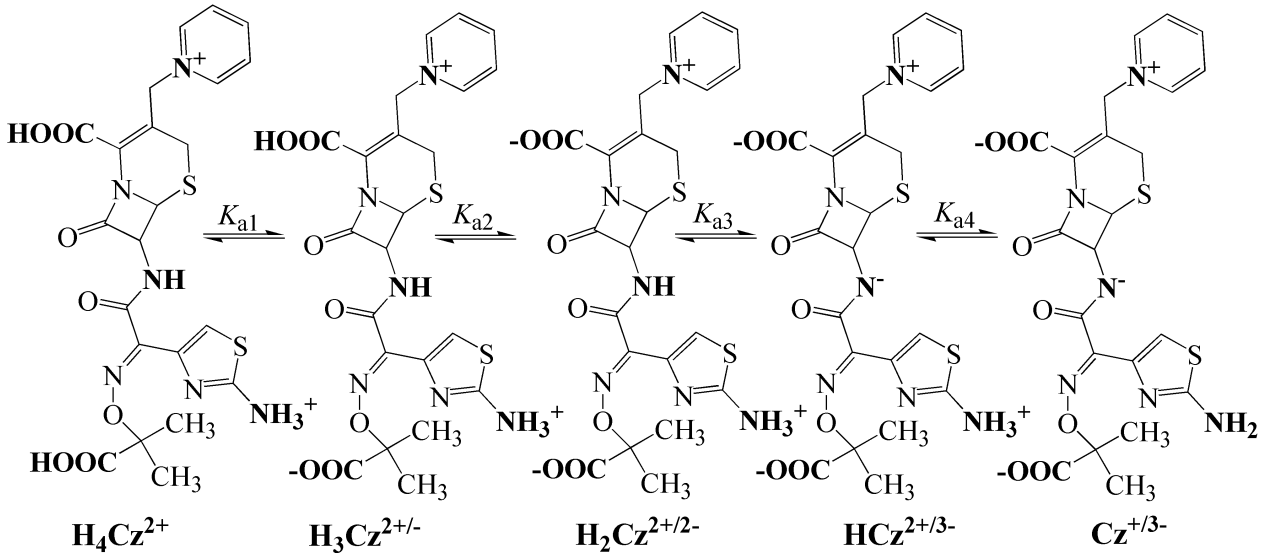

Figure 1. The ionization profile of ceftazidime (Cz).

ionization of four ionizable centers of ceftazidime and two step ionization process of sodium carbonate. Literature data on the pK_a values of ceftazidime [2] are incomplete, indicate only two or three ionization constants, where experimental conditions of determination are not fully described or values are predicted by computer software.

METHODS

A 1 g of mixture containing ceftazidime pentahydrate ((6R,7R)-7-[[(2Z)-2-(2-amino-1,3-thiazol-4-yl)-2-(2-carboxypropan-2yloxyimino)acetyl]amino]-8-oxo-3-(pyridin-1-ium-1-ylmethyl)-5-thia-1-azabicyclo[4.2.0]oct-2-ene-2-carboxylate; pentahydrate) and anhydrous sodium carbonate equivalent to 52 mg of sodium (Ceftazidime Facta Pharmaceuticals) was used for determination of the pK_a values of ceftazidime. A mole ratio of ceftazidime and sodium carbonate was 1.22 : 1. Automatic titrator 798 MPT Titrino (Metrohm, Switzerland) with a combined electrode LL unitrode Pt 1000 (Metrohm, Switzerland) was used for potentiometric determinations. The electrode was regularly calibrated with standard buffer solutions (pH 4.01, 7.00, and 9.21). Standard HCl and CO_2-free NaOH solutions were standardized by potentiometry.

Potentiometric titrations were carried out at 25°C with a continuous magnetic stirring. Constant ionic strength was adjusted to 0.1 M with NaCl. In order to prevent protonation of the aminothiazole and to achieve total deprotonation of two carboxyl groups and amide, 1 mL of NaOH solution (0.0992 M) was added to 40 mL solutions of mixture (containing 10^{-4} M ceftazidime) and titrated with the 0.02 mL aliquots of standard HCl solution (0.1028 M). A representative titration curves are shown on Figure 2.

The measured pH values are expressed as pcH values (pcH = -log [H^+]), according to the relation pcH = pH - A. The correction factor A was determined experimentally. Experimental data obtained by potentiometric titrations were analyzed in computer program Hyperquad.

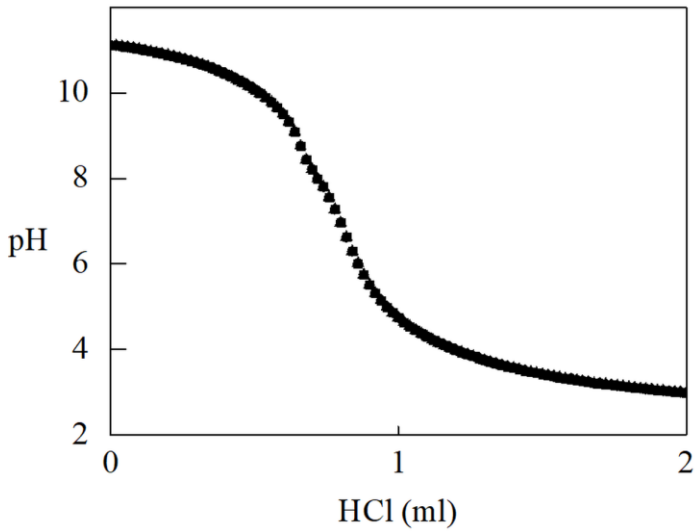

Figure 2. Potentiometric curves for ceftazidime – sodium carbonate mixture titrated with standard HCl solution. I = 0.1 M (NaCl) and t = 25°C.

RESULTS AND DISCUSSION

Investigation of the protolytic equilibria represents a particular challenge in the case of ceftazidime in the mixture with sodium carbonate because a complex system of six overlapped protolytic equilibria is established in solution. To determine the pK_a values of ceftazidime, it is necessary to solve complex systems of equations that define these processes, which can only be achieved by using

computer software. Experimentally obtained data were analyzed in program Hyperquad which enables determination of equilibrium constants in complex systems containing the overlapped acid-base equilibria.

Four pK_a values which define the ceftazidime ionization in aqueous media were determined in this study (pK_{a1}=2.55±0.02, pK_{a2}=3.94±0.02, pK_{a3}=4.54±0.04, pK_{a4}=7.55±0.04). The main significance of the experimental determination of the pK_a values in this study lies in the fact that we took into the account the ionization of all ionizable centers of ceftazidime, since in the literature [2] only two pK_a values had been experimentally determined, pK_{a1} 2.19, pK_{a2} 3.98, determined by capilary electrophoresis and pK_{a1} 2.91, pK_{a2} 3.81, potentiometrically determined. For literature values an overall ionization was attributed only to the ionization of carboxyl groups, but literature values are in good agreement with the pK_a values determined in this study. The lowest value (pK_{a1} 2.55) can be assigned to the ionization of carboxyl group attached to the β-lactam ring. The difference in the acidity of the two carboxyl groups are influenced by electrical effects. The electron density of the β-lactam ring contributes to the delocalization of the electrons of the carboxyl group which facilitates deprotonation and results in higher acidity and lower pK_a value compared to the carboxyl group in the side chain.

On the other hand, the carboxyl group in the side chain is significantly less affected by the electrical effects of aromatic moieties where two methyl groups enrich the electron density of oxygen thus decreasing the acidity of this carboxyl group (pK_{a2} 3.94). The pK_{a3} 4.54 corresponds to the ionization of a resonantly stabilized aminothiazole moiety according to pK_a 5.39 for 2-aminothiazole [3]. The highest value (pK_{a4} 7.55) can be assigned to weakly acidic amide group, which ionization is affected by electrical effects in the molecule and probably by intramolecular interactions occurring in the solution.

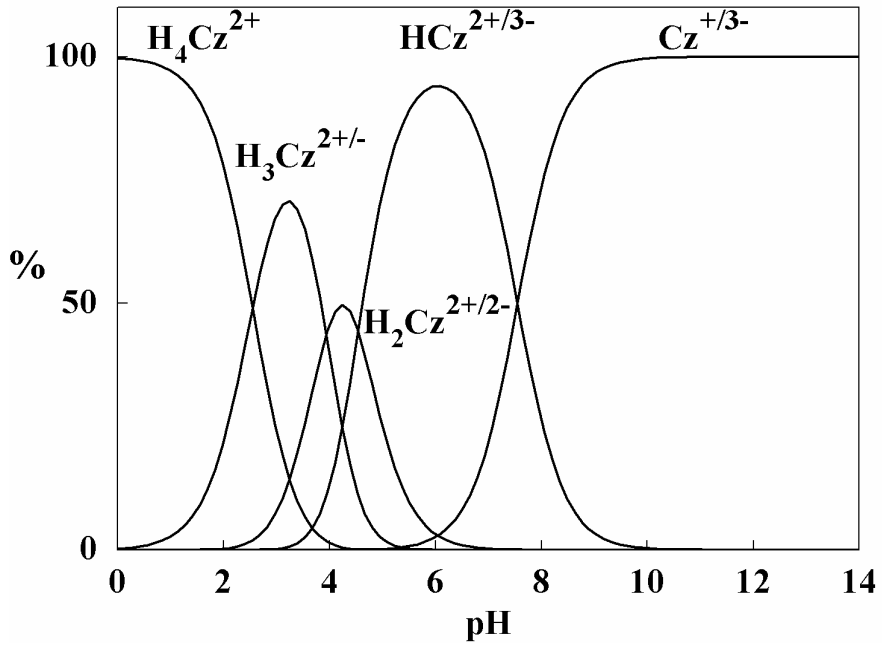

Figure 3. Distribution of the ceftazidime (Cz) equilibrium forms as a function of pH.

On the basis of equations which describe the ionization of compound with four ionization centers and the pK_a values experimentally determined in this study distribution of equilibrium forms as function of pH have been calculated and showed in Figure 3.

The distribution of the equilibrium forms of ceftazidime at pH values of biopharmaceutical significance is shown in Table 1. At a pH value of 1.2 corresponding to gastric conditions, where pharmacologically active substances are usually released from pharmaceutical formulations, H_4Cz^{2+} form of the drug is predominant (96%).

Table 1. Percentage of the equilibrium forms of ceftazidime (Cz) at pH values of biopharmaceutical importance.

pH	H_4Cz^{2+}	$H_3Cz^{2+/-}$	$H_2Cz^{2+/2-}$	$HCz^{2+/3-}$	$Cz^{+/3-}$
1.2	96	4	0	0	0
4.5	0	13	46	42	0
6.8	0	0	0	85	15
7.4	0	0	0	59	41

At pH values related to different parts of the small intestine (pH 4.5 and 6.8), most of the orally administered drugs are absorbed and absorption requires the uncharged and lipophilic form of the drug to be able to pass through biological membranes. At this pH values the content of ionized forms of ceftazidime is the largest (Table 1), $H_2Cz^{2+/2-}$ (46%), $HCz^{2+/3-}$ (42%) and $HCz^{2+/3-}$ (85%). These results can help in explanation of the reasons that make oral administration of ceftazidime difficult. On the other hand, for adequate solubility in blood plasma the ionized form of the drug is required. At pH 7.4 the dominant presence of ceftazidime ionized forms ($HCz^{2+/3-}$ 59% and $Cz^{+/3-}$ 41%) are observed (Table 1).

CONCLUSION

Complex protolytic equilibria of ceftazidime have been defined. The four pK_a values have been determined potentiometrically and attributed to the corresponding ionizable centers. Obtained results provide a real insight into the ionization and the presence of all equilibrium forms of ceftazidime in solution which can serve to improve pharmaceutical formulations and for further estimation of pharmacokinetic parameters.

Acknowledgment

This work was supported by the Ministry of Education, Science and Technological Development of the Republic of Serbia (grant no 452-03-9/2020-14/200014-0902105).

REFERENCES

[1] T. L. Lemke, D. A. Williams, V. F. Roche, S. W. Zito, Foyeś Principles of Medicinal Chemistry, 7th edition, Lippincott Williams & Wilkins, Philadelphia, PA, 2013.
[2] V. G. Alekseev, Pharm. Chem. J., 44 (2010) 14.
[3] T. Eicher, S. Hauptmann, A. Speicher, The Chemistry of Heterocycles: Structures, Reactions, Synthesis, and Applications, John Wiley & Sons, 2013.

MEMBRANE CURRENTS OF C6 CELLS IN PHARMACOLOGICAL INVESTIGATION

Lj. Nikolić[1], D. Savić[1], J. Korać Jačić[2], B. Petković[1], G. Stojadinović[1], Lj. Martać[1] and J. Bogdanović Pristov[2]

[1]*Institute for Biological Research "Siniša Stanković" - National Institute of Republic of Serbia, University of Belgrade, Bulevar despota Stefana 142, 11000 Belgrade, Serbia. (ljnikolic@ibiss.bg.ac.rs)*
[2]*University of Belgrade, Institute for Multidisciplinary Research, Kneza Višeslava 1, 11030 Belgrade, Serbia.*

ABSTRACT
Living cells exhibit multiple ion channel proteins and malfunction of these channels underlies numerous diseases. Channelopathies include diseases of the nervous, cardiovascular, respiratory, endocrine, urinary, and immune system. Currently, ion channels represent the second-largest target for existing drugs. Here, using the whole-cell patch-clamp technique, we explored the epinephrine effect on membrane ionic currents in glioma C6 cells. We demonstrate that epinephrine specifically evokes an increase of C6 cells outward ionic currents that is stable within 10 min, while it does not affect inward currents. Our results thus provide fine resolution and time frame for targeting ion channel activity that is crucial in pharmacological investigations.

INTRODUCTION
Ion channels are transmembrane proteins in the form of highly selective hydrophilic pores that connect the cytosol to the cell exterior. The role of ion channels is to allow specific inorganic ions, primarily Na^+, K^+, Ca^{2+}, or Cl^- to cross the membrane downs their electrochemical gradients [1]. Ion channels are not continuously open. Instead, they exist in either open or closed conformations and are gated, which allows them to open briefly and then close again. When open, ion channels enable the passage of specific ions across the plasma membrane and into the interior of a cell, and when closed, ion passage is stopped. The gate of the ion channel opens in response to a specific stimulus. The type of stimuli that can cause the ion channel to open is a change in the voltage across the membrane. These channels are voltage-gated, also known as voltage-dependent ion channels. Their permeability is influenced by the membrane potential, and they open or close in response to changes in membrane potential. With prolonged stimulation, most channels go into a closed, desensitized state, in which they are refractory to further opening until the stimulus is present. Ion channels are physiologically important in a vast variety of functions in all cells. In excitable cells, nerves and muscles, ion channels generate and shape electrical signals leading to action potential propagation, neurotransmitter release, and muscle contraction. In non-excitable cells, ion channels are involved in hormonal secretion, immune cell responsivity, cell cycling, and ion distribution [2]. Furthermore, they are crucial for the transepithelial transport of salt and water, for the regulation of cellular volume and pH, and for the chemical signalling.

Hence, although numerous ion channel diseases affect the neuromuscular system and cause epilepsy, ataxia, myotonia, and cardiac arrhythmia, they may affect many other organs. The number of known ion channel diseases (channelopathies), has increased dramatically over the past decade [3]. Many ion channels have been pursued as key therapeutic targets and approximately 15% of the most successful drugs target ion channels [4].

The gold standard for the study of ion channels is patch-clamp electrophysiology and the most appropriate variant is the whole cell patch-clamp technique, a direct method of ionic current flow

measurement over the whole-cell membrane. In pharmacological research, this technique enables understanding of how different drugs, ions, or other analytes modify and affect the ion channel functioning.

Here we describe the use of the whole-cell voltage-clamp recordings to investigate changes in the membrane currents of glioma C6 cells evoked by epinephrine.

METHODS

Rat C6 astroglioma cells were cultured under standard conditions (at 37°C, in 95%/5% (v/v) O2/CO2 atmosphere) in Dulbecco's modified Eagle's medium (Life Technologies Limited, Paisley, UK), supplemented with 10% heat-inactivated fetal bovine serum (Gibco, Waltham, MA, USA), and 1% penicillin/streptomycin (Invitrogen, Carlsbad, CA, USA). Plated cells were transferred into a recording chamber with an extracellular solution composed of (in mM, all chemicals from Sigma-Aldrich, MO, USA): 140 NaCl, 4 KCl, 2 $MgCl_2$, 2 $CaCl_2$, 10 HEPES, and 5 glucose (pH 7.4 adjusted with NaOH). To perform the whole-cell voltage-clamp recordings, we used pipettes (4–7 MΩ) filled with intracellular solution containing (in mM): 144 KCl, 2 $MgCl_2$, 5 EDTA, 10 HEPES (pH 7.2 adjusted with KOH), and Tecella Pico 2 amplifier with TecellaLab software (Tecella, Foothill Ranch, CA, USA). Olympus BH-2 upright microscope with a z-axis movable stage was used to perform patch-clamp experiments [5]. Signals were sampled at 10 kHz, filtered at 5 kHz, and analyzed off-line using pClamp software (Molecular Devices, San Jose, CA, USA). All recordings were performed at room temperature. Epinephrine (Sigma-Aldrich, MO, USA) was added to the extracellular solution to a final concentration of 20 μM. C6 cells were voltage-clamped at the holding potential of −50 mV. The whole-cell currents were evoked in response to 20 mV depolarizing steps from −90 mV to 90 mV. Steady-state currents were analyzed. Data were analyzed and plotted using SigmaPlot software (Systat Software Inc., San Jose, CA, USA). Graphs were made with CorelDRAW software. Comparison of two data sets was carried out using a two-tailed paired t-test, $p<0.05$ was considered statistically significant, and exact p values are indicated in the figure. Data are presented as mean ± SEM, and box and whisker plots. In the box plots, the central line shows the median, the edges of the box define the upper and lower quartile values, and the whiskers show the minimum-maximum range.

RESULTS AND DISCUSSION

In view of our previous findings that the brief application of epinephrine (20 μM) caused an increase of outward currents in glioma C6 cell, here we have examined the effect of long-lasting bath-applied epinephrine (10 min, 20 μM) on the membrane currents changes in C6 cells using the patch-clamp whole-cell configuration (Figure 1a**.**) [6]. We examined changes in membrane currents as a measure of the activity of ion channels. In our experiment, 5 cells were used and the same cells were monitored before and 10 min after epinephrine application. Typical membrane current responses are illustrated in figure (Figure 1b.). First, we recorded current traces in C6 cells in control conditions. When epinephrine was subsequently administered the outward membrane currents increased and the inward currents remained unchanged. During the period of 10 minutes, the whole-cell current responses to the applied voltages in the presence of 20 μM epinephrine remained stable. To provide in more detailed analyses of epinephrine effects, we obtained epinephrine-evoked currents by subtracting control current traces from the traces in the presence of epinephrine (Figure 1c.). The I/V plot of the isolated epinephrine-evoked currents confirmed that epinephrine increased outward currents (Figure 1c.). Analysis of control and epinephrine-evoked membrane ionic currents revealed no difference in their amplitudes at −90, −70, and −30 mV (Figure 1d, 1e, 1f.). Oppositely, epinephrine-evoked outward membrane current exhibited significantly higher amplitudes compared with control at 30, 50, 70, and 90 mV (Figure 1g, 1h, 1j, 1i.). The 10 min stable epinephrine-evoked increase of C6 cells

outward currents demonstrates that ion channels are in prolonged open state activity, and also reveals the absence of desensitization.

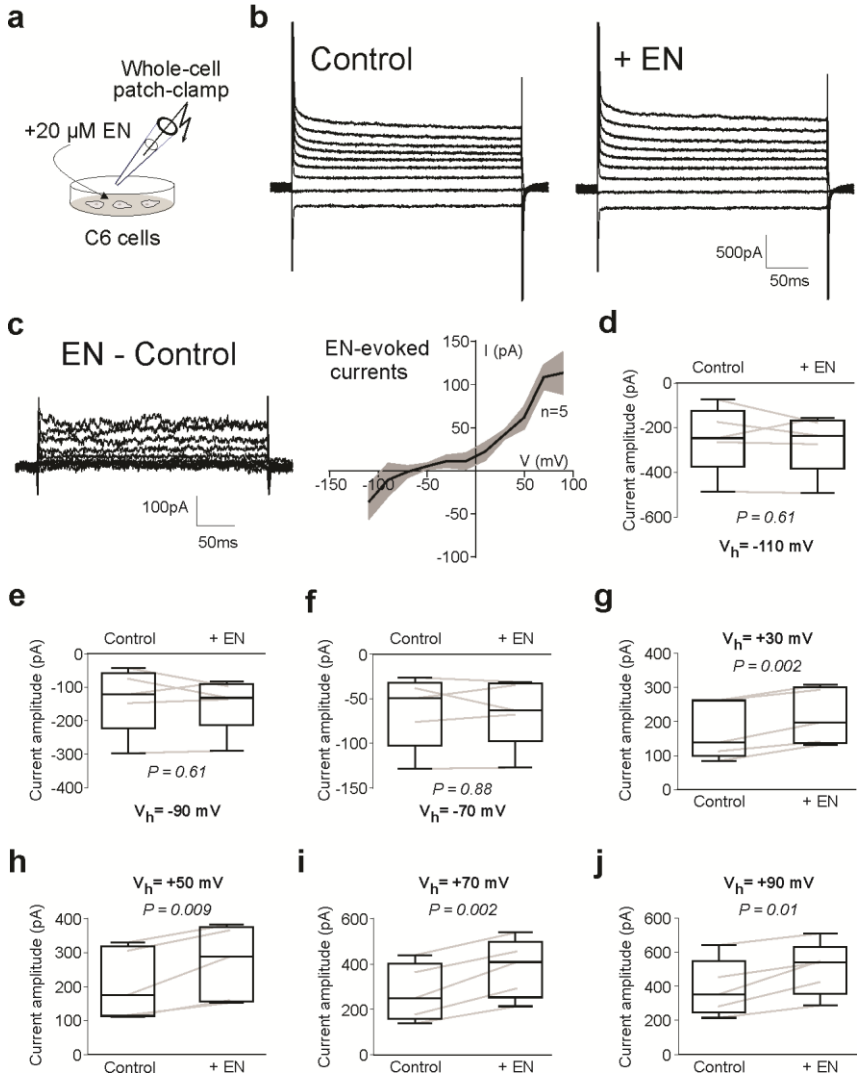

Figure 1. Epinephrine evokes changes of outward currents in glioma C6 cells:
a) Schematic showing the whole-cell patch-clamp recording of glioma cells membrane currents.
b) Example traces of the whole-cell current changes in response to a series of applied stepwise membrane potentials (from −90 to 90 mV in 20 mV increments, V_h= −50mV) of glioma cell in Control and after the addition of 20 μM epinephrine (EN).
c) Left, epinephrine-evoked currents were determined by subtracting current traces obtained in Control (before EN application) from those after EN application at respective voltages. Right, the I–V curve showing the mean epinephrine-evoked current in all examined glioma cells. The number of cells (n) is displayed on the graph. Data were taken 10 min after EN addition. Data are shown as mean ± SEM.
d-j) Comparison of current amplitudes between Control and EN at different holding potentials as specified for each panel, lines connect data points from individual cells.

CONCLUSION

In the present study, we have demonstrated that the bath-applied epinephrine increases the outward membrane ionic currents of glioma C6 cells which are stable over the time of the experiment, up to 10 min. This extended time of membrane ion channel activity in the open state and prolonged sensitization offers suitable research tools to study state-dependent smart drugs that only, for example, block ion channels after they have opened.

Acknowledgment

This work was supported by the Ministry of Education, Science and Technological Development of the Republic of Serbia (Contracts no. 451-03-68/2022-14/200007, and 451-03-68/2022-14/200053).

REFERENCES

[1] B. Hille, Ionic Channels of Excitable Membranes., Sinauer Verlag, Sunderland, 1992.
[2] Jentsch, T., Hübner, C., and Fuhrmann, J., Nat. Cell. Biol., 6 (2004) 1039.
[3] Hübner, C. A., and Jentsch, T. J., Hum. Mol. Genet., 11 (2002) 2435.
[4] Overington, J.P., Al-Lazikani, B., and Hopkins, A.L., Nat. Rev. Drug Discov., 5 (2006) 993.
[5] Perić, M., Bataveljić, D., Bijelić, D., Milićević, K., Andjus, P.R., Bogdanović Pristov, J., and Nikolić, L., Microsc. Res. Tech., doi: 10.1002/jemt.24066 (2022).
[6] Jačić, J. K., Nikolić, L., Stanković, D.M., Opačić, M., Dimitrijević, M., Savić, D., Šipka, S.G., Spasojević, I., Pristov, J.B., Free Radic. Biol. Med., 148 (2020) 123.

^{177}Lu-PHOSPHATE AND PHOSPHONATE MAGNETIC NANOPARTICLES AS POTENTIALTHERANOSTIC NANOAGENTS

M. Radović, M. Mirković, M. Perić, A. Vukadinović, D. Stanković, Z. Milanović, Đ. Petrović, D. Janković and S. Vranješ-Đurić

"VINČA" Institute of Nuclear Sciences - National Institute of the Republic of Serbia, University of Belgrade, Belgrade, Serbia (magdalena.lazarevic@vin.bg.ac.rs)

ABSTRACT

Development of magnetic nanoparticles (MNPs with excellent heating abilities, yet easy to be radiolabeled, suitable for dual magnetic hyperthermia/radionuclide cancer therapy is still a challenge. Aiming to explore MNPs as potential theranostic nanoagent, we used phosphates (IDP and IHP) and phosphonates (MDP and HEDP) coated Fe_3O_4 magnetic nanoparticles (MNPs). The magnetic hyperthermia efficiency of MNPs was evaluated in an alternating magnetic field at 30 mT and 397 kHz. Phosphate-coated MNPs were radiolabeled with ^{177}Lu in a reproducible high yield (99.1% for Fe_3O_4–IDP MNPs and 99% for Fe_3O_4–IHP MNPs, while the radiolabelling yield of phosphonate-coated MNPs was 78.7 % for ^{177}Lu-MDP MNPs and 75.0 % for ^{177}Lu-HEDP MNPs. *In vitro* stabile radiolabeled nanoparticles in saline and HSA were obtained. Overall, *in vitro* stability as well as heating ability indicate that biocompatible radiolabeled phosphate and phosphonate MNPs exhibit promising potential as a theranostic nanoagent.

INTRODUCTION

Many studies on diagnostic and therapeutic use of iron-oxide based magnetic nanoparticles for various diseases including cancer have been massively exploited during the last decades [1]. MNPs radiolabeled with beta-emitting radionuclides yttrium (90Y) and lutetium (177Lu) can be potentially used in cancer radionuclide therapy [2]. However, magnetic hyperthermia applied in cancer therapy is a process based on the harmful heat that magnetic nanoparticles produce under the oscillating magnetic field [3]. Combining diagnostic and therapy approach into one, theranostic, researchers open new avenues for their further improvement.

Coating of MNPs increases the colloidal stability, prevents aggregation and agglomeration of the particles and provides nontoxicity in physiological conditions. Different phosphates and phosphonates have shown excellent coating ability toward magnetic nanoparticles, improving their stability and biocompatibility which enables their biomedical application [4].

In the present study heating capacity of Fe_3O_4 based MNPs coated with inositol hexaphosphate (IHP), imidodiphosphate (IDP), hydroxyethylidene diphosphonic acid (HEDP), and methanediylbis (phosphonic acid) (MDP) have been investigated for possible hyperthermia treatment. Further, phosphate and phosphonate functionalized MNPs were labeled with ^{177}Lu with the aim to investigate their potential for use in diagnosis or hyperthermia cancer therapy.

METHODS

The heating abilities of Fe_3O_4-MPD, Fe_3O_4-HEDP, Fe_3O_4-IDP, and Fe_3O_4-IHP MNPs were analyzed by using a Commercial AC applicator (model DM100, nB nanoscale Biomagnetics). The heat generation under an alternating magnetic field (30 mT) and the resonant frequency of 397 kHz was measured directly on the samples dispersed in water. The heating ability of MNPs (2 mg/ml), defined as specific power absorption (SPA), is calculated according to the following formula: $SPA = (Cp \cdot m_w/m_m) \cdot (\Delta T/\Delta t)$, where Cp is the specific heat capacity of the medium (Cp ~ Cwater =

4.18 Jg−1 K−1), m_w and m_m are the masses of the medium (water) and the magnetic nanoparticles, and ΔT/Δt is the initial slope of the time-dependent temperature curve [5].

^{177}Lu-labeling of phosphates and phosphonates coated Fe_3O_4 MNPs was obtained using the method previously described [6, 7]. Briefly, $^{177}LuCl_3$ solution (approximately 185 MBq in 5 μl) was added to an aqueous suspension of coated Fe_3O_4 MNPs (5 mg/ml at pH 4.5) and incubated at room temperature with continuous stirring for 1 h. To quantify the radiolabeling yield of ^{177}Lu-labeled MNPs and their radiochemical purity after purification by magnetic decantation, ITLC was performed on SG sheets with 0.1 M acetate buffer as the mobile phase. In this system, ^{177}Lu-labeled MNPs remained at the origin (Rf = 0.0–0.1), while the unbound $^{177}Lu^{3+}$ migrated with the solvent front (Rf = 0.8–0.9).

The stability studies were performed by measuring the free, unbound ^{177}Lu in relation to the ^{177}Lu-labeled coated MNPs (bound ^{177}Lu) during incubation of ^{177}Lu –MNPs in 2 ml of human serum or saline (0.9% NaCl, pH=7.3) at 37 °C up to 96 h. At different time points after the radiolabeling (1, 24, 48 and 96 h), samples were analyzed by ITLC using the above-mentioned solvent system as the mobile phase.

RESULTS AND DISCUSSION

In order to apply magnetic hyperthermia, it is necessary to take into account physiological limitations. Due to the eddy currents, MFs of high frequencies can cause local heating also in the sections of the tissue where no magnetic particles have been found. Along with clinical restrictions, technical issues should be also taken into account, since most studies on biological samples encompass a tight frequency range. The applied frequencies, together with the amplitude of the alternating field, are mainly based on literature data [8, 9]. The temperature increase of Fe_3O_4-MPD, Fe_3O_4-HEDP, Fe_3O_4-IDP, and Fe_3O_4-IHP MNPs (5 mg/ml) as a function of the time was evaluated under a frequency of 397 kHz and magnetic field strength of 30 mT (Figure 1.). Although all specimens under investigation have shown substantial heating capacity, it is obvious that Fe_3O_4-HEDP MNPs achieved the highest temperature values.

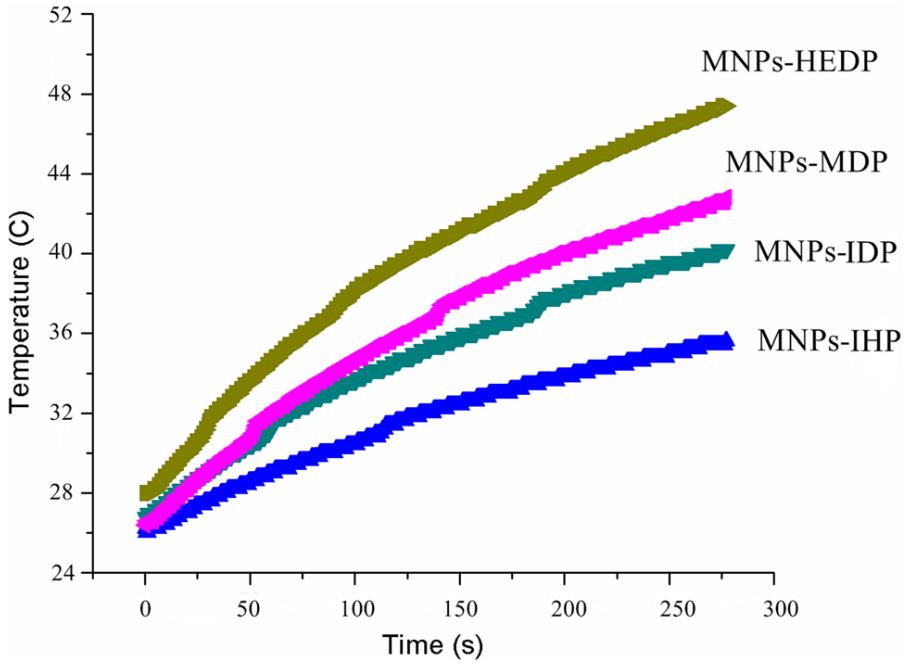

Figure 1. The magnetic hyperthermia efficiency of Fe_3O_4-MPD, Fe_3O_4-HEDP, Fe_3O_4-IDP, and Fe_3O_4-IHP MNPs at 30 mT and 397 kHz

The aim was to optimize the ^{177}Lu radiolabeling of coated MNPs toward their further *in vivo* applications. ^{177}Lu as trivalent metal usually easily make complexes at room temperature with MNPs that possess available phosphates and phosphonates functional groups on the surface. The radiolabeling yield of ^{177}Lu-MNPs, as well as their radiochemical purity after purification by magnetic decantation, was determined using ITLC-SG chromatography with 0.1 M acetate buffer as the mobile phase (Table 1). Radiolabeling yield after 30 min of reaction time was over 99% for ^{177}Lu- IDP-MNPs and ^{177}Lu-IHP-MNPs while the radiolabelling yield of ^{177}Lu-MDP-MNPs and ^{177}Lu-HEDP-MNPs was 78.7 ± 0.7% and 75.0 ± 1.1% respectively. Both radiolabeled phosphonate-coated MNPs can be further purified from free ^{177}Lu using magnetic purification reaching radiochemical purity of over 95% (Table 1.).

Table 1. Radiolabeling yield and radiochemical purity of ^{177}Lu-MNPs after magnetic decantation

177Lu-MNPs	**Radiolabeling yield (%)**	**Radiochemical purity after purification using magnetic decantation (%)**
177Lu-MDP-MNPs	78.7 ± 0.7	95.4 ± 0.5
177Lu-HEDP-MNPs	75.0 ± 1.1	95.9 ± 0.6
177Lu-IDP-MNPs	99.1 ± 1.3	99.7 ± 1.2
177Lu-IHP-MNPs	99.0 ± 0.9	99.9 ± 0.7

In vitro stability of ^{177}Lu-MNPs is shown in (Figure 2.). ^{177}Lu-IDP-MNPs and ^{177}Lu-IHP-MNPs were quite stable, showing the minimal release of ^{177}Lu after 96 h, confirming the strong metal binding to Fe_3O_4-IDP and Fe_3O_4-IHP MNPs. ^{177}Lu-MDP-MNPs and ^{177}Lu-HEDP-MNPs show about 10% of released ^{177}Lu after 96 h indicating their less desirable *in vivo* behavior in relation to phosphate-coated MNPs.

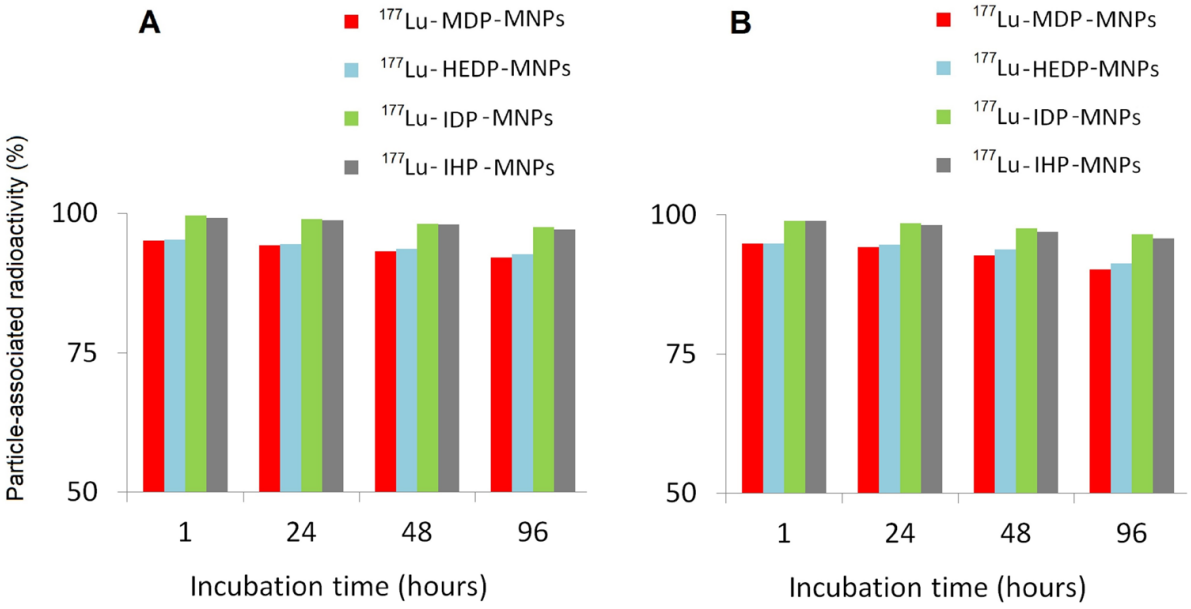

Figure 2. *In vitro* stability of ^{177}Lu-MDP-MNPs, ^{177}Lu-HEDP-MNPs, ^{177}Lu-IDP MNPs, and ^{177}Lu-IHP-MNPs in (**A**) saline and (**B**) human serum after incubation at 37 °C over 96 h

CONCLUSION

The results shown indicate that the MDP, HEDP, IDP, and IHP-coated MNPs could achieve significant heating capacity at 397 kHz and 30 mT frequencies and thus show potential for biomedical applications. Furthermore, phosphate and phosphonate coated MNPs were radiolabeled with ^{177}Lu. Phosphate coated MNPs were radiolabeled in high radiolabeling yield (> 99%) while phosphonate coated MNPs reached a maximum radiolabeling yield of 78%. Regardless of lower radiolabeling yield both radiolabeled phosphonate MNPs may be further purified reaching radiochemical purity of more than 95%. The high heating ability of phosphates and phosphonates coated MNPs and satisfactory radiolabeling yield justifies their further research in order to develop new theranostic agents.

Acknowledgment

This work was supported by the Ministry of Education, Science and Technological Development of the Republic of Serbia (grant no 451-03-68/2022-14/200017) and through funding the VINCENT Center of Excellence.

REFERENCES

[1] Goya G. F., Grazu, V., Ibarra, M. R., Curr. Nanosci., 4 (2008) 1−16.
[2] Radović M., Mirković M., Perić M., Janković D., Vukadinović A., Stanković D., Petrović Đ., Bošković M., Antić B., Marković M., Vranješ-Đurić S., J. Mater. Chem. B, 5 (2017) 8738−8747.
[3] Pankhurst Q. A., Connolly J., Jones S. K., Dobson J. J., J. Phys. D, Appl. Phys., 36 (2003) R167.
[4] Karageorgou M.-A., Vranješ-Djurić S., Radović M., Lyberopoulou A., Antić B., Rouchota M., Gazouli M., Loudos G., Xanthopoulos S., Sideratou Z., Stamopoulos D., Bouziotis P., Cont. Med. Mol. Imag., 2017 (2017) 6951240–6951253.
[5] Shete, P. B., Patil R. M., Thorat N. D., Prasad A., Ningthoujam R. S., Ghosh S. J., and Pawar S. H., Appl. Surf. Sci., 288 (2014) 149–157.
[6] Mirković M., Milanović Z., Stanković D., Petrović Đ., Vranješ-Đuric S., Janković D., and Radović M., J.Radiat. Res. Appl. Sci., 13 (2020) 27–36.
[7] Ognjanović M., Radović M., Mirković M., Prijović Ž., Del Puerto Morales M., Čeh M., Vranješ-Đurić S., and Antić B., ACS Appl. Mater. Interfaces, 11 (2019) 41109–41117.
[8] Atkinos W. J., Brezovich I. A., and Chakraborty D. P., IEEE Trans. Biomed. Eng., 31 (1984) 70–75.
[9] Brezovich I., Med. Phys. Monogr., 16 (1988) 82–111.

THE ELECTROCHEMICAL CHARACTERIZATION, RADIOLABELING, AND BIODISTRIBUTION IN TUMOR-BEARING MICE OF ^{177}Lu-DOXYCYCLINE

Z. Milanović, M. Radović , D. M. Stanković, M. Perić, A. Vukadinović, Đ. Petrović, D. Janković , S. Vranješ Đurić and M. Mirković

„VINČA" Institute of Nuclear Sciences - National Institute of the Republic of Serbia, University of Belgrade, 11001 Belgrade, Serbia(zoranamilanovic89@gmail.com)

.

ABSTRACT

Doxycycline as adjuvant therapy to conventional chemotherapy has shown promising results in cancer therapy. We aimed to examine the capability of ^{177}Lu-labeled doxycycline hyclate, as anticancer agent. Doxycycline was radiolabeled with beta-emitting radioisotope ^{177}Lu. Complex formation and DNA interaction was investigated electrochemicaly. Biodistribution of ^{177}Lu-doxycycline was examined in CT26 colon carcinoma tumor bearing mice. Radiolabeling yield was over 99%. ^{177}Lu-doxycycline was stable *in vitro* in saline and human serum over 72 h. Non-radioactive Lu-doxycycline complex formation was demonstrated electrochemically as well. Tumor accumulation of ^{177}Lu-doxycycline after 3 h was 2.88±0.85% ID/g. ^{177}Lu-doxycycline complex, due to its excellent electrochemical and biological characteristics, and significant accumulation in the tumor, is suitable for further *in vivo* studies to investigate its potential use in cancer treatment.

INTRODUCTION

The chemical structure of doxycycline is closely related to the structure of chemotherapeutic doxorubicin which binds to DNA. Different authors point out to intercalative mechanism of binding of doxycycline to DNA [1,2] . According to the literature doxycycline interacts with DNA via guanine-cytosine and adenine-thymine, and a phosphate (PO_2) group [3]. Considering the chemical properties of tetracyclines, they are good chelating ligands for different metal ions. Tetracyclines have many potential binding sites for different metals, such as oxygens at the C10-C12 phenolic β-diketone system, enolicoxygens and the nitrogens at C4 and at the carboxamide group in ring A [4,5].

According to the study by Silva et al. complexation of platinum(II) with doxycycline, complex binding to DNA, and inhibition of tumor growth *in vitro* was confirmed [1]. Another study demonstrated the diagnostic potential of ^{99m}Tc complex of doxycycline for bacterial infections [6]. Based on these results it seemed to be of interest to examine radiolabeled doxycycline as a potential therapeutic radiopharmaceutical. To date, doxycycline has not been labeled with therapeutic, beta-emitting radioisotope ^{177}Lu.^{177}Lu (half-life 6.7 days) is the perfect β− radionuclide for therapy of solid tumors, as it has a particulate emission (β−or Auger electron) for effective therapy and emits several accompanying γ-photons of 208 keV (11%) and 113 keV (6.4%), which are used for diagnostic evaluation and dosimetry.

METHODS

After dissolving 10 mg of doxycycline hyclate in 1 ml of 0.9% NaCl, pH was adjusted to 6-7 using 0.1 M NaOH solution. To 0.5 ml of dissolved doxycycline was added 37 MBq of $^{177}LuCl_3$ solution, and incubated for one hour at room temperature or in a water bath at 60 ºC. The radiochemical purity (RCP) was checked by ascending paper and Instant Thin Layer Chromatography. The radioactivity was measured using a gamma counter. The percentage of the ^{177}Lu-doxycycline complex was calculated. *In vitro* stability of ^{177}Lu-doxycycline complex was evaluated by

radiochromatography studies at 1, 24, 48 and 72 h after the storage at room temperature and after incubation in saline and human serum at 37 °C. Spectrophotometric and electrochemical tests were done for the investigation of the DNA binding interactions. For the adsorption titration experiments concentration of the DNA was kept constant, while doxycycline and non-radioactive Lu-doxycycline complex concentrations were varied from 0-150 mM. Absorbance was recorded from 200 to 800 nm. All voltammograms were recorded in the three electrode system where a glassy carbon electrode was used as working electrode, Ag/AgCl (3M) as a reference, and platinum wire as a counter electrode, controlled by Autolab 302 N (The Netherland). Biological distribution of the ^{177}Lu-doxycycline complex was tested in BALB/c mice bearing CT26 murine colon carcinoma (males, 10 weeks old, n=5). After cultivation, CT26 cells were resuspended in 0.9% NaCl solution. Tumors were induced by s.c. injection into loins of single dose of cells ($2x10^6$cells/0.1 ml 0.9% NaCl). Radiolabeled complex, in a volume of 0.1 ml, was injected intraperitoneally (1.85 MBq/animal). After 3h, mice were sacrificed. Organs were removed, weighed, and radioactivity was measured. The percentage of injected activity per gram (%ID/g) of the organ was calculated. The data are expressed as mean ± standard deviation.

RESULTS AND DISCUSSION

Under optimized conditions, by radiolabelling of 10 mg of doxycycline hyclate with ^{177}Lu (37 MBq) in a final volume of 1.0 ml (0.9% NaCl) at pH 6-7 and incubation at room temperature for 60 min, the radiochemical purity of ^{177}Lu-doxycycline complex was 99%. No significant dissociation of ^{177}Lu from the complex was observed after 72 h (<10%) indicating high stability of ^{177}Lu-doxycycline complex at all studied conditions. Electrochemical behavior of the doxycycline, before and after formation of the Lu-doxycycline complex, was investigated using three electrode systems with GC electrode as working electrode in acidic media (pH 3.5). The effect of the time on the complex formation was also monitored. Results are given in Fig. 1. At the tested conditions (operating potential -1.3 to 1.3 V) doxycycline provides one well-defined and oval shaped oxidation peak. On the other hand, in the opposite direction, no reduction peak was observed. Based on signal shape, current and potential this signal can be attributed to the phenol group in the doxycycline structure. Similar behavior was reported by other authors [7]. After the addition of the lutetium (1:1 ratio), oxidation peak current reduce to the 5% of its initial value. This confirms formation of the complex Fig. 1.

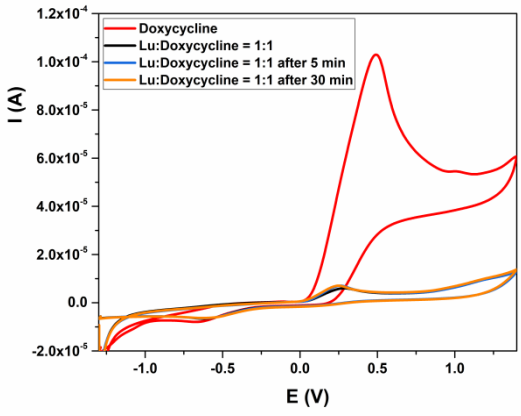

Figure 1. Electrochemical behavior of doxycycline, before and after the formation of the Lu-doxycycline complex. Time dependence. Working electrode GC, scan rate 50 mV/s, pH 3.5.

Increasing amounts of the ligand and complex on the spectra of DNA showed similar behavior. In both cases, spectrums exhibit hyporchromism of about 26%, followed by bathochromic shift. Analyzing doxycycline and Lu-doxycycline incidents in hypochromisms and red shifts, it was noticed that there are no significant changes in their behavior and that both compounds bind to the DNA chain via intercalative interaction.

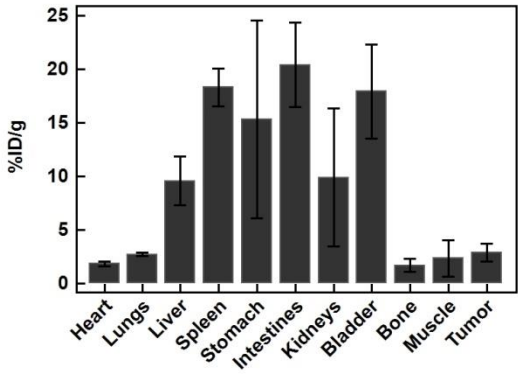

Figure 2. Biodistribution of ^{177}Lu-doxycycline in BALB/c mice bearing CT26 murine colon carcinoma 3 h after intraperitoneal injection

Biodistribution studies of ^{177}Lu-doxycycline complex in BALB/c mice bearing CT26 murine colon carcinoma are illustrated in Fig. 2. Three hours after intraperitoneal injection, ^{177}Lu-doxycycline reach 2.88±0.85% ID/g in tumor, 1.83±0.21% ID/g in heart, 2.71±0.16% ID/g in lungs, 9.55±2.27% ID/g in liver, 18.31±1.74% ID/g in spleen, 15.33±9.23% ID/g in stomach, 20.39±3.94% ID/g in intestines, 9.88±6.45% ID/g in kidneys, 17.94±4.38% ID/g in bladder, 1.68±0.61% ID/g in bone and 2.35±1.69% ID/g in muscle. Taking into account the biological half-life of doxycycline (18 to 22 h), radioactivity detected in the liver, intestines, stomach, kidney, and bladder resembles to excretion routes of doxycycline which is mainly excreted into the gut (in part via the gallbladder, in part directly from blood vessels), and partially (about 40%) via the kidneys [8,9].

CONCLUSION

Doxycycline was successfully labeled with ^{177}Lu in high radiolabeling yield (>99%). The ^{177}Lu-doxycycline complex was found to be stable at room temperature as well as in saline and human serum over 72 h. Complexation between non-radioactive Lu^{3+} and doxycycline was proven using electrochemical measurements. The binding ability of Lu-doxycycline to DNA was confirmed. Satisfactory tumor uptake was obtained in tumor bearing mice. Radiolabeling of DNA-intercalating agents with therapeutic radionuclides, which show satisfactory accumulation in the tumor, grants further investigations to evaluate their possible use as anticancer drugs.

Acknowledgment
This work was supported by the Ministry of Education, Science and Technological Development of the Republic of Serbia (grant no 451-03-68/2022-14/200017).

REFERENCES

[1] Silva P.P., De Paula F.C.S., Guerra W., Silveira J.N., Botelho F. V., Vieira L.Q., Bortolotto T., Fischer F.L., Bussi G., Terenzi H., and Pereira-Maia E.C., J. Braz. Chem. Soc. 21 (2010) 1237–1246.
[2] Aleksić M.M., Kapetanović V., Acta Chim. Slov. 61 (2014) 555–573.
[3] Bagheri A., Masoudinia M., J. Struct. Chem. 59 (2018) 1478–1483.
[4] De Paula F.C.S., Carvalho S., Duarte H.A., Paniago E.B., Mangrich A.S., and Pereira-Maia E.C., J. Inorg. Biochem. 76 (1999) 221–230.
[5] Guerra W., Silva I.R., Azevedo E.A., Monteiro A.R.D.S., Bucciarelli-Rodriguez M., Chartone-Souza E., Silveira J.N., Fontes A.P.S., and Pereira-Maia E.C., in: J. Braz. Chem. Soc., Sociedade Brasileira de Quimica, (2006)1627–1633.
[6] İlem-Özdemir D., Asikoglu M., Ozkilic H., Yilmaz F., Hosgor-Limoncu M., and Ayhan S., J. Label. Compd. Radiopharm. 57 (2014) 36–41.
[7] Nagles E., Alvarez P., Arancibia V., Baez M., Garreton V., and Ehrenfeld N., Int. J. Electrochem. Sci., 7 (2012) 11745 – 11757.
[8] Saivin S., Houin G., Clin. Pharmacokinet. 15 (1988) 355–366.
[9] Agwuh K.N., MacGowan A., J. Antimicrob. Chemother. 58 (2006) 256–265.

CHARACTERIZATION OF UNKNOWN DEGRADANT OF ZIPRASIDONE WITH NMR SPECTROSCOPY

M. Čarapić[1], M. Petković[2], B. Marković[3], M. Popović Nikolić [3], D. Agbaba[3] and K. Nikolic[3]

[1]Medicines and Medical Devices Agency of Serbia,
Vojvode Stepe 458, 11000 Belgrade, Serbia. (marija.carapic@alims.gov.rs)
[2]Department of Organic Chemistry,
[3]Department of Pharmaceutical Chemistry, University of Belgrade - Faculty of Pharmacy,
Vojvode Stepe 450, PO Box 146,11000 Belgrade, Serbia.

ABSTRACT

Ziprasidone (ZIP) is the second generation antipsychotic drug with unique G-protein-coupled (GPCR) receptor binding profile. It is a highly lipophilic and unstable compound. Our group developed and validated the single liquid chromatographic (LC) system for simultaneous determination of ZIP and its five main impurities (IMPs) and we modelled the Quantitative Structure Retention Relationship (QSRR) of the additional ten compounds including unknown detected degradant. One of two proposed structures were confirmed by UPLC-MS/MS study. The further characterisation of unknown degradant was performed with NMR studies as un versatile tool for characterisation of each compound and it is presented. Through several experiments which consists of investigation of chemical shitfs in NMR spectra of ZIP degradation products the structure of unknown degradant was proposed and confirmed as in previous experiments.

INTRODUCTION

ZIP is atypical or second-generation antipsychotic drug with multiple GPCRs receptors affinity and very promiscuous pharmacology [1]. ZIP multipotent mechanism of action and complex therapeutic effects haven't been clearly elucidated yet [2]. Recently, its *in vitro* neuroprotective effects were confirmed [3]. Reactivity of the alpha position of the 2-indolinone moiety of ZIP is a consequence of its instability, thus, mostly ZIP degradants structurally differs at this position. A single LC system was developed for the simultaneous determination of ZIP and its five main IMPs for the first time by our research group [4]. The QSRR model of the LC separation of 10 structurally related compounds to ZIP (IMPs/metabolites), including unknown detected degradant was made [5]. Based on the QSRR predicted retention time (t_R) value two most possible structures were proposed from the test set. A rapid and highly sensitive UHPLC-MS/MS method was developed for chemical characterization of unknown degradant and quantitation of ZIP and its IMPs [6]. The performed UHPLC-MS/MS have confirmed the structure of unknown degradant proposed by QSRR study. The literature data showed that it could be an oxidative degradant formed by aldol condensation between Zip-oxide and ZIP [7]. It was assumed that it could be also formed by dehydration of Zip-dimer (Figure 1).

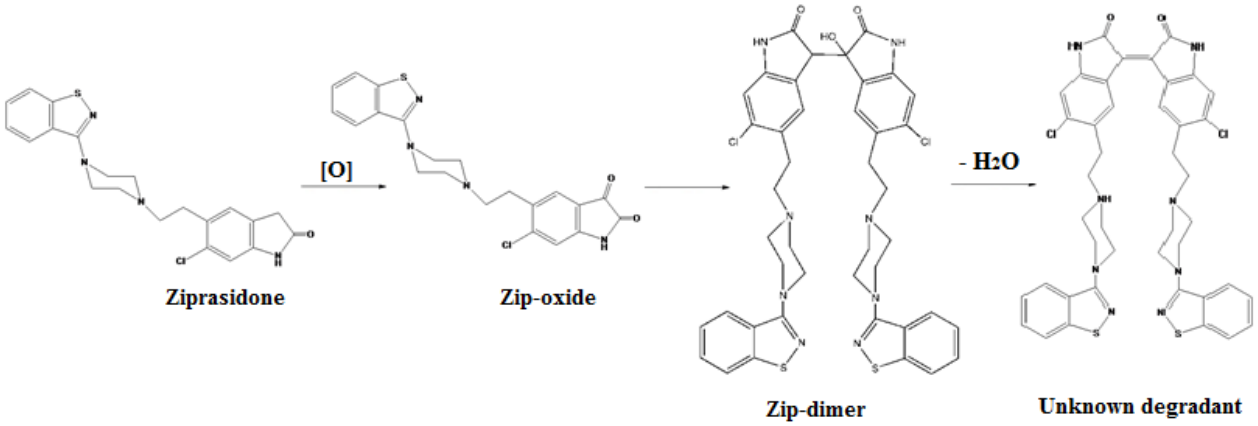

Figure 1. Potential mechanism of degradation of ziprasidone

As per regulatory requirements there is need to use minimum two analytical tools based on different principles for characterization of compounds. This prompted us to investigate unknown degradant by NMR analysis, an advanced selective characterization technique which very recently is used as quantitative tool for API assay [8]. The whole study is important for the further estimation of structures of other unknown IMPs of ZIP which might be of the possible toxicological concern.

METHODS

Working standard of Zip-dimer (5,5'-bis[2-[4-(1,2-benzisothiazol-3-yl)-1-piperazinyl]ethyl]-6,6'-dichloro-1,1',3,3'-tetrahydro-3-hydroxy-[3,3'-bi-2H-indole]-2,2'-dione) was kindly supplied by Pfizer, Conneticut, USA. All the reagents used in the experiment were of analytical grade. Water was of the HPLC grade (purified by the Simplicity 185 system, Millipore, Billerica, MA). Hydrochloric acid (Merck, Darmstadt, Germany), methanol (Chromasolv® for HPLC, ≥99.9%), sulphuric acid (Merck, Darmstadt, Germany) and dimethyl sulfoxide-D6 (DMSO-D6) (Merck, Darmstadt, Germany) were used for the preparation of the solutions and instrumentation.

The standard of Zip-dimer was dissolved directly in DMSO-D6 and analysed. Force degradation studies were performed under two different acidic conditions in order to obtain the unknown degradant from the Zip-dimer and both degradation solutions (I & II) were analyzed with NMR. At first, the working standard of Zip-dimer (3.4 mg) was dissolved in 1 mL of the solution of HCl in methanol (0.5% v/v). After two weeks the red precipitate formed and then dried. Dried precipitate was dissolved in DMSO–D6 (degradation solution I).

For degradation solution II different acid conditions was applied directly in NMR tube with solution of working standard of Zip-dimer in DMSO-D6. One drop of dehydration agent, sulphuric acid was added into NMR tube at elevated temperature 70 ^{o}C (water bath)

NMR spectra were recorded at 25 °C on a Bruker Ascend 400 (400 MHz) spectrometer. Chemical shift are given in parts per million (δ). Chemical shift of the residual solvent signal was used as the reference

RESULTS AND DISCUSSION

^{1}H NMR spectra of solution of standard Zip-dimer showed that there were two different chemical shifts of signals for N-H hydrogens (δ 10.45 and 10.27) and aromatic C-H hydrogens from indolone rings (in the range δ 8.03-6.70 mixed with benzoisothiazole hydrogens) which indicated that Zip-dimer is non-symmetric compound. Furthermore, the characteristic signal for sp^{3} C-H hydrogen from indolone ring was obtained at δ 6.10 (Figure 2.). According to the literature [9], for similar

bisindolone structure signals, the sp3 CH and OH groups are found at 6.16 and 4.00, respectively, which is in good agreement with our results. Very recently the similar investigation for unknown ZIP impurity has been done and ^{1}H NMR assignment for ZIP is presented, but yet without H-NMR spectra for the our investigated compounds [10].

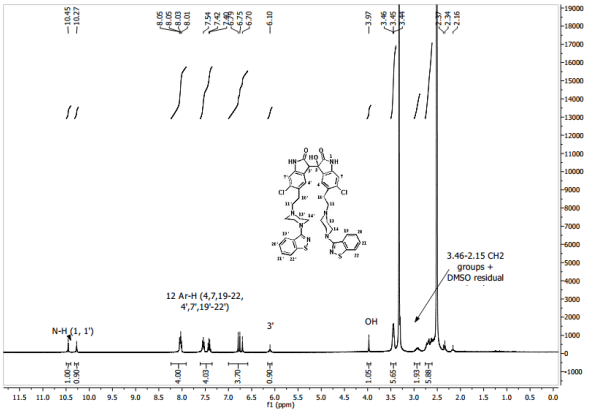

Figure 2. ^{1}H NMR spectra of solution of standard Zip-dimer in DMSO-D6

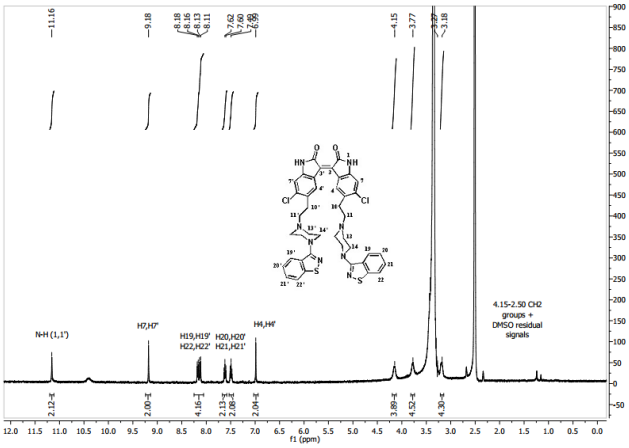

Figure 3. ^{1}H NMR spectra of obtained unknown degradant from precipitate in DMSO-D6 (degradation solution I)

Further experiment was conducted on the degradation solution I. Two weeks from the dissolving of Zip-dimer in the acidic conditions (0.5% v/v HCl in methanol) red precipitate was dissolved in DMSO-D6 and analysed by NMR. There was only one signal for N-H hydrogens (δ11.16) and only two signals for aromatic C-H hydrogens from indolone rings (δ 9.18 and 6.99) indicating that the obtained unknown degradant from precipitate is a symmetric compound. Loss of the sp^3 C-H hydrogen signal (δ 6.10) indicate elimination of water molecule and double bond formation between two indolone rings **(**Figure 3).

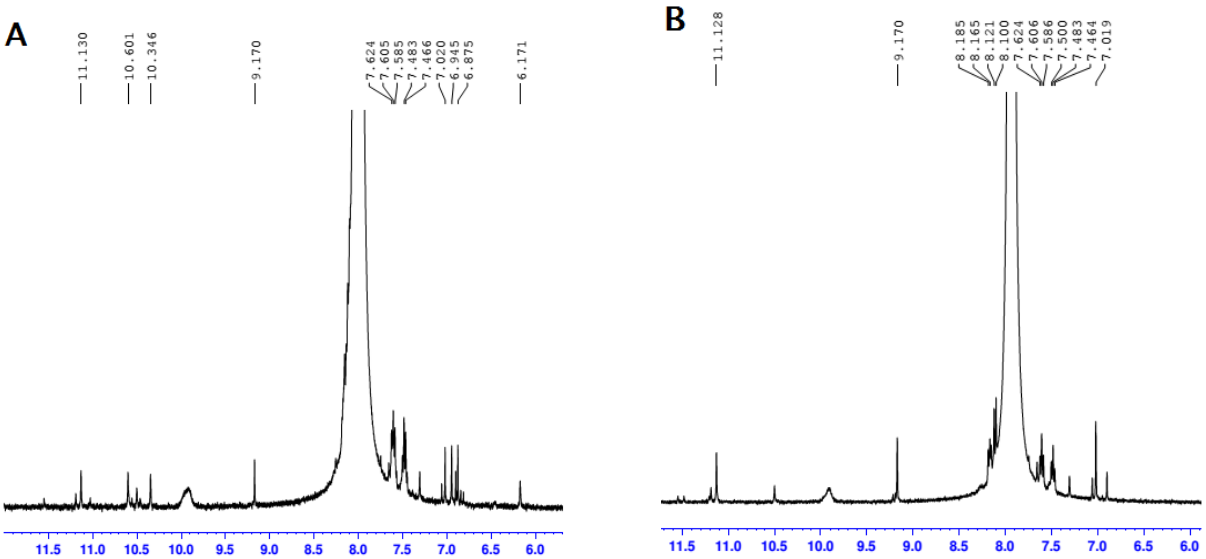

Figure 4. ^{1}H NMR spectra of standard Zip-dimer after addition of H_2SO_4 after: 3 hours at 70 ^{o}C (**A**) and 18 hours at 70 ^{o}C (**B**) (degradation solution II)

The degradation solution II was analyzed in two time points: after 3 hours from addition of one drop of dehydration agent, sulphuric acid at 70 ^{o}C (water bath temperature) and after 18 hours at 70 ^{o}C. After 3h the characteristic signals for unknown degradant from precipitate started to appear (Figure 4, A). After 18 hours at 70 ^{o}C signal for sp^3 C-H hydrogen (δ 6.10) completely disappeared (Figure 4, B).

Based on all NMR experiments, the proposed structure of unknown degradant from the MS/MS and QSRR study was confirmed (Figure 1).

CONCLUSION

The obtained data from NMR experiments proposed the probable structure of unknown degradant (**Figure 1**) the same as in previous studies. To our knowledge, we are the first to report such NMR study. Our results represent valuable data dedicated to the understanding mechanism of degradation of ziprasidone guiding us into further research on novel ziprasidone impurities which might be of possible toxicological cocern.

Acknowledgment

This research was funded by the Ministry of Education, Science and Technological Development, Republic of Serbia through Grant Agreement with University of Belgrade-Faculty of Pharmacy No: 451-03-68/2022-14/200161 and COST Action CA18133.

REFERENCES

[1] Roche V.F., Zito, S.W., Lemke, T.L., Williams, D.A., Foye's Principles of Medicinal Chemistry (8th ed.). Walters Kluwer, 2020.
[2] Moriya S., Takahashi H., Masukawa D., Yamada M., Ishigooka J., Nishimura K. J. Pharmacol. Sci. 144 (2020) 57.
[3] Terada K., Murata A., Toki E., Goto S., Yamakawa H., Setoguchi S., Watase D., Koga M., Takata J., Matsunaga K., Karube Y. Molecules 25 (2020) 4206.
[4] Pavlovic M., Malesevic M., Nikolic K., Agbaba D. J. AOAC Int. 94(3) (2011), 713.
[5] Nikolic K., Pavlovic M., Smoliński A., Agbaba D. Comb. Chem. & High Throughput Screening 15 (2012) 730.
[6] Čarapić M., Nikolic K., Marković B., Petković M., Pavlovic M., Agbaba D. Biomed. Chromatogr. 33(2) (2019) e4379
[7] Li M. Organic Chemistry of Drug Degradation. Cambridge, UK: RSC Publishing; 2012 pp. 124
[8] ICH guideline Q2 (R2) on validation of analytical procedures, step 2b, march 2022
[9] Meilin L., Shaozhong Q., Yu Y., Guodong Y., Tetrahedron Letters, 57(52) (2016.), 5856.
[10] Murkute S.R., Singh G.P., Vasantharaju S.G., Bhat K., Godbole H.M., Upadhyay P.R., Trivedi A., Journal of Pharmaceutical and Biomedical Analysis, 207 (2021) 114416.

INHIBITION OF KAPPA OPIOID RECEPTOR (KOR) AUGMENTS KETAMINE ANTI-DEPRESSIVE PROPERTIES IN THE MOUSE MODEL OF DEPRESSION

A. Zivanovic, M. Mitic, E. Glavonic, I. Lukic, M. Adzic* and S. Ivkovic *

Vinca – Institute of Nuclear Sciences, National Institute of Republic of Serbia, University of Belgrade, Mike Petrovica Alasa 12-14, 11351, Vinca, Belgrade, Serbia, sivkovic@vinca.rs
** shared last authorship*

ABSTRACT
Ketamine emerged recently as a novel and highly effective anti-depressant drug. However, the effects of ketamine, although rapid and robust, are transient and may involve the unwanted side effects. Thus, the enhancement of ketamine-based anti-depressive therapies is essential. Ketamine action depends on opioid signaling and kappa opioid receptor (KOR) inhibition can have antidepressive effect. In this study, the combined ketamine and KOR antagonist norbinaltorphimine (NorBni) treatment augmented the anti-depressant effects of ketamine in the cumulative unpredicted stress (CUS) mouse model of depression. The combined treatment had a bidirectional effect on mTOR and JNK signaling pathways in the striatum (STR), one of the brain structures implicated in the pathology of depression. These results strongly suggest that the simultaneous modulation of glutamate and opioid signaling can improve the anti-depressive effects of ketamine.

INTRODUCTION
Major depressive disorder (MDD) is one of the most prevalent and debilitating mental disorders affecting over 300 million people worldwide [1]. Classical anti-depressant medications have the late onset of their therapeutic effects and are not effective in about 30% of MDD patients. Recent findings that the subanesthetic doses of intravenous ketamine can elicit rapid and robust anti-depressant effects in MDD patients led to the approval of ketamine as a novel drug for the MDD treatment [2]. Unfortunately, ketamine's anti-depressant effects are transient, lasting an average of 1 week following a single infusion and can be accompanied with unwanted side effects (i.e., psychotomimetic effects and dissociation). Therefore, the need for the improvement of of the ketamine-based MDD therapy arose as an urgent challenge.

Ketamine is a noncompetitive glutamatergic N-methyl-D-aspartate receptor (NMDAR) antagonist that exerts its effects through the block of NMDARs, the upregulation of α-amino-3-hydroxy-5-methyl-4-isoxazole propionic acid receptor (AMPAR), and brain-derived neurotrophic factor (BDNF). In such a way, ketamine therapy promotes neurotrophic signaling and the development of the new synaptic connections via activation of mammalian target of rapamycin (mTOR) signaling [3]. Recent findings showed that the ketamine antidepressant effects depend on the activation of the opioid signaling [4]. Kappa opioid receptor (KOR) is of the particular interest as it mediates stress-related behavioral dysfunction and KOR antagonists NorBni have the unique potential as anti-depressant therapeutic agents and acts through the increased phospho-JNK signaling [5,6].

We hypothesized that the combination of ketamine and NorBni can augment ketamine's anti-depressant effects in the CUS model of depression through the modulation of mTOR and JNK signaling pathways. We performed our analyses in the striatum (STR), as it is one of the key structures involved in mediating motivational and emotional processes, and the effects of certain psychoactive drugs. [7,8].

METHODS

Animals: We used male C57BL/6J mice, maintained on a 12 h light/dark cycle with food (commercial animal pellets) and water *ad libitum*. Animals were housed 3-4 per cage, and temperature was maintained at 22°C. **Chronic Unpredictable Stress:** Mice were exposed to CUS starting from postnatal day 28 (P28) till P40. The CUS paradigm was adapted from Yohn and Blendy [9]. **Drug administration:** Animals exposed to the CUS were randomly divided into 4 groups (n=10) for the i.p. drug administration on the P70: I CUS group was treated with the mass-adjusted volume of vehicle (saline, 0.9% NaCl); II K group was treated with ketamine (Ketamidor, Richter Pharma AG, 6mg/kg) diluted in saline; III NorBni group was i.p. injected with NorBni (Sigma-Aldrich,10mg/kg) diluted in saline, IV K/NorBni group was i.p injected with ketamine (6mg/kg) and NorBni (10mg/kg) diluted in saline, 30 min apart. The control group consisted of non-stressed mice treated with mass-adjusted saline. **Behavioral tests:** Behavioral testing was performed 8 days (8d) after the injection with designated drugs or vehicle. Animals were exposed to the tail suspension test (TST) as the measure of their depressive-like behavior. **TST:** Mice were suspended by their tails with a tape and the resulting escape-oriented behavior was recorded and quantified by the observer [10]. On the 9^{th} day, animals were sacrificed and brain structures were isolated for further molecular analyses. **Sample preparation:** Animals were sacrificed on the 8^{th} day from the day of injection, and striatum (STR) was isolated for the isolation of whole cell fraction. The concentration of proteins was determined by the method of Markwell (11). **Western blot detection of proteins:** Samples were mixed with denaturing buffer according to Leammli [12], boiled for 5 min at 100°C, and 25 μg of proteins were subjected to SDS-PAGE electrophoresis on 12% gels. Subsequently, proteins were transferred onto PVDF membrane (Immobilon-P membrane, Millipore) using a blot system (Transblot, Bio-Rad). The membranes were blocked with 5% milk in PBST (137 mM NaCl, 2.7 mM KCl, 10 mM Na_2HPO_4, and 1.8 mM KH_2PO_4, 0.1 % Tween 20), and incubated in primary antibodies – mouse anti-mTOR (1:500, Santa Cruz, sc-517464), rabbit anti-p-mTOR (Ser 2448, 1:500, Santa Cruz, sc-101738), rabbit anti-JNK (1:2000, Santa Cruz, sc-571), and mouse anti-p-JNK (Thr 183, Tyr 185, 1:500, Santa Cruz, sc-6254) and secondary antibodies (rabbit anti-mouse IgG H&L (HRP), Abcam, ab6728, or goat anti-rabbit IgG H&L (HRP), Abcam, ab6721). Signal was developed using enhanced chemiluminescent reagent (Pierce) and exposed to X-ray film (Fuji Photofilm, Bedfordshire, UK). Ponseau-S staining was used as a loading control. Densitometry of protein bands on X-ray film was performed by Image J analysis and normalized to internal referent control sample and Ponseau-S measurements. **Statistical analysis:** All data are presented as mean ± standard error of the mean (SEM). Statistical analyses were performed by Prisma software (GraphPad Prism 6). Results were analyzed using t-test and one-way ANOVA followed by a posthoc Tukey's test. $p < 0.05$ was defined as statistically significant.

RESULTS AND DISCUSSION

Depressive-like behavior in stressed (CUS) group was verified in comparison to the non-stressed mice (Control) by TST 8 days after the saline injections. CUS mice were more immobile than controls (t-test, $p<0.001$, Fig.1A) which confirmed that they exhibit depressive-like behavior. The anti-depressive effects of different treatments were also assessed by TST (Fig.1.A) 8 days after the drug administration. Mice treated with ketamine (K) and NorBni (NorBni) had the same immobility time as the CUS group. However, the K/NorBni group had a significantly lower immobility time compared either to the CUS, K group, or NorBni group ($F=7.174$, $p<0.001$) confirming that K/NorBni can improve the anti-depressive effects of ketamine.

We further examined how different drug treatments affected the expression levels of pJNK (phospho JNK), tJNK (total JNK), pmTOR (phospho mTOR), and tmTOR (total mTOR) in

comparison to the CUS group (Fig.1B-E). Western blot analyses were performed in the STR, the brain structure involved in the development of symptoms associated with psychiatric conditions. Our results showed that the pJNK was decreased in the K/NorBni and K groups, and unaltered in the NorBni group ($F=16.07$, $p<0.001$, Fig.1.B). At the same time, the levels of tJNK were decreased only in the K group ($F=4.555$, $p<0.05$, Fig.1.B). The expression levels of pmTOR were elevated in the NorBni and K/NorBni groups, and unaltered in K group ($F=20.61$, $p<0.001$, Fig.1.C). The levels of tmTOR were decreased in K and K/NorBni, and unaltered in NorBni group ($F=5.303$, $p<0.01$, Fig.1.C). The calculated ratio between the phospho and total forms of JNK and mTOR proteins showed their activation under different treatments. JNK activation was significantly decreased in K and K/NorBni groups, and unaltered in NorBni group ($F=12.84$, $p<0.0001$). The mTOR activation was increased only in K/NorBni group ($F=7.515$, $p<0.001$) (Fig.1.E).

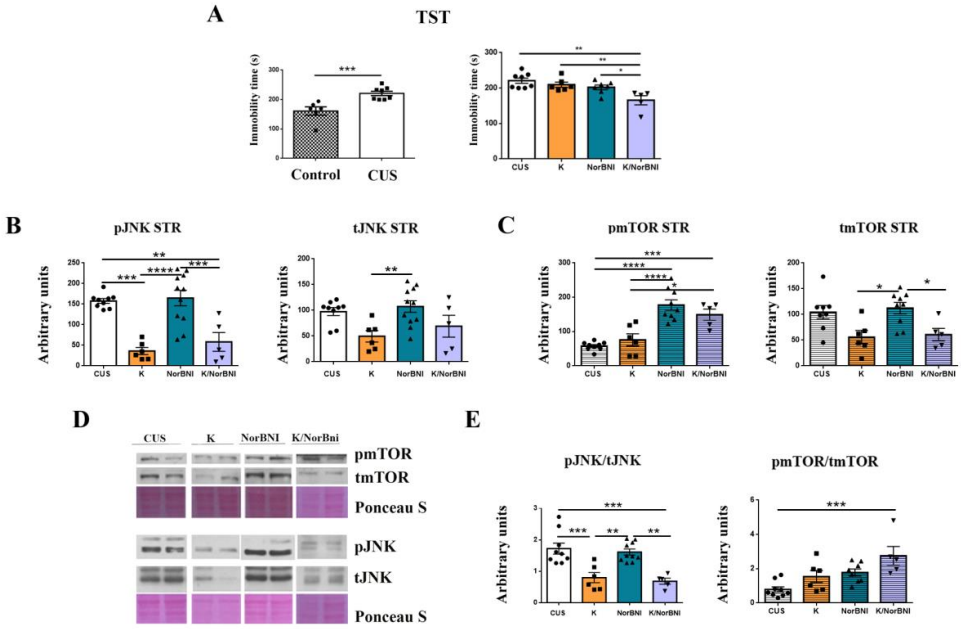

Figure 1. K/NorBni treatment improved ketamine-only anti-depressant effects and modified JNK and mTOR signaling in the STR. (A) TST analyses of the control, CUS, and treatment groups. (B) The expression of pJNK and tJNK in the STR of treated mice. (C) The expression of mTOR and pmTOR in the STR of treated mice. (D) Representative western blots and PonseauS staining. (E)The calculated ratio between pJNK and tJNK, and pmTOR and tmTOR in the STR of treated mice. Data are presented as the mean ± SEM, (*p < 0.05, **p < 0.01, ***p < 0.001, ****p<0.0001).

Ketamine was shown to decrease JNK [13] and both the inhibition of JNK signaling [14] and the activation of mTOR signaling [15] are strongly associated with anti-depressive effects. The significant decrease in the levels of JNK activation was observed in both K/NorBni and K groups but only the K/NorBni group exhibited the sustained non-depressive-like behavior. Remarkably, the increase in mTOR activity was observed only in the K/NorBni group. Thus, our results suggest that the simultaneous JNK inhibition and mTOR activation, at least in the striatum, might be necessary for the sustained anti-depressant effect (Fig.1.E).

The striatum is one of the key structures involved in the pathology of depression and more than 80% of patients with striatal lesions develop depression. However, ketamine was shown to

normalize the connections between the striatum and prefrontal cortex (PFC) [16], implicating the role of other brain structures in ameliorating depressive-like behavior. Similarly, NorBni asserted its anti-depressive effects when injected in the specific striatal regions in animal models of depression but no effect was observed when NorBni was injected in the hippocampus [17]. Thus, the differences in JNK and mTOR signaling in different brain structures involved in the pathology of depressive-like behavior are warranted in order to devise appropriate and effective novel anti-depressive therapies.

CONCLUSION

Our results suggest that the simultaneous modifications of glutamate and opioid signaling can serve as the base for the development of more sustainable anti-depressive therapies but more comprehensive analyses of the brain region-specific molecular effects of these treatments are warranted.

Acknowledgment

This work was supported by the Ministry of Education, Science and Technological Development of the Republic of Serbia (grant No. 451-03-68/2022-14/200017).

REFERENCES

[1] WHO. Depression. 2019. https://www.who.int/news-room/fact-sheets/detail/depression.
[2] U.S. Food & Drug Administration. 2019. http://www.fda.gov/news-events/press-announcements/fda-approves-new-nasal-spray-medication-treatment-resistant-depression-available-only-certified. Accessed 27 June 2019.
[3] R. S. Duman, N. Li. Philos. Trans. R. Soc. Lond. B. Biol. Sci., 367 (2012) 2475.
[4] Williams, N. R., Heifets, B. D., Blasey, C., Sudheimer, K., Pannu, J, Pankow, H., Hawkins, J., Birnbaum, J., Lyons, D. M., Rodriguez, C.I., and Schatzberg, A. F.. Am. J. Psychiatry., 175 (2018) 1205.
[5] Zhang H, Shi YG, Woods JH, Watson SJ, Ko MC. Eur. J. Pharmacol. 570 (2007) 89.
[6] Bruchas, M. R., Yang, T., Schreiber, S., Defino, M., Kwan, S. C., Li, S., and Chavkin, C. J. Biol. Chem., 282 (2007) 29803.
[7] S. S. Kaplitt, Ster. Funct. Neurosurg. 93 (2015) 75.
[8] Gabbay, V., Ely, B. A., Li, Q., Bangaru, S. D., Panzer, A.M., Alonso, C. M., Castellanos, F.X., and Milham, M. P. J. Am. Acad. Child Adolesc. Psychiatry, 52 (2013) 628.
[9] N. L. Yohn, J. A. Blendy Neuropsychopharmacol., 42 (2017) 1670.
[10]Can, A., Dao, D. T., Terrillion, C. E., Piantadosi, S. C., Bhat, S., and Gould, T. D. J.Vis.Exp., (2011) 3769.
[11]Markwell, M. A. K., Haas, S. M., Bieber, L. L., Tolbert, N. E. Anal. Biochem., 87 (1978) 206.
[12]U. K. Laemmli, Nature, 227(1970) 680.
[13]Mei, X-P, Zhang, H., Wang, W., Wei, Y-Y., Zhai, M-Z., Wang, W, and Li, Y-Q. J. Neuroinflam., 8 (2011) 6.
[14]Hollos, P., Marchisella, F., and Coffey, E.T. Brain Plast., 3 (2018) 145.
[15]Réus, G. Z., Abelaira, H. M., Tuon, T., Titus, S. E., Ignácio, Z. M., Rodrigues, A. L., Quevedo, J., Adv. Protein Chem. Struct. Biol., 103 (2016)169.
[16]Mkrtchian, A., Evans, J. W., Kraus, C., Yuan, P., Kadriu, B., Nugent, A. C., Roiser, J. P., and Zarate, C. A., Jr (2021). Mol.Psych., 26 (2021) 3292.
[17]Newton, S.S., Thome, J., Wallace, T.L, Shirayama, Y., Schlesinger, L., Sakai, N., et al., et al. J Neurosci., 22 (2002) 10883.

QUENCHING OF BOVINE SERUM ALBUMIN FLUORESCENCE BY METHIONINE COATED SILVER NANOPARTICLES: INSIGHT IN THE MECHANISM OF INTERACTION

A. M. Bondžić and D. Jovanović

Vinča Institute of Nuclear Sciences, National Institute of the Republic of Serbia, University of Belgrade, P.O. Box 522, 11000 Belgrade, Serbia (aleksandrab@vin.bg.ac.rs)

ABSTRACT

The main goal of this work was the elucidation of the binding interactions between bovine serum albumin (BSA) and methionine coated silver nanoparticles (AgNPs) under physiological like conditions using fluorescence spectroscopy techniques. The quenching of BSA's tryptophan fluorescence has occurred at the concentration-dependent manner. The linear shape obtained for Stern-Volmer plots and its larger slope at higher temperatures indicated mixed static and dynamic quenching mechanisms. The values of quenching constants, K_{sv} and the bimolecular quenching rate constants, k_q, pointed out the existence of binding interactions between BSA and AgNPs. The binding constants, K, with values around 1×10^4 M^{-1}, indicated low to moderate binding interaction with one binding site. Determined thermodynamic parameters $\Delta H^o < 0$, $\Delta S^o < 0$ and $\Delta G^o < 0$ at different temperatures pointed out spontaneous processes, where hydrogen and van der Waals interactions play a major role in the binding.

INTRODUCTION

Silver nanoparticles (AgNPs) attract considerable attention in various fields due to their fascinating physical and chemical properties, including small-scale effects, optical effects, antimicrobial activity, excellent stability and biocompatibility. Owing to these properties, AgNPs are widely used in medical, environmental and material science. After the administration of AgNPs into the bloodstream, they are getting exposed to transport proteins, primarily serum albumin, forming the so-called "protein corona" entity. This new entity is responsible for the final biological response of AgNPs. Therefore, studying the interactions between AgNPs and proteins has great potential, facilitating the understanding of biological effects and safe application of AgNPs in a biological milieu [1]. The intrinsic fluorescence of BSA origins from two tryptophan residues. One of them is located on the surface of the protein, Trp-134, while the other Trp-212 is buried deep into the hydrophobic interior of the protein. Here, we analyzed the interaction between BSA and methionine (Met) capped AgNPs using the fluorescence spectroscopy technique in order to obtain deep insight into these interactions. Experiments performed at different temperatures indicated the existence of mixed static and dynamic mechanism of quenching, while the values of k_q higher than the diffusion-controlled limit, 1×10^{10} $M^{-1}s^{-1}$ pointed out some type of binding interaction. The obtained values for thermodynamic parameters indicated the spontaneous process in which the hydrogen binding and van der Waals interactions play a major role.

METHODS

Apparatus. The fluorescence measurements were performed on Agilent Cary Eclipse fluorescence spectrophotometer. Fluorescence quenching spectra were recorded in the wavelength range 310-500 nm upon excitation at 295 nm at 300, 310 and 315 K. Excitation and emission slits were set at 5 nm, the scaning rate was set at 9600 nm/min, and voltage of the excitation source was set at 450V.

Chemicals. Bovine serum albumin (BSA), $AgNO_3$, L-methionine and KOH were purchased from Sigma-Aldrich (Germany). The stock solution of BSA was prepared in a 10mM phosphate buffer of pH 7.4 and stored at 4°C. The working solution of BSA was 1×10^{-5} M. Silver nanoparticles with L-methionine as a reducing and capping agent were synthesized as previously reported [2]. The concentration of AgNPs stock solutions was 1.06×10^{-9} M.

RESULTS AND DISCUSSION

In our previous study we found that BSA could be adsorbed on the surface of the methionine coated AgNPs by forming "soft protein corona" entity (data not published). In order to gain deep insight into the mechanism of interaction, herein we performed fluorescence quenching titration study. The fluorescence spectra of 1×10^{-5} M BSA in the presence of increasing concentration of AgNPs were recorded in 10 mM phosphate buffer, pH 7.4, after excitation at 295 nm (Figure 1, left). The obtained fluorescence spectrum contained one emission peak at 343 nm. After addition of AgNPs, we observed 4 - 5 nm blue shift followed by gradual decreasing of emission maximum at 343 nm. The obtained Stern-Volmer plot exhibited a linear behavior, indicating possibility of the existence of the static or/and the dynamic quenching processes. In order to distinguish dynamic from static quenching process, the quenching titrations were performed at different temperatures. The Stern-Volmer plots at different temperatures differed in the slopes; with the temperature increase the slopes increased, pointing out the static quenching mechanism. The obtained Stern-Volmer, K_{sv} and bimolecular quenching rate, k_q constants are shown in the Table 1. The obtained k_q values are six orders of magnitude higher than k_q for the diffusion-controlled process, 1×10^{10} $M^{-1}s^{-1}$, pointing out the existence of some type of binding interaction, while synchronic increase of K_{SV} values with temperature implied that process may be dynamic in nature. The binding parameters, the binding constant (K) and number of biding sites (n), between AgNPs and BSA were determined graphically (Figure 1, right) using the double logarithmic plot, eq. 1 [3] and tabulated below (Table 1):

$$\log\left[{(F_0 - F)}/{F}\right] = logK + nlog[Q] \qquad (1)$$

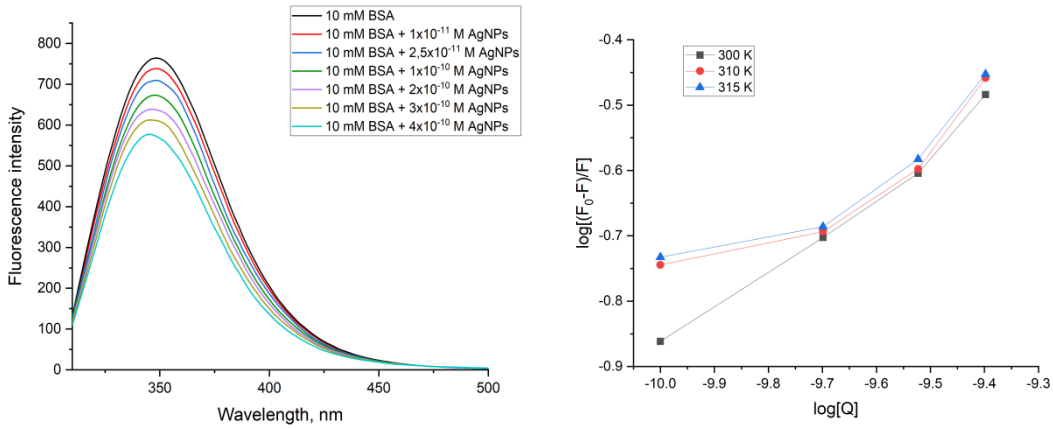

Figure 1. a) The fluorescence spectra of 1×10^{-5}M BSA in the presence of the increasing concentration of AgNPs. b) The plots of the AgNPs quenching effect on BSA fluorescence at different temperature.

where F_0 and F represent the fluorescence intensities in the absence and in the presence of quencher, [Q] is the concentration of the AgNPs [4]. The double logarithmic plot for the experiments performed at 310 K and 315 K (Figure 1, right) can be divided into two segment, indicating that the binding of AgNPs to BSA takes place with different affinity, depending of the AgNPs concentration while the n values lower than 1, in the both segment indicated negative cooperative binding.

Table 1. The Stern - Volmer quenching constants, K_{sv}, the binding parameters and the thermodynamic parameters for the interaction of AgNPs with BSA at the different temperatures.

Temperature (K)	300	310	315
K_{SV} (M)	$(8.7 \pm 0.6) \times 10^8$	$(8.9 \pm 0.8) \times 10^8$	$(9.3 \pm 0.6) \times 10^8$
k_q ($M^{-1}s^{-1}$)	$(8.7 \pm 0.6) \times 10^{16}$	$(8.9 \pm 0.8) \times 10^{16}$	$(9.3 \pm 0.6) \times 10^{16}$
K (M^{-1})	$(3.3 \pm 0.2) \times 10^4$	$(0.4 \pm 0.2) \times 10^4$	$(0.4 \pm 0.2) \times 10^4$
		$(3.2 \pm 0.5) \times 10^4$	$(3.6 \pm 0.2) \times 10^4$
n	0.54 ± 0.08	0.4 ± 0.1	0.4 ± 0.1
		0.5 ± 0.1	0.5± 0.1
ΔH^o (kJmol^{-1})	-115.64		
ΔS^o ($JK^{-1}mol^{-1}$)	-299.96		
ΔG^o (kJmol^{-1})	-25.65	-22.65	-21.15

The thermodynamic parameters responsible for the binding between BSA and AgNPs have been calculated using vant Hoff equation (eq. 2) and equation (3) [3]:

$$lnK = -{}^{\Delta H^\circ}/_{RT} + {}^{\Delta S^\circ}/_{R} \quad (2)$$

$$\Delta G^\circ = \Delta H^\circ - T\Delta S^\circ \quad (3)$$

where K is the previously calculated binding constant at the corresponding temperature, R is the molar gas constant. The obtained values for ΔH^o, ΔS^o and ΔG^o are showed in Table 1. The negative sign for the Gibbs free energy, ΔG^o, indicated spontaneous binding process between BSA and AgNPs, which is enabled by hydrogen binding and van der Waals interactions. [3].

CONCLUSION

In conclusion, methionine coated AgNPs have strong ability to quench the intrinsic tryptophan fluorescence of bovine serum albumin. The fluorescence quenching is the consequence of the combination of the dynamic and the static mechanism of quenching. The binding constants pointed out weak to moderately strong interactions, while the thermodynamic parameters indicated spontaneous process where hydrogen binding and van der Waals interactions play pivotal role. The results obtained in this study confirmed our previous findings in which bovine serum albumin can form “soft protein corona” with the methionine coated AgNPs. The “soft protein corona” is probably consequence of the lower affinity of the BSA toward negatively charged surface of AgNPs at pH value higher than its isoelectric point. Formation of “soft protein corona” enables unchanged bioidentity of AgNPs and facilitates the interaction of “bare” AgNPs with the target molecules. The obtained results could help in the prediction of AgNPs fate after administration in bloodstream as well as in their further surface modifications.

Acknowledgment

This work was supported by the Ministry for Education, Science and Technological Development of the Republic of Serbia, grant numbers: 451-03-68/2022-14/200017. The authors would like to thank dr Bojana Laban for sending some aliquots of silver nanoparticles.

REFERENCES

[1] A.C. Burdușel, O. Gherasim, A.M. Grumezescu, L. Mogoantă, A. Ficai, E. Andronescu, Nanomaterials, 8 (2018) 681.

[2] B. Laban, U. Ralević, S. Petrović, A. Leskovac, D. Vasić-Anićijević, M. Marković, V. Vasić, Green synthesis and characterization of nontoxic L-methionine capped silver and gold nanoparticles, J. Inorg. Biochem., 204 (2020), 110958.

[3] G. Wang, Y. Lu, H. Hou, Y. Liu, RSC Advances, 7 (2017) 9393-9401.

[4] J., R. Lakowicz, Principles of Fluorescence Spectroscopy, Springer, New York, 1999.

NEW DERIVATES OF 2-PHENYL-1,2,3,4-TETRAHYDROISOQUINOLINE AS DUAL INHIBITORS OF CHOLINERGIC ENZYMES

A. M. Bondžić[1], D. Jovanović[1], Z. Džambaski[2], A. Filipović[2] and B. P. Bondžić[2]

[1]Vinča Institute of Nuclear Sciences, National Institute of the Republic of Serbia, University of Belgrade, P.O. Box 522, 11000 Belgrade, Serbia
[2]University of Belgrade-Institute of Chemistry, Technology and Metallurgy, National Institute of the Republic of Serbia, Njegoševa 12, 11000 Belgrade, Serbia
(aleksandrab@vin.bg.ac.rs)

ABSTRACT

The goal of this work was to investigate the inhibitory potency of three derivates of 2-phenyl-1,2,3,4-tetrahydroisoquinoline (THIQ) with different substituents at C3 and C4 positions, namely **65P**,**71P** and **66P**, toward two cholinergic enzymes, acetyl and butyrylcholinesterase. The screening test showed that only compound **65P** possesses inhibition activity higher than 50 % at 10 μM concentration toward both enzymes. The inhibition potency obtained at 10 μM of THIQ was correlated with differences in THIQ's structures in order to predict the structure-activity relationship. It was found that the introduction of the methoxy group at positions C3 and C4 led to decreased inhibition potency, while the removing of fluorine atom from the benzene ring increases selectivity toward acetylcholinesterase. The IC_{50} value gained during the evaluation of inhibition activity of **65P** indicated strong inhibition potency of this compound, while Hill's coefficient ~ 1 indicated the non-existence of cooperativity and one binding site on both enzymes clearly indicating that THIQ could be promising therapeutic drugs in the treatment of Alzheimer's disease.

INTRODUCTION

Tetrahydroisoquinoline derivatives (THIQ) have been widely used in medicinal chemistry owing to their biological functions, such as anti-inflammatory, sedative and anticancer properties [1]. Additionally, published data point out the neuroprotective properties on dopaminergic system in Parkinson's disease by suppressing inflammatory response [1]. To date, it is known that the molecular mechanism of pathogenesis of Alzheimer's disease (AD) includes an extracellular accumulation of amyloid plaques, neurofibrillary tangles' formation in the intracellular domain, decreasing of cholinergic activity, oxidative stress in the basal forebrain and cerebrovascular disorders. Although the complexity of AD requires a multi-target approach, acetylcholinesterase remains the major therapeutical target in the treatment of this disease. Acetyl (AChE) and butyrylcholinesterase (BuChE) enzymes belong to the class of cholinergic enzymes responsible for the hydrolysis of ACh. AChE has a key role in the hydrolysis of acetylcholine (ACh), while BuChE regulates AChE's activity. Therefore, the inhibitors with dual activity toward these enzymes could possess promising therapeutic effects in AD treatment [2].

In this work, we investigated the inhibitory potency of three derivates of 2-phenyl-1,2,3,4 – tetrahydroisoquinoline (Figure 1), which differ in the substitution at C3 and C4 positions against commercially available enzymes, acetylcholinesterase from electric eel and butyrylcholinesterase from equine. Additionally, we attempted to link the observed inhibitory activities with structural features of synthesized molecules in order to enable the design of more potent inhibitors.

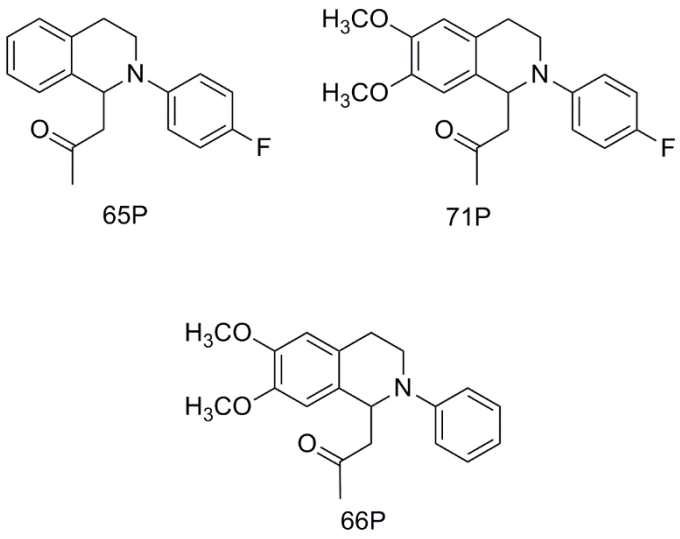

Figure 1. Chemical structures of the investigated tetrahydroisoquinolines.

METHODS

Selected derivates of tetrahydroisoquinoline were synthesized according to reference [3]. THIQs' inhibitory potency was evaluated by performing Ellman's colorimetric assay [4]. 1×10^{-2} M stock solution of the test samples was prepared daily by dissolving the appropriate powder in DMSO and diluting it to the desired concentration. The inhibitory potency was estimated in the concentration range of THIQ from 1×10^{-5} M to 1×10^{-10} M. The enzymes' stock solutions at 1IU/ml concentration were prepared in 50mM TRIS buffer, pH 7.4. Acethylcholineiodide and 5,5'-dithiobis(2-nitrobenzoic acid) were used as substrate and chromogenic reagents. The screening test of the inhibitory potency was performed at 1×10^{-5} M of each THIQ compound, and only compound with inhibitory potency higher than 50 % was further assayed. The assay was performed in the following way: the investigated compounds were incubated with the enzyme for 6 min at 37 C°. After this time, the enzyme's reaction was started by the addition of acetylcholine iodide in the working solution and stopped with sodium dodecyl sulfate 6 min later. At least five increasing concentrations of THIQ were tested at three independent measurements. The obtained results are expressed as mean percentage enzyme activity compared to the corresponding control value. IC_{50} values were determined graphically from log concentration-inhibition curves. Absorbance at 412 nm was recorded on the Perkin Elmer Lambda 35 spectrophotometer with thermostated 1.00 cm quartz cell. pH values of the solutions were measured by a Metrohm pH meter, Model 713.11.

RESULTS AND DISCUSSION

The inhibition potency screening tests for both enzymes were performed at 1×10^{-5} M concentrations of investigated THIQ. The compound with inhibition potency higher than 50 % was **65P** (Table 1). It was observed that the introduction of the methoxy group in C3 and C4 positions of compound **65P** led to decreasing in inhibition potency of compound **71P**. On the other side, replacing the 4-fluorophenyl group with the phenyl group in the compound **71P** led to increased selectivity toward acetylcholinesterase. Compound **65P,** the compound with the best inhibition potency, is selected as the lead compound and further assayed toward both enzymes.

Table 1. % inhibitions of AChE and BuChE by investigated compounds at 10 μM concentration.

Compound	% of AChE Inhibition	% of BuChE Inhibition
65P	64	47
71P	12	14.5
66P	20	/

In the concentration range of **65P** from 1×10^{-5} to 1×10^{-10}, sigmoidal-shaped concentration-dependent inhibition curves were obtained for both enzymes (Figure 2). IC_{50} values, graphically determined from log concentration-inhibition curves, pointed out strong inhibition potency against both enzymes, while Hill's coefficients values around 1 indicated a single binding site for this inhibitor on the surface of the enzymes.

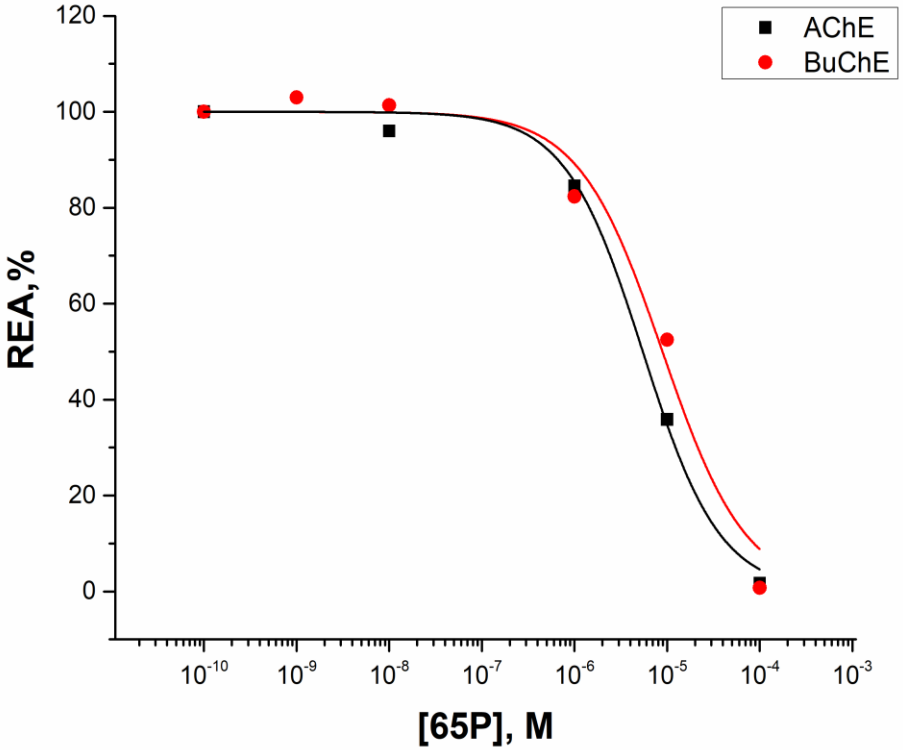

Figure 2. Inhibition of AChE (red circles) and BuChE (black circles) by compound **65**.

Table 2. IC_{50} values and Hill's coefficients obtained for compound **65P** by Ellman's assay.

AChE		BuChE	
IC_{50}, μM	n_H	IC_{50}, μM	n_H
5.46 ± 0.58	0.96 ± 0.21	8.90 ± 2.03	1.04 ± 0.10

CONCLUSION

Based on the obtained results, it is possible to conclude that the selected class of 2-phenyl-1,2,3,4-tetrahydroisoquinoline represents potent inhibitors of cholinergic enzymes, acetyl and butyrylcholinesterase, with IC_{50} values in the micromolar range of concentration. The structure-activity analysis showed that the electron-withdrawing fluoride atom, present in the *para* position of the *N*-aryl group, plays an important role in the increasing selectivity toward acetylcholinesterase. On the other side, introducing the methoxy group in the C3 and C4 positions of THIQ leads to decreasing inhibition potency. We believe that this work could contribute to the development and design of better and more effective drugs in the therapy of Alzheimer's disease based on THIQ's structures.

Acknowledgment

This work was supported by the Ministry for Education, Science and Technological Development of the Republic of Serbia, grant numbers: 451-03-68/2022-14/200017 and 451-03-68/2022-14/200026

REFERENCES

[1] H. Sun, X. He, C. Liu, L. Li, R. Zhou, T. Jin, S. Yue, D. Feng, J. Gong, J. Sun, J. Ji, L. Xiang, ACS Chem. Neurosci. 8 (2017) 155e164.

[2] A.M. Bondžić, M.V. Senćanski, A.V. Vujačić Nikezić, M.V. Kirillova, V. André, A.M. Kirillov, B.P. Bondžić, J. Inorg. Biochem. 205 (2020) 110990.

[3] A. Filipović, Z. Džambaski, D. Vasiljević-Radović, B.P. Bondžić B, Org. Biomol. Chem., 19 (2021**)** 2668 – 2675.

[4] G. L. Ellman, K. D. Courtney, V. Jr. Andres, R.M. Feather-Stone, Biochem. Pharmacol. 7 (1961) 88–95.

Zr(IV)-SUBSTITUTED KEGGIN TYPE POLYOXOTUNGSTATES AS ACETYLCHOLINETERASE INHIBITORS

A.M. Bondžić[1], N. D. Savić[2] and T.N. Parac-Vogt[2]

[1]Vinča Institute of Nuclear Sciences, National Institute of the Republic of Serbia, University of Belgrade, 11000 Belgrade, Serbia (aleksandrab@vin.bg.ac.rs)
[2]Department of Chemistry, KU Leuven, 3001 Leuven, Belgium

ABSTRACT

The aim of this study was to investigate the inhibition potency of two Zr-based POMs, $(Et_2NH_2)_{10}[Zr(PW_{11}O_{39})_2]\cdot 7H_2O$ and $(Et_2NH_2)_8[(\alpha\text{-}PW_{11}O_{39}Zr\text{-}(\mu\text{-}OH)(H_2O))_2]\cdot 7H_2O$, named **POM1** and **POM2** respectively, against acetylcholinesterase, in order to evaluate their anti-Alzheimer potential. Additionally, the effect of net POMs' charge and the number of Zr atoms on the inhibition potency was evaluated. In the POMs' concentration range from 1×10^{-3} - 1×10^{-10} M, sigmoidal-shaped concentration-dependent curves for the inhibition of acetylcholinesterase activity were observed for both POMs. The IC_{50} values indicated inhibition potency with IC_{50} $(2.07 \pm 0.65) \times 10^{-5}$ M and $(3.82 \pm 0.58) \times 10^{-5}$ M for **POM1** and **POM2**, respectively. The obtained negative values of Hill's coefficient, 0.69 ± 0.07 for **POM1** and 0.63 ± 0.11 for **POM2** indicate negative cooperativity, while POMs' net charge and the number of Zr atoms influenced the inhibition. The obtained results suggest that selected POMs show potential to be further developed into more potent anti-Alzheimer Zr-based POM drugs.

INTRODUCTION

Polyoxometalates (POMs) are a class of negative charged inorganic compounds with large structural diversity, which have shown pronounced antiviral, antibacterial and anticancer properties [1]. In recent years, due to their ability to inhibit cholinergic enzymes as well as amyloid aggregation, POMs have also been investigated as effective agents in combat against Alzheimer's disease (AD) [2]. Until today, despite the tremendous improvement in understanding of the pathophysiology of AD, only one inhibitor of amyloid aggregation, Aducanumab, is approved by FDA, while the rest of the drugs are the compounds whose mechanism of action is based on the inhibition of acetylcholinesterase. Acetylcholinesterase (AChE) is the cholinergic enzyme responsible for the hydrolysis of the neurotransmitter acetylcholine at the synaptic cleft or the neuromuscular junction [3]. Since the molecular mechanism of pathogenesis of AD is associated with the decrease of cholinergic activity, the AChE presents the major target enzyme in the pharmacological treatment of AD. The cholinesterase inhibitors are still the most effective treatment for AD disease, owing to their ability to prolong the activity of ACh molecules [1, 4] and to improve the cognitive symptoms in AD patients.

Herein, the influence of two Zr-substituted tungsten-based Keggin type polyoxometalates, $(Et_2NH_2)_{10}[Zr(PW_{11}O_{39})_2]\cdot 7H_2O$ (**POM 1**) and $(Et_2NH_2)_8[(\alpha\text{-}PW_{11}O_{39}Zr\text{-}(\mu\text{-}OH)(H_2O))_2]\cdot 7H_2O$ (**POM 2**), on the activity of commercially available acetylcholinesterase from electric eel was investigated (Figure 1). In addition, an attempt to correlate the POM's structural properties with inhibition potency has been made.

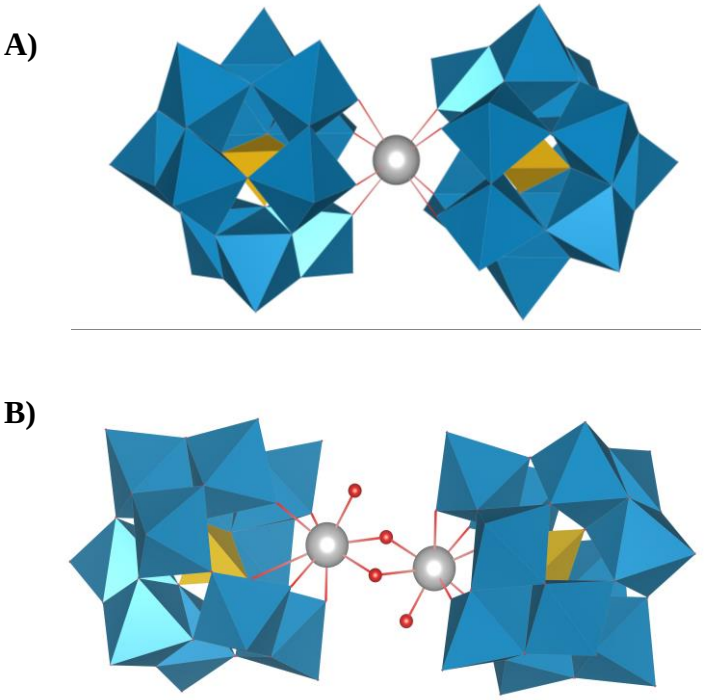

Figure 1. The structures of the investigated POMs. A) POM1; B) POM 2. Zr (IV) metal center in grey; oxygen in red; WO_6 – octahedra in blue and PO_4-tetrahedra in yellow color.

METHODS

POM1 and **POM2** were synthesized using the previously published method [5]. 10 mM stock solutions of POMs compounds were prepared daily by dissolving the solid compound in deionized water and diluting them to desired concentrations. AChE stock solutions (2IU/ml) were prepared by diluting previously dissolved the lyophilized powder in 50mM phosphate buffer (pH 8). The ability of selected POMs to inhibit AChE activity was determined using Ellman's procedure [6]. ASChI was applied as the enzyme-substrate in combination with DTNB as a chromogenic reagent. At least seven concentrations of each POM were tested toward enzyme activity inhibition. All experiments were made in triplicate, and the results were expressed as the mean percentage of enzyme activity compared to the corresponding control value. IC_{50} values were determined graphically from log concentration-inhibition curves. Absorbance at 412 nm was recorded on the Perkin Elmer Lambda 35 spectrophotometer with a thermostatic 1.00 cm quartz cell. pH values of the solutions were measured by a Metrohm pH meter, Model 713.

RESULTS AND DISCUSSION

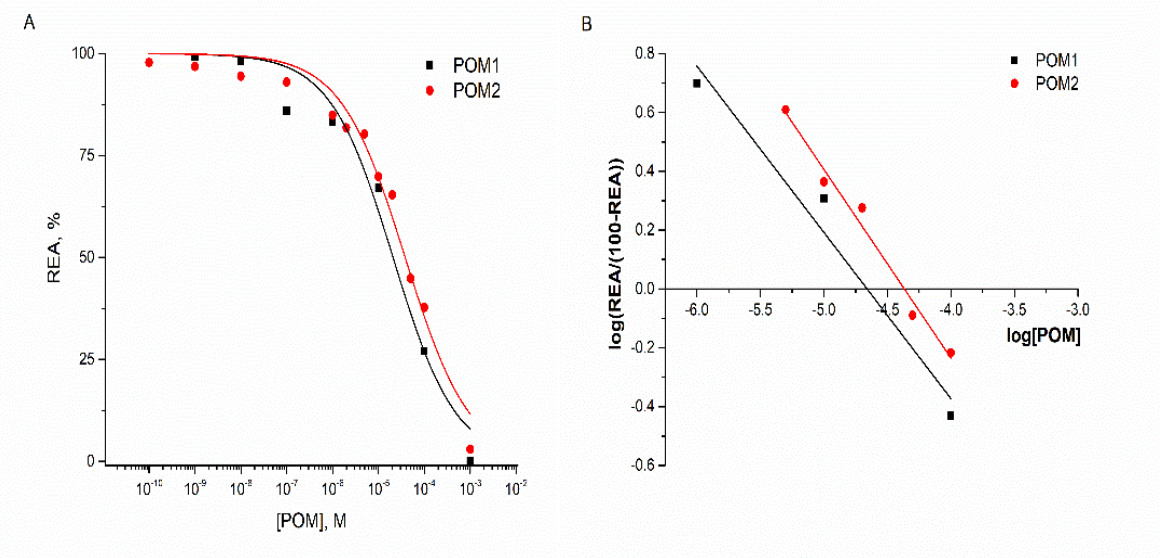

Figure 2. A) Inhibition of AChE induced by selected POMs. B) Hill analysis of inhibition curves.

Both Zr-substituted POMs have a Keggin structure and similar molecular weight but differ in the number of Zr atoms in the structure and in the net charge. Their inhibition potency toward AChE was investigated (Figure 2), and the inhibitory effect was correlated with the POM structural features. Obtained results are summarized in Table 1. It is evident that both POMs showed activities toward AChE with IC_{50} values in a higher micromolar range of concentration. **POM 2** has twice higher IC_{50} in comparison with **POM 1,** indicating better inhibition activity of **POM 1**. Additionally, the latter POM has a higher negative net charge as a result of one Zr atom less in its structure. In our previously published work, the influence of 12-tungstosilicic acid and 12-tungstophosphoric acid on the activity of acetylcholinesterase was investigated, and the mechanism of inhibition was studied in detail [1]. For the first time, it was found that POMs bind on the new allosteric site of AChE, which we characterized as a new site for the binding of negatively charged voluminous molecules. Although these previously investigated POMs, which were Zr-free, had similar molecular weight, they differed in the surface's charge, and POM with lower surface charge showed better inhibitory potency. On the contrary, in this work POM with lower net charge showed better inhibitory potency, which could be explained by the presence of Zr atoms in the structure of POMs, which contribute to the overall net charge. Namely, the introduction of the Zr atom in the POM's Keggin structure leads to the decrease of inhibitory potency of POM as the consequence of the lower electrostatic interactions, which are the main observed interaction between POMs and the proteins.

Table 1. Inhibition potency of selected POMs as inhibitors of AChE was obtained by Ellman's assay.

POM	Formula	POM charge	Metal charge	Net charge	Zr atom	(IC_{50} ± SD), μM
POM1	$(Et_2NH_2)_{10}$ $[Zr(PW_{11}O_{39})_2]$	-14	+4	-10	1	24.3 ± 5.5
POM2	$(Et_2NH_2)_{10}$ $[(\alpha\text{-}PW_{11}O_{39}Zr\text{-}(\mu\text{-}OH)(H_2O))_2]$	-14	+8	-8	2	43.8 ± 3.5

IC50 values represent the concentration of inhibitor required to decrease enzyme activity by 50 % and are the means of three independent measurements, each performed in triplicate (SEM standard error of the mean)

CONCLUSION

In conclusion, investigated Zr-based polyoxotungstates represent a novel class of acetylcholinesterase inhibitors with inhibition potency in a micromolar range of concentrations. Different activity toward AChE could be explained by the differences in the POMs' structures, especially in the net charges, which could influence electrostatic interactions between POMs and protein. Although, in this case, the more negative POM showed higher inhibition potency toward AChE, careful POMs' design is needed because of the necessity of the anti-Alzheimer drugs to cross the blood-brain barrier. This could be overcome by encapsulating POMs into non-toxic matrices, which could prompt the design of more active POMs as therapeutic agents for Alzheimer's disease.

Acknowledgment

This work was supported by the Ministry for Education, Science and Technological Development of the Republic of Serbia, grant numbers: 451-03-68/2022-14/200017.

REFERENCES

[1] A.M. Bondžić, T.D. Lazarević-Pašti, A.R. Leskovac, S. Ž. Petrović, M. B. Čolović, T.N. Parac-Vogt, G.V. Janjić, Eur. J. Pharm. Sci., 151 (2020) 105376.

[2] M. B. Čolović, M. Lacković, J. Lalatović, A.S. Mougharbel, U. Kortz, D. Z. Krstić, Curr. Med. Chem., 27 (2020) 362-379.

[3] H. Dvir, I. Silman, M. Harel, T.R. Rosenberry, J. L. Sussmana, Chem. Biol. Interact., 187 (2010) 10 - 22.

[4] A.M. Bondžić, M.V. Senćanski, A.V. Vujačić Nikezić, M.V. Kirillova, V. André, A.M. Kirillov, B.P. Bondžić, J. Inorg. Biochem. 205 (2020) 110990.

[5] K. Stroobants, G. Absillis, E. Moelants, P. Proost, T.N. Parac-Vogt, Chem. Eur. J., 20 (2014) 3894-3897.

[6] G. L. Ellman, K. D. Courtney, V. Jr. Andres, R.M. Feather-Stone, Biochem. Pharmacol. 7 (1961) 88–95.

KINETIC RELEASE STUDY OF SYNTHETIC LIGNIN (DHP) FROM CALCIUM ALGINATE BEADS

D. Spasojević, D. Mutavdžić, J. Simonović Radosavljević, A. Lj. Mitrović[1], D. Đikanović and K. Radotić

University of Belgrade, Institute for Multidisciplinary Research, Kneza Višeslava 1, 11000 Belgrade, Serbia. (dragica@imsi.rs)

ABSTRACT

Controlled drug delivery systems are of great interest in modern science and medicine. This study was oriented towards encapsulation of synthetic lignin (DHP) into alginate beads and investigation of its release kinetic. Encapsulation was achieved by the ionotropic gelation method. In vitro release profiles were fitted into four release kinetic models (zero-order, first-order, Higuchi, and Korsmeyer-Peppas). According to the *in vitro* release, data alginate beads showed initial burst release followed by prolonged release. The best correlation was found for the Korsmeyer-Peppas model (R^2 = 0.948), with an n value lower than 0.43, indicating the DHP transport mechanism was controlled by quasi-Fickian diffusion. This delivery system could be promising for chronic wound care and antibacterial treatment.

INTRODUCTION

In recent years, numerous studies were conducted to develop new controlled drug delivery systems. Most of them explore hydrogels, composites, micro- and nanospheres as matrix carriers for different drugs, other therapeutics, or cells. Alginate is widely used as a hydrogel for drug delivery because of its availability, biocompatibility, and biodegradability [1]. Lignin and lignin-derived compounds have been proposed to be good candidates for biomedical uses. The antibacterial and antiviral properties of lignin have already been reported. Since antimicrobial resistance poses a serious threat to human health worldwide, there is an urgent need for new antimicrobial agents [2]. Lignin model compound dehydrogenate polymer (DHP), synthesized from coniferyl alcohol by the enzyme peroxidase, is the best lignin substitute, with potential wound healing capacities, as we have shown in our previous studies [3,4].

This study aimed to identify the release mechanism of DHP alginate beads. Calcium alginate beads with encapsulated DHP were prepared using the ionotropic gelation technique, as a relatively fast and mild gelation process. Experimental data of DHP release were fitted into different kinetic mathematical models to obtain information on its transport mechanism.

METHODS

DHP was synthesized from coniferyl alcohol in the presence of HRP (horseradish peroxidase) and hydrogen peroxide in phosphate buffer (pH 7.3). The reaction was left for 48 hours at 37 °C and with constant horizontal shaking. After centrifugation, the precipitate (DHP) was washed with phosphate buffer and with bidistilled water. Obtained DHP was air-dried at room temperature.

The DHP (0.8 mg) was added to 2 ml 2% (w/v) sodium alginate (low viscosity). The solution was transferred in a syringe with a needle and placed above the solution of calcium chloride (5.5 %) in water with constant stirring. The solution was mildly stirred for 1 h to allow beads to harden. After hydrogel beads were formed, they were collected and washed.

In vitro release of DHP was monitored in 10 mL of distilled water at 37 ºC with constant shaking at 100 rpm. Aliquots were taken at predetermined time intervals (1, 2, 3, 4, and 24 h) and the concentration of DHP was determined spectrophotometrically at 272 nm. Immediately after

measuring absorbance, aliquots were poured back into dissolution media, to maintain a constant volume. The dissolution tests were performed in duplicate.

The kinetics of DHP release from prepared beads was analyzed by fitting the release data to the following equations:

Zero-order: $Mt/M\infty = kt$

First-order: $ln\ (Mt/M\infty) = kt$

Higuchi: $Mt/M\infty = kt^{1/2}$

Korsmeyer-Peppas: $Mt/M\infty = ktn$

where $Mt/M\infty$ is a fraction of DHP released at time t (Mt and $M\infty$ are the amounts of released DHP at an arbitrary time t, expressed in hours, and at equilibrium state), k is a release rate constant and n is the release (or diffusional) exponent, used to characterize the mechanism of drug release.

RESULTS AND DISCUSSION

Obtained alginate beads had diameters of approximately 1.5 – 1.7 mm. Released DHP was calculated from the initial amount of DHP and its concentrations in dissolution media. As Figure 1 shows, after an initial burst release in the first hours, alginate beads allowed slow and continuous release of DHP for at least 24 hours. After that time, the released amount of DHP was 40 %, suggesting that the time of monitoring should be prolonged. Intensive release of DHP in the first hours could be beneficial for wound treatment to prevent spreading infection at the beginning of the therapy while keeping the constant higher concentration of the drug for the next 24 and further is suitable for maintaining antimicrobial capacity.

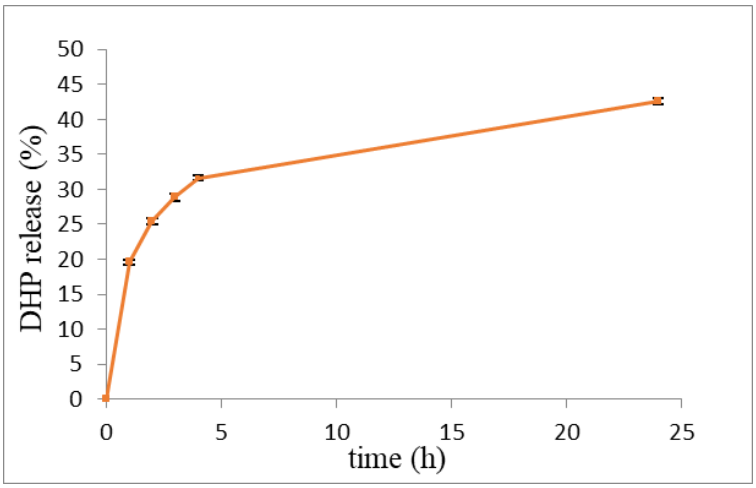

Figure 1. The release profile of DHP from alginate hydrogels.
Data are presented as the mean ± SD.

To characterize the mechanism of DHP release, the experimental data were fitted into different mathematical models, such as zero-order, first-order, Higuchi, and Korsmeyer-Peppas kinetic models. The approximation accuracy for each model was assessed in terms of correlation coefficient values. The highest value of the correlation coefficient (R^2 = 0.948) was obtained for the Korsmeyer-Peppas model (Table 1).

Table 1. Correlation coefficient (R^2) obtained for DHP-alginate beads through release kinetic models

Release kinetic model	R^2
Zero-order	0.5147
First-order	0.6088
Higuchi	0.7861
Korsmeyer–Peppas	0.9475

For the delivery system of the spherical particles release exponent, n = 0.43 mean the drug release mechanism was driven by the Fickian diffusion, and n = 0.85 correspond to case II transport. Values between 0.43 and 0.85 correspond to anomalous release and for n below 0.43 the release type was considered as a quasi-Fickian diffusion. The obtained release exponent is 0.234, as can be seen from the equation in Figure 2, suggesting that the release of the lignin model compound was largely governed by diffusion throughout large pores of alginate polymeric mesh. Since synthetic lignin consists of a mixture of oligomers and polymers of variable sizes, the smaller oligomers of DHP will diffuse faster from hydrogel beads, and the larger polymers enable the delivery of the drug for a prolonged time period.

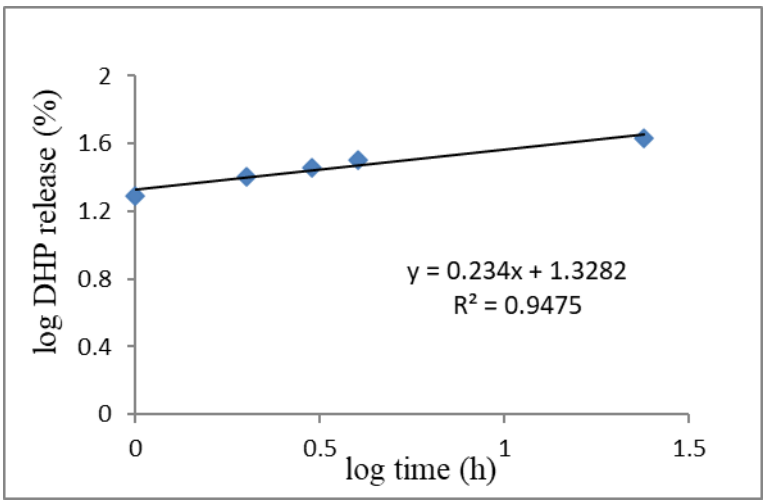

Figure 2. DHP-alginate release data fitted to Korsmeyer-Peppas kinetic model.

CONCLUSION

The obtained results showed that alginate beads could be suitable for sustained DHP release. After 24 hours 40% of initial DHP was released, suggesting that the duration of the experiment should be prolonged. Intensive release at the beginning to firstly prevent spreading infection and later prolonged release of the antibacterial compound for maintaining antimicrobial capacity, confirm that DHP – alginate beads have potential as a chronic wound healing agent. Release results were fitted in four mathematical kinetic models and the Korsmeyer-Peppas model showed the best correlation. The value of the diffusional exponent (n = 0.23) suggests that the release is in agreement with a quasi-Fickian diffusion mechanism.

Acknowledgment

This work was supported by the Ministry of Education, Science and Technological Development of the Republic of Serbia (grant no 451-03-68/2022-14/200053).

REFERENCES

[1] Zhao J., Guo B., and Ma P. X., RSC Adv., 4 (2014) 17736.
[2] Álvarez-Martínez F. J., Barrajón-Catalán E., and Micol V., Biomedicines, 8 (10) (2020) 405.
[3] Spasojević D., Zmejkoski D., Glamočlija J., Nikolić M., Soković M., Milošević V., Jarić I., Stojanović M., Marinković E., Barisan-Asenbauer T., Prodanović R., Jovanović M., and Radotić K., Int J Antimicrob Agents, 48 (2016) 732.
[4] Zmejkoski D., Spasojevic D., Orlovska I., Kozyrovska N., Sokovic M., Glamoclija J., Dmitrovic S., Matovic B., Tasic N., Maksimovic V., Sosnin M., and Radotic K., Int J Biol Macromol, 118 (2018) 494.

ZEOLITE CARRIERS FOR THE ACRIDINE DERIVATIVES DELIVERY

M. Ranković[1], A. Janošević Ležaić[2], A. Jevremović[1], A. Arsenijević[3], V. Dobričić[2], B. Nedić Vasiljević[1], D. Bajuk-Bogdanović[1] and M. Milojević-Rakić[1]

[1]*University of Belgrade-Faculty of Physical Chemistry, University of Belgrade, 11000 Belgrade, Serbia. (anka@ffh.bg.ac.rs)*
[2]*University of Belgrade-Faculty of Pharmacy, 11000 Belgrade, Serbia.*
[3]*University of Kragujevac–Faculty of Medical Sciences, Center for molecular medicine and stem cells research, 34000 Kragujevac, Serbia.*

ABSTRACT
This study investigated acridine and its derivatives (9-chloroacridine and 9-aminoacridine), heteroaromatic compounds, as potential anticancer agents supported on FAU type zeolite Y. Samples were characterized with the Fourier-transform Infrared spectroscopy, while spectrofluorimetry was employed for drug quantification. To investigate the effects of the tested compounds on cell viability, *in vitro* the methylthiazol-tetrazolium (MTT) colorimetric technique against human colorectal carcinoma (cell line HCT-116), was used. Zeolite structure remained unchanged during drug impregnation and derived drug loadings were 17.9 mg/g for acridine, 21.4 mg/g for 9-chloro- and 18.7 mg/g for 9-aminoacridine. The highest release of μM concentrations and favourable kinetics was established for zeolite-supported 9-aminoacridine. Cytotoxicity results are well correlated with the pH-dependent release study, giving promising results for applicative purposes.

INTRODUCTION
Despite the development of new generation drugs with improved characteristics, there is still a problem with maintaining the required drug concentration for a prolonged period. A widely applied solution to this problem is the development of drug carriers. By using such systems, it is possible to reduce the harmful effect of the drug on healthy tissue, control the dosage, and achieve optimal concentration. In addition to liposomes and various polymeric materials, zeolites have been the focus of drug release system research due to their versatile structures that could tailor their performance. Biocompatibility, low toxicity and adjustable pore size that could be matched to drug molecule size, make zeolites perfect candidates for carriers [1]. Clinoptilolite, as natural zeolite, is readily available, used as a food supplement and widely tested as a drug carrier, while synthetic zeolites are dominantly used in research studies due to the higher purity degree of crystalline products [2]. It is particularly important to design drug delivery systems for anticancer drugs, and this field is a fast-growing one, along with the development of drugs themselves.

Acridines and their derivatives are heteroaromatic compounds with a wide range of biological activities as anticancer, anti-inflammatory, and antimicrobial agents. Acridines can bind nucleic acids by intercalation, thereby influencing many cell processes or directly interacting with biologically important proteins [3]. Thus, acridines have been recently explored as potential anti-cancer compounds [4]. Regarding acridine structures, along with the acridine core, there are several possible, multi-substituted functional group positions at hand for interaction with inorganic support/drug carriers. Potentially important substances, with anticancer potential, are amino-acridines as their amino group enables a number of bonding interactions, making them excellent candidates for zeolite loading.

The aim of this work is to prepare acridine and its derivatives supported on FAU zeolite, to employ characterization and drug-release study, and to investigate the cytotoxicity potential of the

prepared samples toward cancer cells. The selection of the zeolite framework was supported by a recent cytotoxicity study [5].

METHODS

Y zeolite (CBU780, SiO_2/Al_2O_3=80, and specific surface area of 780 m^2/g) was purchased from Zeolyst International and used as-is. Tested bioactive molecules are acridine (abbreviation A, 97%, M = 179.22 g/mol, Sigma Aldrich) and derivatives, 9-chloroacridine (abbreviation 9ClA, M = 213.662 g/mol) and 9-aminoacridine (abbreviation 9NA, M = 194.232 g/mol). The impregnation solutions were prepared in 96% ethanol.

Drug supporting procedure involved suspension preparation comprising 10 mL of target drug (1 mM) and 100 mg of zeolite, thermostated at a laboratory shaker at 23 °C/110 rpm for 24 h. The amount of drug remaining in the solution after adsorption and centrifugation is measured at the Agilent Cary Eclipse Fluorescence Spectrophotometer. The prepared drug-loaded zeolites are denoted as A/Y, 9ClA/Y and 9NA/Y, respectively.

The Fourier-transform Infrared (FTIR) spectra of samples were recorded with an iS20, Nicolet spectrometer (Thermo Scientific), in the range from 4000 to 400 cm^{-1} with 2 cm^{-1} resolution employing the KBr pellet technique.

The release study was conducted in the acetic buffer medium with pH values of 2.6 and 4.6 and in a 5mg/5mL and 5mg/10mL solid to liquid ratio. Leached drug quantity was recorded after 2h dissolution with kinetics recorded for 5 mg/10 mL suspension.

In vitro cytotoxicity test employed the methylthiazol-tetrazolium (MTT) colorimetric technique [6] against cell line HCT-116 (human colorectal carcinoma) in triplicate. The cells were incubated with the medium alone or with a two-fold serial dilution of drug-loaded samples and pristine Y zeolite suspensions (5 mg/mL). The cells were incubated under a CO_2 atmosphere (5%) for 48 h at 37 °C. MTT was dissolved (5 mg/mL) in phosphate buffer saline having a pH of 7.2 to reflect acidity in the colorectal region and filtered through a 0.22 μm Millipore filter before use. The optical density of each well was determined at 595 nm using a microplate Zenyth 3100 Multimode detector.

RESULTS AND DISCUSSION

Optimization of experimental conditions due to sensitive fluorescent detection is performed with calibration curves setting at 0.999 correlation coefficients.

Drug impregnation, leaves no change in the Y zeolite structure, as shown by FTIR (Figure 1.). The most intense acridine band which does not overlap with the zeolite bands, at about 740 cm^{-1}, corresponds to C-H out-of-plane bending vibration, and it is visible in the spectrum of the impregnated zeolite sample A/Y.

Gained acridine precursor (Figure 2., left) and derived drug loadings were determined to be 17.9 mg/g for A/Y, 21.4 mg/g for 9ClA/Y and 18.7 mg/g for 9NA/Y sample.

The drug release was performed in two buffer solutions to mimic release in tum with pH 2.6 and 4.6. A slightly lower release concentrations are obtained for A/Y and 9ClA/Y at pH 4.6, in comparison to release at pH 2.6. For the 9NA/Y sample, it is clear that the released amount remains independent of pH and is significantly higher than that released from A/Y and 9ClA/Y samples (Figure 2., left). Additionally, the concentration of the drug released is independent of whether the experiment is performed in a 1 mg/mL or 0.5 mg/mL solid-liquid ratio, which indicates a steady release of the drug into available volume. Kinetics of the process confirms sustained release over the period of a targeted two hours period (Figure 2., right).

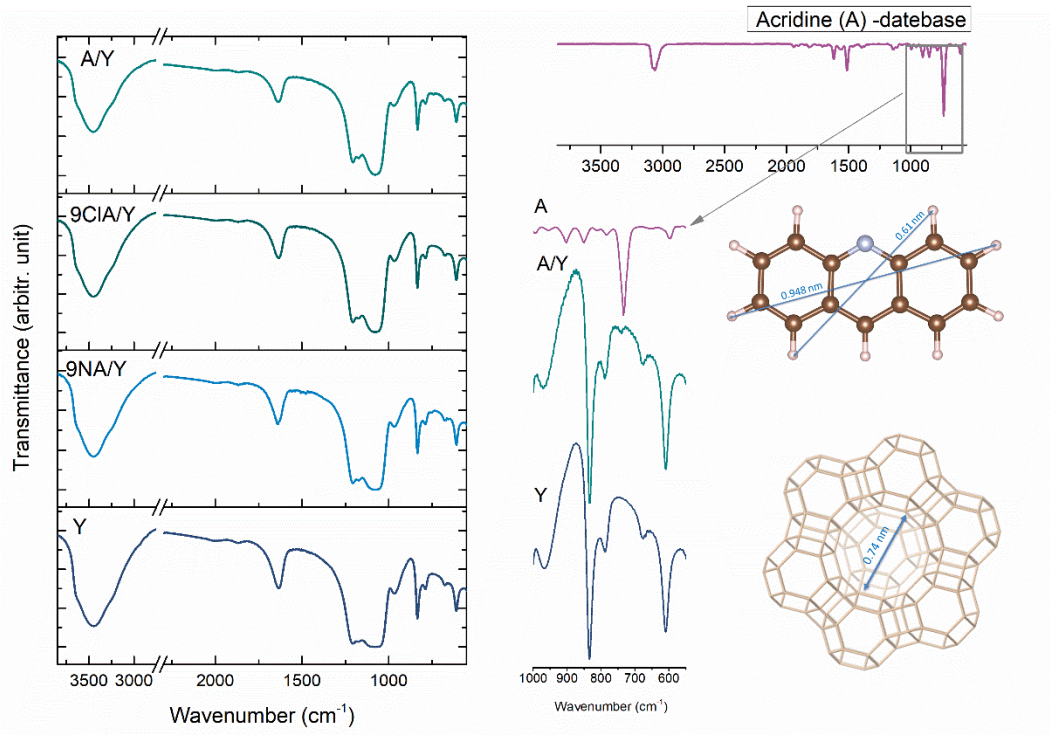

Figure 1. FTIR spectra of prepared samples (left) and acridine-originated vibration in selected A/Y sample with corresponding structures of acridine and Y zeolite precursors (right).

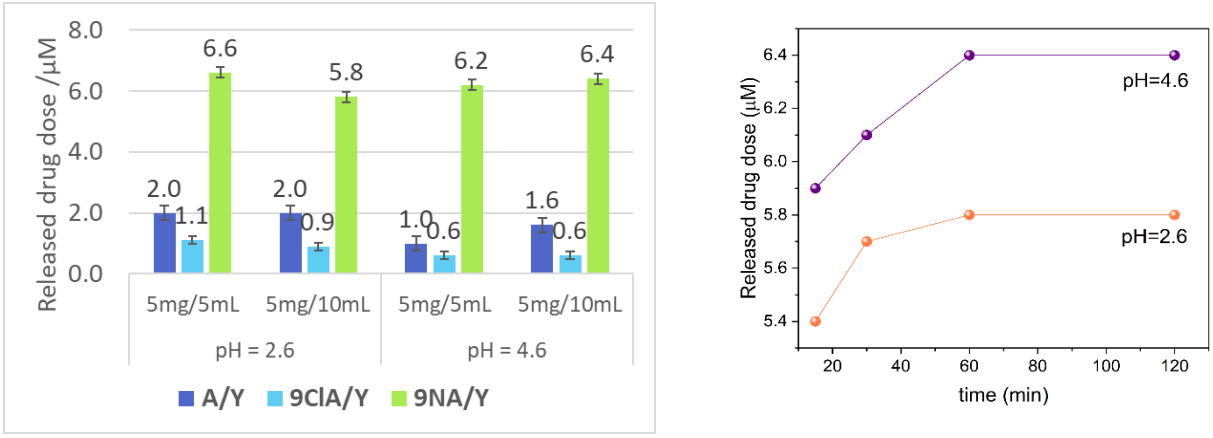

Figure 2. pH-dependent drug release (left) overall quantity and (right) from 9NA/Y over time, in buffer release study.

Prepared drug-loaded zeolites were tested in terms of their toxicity toward cancer cells (Figure 3.). Within 48h incubation, drug-loaded samples were more active than the pristine Y zeolite. Moreover, it appears that zeolite-supported amino and chloro-derivatives impose higher toxicity than the A/Y sample. Figure 3 shows the continuously decreasing dependence of cell viability on suspension concentration for all samples. The highest cytotoxic impact, up to 5 mg/mL is witnessed for 9NA/Y, delivering µM concentration (Figure 2.), and is related to previous findings documenting the anticancer activity of acridine derivatives alone in the targeted µM range [4]. After 5 mg/mL suspension concentration, pristine and drug-loaded Y zeolites express the same toxicity effect, less than 8 % of viable cells remained for 9NA/Y and 9Cl/Y.

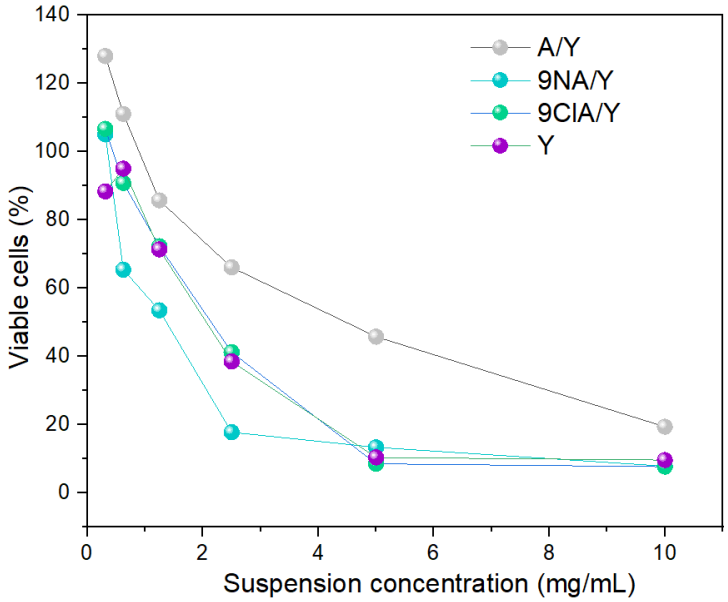

Figure 3. Cytotoxicity testing of Y zeolite, zeolite-supported acridine and its derivatives.

CONCLUSION

Herein we report a novel drug delivery system based on newly proposed acridine derivatives as anticancer compounds within the Y zeolite carrier. Prepared drug-loaded zeolites delivered necessary cytotoxic drug concentrations, in the μM range, in both buffer solutions. Cytotoxicity investigation confirmed the intended steady release effects of the prepared samples with 9NA/Y amino-derivative as the best among the tested drug-carrier systems.

Acknowledgment

This work was supported by the Ministry of Education, Science and Technological Development of the Republic of Serbia (no. 451-03-68/2022-14/200146, 451-03-68/2022-14/200111 and 451-03-68/2022-14/200161) and grant for collaboration with JINR Dubna (JINR-Serbia_P12).

REFERENCES

[1] P. Horcajada, A. Rámila, J. Pérez-Pariente, M. Vallet-Regí, Micro. Meso. Mater. 68 (2004) 105-109.

[2] M. Servatan, P. Zarrintaj, G. Mahmodi, S. J. Kim, M. R. Ganjali, M. R. Saeb, M. Mozafari, Drug Discov. Today. 25 (2020) 642-656.

[3] J. Šebestík, M. Šafařík, I. Stibor, J. Hlaváček, Biopolymers (Pept. Sci.) 84 (2006) 605-614.

[4] J. Rupar, V. Dobričić, J. Grahovac, S. Radulović, Ž. Skok, J. Ilaš, M. Aleksić, J. Brborić, O. Čudina, RSC Med. Chem. 11 (2020) 378-386.

[5] A. Jevremović, A. Stanojković, D. Arsenijević, A. Arsenijević, G. Arzumanyan, K. Mamatkulov, J. Petrović, B. Nedić Vasiljević, D. Bajuk-Bogdanović, M. Milojević-Rakić, J. Hazard. Mater. 436 (2022) 129226

[6] D. C. Marks, L. Belov, M. W. Davey, R. A. Davey, A. D. Kidman, Leuk. Res. 16 (1992) 1165-1173.

ANTIBACTERIAL ACTIVITY OF COPPER/POLYPYRROLE NANOCOMPOSITE

D. Mašojević[1], V. Vodnik[1], J. Spasojević[1], T. Barudžija[1], M. Otoničar[2], S. Davidović[3] and U. Stamenović[1]*

[1]*Vinča Institute of Nuclear Sciences – National Institute of the Republic of Serbia, University of Belgrade, 11351 Vinča, Belgrade, Serbia*
(una@vin.bg.ac.rs)*
[2]*Jožef Štefan Institute, Department of Advanced Materials, 1000 Ljubljana, Slovenia*
[3]*Faculty of Technology and Metallurgy, University of Belgrade, Karnegijeva 4, 11000 Belgrade, Serbia.*

ABSTRACT
A novel and favorable antibacterial agent as a combination of copper nanoparticles (CuNPs) and polypyrrole (PPy) is presented. By simple *in situ* polymerization method, copper/polypyrrole (Cu/PPy) nanocomposite with spherical CuNPs, around 25 nm in diameter, uniformly dispersed throughout PPy matrix with granular morphology, was characterized and subjected to determination of antibacterial activity toward bacteria *Escherichia coli* and *Staphylococcus aureus*. Knowing that when acting alone, CuNPs and PPy have already shown antimicrobial responce, their mutual and synergetic engagement against bacteria in this survey is somewhat expected. After a twenty-four-hour interaction with *S. aureus*, already 2 ppm of Cu/PPy with only 9.45 wt% content of Cu is acting almost completely cidal, with 99.17% of bacterial growth inhibition. Such nanocomposite could easily find application in water disinfection, soil sterilization and food preservation.

INTRODUCTION
The widespread overuse of antimicrobials has led to the strengthening of microbes to drug-resistant ones, that could easily be transmitted to human beings, either through contaminated water/wastewater and soil, or even food chain. Therefore, one should strive to the improvement of existing and development of novel materials with exceptional achievements in disinfection and decontamination applications. Beside that, these materials should be easily prepared at low cost and with high stability, and show cidal antimicrobial effects at short contact time toward broad spectrum of pathogenic microbes [1]. One of the trends in this endeavor is considering nanocomposites of metal NPs (silver (Ag), Cu) and conductive polymers such as polyaniline (PANI) or PPy as materials with promising antimicrobial characteristics [2,3]. Combining polymeric chains that modify function of microbes' functional groups through electrostatic interaction, with a large number of the low-coordinate atoms on the surface of metal NPs that interact with microbes or release metal ions which further cause microbial damage, make these nanocomposites impressive antimicrobial agents [2,3]. In this paper, we represent low cost and stable Cu/PPy nanocomposite with quite satisfactory antibacterial activity toward Gram-negative and Gram-positive bacteria, *E. coli* and *S. aureus*, respectively.

EXPERIMENTAL
In situ polymerization of pyrrole monomer by copper ions, in water as a medium, and in the presence of sodium dodecyl sulfate (SDS) as surfactant and dopant, was used for the formation of Cu/PPy nanocomposite. In a round bottom flask, $5 \cdot 10^{-2}$ M of copper salt was dissolved in 50 ml of water. Upon its stirring with SDS ($5 \cdot 10^{-3}$ M), $1 \cdot 10^{-2}$ M of pyrrole monomer was added. The reaction was continued at room temperature for 24h, i.e. until the color of the reaction mixture became

black. The resulting solution was centrifugated (20 min at 9000 rpm), rinsed with ethanol, and dried for several hours at 30 °C. In the powdered sample, the amount of the Cu, determined by inductively coupled plasma – atomic emission spectrometry (ICP-AES), was found to be 9.45 wt%. For the comparison pure PPy was synthesized by the same method, only instead of copper ions, for the oxidation, ammonium peroxydisulfate (APS, $2 \cdot 10^{-2}$ M) was used.

Antibacterial assay of as prepared samples, in the concentration range 1-20 ppm, for 24 h incubation time, was tested against *E. coli* and *S. aureus*, as described in our previous work with Cu-PANI nanocomposite [2].

RESULTS AND DISCUSSION

In this simple process of nanocomposite's formation that implies an interaction between Cu^{2+} ions as an oxidizing agent, and pyrrole monomer as reducing, there is a simultaneous Cu^{2+} ions reduction to Cu^0, i.e., their nucleation and further growth to CuNPs, and polymerization of pyrrole. Besides, the presence of SDS as surfactant and stabilizer of formed CuNPs, will probably accelerate the polymerization reaction, acting as an acid dopant. After the visual assumption of Cu/PPy nanocomposite formation (the coloration of the reaction mixture to black, which is indicative of π-conjugated PPy form), UV-Vis spectrum (Fig. 1a, Inset: right) confirmed it, since two bands characteristic for oxidized and conductive PPy at 460 nm and 800 nm, attributable to π–π* transition

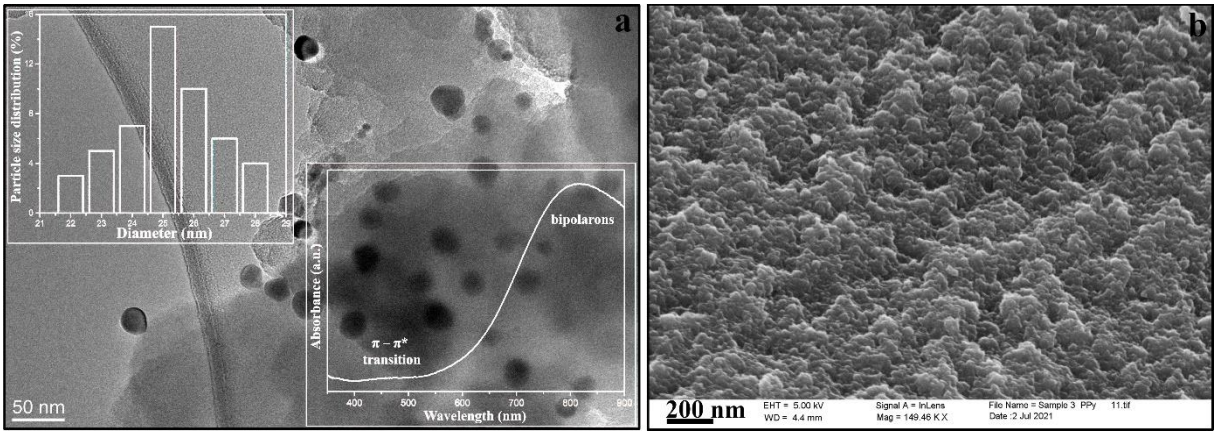

Figure 1. a) TEM image of Cu/PPy nanocomposite with PSD and UV-Vis spectrum (Insets left and right), and b) FESEM image of Cu/PPy nanocomposite.

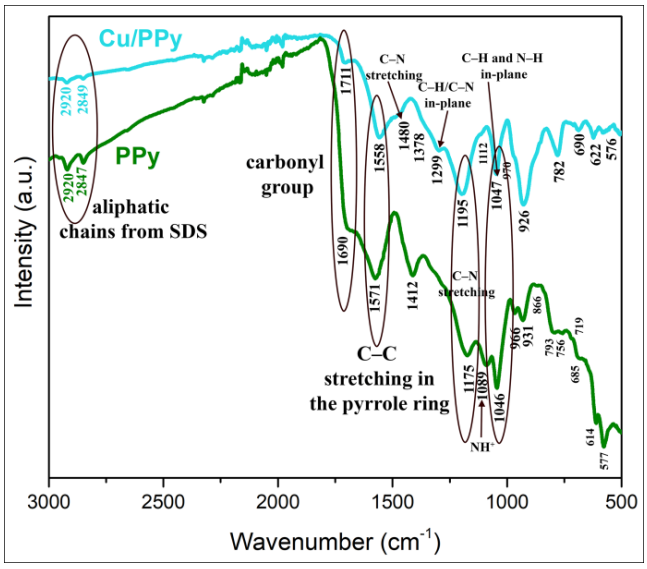

Figure 2. FTIR spectra of Cu/PPy and PPy.

and bipolarons, respectively, are manifested [4]. As can be seen, the spectrum is lacking in the surface plasmon resonance (SPR) band of CuNPs, probably because it's overlapped by strong and wide PPy absorption. However, the formation of CuNPs is evident through the TEM image (Fig. 1a), where spherical NPs with a mean diameter ≈ 25 nm (Fig. 1a, Inset: left) and uniformly dispersed throughout the granular PPy matrix (Fig. 1b) are clearly seen.

The molecular structure of Cu/PPy nanocomposite and PPy was determined by FTIR spectroscopy (Fig. 2). In the spectra of both samples, there is strong evidence for SDS incorporation in the polymer chains, as bands characteristic for aliphatic chains, at 2920 and 2849 cm^{-1}, and 2920 and 2847 cm^{-1}, for Cu/PPy and PPy, respectively, are expressed [5]. Besides, bands at 622 and 614 cm^{-1}, in Cu/PPy and PPy, respectively, corresponding to the sulfate anions, either from SDS or APS, that contribute protonation of the polymer chain, are visible as well. Furthermore, the bands from in-plane =C–H vibration at 1299 cm^{-1} for Cu/PPy, and at 1558 and 1571 cm^{-1} from C–C stretching in the pyrrole ring, and 1195 and 1175 cm^{-1} from C–N stretching for Cu/PPy and PPy, respectively, indicate the formation of PPy in its doped, oxidized state in both samples. Such nanostructures, with sufficiently small particles that offer a great number of active places, and a conductive polymer matrix that provides large contact area, could be convenient as antibacterial agents, which has been experimentally demonstrated.

Table 1. Antibacterial activity of Cu/PPy nanocomposite after 24 h incubation time

Cu/PPy (ppm)	*E. coli* cell reduction (%)	*S. aureus* cell reduction (%)
1	83.75	98.75
2	91.67	99.17
5	97.92	99.27
10	99.96	99.99
20	99.99	99.99

The results of quantitative antibacterial efficiency of different Cu/PPy nanocomposite concentrations (1, 2, 5, 10, and 20 ppm) over 24 h incubation time with indicator strains of pathogenic bacteria, are presented in Table 1. As can be seen, with increasing nanocomposite's concentrations, its antibacterial activity also increases, reaching cidal value of 99.99% with 20 and 10 ppm of Cu/PPy for *E. coli* and *S. aureus*, respectively. Even 2 ppm of Cu/PPy was sufficient for proper antibacterial perfomance toward *S. aureus*.

There is a synergistic action of CuNPs and PPy inside the nanocomposite in its antibacterial activity. Beside that polymer matrix provides greater area for the contact with pathogens, allowing increased interaction between CuNPs and microbes, it disables nutrition process of the bacteria by blocking their communication with the surrounding medium. Together with CuNPs, an important role in preventing bacteria from performing basic functions for self-preservation and reproduction have partially oxidized nanoparticles and cycling redox Cu^{2+}/Cu^{+} species, that will interact with

microbes' biomolecules from the cell wall, accompanied by their conformational changes, leading to altering of their biological functions, and final death. Furthermore, the role of SDS, as a surfactant should not be ignored, since it has been used for solubilization of membrane proteins and disruption of bacterial membranes [6].

Comparing this nanocomposite with the similar one (Cu-PANI, [2]), it is evident that Cu/PPy has somewhat weaker antibacterial activity, eventhough one may say that the mechanism of antimicrobial action is the same. One of the main differences is the concentration of Cu in the samples (9.45 wt% *vs.* 14.25 wt%, for Cu/PPy and Cu-PANI, respectively), and the fact that in the case of Cu/PPy antibacterial assessment was not determined relative to the concentration of the active component (Cu species), but whole nanocomposite. Bearing that in mind, for example, in 10 ppm of Cu/PPy nanocomposite, there is only 0.95 wt% of Cu species as active components, and direct comparison with Cu-PANI is not relevant. Besides, there is a difference in the type of polymer matrices (PPy *vs.* PANI) and their morphologies (granular *vs.* dendritic). However, the great advantage of such antibacterial system is low Cu concentration, which would make it safe for wider use, while the assessment of PPy cytotoxicity toward Dalton's lymphoma ascites (DLA) cells suggested that it is safe and ecofriendly for the concentrations lower than 100 ppm [7].

CONCLUSION

The presented Cu/PPy nanocomposite has shown interesting and satisfactory antibacterial activity toward *E. coli* and *S. aureus*, after 24 h of the bacterial strains' exposure. Since the concentration of the active component in the nanocomposite is low, this contact time is somewhat expected. However, such results leave room for improving the properties of this nanocomposite, in order to achieve greater activity for shorter contact times. Nevertheless, Cu/PPy could easily find application in water disinfection, soil sterilization, and food preservation.

Acknowledgment

The research was funded by the Ministry of Education, Science and Technological Development of the Republic of Serbia, *via* direct financing of Vinča Institute of Nuclear Sciences – National Institute of Republic of Serbia (contract number: 451-03-68/2022-14/200017).

REFERENCES

[1] M. Maruthapandi, A. Saravanan, A. Gupta, J. H. T. Luong, and A. Gedanken, Macromol., 2 (2022) 78.
[2] U. Bogdanović, V. Vodnik, M. Mitrić, S. Dimitrijević, S. Škapin, V. Žunič, M. Budimir, and M. Stoiljković, ACS Appl. Mater. Inter., 7 (2015) 1955.
[3] U. Stamenović, S. Davidović, S. Petrović, A. Leskovac, M. Stoiljković, and V. Vodnik, New J. Chem., 45 (2021) 12711.
[4] J. Milikić, A Tapia, U. Stamenović, V. Vodnik, M. Otoničar, S. Škapin, D.M.F. Santos, and B. Šljukić, Int. J. Hydrogen Energ., (2022) *Article in Press*.
[5] P. Dallas, D. Niarchos, D. Vrbanic, N. Boukos, S. Pejovnik, C. Trapalis, and D. Petridis, Polymer, 48 (2007) 2007.
[6] A.J. Kora, R. Manjusha, and J. Arunachalam, Mat. Sci. Eng. C-Bio. S, 29 (2009) 2104.
[7] A. Radhakrishnan, P. Rejani, and B. Beena, Main Group Met. Chem., 38 (2015) 133.

Index

CIP - Каталогизација у публикацији - Народна библиотека Србије, Београд

544(082)
66.017/.018(082)
502/504(082)

INTERNATIONAL Conference on Fundamental and Applied Aspects of Physical Chemistry (16 ; 2022 ; Beograd)
Physical Chemistry 2022 : proceedings. Vol. 2 / 16th International Conference on Fundamental and Applied Aspects of Physical Chemistry, September 26-30, 2022, Belgrade, Serbia ; [editors Željko Čupić and Slobodan Anić]. - Belgrade : Society of Physical Chemists of Serbia, 2022 (Belgrade : Jovan). - VI str., str. 323-640 : ilustr. ; 30 cm

Tiraž 200. - Bibliografija uz svaki rad. - Registar.

ISBN 978-86-82475-43-9
ISBN 978-86-82475-41-5 (niz)

a) Физичка хемија - Зборници b) Наука о материјалима - Зборници c) Животна средина - Зборници

COBISS.SR-ID 82228745